High-Fidelity Colour Reproduction for High-Dynamic-Range Imaging

Min Hyuk Kim

A dissertation submitted in partial fulfillment
of the requirements for the degree of
Doctor of Philosophy
of the
University College London.

Department of Computer Science
University College London

2010

I, [Min Hyuk Kim], confirm that the work presented in this thesis is my own. Where information has been derived from other sources, I confirm that this has been indicated in the thesis.

Signed:

Min H Kim

Abstract

The aim of this thesis is to develop a colour reproduction system for high-dynamic-range (HDR) imaging. Classical colour reproduction systems fail to reproduce HDR images because current characterisation methods and colour appearance models fail to cover the dynamic range of luminance present in HDR images. HDR tone-mapping algorithms have been developed to reproduce HDR images on low-dynamic-range media such as LCD displays. However, most of these models have only considered luminance compression from a photographic point of view and have not explicitly taken into account colour appearance. Motivated by the idea to bridge the gap between cross-media colour reproduction and HDR imaging, this thesis investigates the fundamentals and the infrastructure of cross-media colour reproduction. It restructures cross-media colour reproduction with respect to HDR imaging, and develops a novel cross-media colour reproduction system for HDR imaging. First, our HDR characterisation method enables us to measure HDR radiance values to a high accuracy that rivals spectroradiometers. Second, our colour appearance model enables us to predict human colour perception under high luminance levels. We first built a high-luminance display in order to establish a controllable high-luminance viewing environment. We conducted a psychophysical experiment on this display device to measure perceptual colour attributes. A novel numerical model for colour appearance was derived from our experimental data, which covers the full working range of the human visual system. Our appearance model predicts colour and luminance attributes under high luminance levels. In particular, our model predicts perceived lightness and colourfulness to a significantly higher accuracy than other appearance models. Finally, a complete colour reproduction pipeline is proposed using our novel HDR characterisation and colour appearance models. Results indicate that our reproduction system outperforms other reproduction methods with statistical significance. Our colour reproduction system provides high-fidelity colour reproduction for HDR imaging, and successfully bridges the gap between cross-media colour reproduction and HDR imaging.

Acknowledgements

I sincerely appreciate my PhD supervisor, Dr. Jan Kautz. His encouragement, support, mentoring, and friendship were essential to completing this PhD thesis. I also am grateful to Dr. Celine Loscos for offering me a doctorate opportunity at University College London (UCL). Further, I would like to thank Dr. Simon Julier for his helpful advice as an assessor. I also am grateful to Prof. Zhaopeng Li for kindly allowing me to use her Vision Laboratory. I am very grateful to Prof. Stuart Robson and Dr. Erik Reinhard for kindly agreeing to serve as internal and external examiners.

Without the help of the following friends in the computer graphics group at UCL, it would have been impossible to complete this thesis. I would like to thank James Tompkin and Martin Parsley for their untiring help and support in proofreading. I also would like to thank my friends (in alphabetical order): Jeren Chen, Andrew Cox, and Harsha Sri-Narayana.

Thanks also to my colleagues in the computer science department for their generous help (in alphabetical order): Jania Aghajanian, Frederic Besse, Dr. Gabriel Brostow, Yun Fu, Oscar Kozlowski, Dr. Peng Li, Soo Ling Lim, Umar Mohammed, Dr. Wole Oyekoya, Dr. Xueni Pan, Dr. Simon Prince, Aitor Rovira, Prof. Anthony Steed, William Steptoe, Fotios Tzellos, Sara Vicente, Dr. Jonathan Warrell, Dr. Tim Weyrich, and Insu Yu.

In addition, I would like to thank these people for mentoring my research through their excellent publications (in alphabetical order): Dr. Roy Berns, Dr. Paul Debevec. Dr. Mark Fairchild, Dr. Robert Hunt, Dr. Youngshin Kwak, Dr. Ronnier Luo, Prof. Lindsay MacDonald, Dr. Jan Morovic, Dr. Jack Tumblin, and Dr. Günter Wyszecki.

Finally, I would like to thank my parents and parents-in-law: Hun Kim, Mi Lim Kim, Hae Duck Jang, Mae Ja Park, my sister: Hey Lee Kim, and my own family: Jung Hyun Kim, Sue Hyun Kim, and Jin Hee Jang for understanding and untiring supporting during this doctorate.

Contents

List of Figures

List of Tables

Chapter 1

Introduction

This chapter provides a brief introduction to motivate the thesis and describes its principal contributions. It summarises the main structure of this document with a short overview of the methodology and results.

1.1 Motivation and Objective

We live in a world of image-driven media. On a computer, a television, or in a newspaper, we look at reproduced images every day. We are communicating and archiving visual information of the real world through image reproduction. *Faithfulness* is the most important factor in this visual communication. If the original and reproduction were different, our visual communication would be deteriorated, introducing miscommunication. In order to achieve *high fidelity* in reproducing an image, the image data captured by a camera should match the original scene, and the captured image should be displayed on a monitor or in a photograph as faithfully as recorded in the image data. The image in visual communication comprises various information, e.g., colour, texture, and visual story. Among them, colours form a fundamental base of visual communication. It is important to achieve high fidelity in reproducing colours for visual communication. This topic has been broadly researched as the study of *cross-media colour reproduction* [Morovic, 2008].

In the past decade, imaging technology has leaped into a new era by significantly extending the *dynamic range* in capturing real-world luminance. The working range of common imaging devices is limited by the capacity of the hardware. For instance, a common digital camera captures luminances by using a solid-state sensor, which yields 12-bit depth of signals as integers (e.g., Nikon D100). If a scene that we need to capture with the camera contains a wider range of luminances, such as ten orders of magnitude, we would only be able to capture partial luminance information due to the bleaching and saturation of sensor signals [see Figure 1.1(a)]. This problem was first addressed by Mann [1993]. To overcome the saturation problem in sensing real-world luminance, Mann introduced an innovative capture technology called high-dynamic-range (HDR) imaging. Instead of taking only one picture, Mann captured the scene (that may have high-dynamic-range luminances) as multiple images, scanning the required dynamic range with various exposure settings with a low-dynamic-range (LDR) camera. The multiple exposures were then concatenated into an HDR image.

As a result, HDR imaging can cover most of the dynamic range of real-world luminance, solving the sensor saturation problem of the camera [see Figure 1.1(b)].

HDR imaging was a sensational innovation in capturing the real world and has been broadly used in the graphics and electronic engineering fields. However, even though HDR imaging solves the sensing problem when capturing, it introduces another problem in reproducing the HDR image data. As shown in Figure 1.1(b), the dynamic range of the captured HDR image exceeds that of the displays significantly. Simple scaling methods are not enough to compress the range of the HDR data. Consequently, most of the interesting information in the HDR image is lost by discretisation of the display signal resolution. Hence, Tumblin and Rushmeier [1993] addressed this reproduction problem. They proposed a non-linear mapping to reproduce the HDR image with a similar appearance to that observed by the human visual system, called a *tone reproduction operator* or *tone-mapping algorithm*.

In fact, HDR imaging [Mann, 1993; Debevec and Malik, 1997; Mitsunaga and Nayar, 1999] and tone reproduction operators [Tumblin and Rushmeier, 1993; Fattal et al., 2002; Durand and Dorsey, 2002; Reinhard et al., 2002] can be understood as advanced colour reproduction methods. However, the state of the art in HDR imaging has focused on the extendibility of the dynamic range from a tone-reproduction point of view and has not yet approached classical cross-media colour reproduction. For example, the state of the art in HDR imaging does not have infrastructure such as a modulated colour reproduction pipeline. As shown in Figure 1.1, the data flows in LDR and

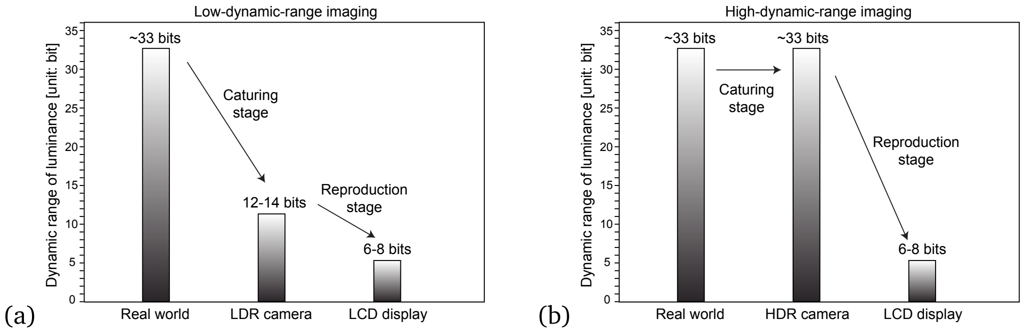

Figure 1.1: *These two plots compare dynamic-range changes in low-/high-dynamic-range image reproduction. Imagine that we capture a real-world scene on a bright sunny day. In both plots, the real-world scene is represented as the highest grey-scales bar on the left-hand side. We assume that the luminance ranges ten orders of magnitude. We recalculate the intensity as a bit depth to compare with digital signal depth (*$33 \approx \log_2 10^{10}$ *cd/m*^{2}*). The middle bars in both plots represent dynamic ranges of camera data. The middle bar in Plot (a) shows ∼12 bits signal depth. This means the sensor in LDR imaging is able to capture only a partial range of the real-world luminance. The middle bar in Plot (b) shows the dynamic range of HDR image data, which is almost identical to that of the real world. Finally, the bars on the right-hand side show the dynamic range of a typical display (about 8 bits of signal depth). While the dynamic range of the display shows a minor difference to the LDR camera, the display range shows a significant difference to that of the camera data for HDR imaging.*

HDR imaging are significantly different; hence, current cross-media colour reproduction technology is not compatible. Historically, there have been efforts to bridge the gap between classical reproduction technology and HDR imaging. Göesele et al. [2001] utilised a colour management profile to build an HDR image. Johnson and Fairchild [2003], Akyüz and Reinhard [2006], and Kuang et al. [2007] attempted to combine a tone-mapping algorithm with a colour appearance model. However, without radical restructuring of the colour reproduction system, such hybrid solutions have struggled with performance. With motivation to bridge the gap between cross-media colour reproduction and HDR imaging, this thesis investigates fundamentals and infrastructure of cross-media colour reproduction. It restructures cross-media colour reproduction with respect to HDR imaging, aiming *to develop a novel cross-media colour reproduction system for HDR imaging*.

1.2 Scope

Classical *cross-media colour reproduction* has been understood as a set of reproduction chains that have three elements: device characterisation, colour appearance modelling, and gamut mapping [MacDonald, 1993]. *Device characterisation* describes a set of transforms to convert input/output device signals to physically-meaningful device-independent signals, e.g., CIEXYZ coordinates. *Colour appearance modelling* interprets these physically-meaningful device-independent signals to perceptually-meaningful coordinates by taking the viewing environmental conditions into account. Finally, *gamut mapping* is a visual enhancement procedure to minimise the perceived gamut differences between the target and source media, aiming for plausible reproductions.

In this thesis, these fundamentals were investigated in the context of HDR imaging, resulting in the development of a high-fidelity colour reproduction system for HDR imaging. First, the capturing stage in HDR imaging was researched with respect to device characterisation [see Figure 1.1(b)]. We suggest a novel device characterisation for HDR imaging. HDR characterisation converts the colour specifications of device-dependent HDR images into highly accurate and physically-meaningful radiance values in the form of *absolute* CIEXYZ. This thesis focuses on generating physically accurate HDR radiance maps of static scenes, whereas constructing HDR images of moving objects or transforming LDR images to HDR images is not handled in this thesis.

Acquiring physically-meaningful radiance maps is not sufficient for HDR colour communication as the given physical colours under high luminance levels are perceived differently depending on their viewing conditions (see Chapter 4 on more details of our experimental findings). Therefore, perceptual attributes, e.g., lightness, colourfulness, and hue, of the given physical colour stimuli under high luminances were measured experimentally and modelled as a novel colour appearance model. Our colour appearance model links the description of physically-meaningful HDR radiance maps to perceptually-uniform appearance attributes under extended luminance levels. In theory, these two elements, HDR device characterisation and colour appearance modelling for high luminances, are sufficient for colour image reproduction unless the size of the colour gamuts of the input/output media are significantly different [Morovic, 2008]. According to our measurements (see Section 2.4), the gamut size of the input device is smaller. Especially the input gamut is smaller regarding highly saturated colours. Aiming to achieve the highest fidelity of perceived colour reproduction, we directly mapped perceived colour attributes (input gamut) into perceived output colour attributes (output gamut) with a direct 1:1 gamut mapping, similar to *relative colorimetric* intent (see Section 2.4 for more details). Plausible aspects in user preference (e.g., gamut mapping study) are not handled in this thesis. In summary, this thesis focuses on *accuracy* in both physical acquisition (device characterisation) and perceptual prediction (colour appearance modelling) in HDR colour reproduction. Finally, this thesis provides a complete colour reproduction system for HDR imaging as an application at the end. Possible applications for this system may be as a high-fidelity reproduction pipeline in an HDR broadcasting system (from HDR input to home displays) or as a measuring device for physical radiance and its corresponding perceptual response.

1.3 Contributions

In the context of this thesis, the following contributions have been made.

- **Device characterisation for HDR camera systems.** A novel characterisation method is introduced in Chapter 3. A novel colour reference target was built, specifically designed for HDR imaging. The reference target has a larger gamut and higher dynamic range than common camera calibration targets. It enables highly accurate calibration of an HDR camera system. The proposed method yields physically-meaningful HDR radiance maps to a high accuracy from digital cameras. See Chapter 3 for more details on HDR characterisation.

- **Colour constancy algorithm.** A novel colour constancy algorithm is proposed to reproduce colour constant hues on output media. This technique produces the estimated white point of the scene illumination that is used for white balancing of the calibrated HDR radiance map and can be used to estimate the white point as input to our CAM. See Chapter 3 for more details on white balancing.

- **Colour appearance data under high luminance levels.** A novel high-luminance display device was built to yield a controllable high-luminance viewing environment, where a series of psychophysical experiments were conducted to produce colour appearance data under high luminance levels (up to 16 860 $\mathrm{cd/m^2}$). This data set provides novel measurements of human colour perception in the full working range of the human visual system (five orders of magnitude). See Chapter 4 for more details on the experiments and analysis of the data set. The appearance data set can be found in Appendix A.

- **Colour appearance model for high luminance levels.** A novel colour appearance model was developed from our experimental data set (see Chapter 4 for the experiments), which enables us to model the human visual system under high luminance levels. The model covers a larger range of luminance than existing colour appearance models, and it is directly applicable to HDR imaging. Owing to the proposed colour appearance model, no extra tone-mapping algorithm is required to complete colour reproduction in HDR imaging. Chapter 5 describes the development of our colour appearance model.

- **Cross-media colour reproduction system for HDR imaging.** A complete colour reproduction pipeline is introduced in Chapter 6. This system is built using the HDR characterisation (in Chapter 3) and our colour appearance model (in Chapter 5). It enables reproduction of human observations of a real-world scene onto an output display device. Chapter 6 describes the organisation of the novel elements for colour reproduction in HDR imaging. Results indicates that the proposed colour reproduction system produces high fidelity on output media.

Most of these contributions have been presented in the following publications:

1. **Min H. Kim**, Tim Weyrich, and Jan Kautz. 2009. Modeling Human Color Perception under Extended Luminance Levels. *ACM Transactions on Graphics (Proc. SIGGRAPH 2009)*, 28(3):27:1-9.

2. **Min H. Kim** and Jan Kautz. 2008. Characterization for High Dynamic Range Imaging. *Computer Graphics Forum (Proc. EUROGRAPHICS 2008)*, 27(2):691-697.

3. **Min H. Kim** and Jan Kautz. 2009. Consistent Scene Illumination using a Chromatic Flash. In *Proc. Eurographics Workshop on Computational Aesthetics in Graphics, Visualization, and Imaging (CAe 2009)*, pages 83-89, British Columbia. Eurographics Association.

4. **Min H. Kim** and Jan Kautz. 2008. Consistent Tone Reproduction. In *Proc. IASTED Conference on Computer Graphics and Imaging (CGIM 2008)*, pages 152-159, Innsbruck. IASTED/ACTA Press.

5. **Min H. Kim** and Lindsay W. MacDonald. 2006. Rendering High Dynamic Range Images. In *Proc. EVA 2006 London Conference, EVA Conferences International*, pages 22.1–11, Middlesex. EVA Conference International (ECI).

Other publications during this doctorate:

6. Tobias Ritschel, Thorsten Grosch, **Min H. Kim**, Hans-Peter Seidel, Carsten Dachsbacher, and Jan Kautz. 2008. Imperfect Shadow Maps for Efficient Computation of Indirect Illumination. *ACM Transactions on Graphics (Proc. SIGGRAPH Asia 2008)*, 27(5):129:1-8.

7. Insu Yu, Andrew Cox, **Min H. Kim**, Tobias Ritschel, Thorsten Grosch, Carsten Dachsbacher, and Jan Kautz. 2009. Perceptual Influence of Approximate Visibility in Indirect Illumination. *ACM Transactions on Applied Perception (presented at Symposium on Applied Perception in Graphics and Visualization, APGV 2009)*, 6(4):24:1-14.

1.4 Thesis Outline

Chapter 2 presents the fundamentals of colour reproduction, device characterisation, colour appearance modelling, and HDR imaging in general. It also provides an overview of the state of the art in colour appearance modelling and HDR imaging. In Chapter 3, we present a novel reference target designed for HDR camera systems and a novel technique to build physically-meaningful HDR radiance maps with significant accuracy, called HDR characterisation. We also introduce an efficient and accurate method to estimate the scene illumination for white balancing. Chapter 4 describes the high-luminance colour experiments, conducted with a high-luminance display device that was specifically designed and build for producing high-luminance colour stimuli. A novel colour appearance model for high luminance levels is presented in Chapter 5. It is derived from the acquired experimental data in Chapter 4. Chapter 6 describes an HDR colour reproduction pipeline using our novel fundamentals. Chapter 7 summaries this thesis and discusses potential directions for future work, and Chapter 8 concludes this thesis. Appendix A lists experimental data.

Chapter 2

Background and Previous Work

This chapter introduces the background to this thesis and discusses related work. Section 2.1 introduces colour reproduction. In Section 2.2, fundamentals of device characterisation are presented. Section 2.3 describes human colour vision and the state of the art in modelling colour appearance. The fundamentals of gamut mapping are presented in Section 2.4. Section 2.5 describes the related work in high-dynamic-range imaging with respect to colour reproduction. Section 2.6 discusses this chapter.

2.1 Colour Reproduction

Cross-media colour reproduction can be presented as a process which comprises three essential elements: device characterisation, colour appearance modelling, and gamut mapping. A set of

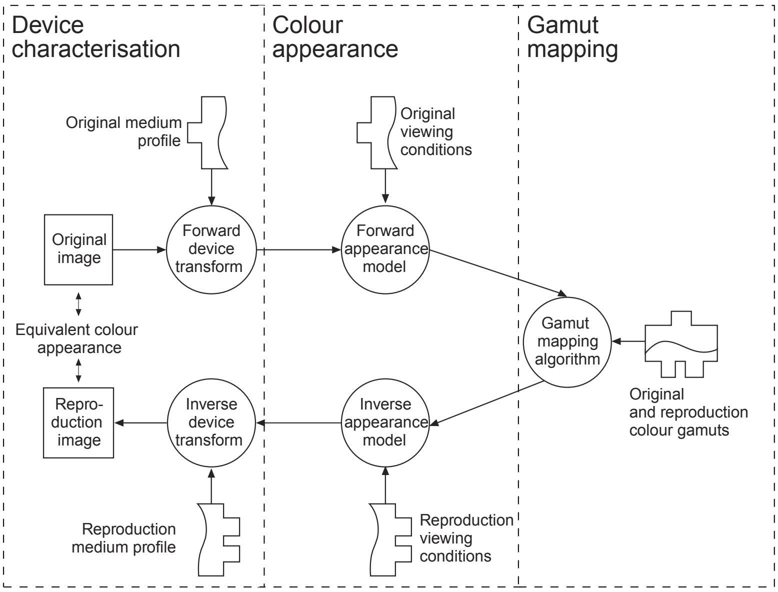

Figure 2.1: *Five-stage colour reproduction system. Procedures for reproducing a source image on a target medium can be described as a set of five different stages: (1) forward device characterisation, e.g., a camera or a scanner, (2) forward colour appearance model, e.g., CIECAM02, (3) perceptual gamut mapping, (4) inverse colour appearance model, and (5) inverse device characterisation. Adapted from [MacDonald, 1993; Morovic, 1985].*

these elements can be interpreted as a five-stage transform [MacDonald, 1993] from the point of view of reproducing a source image on a target medium (see Figure 2.1).

Initially, the original image is specific on the source medium. For instance, the RGB 8-bit signals of a camera. At the target device the image is also shown in a medium-dependent way. In order to match the colour appearance on the two different media, it important to describe the different media in some medium-independent way. *Device characterisation* describes colour reproduction devices, e.g., a camera, a scanner, and a printer, by relating their device-dependent colour specification to device-independent coordinates, e.g., physically-meaningful tristimulus values such as CIEXYZ. However, this is not sufficient for colour reproduction as a given physical stimuli can be perceived differently depending on its viewing conditions. Perceptual attributes, e.g., the lightness, chroma, and hue of a physical colour stimulus, need to be communicated instead of physical stimuli values. Hence, a *colour appearance model* links the description of the physical stimuli to the perceptual appearance attributes, considering a given viewing environment. Technically, these two elements, device characterisation and colour appearance modelling, are sufficient for colour image reproduction unless the size of the colour gamuts of input/output media is different [Morovic, 2008]. However, if there is a considerable difference between the colour gamuts, it is necessary to map the input colour gamut into the output in an intelligent way, so-called *gamut mapping*.

2.2 Characterisation

Colours on imaging devices are specific to their media. *Device characterisation* converts the device-dependent colour specification to device-independent coordinates. It bridges the meaningless imaging device signals to physically-meaningful values. The following sections present the physical background and technical details of device characterisation.

2.2.1 Measuring Optical Radiation

Imaging devices like digital or film cameras sense a certain range of optical radiation to yield images. *Radiometry* is the measurement of the optical radiation, which is an electromagnetic radiation within the frequency range from 3×10^{11} to 3×10^{16}Hz [CIE, 1983]. In contrast, *photometry* is the measurement of light, which is defined as electromagnetic radiation detectable by the human eye within the wavelength range from 380nm to 780nm. It is defined as the CIE $V(\lambda)$ function [CIE, 1986]. Therefore, radiometric units include infrared, visible, and ultraviolet wavelengths without specific consideration of the human visual system, and luminous units account for the perceptual aspect of the radiation on the human eye.

There are various ways to quantify the optical radiation in physics. The quantification units are described here. Suppose there is a tungsten light, which emits a beam of light on subjects in a room. The beam contains a certain amount of light. When it is near the lamp, it occupies a small area; when it is further away, it occupies a larger area (like a spot light). However, the amount of light in the beam is the same. Its beam looks like a circular cone (see Figure 2.2). The *total amount of light visible in the beam* is called *luminous flux* [unit: *lumen*] F. It is a summation of the products of the power per unit wavelength interval $P(\lambda)$, the spectral luminous efficiency function $V(\lambda)$ [CIE, 1986], and the width of each wavelength band $\Delta\lambda$. To obtain a physically-meaningful scale, it is scaled by a constant relating units of flux to units of power (683 lumens per watt) K_m:

$$F = K_m \sum_{\lambda} P(\lambda)V(\lambda)\Delta\lambda \,. \tag{2.1}$$

The only difference between calculating radiometric units and calculating photometric units is to exclude the CIE $V(\lambda)$ function of luminance. The calculation of *radiant flux* excludes the $V(\lambda)$ function in Equation (2.1) and uses the *watt* unit instead.

Luminous flux measures the visible light in passage from one place to another. *Illuminance* is the *amount of luminous flux falling on a unit area of a surface*. Its unit is *lux*, which means one lumen falls on an area of one square metre. For irradiance, the unit is w/m^2.

There are two interesting laws related to illumination. Illumination E is inversely proportional to the square of the distance between the light and the surface d, $\frac{E_1}{E_2} = \frac{d_2^2}{d_1^2}$, called *Inverse Square Law of Illumination*. The illumination E on an inclined surface E at distance d is proportional to the cosine of the angle θ of incident light and the surface normal, $E = \frac{I\cos\theta}{d^2}$, where I is luminous intensity, called the *Lambertian Cosine Law of Illumination* (see Figure 2.2).

On the light emitting surface, the *amount of light leaving a light source* can be measured. It is called the *luminous intensity*, and is measured in *candela*. One *candela* occurs when a source radiates one *lumen* into a solid angle of one *steradian (sr)*. The unit for radiant intensity is w/sr.

Luminance describes a measure of the light leaving a surface, equal to the *luminous intensity per unit area*. The unit of luminance is cd/m^2; the unit for radiance is $w/(m^2 \cdot sr)$. In particular, the iterative travel of radiance L at a certain *solid angle* (a steradian w is an area A per squared radius r: $w = A/r^2$) ω_o can be modelled mathematically like Equation (2.2), so-called the *rendering equation* [Kajiya, 1986]. It is a summation of emitted radiance $L_e(p, \omega_o)$ at a point p and the integral of reflected light in hemisphere Ω:

$$L(p,\omega_o) = L_e(p,\omega_o) + \int_{\Omega} f(p,\omega_i,\omega_o)L(p',-\omega_i)\cos\theta_i d\omega_i \,, \tag{2.2}$$

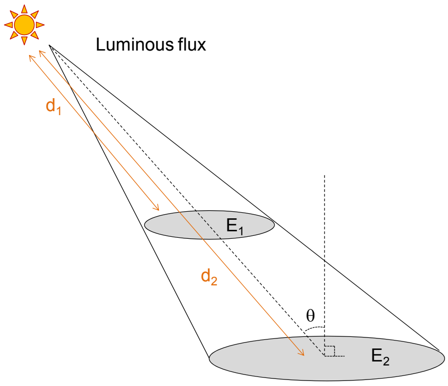

Figure 2.2: *Schematic diagram of illumination laws. E_1 surface illuminated by a near light source; E_2 surface illuminated by a more distance of light source.*

where $f(p,\omega_i,\omega_o)$ is the reflectance property (a scalar function from zero to one) at point p in the incoming direction ω_i and outgoing direction ω_o. This is the bi-directional reflectance distribution function (BRDF). $L(p',-\omega_i)$ is the incoming radiance from direction $(-\omega_i)$ in one dimensional angle θ from the surface p normal.

In practice, a perfect diffusion assumption is often used for mathematical convenience, called a *Lambertian surface*. Theoretically, a Lambertian surface provides uniform diffusion of the incident radiation so that its luminance is the same in all directions from which it can be measured. For instance, if the Lambertian surface is illuminated uniformly with an illuminance of 3.1416 (π) lux, then the measure of its luminance on that surface will be 1.0 cd/m^2 in 100% reflectance.

2.2.2 Colorimetry

Colorimetry is the measurement of human colour perception, concerned with reducing spectra to the physical correlates of colour perception. To perform colorimetry, we need three essential elements: a light source (illuminant), an object (with standard measuring geometry), and a standard observer. In 1931, Commission Internationale de l'Eclairage (CIE) conducted psychophysical experiments, the CIE 1931 standard colorimetric observation, for quantifying trichromatic colour perception of humans to yield *colour matching functions* (CMF). In the experiment, two colours are shown to normal colour vision observers who are asked to adjust one of the stimuli colours to match the appearance of the other colour. They used red, green, and blue lights that produced a metameric match. The transform has since been updated by Stiles and Burch [1959] and Vos [1978]. These functions became the official standard for the transform from visible spectrum to trichromatic colour coordinates, the so-called CIE tristimulus values, CIEXYZ.

However, the physiological long-/middle-/short-wave (LMS) cone responses were discovered to be different from these psychophysical colour matching functions [Estévez, 1979; Hunt and Pointer, 1985]. A transform for cone response was suggested by Estévez [1979], which is broadly

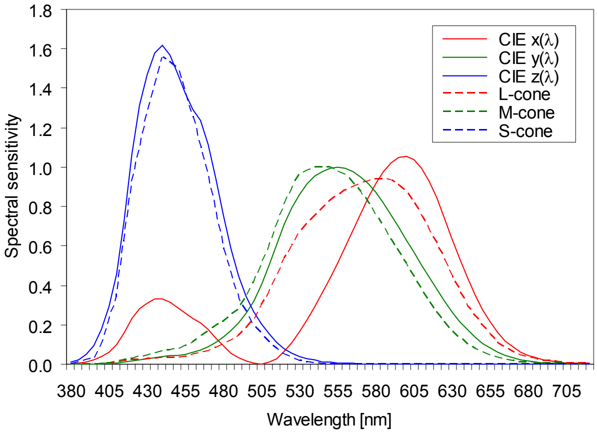

Figure 2.3: *CIE 1931 colour matching functions vs. physiological cone spectral sensitivity curves. Solid R/G/B coloured lines present CIE 1931 colour matching functions (version: Vos [1978] modification), broken R/G/B coloured lines show the physiological cone responses originated by Estévez [1979]. In particular, the red colour response (L-cone) appears significantly different from CIE $\overline{x}(\lambda)$ function.*

used as a fundamental transform for computational cone responses (see Figure 2.3 for comparison between the CIEXYZ and LMS cone responses). See Section 2.3.4 for more details on colour spaces.

Radiation that raises the colour sensation is measurable by a photo-detector. Such devices comprise of a diffraction grating and light-detecting diodes; for instance, a colorimeter, spectroradiometer, or spectrophotometer. The measured energy on each band of wavelengths is recorded as a spectrum. The spectrum can be converted to tristimulus values (CIEXYZ). Depending on the type of measuring device, there are two different types of tristimulus values. Spectroradiometers normally yield tristimulus values XYZ by the summation of products of spectral radiance distributions $L_{e,\lambda}$ [unit: W/(sr·m^2·nm)] and CIE colour matching functions $\overline{x}(\lambda)$, $\overline{y}(\lambda)$, and $\overline{z}(\lambda)$, scaled by maximum photographic luminous efficacy, K_m, 683lm/W, where the Y value corresponds to luminance L_v (unit: cd/m^2) [Ohta and Robertson, 2005]:

$$\begin{aligned} X &= K_m \sum_{\lambda} L_{e,\lambda} \overline{x}(\lambda) \Delta\lambda \,, \\ Y &= K_m \sum_{\lambda} L_{e,\lambda} \overline{y}(\lambda) \Delta\lambda = L_v \,, \\ Z &= K_m \sum_{\lambda} L_{e,\lambda} \overline{z}(\lambda) \Delta\lambda \,. \end{aligned} \tag{2.3}$$

In contrast, spectrophotometers yield the CIEXYZ by the normalised (usually $Y = 100$) summation of products of *reference viewing illumination* $P(\lambda)$ (*CIE standard illumination, D50*), which is the spectral power distribution normalised to 100 at 560nm wavelength, surface reflectance basis $S(\lambda)$ [unit: W/(sr·m^2·nm)], and CIE CMFs [CIE, 1986] [Hunt, 1998]. As it turns out, spectrophotometers yield normalised *D50 illumination-adapted* radiance measurements. However, both are confusingly called CIEXYZ values even though they are not identical:

$$\begin{aligned} X &= k \sum_{\lambda} P(\lambda) S(\lambda) \overline{x}(\lambda) \Delta\lambda \,, \\ Y &= k \sum_{\lambda} P(\lambda) S(\lambda) \overline{y}(\lambda) \Delta\lambda \,, \\ Z &= k \sum_{\lambda} P(\lambda) S(\lambda) \overline{z}(\lambda) \Delta\lambda \,, \\ &\text{where } \; k = \frac{100}{\sum_{\lambda} P(\lambda) \overline{y}(\lambda) \Delta\lambda} \,. \end{aligned} \tag{2.4}$$

The International Electrotechnical Commission (IEC) standardises a common colour transform from sRGB primaries to CIEXYZ values [IEC, 2003], which returns the *radiometric* tristimulus values without including the reference illumination adaptation. In contrast, most present colour transform matrices in colour science were derived from the measurements of a spectrophotometer, e.g., CIECAT02, Bradford chromatic transform, or Hunt-Pointer-Estévez (HPE) transform, as most psychophysical experiments were conducted with reflective materials. To this end, Nielsen and Stokes [1998] proposed a D50-adapted transform of sRGB primaries. The transform bakes the D50 illuminant adaptation in the original sRGB transform [IEC, 2003] through the Bradford chromatic adaptation [Lam, 1985]. This transform is used as an International Color Consortium (ICC) profile

	Forward transform		
	R	G	B
X	0.4124	0.3576	0.1805
Y	0.2126	0.7152	0.0722
Z	0.0193	0.1192	0.9505

	Inverse transform		
	X	Y	Z
R	3.2406	-1.5372	-0.4986
G	-0.9689	1.8758	0.0415
B	0.0557	-0.2040	1.0570

Table 2.1: *Transform from sRGB into CIEXYZ [IEC, 2003].*

	Forward transform		
	R	G	B
X	0.4361	0.3851	0.1431
Y	0.2225	0.7169	0.0606
Z	0.0139	0.0971	0.7141

	Inverse transform		
	X	Y	Z
R	3.1336	-1.6168	-0.4907
G	-0.9787	1.9161	0.0335
B	0.0721	-0.2291	1.4054

Table 2.2: *Transform from sRGB into D50-adapted CIEXYZ [Nielsen and Stokes, 1998].*

colour space (PCS) [ICC, 2004] (see Table 2.1 and 2.2 for both transform details). In our colour reproduction system, the D50-adapted transform is used for transforming sRGB signals to CIEXYZ values. See Chapter 6 for more details of our colour reproduction system.

When the photo-detector measures the surface reflectance (colour), the measurements can be changed due to the geometric positions of the light source, the photo-detector and the surface object. The CIE defined four illumination and viewing geometries for reflectance (transmittance) measurements [CIE, 1986]: 45/normal (45/0), normal/45 (0/45), diffuse/normal (d/0), and normal/diffuse (0/d) (see Figure 2.4). In the 45/normal geometry, the sample is illuminated with an incident light at an angle of 45° from the normal, and the photo-detector is located along the normal. The normal/45 geometry is the reverse order of the 45/normal geometry. Common hand-held spectrophotometers, e.g., GretagMacbeth Spectrolino and EyeOne, use the 45/normal geometry. In

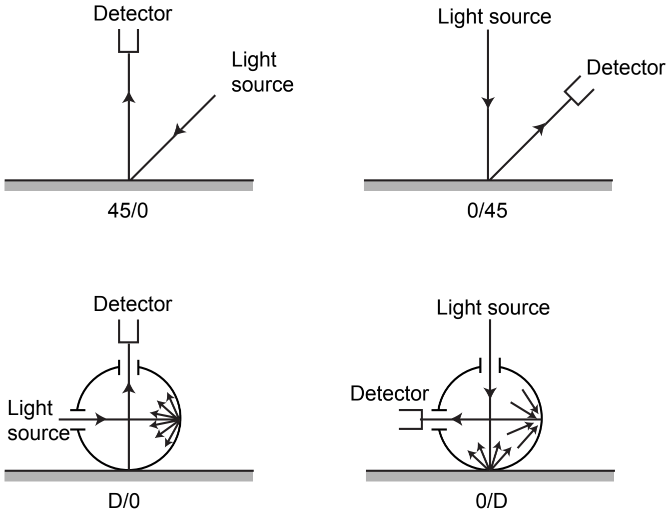

Figure 2.4: *CIE-recommended illuminating and viewing geometries. Adapted from [Battle, 1997].*

the diffuse/normal geometry, the colour object is illuminated from all angles using an integrating sphere, of which the inner surface is painted with white material, and measured at the angle near the normal to the surface (generally 8° from the normal to avoid specular highlights). This geometry provides an option for measuring specular highlights (included or excluded). The normal/diffuse geometry is the reverse order of the diffuse/normal geometry. Generally, high-end spectrophotometers use normal/diffuse geometry, e.g., the Datacolor Spectraflash.

2.2.3 Camera Optics for Capturing Radiance

Electromagnetic radiation can be captured physically by an optical mechanism. The simplest formation of an optical image is an image on a *plane mirror*. As further evolution of the image formation device, Greeks such as Aristotle and Euclid discovered the optical principle of the *pinhole camera* in the 4th century BC. This is a precursor to the *camera obscura*: an optical device used in drawing that lead to the invention of photography. In this camera system, the bundles of rays from points on the subject pass through a pinhole and diverge to form an image on a photoplane surface. The pinhole image is inverted, reversed, smaller and lacks sharpness. In modern camera systems, the pinhole is replaced with a series of negative and positive spherical lenses in order to improve the image formation in terms of geometric/radiometric distortion, sharpness, vignetting, and brightness.

A lens is usually fitted with aperture, which controls the transmittance of light, calibrated in units of *relative aperture*. This is represented by a number N, which is defined as the equivalent focal length f of the lens divided by the diameter d of the entrance pupil: $N = f/d$, for example, a lens with an entrance pupil size 25mm in diameter and a focal length of 50mm has a relative aperture of 2 (=50/25). The numerical value of relative aperture is usually prefixed by the italic letter f and an oblique stroke, e.g., $f/2$, which provides a reminder of its derivation. The denominator of the expression used is usually referred to as the *f-number* of the lens, and the relative aperture of a lens is commonly referred to simply as its *aperture* or even as the *f-stop*. If there are two different aperture and shutter speed settings, they satisfy the ratio of shutter times to the ratio of squared aperture sizes: $\frac{t_1}{t_2} = \frac{N_1^2}{N_2^2}$ [Ray, 2000b].

To simplify exposure calculations, f-numbers are usually selected from a standard series of numbers. As the amount of light passed through a lens is inversely proportional to the square of the f-number, the numbers in the series increase by a factor of $\sqrt{2}$. The standard series of f-number is $f/1.0$, 1.4, 2.0, 2.8, 4.0, 5.6, 8.0, 11, 16, 22, 32, 45, and 64. A change in relative aperture corresponding to a change in exposure by a factor of 2 (larger or smaller) is referred to as a change of *one stop*.

The change of aperture size influences not only exposure, but also sharpness. This is called the *depth of field*. The depth of field T_d is proportional to the squared of focused distance u of an object and relative aperture N. T_d is also proportional to the diameter of the circle of confusion of the lens C, but is inversely proportional to the square of the focal length f of the lens: $T_d = \frac{2u^2NC}{f^2}$.

The amount of incident radiation can be controlled by a *shutter* by opening and closing its shield at a user's command and exposing the sensing material to light for a predetermined time. It can be decided by the user or by an automatic exposure-metering system. On older shutters before 1950s, the series of shutter speeds was 1, 1/2, 1/5, 1/10, 1/25, 1/50, 1/100, 1/250, and 1/500 second. Modern shutters provide 1, 1/2, 1/4, 1/8, 1/15, 1/30, 1/60, 1/125, 1/250, and 1/500 second in order to provide a progression of exposure increases similar to the standard series of lens aperture numbers (by a factor of 2) for easy calculation of the exposure. The latter shutter system permits a mechanical interlock between the aperture and shutter speed controls to keep the two in a reciprocal relationship with reference to *exposure values* [Ray, 2000a]. However, modern shutters introduce rounding errors with respect to a factor of 2, e.g., 1/15 and 1/16. Debevec and Malik [1997] tested their Canon EOS Elan camera by audio recording of the camera shutters. Their measurements verified that the actual exposure times varied by powers of two, e.g., 1, 1/2, 1/4, 1/8, 1/16, 1/32, 1/64, 1/128, 1/256, and 1/512. We used these actual shutter speeds for the exposure time calculation.

When the shutter system opens, the light from a subject falls on to the corresponding area of the photo-sensing material inside a camera. The effect produced on the material, *exposure* H, is proportional to the product of the illuminance E and the exposure time t: $H = Et$. The unit for exposure is $lux\ seconds$ [unit: $lx \cdot s$] [Attridge, 2000]. The decision of how much to exposure is made not using radiance, but luminance that excludes the ultraviolet and infrared regions of the electromagnetic spectrum.

The *luminance* L of a small off-the-axis area of the subject is imaged in the focal plane of the camera as illuminance E. The amount of *illuminance* E on the sensor site that comes from the subject's *luminance* L increases with a lens of higher transmittance T, but decreases with squared f-number of aperture N:

$$E = \frac{T \pi \cos^4 \theta}{4N^2} L \, , \tag{2.5}$$

where illumination E reduces according to the distance from the optical axis of the lens in proportional to $\cos^4 \theta$, called the *vignetting* effect (θ is an angle from the optical axis).

In addition, the equivalent series of the combinations of shutter times and apertures can be defined as a absolute figure, called exposure value (EV) [Ray, 2000a]: $\log_2 \left(\frac{N^2}{t} \right)$. Assuming a film speed of ISO 100, the overall luminance level can be determined as a proportion of 2^{EV-3}. For instance, if an EV measurement is 5, the scene luminance is approximately 4 $\mathrm{cd/m^2}$.

2.2.4 Sensing Radiance

Once the optical radiation has travelled through the optical mechanism, the amount of radiation can be detected by certain materials to accomplish image formation. Early image-sensing technology started with *Daguerreotype* (the first photography, introduced in 1839) in which *silver halide* is coated on the surface of a mirror as photodetectors [Walls and Attridge, 1977]. Once an image is exposed on the silver halide, the *latent image* is deposited by *iodine* vapour. In recent film photography, the mirror is replaced with light-sensitive emulsion, which comprises transparent celluloid or acetate base, coated with an emulsion, containing the silver halide. The developing method of the latent image is also improved with *bromine* and *chlorine* to enhance the spectral sensitivity of films.

The film-based image-sensing method has been replaced by solid-state-based devices over many years for efficiency and accuracy. Charge-coupled device (CCD) refers to a semiconductor architecture in which the electronic charge is transferred to its storage areas. The CCD architecture has three basic functions: charge collection, charge transfer, and the conversion of charge into measurable voltage [Janesick, 2001]. Recently, complementary-metal-oxide semiconductor (CMOS) has become more popular than CCD sensors in solid-state cameras as it provides more efficient energy consumption. In general, CCDs are regarded as passive pixel sensors and CMOSs are regarded as active pixel sensors, since each pixel on the CMOS includes its own amplifier to yield amplified charge voltage per pixel [Holst, 1998].

Note that solid-state-based sensors have a wider bandwidth of spectral sensitivity than the human visual system (see Figure 2.5). In particular, the sensitivity of such sensors is spread more toward infrared (IR) wavelengths (beyond red colour). In order to have a similar response to human vision, the sensors need to be calibrated with an IR-blocking filter that cuts out the wavelengths longer than 700-800nm [Gilblom and Yoo, 2004]. Once the incident light is filtered through the IR blocking filter, individual pixels are filtered with either red, green, or blue filters arranged in a mosaic pattern. These colour filters mimic the spectral responsivity of the human visual system [see Figure 2.8(a) for the spectral sensitivity of a digital camera and Figure 2.3 for that of the human visual system].

The amplified charge voltage is transported to an *analogue-to-digital converter* (ADC), which converts voltage into measurable voltage, i.e., an electronic signal. For consumer cameras, an 8-bit ADC is used; for professional or scientific photographic cameras, a 12- or 14-bit ADC is used. Its linearity is specified by *differential nonlinearity* (DNL) and *integral nonlinearity* (INL). In theory, the voltage of charge in a detector should increase linearly in proportion to the illuminance on the surface of each pixel, but its linearity often requires additional calibration inside the solid state device [Inglis and Luther, 1996]. In addition, recent digital single-lens reflex (DSLR) cameras provide an alternative output in addition to ordinary 8- or 16-bit red, green, and blue (RGB) outputs.

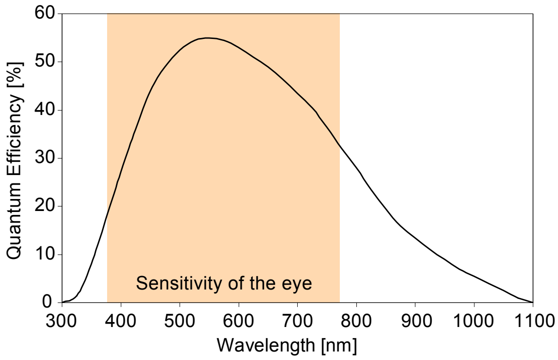

Figure 2.5: *Quantum efficiency of a solid-state-based sensor. The raw spectral sensitivity of solid-state-based sensors is much wider (between 300 and 1100nm) than that of the human visual system (380–780nm). Infrared-blocking filters are necessary to make the response similar to the human eye. Adapted from [Gilblom and Yoo, 2004].*

It is often called *RAW image format*, which directly stores the ADC sensor signals in the Bayer-pattern as one mosaic colour channel of red, green, blue, and green (RGBG). It excludes the post-image processing, e.g., white balancing, gamma correction, tone mapping, or post noise reduction process, merely including hardware-level noise reduction (pattern noise), scaling constants for white point in the captured scene, and meta data of the camera settings [Coffin, 2009]. The method in Chapter 3 utilises these RAW files to generate high-dynamic-range images and characterises them to achieve image measurements of radiance on an absolute scale.

The *dynamic range* of solid-state sensors is often limited by two main factors: overflow drain in the highest saturation level of illuminance, called *blooming effect*; and *noise floor* in the lowest saturation level of illuminance (see Figure 2.6). First, when an electron-detector (*well*) overflows, the charge spills over to adjacent pixels in the same column resulting in an undesirable overload, called *blooming*. In order to overcome the blooming effect, usually *anti-bloom drains* or *overflow drains* are installed in the imaging sensor. The drains are attached to every pixel, where any photoelectron is swept into the drain and instantly removed. In an ideal imaging system, the output increases linearly in proportion to the incident light up to the anti-bloom drain limit. However, in real arrays, a *knee* is created because of imperfect drain operation [Janesick, 2001] (see Figure 2.6).

Second, the dark saturation point of the image is limited by sensor *noise*, which falls into five main categories [Holst, 1998]: *Shot noise* is due to the discrete nature of electrons. It occurs when the photoelectrons are created while the dark current electrons are present. Cooling the array can reduce the *dark current* (relatively small electric current that flows through the solid state even without exposed to light) to a negligible value and thereby reduce the shot noise to a negligible level; *Reset noise* is associated with resetting the sense node capacitor. It occurs due to *thermal noise* (a signal generated by the thermal agitation of the charge carriers in the conductor) generated by the resistance; *Amplifier noise* comprises two components: *1/f noise* (a signal with a frequency spectrum such that the spectral power density is proportional to the reciprocal of the frequency) and *white noise* (random signals independent of the spectral power density). It occurs in on-chip amplifiers as well as off-chip amplifiers; *quantisation noise* is due to the ADC discretisation of the output level; *Pattern noise* refers to pixel-to-pixel variation that occurs (when the array is even in the dark) due to the *dark current* differences. It is a signal-independent noise, which occurs in CMOS sensors. The noise level is often evaluated as root-mean-squared (RMS) noise on the capture of a uniform surface:

$$\mathrm{RMS} = \sqrt{\frac{1}{MN}\sum_{x=0}^{M-1}\sum_{y=0}^{N-1}\left[f(x,y)-g(x,y)\right]^2}, \tag{2.6}$$

where M and N are horizontal and vertical image resolutions; f is each pixel level, and g contains the mean of the entire pixel levels.

The dynamic range can be described as the difference between the maximum and minimum intensities (or densities) of imaging signal (or colorant), where the intensity (or density) is often calculated by taking the 10-based logarithm of the ratio between the reference maximum luminance measure I_{max} and the minimum luminance measure I_{min}: $\log_{10}\left(\frac{I_{max}}{I_{min}}\right)$. In electronic imaging, the dynamic range often describes the number of electrons of full capacity of the well N_{signal}, which is limited by the noise floor N_{noise} [Holst, 1998]. The dynamic range that considers the noise floor is presented by the *signal-to-noise ratio* (SNR) (dynamic range multiplied by 20, unit: dB): $20\log_{10}\left(\frac{N_{signal}}{N_{noise}}\right)$, where N_{noise} is usually calculated as RMS noise.

2.2.5 Device Characterisation

Once we measure the optical radiation of a reference target and simultaneously capture it as an image with a sensing device, it is possible to derive a mathematical model to describe the colour specification of the imaging device in physically-meaningful device-independent coordinates. The device signals or output colours in imaging devices vary due to their manufacturer settings or hardware design. They can also vary even with the same specification of identical models due to their manufacturing process. Device characterisation overcomes the variation of imaging devices to build a mathematical bridge between device signals and physical coordinates so that we can describe the device-dependent signals as device-independent signals. A colour space, e.g., CIEXYZ or CIELAB, can be used device-independent signals. To this end, we are able to utilise imaging devices to measure some physical property or to produce specific target colours on the output devices. Device characterisation often requires two procedures [Johnson, 2002]:

- **Calibration:** the setting up of a device or process so that the device gives repeatable data.
- **Characterisation:** the relationship between device colour space and the device-independent colour space, e.g., CIE tristimulus values.

Once a device is calibrated in repeatable conditions, a mathematical model can be derived to yield physically-meaningful coordinates. The characterisation of a target device then comprises two elements: estimating a tone-reproduction curve for each colour channel, the so-called *opto-electronic transfer function* (OETF), and deriving a *colour transform* between the device-dependent signals and

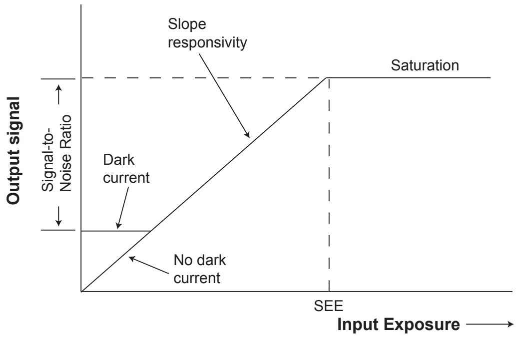

Figure 2.6: Average responsivity of solid-state imaging. Its average responsivity is the slope of the output-input transformation. The maximum input or the saturation equivalent exposure (SEE) is the input that fills the charge wells. SEE is used to define the dynamic range. Dark current limits the available signal strength. Cooling can reduce the dark current to a negligible level. Adapted from [Holst, 1998].

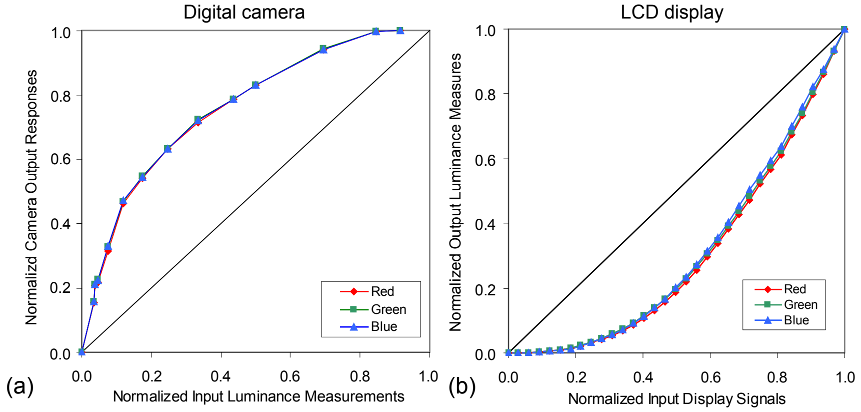

Figure 2.7: Measured OETFs of a digital camera and an LCD display. Plot (a) shows the measured OETF of RGB output of a Nikon D100 camera, where the horizontal axis presents normalised incident luminance and the vertical axis shows normalised camera outputs. Plot (b) shows the measured OETF of an Apple Cinema HD Display (LCD panel), where the horizontal axis indicates normalised input display signals and the vertical axis presents the normalised corresponding measurements of luminance levels.

the device-independent coordinates.

Opto-Electronic Transfer Function OETF describes a non-linear tone-reproduction function for each colour channel of an imaging device. For instance, the 709 phosphor in a cathode-ray tube (CRT) display yields non-linear luminance responses according to its voltage input [Inglis and Luther, 1996]. Its responses are raised to the power of approximately 2.2, which is similar to the inverted function of the human cone responses (raises to the power of approximately 0.45, see Chapter 4 for the measured human response). To this end, the non-linear response of CRT monitors cancels out the non-linear response of human perception. The OETF for the 709 phosphor became an international standard for tone reproduction of the sRGB colour space [IEC, 2003]. Figure 2.7 shows the measured OETFs of a DSLR camera and a liquid-crystal display (LCD) monitor. One is associated with the other as an inverse function with minor differences. Even though an LCD panel has a linear response to input voltage [Kwak and MacDonald, 2001], the complete product of the LCD display replicates the OETFs of the CRT monitor to maintain backward compatibility with the sRGB colour system.

Display device radiance level measurements (corresponding to its input signals) allow us to derive OETFs for the colour primaries of the device. For instance, if the rough estimate of the tone-reproduction curve appears similar to the power function, we can model the OETF as a power function [Berns et al., 1993], called a gain-offset-gamma (GOG) model. It models the tone reproduction of each channel as a power function with a conditional clamp:

$$C = \begin{cases} \left[k_{gain} \cdot d + k_{offset}\right]^{\gamma}, & \left[k_{gain} \cdot d + k_{offset}\right] > 0 \\ 0, & \left[k_{gain} \cdot d + k_{offset}\right] \leq 0 \end{cases}, \tag{2.7}$$

where the summation of k_{gain} and k_{offset} is one; d is a normalised display signal for each channel; k_{gain} is a scaling constant; k_{offset} is an offset value; the radiance raises to the exponent of γ. C is the radiance level of red (R), green (G), and blue (B) primaries respectively.

To provide a linear relationship in the complete camera-display system, an inverse gamma power function is used in digital cameras as an image processing procedure, so-called *gamma correction*. This is an essential step to transform the trichromatic radiance values to sRGB display signals (camera output). Note that gamma correction does not exist in HDR imaging camera output as this is normally conducted in the tone-reproduction stage of HDR imaging. When the radiance level C of each primary is normalised to 1.0, the normalised camera output will be:

$$d = \begin{cases} 1.055C^{\gamma} - 0.055, & C > 0.00304 \\ 12.92C, & C \leq 0.00304 \end{cases}, \tag{2.8}$$

where γ value is 1/2.4 (0.42) which compensates for the 2.2 gamma reproduction in the sRGB system (with linear ramp for dark colours) [IEC, 2003].

OETFs of output devices should be invertible for actual applications. See Chapter 6 for more details on the practical application of display characterisation. In contrast, it is not necessary for digital camera OETFs to be invertible as only a forward transform (from the device signals to the device-independent signals) is required (see Chapter 6 for more details). Hence, high-ordered polynomials are often used for better performance instead of the simple power function [Pointer et al., 2001; MacDonald and Ji, 2002; ISO, 2006].

Colour Transform Modelling characteristics of non-linear tone reproduction for each colour channel yields linearised device signals, which correspond to physical measurements of device-dependent colours. It enables us to derive a linear transform between device signals and physical measurements. The use of colour transforms is based on a theory, called *Grassmann's Additivity Law* [Hunt, 1998], which describes that any colour can be matched by certain amounts of multiple primaries. For instance, if we have three device primaries and three-dimensional colour coordinates, a 3×3 linear transform is sufficient to map device colours to colour coordinates such that they are linearly associated.

Suppose we have a digital camera which captures a measured colour target. The trichromatic response value [red (R), green (G), and blue(B)] of a specific pixel on the sensor is given as the sum of the product of the spectral power distribution (irradiance) of the light source $P(\lambda)$, the surface reflectance (or transmittance) of the imaged object $S(\lambda)$, and the spectral responsivities of the colour filters $D_{r/g/b}(\lambda)$. Assuming that incident light is reflected from object surfaces:

$$\begin{aligned} R &= \sum_{\lambda} P(\lambda)S(\lambda)D_r(\lambda)\Delta\lambda\,, \\ G &= \sum_{\lambda} P(\lambda)S(\lambda)D_g(\lambda)\Delta\lambda\,, \\ B &= \sum_{\lambda} P(\lambda)S(\lambda)D_b(\lambda)\Delta\lambda\,. \end{aligned} \tag{2.9}$$

The summation is taken over a suitable wavelength range in the visible part of the spectrum from 380nm to 780nm for instance [ISO, 2006]. The calculation of these response values is similar to the computation of device-independent tristimulus values, such CIEXYZ:

$$\begin{aligned} X &= \sum_{\lambda} P(\lambda)S(\lambda)\overline{x}(\lambda)\Delta\lambda\,, \\ Y &= \sum_{\lambda} P(\lambda)S(\lambda)\overline{y}(\lambda)\Delta\lambda\,, \\ Z &= \sum_{\lambda} P(\lambda)S(\lambda)\overline{z}(\lambda)\Delta\lambda\,, \end{aligned} \tag{2.10}$$

where $\overline{x}(\lambda)$, $\overline{y}(\lambda)$ and $\overline{z}(\lambda)$ are the CIE color matching functions (CMF) [CIE, 1986]. The only difference between Equations (2.9) and (2.10) is the use of different weighting functions $D_{r/g/b}$ and $\overline{x},\overline{y},\overline{z}$.

Various camera characterisation techniques have been proposed to find a mapping between these colour spaces. They can be categorised into two main classes: models based on targets with known reflectances [Pointer et al., 2001; MacDonald and Ji, 2002; Johnson, 2002; ISO, 2006] and models based on the measurement of spectral responsivity using a monochromatic light source [Martínez-Verdú et al., 2000; MacDonald and Ji, 2002; Martínez-Verdú et al., 2003; ISO, 2006; Normand et al., 2007].

The reflectance-based techniques use a colour target, such as the GretagMacbeth ColorChecker, where the tristimulus values of each colour patch are measured first or already known (e.g., in CIEXYZ). A picture of the colour target is then taken and a direct mapping between the image's RGB-values and the measured XYZ values is derived via linear regression (or polynomial regression in case of non-linearised images). While these techniques are very simple, they are only valid for the current illumination condition [ISO, 2006], as $P(\lambda)$s in Equation (2.9) and (2.10) are not the same

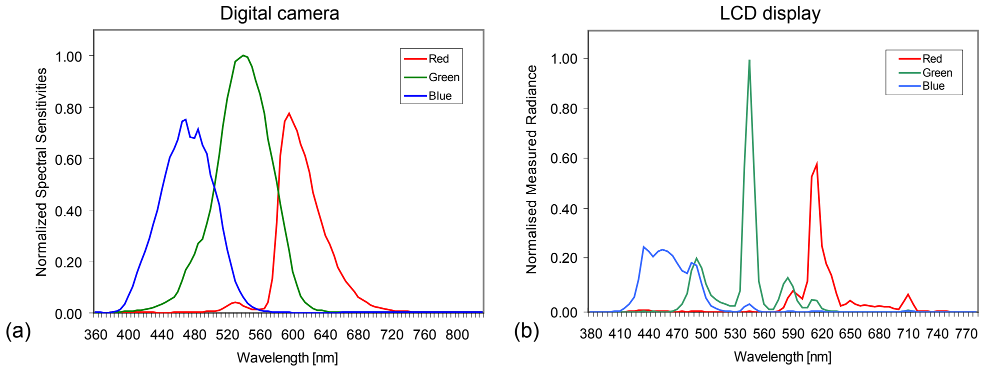

Figure 2.8: *Spectral responsivity of a digital camera and an LCD display. Plot (a) shows the measured spectral sensitivities of the RGB filters respectively on the single wavelength lights (Nikon D70). The responsivity appears to be similar to the human colour matching functions in wavelengths between 380 and 730nm. Plot (b) presents the measured spectral characteristics of the RGB primaries respectively. The bandwidth of the trichromatic primaries is relatively narrower in the LCD display (Apple Cinema HD Display), compared to the width of the camera filters, as the florescent lamp or LED diode is used as a back-light source instead of broadband width light sources (e.g., a Xenon lamp).*

with these methods. $P(\lambda)$ in Equation (2.9) is the spectrum of the light source at a scene; $P(\lambda)$ in Equation (2.10) is usually CIE D50 illuminant in colorimetry and ICC profiles (see Section 2.2.2). As soon as the lighting changes, a new mapping is required. Therefore, this characterisation method is very limited in practical applications. Nonetheless, it is universally used for ICC input profiles [ICC, 2004] and is part of the ISO standard [ISO, 2006]. Reflectance-based techniques have also been extended to HDR imaging by assembling characterised LDR images into an HDR image by using the ICC method [Göesele et al., 2001]. However, this extension shares the same assumption of fixed geometric and spectral illumination characteristics, and also does not allow us to characterise absolute luminance.

The monochromator-based techniques use a white integrating sphere of known reflectance and a monochromatic light source of which wavelength can be adjusted. By illuminating the integrating sphere with every single wavelength within the visible spectrum, the spectral responsivity $D_{r/g/b}$ can be measured directly, which allows derivation of a simple linear mapping to CIEXYZ. In this case, $P(\lambda)$ is the same for Equation (2.9) and (2.10). While this method is much more universal than reflectance-based techniques, monochromator-based techniques are very time-consuming, each wavelength must be measured individually and a picture needs to be taken for every wavelength. These techniques can, in theory, be used for camera characterisation in HDR imaging. However, only colour could be characterised and not luminance, as the employed illumination and target only offers a low dynamic range. Figure 2.8(a) presents spectral characteristics of a digital camera, obtained through the monochromator-based technique, compared to spectral characteristics of a trichromatic LCD display [Figure 2.8(b)].

Inanici and Galvin [2004] and Krawczyk et al. [2005] proposed to rescale the measured luminance values in HDR radiance maps by comparing them with measurements from a luminance meter. However, they only take into account luminance scales without considering radiometric measurements of colours.

2.2.6 White Balancing

The characterisation model of a digital camera transforms input device-dependent camera signals into device-independent colour coordinates. However, in case an image is not intended for measurement purposes but for display on an output monitor, we need to take the human visual system (which adapts to a given illumination condition) into account. This is a classical issue and is traditionally called *white balancing* (for cameras) or *colour constancy* (for human vision) [d'Zmura and Lennie, 1986] for digital cameras. These computational methods are distinct from human chromatic adaptation. *Colour constancy* methods pursue accurate estimation of scene illumination and assume 100% adaptation to the given illumination, but *chromatic adaptation* in the human visual system shows *inconsistent* adaptation to a given illumination; hence, a chromatic adaptation model focuses on formulating these inconsistent trends in perceiving hue (see Section 2.3.4 for more details). Many colour constancy methods have been proposed and we can only mention the most related methods; for a more complete overview, see [Hordley, 2006].

In order to estimate the unknown scene illumination from camera signals only, assumptions are usually made about aspects of real-world images. The grey-world method [Buchsbaum, 1980; van de Weijer and Gevers, 2005] assumes that the average reflectance or colour derivative in a scene is grey, whereas the maxRGB method [Land, 1977] assumes the respectively brightest channel levels in an image correspond to the white point. Instead, prior information about the gamut distribution can be acquired in a learning phase, which is used in the colour-by-correlation method, for instance in [Finlayson et al., 2001]. Statistical prior probability of the training data set can be used to improve the performance of the grey-world method [Barnard et al., 2002; Gijsenij and Gevers, 2007; Gehler et al., 2008]. This requires a large set of training data and long precomputation times.

Despite the large variety of available methods, no algorithm can be regarded as universal. In practice, the grey-world and maxRGB approaches perform well on natural, real-world images [Hordley, 2006; Gijsenij and Gevers, 2007]. We therefore propose an enhanced version of the grey-world algorithm to estimate the scene's correlated colour temperature, which is inspired by Barnard et al. [2002]'s method. However, we derive a linear transform from real-world training images with radiometric measurements instead of synthetic images, and we further apply a weighting scheme that combines the maxRGB and grey-world methods. See Chapter 3 for more details.

2.3 Colour Appearance

Device characterisation describes colour reproduction devices by relating their device-dependent colour specification to device-independent coordinates, e.g., physically-meaningful CIEXYZ. However, this is not sufficient for colour reproduction as given physical stimuli can be perceived differently due to their viewing conditions. Therefore, perceptual attributes, e.g., lightness, chroma, and hue, of a physical colour stimulus need to be communicated rather than physical stimuli. Colour spaces commonly try to ensure that equal scale intervals between stimuli represent approximately equally perceived differences in the attributes considered. Colour appearance models additionally try to model how the human visual system perceive colours under different viewing conditions, e.g., against different backgrounds. The following section presents the background and related work of the human visual system, psychophysical methodology, and colour appearance models.

2.3.1 Human Colour Vision

Colour is caused by the spectral characteristics of reflected or emitted radiance, which is seemingly easy to understand as a physical quantity. However, colour is really a perceptual quantity that occurs *in one's mind, and not in the world*. Therefore, the physical spectrum is commonly decomposed into perceptual quantities using physiological and psychophysical measurements that try to quantify the *human visual system*; e.g., the CIE 1931 standard colorimetric observation [CIE, 1986].

Müller's zone theory of trichromatic vision [Müller, 1930] is commonly used as a basis for deriving computational models of human vision. It describes how the combined effect of retina, ganglion neurons, nerve fibers, and the visual cortex constitutes colour perception (see Figure 2.9).

The retina features cones and rods with different spectral sensitivity. Long (L), middle (M), and short (S) cones are stimulated by approximately red, green, and blue wavelengths respectively, while the rods have achromatic sensitivity. The ratio of the numbers of the three cone types varies significantly among humans [Carroll et al., 2002], but on average it can be estimated as 40:20:1 (L:M:S) [Vos and Walraven, 1971].

In the first stage of the visual system, the eye adapts to the observed brightness level. Two adaptation mechanisms control the effective *cone response*. The pupil changes size and controls the amount of light reaching the retina to a limited extent. In addition to physical adaptation, the retina itself adapts neurologically. Based on measurements of cone responses of primates under varying (flashed) incident retinal light levels I of up to 10^6 td (Troland units: luminance in cd/m^2 × pupil area in mm^2), Valeton and van Norren [1983] found that the response satisfies the *hyperbolic ratio* equation of Naka and Rushton [1966], called Naka-Rushton equation [Equation (2.11)], which originated from the Michaelis-Menten equation [$V/V_m = I/(I+\sigma)$] [Michaelis and Menten, 1913], effectively compressing the response. Normalising the cone response V by the maximum physiological cone response V_m, they derive a general response function:

$$\frac{V}{V_m} = \frac{I^n}{I^n + \sigma^n}\,, \tag{2.11}$$

where n was found to be 0.74 and σ was found to depend directly on the adaptation luminance (varying from 3.5 to 6.3 log td), which shifts the response curve along the log-intensity axis, see Figure 2.10.

In contrast, Boynton and Whitten [1970] assume σ to be constant and that all sensitivity loss is caused by response compression and *pigment bleaching*, which is the basis of many colour appearance models, such as Hunt94, CIECAM97s, and CIECAM02 [Hunt, 1994; CIE, 1998; Moroney et al., 2002]; however, we will demonstrate that for accurate prediction of lightness, σ should be

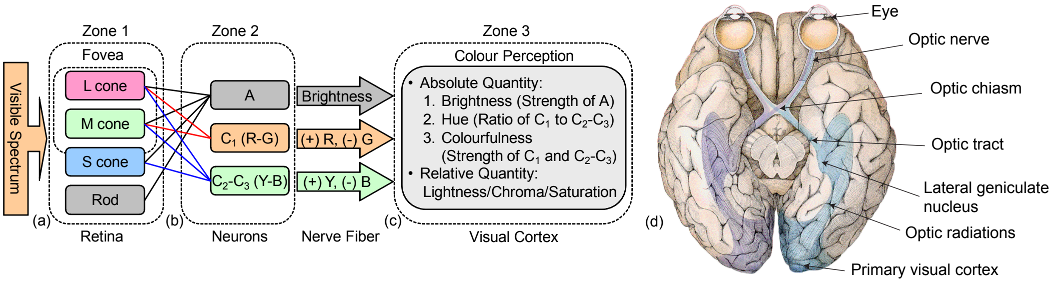

Figure 2.9: *Schematic illustration of human colour vision based on the zone model [Müller, 1930]. Light enters through the pupil and stimulates cones and rods. The given stimulus is sensed by long (L)- and middle (M)-wave cones in the fovea, and short (S)-wave cones and rods outside the fovea (a). The strengths of the four responses are combined to yield achromatic brightness, and the ratio and strength of the C_1 $(L-M)$ channel and the combined C_2 $(M-S)$ and C_3 $(S-L)$ channels yield the* hue *and* colourfulness *sensations. The signals travel along the nerve fiber (crossed at the optical chiasm), are merged into one image in the left and right lateral geniculate nucleus (LGNs), and cause the final visual sensation at the visual cortex (c). Image (d) presents a corresponding anatomical chart of the head.*

allowed to vary. See Chapter 5 for more details on modelling the cone response.

Humans perceive object colours as constant under different illumination; this effect is called colour constancy. It is believed that the underlying mechanism is caused by a slightly different adaptation of each cone type but the details are still debated [Lam, 1985]. It may even be a combination of cone adaptation and processing in the cortex.

According to the zone theory, the cones' and rods' responses are transformed into three neural signals, which are passed along the nerve fibers. A weighted combination of the three cone- and rod-responses yields one achromatic signal A that is perceived as *brightness*. Colour information is transformed in the form of two difference signals: the red/green *opponent colour attribute* is the difference of the L and M cone sensations, $C_1 = L - M$; the yellow/blue opponent colour attribute is the difference of the two difference signals $C_2 = M - S$ and $C_3 = S - L$, that is, $C_2 - C_3$. The ratio of C_1 and $C_2 - C_3$ causes a *hue* sensation in our visual cortex, and their strength conveys *colourfulness*.

Brightness, hue, and colourfulness are the fundamental attributes of colour sensation. They can be used to derive relative quantities that model human colour perception. The ratio of a surface's brightness A and the brightness A_n of the reference white defines the *lightness* sensation [Land and McCann, 1971]. Setting a surface's colourfulness in proportion to the reference brightness A_n yields *chroma*. Similarly, comparing a surface's colourfulness to its own brightness level provides the *saturation* sensation.

Hunt [1998] defines common colour appearance terminologies clearly:

- **Brightness:** attribute of a visual sensation according to which an area appears to exhibit more or less light.
- **Lightness:** the brightness of an area judged relative to the brightness of a similarly illuminated area that appears to be white or very highly transmitting.
- **Colourfulness:** attribute of a visual sensation according to which an area appears to exhibit more or less of its hue.
- **Chroma:** the colourfulness of an area judged in proportion to the brightness of a similarly illuminated area that appears to be white or highly transmitting.

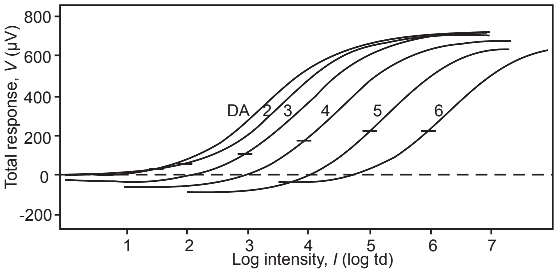

Figure 2.10: *Cone response (V) vs. intensity (log I) curves in the presence of adapting background illumination from dark adapted luminance (DA) to brighter adaptation luminances (2, 3, 4, 5, and 6 log td). Adapted from [Valeton and van Norren, 1983].*

- **Saturation:** the colourfulness of an area judged in proportion to its brightness.
- **Hue:** attribute of a visual sensation according to which an area appears to be similar to one, or to proportions of two, of the perceived colours, red, yellow, green, and blue.

In this thesis, colour appearance attributes will be discussed by using these terminologies.

2.3.2 Quantifying Perception

Colorimetry in Section 2.2.2 describes colour as it directly relates to physical properties. Considering that colour is a perceptual sensation triggered by physical stimuli and that electrophysiological measurements of the human eye and brain are quite limited, experimental psychology is an alternative option to measure human colour perception. Many of the psychophysical measurements necessary for modelling human colour vision have been conducted in recent decades. Psychophysics is the scientific study to derive the relationships between the physical stimuli and the perceptual sensations that those stimuli evoke [Fairchild, 2005]. We conducted psychophysical experiments to quantify human colour perception under high luminance levels to achieve a full range of measurements of the human visual response (see Chapter 4) and to assess and evaluate the accuracy of our colour reproduction system, compared with previous work (see Chapter 6).

Psychophysical analysis originates from *Weber's Law*, which states that the ratio of the change in stimulus intensity that achieve a just noticeable difference to the stimulus intensity is constant, and *Fechner's Law* that defines the relationship between the magnitudes of physical stimuli X and their resulting perceptions S as logarithmic ($S = \ln X$). In modern psychophysics, the relationship between the stimuli and their perceptions is described as a power function ($S = \alpha X^{\beta}$), instead of logarithmic, by *Stevens' Law* [Laming, 1997].

Psychophysical experiments fall into two main categories: *threshold and matching* to measure visual sensitivity to small changes in stimuli (or perceptual equality), e.g., measuring just-noticeable difference (JND) as visual tolerances, and *scaling* to define a supra-threshold relationship between the physical stimuli and the perceptual magnitudes from those stimuli, e.g., LUTCHI colour appearance experiments [Luo et al., 1991a].

Threshold and Matching Two different stimuli are presented to observers who are asked whether they can sense the difference of those stimuli (threshold) or to adjust one of the presented stimuli to match with the other (matching). In general, these methods yield more accurate measurements than the sensory scaling methods. For instance, CIE 1931 standard colorimetric observations were derived from metameric matching experiments [Hunt, 1998]. In these experiments, one colour is presented to one eye and another colour presented to the other eye with a haploscopic device. Colour-normal participants are then asked to adjust one colour to match the other by controlling the proportion of red, green, and blue primary colours. This experiment is based on the assumption that the adaptation of one eye does not influence the other. Unfortunately it imposes unnatural viewing conditions with constrained eye movement.

Sensory Scaling For a given stimulus, observers are asked to produce a numerical *scale* with respect to the intensity of a "*-ness*" property [Engeldrum, 2000], e.g., lightness, colourfulness, or similarity. The scales belong to one of four different categories. A *nominal scale* is an indexing number for classification or identification purposes. An *ordinal scale* presents the rank of a specific property of given candidate stimuli. An *interval* (between scales) describes the difference or distance between the measured property or characteristic. A *ratio* scale is a combined scale of the ordinal and interval scales. This scale includes the zero amount [Fairchild, 2005].

The sensory scaling experiments fall into three main categories: pair comparison, category judgment, and magnitude estimation types. *Pair comparison* is an experiment where each pair combination of a set of stimuli is presented to observers. Observers are then asked to choose which stimulus exhibits more of a property or characteristic being evaluated. So that the experiment is not forced-choice, the observers are allowed to choose that both stimuli are equal. Thurstone's *Law of Comparative Judgement* [Thurstone, 1959] is often used to analyse the collected data to quantify properties of stimuli by transforming them into an interval scale. This method is generally believed to provide better accuracy in quantifying a property compared with other scaling methods.

Category judgement is a method where a possible magnitude of a property (given to observers) is scaled in equal intervals. Observers are asked to judge which category a given stimulus falls into. Torgerson's *Law of Categorical Judgement* [Torgerson, 1958] (extended Thurstone's Law of Comparative Judgement) allows us to transform the equal-interval scales into relatively-positioned interval scales with respect to category boundaries.

Magnitude estimation is an experiment where observers are asked to judge a property of a given stimulus as a ratio scale to represent the extent. Each observer produces different scales, which are different from other observers. *Stevens' Power Law* [Stevens, 1957] is used to manage a large variation of subjective ratio scales of each observer. We used this magnitude estimation method for obtaining human colour perception under high luminance levels. See Chapter 4 for more details on experimental setting and data analysis.

2.3.3 Colour Appearance Phenomena

Colour appearance phenomena occur when identical optical radiation levels are perceived differently in varying viewing environments. The human visual system presents certain characteristics in how it perceives the appearance of colour in specific viewing conditions. These are defined as stimulus, proximal field, background, surround, and adapting field [Hunt, 1998]. *Stimulus* describes the physical radiation that invokes colour appearance, generally in a 2° angle subtended from the visual axis of the human eye. The *proximal field* is the extended area from the edge of a 2° stimulus in all directions. The *background* presents the environment of the main colour stimulus in a 10° area, outside the 2° stimulus. The *surround* is the field outside the background. See Figure 2.11.

Perceived appearance depends on the environmental viewing conditions. Among the various effects, this section presents phenomena with respect to our experiments in Chapter 4 (see [Fairchild, 2005] for more details on other phenomena):

- **Luminance Effect on Brightness:** Stevens and Stevens [1963] describe brightness perception

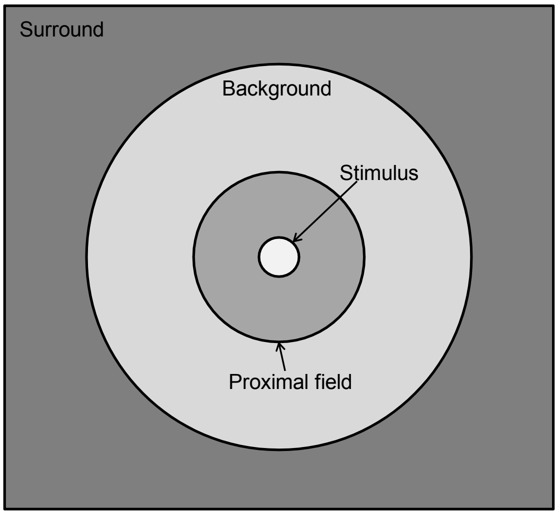

Figure 2.11: *Specification of components of the viewing field. Stimulus describes the physical radiation, generally in a 2° angle subtended from the visual axis of the human eye. The proximal field is the extended area from the edge of a 2° stimulus in all directions. The background presents the environment of the main colour stimulus in a 10° area, outside the 2° stimulus. The surround is the field outside the background. Adapted from [Fairchild, 2005].*

trends with respect to luminance. They state that the perceived brightness changes according to luminance and model brightness perception as a power function where the exponent depends on a luminance. This is the *Stevens effect*. Suppose two identical grey-scales are placed in a dark room and a bright room. The contrasts of the perceived brightnesses appear differently. At a low luminance level, the contrast of the perceived grey-scale appears decreased, while at a high luminance level, the perceived contrast increases, i.e., the dark colours appear darker, and middle or brighter colours appear brighter under higher luminance levels. This effect is observed in our experimental data. However, the trend appears more complicated than a simple power raise. See Chapter 5 for more details on our proposed numerical model for the Stevens effect.

- **Luminance Effect on Colourfulness:** The level of luminance influences not only contrast, but also colourfulness. Suppose we look at colourful objects under bright sun light but we also observe the identical objects in a dim room. Comparison of the perceived colourfulness find that the colourfulness of a given stimulus increases with the luminance level; the so-called *Hunt effect* [Hunt, 1952]. The Hunt effect is also confirmed by our colour experiments (see Chapter 4). While Hunt [1952] uses a haploscopic device where two different levels of luminance are presented to the left and the right eyes respectively, we conducted a psychophysical memory experiment (see Chapter 4 for more details on the experiments).
- **Background Effect:** Suppose two identical grey patches are placed on two different backgrounds, white and black. The grey patch on the black background appears lighter, while

the identical patch on the white background appears darker. This is called the *simultaneous contrast effect*. The change in the background causes the change of colour appearance [Albers, 1963]. The simultaneous contrast for these stimuli depends on the spatial structure of the environment, rather than colours or edges. These changes were observed for not only lightness but also for colourfulness in our colour experiments (see Chapter 4 for more details on the initial findings).

- **Surround Effect:** Breneman [1977] describes the effects of surround with respect to luminance. Suppose two identical grey-scales are placed under average and dark surround respectively. The perceived contrast of lightness under the dark surrounds increases while the contrast under the average surround decreases. Our experimental data indicates that lightness contrast decreases while colourfulness increases as the luminance level of the surround increases. However, as observed in Breneman [1977], our data confirms that the difference was small and statistically insignificant(see Chapter 4).
- **Helson-Judd effect:** Helson [1938] states that the chromatic adaptation mechanism works imperfectly depending on the lightness of the objects. For instance, if a grey scale is illuminated by a yellowish light source like tungsten light, the lighter patches will appear yellowish exhibiting a certain amount of the hue of the light source. In contrast, the darker patches in the grey scale will appear bluish.
- **Purkinje Break & Shift:** Purkinje [1825] describes the activity transition of cones and rods with respect to luminance. In the luminance range between 0 and $\sim$100 cd/m^2 (called mesopic vision), as luminance decreases, cones are gradually deactivated, and rods start to contribute in sensing luminance. At a certain luminance level (called Purkinje break), the threshold of luminance increases such that the cones and rods both contribute to luminance perception. However, further decreases of luminance deactivates cones, and then only rods contribute to vision. Under dark luminance conditions, the scotopic vision (only rods) also presents different spectral sensitivity, called Purkinje shift, from photopic vision (only cones). In dark viewing conditions, the eye's luminance sensitivity shifts toward short-wavelengths (bluish) a little, defined as the CIE $V'(\lambda)$ function [CIE, 1986]. Peak sensitivity of luminance shifts from 560nm to 510nm. Targeting extended luminance levels, our model covers photopic vision only. This phenomenon is not modelled in our appearance model.

LUTCHI Colour Appearance Experiments In order to quantify colour appearance phenomena, many extensive experiments have been conducted. In particular, the magnitude estimation experiments conducted at the Loughborough University of Technology Computer Human Interface (LUTCHI) Research Centre provide a significant amount of measurements of colour appearance on a large variety of media from reflective materials to CRT monitors [Luo et al., 1991a,b, 1993a,b, 1995]. The LUTCHI data set includes relative tristimulus values, viewing conditions (e.g., reference white, background luminance level, and medium type), and corresponding colour appearance measurements. The data set has been used to revise the Hunt colour appearance model [Hunt, 1991] and to derive the LLAB model [Luo et al., 1996]. International standard colour appearance models, CIECAM97s [CIE, 1998] and CIECAM02 [Moroney et al., 2002], are also derived from this data set.

In [Luo et al., 1991a], six to seven trained colour-normal participants were asked to rate scales with respect to lightness, colourfulness, and hue of the given stimuli. The viewing environments varied the level of illumination (low and high, up to ∼250 cd/m^2), medium type (reflective and CRT), background (white, grey, and black), and white point (CIE A, D50, D65 illuminant). The results show that the background and reference white influence colour appearance significantly. In our experiments, we used the almost identical experimental settings to these LUTCHI experiments. See Sections 4.2 and 4.3.1 for more details. Luo et al. [1991b] compares the performance of a several colour appearance models, namely CMC, CIELAB, Nayatani's, Hunt's 87, and Hunt-ACAM (being the Alvey Colour Appearance Model), in terms of lightness, colourfulness, and hue. Overall, the Hunt-ACAM model performs better than the others.

In particular, Luo et al. [1993a] measured brightness along with lightness perception, which is the only available data set for the relationship between lightness and brightness. Those properties were measured under six different luminance levels of CIE D50 illuminant. Luo et al. [1993b] describe the measurements of colour appearance on cut-sheet transparency and 35mm projection, which are under high levels of luminance up to 1 272 cd/m^2. However, they used only four colour samples between 1 000 and 1 272 cd/m^2. Luo et al. [1995] specifically examined the simultaneous contrast effect. Five observers scaled lightness, colourfulness, and hue on a CRT display with varying proximal fields around the main colour samples. This is used for testing the performance of predicting simultaneous contrast in the Hunt model.

The LUTCHI colour appearance experiments provide an excellent methodology to measure the perceived colour appearance in a scientific way, and it covers a very wide range of media from reflective materials to CRT displays. However, most of the luminance levels in the experimental data are under approximately 690 cd/m^2, which was limited by the available display technology in the 90s. This range of luminance falls short of covering the full range of the human visual system (which is five-orders of magnitude). Consequently, perceptual colour appearance under extended luminance levels has not been studied, mainly due to the unavailability of psychophysical data. Therefore, we conducted psychophysical colour experiments in order to acquire appearance data for many different luminance levels (up to 16 860 cd/m^2) covering most of the dynamic range of the human visual system (see Chapter 4 for more details). These experimental data allow us to quantify human colour perception under extended luminance levels, yielding a new colour appearance model.

Coefficient of Variation In order to evaluate the performance of the colour appearance models, Luo et al. [1991b] compared models' predicted attributes to their perceptual measurements of colour appearance. They evaluated the qualitative difference by employing *coefficient of variation* (CV); RMS error with respect to mean in percentage scale. Suppose there are two different data sets x

and y. The calculation of CV is:

$$\mathrm{CV} = \frac{100}{\overline{y}} \sqrt{\frac{1}{N} \sum_i (x_i - y_i)^2}\,, \tag{2.12}$$

where $\overline{y}$ is the mean of the data set y; N number of y elements. The deviation in this CV is calculated from the difference between two elements $(x_i - y_i)$ like RMS error, which is then normalised by the mean. As opposed to this paired comparison, when evaluating the *sample variation* of a group x, like inter-observer variation, the difference between each element and the mean $(x_i - \overline{x})$ is used instead of the difference of each element $(x_i - y_i)$ in Equation (2.12):

$$\mathrm{CV} = \frac{100}{\overline{x}} \sqrt{\frac{1}{(N-1)} \sum_i (x_i - \overline{x})^2}\,, \tag{2.13}$$

where $(N-1)$ is the degree of freedom. We only have $(N-1)$ independent deviations such that the sum of the N deviations from the mean is always zero: $\sum_i (x_i - \overline{x}) = 0$. We employed these CV error methods for evaluating our experiments and model performance in qualitative comparison with others.

2.3.4 Colour Appearance Models

A colour appearance model (CAM) is a numerical model of the human *colour vision* mechanism. Common colour appearance models largely follow the zone theory by modelling human colour vision as a four-stage procedure, shown in Figure 2.12, comprising chromatic adaptation, dynamic cone adaptation, achromatic/opponent colour decomposition, and computation of perceptual attribute correlates. Generally, colour appearance models take tristimulus XYZ values (of the colour to be perceived) and parameters of the viewing condition to yield perceptual attributes predicting the perceived colour (commonly lightness, chroma, and hue). Colour appearance models mostly differ in the specific functions that transform colour quantities across these four stages, the quality of their prediction, and the different viewing conditions that can be modelled. Popular models are

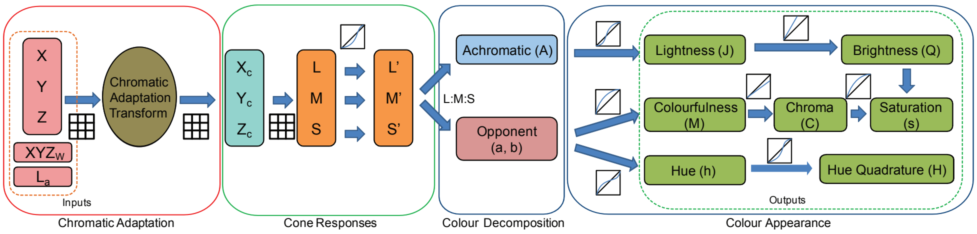

Figure 2.12: *Modern colour appearance models roughly follow these four stages. First, the incoming spectrum, sampled as an XYZ triple, is transformed for chromatic adaptation. This is usually done in a specialised colour space (though not always). Then, the white-adapted XYZ_c is transformed into the cone colour space, where a cone-response function is applied (commonly a power or hyperbolic function). After that, the signal is decomposed in the achromatic channel A and the colour opponent channels a and b. The perceptual correlates are based on these three channels. This is where colour appearance models differ most, as a large range of functions are applied to yield perceptual values.*

the simple CIELAB model, RLAB [Fairchild, 1991], Hunt94 [Hunt, 1994], LLAB [Luo et al., 1996], CIECAM97s [CIE, 1998], up to the recent and currently widely accepted CIECAM02 [Moroney et al., 2002].

Many different colour appearance models have been proposed over the years. We will briefly review the common models with more details on their mathematical modelling (see [Fairchild, 2005] for a complete overview of other colour appearance models). For the purpose of developing our colour appearance model, we conducted a review of the mathematical details of other colour appearance models.

This section contains detailed description of the mathematics of the models. This is included as a reference to the reader for completeness. Section 2.3.6 summarises the following models in sufficient detail for those readers not requiring the reference.

CIELAB CIELAB (or CIELCH) [CIE, 1986] is a very simple colour appearance model that is purely based on XYZ tristimulus values. Chromatic adaptation is performed by dividing XYZ values by normalised white point values XYZ_w. This is a modified form of the von Kries chromatic adaptation transform [von Kries, 1970], and the cone response is modelled as a cube root. Only lightness, chroma, hue, and colour opponents (a and b) are predicted. It does not model any adaptation to different backgrounds or surround changes. Despite these simplifications, it still performs rather well (see Chapter 5 for more details on its performance).

Input parameters to the CIELAB model are:

- Normalised (Y equal to 100) CIE tristimulus values (observed main colours): XYZ,
- Normalised tristimulus values of the reference white point: $X_nY_nZ_n$.

CIELAB takes only normalised input values without taking any environmental viewing conditions into account. The colour appearance attributes are modelled as follows:

$$\text{Lightness} \qquad L^* = 116 f\left(Y/Y_n\right) - 16\,, \tag{2.14}$$

$$\text{Redness} - \text{Greenness} \qquad a^* = 500\left[f\left(X/X_n\right) - f\left(Y/Y_n\right)\right]\,, \tag{2.15}$$

$$\text{Yellowness} - \text{Blueness} \qquad b^* = 200\left[f\left(Y/Y_n\right) - f\left(Z/Z_n\right)\right]\,, \tag{2.16}$$

$$\text{where}\quad f(x) = \begin{cases} x^{1/3}\,, & x > 0.008856 \\ 7.787x + 16/116\,, & x \leq 0.008856 \end{cases}\,, \tag{2.17}$$

$$\text{Chroma} \qquad C^*_{ab} = \sqrt{(a^*)^2 + (b^*)^2}\,, \tag{2.18}$$

$$\text{Hue angle} \qquad h_{ab} = tan^{-1}(b^*/a^*)\,. \tag{2.19}$$

CIELAB is the oldest model that was derived from the psychophysical approach in 1976. Although CIELAB does not consider background or surround environmental conditions, it performs considerably well for general purposes (see Chapter 5 for quantitative comparison).

RLAB RLAB [Fairchild, 1991] is a revised version of CIELAB that takes different viewing conditions into account. In particular, it supports different media and different surround conditions.

RLAB comprises a chromatic adaptation transform and appearance attribute calculation. Chromatic adaptation is performed in LMS cone colour space, but colour attributes are still computed from white-adapted XYZ values.

Input parameters to the RLAB model are:

- Normalised (Y equal to 100) CIE tristimulus values (observed main colours): XYZ,
- Normalised tristimulus values of the reference white point: $X_nY_nZ_n$,
- Level of luminance of the reference white point: Y_N [unit: cd/m^2],
- Model parameters: D and σ,

where D depends on a medium type: $D = 1.0$ corresponds to hard-copy print, soft-copy CRT display yields $D = 0.0$, and an intermediate value is used for projected images in a darkroom. ($D = 0.5$ is used with no available data.) σ corresponds to the surround condition: 1/2.3 (for dark), 1/2.9 (for dim), and 1/3.5 (for average) respectively.

First, the input tristimulus XYZ values are transformed into LMS cone signals by using the Hunt-Pointer-Estévez (HPE) transform, $\mathbf{M}_{\text{HPE}}$, originated from [Estévez, 1979]:

$$\begin{bmatrix} L \\ M \\ S \end{bmatrix} = \mathbf{M}_{\text{HPE}} \cdot \begin{bmatrix} X \\ Y \\ Z \end{bmatrix}, \ \mathbf{M}_{\text{HPE}} = \begin{bmatrix} 0.38971 & 0.68898 & -0.07868 \\ -0.22981 & 1.18340 & 0.04641 \\ 0.00000 & 0.00000 & 1.00000 \end{bmatrix}. \tag{2.20}$$

From the transformed cone signals, the model computes von Kries chromatic adaptation scalars a_L, a_M, and a_S to accomplish chromatic adaptation in the LMS cone colour space:

$$a_L = \frac{p_L + D(1-p_L)}{L_n}, \quad a_M = \frac{p_M + D(1-p_M)}{M_n}, \quad a_S = \frac{p_S + D(1-p_S)}{S_n}, \tag{2.21}$$

where the inner parameters p_L, p_M, and p_S are calculated as follows:

$$p_L = \frac{(1+Y_N^{1/3}+l_E)}{(1+Y_N^{1/3}+1/l_E)}, \quad p_M = \frac{(1+Y_N^{1/3}+m_E)}{(1+Y_N^{1/3}+1/m_E)}, \quad p_S = \frac{(1+Y_N^{1/3}+s_E)}{(1+Y_N^{1/3}+1/s_E)}, \tag{2.22}$$

$$\text{where} \quad l_E = \frac{3L_n}{L_n+M_n+S_n}, \quad m_E = \frac{3M_n}{L_n+M_n+S_n}, \quad s_E = \frac{3S_n}{L_n+M_n+S_n}. \tag{2.23}$$

The adaptation scalars form a diagonal matrix $\mathbf{A}$ to apply to the adaptation transform, then the cone signals are transformed into tristimulus values with respect to the model's reference viewing condition (CIE D65 illuminant in 318 cd/m^2).

$$\begin{bmatrix} X_{ref} \\ Y_{ref} \\ Z_{ref} \end{bmatrix} = \mathbf{R} \cdot \mathbf{A} \cdot \mathbf{M}_{\text{HPE}} \cdot \begin{bmatrix} X \\ Y \\ Z \end{bmatrix}, \ \mathbf{R} = \left(\mathbf{A}_{ref} \cdot \mathbf{M}_{\text{HPE}}\right)^{-1} = \begin{bmatrix} 1.9569 & -1.1882 & 0.2313 \\ 0.3612 & 0.6388 & 0.0000 \\ 0.0000 & 0.0000 & 1.0000 \end{bmatrix}. \tag{2.24}$$

Then, the colour appearance attributes are modelled as follows:

$$\text{Lightness} \qquad L^R = 100\left(Y_{ref}\right)^{\sigma}, \tag{2.25}$$

$$\text{Redness} - \text{Greenness} \qquad a^R = 430\left[\left(X_{ref}\right)^{\sigma} - \left(Y_{ref}\right)^{\sigma}\right], \tag{2.26}$$

$$\text{Yellowness} - \text{Blueness} \qquad b^R = 170\left[\left(Y_{ref}\right)^{\sigma} - \left(Z_{ref}\right)^{\sigma}\right], \tag{2.27}$$

$$\text{Chroma} \qquad C^R = \sqrt{(a^R)^2 + (b^R)^2}, \tag{2.28}$$

$$\text{Saturation} \qquad s^R = \frac{C^R}{L^R}, \tag{2.29}$$

$$\text{Hue angle} \qquad h^R = tan^{-1}(b^R/a^R). \tag{2.30}$$

Finally, hue composition H^R is calculated by linear interpolation of the values in Table 2.3.

h^R	Red	Blue	Green	Yellow	H^R
24	100	0	0	0	R
90	0	0	0	100	Y
162	0	0	100	0	G
180	0	21.4	78.6	0	B79G
246	0	100	0	0	B
270	17.4	82.6	0	0	R83B
0	82.6	17.4	0	0	R17B
24	100	0	0	0	R

Table 2.3: *Hue angle conversion to hue composition in the RLAB model.*

The RLAB model includes a rigorous medium parameter D, accepting that colour appearance depends on medium type. On the other hand, it conducts the chromatic adaptation in the physiological cone colour space; but we experienced that its hue and colourfulness estimation performance is reduced when compared to the original, CIELAB (see Chapter 5 for more details on comparison). Thus, we were skeptical that the physiologically-plausible structure is a better choice than the hybrid structure (psychophysical chromatic adaptation and physiological pipeline), and our model inherits the hybrid structure instead of the physiologically-plausible structure for chromatic adaptation (see Chapter 5).

Hunt94 Hunt94 is the latest in a series of colour appearance models by the author [Hunt, 1982; Hunt and Pointer, 1985; Hunt, 1987, 1991, 1994]. The Hunt94 model is a predecessor to the CIECAM97s model. The Hunt94 model is based on the physiological zone theory [Müller, 1930]. For instance, the Hunt94 model does not have the separate chromatic adaptation procedure at the beginning, whereas the adaptation is generally adopted for high accuracy in other colour appearance models. To place chromatic adaptation before the cone responses using the von Kries transform is not physiologically plausible, at least under the assumption that not the cones but the visual cortex interprets the hue of colours. Differing from CIECAM97s and CIECAM02, the chromatic adaptation in the Hunt94 model is implemented as part of the cone adaptation calculation. Nonetheless, the Hunt94 model provides a basic structure in comparison to other colour appearance models. However, its application has been limited by the mathematical complexity of the model (the most complicated model ever).

The model comprises three stages: dynamic cone adaptation, colour decomposition (achromatic and colour opponent signals), and colour appearance attribute modelling. It has the largest number of input parameters among colour appearance models:

- Normalised (Y equal to 100) CIE tristimulus values (observed main colours): XYZ,
- Normalised tristimulus values of the reference white point: $X_W Y_W Z_W$,
- Level of luminance adaptation: L_A [unit: cd/m^2]
  (L_A is normally taken to be 20% of the luminance of the reference white.),
- Normalised luminance of background: Y_b,
- Scotopic luminance of the adapting field: L_{AS} [unit: scotopic cd/m^2]
  (L_{AS} can alternatively be approximated from the photopic luminance adaptation: $L_{AS} = 2.26 L_A (T/4000 - 0.4)^{1/3}$ where T is correlated colour temperature),
- Scotopic normalised luminance of colour sample to the reference white: S/S_W,
  (If it is not available, Y/Y_W can be substituted instead.)
- Background parameters: N_{cb} and N_{bb} [$N_{cb} = N_{bb} = 0.725(Y_W/Y_b)^{0.2}$],
- Surround parameters (specified in Table 2.4): N_b and N_c.

Surround conditions	N_b	N_c
Small areas in uniform backgrounds and surrounds	300	1.0
Normal scenes	75	1.0
Television and CRT displays in dim surrounds	25	1.0
Cut-sheet transparencies on light boxes	25	0.7
Projected transparencies in dark surrounds	10	0.7

Table 2.4: *Surround parameters in the Hunt94 model.*

First, the input tristimulus values are transformed into a physiological cone colour spaces using the HPE transform (see 2.20 for more details of the transform):

$$\begin{bmatrix} \rho \\ \gamma \\ \beta \end{bmatrix} = \mathbf{M}_{\text{HPE}} \cdot \begin{bmatrix} X \\ Y \\ Z \end{bmatrix}. \tag{2.31}$$

They are then compressed by the revised Naka-Rushton equation [see Equations (2.11) and (2.33)]:

$$\begin{aligned} \rho_a &= B_\rho [f_n(F_L F_\rho \rho/\rho_W) + \rho_D] + 1\,, \\ \gamma_a &= B_\gamma [f_n(F_L F_\gamma \gamma/\gamma_W) + \gamma_D] + 1\,, \\ \beta_a &= B_\beta [f_n(F_L F_\beta \beta/\beta_W) + \beta_D] + 1\,, \end{aligned} \tag{2.32}$$

where the function f_N is defined as:

$$f_n(I) = 40[I^{0.73}/(I^{0.73}+2)]\,. \tag{2.33}$$

Here we can observe the exponent constant is almost identical to [Valeton and van Norren, 1983] (0.73 ≈ 0.74), which is derived from primate cone measurements. The luminance-level adaptation is modelled as F_L, which is inherited in CIECAM97s and CIECAM02:

$$F_L = 0.2k^4(5L_A) + 0.1(1-k^4)^2(5L_A)^{1/3},\ k = 1/(5L_A+1)\,. \tag{2.34}$$

The formulae below also include the chromatic adaptation factors F_ρ, F_γ, and F_β, which are modelled as follows:

$$\begin{aligned} F_\rho &= (1+L_A^{1/3}+h_\rho)/(1+L_A^{1/3}+1/h_\rho)\,,\\ F_\gamma &= (1+L_A^{1/3}+h_\gamma)/(1+L_A^{1/3}+1/h_\gamma)\,,\\ F_\beta &= (1+L_A^{1/3}+h_\beta)/(1+L_A^{1/3}+1/h_\beta)\,, \end{aligned} \tag{2.35}$$

where parameters h_ρ, h_γ, and h_β are modelled:

$$h_\rho = 3\rho_W/(\rho_W+\gamma_W+\beta_W)\,,\ h_\gamma = 3\gamma_W/(\rho_W+\gamma_W+\beta_W)\,,\ h_\beta = 3\beta_W/(\rho_W+\gamma_W+\beta_W)\,. \tag{2.36}$$

As opposed to other appearance models, the Hunt94 model predicts the Helson-Judd effect (see Section 2.3.3 for more details on the effect) and the cone pigment bleaching effect. In the above formulae, scalars ρ_D, γ_D, and β_D are used for modelling the Helson-Judd effect:

$$\begin{aligned} \rho_D &= f_n[(Y_b/Y_W)F_L F_\gamma] - f_n[(Y_b/Y_W)F_L F_\rho]\,,\\ \gamma_D &= 0.0\,,\\ \beta_D &= f_n[(Y_b/Y_W)F_L F_\gamma] - f_n[(Y_b/Y_W)F_L F_\beta]\,. \end{aligned} \tag{2.37}$$

The pigment bleach is modelled as follows:

$$\begin{aligned} B_\rho &= 10^7/[10^7+5L_A(\rho_W/100)]\,,\\ B_\gamma &= 10^7/[10^7+5L_A(\gamma_W/100)]\,,\\ B_\beta &= 10^7/[10^7+5L_A(\beta_W/100)]\,. \end{aligned} \tag{2.38}$$

For the next stage, the Hunt94 model calculates achromatic signals and colour opponent signals. The achromatic signal transform in the Hunt94 model is rather complicated. The Hunt94 model even considers the photopic and scotopic vision. First, photopic vision is modelled by taking a weighted average of the three cones (L:M:S ≈ 40:20:1) [Vos and Walraven, 1971]:

$$A_a = 2\rho_a + \gamma_a + (1/20)\beta_a - 3.05 + 1\,. \tag{2.39}$$

Second, the scotopic vision is modelled in a more complex way as follows:

$$A_S = 3.05B_S[f_n(F_{LS}S/S_W)] + 0.3\,, \tag{2.40}$$

where the parameters F_{LS} and B_S are defined as:

$$F_{LS} = 3800j^2 5L_{AS}/2.26 + 0.2(1-j^2)^4(5L_{AS}/2.26)^{1/6}\,, \tag{2.41}$$

$$\text{where} \quad j = 0.00001/(5L_{AS}/2.26 + 0.00001)\,, \tag{2.42}$$

$$B_S = 0.5/\{1 + 0.3[(5L_{AS}/2.26)(S/S_W)]^{0.3}\} + 0.5/[1 + 5(5L_{AS}/2.26)]\,. \tag{2.43}$$

The photopic and scotopic achromatic signals, A_a and A_S, are combined to an achromatic signal:

$$A = N_{bb}(A_a - 1 + A_S - 0.3 + \sqrt{1^2 + 0.3^2})\,. \tag{2.44}$$

Then, the intermediate colour opponent signals C_1, C_2, and C_3 are derived from zone theory:

$$C_1 = \rho_a - \gamma_a,\;\; C_2 = \gamma_a - \beta_a,\;\; C_3 = \beta_a - \rho_a\,. \tag{2.45}$$

These parameters yield redness–greenness and yellowness–blueness coordinates:

$$\text{Redness} - \text{Greenness} \qquad M_{RG} = 100[C_1 - (C_2/11)][e_S(10/13)N_c N_{cb}]\,, \tag{2.46}$$

$$\text{Yellowness} - \text{Blueness} \qquad M_{YB} = 100[(1/2)(C_2 - C_3)/4.5][e_S(10/13)N_c N_{cb} F_t]\,, \tag{2.47}$$

$$\text{where} \quad e_S = e_1 + (e_2 - e_1)\frac{(h_S - h_1)}{(h_2 - h_1)}, \tag{2.48}$$

$$F_t = L_A/(L_A + 0.1)\,. \tag{2.49}$$

Finally, the following colour appearance attributes are modelled, where the Hunt94 model calculates the brightness level first, then computes lightness:

$$\text{Brightness} \qquad Q = [7(A + M/100)]^{0.6}N_1 - N_2\,, \tag{2.50}$$

$$\text{where} \quad M = \sqrt{M_{RG}^2 + M_{YB}^2}\,,\; N_1 = \frac{(7A_W)^{0.5}}{5.33N_b^{0.13}},\; N_2 = \frac{7A_W N_b^{0.362}}{200}\,, \tag{2.51}$$

$$\text{Lightness} \qquad J = 100\left(\frac{Q}{Q_W}\right)^z, \text{ where } \; z = 1 + (Y_b/Y_W)^{0.5}\,, \tag{2.52}$$

where the achromatic signal Q_W of the reference white point XYZ_W is calculated in the same way as XYZ main colours. In this model, lightness and brightness are related with saturation, chroma, and colourfulness through the chromatic response parameter M [see Equation (2.51)]:

$$\text{Saturation} \qquad s = 50M/(\rho_a + \gamma_a + \beta_a)\,, \tag{2.53}$$

$$\text{Chroma} \qquad C_{94} = 2.44s^{0.69}(Q/Q_W)^{Y_b/Y_W}(1.64 - 0.29^{Y_b/Y_W})\,, \tag{2.54}$$

$$\text{Colourfulness} \qquad M_{94} = C_{94}F_L^{0.15}\,. \tag{2.55}$$

The hue angle h_s is computed from the internal colour opponent signals, and the hue quadrature H (0–400) is computed by interpolating with respect to the eccentricity of each hue:

$$\text{Hue} \qquad h_S = \tan^{-1}\left[\frac{(C_2 - C_3)/9}{C_1 - (C_2/11)}\right], \tag{2.56}$$

$$\text{Hue quadrature} \qquad H = H_1 + \frac{100(h_S - h_1)/e_1}{(h - h_1)/e_1 + (h_2 - h)/e_2}\,, \tag{2.57}$$

Unique Hue	Red	Yellow	Green	Blue
Hue angle h_S	20.14	90.00	164.25	237.53
Eccentricity e_S	0.8	0.7	1.0	1.2
Hue quadrature H	0	100	200	300

Table 2.5: *Hue eccentricity parameters in the Hunt94 model.*

where H_1, h_1, and e_1 are the hue quadrature, the hue angle, and the eccentricity values of the nearest lower unique hue angle of a given hue angle h_S; h_2 and e_2 are the hue angle and the eccentricity values of the nearest higher unique hue angle of h_S in Table 2.5.

The Hunt94 model was derived from a long study on photographic media, conducted at the Kodak research lab [Hunt, 1982; Hunt and Pointer, 1985; Hunt, 1987, 1991, 1994]. The formulae and structures were accumulated over many years. However, it involves a high complexity in mathematics, which results in a high computational cost and limits the model's broad application. However, it forms the basic structure of modern colour appearance models.

LLAB The LLAB model [Luo et al., 1996] was derived from the analysis of psychophysical experimental data, namely the LUTCHI colour appearance data set [Luo et al., 1991a,b, 1993a,b, 1995] (see Section 2.3.3 for more details). The LLAB model comprises chromatic adaptation (adopted from the so-called Bradford chromatic adaptation transform [Lam, 1985]) and a revised CIELAB colour space. Its structure is similar in a sense to the RLAB model. The LLAB model takes background measurements and surround parameters in order to predict the change of colour appearance by the luminance levels of background and surround, as observed in their experimental data.

We review the mathematical details of this model that were revised and presented in [Luo and Morovic, 1996]. The input parameters to the LLAB model are:

- Normalised (Y equal to 100) CIE tristimulus values (observed main colours): XYZ,
- Normalised tristimulus values of the reference white point (test): $X_oY_oZ_o$.
- Normalised tristimulus values of the reference white point (target): $X_{o_r}Y_{o_r}Z_{o_r}$
  (The reference illuminant is defined to be CIE illuminant D65,
  $XYZ_{o_r} = [95.05, 100.00, 108.08]$).
- Level of luminance of the reference white point: L [unit: cd/m^2],
- Normalised luminance of background: Y_b,
- Surround parameters: D, F_S, F_L, and F_C (see Table 2.6).

First, normalised input tristimulus values are transformed into a psychophysically *sharpened* (optimised) colour space through the Bradford chromatic adaptation transform $\mathbf{M}_{\mathrm{BFD}}$ [Lam, 1985]:

$$\begin{bmatrix} R \\ G \\ B \end{bmatrix} = \mathbf{M}_{\mathrm{BFD}} \cdot \begin{bmatrix} X/Y \\ Y/Y \\ Z/Y \end{bmatrix}, \quad \mathbf{M}_{\mathrm{BFD}} = \begin{bmatrix} 0.8951 & 0.2664 & -0.1614 \\ -0.7502 & 1.7135 & 0.0367 \\ 0.0389 & -0.0685 & 1.0296 \end{bmatrix}. \tag{2.58}$$

Surround conditions	D	F_S	F_L	F_C
Reflective samples in average surround (>4°)	1.0	3.0	0.0	1.0
Reflective samples in average surround (≤4°)	1.0	3.0	1.0	1.0
Television in dim surround	0.7	3.5	1.0	1.0
Cut-sheet transparencies in dim surround	1.0	5.0	1.0	1.1
35mm projection transparencies in dark surround	0.7	4.0	1.0	1.0

Table 2.6: *Surround parameters in the LLAB model.*

Three cone responses are adapted to the test reference white point as follows:

$$R_r = [D(R_{o_r}/R_o) + 1 - D]R\,, \tag{2.59}$$

$$G_r = [D(G_{o_r}/G_o) + 1 - D]G\,. \tag{2.60}$$

In particular, the blue response is changed nonlinearly:

$$B_r = \begin{cases} [D(B_{o_r}/B_o^{\beta}) + 1 - D]B^{\beta}\,, & B > 0 \\ -[D(B_{o_r}/B_o^{\beta}) + 1 - D]\,|B|^{\beta}\,, & B \leq 0 \end{cases}\,, \quad \text{where} \quad \beta = (B_o/B_{o_r})^{0.0834}\,. \tag{2.61}$$

The above function is added to achieve a better fit of the model to the psychophysical experimental data, improving the accuracy of the chromatic adaptation [Lam, 1985]. However, it leads to non-equal energy of the three cones and also limits the analytical invertibility of the chromatic adaptation. The scaled RGB responses are transformed back to tristimulus XYZ values:

$$\begin{bmatrix} X_r \\ Y_r \\ Z_r \end{bmatrix} = \mathbf{M}_{\text{BFD}}^{-1} \cdot \begin{bmatrix} R_r Y \\ G_r Y \\ B_r Y \end{bmatrix}\,. \tag{2.62}$$

In the second stage, the LLAB model computes colour appearance attributes. Lightness and colour opponent channels are modelled in a similar way to CIELAB:

$$\text{Lightness} \qquad L_L = 116 f(Y_r/100)^z - 16\,,\ \ z = 1 + F_L(Y_b/100)^{1/2}\,, \tag{2.63}$$

$$\text{Redness} - \text{Greenness} \qquad A = 500\left[f\left(X_r/X_{o_r}\right) - f\left(Y_r/Y_{o_r}\right)\right]\,, \tag{2.64}$$

$$\text{Yellowness} - \text{Blueness} \qquad B = 200\left[f\left(Y_r/Y_{o_r}\right) - f\left(Z_r/Z_{o_r}\right)\right]\,, \tag{2.65}$$

$$\text{where} \ \ f(x) = \begin{cases} x^{1/F_s}\,, & x > 0.008856 \\ \left(\frac{0.008856^{1/F_s} - \frac{16}{116}}{0.008856}\right)x + \frac{16}{116}\,, & x \leq 0.008856 \end{cases}\,.$$

The other colour appearance attributes are calculated as follows:

$$\text{Chroma} \qquad Ch_L = 25\ln(1+0.05C), \text{ where } C = \sqrt{A^2+B^2}), \tag{2.66}$$

$$\text{Colourfulness} \qquad C_L = Ch_L S_M S_C F_C\,, \tag{2.67}$$

$$\text{where } S_M = 0.7+0.02L_L - 0.0002L_L^2\,, \tag{2.68}$$

$$S_C = 1.0+0.47\log L - 0.057(\log L)^2\,, \tag{2.69}$$

$$\text{Saturation} \qquad S_L = \frac{Ch_L}{L_L}\,, \tag{2.70}$$

$$\text{Hue angle} \qquad h_L = tan^{-1}(B/A)\,, \tag{2.71}$$

$$\text{Hue quadrature} \qquad H_L = H_{L1} + (H_{L2} - H_{L1})(h_L - h_{L1})/(h_{L2} - h_{L1})\,, \tag{2.72}$$

where H_{L1} and h_{L1} are the hue quadrature and the hue angle of the nearest lower unique hue angle of a given hue angle h_L; H_{L2} and h_{L2} are the hue quadrature and the hue angle of the nearest higher unique hue angle of h_L in Table 2.7.

h_L	H_L	Red	Yellow	Green	Blue	NCS expression
25	0	100	0	0	0	R
62	50	50	50	0	0	R50Y
93	100	0	100	0	0	Y
118	150	0	50	50	0	Y50G
165	200	0	0	100	0	G
202	250	0	0	50	50	G50B
254	300	0	0	0	100	B
322	350	50	0	0	50	B50R

Table 2.7: *Hue angle conversion to hue composition in the LLAB model.*

As observed in the RLAB model, the LLAB model noted that the colour appearance depends on the medium type, so the LLAB model includes medium-dependent parameters, e.g., for cut-sheet transparencies distinctive from other reflective media. We also experienced and include such a change of colour appearance due to the medium type after analysis of our experimental data and LUTCHI data (see Chapter 5 for more details).

CIECAM97s CIECAM97s [CIE, 1998] is a predecessor to CIECAM02 and similar in spirit to, but much more complex than, CIECAM02. Historically, CIECAM97s is a combination of the Hunt94 model (having physiological plausibleness) and the LLAB model (based on psychophysical data). The chromatic adaptation transform, the Bradford chromatic adaptation transform [Lam, 1985], is adopted from the LLAB model. The structure is adopted from the Hunt94 model. It is a considerable challenge to merge the psychophysical (LLAB) and physiologically-plausible (Hunt94) aspects into a model to achieve improved performance. However, its practical applicability is limited. For instance, the Bradford chromatic adaptation transform is non-invertible as it includes non-linear compression of the short cone (blue) signals, and the performance in the prediction of saturation is unstable as it is influenced by its hue and luminance levels. CIECAM02 is in many respects its simpler but more powerful successor, overcoming the drawbacks of CIECAM97s.

We review the mathematical details of the CIECAM97s model. The input parameters for this model are:

- Normalised (Y equal to 100) CIE tristimulus values (observed main colours): XYZ,
- Normalised tristimulus values of the reference white point: $X_W Y_W Z_W$,
- Level of luminance adaptation: L_A [unit: cd/m^2]
  (L_A is normally taken to be 20% of the luminance of the reference white.),
- Normalised luminance of background: Y_b,
- Surround parameters (specified in Table 2.8): c, N_c, F, and F_{LL}.

In particular, the input parameters to the CIECAM97s model includes a medium-dependent parameter F_{LL} for the surround (see Table 2.8). The parameter specifies cut-sheet transparencies data, which is removed in CIECAM02.

Surround conditions	c	N_c	F	F_{LL}
Average surround (>4°)	0.69	1.0	1.0	0.0
Average surround (≤4°)	0.69	1.0	1.0	1.0
Dim surround	0.59	1.1	0.9	1.0
Dark surround	0.525	0.8	0.9	1.0
Cut-sheet transparencies	0.41	0.8	0.9	1.0

Table 2.8: *Surround parameters in the CIECAM97s model.*

For the first stage, the CIECAM97s model uses the Bradford chromatic adaptation transform, $\mathbf{M}_{\mathrm{BFD}}$ [see Equation (2.58) in the LLAB model], which is often called CMCCAT97, which is inherited from the LLAB model:

$$\begin{bmatrix} R \\ G \\ B \end{bmatrix} = \mathbf{M}_{\mathrm{BFD}} \cdot \begin{bmatrix} X/Y \\ Y/Y \\ Z/Y \end{bmatrix} . \tag{2.73}$$

As in the LLAB model, red and green responses are adapted to the test reference white point as follows:

$$R_c = [D(1.0/R_W) + 1 - D]R \,, \tag{2.74}$$

$$G_c = [D(1.0/G_W) + 1 - D]G \,, \tag{2.75}$$

$$B_c = \begin{cases} [D(1.0/B_W^p) + 1 - D]B^p \,, & B > 0 \\ -[D(1.0/B_W^p) + 1 - D]\,|B|^p \,, & B \le 0 \end{cases} , \quad \text{where} \quad p = (B_W/1.0)^{0.0834} \,. \tag{2.76}$$

CIECAM97s suffers the non-invertibility problem of the chromatic adaptation, which is inherited from the LLAB model. It was later on modified in CIECAM02 to address the invertibility problem. After the chromatic transformation, the scaled RGB responses are transformed back to tristimulus XYZ values, and then transformed into the cone colour space by using the HPE transform, $\mathbf{M}_{\text{HPE}}$, as in RLAB [see Equation (2.20) for more details on the transform]:

$$\begin{bmatrix} \rho \\ \gamma \\ \beta \end{bmatrix} = \mathbf{M}_{\text{HPE}} \cdot \mathbf{M}_{\text{BFD}}^{-1} \cdot \begin{bmatrix} R_c Y \\ G_c Y \\ B_c Y \end{bmatrix} . \tag{2.77}$$

Second, a hyperbolic function, originating from the Naka-Rushton equation [Equation (2.11)], compresses the cone signals:

$$\begin{aligned} \rho_a &= \frac{40(F_L \rho/100)^{0.73}}{(F_L \rho/100)^{0.73}+2} + 1 , \\ \gamma_a &= \frac{40(F_L \gamma/100)^{0.73}}{(F_L \gamma/100)^{0.73}+2} + 1 , \\ \beta_a &= \frac{40(F_L \beta/100)^{0.73}}{(F_L \beta/100)^{0.73}+2} + 1 , \end{aligned} \tag{2.78}$$

where parameter F_L is calculated by a polynomial function. This is the same as Equation (2.34) in the Hunt94 model.

Third, the cone responses are transformed into achromatic signals and colour opponent signals. The achromatic signals A are modelled as follows:

$$\text{Achromatic signal} \qquad A = [2R_a^{\prime} + G_a^{\prime} + 0.05B_a^{\prime} - 2.05]N_{bb} , \tag{2.79}$$

$$n = Y_b/Y_W ,\ N_{bb} = N_{cb} = \frac{0.725}{n^{0.2}} . \tag{2.80}$$

The colour opponent signals, redness-greenness (a) and yellowness-blueness (b), are calculated (inherited from Hunt94) as follows:

$$\text{Redness} - \text{Greenness} \qquad a = R_a^{\prime} - \frac{12}{11}G_a^{\prime} + \frac{1}{11}B_a^{\prime} , \tag{2.81}$$

$$\text{Yellowness} - \text{Blueness} \qquad b = \frac{1}{9}(R_a^{\prime} + G_a^{\prime} - 2B_a^{\prime}) . \tag{2.82}$$

Finally, the following colour appearance attributes are modelled as follows:

$$\text{Lightness} \qquad J = 100\left(\frac{A}{A_W}\right)^{cz} ,\ z = 1 + F_{LL} n^{0.5} , \tag{2.83}$$

$$\text{Brightness} \qquad Q = (1.24/c)(J/100)^{0.67}(A_w + 3)^{0.9} , \tag{2.84}$$

where the achromatic signal A_W of the reference white point XYZ_W is calculated in the same way as the XYZ main colours.

$$\text{Chroma} \qquad C = 2.44 s^{0.69}(J/100)^{0.67n}(1.64 - 0.29^n) , \tag{2.85}$$

$$\text{Colourfulness} \qquad M = C F_L^{0.15} , \tag{2.86}$$

$$\text{Saturation} \qquad s = \frac{50\sqrt{a^2+b^2}\,100e(10/13)N_c N_{cb}}{\rho_a + \gamma_a + (21/20)\beta_a} , \tag{2.87}$$

where e is calculated by Equation (2.48) in the Hunt94 model. Hue angle h is derived by converting a and b into polar coordinates:

$$\text{Hue angle} \qquad h = tan^{-1}(b/a)\,. \tag{2.88}$$

The calculation of the hue quadrature H values are identical to those of the Hunt94 model [see Equation (2.57) and Table 2.5].

CIECAM97s forms the basic structure of the current standard appearance model, CIECAM02. The detailed differences are: the chromatic adaptation transform, the Bradford transform, is substituted with a new chromatic transform, CIECAT02, in order to rectify the invertibility problem, and the equations of colour appearance attributes are optimised differently in CIECAM02.

CIECAM02 CIECAM02 [Moroney et al., 2002] is considered one of the most complete and accurate colour appearance models. It originates from the CIECAM97s model through a few modifications [Fairchild, 2001; Hunt et al., 2002] (often called the *Fairchild* model and the *FC* model respectively). It follows the zone theory closely, but includes psychophysical optimisation in the chromatic adaptation.

First, chromatic adaptation is performed using CIECAT02, which supports varying degrees of adaptation. The resulting white-adapted XYZ values are then normalised. The cone response is modelled using Equation (2.11), but with a fixed σ, which causes the response to be similar to a power function (see Chapter 5 for more details on each equation). The opponent colour decomposition follows Section 2.3.1 closely. The final attributes include lightness, brightness, chroma, colourfulness, hue and saturation. CIECAM02 can model different surroundings and adaptation levels.

We review the mathematical details of the CIECAM02 model. Many parts are similar or identical to CIECAM97s, hence we describe only the formulae that are different. Note that the medium dependent parameter F_{LL} in CIECAM97s is removed in CIECAM02 (see Table 2.9). The input parameters for the CIECAM02 model are:

- Normalised (Y equal to 100) CIE tristimulus values (observed main colours): XYZ,
- Normalised tristimulus values of the reference white point: $X_W Y_W Z_W$,
- Level of luminance adaptation: L_A [unit: cd/m^2]
  (L_A is normally taken to be 20% of the luminance of the reference white.),
- Normalised luminance of background: Y_b,
- Surround parameters (specified in Table 2.9): c, N_c, and F.

The main procedures fall into four different stages.

First, the physically-meaningful input tristimulus values XYZ are adapted with respect to the reference white point to yield colour constancy. Chromatic adaptation is calculated in a psychophysically sharpened colour space, called CIECAT02, originating from the revision of the CMCCAT2000

Surround conditions	c	N_c	F
Average surround	0.69	1.0	1.0
Dim surround	0.59	0.9	0.9
Dark surround	0.525	0.8	0.8

Table 2.9: *Surround parameters in the CIECAM02 model.*

transform [Li et al., 2002]:

$$\begin{bmatrix} R \\ G \\ B \end{bmatrix} = \mathbf{M}_{\mathrm{CAT02}} \cdot \begin{bmatrix} X \\ Y \\ Z \end{bmatrix}, \quad \mathbf{M}_{\mathrm{CAT02}} = \begin{bmatrix} 0.7328 & 0.4296 & -0.1624 \\ -0.7036 & 1.6975 & 0.0061 \\ 0.0030 & 0.0136 & 0.9834 \end{bmatrix}. \tag{2.89}$$

The Matrix $\mathbf{M}_{CAT02}$ is normalised such that the tristimulus values for the equal-energy illuminant ($X=Y=Z=100$) produce equal cone responses ($L=M=S=100$) to ensure analytical invertibility. This means that the model handles the responses of three cones equally (which is then re-scaled by the proportion of their respective populations). The degree of chromatic adaptation depends on the absolute luminance level of L_A, which is modelled as a parameter D:

$$D = F\left[1-\left(\frac{1}{3.6}\right)e^{\left(\frac{-(L_A+42)}{92}\right)}\right]. \tag{2.90}$$

Then, the chromatic adaptation is modelled in the CIECAM02 as follow:

$$\begin{aligned} R_C &= [(100D/R_W)+(1-D)]R\,, \\ G_C &= [(100D/G_W)+(1-D)]G\,, \\ B_C &= [(100D/B_W)+(1-D)]B\,. \end{aligned} \tag{2.91}$$

The chromatically adapted values in CIECAT02 are then inverted back to the original CIEXYZ colour space through the inverse matrix, $\mathbf{M}_{CAT02}^{-1}$.

Second, chromatically adapted colours are transformed into the physiological LMS cone colour space by using the HPE transform [see Equation (2.20) in the RLAB model]:

$$\begin{bmatrix} R' \\ G' \\ B' \end{bmatrix} = \mathbf{M}_{\mathrm{HPE}} \cdot \mathbf{M}_{\mathrm{CAT02}}^{-1} \cdot \begin{bmatrix} R_C \\ G_C \\ B_C \end{bmatrix}. \tag{2.92}$$

The linear cone responses are compressed with a hyperbolic function. Although the function is derived from different optimisation (exponent changed from 0.73 to 0.42), they are similar to CIECAM97s' cone response functions:

$$\begin{aligned} R_a^{'} &= \frac{400(F_L R'/100)^{0.42}}{27.13+(F_L R'/100)^{0.42}} + 0.1\,, \\ G_a^{'} &= \frac{400(F_L G'/100)^{0.42}}{27.13+(F_L G'/100)^{0.42}} + 0.1\,, \\ B_a^{'} &= \frac{400(F_L B'/100)^{0.42}}{27.13+(F_L B'/100)^{0.42}} + 0.1\,, \end{aligned} \tag{2.93}$$

where F_L is calculated by Equation (2.34) in the Hunt94 model. In Chapter 5, we claim that the way to model cone responses in current colour appearance models can be improved upon to increase the dynamic range of our colour appearance model. We will discuss modelling cone responses later (see Chapter 5 for more details).

Third, the simulated cone responses are transformed into achromatic signals and colour opponent signals. Achromatic signals are calculated as an average with respect to the population of the three cones (inherited from the Hunt94 model). Compared to CIECAM97s, only the achromatic signal equation is modified:

$$A = [2R_a^{'} + G_a^{'} + (1/20)B_a^{'} - 0.305]N_{bb}\,, \tag{2.94}$$

$$\text{where} \quad n = Y_b/Y_W\,,\ N_{bb} = \frac{0.725}{n^{0.2}}\,. \tag{2.95}$$

The colour opponent signal equations [redness-greenness (a) and yellowness-blueness (b)] are identical to the CIECAM97s model [see Equation (2.81) and (2.82)]. Finally, colour appearance attributes for a given stimulus are calculated: lightness (J), brightness (Q), chroma (C), saturation (s) and hue angle (h), colourfulness (M) and hue composition (H):

$$\text{Lightness} \qquad J = 100\left(\frac{A}{A_W}\right)^{cz}\,,\ z = 1.48 + \sqrt{n}\,, \tag{2.96}$$

$$\text{Brightness} \qquad Q = \frac{4}{c}\sqrt{\frac{J}{100}}\left(A_W + 4\right)F_L^{0.25}\,, \tag{2.97}$$

where the achromatic signal A_W of the reference white point XYZ_W is calculated in the same way as XYZ main colours.

$$\text{Chroma} \qquad C = t^{0.9}\sqrt{J/100}(1.64 - 0.29^{n})^{0.73}\,, \tag{2.98}$$

$$\text{where} \quad t = \frac{(50000/13)N_c N_{cb} e_t \sqrt{a^2 + b^2}}{R_a^{'} + G_a^{'} + (21/20)B_a^{'}}\,, \tag{2.99}$$

$$e_t = 1/4[\cos(h\frac{\pi}{180} + 2) + 3.8],\ N_{cb} = \frac{0.725}{n^{0.2}}\,, \tag{2.100}$$

$$\text{Colourfulness} \qquad M = CF_L^{0.25}\,, \tag{2.101}$$

$$\text{Saturation} \qquad s = 100\sqrt{\frac{M}{Q}}\,. \tag{2.102}$$

The calculation of hue angle h is directly inherited from the CIECAM97s model [see Equation (2.88)], and the calculation of hue quadrature H from the hue angle h is identical to those of the Hunt94 model and the CIECAM97s model [see Equation (2.57) and Table 2.5].

Generally, the performance of the CIECAM02 model is good, and it is the current international standard for colour appearance modelling. However, as we will see in Chapter 5, it has difficulties with higher luminance levels, both in terms of colourfulness as well as lightness. We partially attribute this to the fact that input XYZ values are normalised, which seems to lose important information.

Kunkel and Reinhard [2009] Kunkel and Reinhard [2009] introduced a neurophysiology-inspired colour appearance model, which shows that chromatic adaptation and response compression in

CIECAM02 could be combined and that colour opponent channels could be derived from neurophysiological evidence [De Valois et al., 1997]. Compared to CIECAM02, their model removes the *chromatic adaptation transform* matrix [see Equation (2.89) for the transform] and merges the degree of adaptation in the chromatic adaptation [see Equations (2.90) and (2.91)] into a dynamic cone response function [see Equation (2.93)]. This revision changes the value σ for each cone respectively in the physiological cone response function [see Equation (2.11)]. This models the different responsivity trends (response curve shapes) of the three LMS cones. Consequently, their model employs different LMS ratios (4.19:1.00:1.17) for computing *achromatic signals* [see Equation (2.94)] and three different stages of *colour opponent signals*. First, a set of colour opponent signals (a_c,b_c) is used for modelling the *chroma* attribute:

$$\begin{bmatrix} a_c \\ b_c \\ d \end{bmatrix} = \begin{bmatrix} -4.5132 & 3.9899 & 0.5233 \\ -4.1562 & 5.2238 & -1.0677 \\ 7.3984 & -2.3007 & -0.4156 \end{bmatrix} \cdot \begin{bmatrix} L' \\ M' \\ S' \end{bmatrix}, \tag{2.103}$$

where d is a normalisation constant and L', M', and S' are non-linear cone responses. Then, chroma C is calculated as follows:

$$C = (10^3 t)^{0.9} \sqrt{\frac{J}{100}} (1.64 - 0.29^n)^{0.73}, \quad \text{where} \quad t = \frac{N_c N_{cb} \sqrt{a_c^2 + b_c^2}}{d}, \tag{2.104}$$

and J is lightness, see Equations (2.95) and (2.100) and Table 2.9 for N_c, N_{cb}, and n in CIECAM02. A second set of colour opponent signals (a_h, b_h) is used to compute intermediate hue attributes h [a polar coordinate of (a_h, b_h)]:

$$\begin{bmatrix} a_h \\ b_h \end{bmatrix} = \begin{bmatrix} -15.4141 & 17.1339 & -1.7198 \\ -1.6010 & -0.7467 & 2.3476 \end{bmatrix} \cdot \begin{bmatrix} L' \\ M' \\ S' \end{bmatrix}. \tag{2.105}$$

Finally, a third set of colour opponent signals (a'', b'') is derived from the ganglion-derived colour primaries r_p, g_p, y_p, and b_p:

$$a'' = r_p - g_p, \tag{2.106}$$

$$b'' = y_p - b_p, \tag{2.107}$$

where

$$r_p = \max(0, 0.6581 \cos^{0.5390}(9.1 - h)), \tag{2.108}$$

$$g_p = \max(0, 0.9482 \cos^{2.9435}(167.0 - h)), \tag{2.109}$$

$$y_p = \max(0, 0.9041 \cos^{2.5251}(90.9 - h)), \tag{2.110}$$

$$b_p = \max(0, 0.7832 \cos^{0.2886}(268.4 - h)). \tag{2.111}$$

The colour opponent signals are converted into a polar coordinate h' [see Equation (2.88)].

Their model is simpler and theoretically more plausible in modelling cone response and chromatic adaptation than CIECAM02. It also shows a higher accuracy in predicting *hue* attributes when compared with CIECAM02, although it does not present significant improvements in predicting lightness and colourfulness attributes. In addition, their model is invertible, hence can be used for imaging applications. It is interesting future work to combine their hue prediction with our colour appearance model.

2.3.5 Colour Difference

If a colour space is perceptually uniform, the difference between two colours can be represented as the Euclidean distance between their coordinates. The CIE 1976 uniform colour space, CIELAB, defines colour difference CIE ΔE as the Euclidean distance between two colours:

$$\Delta E^*_{ab} = \sqrt{(L^*_1 - L^*_2)^2 + (a^*_1 - a^*_2)^2 + (b^*_1 - b^*_2)^2}\,. \tag{2.112}$$

However, it was found that perceptual uniformity of colour difference is not consistent, in particular around the blue hue [Luo et al., 2001]. Many other colour difference formulae have been suggested to correct the non-uniformity, e.g., CMC($l:c$) [Clarke et al., 1984], BFD($l:c$) [Luo and Rigg, 1987], CIE94 [CIE, 1995], and CIEDE2000 [CIE, 2001] colour differences. Below, we briefly review the latest standard colour difference, CIEDE2000, ΔE_{00}. This revision is based on psychophysical experiment data accumulated over many years, and its basic structure is similar to that of the BFD($l:c$) colour difference formula.

CIEDE2000 is the Euclidean distance between two CIELCH coordinates, where the difference of each dimension is rescaled by constants and an additional term is introduced for hue and chroma interaction. First CIEDE2000 computes intermediate colour coordinates L', a', b', C'_{ab}, and h'_{ab} for the CIELAB coordinates:

$$L' = L^*\,, \tag{2.113}$$

$$a' = (1+G)a^*\,, \tag{2.114}$$

$$b' = b^*\,, \tag{2.115}$$

$$C'_{ab} = \sqrt{a'^2 + b'^2}\,, \tag{2.116}$$

$$h'_{ab} = \tan^{-1}(b'/a')\,, \tag{2.117}$$

$$\text{where} \quad G = 0.5\left(1 - \left(\frac{\overline{C^*_{ab}}^7}{\overline{C^*_{ab}}^7 + 25^7}\right)^{1/2}\right)\,, \tag{2.118}$$

and $\overline{C^*_{ab}}^7$ is the mean of the C^*_{ab} values for two different colours. Then, each colour difference in each dimension is calculated as $\Delta L'$, $\Delta C'$, and $\Delta H'$:

$$\Delta L' = L'_1 - L'_2\,, \tag{2.119}$$

$$\Delta C'_{ab} = C'_{ab,1} - C'_{ab,2}\,, \tag{2.120}$$

$$\Delta H'_{ab} = 2\sqrt{C'_{ab,1}C'_{ab,2}}\sin\left(\frac{\Delta h'_{ab}}{2}\right)\,, \tag{2.121}$$

$$\text{where} \quad \Delta h'_{ab} = h'_{ab,1} - h'_{ab,2}\,. \tag{2.122}$$

After that, three weighting scalars S_L, S_C, and S_H are computed as follow:

$$S_L = 1 + \frac{0.015(\overline{L'} - 50)^2}{(20 + (\overline{L'} - 50)^2)^{1/2}}\,, \tag{2.123}$$

$$S_C = 1 + 0.045\overline{C'_{ab}}\,, \tag{2.124}$$

$$S_H = 1 + 0.015\overline{C'_{ab}}T\,, \tag{2.125}$$

$$\text{where} \quad T = 1 - 0.17\cos(\overline{h'_{ab}} - 30^\circ) + 0.24\cos(2\overline{h'_{ab}}) + 0.32\cos(3\overline{h'_{ab}} + 6^\circ) - 0.20\cos(4\overline{h'_{ab}} - 63^\circ), \tag{2.126}$$

and $\overline{L'}$ is the mean of two different L's, and $\overline{h'_{ab}}$ is the mean of the two angles:

$$\overline{h'_{ab}} = \begin{cases} (h'_{ab,1} + h'_{ab,2})/2, & \overline{h'_{ab}} \leq 180^\circ \\ (h'_{ab,1} + h'_{ab,2})/2 - 180, & \overline{h'_{ab}} > 180^\circ \end{cases}\,. \tag{2.127}$$

The hue–chroma interaction factor R_T is modelled as follows:

$$R_T = -\sin(2\Delta\theta)R_C\,, \tag{2.128}$$

$$\text{where} \quad \Delta\theta = 30\exp\left\{-[(\overline{h'_{ab}} - 275^\circ)/25]^2\right\}, \tag{2.129}$$

$$R_C = 2\left(\frac{\overline{C'_{ab}}^{\,7}}{\overline{C'_{ab}}^{\,7} + 25^7}\right)^{1/2}. \tag{2.130}$$

Finally, the colour difference CIE ΔE_{00} is calculated as follows:

$$\Delta E_{00} = \left[\left(\frac{\Delta L'}{k_L S_L}\right)^2 + \left(\frac{\Delta C'_{ab}}{k_C S_C}\right)^2 + \left(\frac{\Delta H'_{ab}}{k_H S_H}\right)^2 + R_T\left(\frac{\Delta C'_{ab}}{k_C S_C}\right)\left(\frac{\Delta H'_{ab}}{k_H S_H}\right)\right]^{1/2}, \tag{2.131}$$

where parameters k_L, k_C, and k_H are chosen to best represent the viewing conditions. For general reference conditions, these parameters are set to be 1 ($k_L = k_C = k_H = 1$).

We use CIEDE2000 in our work of the characterisation method for HDR imaging in order to compute perceptual difference values (see Section 3.5.1).

2.3.6 Summary

Colour appearance models are numerically derived from experimental measurements of colour appearance. Colour appearance occurs in the visual cortex; hence, physiological measurements of colour appearance is still challenging. Instead, psychophysical measurements have been broadly used for modelling human colour vision. This is the reason why we still depend on the classical zone theory [Müller, 1930]. The previous methods to model human colour vision fall into three categories. One is the psychophysical modelling approach used by CIELAB and LLAB models. They are derived from psychophysical experimental data so do not try to follow the zone theory. Those models perform comparatively well (see Chapter 5 for more details on qualitative comparison). However, these models are quite limited in their representation of the structure and process of human colour vision. Another approach is physiologically-inspired modelling such as the Hunt94 model. This approach is strongly based on the zone theory and physiological measurements of primate cone responses. Even though it is seemingly more rigorous, it is based on an unproven hypothesis and on physiological response measurements from primates, which may have different characteristics from humans. Finally, hybrid approaches are an empirical combination of three different approaches: zone theory, physiological measurements of primates, and psychophysical measurements of the human,, e.g., CIECAM97s, Fairchild, FC, and CIECAM02. The CIECAM02 model is the latest of the hybrid types. The main structure is based on the zone theory. The chromatic adaptation is from psychophysical measurements. The cone responses are modelled from primate measurements. The colour appearance attributes are modelled from psychophysical measurements again. Our colour appearance model also takes this hybrid structure after analysis of our experiments (see Chapter 5 for more details).

On the other hand, colour appearance modelling largely depends on the psychophysical experimental data. However, available data are geared towards luminances under $690\,\mathrm{cd/m^2}$, which is a low luminance level when compared to real-world luminances. This is the reason why current colour appearance models fail when predicting colour perception under high luminance levels. This also limits the application of current colour appearance models for reproduction of HDR images. Therefore, we built a new experimental environment by using a custom-built high-luminance display; then, we conducted a series of psychophysical colour experiments under high luminance. This enabled us to produce a novel colour appearance data set for high luminance levels. Such wide range of colour appearance data allowed us to build a novel colour appearance model that can cover the working range of the human visual system (about five-orders magnitude). Finally, the appearance model is used to complete cross-media colour reproduction in HDR imaging (see Chapter 4 and 5 for more details on the development of our colour appearance model).

2.4 Gamut Mapping

Device characterisation describes colour device by relating their device-dependent colour specification to device-independent coordinates, e.g., CIEXYZ. Such colour spaces commonly try to ensure that equal scale intervals between stimuli represent approximately equally perceived differences in the attributes considered. Colour appearance models additionally try to model how the human visual system perceives colours under different viewing conditions so that the physically-meaningful coordinates can be transformed into perceptually-uniform coordinates.

In colour reproduction process, a forward device characterisation model of a input device converts device-dependent signals to physically-meaningful coordinates. A forward colour appearance model then interprets these physical values into perceptual correspondence. These applications yield perceptually uniform colour coordinates of the real world. Suppose a reverse order of this colour reproduction process with respect to an output device. An inverse colour appearance model with a target viewing environment of the output device converts the perceived colour attributes (through the input device) to physically-meaningful colour coordinates (for the output device). Successively, inverse device characterisation of an output device changes the physical values into output device-dependent signals, completing the chain of the colour reproduction process (see Figure 2.1). Here colour gamuts of input/output devices can be compared in a perceptual colour space. We reach a point where we need to consider how to map these two perceptual colour spaces in order to achieve *high fidelity* in colour reproduction.

Gamut-mapping algorithms have been broadly researched, and aim to ensure a *plausible correspondence of overall colour appearance* between the original and the reproduction by compensating for the mismatch in the size, shape, and location between the original and reproduced gamuts [MacDonald, 1993; Luo and Morovic, 1996; Stone et al., 1988; Braun and Fairchild, 1999]. See [Morovic, 2008] for a complete overview of gamut-mapping algorithms. As long as the output medium is different from the input, it is impossible to physically reproduce the same number of colours. Gamut-mapping algorithms generally aim for a plausible reproduction of the *image's appearance* rather than the *appearance of individual colours* in the input image. The gamut-mapping algorithms generally fall into two high-level categories. The first is *gamut clipping algorithms*, which aim to preserve all in-gamut colours in their original locations as far as possible, but clip the rest of the out-of-gamut colours to maintain high fidelity. For instance, a common *gamut clipping* method is to project an out-of-gamut colour towards the light axis along paths of constant *lightness* and *hue*

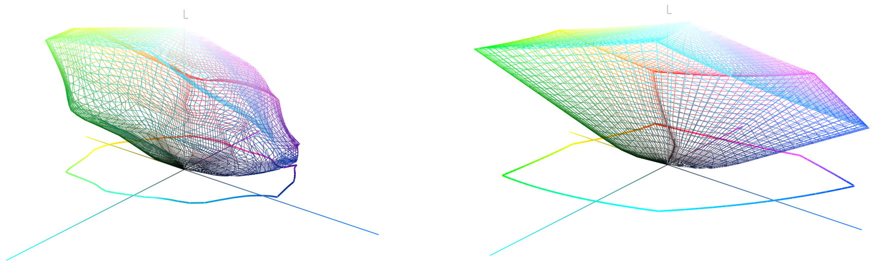

(a) Digital camera

(b) LCD display

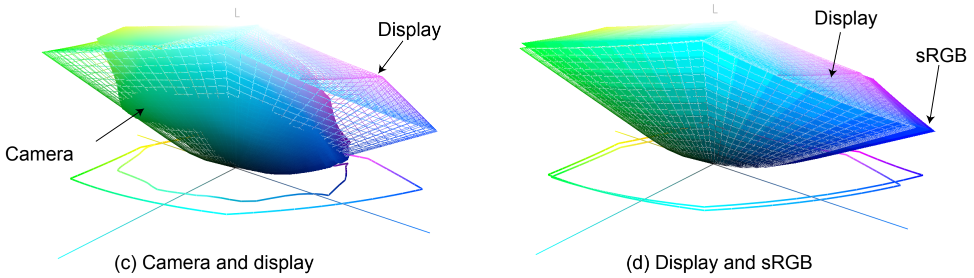

(c) Camera and display

(d) Display and sRGB

Figure 2.13: *Gamut boundary comparison between a digital camera and an LCD display. Image (a) presents the measured gamut boundary of a digital camera, a Canon 350D in the CIELAB colour space. Image (b) shows the gamut boundary of an LCD display, an Apple Cinema HD display. Image (c) presents a comparison of these two different media. Most of the camera gamut is covered by the display gamut so that most of the captured camera gamut can be represented without any gamut mapping (1:1 direct mapping) except in case of extreme saturation. As shown in Image (d), the gamut size of the Apple display is almost identical to sRGB international standard gamut.*

in a lightness, chroma, and hue space. These methods are generally used when gamut mismatch is small, which is true in most cases. The second way is *gamut compression algorithms*, which make changes to all colours from the original gamut so as to distribute the differences caused by gamut mismatch across the entire image. These approaches are used when a larger difference need to be overcome.

Suppose the input and output gamuts are identical to each other. The input media gamut can be mapped directly onto the output media gamut. Even when the input device gamut is smaller than the output one, the input colours can be mapped directly onto the output device colours. In these two cases, simple 1:1 gamut mapping yields a perceptual match between input stimuli and output stimuli. However, if the input gamut is bigger than the output gamut, e.g., the reproduction of a colour transparency film to newspaper, direct mapping leads to gamut clipping of the outside colours.

Rendering attempts to deal with gamut difference between the original and its reproduction, and can be divided into four different categories [Hunt, 2004; ICC, 2004]:

- **Relative colorimetric:** Assuming that the human eye always adapts to the white of the viewed medium, *relative colorimetric intent* uses an output medium white point. This means that the white point of an image is changed to the medium's white point. It preserves all in-gamut

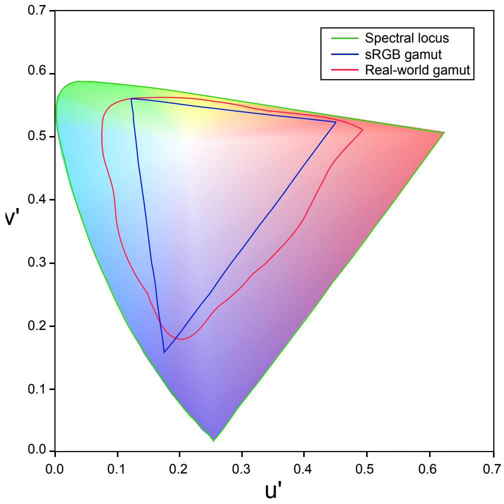

Figure 2.14: *Gamut boundary comparison between the real-world gamut and sRGB colour space. Pointer [1982] measured a maximum gamut for surface colours of the real world from 4089 colour samples including Munsell Limit Color Cascade. The green outer boundary represents possible gamut size yields by single monochromatic light within the visible spectrum (380–780nm in wavelength) in CIE $u'v'$ diagram, the so-called spectral locus. The red-lined boundary shows the possible gamut boundary in the real-world viewing environment, which is smaller than the spectral locus as the actual bandwidth of the spectrum in the real world more spread out than monochromatic lights. Finally, the blue triangle region represent sRGB colour space. As shown above, most of the gamut boundary of the real world is covered by the sRGB colour space. Adapted from [Pointer, 1982]*

colours in their original locations, but clips all out-of-gamut colours. It is regarded as a better choice when the gamuts of the source and the reproduction are similar. This method applies to most common cases and is defined as a default for ICC profiling [ICC, 2004].

- **Absolute colorimetric:** Absolute colorimetric intent preserves the original white point in reproduction so that the original white point is maintained on the output medium that may differ from the original. For instance, this method is broadly used for newspaper and professional proofing prints.
- **Perceptual:** Perceptual intent is the default rendering intent in gamut mapping. It preserves all of the source gamut by compressing through scaling. This method also uses the output medium's white point. No clipping of the source gamut happens. It is a reasonable choice for source images that contains significant out-of-gamut colours.
- **Saturation:** Without concerning itself with accuracy, saturation intent converts saturated colours in the source to saturated colours in the destination by expanding the source image's colour gamut to the output device's gamut. All colours are changed and the white point is decided by the output medium.

We measured and characterised a digital camera (Canon 350D) and an LCD display (Apple Cinema HD Display) with a spectrophotometer (GretagMacbeth EyeOne Pro). These were used as input and output devices during the work that makes up this thesis. The gamut boundaries of these two devices are compared in Figure 2.13 and the sRGB colour space is also compared with the real-world colour gamut (see Figure 2.14). As it turns out, the measured colour gamut of the digital camera is smaller than that of the display in most regions of the gamut boundary. *1:1 gamut mapping* is used for faithful reproduction so that all in-gamut colours in the input medium are directly mapped (1:1) in their original locations in the output medium (see Chapter 6 for more details). Our colour appearance model handles the luminance difference of input/output media (see Chapter 5 for more details). Other gamut mapping techniques are not handled in this thesis.

2.5 High-Dynamic-Range Imaging

The previous sections discussed background and related work of the three essential elements in classical cross-media colour reproduction. However, this classic system was established and developed with low-dynamic-range (LDR) imaging fundamentals. It is well known that the LDR imaging system has obvious limitation in capturing and representing real-world optical radiation, as mentioned in Section 1.1.

Current LDR imaging and LDR displays are based on a discretised signal structure, e.g., using 8-bit or 16-bit integer levels, which has obvious limitations. For instance, the camera cannot capture higher dynamic ranges than 16bits, or the display cannot produce colours of less than 1-bit signal depth. High-dynamic-range (HDR) imaging [Mann, 1993] and HDR display systems [Seetzen et al., 2004] have been developed to overcome these dynamic range limits. Owing to the new technology, we can capture a much higher dynamic range of luminance, a range similar to human vision, and we can display the captured higher dynamic range of data. However, the state of the art has mainly focused on the extendability of dynamic range from a tone-reproduction point of view, and has not considered colours rigorously. The work merely extended the dynamic range of each sensing/display channel on the existing platform. Current colour HDR imaging is achieved by merely combining the extended multi-chromatic channels, e.g., of red, green, and blue, together as a colour image.

On the other hand, although we can overcome the dynamic range limit in the capturing stage, we are facing a reproduction problem at the display stage since HDR displays are not yet available. As presented in Figure 1.1(b), the range of the captured HDR image exceeds that of common LDR displays significantly. Gamma correction is not enough to compress the dynamic range of the captured images. Consequently, HDR images cannot be reproduced by simply rescaling the values of the HDR images to that of the display. If done nonetheless, most of the interesting information in the HDR images is lost by the discretisation of the display signal. Tumblin and Rushmeier [1993] proposed a non-linear mapping to reproduce HDR images on common LDR displays with a similar appearance to that observed by the human visual system, so-called *tone mapping* or *tone reproduction*.

Many different HDR image acquisition algorithms and tone-mapping algorithms have been developed over the years. We will briefly review the common algorithms. In HDR imaging, we review how to solve a camera exposure function to derive a radiance map from LDR camera signals. We briefly review the structure of HDR displays. Finally, we review the state-of-the-art tone-mapping algorithms with respect to colour reproduction and appearance modelling.

2.5.1 High-Dynamic-Range Image Acquisition

Imaging sensors digitise incident illumination into digital signals within a certain range, which is often limited by the capacity of the solid-state wells and the ADC. State-of-the-art ADCs produce 12- or 14-bit discrete signals as integers. If the dynamic range of illumination exceeds the ADCs' capacity, the output signal is saturated. To this end, Mann [1993] proposed a novel method to overcome the dynamic range limit. By taking the exposure time factor into account, the method concatenates a series of different exposures as a continuum, resulting in an HDR image. Exposure on the sensor H is the product of irradiance E and exposure time Δt. Once we have the response function of a camera $f(x)$ to output camera signal Z for a given exposure H, the inverse application of the function $f^{-1}(x)$ yields the exposure H. As a result, the summation of the exposure H divided by the time interval Δt yields irradiance E at each pixel location (x,y). Supposing the irradiance on the sensor is linear to the scene radiance [see Equation (2.5)], we can derive relative radiance measures up to a scalar from the camera signal:

$$E(x,y)=\sum_{j=0}^{N-1}\frac{H_j(x,y)}{\Delta t_j(x,y)}, \quad \text{where} \quad H(x,y)=f^{-1}(Z(x,y)), \tag{2.132}$$

and j represents the multi-exposure sequence number and N indicates the total number of exposure sequences.

HDR radiance maps can be generated from ordinary sensor responses as a solid-state sensor produces linear responses to incident luminances [Mann and Picard, 1995; Yamada et al., 1995; Xiao et al., 2002]. These methods employ *raw* sensor signals by taking into account exposure times. In practice, digital cameras output non-linear response characteristics given incident light (see Figure 2.7 for the typical OETF of digital cameras); hence, a camera response function is generally required to derive exposure levels from given camera signals. As it turns out, this response function can be directly derived from the camera signals. Many such HDR image acquisition algorithms have been developed over the years. We will briefly review the common techniques.

Debevec and Malik [1997] introduced a method to generate HDR images from multi-exposed ordinary photographs (not sensor signals). The key contribution of this method is to estimate a camera exposure function for a given exposure without requiring extra physical measurements of the cameras properties. The function is estimated from pixel data with exposure time information in a curve fitting sense. They assume that the camera response is a smooth and monotonically increasing function $f(x)$ as a constraint to solve the under-determined function. If $\ln f^{-1}(x)$ at pixel Z_{ij} is defined as $g(Z_{ij})$, the camera response function can be estimated by minimising the following error function:

$$O = \sum_{i=1}^{N} \sum_{j=1}^{P} \{w(Z_{ij})[g(Z_{ij}) - \ln E_i - \ln \Delta t_j]\}^2 + \lambda \sum_{z=Z_{\min}+1}^{Z_{\max}-1} [w(z) g''(z)]^2, \tag{2.133}$$

where N is a number of pixel locations, P is a number of exposure sequences, Z is a pixel response, Δt_j is a relative exposure time, λ is the weighting constant, $g''(z)$ is the second derivative of the function $g(Z_{ij})$, and $w(z)$ is a pyramid weighting factor:

$$w(z) = \begin{cases} z - Z_{\min} \ , & z \leq \frac{1}{2}(Z_{\min} + Z_{\max}) \\ Z_{\max} - z \ , & z > \frac{1}{2}(Z_{\min} + Z_{\max}) \end{cases} . \tag{2.134}$$

In Equation (2.133), the first term is for concatenating the camera responses in different exposures; the second term is a smoothness term at each joint point of the LDR responses; the λ is empirically determined.

Once the inverse logarithmic camera response function $g(z)$ is recovered, the radiance values of each pixel in different exposure sequences are accumulated with a pyramid-weighting factor [see Equation (2.134)]; consequently, it yields a relative HDR radiance value (up to a scalar) at each pixel E_i:

$$\ln E_i = \frac{\sum_{j=1}^{P} w(Z_{ij})(g(Z_{ij}) - \ln(\Delta t_j))}{\sum_{j=1}^{P} w(Z_{ij})}. \tag{2.135}$$

The main impact of their method is to allow greater access to HDR imaging so that any digital camera can be used to build HDR images without requiring any specific hardware such as a spectroradiometer. However, their estimation approach may produce noise depending on the sampleddata. Even though the parameter λ is helpful for stabilising performance, it may result in the loss of important information when estimating the camera exposure function.

Mitsunaga and Nayar [1999] model the camera exposure function as a high-order polynomial function, while Debevec and Malik [1997] and Robertson et al. [1999, 2003] solve the camera function without assuming a polynomial function. The camera exposure function $f(x)$ of pixel value Z is modelled as a polynomial function:

$$f(Z)=\sum_{n=0}^{N} c_n Z^n. \tag{2.136}$$

The exposure function is solved by minimising the below error function ε:

$$\varepsilon=\sum_{q=1}^{Q-1}\sum_{p=1}^{P}\left[\sum_{n=0}^{N} c_n Z_{p,q}^n - R_{q,q+1}\sum_{n=0}^{N} c_n Z_{p,q+1}^n\right]^2, \tag{2.137}$$

where Q is a total number of images used, N is a polynomial degree, and P represents each pixel location. c_n is the coefficient to the polynomial. The optimisation can be solved by determining where the partial derivatives are all zero with respect to the polynomial coefficients $\partial\varepsilon/\partial c_n = 0$.

The equation is solved iteratively until the minimum error reaches a certain level. They also constrain the maximum order of the polynomial degree up to the tenth order. Once the camera response function is recovered, the radiances in different exposures (scaled by the time intervals) at each pixel are accumulated as in [Debevec and Malik, 1997] [see Equation (2.135)].

While the assembly algorithm of [Debevec and Malik, 1997] requires the complete information of a series of exposure time intervals, Mitsunaga and Nayar [1999]'s algorithm needs only the first exposure time interval and computes the other time intervals. However, considering that the LDR source images are usually taken in identical exposure intervals, it is not a big benefit in practice. Nonetheless, [Mitsunaga and Nayar, 1999] is computationally more efficient and robust than [Debevec and Malik, 1997] such that the camera response function is smoothly increasing and monotonic.

Nayar and Mitsunaga [2000] introduced the application of one-shot HDR imaging, so-called *spatially varying exposure (SVE)* imaging, by placing a set of mosaic neutral density filters in front of the sensor. This avoids the registration problem of the previous multi-exposure HDR imaging, e.g., [Debevec and Malik, 1997]. In their hardware, four neighboring pixels have different exposures respectively, and this pattern is repeated over the detector array. It is an innovative approach to produce HDR images without taking multi-exposure sequences that enables the capture of moving objects as HDR video.

Göesele et al. [2001] solves the exposure function by using the ICC profile, which converts device-dependent signals (non-linear RGB) into device-independent signals, so-called *profile-connect space (PCS)*, e.g., CIEXYZ coordinates — colour space adapted in the D50 illuminant [ICC, 2004]. Then the exposure sequence $x_{i,j}$, $y_{i,j}$, and $z_{i,j}$, scaled by the time interval T_j, are averaged with

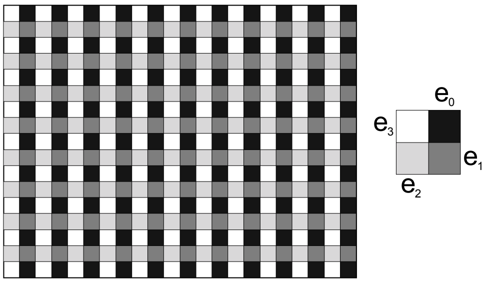

Figure 2.15: *Mosaic neutral-density filter for spatial varying exposure imaging. Four different exposures of neutral density filter are installed in front of the detector array. The difference between neutral density is* $e_3 = 4e_2 = 16e_1 = 64e_0$. *Adapted from Nayar and Mitsunaga [2000].*

weighing factor w:

$$X_i = T_n \frac{\sum_j X_{i,j} T_j^{-1} w(X_{i,j}, Y_{i,j}, Z_{i,j})}{\sum_j w(X_{i,j}, Y_{i,j}, Z_{i,j})},$$
$$Y_i = T_n \frac{\sum_j Y_{i,j} T_j^{-1} w(X_{i,j}, Y_{i,j}, Z_{i,j})}{\sum_j w(X_{i,j}, Y_{i,j}, Z_{i,j})}, \quad (2.138)$$
$$Z_i = T_n \frac{\sum_j Z_{i,j} T_j^{-1} w(X_{i,j}, Y_{i,j}, Z_{i,j})}{\sum_j w(X_{i,j}, Y_{i,j}, Z_{i,j})}.$$

After that, the HDR XYZ image is transformed into the display signals through an output ICC profile, which converts the device-independent signals (CIEXYZ) into device-dependent signals (non-linear display RGB).

This approach is a method to utilise HDR images in the colour management workflow, which can produce better colour reproduction across its pipeline. However, this method inherits drawbacks from the ICC profile mechanism. The proposed method needs to measure the white point of the captured scene to achieve colour consistency; otherwise it needs to capture the reference target in every capture as the ICC input profile is specific only to a certain illumination condition (where it was generated). In practice, this aspect limits their application for capturing HDR images. The method also does not include a tone-mapping algorithm to reproduce images. It merely applies gamma correction, which is built in the ICC profile mechanism.

HDR Image Formats Captured HDR radiance is usually represented as floating-point data. Any image format that supports floating-point data can be used for storage of the HDR images, e.g., RGBE format [Ward, 1992], OpenEXR [Lucas Digital Ltd., 2006], or Portable Float Map (PFM) [IEEE, 1985].

The RGBE file format has been distributed as a part of the freely available application *Radiance* [Ward, 1992]. It is broadly used in HDR and graphics applications. It has four channels:

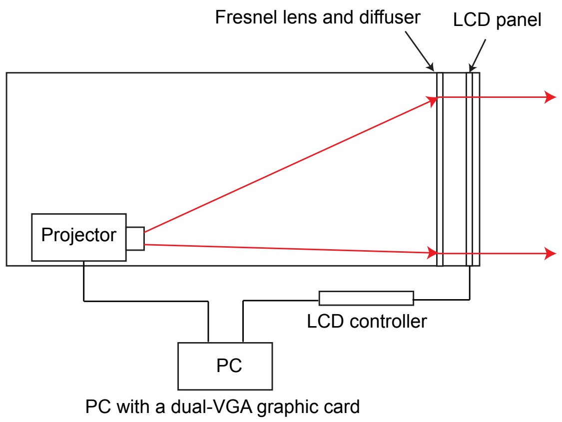

Figure 2.16: *Design of a high-dynamic-range display. In the general structure of the LCD display, a DLP projector or LED panel is substituted for the fluorescent back-light unit. Consequently, the HDR display can produce higher contrast resolution than the ordinary display does and higher luminance levels. Adapted from [Seetzen et al., 2004].*

three mantissas for red, green, and blue, and one exponent that is shared by these three colour channels; therefore, each colour value comprises two bytes of a mantissa and a shared exponent (half-precision float). The memory size for a pixel is 32 bits (4 bytes). However, it cannot cover the whole visible colour gamut, and colour saturation may occur as the three mantissa channels share one exponent. For example, if there is a colour which has large variation of colourfulness, the colour information will be clamped when it is encoded. The other drawback is that the number of mantissa bits (8bits) is rather smaller; hence, the RGBE format has limited precision.

Lucas Digital Ltd. [2006] introduced open-source file input/output interface, called *OpenEXR*. This format is a general purpose wrapper for 16bits half-precision float type. It comprises a sign bit for the exponent, five bits for the exponents, and ten bits for the mantissa. It further supports wavelet compression. The memory size for a pixel is 48 bits (6 bytes). However, considering that most of HDR applications use single or double precision float internally, it loses tone precision of when restoring image data. In addition, the maximum value that can be stored is limited to 65504.0.

The *PFM* file format stores single precision data directly without loss (IEEE storage format for the 32bits (4bytes) single precision float type [IEEE, 1985]). It comprises a sign bit for the exponent, 8bits for the exponent, and 23bits for the mantissa per each pixel in the interleaved mode. The total memory size for a pixel is 96bits (12bytes). The precision is high, but the file size is larger when compared to other HDR formats.

2.5.2 High-Dynamic-Range Display

Seetzen et al. [2004] introduced an HDR display system, which was created by substituting a digital light processing (DLP) projector for the fluorescent back-light unit of an ordinary LCD display. As a result, the display can display images with a higher dynamic range and a contrast ratio of 1:50 000 as the *backlight* is now spatially varying. Depending on the exact configuration, the maximum luminance goes up to 2 700 cd/m^2. As shown in Figure 2.16, the projector-based HDR display requires 100cm in depth, which is a drawback. Hence, they developed another type with light-emitting diode (LED)-based back-light modulator. The LED-based model has a low-resolution back light behind the diffuser of the LCD panel. It has a higher maximum output luminance of up to 8 500 cd/m^2. The LEDs are powered individually to form a low-frequency luminance map behind the displayed image. Thus the HDR display makes dark regions appear darker and in higher contrast than a uniform back-light modulation.

In order to build a controllable viewing environment of our psychophysical experiment under high luminance levels, we built a high-luminance display. Our display substitutes hydrargyrum medium-arc iodide (HMI) bulbs for the florescent back-light unit of an LCD display so that its maximum luminance increases to 16 860 cd/m^2 (see Chapter 4 for more details on our high-luminance display).

2.5.3 Tone Reproduction in High-Dynamic-Range Imaging

HDR imaging has been introduced to record real-world radiance values, which can have a much higher range than that of ordinary imaging devices. HDR radiance maps can have a dynamic range of about nine to ten orders of magnitude. Photographic HDR images or artificial radiance maps cannot be displayed properly on low-dynamic-range (LDR) output devices (with about two orders of magnitude) due to the huge difference in dynamic range (see Figure 1.1). Consequently, the dynamic range of the HDR scene needs to be mapped into the range of an output device, which is called *tone reproduction* or *tone mapping*.

Tone Mapping Tone mapping is related to colour appearance modelling and cross-media colour reproduction as it tries to preserve the perception of an image after remapping to a low-luminance display; however, generally only tone (and not colourfulness) is considered. Over the years, many different tone reproduction operators have been developed since [Miller and Hoffman, 1984]. The majority of research has focused on improving local contrast, pursuing fewer artifacts and more efficient computation times [Schlick, 1994; Rahman et al., 1996; Ferwerda et al., 1996; Pattanaik et al., 1998; Tumblin and Turk, 1999; Pattanaik et al., 2000; Funt et al., 2000; Fattal et al., 2002; Reinhard et al., 2002; Durand and Dorsey, 2002; Johnson and Fairchild, 2003; Meylan and Süsstrunk, 2004; Li et al., 2005]. Global operators have received less attention [Tumblin and Rushmeier, 1993; Ward, 1994; Ward et al., 1997; Drago et al., 2003; Reinhard and Devlin, 2005] since high contrast appearance is difficult to achieve, but on the plus side they do not suffer from halo-artifacts like many local operators and are much more efficient.

Among the previous tone-mapping algorithms, we will briefly review the relevant techniques (see [Reinhard et al., 2005] for a complete overview of other tone-mapping algorithms). This section also contains detailed mathematics of the methods. They are included here as a reference, and the reader is welcome to continue to Section 2.5.4 for a general summary of HDR imaging. First, we will briefly review the global operators.

Global Operators Tumblin and Rushmeier [1991, 1993] were pioneers in addressing the research question of how to render computer-generated HDR images. Their approach is to manipulate the tone-reproduction curves of HDR images by utilising the brightness perception model by [Stevens and Stevens, 1963]. It originates from scientific insights of the colour reproduction mechanism in humans with respect to tone mapping. Their tone-reproduction operator comprises three elements: a real-world observer function, an inverse display observer function, and an inverse display device function so that the perceived brightness on the display B_d matches that of the original scene B_{rw} (See Figure 2.17).

In particular, their insight into the HDR reproduction pipeline influenced our approach. They are only concerned with luminance mapping and derive their formulae from previous psychophysical assumptions, whereas we conducted psychophysical experiments to measure colour appearance attributes and modelled them for use in the reproduction pipeline (see Chapter 6 for more details on our method).

Ward [1994] introduced a simple tone-mapping operator, which controls the contrast of HDR images with respect to the threshold in the human visual system to a given luminance intensity. The simplest way to achieve tone-mapping is to scale the captured real-world luminance L_w at pixel (x,y) to the range of a display luminance L_d with an appropriate scalar m:

$$L_d(x,y) = m \cdot L_w(x,y)\,. \tag{2.139}$$

Considering the non-linear responsivity of the human visual system to given luminance, a threshold-versus-intensity function t (a human observation function, corresponding to the forward colour appearance model) is used:

$$t[L_d(x,y)] = m \cdot t[L_w(x,y)]\,, \tag{2.140}$$

where m is derived by solving $t[L_d(x,y)]/t[L_w(x,y)]$, based on [CIE, 1981]. Finally, the tone-

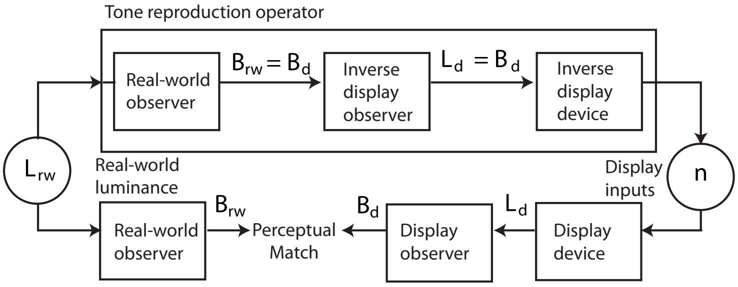

Figure 2.17: *Schematic diagram for tone reproduction operators, adapted from [Tumblin and Rushmeier, 1993]. Their proposed tone-reproduction operator comprises real-world observations, inverse display observations, and an inverse display device function that achieves a perceptual match between real-world observation and the observation of the reproduced image on the display.*

mapping function m is modelled as:

$$m = \frac{1}{L_{d,max}} \left(\frac{1.219 + \left(\frac{L_{d,max}}{2} \right)^{0.4}}{1.19 + L_{wa}^{0.4}} \right)^{2.5} , \tag{2.141}$$

where $L_{d,max}$ is the maximum display luminance assumed in the range 30–100 cd/m^2; the level of real-world luminance adaptation L_{wa} is estimated as the log average of the image's luminance levels:

$$L_{wa} = \exp \left(\frac{1}{N} \sum_{x,y} \log(10^{-8} + L_w(x,y)) \right) . \tag{2.142}$$

This method and [Tumblin and Rushmeier, 1993] form fundamentals for later tone-mapping algorithms. While Tumblin and Rushmeier [1993] suggest a fundamental pipeline for tone-mapping algorithms, Ward [1994] suggests a more practical idea to achieve tone mapping with respect to the human visual system. In particular, Equation (2.142) is adopted in many other tone-mapping algorithms for estimating the real-world luminance adaptation in HDR images [Pattanaik et al., 1998; Reinhard et al., 2002]. Equation (2.141) is extended further by Ferwerda et al. [1996] based on real measurements of the luminance response of the human visual system.

Ward et al. [1997] suggested a global adaptation approach, which is based on histogram equalisation; furthermore, it models the subjective perception of the scene by borrowing the perceptual measurements of the contrast threshold. Their histogram equalisation decreases the contrast of less populated luminances and increase the contrast of more populated luminances respectively. This method first computes a histogram and cumulative distribution function from the logarithmic values of luminance, which is only used for obtaining a distribution. However, they found that the naive histogram equalisation method exaggerates contrast; hence, they imposes an upper bound onto the slope of the cumulative histogram remapping curve. But this changes the total pixel count in the histogram, which also affects the upper bound. They conduct histogram adjustments iteratively to a certain tolerance level. The level is decided in an empirical manner. The histogram is taken between the minimum and maximum values in equalised bins in the logarithmic scale of luminance (100 bins are used). The histogram equalisation function B_{de} is applied in pixel values between $\log(L_{dmin})$ and $\log(L_{dmax})$. The function B_{de} follows:

$$B_{de} = \log(L_{d\,\mathrm{min}}) + [\log(L_{d\,\mathrm{max}}) - \log(L_{d\,\mathrm{min}})] cdf(B_w) , \tag{2.143}$$

where B_{de} is the computed display brightness $\log(L_d)$, L_{dmin} is the minimum of the display luminance (black level) $[cd/m^2]$, L_{dmax} is the maximum of the display luminance (white level) $[cd/m^2]$, B_w is the world brightness $\log(L_w)$, and $cdf()$ is the cumulative distribution function.

Their method also considers the limitations of human vision: glare, colour sensitivity, and visual acuity. It includes functions to simulate glare that is caused by bright sources in the visual periphery and which scatter light into the lens of the eye; furthermore, it includes a term to simulate colour sensitivity which is reduced in dark environments as the light-sensitive rods take over from the colour-sensitive cone system. The proposed method is able to compress HDR images very effectively and also provides relatively stable colourfulness in the results. The details in the shadow area are very well preserved. However, the physical relationship between the display signal and the HDR radiance map is changed considerably.

Drago et al. [2003] introduced a global tone-mapping model which is based on logarithmic compression following the hypothesis by Fechner [1963] (see Section 2.3.2 for more details). They manipulate the base of the logarithm to adjust the contrast of images. The method originates from *Fechner's Law*:

$$B = k_1 \ln\left(\frac{L}{L_0}\right), \tag{2.144}$$

where L_0 denotes the luminance of the background and k_1 is a constant factor. The proposed logarithmic compression is structured to compute display luminance L_d through dividing real-world luminance L_W by the maximum luminance in the scene L_{max}:

$$L_d = \frac{\log(L_w + 1)}{\log(L_{\max} + 1)}. \tag{2.145}$$

However, this simple logarithmic compression is not enough to handle various HDR radiance maps, hence the base of the logarithm is varied from two to ten with appropriate interpolation. This is computed by Perlin and Hoffert's *bias* power function [Perlin and Hoffert, 1989]. The bias function is a power function defined over the unit interval where an intuitive parameter b remaps an input value to a higher or lower value (0.85 is used for b):

$$bias_b(t) = t^{\frac{\log(b)}{\log(0.5)}}, \tag{2.146}$$

where t is the relative intensity of luminance. Finally, the bias function of Equation (2.146) is merged with the compression function of Equation (2.145) to vary the base of logarithm to differing contrast:

$$L_d = \frac{L_{dmax} \cdot 0.01}{\log_{10}(L_{wmax} + 1)} \cdot \frac{\log(L_w + 1)}{\log\left(2 + \left(\left(\frac{L_w}{L_{wmax}}\right)^{\frac{\log(b)}{\log(0.5)}}\right) \cdot 8\right)}. \tag{2.147}$$

The first factor in Equation (2.147) is the adaptation scale factor, which is derived from the denominator of Equation (2.145). It is the ratio of the maximum luminance of the display (assumed to be $100 cd/m^2$) to the logarithm of the maximum world luminance. The denominator of the second factor in Equation (2.147) is the base of the logarithm, which is the interpolated ratio of world luminance to maximum world luminance from two to ten by using the bias function ($b = 0.85$). After that, the compressed luminance values are gamma-corrected to fit the display gamma (ITU-R BT.709):

$$E' = \begin{cases} slope \cdot L\,, & L \le start \\ 1.099 L^{\frac{0.9}{\gamma}} - 0.099\,, & L > start \end{cases}, \tag{2.148}$$

where $slope$ is the elevation ratio ($slope$=4.5) of the line passing by the origin and tangent to the curve, $start$ is the abscissa ($start$=0.018) at the point of tangency, and γ is 2.2. The proposed method provides not only computational efficiency but also relatively plausible reproduction. However, the performance of this method is affected by the default parameter settings and image characteristics. Some images are overly bright or dark while others look fine.

Reinhard and Devlin [2005] introduced an efficient global method, inspired by the physiological response of photoreceptors (cones), based on [Kleinschmidt and Dowling, 1975; Hood et al., 1979]. The photoreceptor response V according to intensity I is defined similarly to the Michaelis-Menten equation [Valeton and van Norren, 1983] [see Equation (2.11)]:

$$V = \frac{I}{I + (I_a)^m} V_{\max} , \tag{2.149}$$

where the exponent m is $0.3 + 0.7k^{1.4}$, k is $(L_{\max} - L_{av})/(L_{\max} - L_{\min})$, L_{av} is the geometric mean of the luminance, and the adapted pixel intensity I_a is computed through interpolation of local (pixel intensity itself) and global (geometric mean of luminance) adaptation as follow:

$$I_a = a\, I_a^{local} + (1-a) I_a^{global} , \tag{2.150}$$

where a is 0.5 (which means the arithmetic mean of the *geometric mean of luminance* and *pixel value*), $I_a^{local} = L$, $I_a^{global} = I_{r/g/b}^{av}$, where L is the luminance level of each pixel, and $I_{r/g/b}^{av}$ is the exponent of L_{av} [Reinhard et al., 2005]. Finally the pixel value $V_{r/g/b}$ is gamma-corrected by 2.0 [Reinhard et al., 2005]:

$$V'_{r/g/b} = V_{r/g/b}^{1/2.0} . \tag{2.151}$$

The proposed algorithm takes a similar strategy to the global adaptation part of [Reinhard et al., 2002]. Both methods describe the modified version of the Michaelis-Menten hyperbolic equation. However, the global operator of [Reinhard et al., 2002] produces more stable and plausible results than this proposed method [Reinhard and Devlin, 2005] (see Chapter 6 for a more detailed comparison). Furthermore, like [Drago et al., 2003], the performance of the proposed method is affected by the default parameter settings and image characteristics. For instance, some images appear overly bright or dark with the default parameter settings (see Chapter 6 for more details on comparison).

Kim and Kautz [2008b] introduced a global tone reproduction operator which provides consistent tone reproduction. This method was tested with a large variety of HDR images and produced *consistent* results without adjusting parameters.

Their method is inspired by the *characteristic curve* in photography, called *DlogE* plot [Hunt, 2004], which plots density (logarithm of reflective luminance) against logarithm of the luminance incident on the photographic material.

For instance, the Stanford Church HDR image [Debevec and Malik, 1997] (see Figure 6.5) has a dynamic range (luminance) of 5.5 orders of magnitude (1:343 512). Imagine that the radiance map is observed on a display which has a dynamic range of 2.4 orders of magnitude (1:256, 8-bits [Berns and Katoh, 2002]). By linearly scaling the HDR radiance map to the range of display luminance in the DlogE domain (scaled by approximately 0.43), the dynamic range of the HDR radiance map is adjusted to that of the display luminance. The dynamic range of these two is then identical. The scaling factor k_1 is computed as follows:

$$k_1 = \frac{\log L_{d_{max}} - \log L_{d_{min}}}{\log L_{s_{max}} - \log L_{s_{min}}}, \tag{2.152}$$

where $\log L_{d_{max}}$ and $\log L_{d_{min}}$ are the maximum and minimum luminances of the display signals and $\log L_{s_{max}}$ and $\log L_{s_{min}}$ are the maximum and minimum luminances of the HDR radiance map. The dynamic-range compressed image can be computed as:

$$L_1(x,y) = \exp\left(k_1 \log L_0(x,y)\right), \tag{2.153}$$

where L_1 is the compressed luminance at pixel address (x,y) and L_0 is the luminance of the HDR image at each pixel.

When a linear scaling factor is applied, the slope of the tone reproduction line decreases in the DlogE domain. The rotating point in changing the slope is moved to the averaged log-luminance μ by subtracting the mean μ before scaling, and then adding it back in the DlogE domain. The linear scaling factor is then replaced with a non-linear function. A Gaussian-weighting of the scale factor k_1 is performed such that it has a peak at the averaged log-luminance μ and a minimum at k_1 (see Figure 2.18). This new Gaussian-weighted scale factor $k_2(L)$ depends on the log-luminance $L = \log L_0(x,y)$ and has a range of $k_1 \leq k_2(L) \leq 1.0$. This non-linear scale factor is computed as:

$$k_2(L) = \left(1 - k_1\right) w(L) + k_1, \tag{2.154}$$

$$w(x) = \exp\left(-\frac{1}{2}\frac{\left(x-\mu\right)^2}{\sigma^2}\right),\ \sigma = \frac{d_0}{c_1}, \tag{2.155}$$

where σ is the ratio of the *dynamic range* d_0 of the *log-luminances of the HDR image* to the user-parameter c_1. This adjusts the shape of Gaussian fall-off within the width of its characteristic curve. The parameter c_1 influences the resulting brightness and local details of the tone-mapped image. They found that $c_1 \approx 3.0$ is the maximum level that can compress contrast without losing detail in the bright areas of images.

The final non-linear mapping function is as follows (including the rotation around μ):

$$L_1(x,y) = \exp\left[c_2 k_2 \left(\log L_0(x,y) - \mu\right) + \mu\right]. \tag{2.156}$$

Parameter c_2 is also introduced, referred to as the *efficiency factor*, which scales the intensity of the non-linear weighting. Even though the display signal depth may have a dynamic range of 2.4 (1:256), the actual dynamic range of the display luminance is often lower than that of the signal (e.g., an Apple Cinema HD Display has a measured dynamic range of only 2.01). Therefore, the dynamic range of an HDR radiance map should be compressed more than that of the display signal depth. Parameter c_2 is 0.84 (= 2.01/2.4) for this specific display. However, based on the testing of

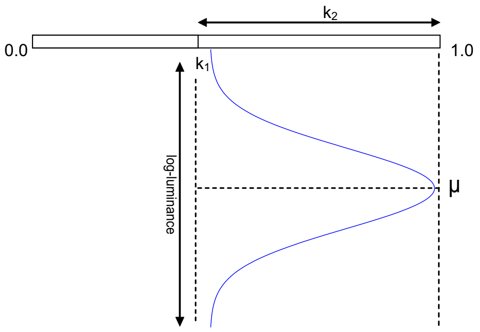

Figure 2.18: *Range of the dynamic scale factor k_2.*

other displays with lower dynamic ranges, the c_2 parameter should be set to lower than the above for *general purpose*. Setting $c_2 \approx 0.5$ works for a wide variety of images and displays.

The Y coordinate of CIEXYZ is used as the luminance input value L_0 for the proposed tone reproduction operator. After obtaining the mapped luminance layer L_1, the X and Z channels are scaled by the ratio of mapped luminance to original luminance as [Schlick, 1994]. After obtaining the tone-mapped radiance map, they use the international specification for the sRGB colour space [IEC, 2003] to map the LDR radiance map onto the display colour space (CIEXYZ values are transformed into sRGB signals through the inverse transform matrix and gamma correction, corresponding to $\gamma = 2.2$ including a linear ramp for dark values [IEC, 2003]). In order to optimise the dynamic range of the display, a histogram is computed of the tone-mapped image and used to stretch the pixel levels between 1% and 99% of the range of display signals (effectively clamping values below 1% and above 99% and re-normalising to the 0%-100% range).

Global tone-mapping algorithms often produces inconsistent reproduction results for the same default parameter set — some images are overly bright or dark while others look fine. It is beneficial for tone reproduction operators not to require any per-image parameter tweaking. Their proposed method shows consistent results across the set of images (photographic and computer-generated) without any need for parameter tweaking. However, this model is developed with theoretical assumptions in an empirical manner, without taking into account colour reproduction.

Local Operators Chiu et al. [1993] introduced the pioneering concept of local adaptation for HDR tone-mapping. As the human visual system has different sensitivities to different spatial frequencies, the contrast of the pixel intensity f at pixel location (i,j) is controlled with a low-pass filter $S(i,j)$ in order to simulate the change of frequency sensitivity:

$$\hat{f}(i,j) = \hat{S}(i,j) f(i,j). \tag{2.157}$$

The contrast scaling function $S(i,j)$ is modelled as follows:

$$\hat{S}(i,j) = \begin{cases} S(i,j), & S(i,j) < \frac{1}{f(i,j)} \\ \frac{1}{f(i,j)}, & S(i,j) \geq \frac{1}{f(i,j)} \end{cases}, \text{ where } S(i,j) = \frac{1}{k f_{blur}(i,j)}, \ 0 \leq S(i,j) \leq \frac{1}{f(i,j)}, \tag{2.158}$$

and $\hat{S}(i,j)$ is proportional to the reciprocal of a filtered (blurred) function f_{blur}; $S(i,j)$ has the value between 0 and $\frac{1}{f(i,j)}$, which accents dark areas and dims bright areas. f_{blur} is generated by a low-pass filtering through the Perlin and Hoffert interpolation [Perlin and Hoffert, 1989] between two intensities at two local points c_0 and c_1 as $c = (-2t^3 + 3t^2)c_0 + (2t^3 - 3t^2 + 1)c_1$, where t varies from zero to one between c_0 and c_1. Although the spatially-varying adaptation of luminance was a pioneering idea to overcome the difference of dynamic range, their results yield artifacts such as halos (see Figure 2.19 for more details).

Tumblin and Turk [1999] introduced the concept of diffusion imaging, which involves gradient mapping using a partial differential equation solver. The common local adaptation methods convert HDR images into the frequency domain and scale down only the low bandwidth channel. These methods compress the low frequency luminance selectively into the display's range with the same details as the original. However, this yields typical artifacts, called halos [see Figure 2.19(a)]. On the contrary, they introduced a method to control the gains of pixel intensities in the gradient domain instead of the frequency domain. In order to detect the edge, the method uses the diffusion theory [Perona and Malik, 1990] with an assumption that the image intensity is the temperature of a large flat plate of uniform thin material. This method scales down the higher gain selectively in the gradient domain so that such halo artefact is not included in output images [see Figure 2.19(b)].

Fattal et al. [2002] extended the gradient approach of [Tumblin and Turk, 1999] and improved computational efficiency. This method calculates the gradient of logarithm of luminance, following the approximation of human perception by [Fechner, 1963]. The computed gradients are compressed in a multi-scale pyramid. The compressed gradients are then converted back to intensities

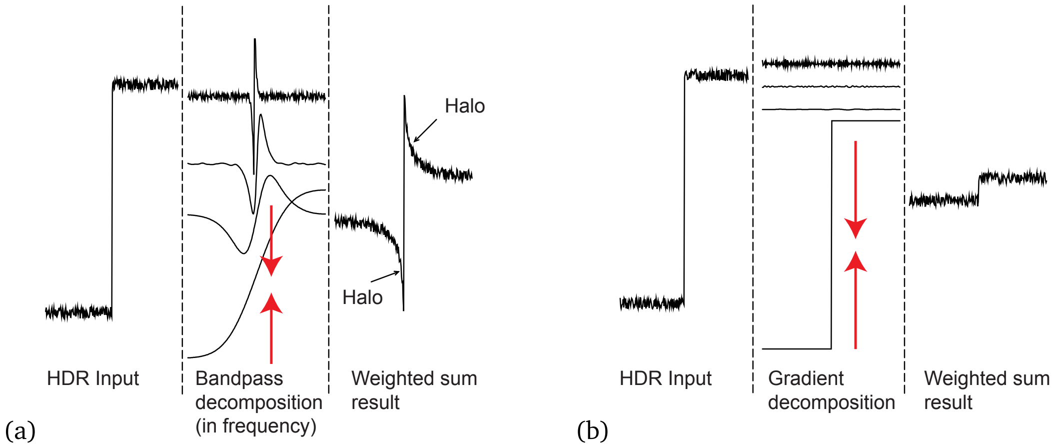

Figure 2.19: *Comparison between frequency and gradient decomposition in tone mapping. Image (a) presents three stages of tone mapping in the frequency domain. On the left, an HDR image has very high contrast ratio with details. In the middle, the image is decomposed into different bandwidth channels, and the lower bandwidth is selectively scaled down for tone mapping. The result on the right presents halo artifacts as the higher bandwidth is spatially associated with the lower bandwidth. Image (b) presents three stages of tone mapping in the gradient domain. The HDR input on the left is decomposed into different level of gradient. The high gradient is selectively scaled down so that this method reduces any halo-like artifacts. Adapted from [Tumblin and Turk, 1999].*

via the Poisson equation. This method is faster than [Tumblin and Turk, 1999], but it often produces halo artefacts around high frequency regions as this method compresses not the gradient of pixel intensity, but the gradient of logarithmic luminance.

Durand and Dorsey [2002] proposed an HDR tone-mapping operator based on bilateral filtering [Tomasi and Manduchi, 1998]. The main idea of bilateral filtering is that not only a spatial Gaussian filter $f(p-s)$ is applied, but is weighted by an intensity Gaussian filters $g(I_p - I_s)$ between two points p and s, which scales signal intensity of the corresponding pixels I_p within an image Ω. As a result, the filter detects edges J_s at each pixel s while smoothing high frequency details:

$$J_s = \frac{1}{k(s)} \sum_{p \in \Omega} f(p-s)\, g(I_p - I_s)\, I_p \,. \tag{2.159}$$

where $k(s)$ is a normalisation term: $k(s) = \sum\limits_{p \in \Omega} f(p-s)\, g(I_p - I_s)$. Hence, a pixel closer to s and more similar to s in intensity will be weighted more greatly to detect edges. The method then is accelerated by a piecewise-linear approximation in the intensity domain and appropriate subsampling through the fast Fourier transform to improve the computational cost over the original bilateral filter. Finally, this filter is used to decompose an image into a base layer (obtained from the bilateral filter) and a detail layer. Only the base layer is compressed and the detail layer is added back in. Even though the method was developed empirically, according to [Kuang et al., 2004], its tone-mapping results are as plausible as [Reinhard et al., 2002]. It was adopted into an image appearance model by Kuang et al. [2007], called iCAM06, to mimic the spatially-varying adaptation of the human vision system.

Reinhard et al. [2002] presented a mixed approach of the global and local operators, which produces consistent and plausible results. It has been used broadly in graphics applications. For the local operation, they employed low-pass filtering through the Fast Fourier Transform. The global operation starts from calculating luminances from pixel values. Then, an adapting level of luminance $\overline{L}_w$ is calculated, which is similar in a sense to the geometric mean of the luminance:

$$\overline{L}_w = \exp\left(\frac{\sum\limits_{x,y} \log(\delta + L_w(x,y))}{N} \right) , \tag{2.160}$$

where δ is 0.0001 to avoid infinite error. The estimated average of luminance produces a normalisation of the scene luminances with key values (representing 18% neutral grey):

$$L(x,y) = \frac{a}{\overline{L}_w} L_w(x,y)\,, \tag{2.161}$$

where $L(x,y)$ is a scaled luminance, and a is a user parameter, 0.18 (as default). Finally, the global adaptation is defined in a form:

$$L_d(x,y) = \frac{L(x,y)}{1+L(x,y)} \cdot \left(1 + \frac{L\,(x,y)}{(L_{white})^2} \right) , \tag{2.162}$$

where $L_d(x,y)$ is a global tone mapped image, and L_{white} is the maximum luminance of $L(x,y)$ (limited to $1{\times}10^{20}$).

After that, the photographic local adaptation function is appended as a Gaussian convolution. The convoluted profile R_i of each scale s at each pixel (x,y) is defined:

$$R_i(x,y,s) = \frac{1}{\pi(\alpha_i s)^2}\left(-\frac{x^2+y^2}{(\alpha_i s)^2}\right). \tag{2.163}$$

The computed profile R_i of each scale s is convoluted with the luminance value L: $V_i(x,y,s) = L(x,y) \otimes R_i(x,y,s)$. Then the centre convolution V_1 and surround convolution V_2 are merged to a layer of each scale:

$$V(x,y,s) = \frac{V_1(x,y,s) - V_2(x,y,s)}{2^{\phi} a/s^2 + V_1(x,y,s)}, \tag{2.164}$$

where ϕ is a sharpening parameter, 8.0. Finally, Equation (2.162) and (2.164) are combined as follows:

$$L_d(x,y) = \frac{L(x,y)}{1 + V_1(x,y,s_m(x,y))}, \tag{2.165}$$

where $V_1(x,y,s_m(x,y))$ is the blurred luminance level when $s_m(x,y)$ satisfies $|V(x,y,s_m)| < \varepsilon$ (a threshold).

The resulting quality is more consistent compared to other approaches. According to [Kuang et al., 2004], its tone-mapping results are psychophysically rated to be as highly plausible as [Durand and Dorsey, 2002]. The performance of this method is presented in Chapter 6 with comparison to our reproduction model.

Colour in Tone Mapping Commonly, tone-mapping algorithms only modify lightness while keeping the colour channels untouched. The Schlick [1994] tone-mapping method was the first to take colour into account in HDR tone mapping. He concentrated on preserving the ratio of colour primaries. Instead of scaling all three colour channels with a non-linear function, the luminance information L (corresponding to the Y channel in CIEXYZ colour space) is derived from the original image. The contrast response function takes the luminance level L to yield the tone-mapped luminance L'. Finally, the ratio of L' to L is used to compress the luminance without altering the physical colour property of each pixel in the source image:

$$C'_{r/g/b} = \frac{L'}{L} \cdot C_{r/g/b}, \tag{2.166}$$

where $C'_{r/g/b}$ is the tone-mapped primaries, and $C_{r/g/b}$ is the original colour primary value. This colour reproduction method is used by many other tone-mapping algorithms [Reinhard et al., 2002; Reinhard and Devlin, 2005; Kim and Kautz, 2008b].

However, this may lead to perceptually flawed colour reproduction (either washed-out colours or over saturation), as has been shown in [Tumblin and Turk, 1999; Mantiuk et al., 2009]. Tumblin and Turk [1999] experienced washed-out colours after applying their tone-mapping operator and suggested a *luminance preserving correction* method:

$$C'_{r/g/b} = \left(\frac{C_{r/g/b}}{L}\right)^{s} \cdot L', \tag{2.167}$$

where s is a saturation factor, which was suggested to control the saturation of tone-mapped images.

Mantiuk et al. [2009] also demonstrate how to improve colour reproduction after contrast compression and enhancement. They conducted a series of subjective appearance matching experiments to measure the change. Even though they did not provide a full colour appearance model, they proposed colour correction formulae for current tone-mapping algorithms.

In addition to [Tumblin and Turk, 1999], Mantiuk et al. [2009] suggests a *non-linear colour correction* formula:

$$C'_{r/g/b} = \left(\left(\frac{C_{r/g/b}}{L} - 1 \right) s + 1 \right) L'. \tag{2.168}$$

The saturation parameter s is estimated with respect to a given luminance-specific tone-curve (depending on a contrast compression factor c). The tone curve is defined in a simplified form:

$$L' = (L \cdot b)^c , \tag{2.169}$$

where b is the brightness adjustment. Finally, Mantiuk et al. [2009] define the relationship between contrast c and saturation s as follows:

$$s(c) = \frac{(1 + k_1)\, c^{k_2}}{1 + k_1 c^{k_2}}, \tag{2.170}$$

where the parameters k_1 and k_2 are derived from their experimental data by a least-squares fit. The best fit for non-linear colour correction is k_1=1.6774 and k_2=0.9925 in Equation (2.168); the best fit for luminance preserving correction is k_1=2.3892 and k_2=0.8552 in Equation (2.167).

Mantiuk et al. [2009]'s method provides a practical solution for compensating colour reproduction with respect to tone-mapping algorithms. However, their non-linear colour correction formulae strongly distorts lightness, and while the hue is less distorted than the luminance when using the preserving formula. In addition, they also observed that an existing colour appearance model (CIECAM02) cannot explain the relationship between perceived brightness and colourfulness.

Image Appearance Advanced models exist that try to combine colour appearance models with spatial vision. Ferwerda et al. [1996] proposed a computational model of human vision that includes spatial adaptation. It was mainly based on previous psychophysical threshold experiments. It includes a *threshold* detection experiment that quantifies the perceptual threshold of luminance up to 10 000 cd/m^2. The experiment does not measure the suprathreshold appearance of luminance (e.g., magnitude experiments as in LUTCHI), but instead the threshold level of luminance. In contrast, we conducted suprathreshold measurements of perceived colour attributes (not only luminance) up to 16 860 cd/m^{2}of luminance (see Chapter 4 for more details on our experiments). Adopting Ward [1994]'s tone-mapping concept, Ferwerda et al. [1996] assume that the display luminance level L_d is achievable by scaling real-world luminance L_w with an appropriate scalar m: $L_d(L_w) = mL_w$. Ward [1994] defines a function to define the scalar m, which depends on real-world adaptation luminance L_{wa} and display adaptation luminance L_{da} as follows:

$$m\left(L_{wa}, L_{da}\right) = t\left(L_{da}\right) / t\left(L_{wa}\right) . \tag{2.171}$$

Ferwerda et al. [1996] replace the threshold function t with their threshold function, derived from their psychophysical measurements. Like the Hunt94 colour appearance model (see Section 2.3), they modelled the threshold function t on three different vision categories. First, the threshold function for photopic vision (cone only) $t_p(L_a)$ is modelled as follows:

$$\log t_p(L_a) = \begin{cases} -0.72\,, & \log L_a \leq -2.6 \\ \log L_a - 1.255\,, & \log L_a \geq 1.9 \\ (0.249 \log L_a + 0.65)^{2.7} - 0.72\,, & -2.6 < \log L_a < 1.9 \end{cases}, \tag{2.172}$$

where L_a is luminance $[cd/m^2]$. The function for scotopic vision (rod only) $t_s(L_a)$ is:

$$\log t_s(L_a) = \begin{cases} -2.86\,, & \log L_a \leq -3.94 \\ \log L_a - 0.395\,, & \log L_a \geq -1.44 \\ (0.405 \log L_a + 1.6)^{2.18} - 2.86\,, & -3.94 < \log L_a < 1.44 \end{cases}. \tag{2.173}$$

For mesopic vision (scotopic plus photopic vision) L_d, these two responses, photopic L_{dp} and scotopic L_{ds}, are summed with a scaling constant k :

$$L_d = L_{dp} + k(L_a) L_{ds}\,, \tag{2.174}$$

where k is a constant from 0 to 1 replacing the adaptation level. Finally, they employed a Gaussian convolution filter with respect to spatially-varying local adaptation as shown in [Reinhard et al., 2002]. The filter cuts off high frequency (high contrast) of luminance to match the observer's contrast threshold:

$$f^*\left(w_c\left(L_{wa}\right)\right) = \frac{t\left(L_{wa}\right)}{L_{wa}}, \tag{2.175}$$

where f^* is the Fourier transform of the convolution filter and $w_c(L_{wa})$ is the threshold frequency for real-world adaptation.

This method aims to produce the closest rendering results to human perception with high-dynamic-range scenes. In particular, it presents a rigorous approach in modelling the Purkinje break effect (see Section 2.3.3 for the phenomenon). However, their model considers only luminance perception. Accurate colour appearance phenomena were not modelled, e.g., Hunt effect, Stevens effect, or simultaneous contrast effect (see Section 2.3.3 for more details on the phenomena). In contrast, we conducted a full range of colour experiments, and derived a suprathreshold colour appearance model in a wider range of luminance levels (up to 16 860 cd/m^2).

Pattanaik et al. [1998] improved on [Ferwerda et al., 1996] using a multiscale model of adaptation and spatial vision, combined with the CIECAM97s model [CIE, 1998] (see Section 7.3.4 in [Reinhard et al., 2005] for more details of the mathematics). Their model is based on a rigorous survey of previous psychological literature, but they only use previous experimental data without any new experiment. Their method is a two-staged mechanism. The first stage is a visual encoding which aims to simulate cone and rod response with respect to spatially-varying adaptation, corresponding for a forward colour appearance model. The second stage is a display mapping that converts the perceptual information to a display signal. This stage is a combination of the partial inverse appearance model and a partial inverse device characterisation. Their tone-mapping algorithm is a simplified application of the CIECAM97s model.

The main structure of the visual encoding stage follows a Hunt-style structure (see the Hunt94 and CIECAM97s model in Section 2.3). The first step in visual encoding is to convert RGB input to LMS cone and rod signals through sRGB (see Section 2.2.2) and a HPE transform [see Equation (2.20)]. These four channel images are spatially decomposed into four seven-level Gaussian pyramids (a stack of seven Gaussian-blurred images). By subtracting adjacent Gaussian-blurred images $L/M/S_s^{blur}$in the pyramid, they compute four six-level difference-of-Gaussian (DoG) stacks $L/M/S_s^{DoG}$ at pixel (x,y), which are then normalised. After that, each of the DoGs in each of four channels are scaled by the gain function (equivalent to the threshold function in [Ward, 1994; Ferwerda et al., 1996]):

$$\begin{aligned} L_s^{DoG}(x,y) &= (L_s^{blur}(x,y) - L_{s+1}^{blur}(x,y)) \cdot G(L_{s+1}^{blur}(x,y)), \\ M_s^{DoG}(x,y) &= (M_s^{blur}(x,y) - M_{s+1}^{blur}(x,y)) \cdot G(M_{s+1}^{blur}(x,y)), \\ S_s^{DoG}(x,y) &= (S_s^{blur}(x,y) - S_{s+1}^{blur}(x,y)) \cdot G(S_{s+1}^{blur}(x,y)), \end{aligned} \tag{2.176}$$

where s indicates the stack level, and the gain function G is modelled as follows:

$$G(x) = \frac{1}{0.555(L+1)^{0.85}}. \tag{2.177}$$

The blurred image at level seven is retained and will form the basis for image reconstruction [Reinhard et al., 2005]. The pixels in the level (s=7) are adapted to the mean value:

$$\begin{aligned} L_7^{blur}(x,y) &= L_7^{blur}(x,y) G((1-A)\overline{L}_7^{blur} + A \cdot L_7^{blur}(x,y)), \\ M_7^{blur}(x,y) &= M_7^{blur}(x,y) G((1-A)\overline{M}_7^{blur} + A \cdot M_7^{blur}(x,y)), \\ S_7^{blur}(x,y) &= S_7^{blur}(x,y) G((1-A)\overline{S}_7^{blur} + A \cdot S_7^{blur}(x,y)), \end{aligned} \tag{2.178}$$

where A is a user parameter for interpolation. The adapted cone signals are then converted to achromatic and colour opponent signals following the Hunt94 and CIECAM97s models [CIE, 1998]. They then apply another contrast transducer functions on each channel respectively (see [Pattanaik et al., 1998]).

The first step in display mapping is to rescale the basis stack (level seven) with the mean luminance of a typical display $L_{d,mean}$ (∼50 cd/m^2), which is taken by the gain function G [Equation (2.177)]:

$$L_7^{blur}(x,y) = \frac{L_7^{blur}(x,y)}{G(L_{d,mean})}, \quad M_7^{blur}(x,y) = \frac{M_7^{blur}(x,y)}{G(M_{d,mean})}, \quad S_7^{blur}(x,y) = \frac{S_7^{blur}(x,y)}{G(S_{d,mean})}. \tag{2.179}$$

Finally, the stacks of DoGs (from zero to six levels) are accumulated in order to the adapted blurred image at level seven. The computed LMS cone signals are converted back to RGB through XYZ with gamma correction. Even though this method is technically sound, in practice, multi-scale Gaussian pyramid tone mapping presents more obvious halo artifacts than other tone-mapping algorithms.

Akyüz and Reinhard [2006] propose to combine a modified CIECAM02 model with tone mapping [Reinhard et al., 2002], in order to yield a better colour reproduction. As presented in Figure 2.17, when the employed colour appearance model can predict the real-world observation correctly, a tone-mapping algorithm is not required. However, insofar as the current conventional standard for colour appearance (CIECAM02) fails to predict the perception under high-dynamic-range luminances, the combination of the colour appearance model and tone mapping can be a practical solution.

Akyüz and Reinhard [2006] applied a modified colour appearance model with scene viewing conditions (forward) and output device viewing conditions (inverse). After that, tone compression is performed only on luminance (Y in the Yxy domain). When Akyüz and Reinhard [2006] adapts CIECAM02, the chromatic adaptation parameter D in CIECAM02 is modified [see Equation (2.90) for the original CIECAM02 equation] as follows:

$$D' = D(1-3s^2+2s^3), \tag{2.180}$$

$$\text{where } s = \frac{L - L_T + 0.1(L_{\max} - L_{\min})}{L_{T_1} - L_{T_0}}, \tag{2.181}$$

$$L_T = L_{\min} + [0.6 + 0.4(1-k)](L_{\max} - L_{\min}), \tag{2.182}$$

$$L_{T_0} = \max[L_{\min}, L_T - 0.1(L_{\max} - L_{\min})], \tag{2.183}$$

$$L_{T_1} = \min[L_{\max}, L_T + 0.1(L_{\max} - L_{\min})], \tag{2.184}$$

where if the luminance of a pixel is below L_{T_0}, the original D is used. If it is greater than L_{T_1}, D is set to 0 for the pixel. Otherwise, D' is used instead of D. According to colour appearance data such as LUTCHI, the degree of adaptation increases in proportion with luminance. However, D' decreases the degree of adaptation. Therefore, the used modification of the adaptation parameter is observed to conflict with previous findings.

In contrast, our colour reproduction mechanisms do not employ any tone-mapping algorithm. They calculate the human observation as perceptual coordinates, and the perceptual values are reproduced on target medium through an analytical inverse model (see Chapter 5 and 6 for more details on our model and reproduction pipeline). Furthermore, our colour appearance model can be used to keep the perceived colourfulness and hue of colour samples as close to the original as possible during tone-mapping.

iCAM [Johnson and Fairchild, 2003] is an *image appearance* model that is intended to predict the appearance of images, including HDR images. It combines components of traditional colour appearance models with spatial models of vision. iCAM has been developed through empirical modification of a colour appearance model, CIECAM02. iCAM aims to associate CIECAM02 with a spatially-varying tone-mapping algorithm. The goal and approach are similar in a sense to [Akyüz and Reinhard, 2006]. Kuang et al. [2007] introduced a revised image appearance model, called iCAM06, which is essentially a combination of CIECAM02 with tone mapping [Durand and Dorsey, 2002].

We briefly review the mathematical details of the latest version of iCAM [Kuang et al., 2007].

An RGB source image is transformed into XYZ through the sRGB transform (see Table 2.1 for the transform). The XYZ image is then decomposed to a base layer and a detail layer through bilateral filtering [Durand and Dorsey, 2002] [see Equation (2.159)] . The base layer is used as input to the chromatic adaptation and tone mapping (modified from CIECAM02), while the detail layer is combined after the tone-mapping process.

The chromatic adaptation of iCAM06 is inherited directly from CIECAM02 [see Equations (2.89), (2.90), and (2.91)]. They set the luminance adaptation parameter L_A to 20%, and surround factor F to 1 (average surround). The degree of adaptation D is empirically scaled down to 30% (D scaled by 0.3). Instead of using the D50-adapted XYZ transform (see Table 2.2), the white point of the CIECAT02 transform [see Equation (2.89)] is changed into D65. In particular, they assume that the human visual system performs spatially-varying white adaptation. The Gaussian blurred original XYZ image is used as a set of local white points in their implementation of the chromatic adaptation in CIECAM02. However, our experiments (see Chapter 6) find that spatially-varying white balancing yields unrealistic results. After that, the base layer is converted into LMS cone and rod signals. In the Naka-Rushton equation in the CIECAM02 model, they empirically replace the exponent constant 0.43 with 0.75 (similar to 0.73 in CIECAM97s) in Equation (2.93). They also include rod response modelling adapted from the Hunt94 model [see Equations (2.40), (2.41), and (2.43)].

Next, the tone-mapped base layer is converted to XYZ values and combined with the detail layer. The combined layer is converted to the IPT colour space [Ebner and Fairchild, 1998]. In the IPT colour space, the image coordinates (lightness, chroma, and hue in the IPT space) can be used as perceptual coordinates. They also empirically adjusted image attributes (contrast of detail layer, chroma, and surround effect). The detail later is changed by using F_L in CIECAM02 to mimic the Stevens effect:

$$Details_a = Details^{(F_L+0.8)^{0.25}} . \tag{2.185}$$

The chroma is also modified to mimic the Hunt effect:

$$P' = P \cdot [(F_L+1)^{0.2}(\frac{1.29C^2 - 0.27C + 0.42}{C^2 - 0.31C + 0.42})] , \tag{2.186}$$

$$T' = T \cdot [(F_L+1)^{0.2}(\frac{1.29C^2 - 0.27C + 0.42}{C^2 - 0.31C + 0.42})] , \tag{2.187}$$

$$\text{where} \;\; C = \sqrt{P^2 + T^2} . \tag{2.188}$$

With respect to the surround effect, I coordinates (lightness) are modified:

$$I_a = I^{\lambda} , \;\; \text{where} \;\; \lambda_{dark} = 1.5, \, \lambda_{dim} = 1.25, \, \lambda_{average} = 1.0. \tag{2.189}$$

Finally, the IPT colour space values are transformed to RGB signals through the XYZ colour space, then these signals are clamped to the 1^{st} and 99^{th} percent of the image data to achieve improved plausibleness in the final output images.

As opposed to previous colour appearance models, in fact, the modification of CIECAM02 in iCAM is not derived from experimental data (empirical modification in previous equations), although psychophysical experiments were conducted for evaluation purposes. In contrast, our colour appearance model is analytically derived from psychophysical experimental data like other colour appearance models; as a result, our model can achieve better performance than other empirical image appearance models (see Chapter 6 for more details on comparison). However, our aim is not to derive a full image appearance model; instead, we want to derive a pure colour appearance model that enables accurate predictions of colour perception. (see Chapter 5 for more details on our colour appearance model).

2.5.4 Summary

We first reviewed HDR image acquisition algorithms, which enables the creation of HDR images from multiple exposures. HDR image acquisition algorithms comprise two main stages: solving for the camera response function (converting pixel values to exposure) and accumulating radiance (exposure divided by time interval) at each pixel. Curve-fitting [Debevec and Malik, 1997], polynomial regression [Mitsunaga and Nayar, 1999], or ICC profiling [Göesele et al., 2001] yield a camera response function from captured camera signals. As it turns out, the first stage is not necessary if we utilise the solid-state response to incident light directly such as [Mann and Picard, 1995; Yamada et al., 1995; Xiao et al., 2002]. Professional DSLR cameras provides direct output from the sensor, called *RAW images*. With these, we can simplify the HDR imaging algorithm with improved accuracy, skipping the first stage — including non-linear regression (see Chapter 3 for more details on the our HDR imaging algorithm).

Theoretically, if there is a display which can produce luminance as it exists in the real world in terms of dynamic range and maximum luminance, the captured HDR images can be reproduced on the display by simply mapping the camera signals to the display ones. Seetzen et al. [2004] propose an HDR display with a higher dynamic range and brighter maximum luminance than existing displays.

However, the luminance levels of most displays is not identical to that of the real world. We need a specific solution to deal with this difference of luminance levels, called tone-reproduction operators or tone-mapping algorithms. The main aim of tone-reproduction operators is to achieve the same appearance on a output display, which is identical to the human perception of the real scene. The research falls into three categories: global adaptation models, local (spatially-varying) adaptation models, and image appearance models. Global adaptation models [Tumblin and Rushmeier, 1993; Ward, 1994; Ward et al., 1997; Drago et al., 2003; Reinhard and Devlin, 2005; Kim and Kautz, 2008b] attempt to achieve a similar response function to the human response function on incident luminance. They generally provide high computational efficiency, but are less able to handle the variation in dynamic range than local approaches. Local adaptation models [Tumblin and Turk, 1999; Fattal et al., 2002; Reinhard et al., 2002; Durand and Dorsey, 2002] attempt to achieve great flexibility in the compression of dynamic range with the assumption that the human eye is less sensitive to variations at low spatial frequencies than higher ones. They manipulate frequency, gain, or gradient in multi-bandwidths (detail and base layers), and often struggle with high computational cost and halo artefacts. Tone-mapping operators [Schlick, 1994; Tumblin and Turk, 1999; Mantiuk et al., 2009] address colour reproduction problem while compressing luminance and attempt to solve the colour problem in an empirical manner. Finally, image appearance models [Ferwerda et al., 1996; Pattanaik et al., 1998; Johnson and Fairchild, 2003; Akyüz and Reinhard, 2006; Kuang et al., 2007] attempt to make a computation model identical to the human vision system. They are often based on physiological assumptions, measurements from primates, or psychophysical experiments.

Most tone-mapping algorithms are derived from the same assumption that the human visual system has a specific mechanism to observe real-world luminance. They attempt to model the response mechanism from previous experimental evidence or their own hypothesis, where the used data is often limited in dynamic range compared to real-world luminance, or not appropriate, or the hypothesis cannot prove the scientific soundness without experimental observation. These tone-mapping algorithms only modify lightness while keeping the colour channels untouched, suggested by Schlick [1994]. However, as shown in [Tumblin and Turk, 1999; Mantiuk et al., 2009], this may lead to perceptually flawed colour reproduction. Mantiuk et al. [2009] attempt to change colourfulness of tone-mapped images according to experimental data, but they would need to include other colour properties such as lightness and hue in order to obtain plausible colourfulness. On the other hand, image appearance models attempt to solve this colour problem with empirical modification to the current colour appearance model by combining CIECAM02 with a tone-mapping algorithm. However, such hybrid solutions have struggled with performance. In contrast, our approach is to develop a novel colour appearance model derived from new experimental data that covers the full working range of the human visual system. This approach attempts to minimise any empirical modification to previous equations or unproved hypothesis (see Chapter 5 and 6 for more details on our model).

2.6 Discussion

Although HDR imaging technology extends the dynamic range in input/output media, the newly extended dynamic range in HDR imaging is not compatible with previous cross-media colour reproduction systems as they had been developed and optimised for integer-based LDR imaging systems. For instance, first, traditional characterisation techniques for digital cameras fail with HDR imaging, and produce considerable errors. The dynamic range of traditional colour targets and modelling techniques can only cope with the dynamic range of ordinary LDR cameras (see Chapter 3). Second, image appearance on high-luminance displays, e.g., HDR displays, are perceived to be different, compared with their appearance on low-luminance displays like CRT or LCD display. Specific colour appearance phenomena, the Stevens and Hunt effects, are strongly observed on high-luminance displays as our psychophysical experiments validated (see Chapter 4). Third, current colour appearance models fail in predicting such colour appearance phenomena under high luminance levels and are not applicable for HDR image reproduction (see Chapter 5 for results). The reason for the incompatibility is that current colour appearance models were derived from low-luminance experimental data (under about 690 cd/m^2) limited by the available display technology in the 1990s, such as CRT displays. To correct this problems, a newly derived *cross-media colour reproduction system* for HDR imaging is presented in Chapter 6. It comprises three stages: HDR characterisation, a forward colour appearance model, and an inverse colour appearance model. Results indicate that the proposed system yields high-fidelity colour reproduction in HDR images (see Chapter 6 for more details on the reproduction pipeline). The following chapters will describe our experiments in more detail.

Chapter 3

Characterisation for High-Dynamic-Range Imaging

In this chapter, a new practical camera characterisation technique is presented to improve colour accuracy in high-dynamic-range (HDR) imaging. Camera characterisation refers to the process of mapping device-dependent signals, such as digital camera images, into a well-defined colour space (see Section 2.2 for background). This is a well-understood process for low-dynamic-range (LDR) imaging and is part of most digital cameras. It is usually a mapping from the raw camera signal to the sRGB or Adobe RGB colour space. This chapter presents an efficient and accurate characterisation method for HDR imaging that extends previous methods originally designed for LDR imaging. We demonstrate that our characterisation method is very accurate even in unknown illumination conditions, effectively turning a digital camera into a measurement device that measures physically accurate radiance values, in terms of both luminance and colour, and rivals more expensive measurement instruments. We then estimate the correlated colour temperature of the scene as a reference white point for white-balancing the HDR radiance map. Finally, the physically meaningful HDR radiance map is used later on as input to our colour reproduction system.

3.1 Motivation

Recent advances in HDR imaging allow us to easily obtain radiance maps with off-the-shelf digital cameras by combining multiple exposures into a single HDR image [Mann and Picard, 1995; Saito, 1995; Debevec and Malik, 1997; Mitsunaga and Nayar, 1999; Robertson et al., 1999]. These acquired radiance maps are commonly used as environment maps for lighting simulations or for computational photography applications. However, the radiometric accuracy of the acquired HDR radiance maps — in terms of both luminance and colour — has rarely been discussed or evaluated because traditional characterisation methods for LDR imaging [Martínez-Verdú et al., 2000; Pointer et al., 2001; MacDonald and Ji, 2002; Martínez-Verdú et al., 2003; Kim et al., 2005; ISO, 2006; Normand et al., 2007] were not designed to characterise HDR radiance maps. We propose a new camera characterisation method that works well for HDR imaging as it is more accurate than many of the LDR methods and is very efficient in terms of acquisition time and cost. Our method is based on the insight that common reflective targets have two main drawbacks: they only offer a low dynamic range which makes them not a good choice for HDR imaging, and that characterisation based on reflective targets requires both the reflectance of the target and the spectrum of the illuminant to be known. Therefore, we propose to use a novel back-lit transparency target specifically designed for HDR imaging, offering a higher dynamic range and wider colour gamut. Our method only requires the emitted radiance to be known, which can be measured using a spectroradiometer. This enables us to accurately characterise digital cameras used for HDR imaging. We show the effectiveness of the new method by characterising three different digital cameras. The achieved accuracy of the cameras is similar to the accuracy of a spectroradiometer. As we will demonstrate, radiance maps acquired by different cameras are virtually the same when using our characterisation method.

Our goal is to develop a novel method to obtain a *physically-accurate* HDR radiance map with a camera system. Then, the captured radiance maps are white-balanced and tone-mapped for display. The following sections describe a novel HDR characterisation method and a novel white-balancing method for displaying HDR radiance maps.

3.2 Acquisition of HDR Radiance Maps

3.2.1 Response of Digital Cameras

The sensing area of digital cameras is a solid-state sensor upon which incident photons cause charge to accumulate at discrete locations called pixels. This charge is transferred as an output digital signal via an ADC [Yamada, 2006] (see Section 2.2 for more details). The amount of digitised electronic charge is linear to irradiance on the sensing area — excluding the *noise floor* (fixed-pattern noise, sensor dark current, etc. [Holst, 1998]) and *blooming* (overflowing) [Janesick, 2001] of the sensor response (see Section 2.2.4 for more details). Typically, a non-linear function is applied to improve the dynamic range of the camera and at the same time this also takes care of gamma-correction for display. Most DSLR cameras allow the 12–16 bit linear digital signals to be output before non-linear processing (gamma correction, tone mapping, and histogram equalisation) as a *RAW* image [Coffin, 2009]. Within the possible range of camera signals, these RAW images correspond to the amount of charge of all the incident photons on the sensor, effectively measuring scene radiance at each pixel.

Figure 3.1 presents the measured responses of a digital camera. A Canon 350D DLSR camera captured a transparency reference target, IT8.7/1 [ANSI, 1999] [see Figure 3.1(a)], in RAW as non-linear TIFF images. Luminances of greyscales in the target were measured by a spectroradiometer (a Jeti Specbos 1200) which has a luminance accuracy of ±0.05 at $1000 cd/m^2$ and chromaticity repeatability of ±0.0005 (x,y) [Morgenstern et al., 2004]. The corresponding signal levels were read in RAW and non-linear TIFF images. Figure 3.1(b) presents a comparison between the ordinary non-linear response (marked with green triangles) and the RAW response (marked with blue-lined white triangles). As shown in Figure 3.1(b), the RAW camera response is linearly proportional to the incident light while the ordinary camera response presents a non-linear trend (a power function) in response. In this experiment, we use linear RAW signals to generate HDR radiance maps so that we

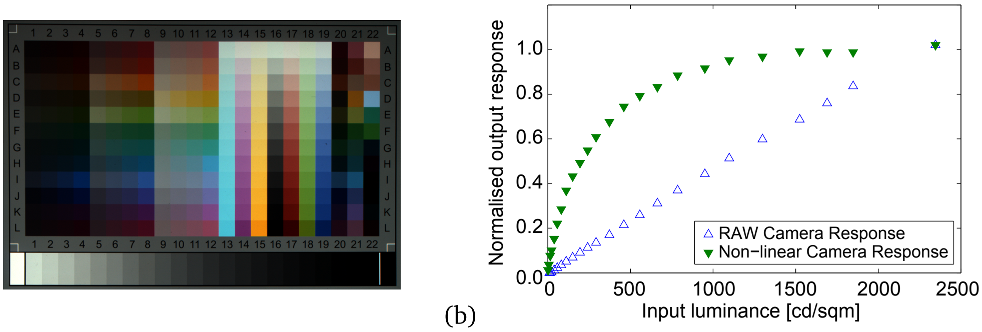

(a) (b)

Figure 3.1: *Image (a) presents the linear RAW sensor response of a Canon 350D digital camera (interpolated into RGB channels, but not gamma-corrected) and shows the captured transparency reference target, IT8.7/1 [ANSI, 1999]. Image (b) presents characteristic curves of the ordinary non-linear response, and the RAW sensor response from the camera. The Y axis, which signifies the acquired response, is normalised in the range [0.0,1.0]. The X axis represents the luminance in greyscales of the target [image (a)] measured by a spectroradiometer. As the plot shows, the RAW response is proportional to the amount of incident light.*

avoid curve fitting regression and its potential inaccuracies. Next, we demonstrate how to generate HDR radiance maps from RAW responses.

3.2.2 Camera Setup

In this experiment, three different DLSR cameras were tested: a Nikon D100 with a 35mm lens, a Canon 350D with an 18–55mm lens, and a Nikon D40 with an 18–55mm lens. These cameras support manual control over exposure parameters. The exposure parameters were manually calibrated with an identical setting of aperture size (f/11), shutter speed (1/4000–30seconds in one-step intervals for exposure bracketing — HDR source images), and film speed (ISO 200). No automatically-estimated exposure parameters were involved in producing the RAW output images.

A white-balancing procedure is required to display the characterised radiance map. Like the exposure parameters, the cameras provide automatic estimation of the white point of captured scenes. The estimated white point information is essential for achieving colour constancy (see Section 3.4). This automated white balancing is generally the default option in digital cameras. However, the cameras' internal colour temperature estimate may not be directly applicable for white balancing, as it is often skewed to accommodate user preference. For instance, with the Canon 350D, we captured a GretagMacbeth ColorChecker DC chart under different illumination conditions with a colour temperature ranging from 2000K to 7500K in 500K intervals. We measured the correlated colour temperature (CCT) of the scene illumination and recorded the white-balancing multipliers estimated by the camera. Then the white-balancing multipliers are converted to CCT. The brown sigmoidal curve in Figure 3.2 shows the Canon 350D's colour temperature estimation of the GretagMacbeth images (derived from white balancing multipliers), which indicates a deliberate choice to overestimate the colour temperature (yielding more yellowish images under lower colour tem-

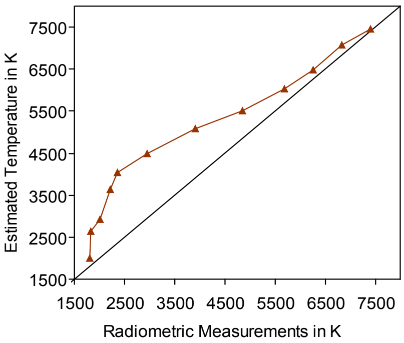

Figure 3.2: *Correlated colour temperature estimates from a digital camera (Canon 350D).*

peratures). Therefore, although the cameras store the estimated white-balancing multipliers in the header of the RAW files, we discard them and use our estimation method of scene illumination in order to display the characterised image more accurately, i.e., we use the raw colour response directly from the sensor instead of the automatically white-balanced image. As a result, the RAW sensor response (without auto white balancing) appears cyan-greenish as the incident light is filtered by an infrared-blocking filter (cutting out the wavelengths beyond red, see Section 2.2.4 for more details) before light reaches the solid-state sensor. Then, instead of using the automatic white balancing from the camera value, we estimate a correlated colour temperature of the scene illumination with our method (see Section 3.4 for more details) and conduct white balancing to display images.

3.2.3 Low-Dynamic-Range Source Images

Previous research [Mann and Picard, 1995; Debevec and Malik, 1997; Mitsunaga and Nayar, 1999; Robertson et al., 1999] presents many HDR imaging methods to derive an exposure function to describe a camera's response to incident light. The exposure function virtually linearises non-linear camera responses in multi-exposed images. These regression methods contain potential computational errors in estimating the non-linear exposure function. With respect to *accuracy*, the best solution for generating HDR images is to use the *linear* response from a RAW image rather than the non-linear response from ordinary images; hence, we choose the RAW response to build HDR

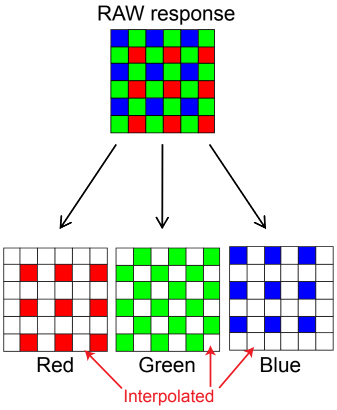

Figure 3.3: *Channel separation from RAW response to RGB channels.*

images. As such, the first step in the HDR imaging algorithm (estimating a camera exposure function, see Section 2.5.1 for more details on HDR imaging algorithms) is not needed. Instead, an additional procedure is required to use a RAW response. A RAW response is a Bayer-pattern mosaic image of a single channel where generally a red, green, blue, and green channel pattern (or CMYM) covers the solid-state sensor. To yield an ordinary RGB image of three channels, we need to interpolate the missing data [Shortis et al., 2005]. (see Figure 3.3). We employed a so-called *adaptive homogeneity-directed method* [Hirakawa and Parks, 2003] for the interpolation process by adapting [Coffin, 2009]. Unlike ordinary conversion of RAW images, we do not perform *gamma correction*, *tone reproduction* (e.g., histogram equalisation), and *white balancing*. The RAW images are stored as 16-bit integer images. Note that these cameras have a 12-bit ADC, so output signals are rescaled up to 16 bits and stored.

3.2.4 High-Dynamic-Range Image Acquisition

We obtained linear 16-bit RAW images with exposure variations P and shutter times T, from which an HDR radiance map was generated. Logarithms of radiance values E at each pixel i are computed from the weighted average of the differences between the pixel response Z_i and the shutter time $\log_2 T$ in shutter intervals j:

$$log_2 E_i = \frac{\sum_{j=1}^{P}[log_2(Z_{ij}) - log_2(T_j)]w(Z_{ij})}{\sum_{j=1}^{P} w(Z_{ij})}, \tag{3.1}$$

where the weighting function w is a normalised pyramid:

$$w(z) = \begin{cases} z - Z_{\min} \ , & z \le \frac{1}{2}(Z_{\min} + Z_{\max}) \\ Z_{\max} - z \ , & z > \frac{1}{2}(Z_{\min} + Z_{\max}) \end{cases}, \tag{3.2}$$

where Z_{max} is 65535, and Z_{min} is 0. This procedure is similar in sense to the second stage [Equation (2.135)] of Debevec and Malik [1997]'s method. Instead of deriving an exposure function from photographs, we take the direct sensor signals as the first stage. By taking RAW responses from the cameras [Debevec and Malik, 1997; Mitsunaga and Nayar, 1999; Robertson et al., 1999], the acquisition of HDR radiance maps is simplified.

Figure 3.4 is a qualitative comparison between the RAW sensor signals and the HDR radiance map. These two sets of values are proportional to measured luminance. We tested the linearity of these two responses to incident luminance by computing the CV against incident luminance [see Equation (2.12) for more details on the CV calculation]. The RAW signal's CV to the incident luminance was 6.66, and the HDR radiance's CV was 2.54. Hence, measuring luminance by using the HDR radiance map is more accurate than simply using the RAW signal. The next section describes how to calibrate colours in the HDR radiance map.

3.3 High-Dynamic-Range Characterisation

Camera characterisation is defined as the transform of device-dependent signals into device-independent coordinates [Johnson, 2002] such as CIEXYZ tristimulus values. Ideally, the same

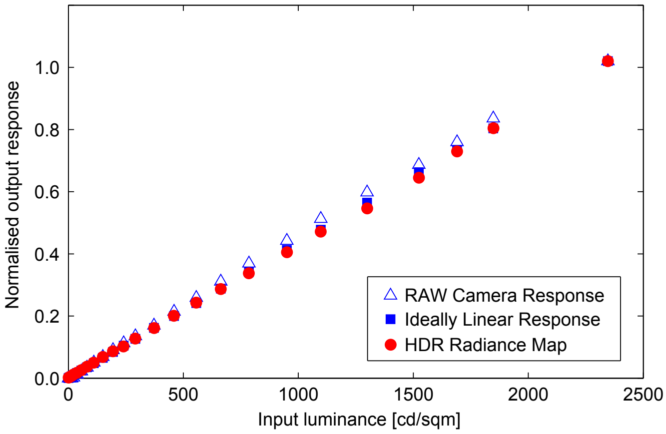

Figure 3.4: *Characteristic curves of: RAW sensor response of the Canon 350D camera and an HDR radiance map is green channel, compared with the ideally-linear response. The Y axis, which signifies the acquired response, is normalised into the range [0.0,1.0]. The X axis represents luminance measured by a spectroradiometer. The square points on the diagonal show the ideally linear response. As the plot shows, the RAW response and the computed HDR radiance map are proportional to the incident light. CVs to the ideally linear signals are 6.66 (RAW signals) and 2.54 (HDR radiance map).*

mapping works for any illumination. However, as mentioned in Section 2.2.5, previous characterisation methods were either limited to known illumination conditions [Pointer et al., 2001; MacDonald and Ji, 2002; Johnson, 2002; ISO, 2006] or required expensive equipment and prohibitive measurement times [Martínez-Verdú et al., 2000; MacDonald and Ji, 2002; Martínez-Verdú et al., 2003; ISO, 2006; Normand et al., 2007]. Furthermore, these characterisation methods were geared towards *low-dynamic-range* imaging.

Inanici and Galvin [2004] and Krawczyk et al. [2005] proposed to rescale the measured luminance values in HDR radiance maps by comparing them with measurements from a luminance meter. In contrast, our method calibrates luminance and colour at the same time. We propose a new technique which offers the simplicity of reflectance-based techniques with the accuracy and the universal applicability of monochromator-based techniques. Furthermore, it is well-suited for HDR imaging and can characterise both colour and luminance. Our experiments show that a digital camera, characterised with our method, can capture measurements of the colour and luminance information of a scene that are almost identical to the measurements from a spectroradiometer that we tested. See Chapter 3 for more details of our characterisation method.

Through HDR imaging (see Section 3.2.4 for more details), we build a *device-dependent* HDR radiance map, where the HDR trichromatic response values (red $\mathbf{r}$, green $\mathbf{g}$, and blue $\mathbf{b}$) of pixels on the sensor are given as the sum of the product of the spectral power distribution of the light source $P(\lambda)$, the reflectance (or transmittance) of the imaged object $S(\lambda)$, and the spectral responsivities of the colour filters $D_{r/g/b}(\lambda)$ — assuming that incident light is reflected from object surfaces:

$$[\mathbf{r},\mathbf{g},\mathbf{b}] = \sum_{\lambda} P(\lambda)S(\lambda)D_{r/g/b}(\lambda)\Delta\lambda\,. \tag{3.3}$$

The sum in Equation (3.3) is taken over a suitable wavelength range in the visible part of the spectrum, for instance, from 380nm to 780nm [ISO, 2006] (see Figure 2.8 for an example). The calculation of these response values is similar to the computation of device-independent tristimulus values, such as CIEXYZ:

$$[\mathbf{x},\mathbf{y},\mathbf{z}] = \sum_{\lambda} P(\lambda)S(\lambda)F_{\overline{x}/\overline{y}/\overline{z}}(\lambda)\Delta\lambda\,, \tag{3.4}$$

where $F_{\overline{x},\overline{y},\overline{z}}(\lambda)$ are the CIE colour matching functions [CIE, 1986]. The only difference between Equation (3.3) and (3.4) is the use of different weighting functions $D_{r/g/b}$ and $F_{\overline{x},\overline{y},\overline{z}}$. Therefore, HDR characterisation finds a mapping between the colour spaces of HDR radiance and tristimulus values by modelling the difference between the $D_{r/g/b}$ and $F_{\overline{x},\overline{y},\overline{z}}$ functions.

Our technique is based on two insights. First, the product of the spectral power distribution of the light source $P(\lambda)$ and the reflectance of the calibration target $S(\lambda)$ can be measured in a single step using a spectroradiometer, allowing camera characterisation that is efficient both in terms of cost and measurement time. Second, a novel back-lit transparency target specifically optimised for HDR imaging has a wider gamut and higher dynamic range than ordinary reflective targets. This makes the characterisation produce accurate measurements of luminance and colour and makes it applicable even in unknown illumination conditions.

3.3.1 Setup

We created our own transparency targets by photographically enlarging the IT8.7/1 [ANSI, 1999] colour chart onto Kodak Ektachrome professional film (8-by-10 inch) such that each patch matches the sensing area of the employed spectroradiometer (approximately 8mm in diameter). Two enlarged identical targets, one placed over three sheets of neutral density (2×) filters (in total 8× darker), are placed on an uniform light emitting table in a darkroom to produce a *training set* with 576 colour patches and a dynamic range of 4.53 orders of magnitude. The light source's correlated colour temperature (CCT) was 5434K. Using a transparency target not only offers a high dynamic range, but also provides a very wide colour gamut, [Figure 3.5 and 3.6(a)].

Two GretagMacbeth ColorChecker targets and two 800W halogen light sources (CCT: 2856K) are used to produce a *test set* with 48 colour patches. One target is illuminated by two halogen-type lights, which have different spectral characteristics from the light source used for the training data set. The other target is placed in a shadow area such that the scene has a large dynamic range (4.00 orders of magnitude). The emitted/reflected radiance of each patch in these two experimental sets were measured with the spectroradiometer, see Figure 3.6. Finally, we took HDR images of these two datasets using three different digital cameras for characterisation (Canon 350D, Nikon D100, and Nikon D40), see Figure 3.7.

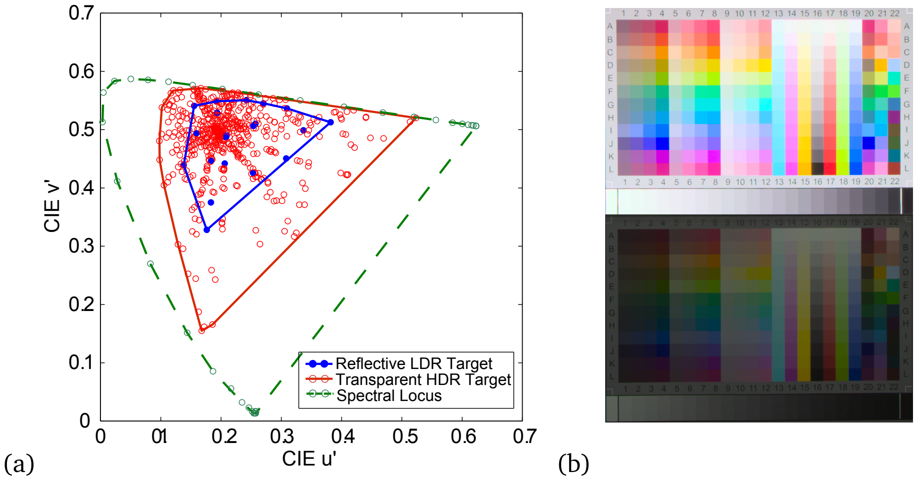

Figure 3.5: *Image (a) shows a comparison of measured gamut boundaries. The transparency HDR target provides a comparatively larger colour gamut than an ordinary reflective target (GretagMacbeth ColorChecker). Each side of our target [as seen on Image (b)] is an enlarged IT8.7/1 [ANSI, 1999] colour chart on Kodak Ektachrome professional film (8-by-10 inch).*

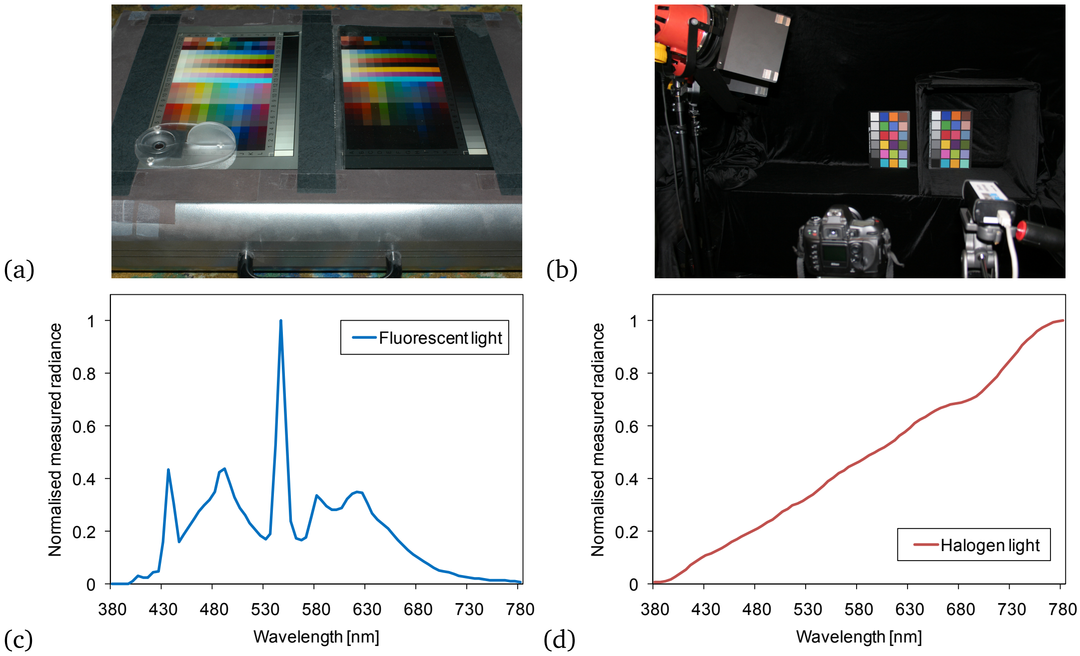

Figure 3.6: *Image (a) presents the training setup of the HDR transparency reference colour samples. 576 colour patches were measured with a spectroradiometer and captured by a camera in a darkroom. Image (b) shows the setup for testing HDR characterisation models. Two GretagMacbeth ColorChecker targets and two 800W halogen light sources on the left (CCT: 2856K) were used to produce a test set with 48 colour patches. Plot (c) shows the spectral power distribution of the fluorescent light bulb (of the training setup) which presents a peak between 530 and 580 nm. Plot (d) presents the spectral power distribution of the halogen light bulb (of the test setup) which is spread more toward infrared wavelengths.*

3.3.2 Characterisation

In traditional colorimetry (see Section 2.2.2), $P(\lambda)$ in Equation (3.4) refers to *relative* spectral power distributions, which are always normalised (100 at 560nm [Hunt, 1998]). This discards the intensity scale of the illumination, which is why previous characterisation models have difficulties calibrating absolute scales. Furthermore, when tristimulus reflectance values are measured by a spectrophotometer (e.g., GretagMacbeth Spectrolino), a calibrated tungsten light is used, which is then converted into a CIE D50 illuminant $P_{D50}(\lambda)$ [Equation (3.4)]. However, the scene illuminant $P(\lambda)$ [in Equation (3.3)] is different from that, effectively building this mismatch into the characterisation, which poses problems when different scene illumination is used after characterisation (see Figure 3.8). Hence, our technique uses identical $P(\lambda)$ and absolute spectral power distributions to solve both scale and illumination problems (see Figure 3.9 for our geometry setup).

Using the above setup, we know the emitted radiance values for each patch of our transparency target (measured using the spectroradiometer), corresponding to Equation (3.4). Furthermore, the linear camera response for each patch is known from the HDR image (corresponding to Equation (3.3), see Appendix A.3 for the measurements of the colour samples). Since the illumination is identical for both, we can now find a (least-squares) linear transform between the RGB camera response and the physical CIEXYZ radiance values that is applicable to unknown lighting [the $P(\lambda)$

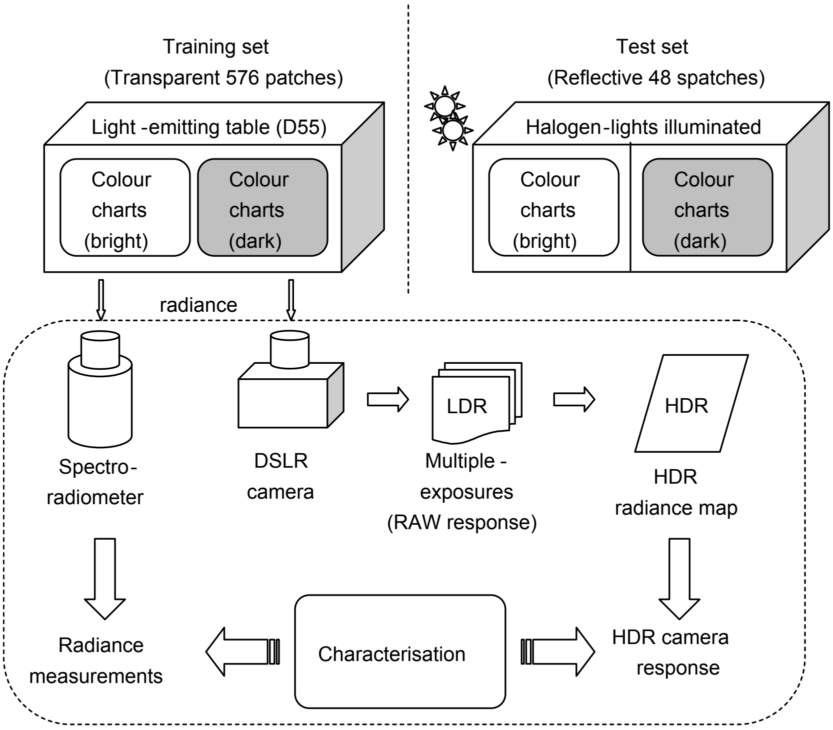

Figure 3.7: *Setup of HDR characterisation. A back-lit transparency colour target is captured by a digital camera and all its colour patches are measured using a spectroradiometer, which forms the training set that is used to compute the characterisation model. A second test set is acquired for validation purposes. It consists of two GretagMacbeth colour charts illuminated by light from a halogen bulb.*

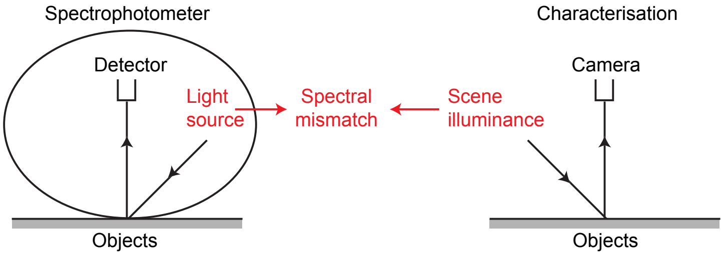

Figure 3.8: *Traditional characterisation setup of reflectance-based models. In order to measure reflectance, spectrophotometers use an internal light source (see Section 2.2.2 for more details on geometry). Generally a tungsten or xenon bulb is used as light source, then converted into a CIE D50 illuminant to yield CIEXYZ measurements. However, the scene illumination that is used in characterisation is different from the CIE D50 illuminant. Such a spectral mismatch is built into the characterisation, which poses problems when different scene illumination is used after characterisation.*

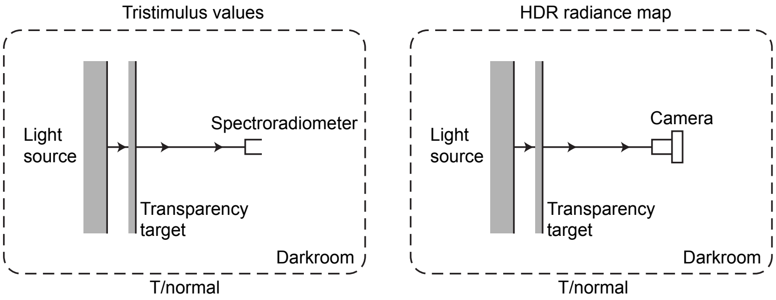

Figure 3.9: *Measuring geometry setup for high-dynamic-range characterisation. Our HDR transparency target is installed on top of the uniform light emitting table in a dark room to produce a set of colours (576 patches). The light source, the colour samples, and measuring device are placed on a straight line (normal to transparency), where the emitted radiances of the patches are measured simultaneously by the spectroradiometer and a digital camera that yields HDR images. Therefore, the identical light source is used in both tristimulus and HDR radiance measurements and will be cancelled out when deriving a characterisation model.*

cancels out]:

$$\mathbf{X} = (\mathbf{A}^\top \cdot \mathbf{A})^{-1} \cdot \mathbf{A}^\top \cdot \mathbf{M}\,, \tag{3.5}$$

where $\mathbf{X}$ is a 3×3 transform for characterisation, $\mathbf{A}$ is a matrix containing the linear RGB camera response $[\mathbf{r}, \mathbf{g}, \mathbf{b}]$ for each patch, and $\mathbf{M}$ is a matrix containing the measured radiometric CIEXYZ values $[\mathbf{x}, \mathbf{y}, \mathbf{z}]$ for each patch.

This transform $\mathbf{X}$ can now be used to map any (high-dynamic-range) RGB value into a physically meaningful CIEXYZ value, independent of the illumination. In our particular setup we find three transforms, one for each digital camera.

3.3.3 Characterisation Models

Table 3.1 presents the matrices of the linear transform from camera HDR into CIEXYZ coordinates, which were computed as outlined in Section 3.3.2. Note that these matrices not only transform colorimetric information but also luminances, because we take absolute scales into account such that the characterised coordinates are identical to the physical radiance measurement. However, the scale of the matrices may be different for other HDR assembly algorithms.

	Canon 350D / 18-55mm lens		
	R	G	B
X	6.8364	1.1685	0.3256
Y	3.0657	4.1205	-1.2861
Z	0.3650	-0.6863	6.3905

	Nikon D40 / 18-55mm lens		
	R	G	B
X	12.9566	1.6246	0.8274
Y	6.0406	6.4671	-1.5985
Z	0.5537	-0.9170	11.5996

	Nikon D100 / 35mm lens		
	R	G	B
X	10.1001	1.4246	0.5921
Y	4.6565	5.2054	-1.5151
Z	0.4985	-0.7648	10.1364

	Averaged		
	R	G	B
X	9.9644	1.4059	0.5817
Y	4.5876	5.2643	-1.4666
Z	0.4724	-0.7894	9.3755

Table 3.1: *Transformation matrices from high-dynamic-range signals into CIEXYZ. The transforms were computed from HDR radiance maps of our transparency target and the corresponding radiance measurements.* Averaged *refers to the mean matrix of the three different cameras.*

3.4 White Balancing of HDR Radiance Maps

Our mapping transforms HDR input images into physically-meaningful CIEXYZ values. However, in case an image is not intended for measurement purposes but for display (e.g., using a tone-mapping method), we need to take the human visual system into account, which adapts to a given illumination condition. This is a classical issue and is traditionally called *white balancing*. There are a variety of techniques available to simulate this adaption [Hubel et al., 1999; Fairchild, 1991; Finlayson et al., 1997].

Colour temperature is defined as the spectral power distribution of a Planckian blackbody radiator [Wyszecki and Stiles, 1982]. Even though many real-world illuminants are not exactly equal to any of the chromaticities of a blackbody radiator, we can compute the *correlated colour temperature* (CCT) [Holm and Krochmann, 1975], which refers to the closest matching temperature. In our work, we estimate the CCT of a scene. While this assumes the scene illumination to be on the blackbody locus, it acts as a constraint which allows us to find good estimates.

Techniques for estimating the correlated colour temperature are usually a part of *computational colour constancy* [d'Zmura and Lennie, 1986], which simulate the human visual system's chromatic adaptation in digital imaging. Conceptually, these algorithms first *estimate* the correlated colour temperature and then *balance* the white point of the image accordingly. In the context of this thesis, we use colour constancy in two ways. First, we propose an efficient method to estimate the correlated colour temperature of a scene; and second, we white-balanced the captured HDR radiance maps for final display.

Many colour constancy methods have been proposed (see Section 2.2.6 for more details), but despite the large variety of available methods, no algorithm can be regarded as universal. In practice, the grey-world and maxRGB approaches perform well on natural, real-world images [Hordley, 2006; Gijsenij and Gevers, 2007]. We therefore proposed an enhanced version of the grey-world algorithm to estimate the scene's CCT. We derive a linear transform from real-world training images with radiometric measurements instead of synthetic images [Barnard et al., 2002], and we further apply a weighting scheme that combines the maxRGB and grey-world methods.

3.4.1 Estimating the Scene Illumination

The camera signal C (for each colour channel $k = r, g, b$) is the sum of the product of surface reflectance $S(\lambda)$, camera response function $D_k(\lambda)$ (e.g., influenced by colour filters), and irradiance $P(\lambda)$ over all wavelengths λ:

$$C_k = \sum_{\lambda} P(\lambda) S(\lambda) D_k(\lambda) \Delta\lambda \,. \tag{3.6}$$

We characterise $D_k(\lambda)$ [Barnard and Funt, 2002] (see Section 3.3 for more details), which allows us to obtain (linearised) estimates of the radiant power $\Phi = P(\lambda)S(\lambda)$.

However, both $P(\lambda)$ and $S(\lambda)$ are unknown, but we need to estimate the correlated colour temperature T of the *scene illuminant* $P(\lambda)$. We start from the grey-world assumption that the average of all surface reflectances in a scene is a neutral reflectance [Buchsbaum, 1980]. However, as mentioned in [Barnard et al., 2002; Gijsenij and Gevers, 2007; Gehler et al., 2008], real-world statistical data shows that the average is different from perfect neutral reflectance. Unlike previous database-based grey-world methods [Barnard et al., 2002; Gijsenij and Gevers, 2007; Rosenberg et al., 2003] that either use synthetic training images or training images without knowing the actual scene illuminant, we use a database of characterised real-world photographs as well as accurately measured scene illuminants $P(\lambda)$.

We first captured 35 training images of real-world scenes (see Figure 3.10) under different illumination conditions with a colour temperature T_m ranging from 2000K to 7500K, which we measured on a Spectralon tile that was placed in each scene using the spectroradiometer. The Spectralon tile was always oriented such that it was facing the main light source. It was usually removed from the scene when the training images were photographed (see Figure 3.10).

The radiant power values Φ of each pixel (in each image) are then projected onto the blackbody locus using Holm and Krochmann [1975]'s method, which is also used by the spectroradiometer that we used to estimate the CCTs of the training data, yielding the (per pixel) correlated colour temperature T:

$$\arg\min_T \left[(u_e - u_T)^2 + (v_e - v_T)^2 \right]^{1/2}, \tag{3.7}$$

where (u_e, v_e) are the radiance chromaticity coordinates of the pixel (derived from their radiance value) and T is the temperature of the nearest point (u_T, v_T) on the Planckian locus. The colour temperatures T_i of pixels Z_i within each image are then averaged together using a weighted average (similar to grey-world):

$$\overline{T} = \frac{\sum_i T_i w(Z_i)}{\sum_i w(Z_i)}. \tag{3.8}$$

Our weighting function $w()$ is proportional to the luminance of a pixel, i.e., zero weights are applied to the pixels with smallest luminance and a weight of one is applied to the brightest pixels. The colour temperatures of the brighter pixels are weighted more than those of the dark area. This weighting takes into account brighter signals more than the dark in a similar sense to the MaxRGB

Figure 3.10: *Examples of the training images for our white balancing. We use raw sensor signals (discarding the camera's auto white balance) and the spectral power distribution of the scene illumination (measured on a Spectralon tile) as our training data.*

method (which considers the brightest signal).

From this training data, we then derive a simple affine transformation $T_m = a \cdot \overline{T} + b$ that maps from $\overline{T}$ to the accurately measured T_m. We estimate the two parameters a and b of this model using linear regression:

$$\mathbf{M}_T = (\overline{\mathbf{T}}^\top \cdot \overline{\mathbf{T}})^{-1} \cdot \overline{\mathbf{T}}^\top \cdot \mathbf{T}_m \,, \tag{3.9}$$

where $\overline{\mathbf{T}}$ refers to the vector containing all training CCTs $\overline{T}$, $\mathbf{T}_m$ refers to the vector containing all measured CCTs T_m, and $\mathbf{M}_T$ is a matrix containing the two parameters. For any new image, we simply compute $\overline{T}$ and map to the actual colour temperature T_a with $\mathbf{M}_T$.

3.5 Results

3.5.1 Colour Accuracy of HDR Characterisation

We have tested our HDR characterisation methods with three different cameras (Nikon D100, Canon 350D, and Nikon D40). For this we have computed three characterisation models, one for each camera, as described in the previous section [using our transparency colour target, see Figure 3.6(a)].

We analyse the radiometric accuracy of each of the three characterisation models (one for each camera) by comparing their results against physical measurements from the spectroradiometer. For each comparison, we compute three different error measures in order to judge the accuracy. First, we compute CIEDE2000 [CIE, 2001] values, which are commonly used to compare colours in a perceptual fashion (see Section 2.3.5 for more details on the formulae). This method is based on the CIELAB colour space [CIE, 1986], and as such is really only valid for low dynamic range values. Nonetheless, we include it for completeness. Second, we compute CIE $Yu'v'$ coordinates [CIE, 1986] for the characterised HDR image as well as the measurements from the spectroradiometer, and compute (relative) median differences between them. Third, we compute the (relative) median differences between the characterised CIEXYZ values and the measured CIEXYZ values.

We first perform these comparisons within the training set [transparency target, see Figure 3.5(b)], i.e., we validate that a linear characterisation model is sufficient. To this end, we take the original HDR images (one for each camera), convert them to CIEXYZ with the characterisation matrices from Table 3.1 and compute the CIEDE2000 values, $Yu'v'$ median differences, and CIEXYZ median differences for each colour patch in the transparency target. As can be seen in Table 3.2(a), the errors are comparatively low.

Furthermore, we validate how well the characterisation models work with test scenes that were taken under different illumination. Figures 3.6(c) and (d) show significant differences in spectral characteristics between the training scene (fluorescent light) and the test scene (halogen light). Our first test scene consists of two ColorChecker charts illuminated under halogen light, shown in Figure 3.6(b). As can be seen again in Figure 3.11 and Table 3.2(b), the errors are quite low, especially for the Canon 350D. We compare this result of our method [Kim and Kautz, 2008a] with the previous reflectance-based LDR characterisation [ISO, 2006] technique and the HDR assembly method using ICC profiles [Göesele et al., 2001] (generated by GretagMacbeth ProfileMaker), see

(a)

Training set	ΔE_{00}	Y	$u'v'$	XYZ
Canon 350D	1.121	0.103	0.013	0.116
Nikon D100	1.311	0.096	0.022	0.117
Nikon D40	1.486	0.066	0.026	0.083

(b)

Test set	ΔE_{00}	Y	$u'v'$	XYZ
Canon 350D	0.480	0.111	0.016	0.114
Nikon D100	3.816	1.214	0.035	1.660
Nikon D100 (IR filter)	1.615	1.193	0.048	1.439
Nikon D40	3.104	0.884	0.038	1.192

(c)

Test set – other methods	ΔE_{00}	Y	$u'v'$	XYZ
Canon 350D (LDR Char.)	7.028	0.225	0.039	0.228
Canon 350D (HDR ICC)	4.130	1.085	0.073	0.919

Table 3.2: *Colour accuracy error of HDR characterisation: (a) the* training set *presents the accuracy of our characterisation models using the training data (576 patches under 5571K illumination). (b) the* test set *shows the accuracy of the same characterisation models using a different test data-set (reflective target under 2946K illumination). Accuracy compared with other methods (c): LDR characterisation (only one target is used [ISO, 2006]) and HDR assembly using ICC profiles [Göesele et al., 2001].* ΔE_{00} *denotes the median CIEDE2000 over all patches between measurement and prediction,* Y *shows the median relative differences of luminance levels, and* $u'v'$ *indicates the median relative differences between measurement and prediction of all patches in CIE* $u'v'$*.* XYZ *shows the median relative differences of CIEXYZ channels between measurement and prediction.* IR filter *means using the improved results with Rosco Thermal Shield infrared-blocking filter.*

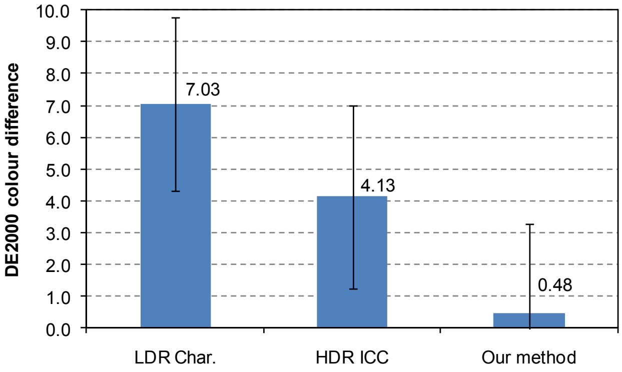

Figure 3.11: *Overall results of accuracy. GretagMacbeth ColorChecker is used for testing colours. This figure compares the median CIEDE2000 colour difference error when the camera (Canon 350D) is characterised with three different methods (LDR characterisation with a ICC camera profile [ISO, 2006], HDR ICC profile [Göesele et al., 2001], and our HDR characterisation method. Average colour differences in CIEDE2000 are: (LDR Char.) 6.72, (HDR ICC) 4.70, and (our method) 1.01.*

Table 3.2(c) and Figure 3.12. As predicted, the achieved accuracy error is lower than with our new method. In order to confirm repeatability, we acquired the test set (Canon 350D) a second time under different illumination (2983K). The median ΔE_{00} was 0.546 over 48 patches, which is very close to the ΔE_{00} of 0.480 for the first test set.

Figure 3.13 compares luminance and chromaticity of the test scene which consists of GretagMacbeth charts under halogen light, acquired by three different cameras and then characterised using our method. As shown in the top plot, the Canon 350D shows very similar performance to the spectroradiometer, whereas the Nikons show overestimation of the luminance.

The Nikon cameras have a slightly higher error which we traced back to an inferior infrared filter. Halogen light emits a large amount of infrared light, which caused the HDR images acquired with the Nikon cameras to have a considerable amount of infrared glare. Using an additional infrared blocking filter (Rosco Thermal Shield) in front of the lights yielded a median ΔE_{00} of 1.6 for the Nikon D100, down from 3.8 [see Table 3.2(b)]. Insofar as the averaged error level decreases with additional infrared-blocking filters, we believe that the inferior infrared-blocking filter with the Nikon camera causes infrared glare under tungsten light.

The bottom left plot shows chromaticity differences of the test patches. The differences are minor, with only one colour (a red patch on the right-hand side) showing a big difference. This colour is located outside the camera's RGB filter gamut because these cameras use wide-band width filters.

Our second test scene is a desk scene illuminated mainly by a fluorescent desk lamp, shown in Figure 3.14, 3.15, and 3.16. The dynamic range of HDR radiance maps is usually much higher than that of typical monitors and cannot be displayed directly (see Section 2.5 for more details). Since simple linear scaling with gamma correction does not achieve satisfactory results when displaying

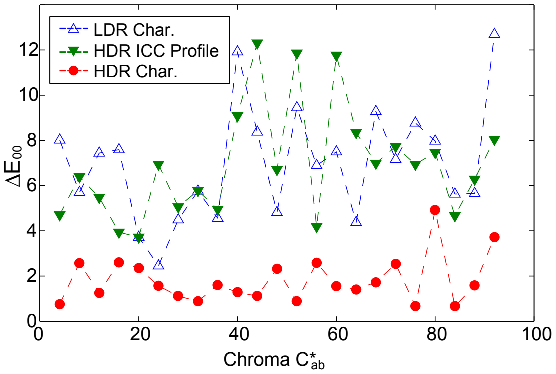

Figure 3.12: *Comparison of colour difference (test set, patches sorted by chromaticity). ΔE_{00} is computed by using a ColorChecker chart in a brightly illuminated area. LDR characterisation is calculated using the reflectance-based method [ISO, 2006]; the HDR ICC method is according to [Göesele et al., 2001]. Our HDR characterisation shows comparatively low errors.*

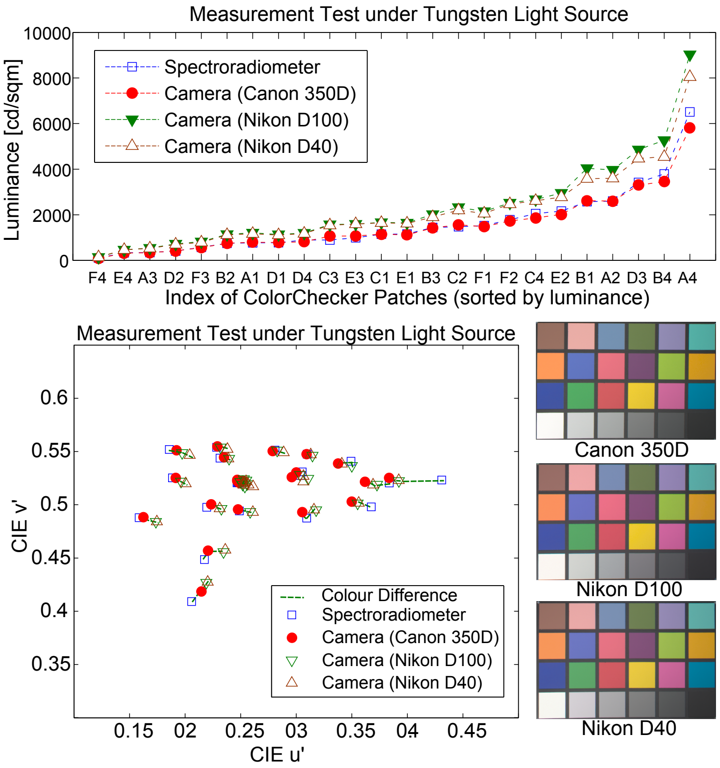

Figure 3.13: *Test scene consisting of GretagMacbeth charts under halogen light, acquired by three different digital cameras and then characterised using our method. The top plot presents luminance differences between radiometric measurements and camera measurements. In particular, the Canon 350D shows very similar performance to the spectroradiometer. Tone-mapped versions of the three characterised images are shown on the right; the differences between them are difficult to spot. For a quantitative comparison, see Table 3.2(b). The bottom left plot shows chromaticity differences of the test patches in a CIE uniform chromaticity diagram. The differences are minor, with only one colour showing a big difference, which is located outside the camera's R/G/B filter gamut.*

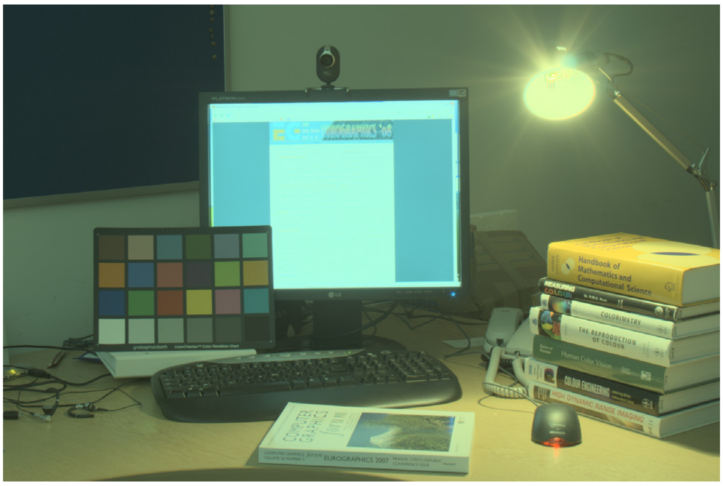

(a) Direct sensor response (RAW)

(b) Absolute CIEXYZ

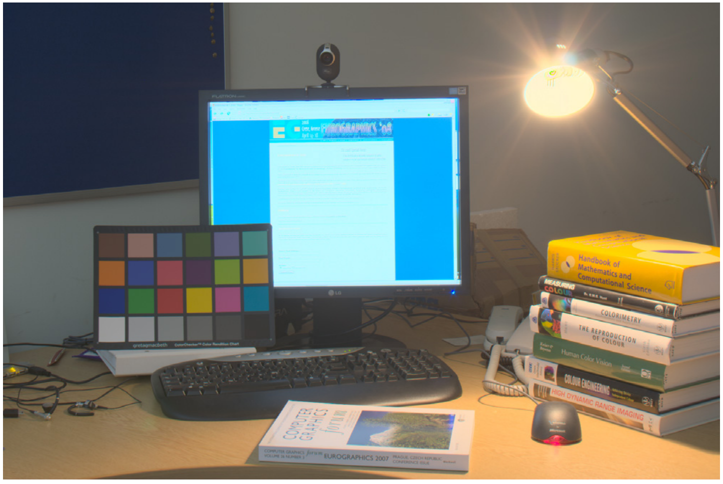

* (c) HDR Characterisation (white-balanced)

Figure 3.14: *Each step of the HDR characterisation method. Image (a) presents the* direct sensor response *and is the acquired RAW image without any white balancing. The greenish appearance is due to the infrared filter in front of the sensor, which will be corrected by the derived mapping. Image (b) shows the characterised CIEXYZ image (which we render using an 1:1 mapping to RGB for illustration purposes). Each pixel value represents a measurement of radiance. Image (c) shows the final resulting image by mapping from characterised and device-independent CIEXYZ to the display sRGB colour space. The white point of the scene is converted to the white point of the display with the estimated reference white.*

(a) Before HDR characterisation

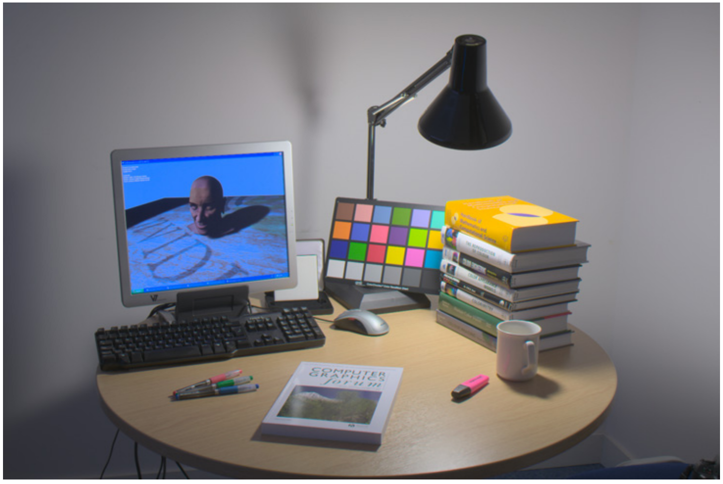

(b) After HDR characterisation

(c) Difference map (mid-grey = mean) amplified by 10

Figure 3.15: *Before and after comparison of HDR characterisation. Image (a) presents an HDR image without characterisation while image (b) shows an HDR radiance map, which is characterised through our proposed method. Image (c) is a difference map which is amplified by 10 (for a visualisation purpose). Mid-grey presents the mean of these two images (before & after). In particular, the blue screen and yellow books (colourful objects) present more of a difference.*

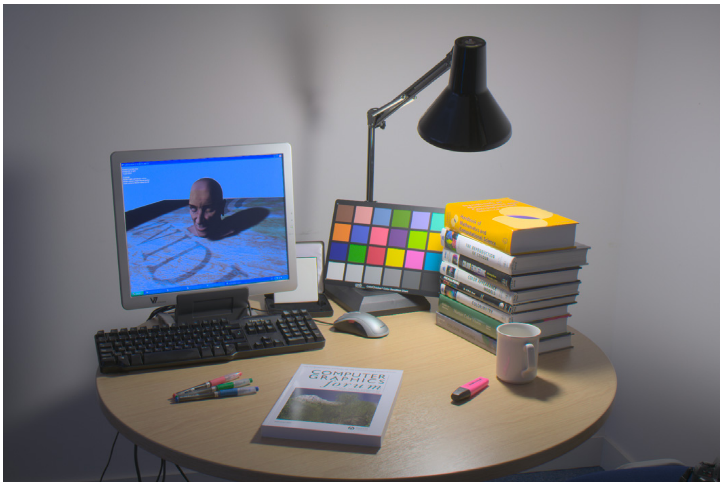

(a) Canon 350D

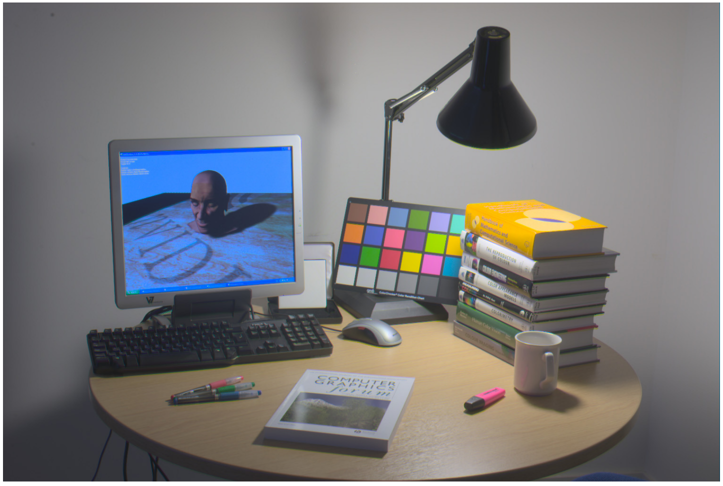

(b) Nikon D100

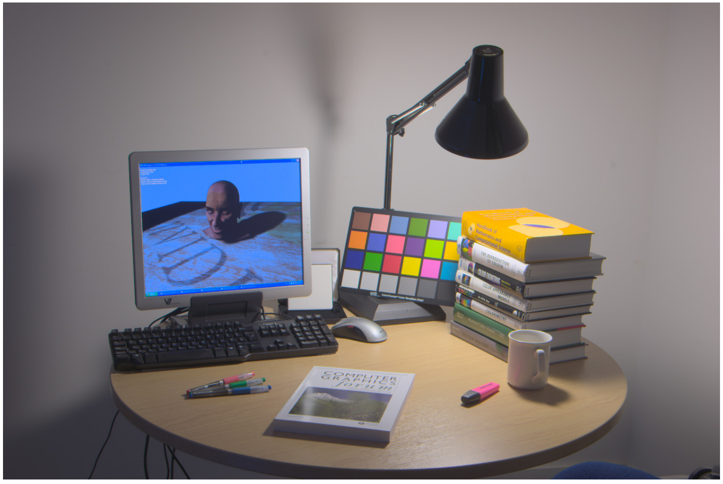

(c) Nikon D40

Figure 3.16: *An HDR desk scene is characterised with our method for three different digital cameras (Canon 350D, Nikon D100, and Nikon D40). Even though they are taken from slightly different perspectives and angles, there are only very minor colour differences between the images. For instance, the measurements of the white tile in the scene are: (spectroradiometer in X/Y/Z) 119.63/112.50/33.07; (Canon 350D)127.00/122.00/30.50; (Nikon D100) 150.00/143.00/39.00; (Nikon D40) 150.00/142.00/38.00.*

HDR images, tone-mapping algorithms have been introduced that compress the dynamic range in a more suitable manner in a global, local, or image appearance fashion. We only deal with the input side of HDR imaging in this chapter. Tone-mapping and colour appearance modelling will be dealt with in Chapters 5 and 6. For now, we use a popular tone-mapping method [Reinhard et al., 2002] to display our characterised images.

Figure 3.14 presents each step of the HDR characterisation. The top image shows the direct sensor response and is the interpolated RAW image without any white balancing. As the infrared blocking filter (cyan-greenish) is located in front of the sensor, the raw sensed image without white balancing appears greenish. The middle image presents the characterised CIEXYZ image, which is rendered using a 1:1 mapping for CIEXYZ to RGB. Finally, the bottom image shows the result by mapping from characterised and device-independent CIEXYZ to the display sRGB colour space. The estimated white point of the scene is converted to the white point of the display. Figure 3.15 compares before and after a HDR characterisation. The top image shows an ordinary HDR image and the middle image presents a characterised HDR radiance map, which is characterised through our proposed method. The bottom image shows a difference map. In particular, the blue screen, yellow book, and colour chart present more of a difference. Tone-mapped versions of the characterised HDR images are shown and as can be seen in Figure 3.16, the colours in all three images are almost identical, even though they were taken with three different cameras.

3.5.2 Illuminant Estimation

Traditional grey-world methods average trichromatic primaries first and then compute the correlated colour temperature from the average. However, we have found that first computing colour temperatures and building a weighted average of those yields better results (squared correlation coefficient of $R^2 = 0.86$ vs. $R^2 = 0.79$).

Initially, we experimented with training images of a GretagMacbeth DC chart instead of natural images. While their average colour temperatures $\overline{T}$ were highly correlated with the measured colour temperatures T_m ($R^2 = 0.99$), the derived linear transform did not generalise well to natural images.

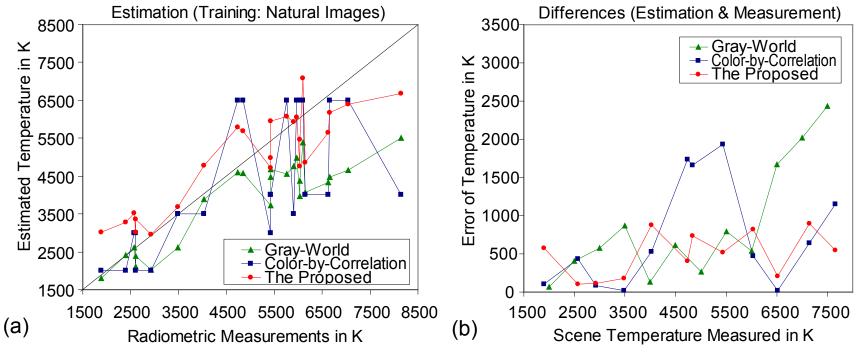

Figure 3.17: *(a) Result of temperature estimation using the training data of natural images (all 35). (b) Difference between temperature estimation and radiometric measurement of new test images.*

Figure 3.17(a) and (b) demonstrate that our database-based grey-world algorithm estimates the colour temperature rather accurately for both the training as well as new natural images. These results of our method [Kim and Kautz, 2009] compare favourably to the original grey-world and colour-by-correlation methods [Finlayson et al., 1997]. In many cases, our colour temperature estimation method is more accurate than the original grey-world or gamut-based model despite using only 35 training images. Yet it allows us to compute an estimate in milliseconds (or even less when only a subset of pixels is used). Of course, when an image deviates too much from our training data, the colour temperature estimate is less accurate.

3.6 Discussion

HDR Characterisation Our characterisation method is applicable to HDR imaging, which is very useful in graphics but also other scientific fields. Our mathematical method of characterisation is rather simple — a linear transformation between colour spaces — and not different from previous methods. However, our *characterisation methodology*, the combination of a new transparency colour target, HDR imaging, and characterisation theory, solves drawbacks of previous characterisation methods. As shown in the results (see Figure 3.11), our characterisation performance is comparatively better than previous methods [Pointer et al., 2001; MacDonald and Ji, 2002; Johnson, 2002; ISO, 2006; Göesele et al., 2001], yet efficient in terms of cost and acquisition time.

However, there are some limitations of our method. The performance depends on the optical quality of the digital camera, including lens flare, vignetting, veiling glare, and the infrared filter. For instance, the optical quality of the camera system could be improved with a fixed lens, which provides less chromatic aberration than a zoom lens [Shortis et al., 2006]. The inaccurate performance of Nikon cameras under tungsten lights could be improved by installing an additional infrared-blocking filter. HDR veiling glare can be solved [Talvala et al., 2007] but acquisition complexity is greatly increased. The measurement used in our method returns radiometric XYZ values, not radiance in each wavelength. In this way, it still allows potential measurement errors with metameric colours like other target-based models.

Illuminant Estimation In many cases, our colour temperature estimation method is more accurate than the original grey-world or gamut-based model, even though we only used 35 training images. Yet, it allows us to compute an estimate in milliseconds (or even less when only a subset of pixels is used). Of course, when an image deviates too much from our training data, the colour temperature estimate is less accurate. When the scene illuminant moves far from the locus, the performance of our algorithm will degrade as we assume the illuminant to lie on the locus. However, in our experience, this case does not seem to occur frequently in natural scenes. Of course, extreme cases such as tinted light bulbs will be difficult to handle for our method. In this case, a classical white balancing method, like MaxRGB or the general grey-world method, can be used for white balancing. In addition, our method seems to perform well, even if the new images are not well represented in our training database. For instance, there is no similar training image (Figure 3.10) to the example from Figure 3.14 and the colour chart example in Figure 3.15. Note that this estimation method is used only for display purposes (white balancing) and can be used to estimate white point (colour) for the CAM and that the characterisation method actually yields physically-meaningful radiance values (not white balanced) in absolute CIEXYZ.

3.7 Summary

We have presented a new technique that can characterise HDR imaging systems, both in terms of luminance and colour. It is more accurate than previous reflectance-based characterisation methods and less time-consuming than monochromator-based techniques, which were designed for LDR imaging. We have validated the accuracy of the method using three different digital cameras and test data sets with radiometric measurements. Even though we have devised our method with HDR imaging in mind, the same technique can also be applied to characterise LDR devices.

The proposed method enables measurement of real-world radiance as an HDR radiance map with significant accuracy. The radiance map contains the full dynamic range of the real-world radiance in a physically-meaningful way. In the next chapter, we will describe how physical stimuli in the real world are perceived by the human visual system. We will describe a series of psychophysical experiments and a colour appearance data set under high-luminance levels.

Chapter 4

High-Luminance Colour Experiments

The previous chapter describes a method to characterise HDR imaging to digitise real-world radiance as an HDR radiance map to a high accuracy. The method yields physically-meaningful HDR radiance maps, equivalent to radiometric measurements of the real world. This chapter will describe how such physical colour stimuli are perceived by the human visual system. We describe the experimental measurement of colour appearance under high luminance levels. This data set was used to develop a new colour appearance model (see Chapter 5) to complete colour communication in HDR imaging.

In order to quantify actual perceptual colour appearance, we have conducted a series of magnitude estimation experiments. Observers are presented with a large number of coloured patches in succession, for which they have to estimate lightness, colourfulness, and hue values. Parameters influencing the estimates are changed across different phases of the experiment: background level, luminance (and colour temperature) of the reference white, and ambient luminance. We designed our psychophysical experiment in a similar way to the LUTCHI experiment, which allows us to leverage their existing data. However, our experiment differs from LUTCHI by including high luminance levels of up to 16 860 cd/m^2 as well as a large number of phases, where the background intensity is varied. (The LUTCHI data set for the *simultaneous contrast effect* [Luo et al., 1995] is not publicly available.)

4.1 High-Luminance Display

As mentioned in Section 2.3.3, current colour appearance data sets, mostly LUTCHI [Luo et al., 1991a,b, 1993a,b, 1995], present the limited dynamic range of luminance. For instance, among the data sets, only Luo et al. [1993b] describe colour appearance of transparency signboards under high levels of luminance up to 1 272 cd/m^2, where only four colour samples were used with more than 1 000 cd/m^2. Most of the colours in the LUTCHI data sets are under 690 cd/m^2, which was limited by the available display technology in the early 1990s.

In order to span an extended range of luminance levels (up to five-order magnitude, equivalent to the working range of the eye's cone), we built a custom high-luminance display device which is capable of delivering up to approximately 30 000 cd/m^2, see Figure 4.1. The setup consists of a light box, powered by two 400W hydrargyrum medium-arc iodide (HMI) bulbs, transmitting light

Figure 4.1: *A custom-built high-luminance display. The display can produce a luminance of 2 200 cd/m^2 when used as an LCD display and up to 30 000 cd/m^2 when used with transparencies.*

through a filter ensemble followed by either a 19″ LCD panel (original backlight removed) or a diffuser onto which transparencies are placed. The light source spectrum conveniently resembles fluorescent backlights, close to a correlated colour temperature of 6500K. Moreover, HMI bulbs stay cool enough to keep the LCD panel from overheating (see Figure 4.2 for overall design).

4.1.1 Design and Manufacturing

The main insight of our display device is to achieve a higher luminance level by replacing the backlight unit in an ordinary LCD display. This simple replacement creates two new issues: over-heating of the LCD panel and calibration of the display. To avoid heat from the high-luminance light bulbs, we first choose an HMI bulb (400W Iwasaki Electric company Ltd — Eye MT400DL) with a 400W electronic ballast as a light source. As shown in Figure 4.4(b), the spectral power distribution of the bulb is quite similar to an ordinary florescent light bulb [see Figure 2.8(b)], as also used in the LUTCHI experiment [Luo et al., 1993b]. The minor differences of these spectrums are calibrated by using an ICC profile (see Section 4.1.2 for more details). The measured CCT of the bulb was 6494K, corresponding to CIE D65 illuminant. In addition, the HMI-type bulb produces more energy toward the visible spectrum, and relatively lower energy in the infrared wavelengths, compared to filament-type halogen bulbs. Consequently, the HMI bulb produces much less heat than other types of bulbs. However, liquid crystals are rather sensitive to heat. Any heat energy can affect crystal liquids to close the pixel by turning the direction of the liquid crystals (becoming black). Generally, LCD panels function under a temperature of 50°C. For this reason, although HMI bulbs produce less energy than halogen bulbs, heat ventilation was required to ensure this LCD panel work properly at under 45°C (ensured by measuring with a thermometer).

Peak luminance (and with it the luminance of the reference white, as well as of all colour

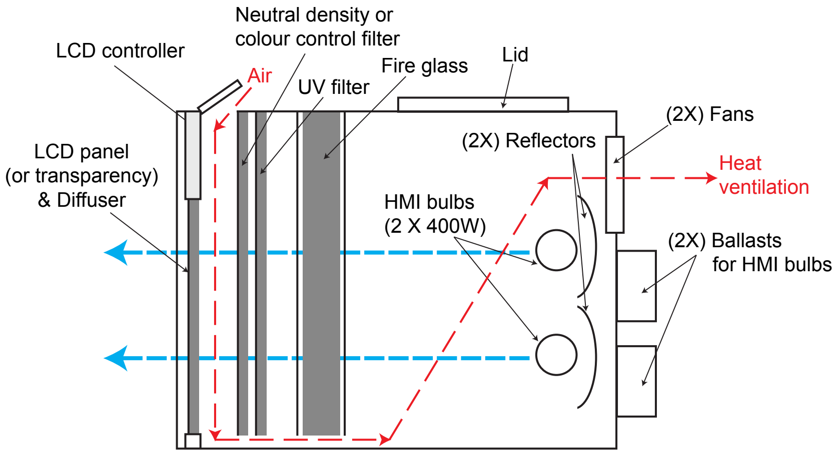

Figure 4.2: *Design of the high-luminance display. From the left, an LCD panel or transparency is placed to produce colour stimuli. A slot is made for neutral density or colour control filters to control luminance and colour temperature of the light source. Double-glazed fire glass is installed to isolate the heat energy against the LCD panel. Two 400W HMI bulbs are used as a light source. Two 400W ballasts and two fans are located outside the box. Heat is vented from the top and the back sides of the display. A thermometer is installed to check the temperature of the inner chamber (keeping the box temperature at approximately 45°C).*


(a) Lighting panel (b) LCD panel and its controller (c) Fans and electronic ballasts


(e) Fire glass, filters, and LCD (f) Overall top view (g) Front view without LCD

Figure 4.3: *Compartments of the high-luminance display. Image (a) presents the inner back side that contains two HMI bulbs, two fans, their power supply, and electronic wires. These elements (except the bulbs) are covered with aluminium tin foil to improve energy efficiency. Image (b) shows the LCD panel, its power supply, and its VGA controller. Image (c) is a photograph of the outer back side panel. To protect the ballasts against heat, two electronic ballasts that produce flicker-free light are installed outside the display. From the top of the image (e), the double-glazed fire glass is installed to isolate infrared light and heat energy from the LCD panel, then (3×) UV filters are installed to avoid ionisation, then finally the LCD panel unit. Image (f) shows overall top view before installing the top panel. Image (g) presents a front view of the display before installing the LCD panel.*

samples) is controlled by placing additional neutral density (ND) filters into the light box (which preserves amplitude resolution). Combinations of different ND filters creates peak luminances of approximately 50, 125, 500, 1 000, 2 200, 8 500, and 16 860 cd/m^2 used in our experiment. In addition, we can modify the colour temperature of our light source by placing Rosco colour-temperature-changing filters inside the light box. Our experiments use four different colour temperatures: 2000K, 6500K, and 8000K with the LCD, and 6000K with transparencies.

We used a Samsung SM931C 19″ SXGA TFT LCD panel, which has a resolution of 1280x1024 (response time: 2ms) and a contrast ratio of approximately 1:1000 (according to its specification). When used with the LCD, the maximum displayable luminance is 2 250 cd/m^2 (similar to the Dolby HDR display [Dolby, 2008]). Owing to the 8-bit LCD, the amplitude resolution is only 256 steps (less than for a real HDR display [Seetzen et al., 2006]). However, this is not critical, as the experiment only requires sparse sampling of the colour space. For transparencies, the maximum luminance reaches 30 000 cd/m^2, with virtually arbitrary contrast and amplitude resolution.

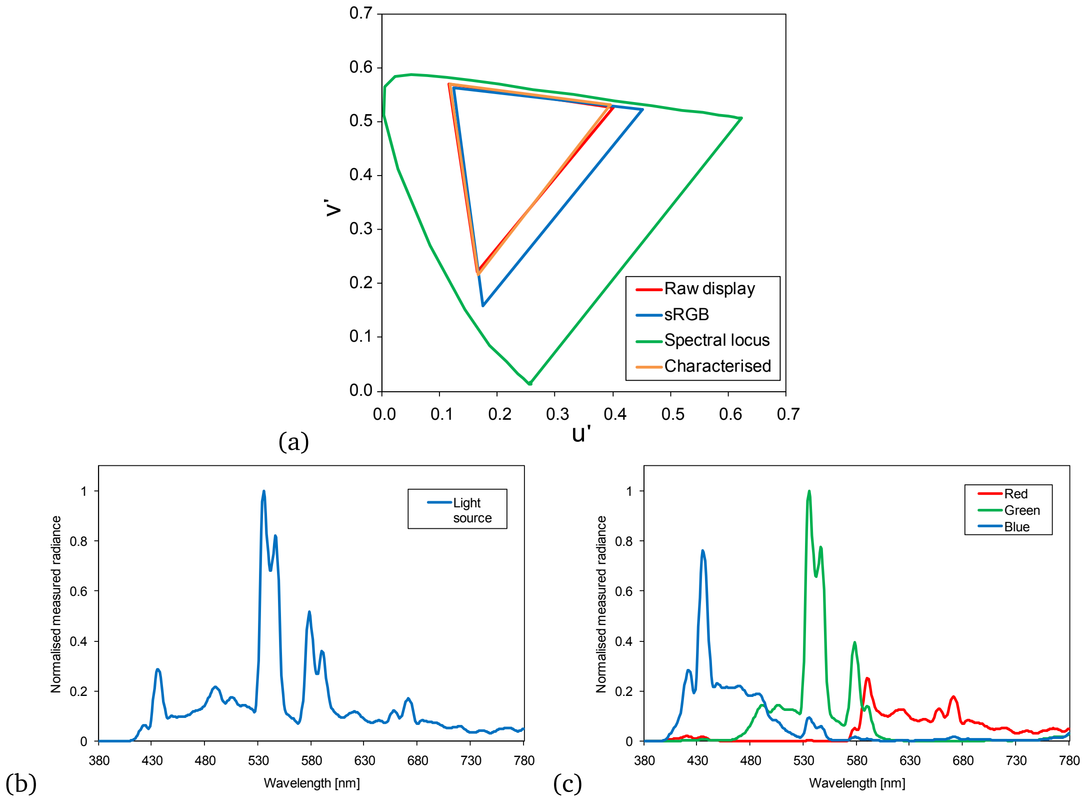

Figure 4.4: *Colour gamut and spectral power distribution of the high-luminance display. In Plot (a), a red triangle presents the gamut of the raw colour primaries, and a orange triangle shows the gamut of characterised primaries of our high-luminance display. Plot (b) and (c) show measured spectral power distributions of the HMI bulb and the calibrated display. The light source presents undesirable strong peaks in the middle of its spectrum, which causes viewing angle dependency in the final display. Therefore, participants' viewing angle was fixed perpendicular to the centre of the display to avoid the colour appearance changes by viewing angle.*

4.1.2 Calibration

Using a Specbos Jeti 1200 spectroradiometer, we colour-calibrated the LCD version of our display to match an sRGB colour gamut and a gamma of 2.2 by generating a ICC [2004] profile (see Appendix A.4 for radiometric measurements for device characterisation), but our light bulbs produce a smaller colour gamut toward the red primary compared to sRGB colour space [see Figure 4.4(a)]. Hence, the display produces a colour space similar to sRGB, but with much higher luminance levels. In addition, when using the transparent film panel, the display covers higher levels of luminance and a wider colour gamut beyond the LCD panel (see Figure 4.6). We further measured the spectra of all displayed colour patches (LCD and transparencies), as well as background and reference white. In addition, the reference white was re-measured at the beginning (after the HMI bulbs output had stabilised after a few hours) and at the end of each day to ensure repeatability. Even though HMI light bulbs are known to change colour temperature over their lifetime (approximately 0.5K for each hour), over the two-week period of our experiments, we recorded only an insignificant variation of about 3% in luminance and a 1% decrease in colour temperature.

4.2 Stimuli

The setup for recording our perceptual measurements is adapted from the LT phases (cut-sheet transparencies) of the LUTCHI experiments [Luo et al., 1993b]. A participant is asked to look at a colour patch presented next to a reference white patch and a reference colourfulness patch (with a colourfulness of 40 and lightness of 40), as shown in the centre of Figure 4.5.

The viewing pattern is observed from 60 cm distance and normal to the line of sight, such that each of the approximately $2\times 2\,\mathrm{cm}^2$ patches covers approximately 2°, and thus the whole display approximately 50° in the field of view of the participant (with the test colour patch being in the centre). The background is black or gray, with 32 random decorating colours at the boundary, simulating a real viewing environment. We selected 40 colour patches as stimuli, carefully chosen to provide a good sampling of the available colour gamut and to provide a roughly uniform luminance sampling. The 40 colour patches, background luminance level, and reference white patch were measured by a spectroradiometer before taking experiments with participants (see Figure 4.7 and Table 4.1 and Appendix A.6 for physical/perceptual measurements). Figure 4.6 shows the distribution of these 40 patch colours for each device. The patch sets for the LCD and transparency setup are different, as it is neither easy to match their spectra nor necessary for the experiment.

Since the perception of lightness, colourfulness, and hue is strongly correlated with parameters such as luminance range, reference white, background level, and surround condition [Stevens and Stevens, 1963; CIE, 1981; Luo et al., 1991a; Luo and Hunt, 1998; Hunt et al., 2003], our study explores relevant slices of this high-dimensional space. We partition the experiment into different phases, with a specific set of parameters in each phase (see Table 4.1). We primarily focus on the influence of luminance range and background level on colour perception as these two dimensions are known to have the strongest perceptual influence [Luo et al., 1991a]. We performed experiments

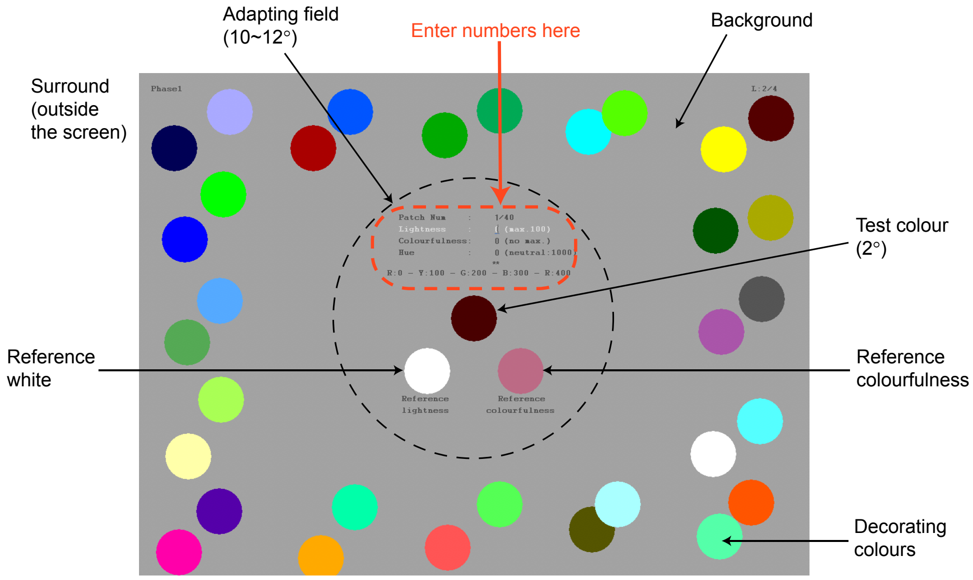

Patch Num : 1/40
Lightness : 0 (max.100)
Colourfulness: 0 (no max.)
Hue : 0 (neutral:1000)
**
R:0 – Y:100 – G:200 – B:300 – R:400

Figure 4.5: *The viewing pattern observed by participants (made with the C/C++ in Microsoft Visual Studio). Participants were presented with a series of test colour samples in the centre of the screen. They entered three estimated magnitude numbers (lightness, colourfulness, and hue) by using a keyboard numeric pad. Reference white is located to the left and below the test colour. The reference white patch is used for lightness estimation on a relative scale. Reference colourfulness is located to the right below to provide an anchor point when observers estimate colourfulness magnitude on an absolute scale. The adapting field (10-degree viewing angle) is used for measuring the luminance adaptation level of the eye. All other screen area is background, which includes decorating colours around edges to simulate the real-world viewing environment. Finally, areas outside of the screen are assumed to be surround, including the luminance level of the room.*

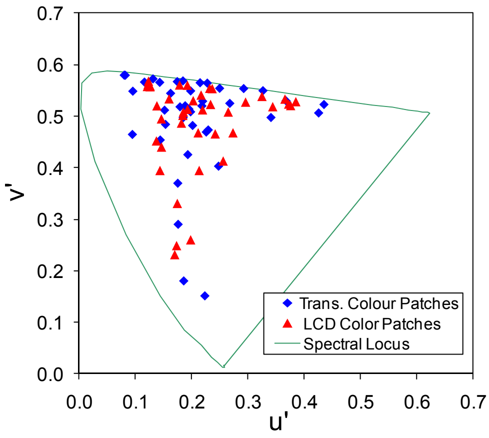

Figure 4.6: *Colour coordinates of the 40 LCD and transparency patches (CIE u′v′).*

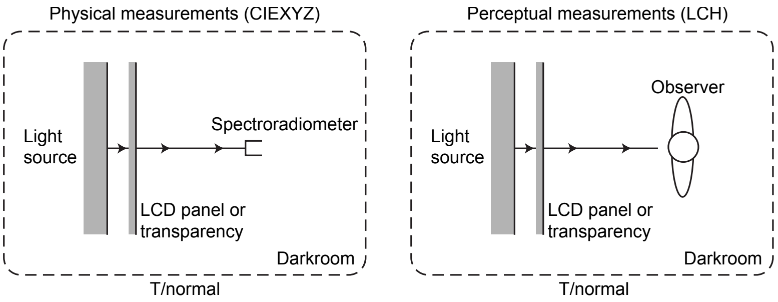

Figure 4.7: *Our high-luminance display device is placed in a dark room where colour patches were measured by a spectroradiometer (physical quantities) and estimated by trained observers (corresponding perceptual quantities) in colour experiments.*

up to a peak luminance of 16 860 cd/m^2 (corresponding to white paper in noon sunlight); higher luminance levels were abandoned as they were too uncomfortable for the participants. As previous colour experiments have already covered low luminance, we conducted only a few low-luminance experiments (phases 1–5 in Table 4.1) to verify consistency.

4.3 Experiments

4.3.1 Experimental Procedures

A crucial point to psychophysical measurements conducted through magnitude estimation is that each observer clearly understands the perceptual attributes being judged. Each observer completed a 3-hour training session with the actual viewing pattern (using a different set of colour patches) to develop a consistent scale for each of the required perceptual attributes (lightness, colourfulness, and hue). For data compatibility, the same scaling units and instructions (see Appendix A.5) were used as in the LUTCHI data sets [Luo et al., 1993b]. We employed six fully trained expert observers, all of whom were research staff from our institution, who had passed the *Ishihara and City University* vision tests for normal colour vision. At the beginning of each phase, observers spent 5 minutes for high luminance and 30 minutes for dark luminance adapting to the viewing conditions. Each observer spent around 10 hours on the experiment in a dark room, usually distributed over two

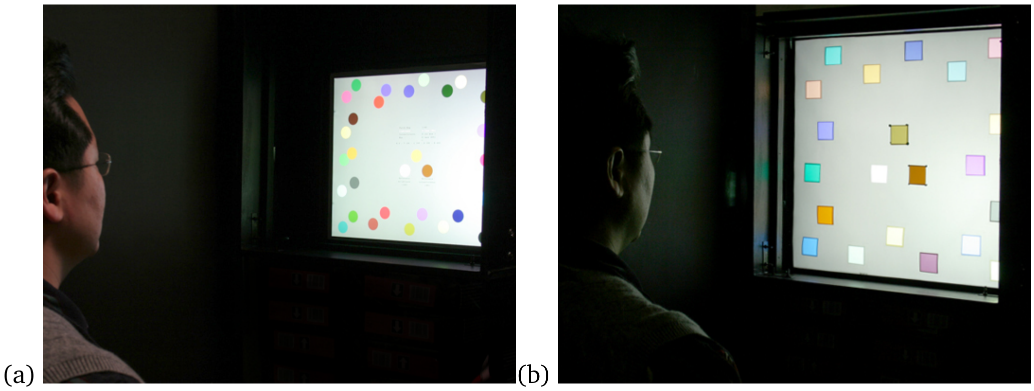
(a) (b)

Figure 4.8: *Viewing pattern observed by participants [(a) with the LCD panel and (b) with transparency].*

	Observers	Phases	Samples	Sequences	Estimates
Numbers	6–7	60	105	9,450	28,350

Phase	Light	Type	Peak Lumin.	Backgrnd.	Ambient
1	5935K	LCD	44 cd/m^2	24%	dark
2	6265K	LCD	123 cd/m^2	21%	dark
3	6265K	LCD	494 cd/m^2	0%	dark
4	6265K	LCD	521 cd/m^2	24%	dark
5	6197K	LCD	563 cd/m^2	87%	dark
6	6197K	LCD	1 067 cd/m^2	0%	dark
7	6197K	LCD	1 051 cd/m^2	22%	dark
8	6390K	LCD	2 176 cd/m^2	0%	dark
9	6392K	LCD	2 189 cd/m^2	12%	dark
10	6391K	LCD	2 196 cd/m^2	23%	dark
11	6387K	LCD	2 205 cd/m^2	55%	dark
12	6388K	LCD	2 241 cd/m^2	95%	dark
13	7941K	LCD	1 274 cd/m^2	21%	dark
14	1803K	LCD	1 233 cd/m^2	19%	dark
15	6391K	LCD	2 201 cd/m^2	23%	average
16	5823K	Trans.	8 519 cd/m^2	6%	dark
17	5823K	Trans.	8 458 cd/m^2	21%	dark
18	5921K	Trans.	16 860 cd/m^2	5%	dark
19	5937K	Trans.	16 400 cd/m^2	22%	dark

Table 4.1: *Summary of the 19 phases of our experiment. In each phase, 40 colour samples are shown. Each participant totalled 2 280 estimations, which took around 10 hours per participant.*

days (see Figure 4.8 for snapshots of the experiments).

After the adaptation time, each colour sample was shown in a random order and the participants had to estimate three perceptual attributes: *lightness*, for which observers used a fixed scale from 0 (imaginary black) to 100 (reference white); *hue*, where observers were asked to produce a number indicating the hue using neighbouring combinations among four primaries — red-yellow (0–100), yellow-green (100–200), green-blue (200–300), blue-red (300–400); and *colourfulness*, where observers used their own open scale, with 0 being neutral and 40 equaling the anchor colourfulness. The participants entered the data using a keyboard. After each phase, participants were asked to judge the colourfulness of the reference colourfulness patch of the next phase relative to the previous one in order to allow inter-phase data analysis.

4.3.2 Colour Appearance Attributes

Colour appearance attributes can be quantified in either relative or absolute scales. An interesting question in designing a psychophysical experiment is which type of scale is a better choice in describing colour attributes. Brightness and colourfulness are attributes on absolute scales; lightness and chroma are relative attributes with respect to the maximum levels of brightness. Hue is a relative attribute describing the proportion of primary colours (see Section 2.3.1 for colour terminology), and hence a *partitioning* experiment is the only available method for this attribute.

Generally, a *partitioning* experiment provides more convenience than *magnitude estimation*. The reason is that magnitude can only be estimated when considering the memory of the previous

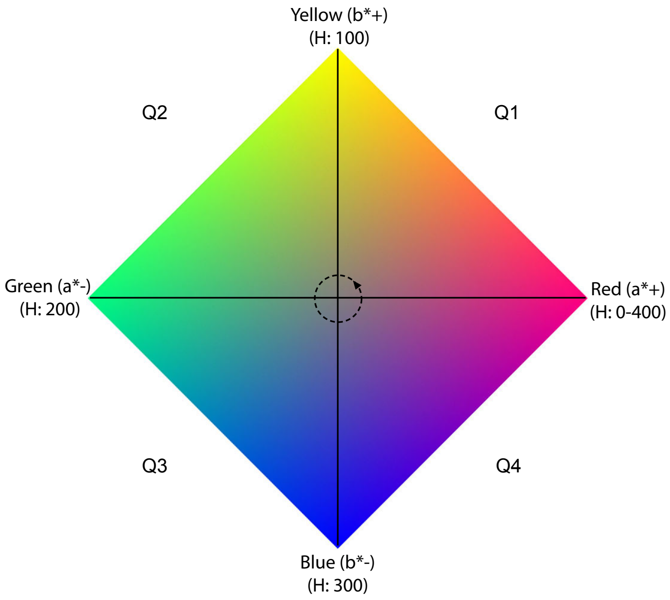

Figure 4.9: *Perceptual colour primaries. Imagine that a participant observes a test colour (suppose purple). He chooses one of the quadrants (Q4) that best matches the test colour. He decides the proportion of the nearest primaries (blue and red) on a percentage scale (like 60% of blue and 40% of red) that make up the test colour. Then, he adds the nearest small primary quadrature value (blue = 300) on the decided proportion (300 + 60) to obtain the hue quadrature value (360) of the test colour.*

trial (often assisted with an anchor point). Obtained data is on a subjective *arbitrary* scale, which depends on each participant individually. Therefore, if *partitioning* is possible, relative scaling is a better choice to improve the efficiency of the experiments. The question is whether relative scaling is possible in colour appearance experiments. Measuring *lightness* is achievable by providing a reference *maximum brightness* (reference white). For instance, each participant can be asked how bright the patch is with respect to the reference white. The participant can estimate a level of *brightness* on a percentage scale without difficulty. Thus, we choose lightness scaling over brightness scaling to allow relative scale assessment.

However, scaling *chroma* is questionable as Kwak [2003] and Fairchild [2005] suggested when commenting on the LUTCHI experiments. Following the colour attribute definition by Hunt [1998] (see Section 2.3.1 for definitions), chroma is a relative judgement of colourfulness with respect to reference white, but it is a very difficult task to normalise a judged colourfulness intensity by the brightness level of the reference *white*. Therefore, simply asking for colourfulness intensity (ignoring maximum brightness level) is more intuitive than asking for normalised colourfulness. In this way, the colourfulness judgements become easier to understand for participants. For saturation, we would need to ask participants to judge their own assigned brightness level for a given test colour and, accordingly, to judge the colourfulness of the patch given this assigned brightness level. This includes the judgements of two different colour appearances. Consequently, it is better to ask for colourfulness directly than to ask for either *chroma* or *saturation*.

Therefore, we asked the participants directly to judge the absolute quantity of colourfulness with the help of an *anchoring* reference colourfulness patch, which was also used in previous LUTCHI experiments [Luo et al., 1991a, 1993a].

4.3.3 Inter-phase Colourfulness

In our experiments, the reference colourfulness patches were chosen to have a colourfulness of 40 according to the CIELAB colour space. It should be noted that the reference colourfulness is only meant to anchor the estimates, and as such any colour or *any* value can be chosen. To allow comparisons between different phases, we asked participants to rate the colourfulness of the reference colourfulness patch based on the reference colourfulness patch from the previous phase (memory experiment). The results are shown in Figure 4.10, where (a) plots the averaged perceived colourfulness of the *reference colourfulness* for different luminance levels (44–16 400 $\mathrm{cd/m^2}$) with a fixed background (20%), and (b) plots perceived reference colourfulness for different background levels (0–95%) with a fixed luminance level (2 200 $\mathrm{cd/m^2}$). Averaged perceived colourfulness increases up to 62.12% in proportion to the logarithm of luminance and decreases up to 31.73% in proportion to the luminance levels of background. The average CV of these colourfulness memory experiments was 20.93%. In particular, the variation of the colourfulness change *by background* is higher than that change *by luminance*; the slope of change by background is also smaller than that of luminance. Our results show that the luminance level has more impact than the background level on colourfulness perception. Finally, as the participants estimate colourfulness by using a same anchor point (colourfulness: 40), we can scale the perceived colourfulness by the change of reference colourfulness between phases.

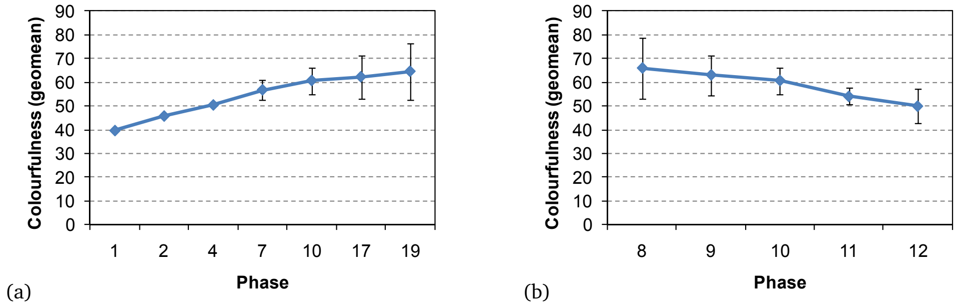

Figure 4.10: *Plot (a) shows the average perceived colourfulness of the reference colourfulness patch for different luminance levels (44–16 400 cd/m^2) with a fixed background (in 20%). Plot (b) presents the perceived reference colourfulness for different background levels (0–95%) with a fixed luminance level (2 200 cd/m^2).*

4.3.4 Observer Repeatability and Variation

The soundness of obtained colour appearance data was tested by evaluating variation at different time (repeatability) and overall CV errors in all phases (accuracy) [see Equation (2.13) for CV calculation]. Three observers repeated two phases (phases 7a and 7b) of the original experiment (phase 7) in order to judge long- and short-term repeatability. Phase 7 was conducted in the first week of December in 2008; the other two phases (7a and 7b) were conducted a month later. The average CV of short-term repeatability between two different experiments (7a and 7b) was 10.06% for lightness, 17.23% for colourfulness, and 7.22% for hue (see Figure 4.11 for qualitative comparison). Comparing one-month different experiments (phases 7 and 7a), the average CV of long-term repeatability was 11.83% for lightness, 22.82% for colourfulness, and 11.42% for hue. In addition, we tested overall observer variation of all phases by calculating CV error. The average CV of all the observers in all phases was 14.89% for lightness, 31.91% for colourfulness, and 9.37% for hue (see Table 4.2 for comparison). In particular, the colourfulness estimation had higher variation than other appearances, but this was also observed in previous colour experiments [Luo et al., 1991a,b, 1993a,b, 1995]. For instance, in the LUTCHI data sets phases of lightness varied 11–18% (CV), colourfulness phases varied 13–27%, and hue phases varied 4–7%. The LUTCHI data sets present similar variations to ours.

Figure 4.11 shows a qualitative comparison of two different experiments (phase 7a and 7b) to measure short-term repeatability. It represents later estimations of the same colour stimuli against former estimations. Although small variation is observed in these two phases, data is scattered along the diagonal of these plots (a straight line on the diagonal indicates an ideal match). The later estimates (the Y axis) of lightness, colourfulness, and hue present the same trend compared to the former estimates (the X axis), and no bias nor skewness is observed.

As shown in Table 4.2, hue estimates were more consistent than lightness and colourfulness estimates. Lightness estimates were more consistent than colourfulness estimates. Similar trends are also observed in the LUTCHI data sets. In particular, the largest variation was observed in colourfulness estimation. In post-experiment interviews, all the participants reported that colourfulness is the most difficult to judge and that open-end magnitude estimation (colourfulness) is more difficult than simple partitioning (lightness and colourfulness). For the larger variation of colourfulness, we could trace back to the difficulty of magnitude estimation, but the quality of our appearance data is consistent with previous experiments.

Observer Variance	Lightness	Colourfulness	Hue
Short-term repeat.	10.06%	17.23%	7.22%
Long-term repeat.	11.83%	22.82%	11.42%
All phases	14.89%	31.91%	9.37%

Table 4.2: *Observers repeatability and all-phases variation.*

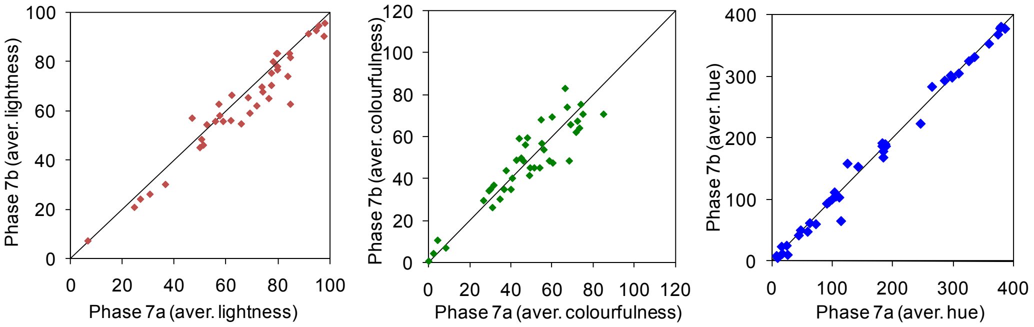

Figure 4.11: *The repeatability of observers was tested by using stimuli in phase 7. The X axis represents the estimations of lightness, colourfulness, and hue in phase 7a. The Y axis shows these estimations in phase 7b that was repeated after phase 7a.*

4.3.5 Differences to Previous Experiments

Previous perceptual attribute correlates have been derived mostly from the LUTCHI data sets because it is publicly available (with one addition: an appearance data set for the *simultaneous contrast effect* [Luo et al., 1995]). The LUTCHI data sets comprise eight different viewing conditions: high-luminance reflective paper (R-HL), low-luminance reflective paper (R-LL), low-luminance reflective paper comparing lightness with brightness (R-VL), reflective textile (R-Textile), CRT display (CRT), transparency (LT), 35mm slide projector film (35mm), and supplemental reflective paper and transparency measurements (BIT) [Luo et al., 1991a,b, 1993a,b, 1995, 1997], but were really geared towards reflective surfaces and low-luminance conditions. Most of their experiments were carried out with a maximum luminances of up to 690 $\mathrm{cd/m^2}$, except the cut-sheet transparency condition [Luo et al., 1993b], which included a total of only four colour patches (used in two different phases) with a luminance over 1 000 cd/m^2.

It should be mentioned that there are some distinct differences in our experiments to previous experiments. The LUTCHI data set was geared towards reflective surfaces and low-luminance conditions — no data are available for extended luminance levels. As a result, colour appearance models derived only from LUTCHI cannot robustly model colour appearance under higher luminance levels. This can be seen in Chapter 6. In addition, data sets used in other experiments are not publicly available.

In order to verify experimental consistency with the LUTCHI data sets, we conducted a few low-luminance experiments (phases 1–5 in Table A.36) as previous colour experiments have already covered low luminance. Figure 4.12 compares one low-luminance phase between LUTCHI (phase 6 in [Luo et al., 1991a] – on a CRT display with a peak luminance of 40.5 cd/m^2) and ours [phase 1 on our high-luminance display with neutral-density (ND) filters, producing a peak luminance of 44 cd/m^2]. Although both experiments were conducted on different display devices (a CRT and an ND-filtered high-luminance display) and different viewing conditions (unknown in LUTCHI), the quantified values of colourfulness and hue in both data sets present a very similar trend [see Plots (b) and (c)]. Lightness perception shows some differences in the perceived lightness of middle-tone colours [see Plot(a)]. We explain the differences with the fact that lightness perception is considerably changed by medium type [Luo et al., 1993b] (see Chapter 5 for more details) and with the (unknown) differences in viewing conditions.

4.4 Data Analysis

For lightness and hue estimates, all observers had to use the same numerical scale with fixed end points. Given minimum and maximum values to judge the lightness and hue attributes, this forced the observers to use a partition technique rather than pure magnitude estimation [Stevens, 1971]. Consequently, we can compute the *arithmetic mean* between all observers in order to find the central tendency measure for *partitioning*. Note that for hue, the scale is circular and care needs to be taken when averaging. If an observer's response were a mixture of R-Y and B-R, one of the responses was moved to the other end of the scale between 0 and 400, e.g., in case of 20 and 390, 390 is converted to -10, and averaged with 20.

For colourfulness scaling, the observers applied their own open-end arbitrary scale (pure magnitude estimation). Colourfulness estimates, on absolute scales, were analysed, following [Bartleson, 1979; Pointer, 1980]. According to [Stevens, 1971], the sensation of a signal always presents a power function. Therefore, the appropriate central tendency measure for magnitude estimation is the geometric mean, but only after relating the observers' responses to each other (since observers use their individual scales). We follow the same method as [Pointer, 1980] and map each observer's responses to the *mean* observer.

Each observer produces their own *scale* unit of sensation b in their own *attribute* a. The ob-

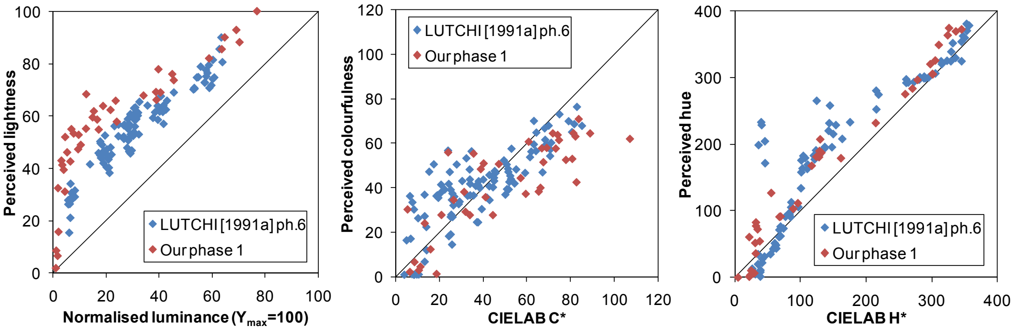

(a) Lightness (b) Colourfulness (c) Hue

Figure 4.12: *Qualitative comparison between LUTCHI and our appearance data. This figure compares low-luminance phases in LUTCHI (phase 6 in [Luo et al., 1991a] – on a CRT display) and ours (phase 1 on our high-luminance display with ND filters). Plot(a) presents perceived lightness against normalised incident luminance. Plot(b) and (c) show perceived colourfulness and hue of our data and LUTCHI data against CIELAB chroma C* and hue H* (scaled to 400). For qualitative comparison of colourfulness and hue (which are not measurable in a physical sense as is luminance), we use CIELAB colour space instead as the CIELAB space does not account for any viewing environmental conditions (see Section 2.3.4 for more details). In Plot(a), lightness perception presents differences in the perceived lightness of middle-tone colours. The differences are explained by the fact that lightness perception is considerably changed by medium type, i.e., LUTCHI data here [Luo et al., 1993b] employs a CRT display and our measurement uses an LCD display. The different spectral characteristics of these media causes different perception of lightness due to unknown differences in viewing conditions.*

servers response magnitude R can be modelled [Stevens, 1971] as follows:

$$R = aS^{b}\,, \tag{4.1}$$

where S is the stimulus magnitude. The observer's scale and attribute can be mapped into a *common scale* (*geometric mean* according to [Stevens, 1971]). When the common geometric mean responses $\overline{\mathbf{R}}$ of all the observers to given stimuli $\mathbf{S}$ is computed, each individual observer's scale and attribute, the constants a and b, can be found by least-squares fitting in log-log domain:

$$\log_{10}\overline{\mathbf{R}} = b\log_{10}\mathbf{S} + a. \tag{4.2}$$

This enables us to correct each observer's data to a common scale. Then, the arithmetic mean of the converted data turns out to match to the geometric mean of original data. As a result, each individual colourfulness measurement is able to be compared with others for arithmetic comparison. The CV was mainly used as a statistical measure to investigate the agreement between any two sets of data [see Equations (2.12) and (2.13)].

4.5 Colour Appearance Phenomena

Before describing our colour appearance model in the next chapter, this section will describe the important findings and trends observed in our data. The findings of our experiments agree with those of previous experiments (see Section 2.3.3 for more details on colour appearance phenomena). However, our experiments quantify known colour appearance phenomena in the full range of the human visual system (five orders of magnitude). Colour appearance data sets have higher variation than other scientific measurements [Luo et al., 1991a] as they are commonly derived via the magnitude estimation method. Therefore, the *central tendency* of colour appearance attributes is broadly accepted and used in colour appearance modelling as opposed to the *student's t-test*.

The following subsections describe qualitative and quantitative findings from our experiments. The observed colour appearance phenomena are presented by plotting them against CIELAB colour appearance. As mentioned earlier, the lightness, chroma, and hue coordinates in CIELAB are assumed here to be physical measures such that they do not take into account the viewing environment (see Section 2.3.4 for more details). Physical measurements from the spectroradiometer in CIEXYZ are simply transformed into L*, C*, and H* (scaled to 400) coordinates in CIELAB for comparison with perceptual measurements.

4.5.1 Luminance Effect on Lightness

Perceived lightness is plotted against physical measurements in Figure 4.13. The Y axis represents perceived lightness, and the X axis shows the lightness value L* (in CIELAB) of the incident light. 40 colour patches were observed by participants with a variation in luminance. Other viewing conditions were fixed: background ratio (23%), colour temperature (6197K), and a dark surround. Luminance (controlled by ND filters in front of the light source) is set at 44, 123, 397, 1 051, and 2 196 cd/m^2. We found that the perceived lightness of the *medium* colours (not dark and not bright) increases when the luminance level increases and that the *shape* of the perceived lightness curve changes due to the luminance difference. The average perceived lightness increases with increased peak luminance, see Figure 4.13(b). Lightness in our data shows a similar trend to the LUTCHI experiments. In our data, the average lightness of the 40 colours increases by 5.26% per magnitude of peak luminance [$\log(peak\,luminance)$]. LUTCHI data sets show that darker colours appears lighter under higher luminance by approximately 4%.

4.5.2 Luminance Effect on Colourfulness

Perceived colourfulness is plotted against physical measurements in Figure 4.14, using the same viewing environment as in Section 4.5.1. The Y axis presents perceived colourfulness, and the X axis shows the chroma value C* (in CIELAB) of the incident light. Colourfulness shows a similar trend. We note that the perceived colourfulness of the *bright* colours mainly increases. The average perceived colourfulness increases with increased peak luminance (fixed background ratio), as shown in Figure 4.14(b). At higher luminance levels perceived colourfulness increases. It is shown that the *slope* of the perceived colourfulness trends changes due to the peak luminance. In our data, the average colourfulness of the 40 colours increases by 13.09% per magnitude of peak luminance [$\log(peak\,luminance)$]. The LUTCHI data sets [Luo et al., 1993b] show that colourfulness increases under higher luminance by approximately 6%.

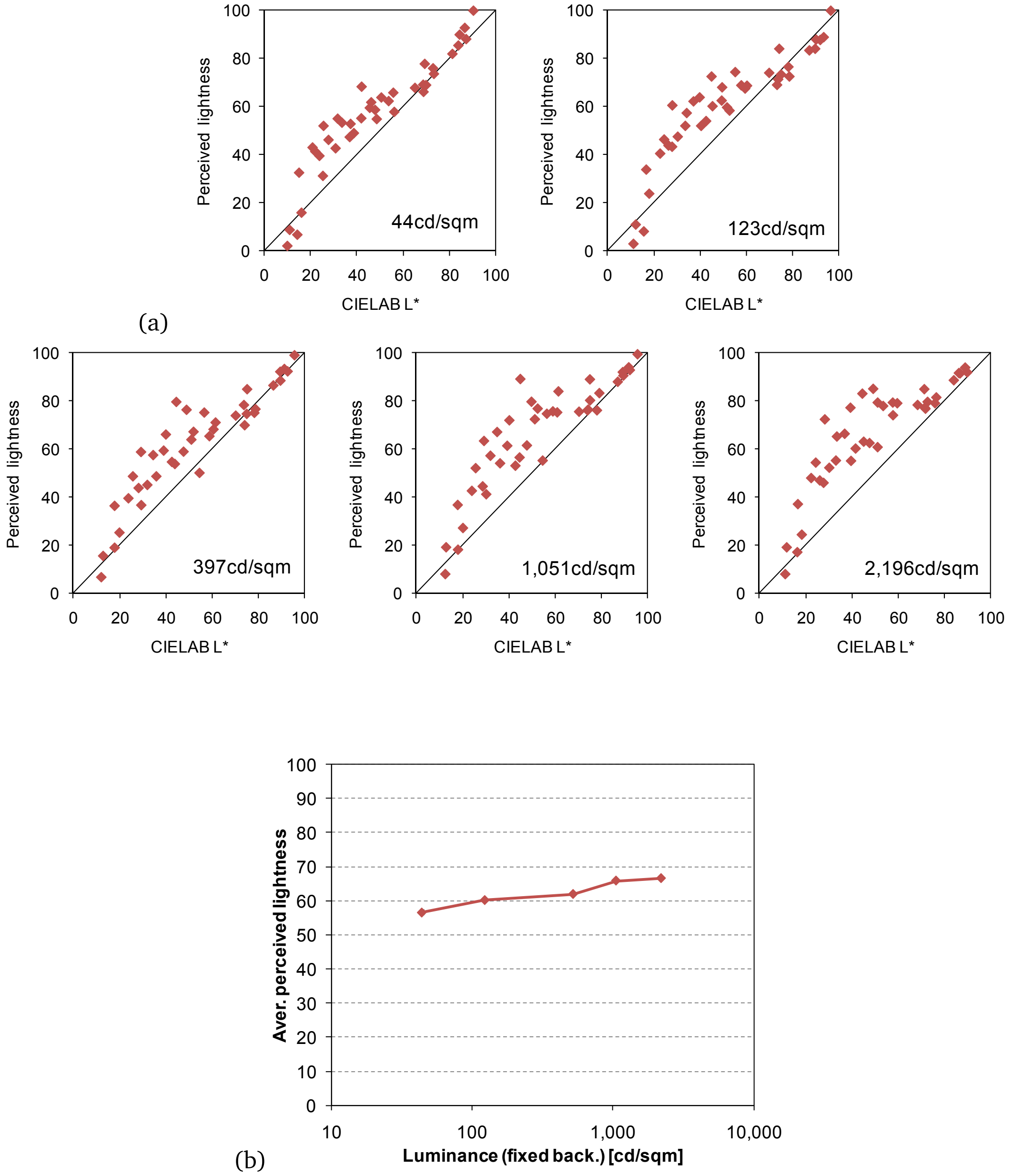

Figure 4.13: *(a) Lightness perception for different luminance levels (phases 1, 2, 4, 7, and 10). (b) Average lightness perception for different luminance levels.*

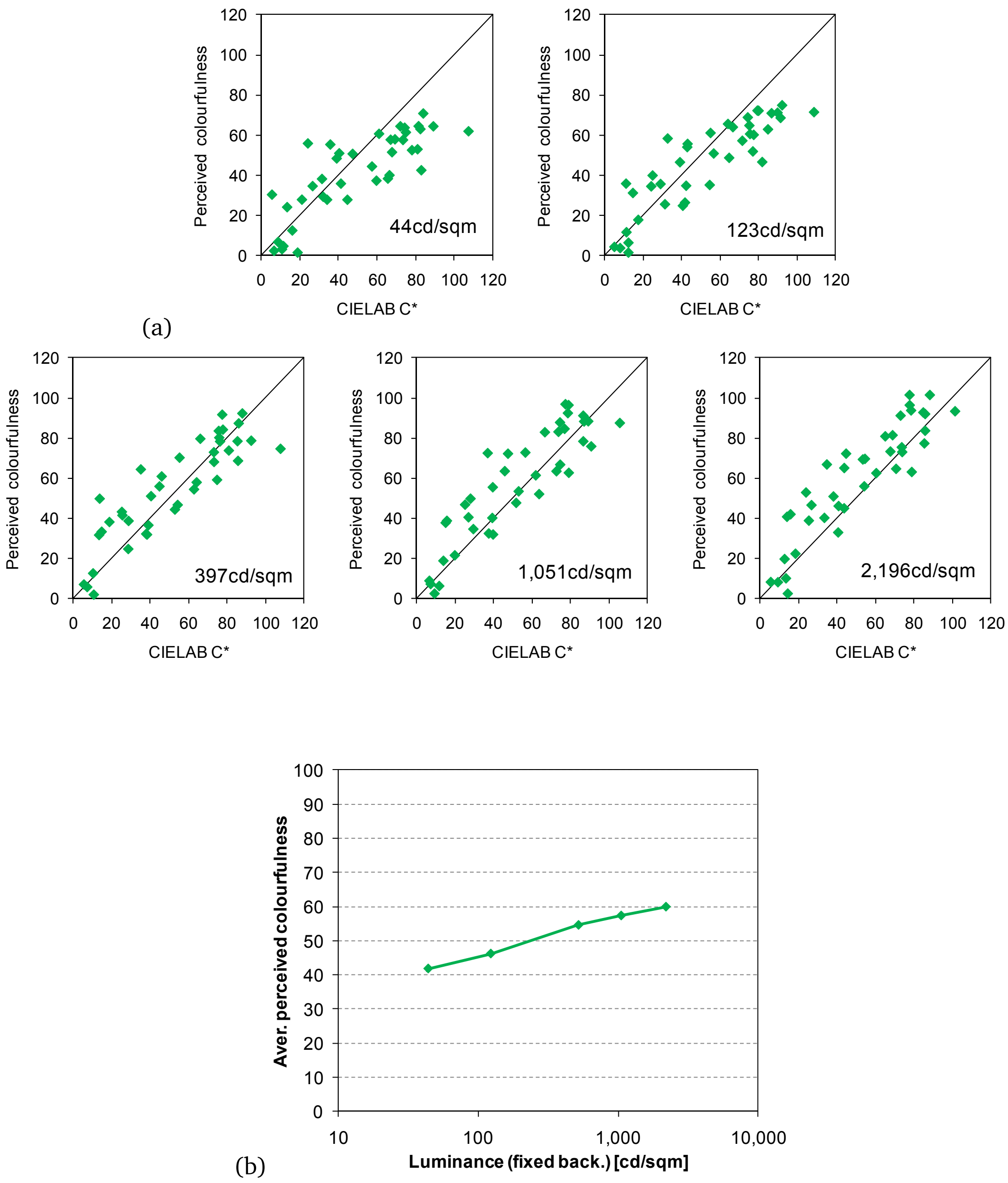

Figure 4.14: *(a) Colourfulness perception for different luminance levels (phases 1, 2, 4, 7, and 10). (b) Average colourfulness perception for different luminance levels.*

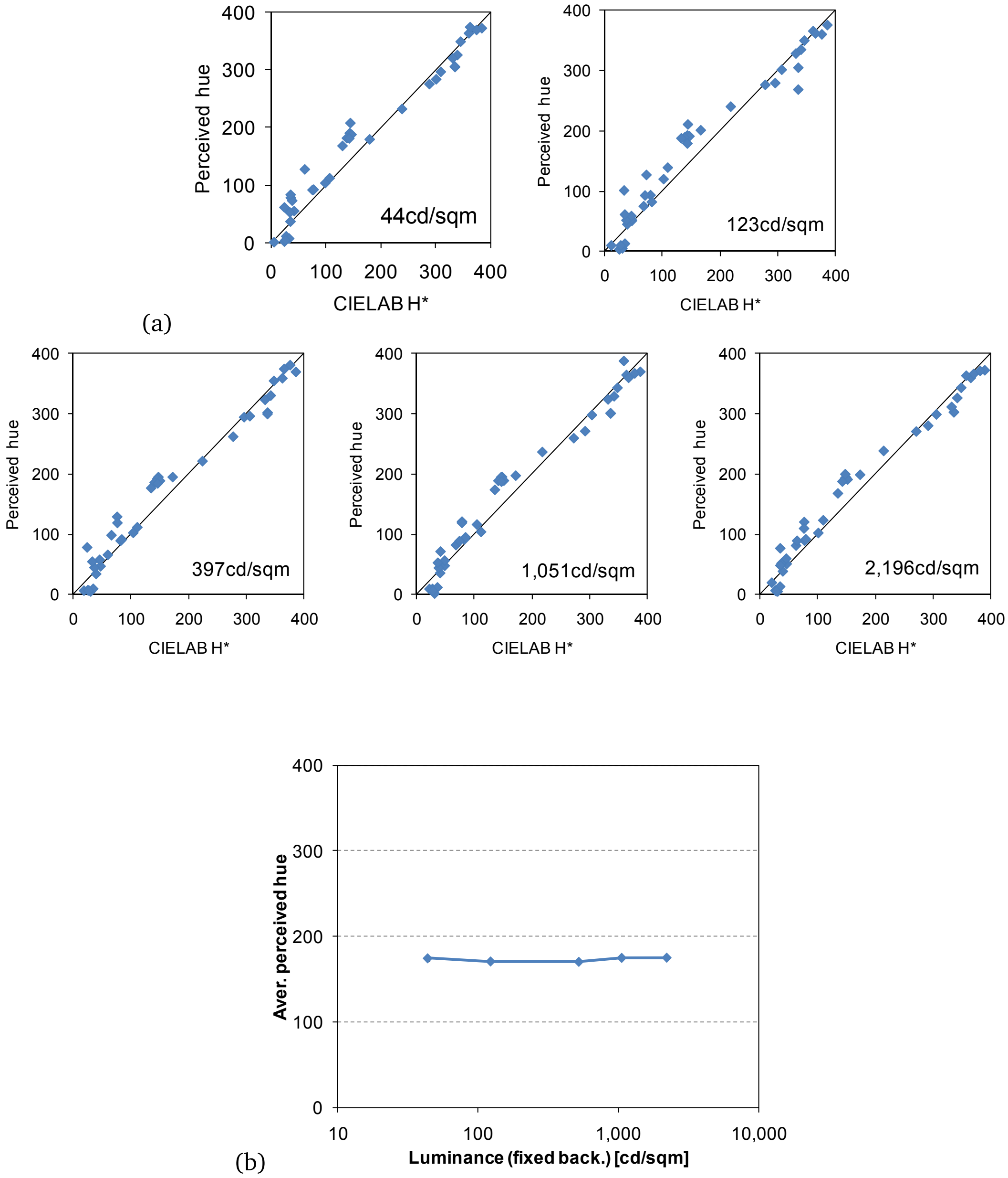

Figure 4.15: *(a) Hue perception for different luminance levels (phases 1, 2, 4, 7, and 10). (b) Average hue perception for different luminance levels.*

4.5.3 Luminance Effect on Hue

Perceived hue is plotted against physical measurements in Figure 4.15. The same colour patches are observed by observers with variations in luminance. Other viewing conditions are the same as in Section 4.5.1. As shown in this qualitative comparison, the perceived hue does not present comparative variation with changes in luminance levels. The CV of the average perceived hue is only 1.98. Hue appears constant with regards to variations in luminance, which is consistent with previous data (LUTCHI), see Figure 4.15.

4.5.4 Background Effect on Lightness

Figure 4.16 presents the perceived lightness trend with variations in the background luminance. The peak luminance level is fixed at 2 241 $\mathrm{cd/m^2}$, but the background ratio is changed to 0% (black), 12%, 23%, 55%, and 95% (white). The colour temperature was fixed at 6197K, and the surround was set to dark. Participants judged 40 colour patches against different backgrounds. The perceived lightness comparatively changes due to the background luminance. We note that the perceived lightness of *all* the colours clearly increases on the dark background. The average perceived lightness increases with decreased background luminance of 8.43% per magnitude of background luminance [$\log(background\, luminance)$]. We note that in case of a black background (0% background ratio), the shape of the perceived lightness curve is also changed.

4.5.5 Background Effect on Colourfulness

Perceived colourfulness is presented with variations in background luminance in Figure 4.17. Other viewing conditions were set as in Section 4.5.4. We found that the perceived colourfulness of the *medium-dark* colours increases. Variation of the perceived colourfulness increases accordingly; however, the slope of the perceived colourfulness trends is not changed by the background ratio. The average perceived colourfulness increases with decreased background luminance by 6.48% per magnitude of background luminance [$\log(background\, luminance)$].

4.5.6 Background Effect on Hue

Figure 4.18 presents the perceived hue with variation of the background ratio. Peak luminance, colour temperature, and surround were fixed as in Section 4.5.4. We found that the perceived hue does not show strong variation against different background ratios. The CV of the average perceived hue is only 1.82, see Figure 4.18(b).

4.5.7 Colour Temperature Effect on Colour Appearance

Figure 4.19 presents the perceived colour appearance with variations in colour temperature of the light source. 40 colour patches were presented against a background of ratio 23%, a fixed peak luminance of 1 233 $\mathrm{cd/m^2}$, and a dark surround. The colour temperature of the light source was changed by using Rosco colour-temperature changing filters (1803, 6197, and 7941K). We found that perceived lightness presents small changes of 7-9% with variations in colour temperature and that perceived colourfulness presents also small changes of 14-18% with temperature variation. However, perceived hue under 1803K (yellowish) presents a different CV from others (6197 and

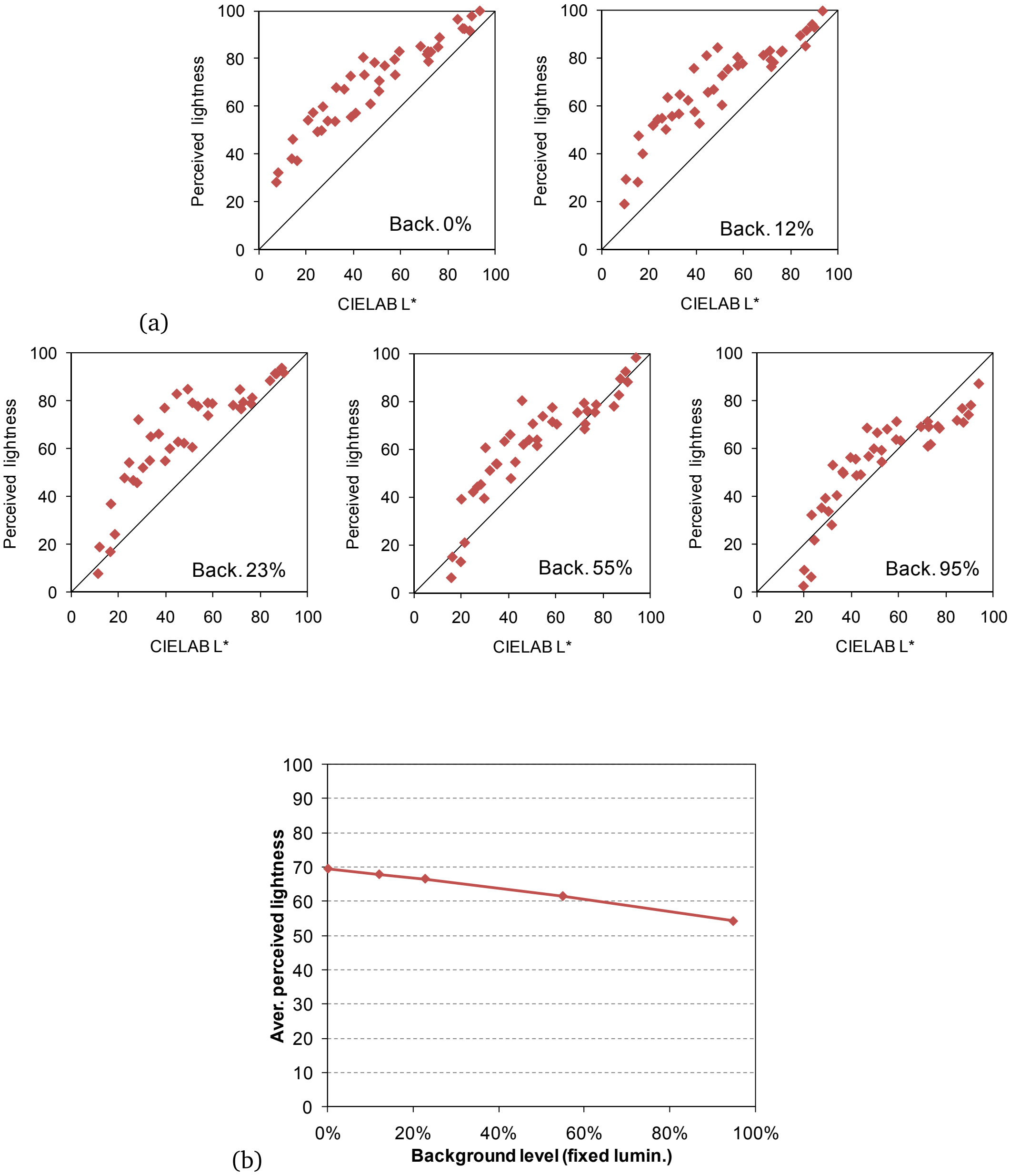

Figure 4.16: *(a) Lightness perception for different background levels (phases 8, 9, 10, 11, and 12). (b) Average lightness perception for different background levels.*

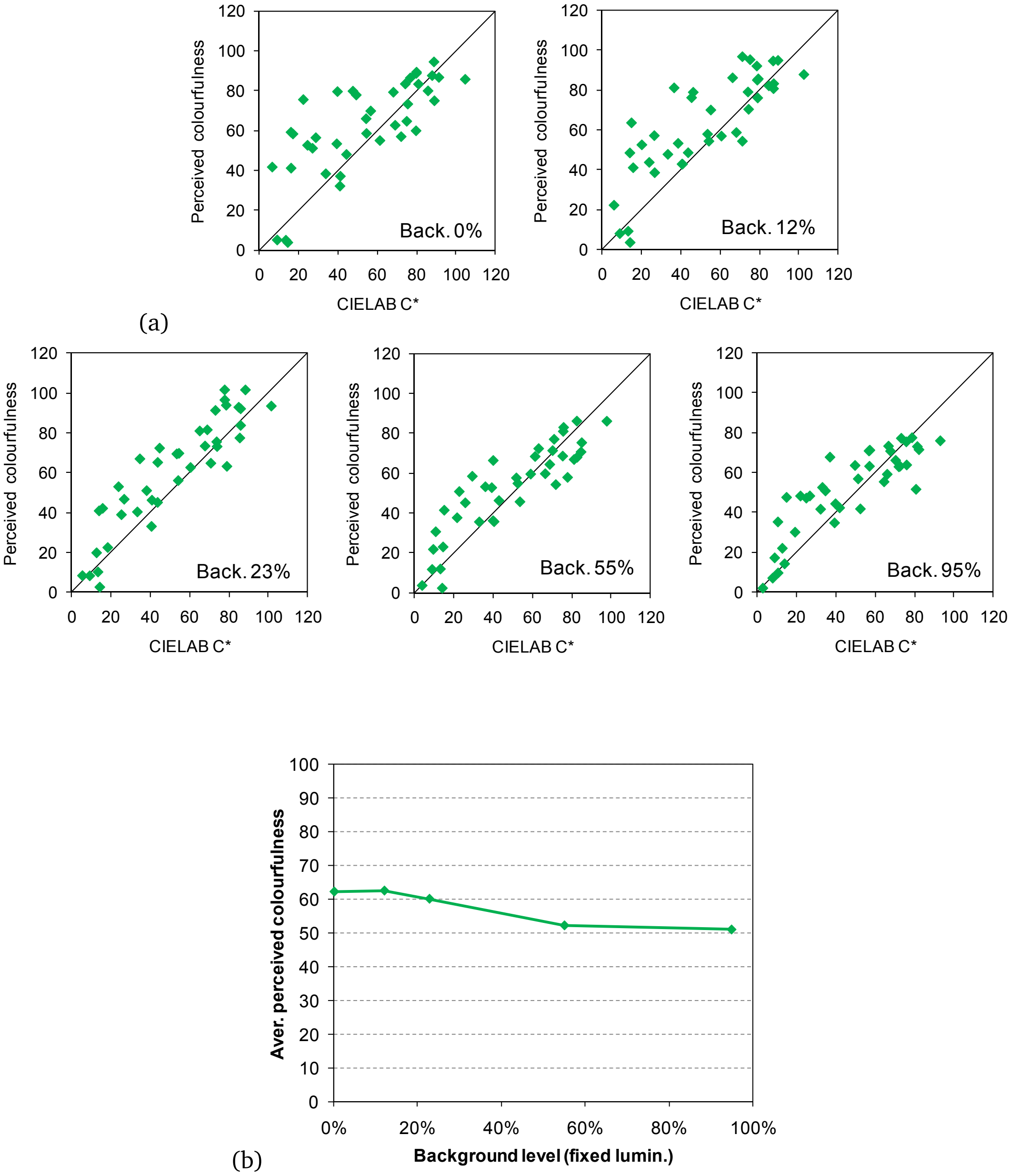

Figure 4.17: *(a) Colourfulness perception for different background levels (phases 8, 9, 10, 11, and 12). (b) Average colourfulness perception for different background levels.*

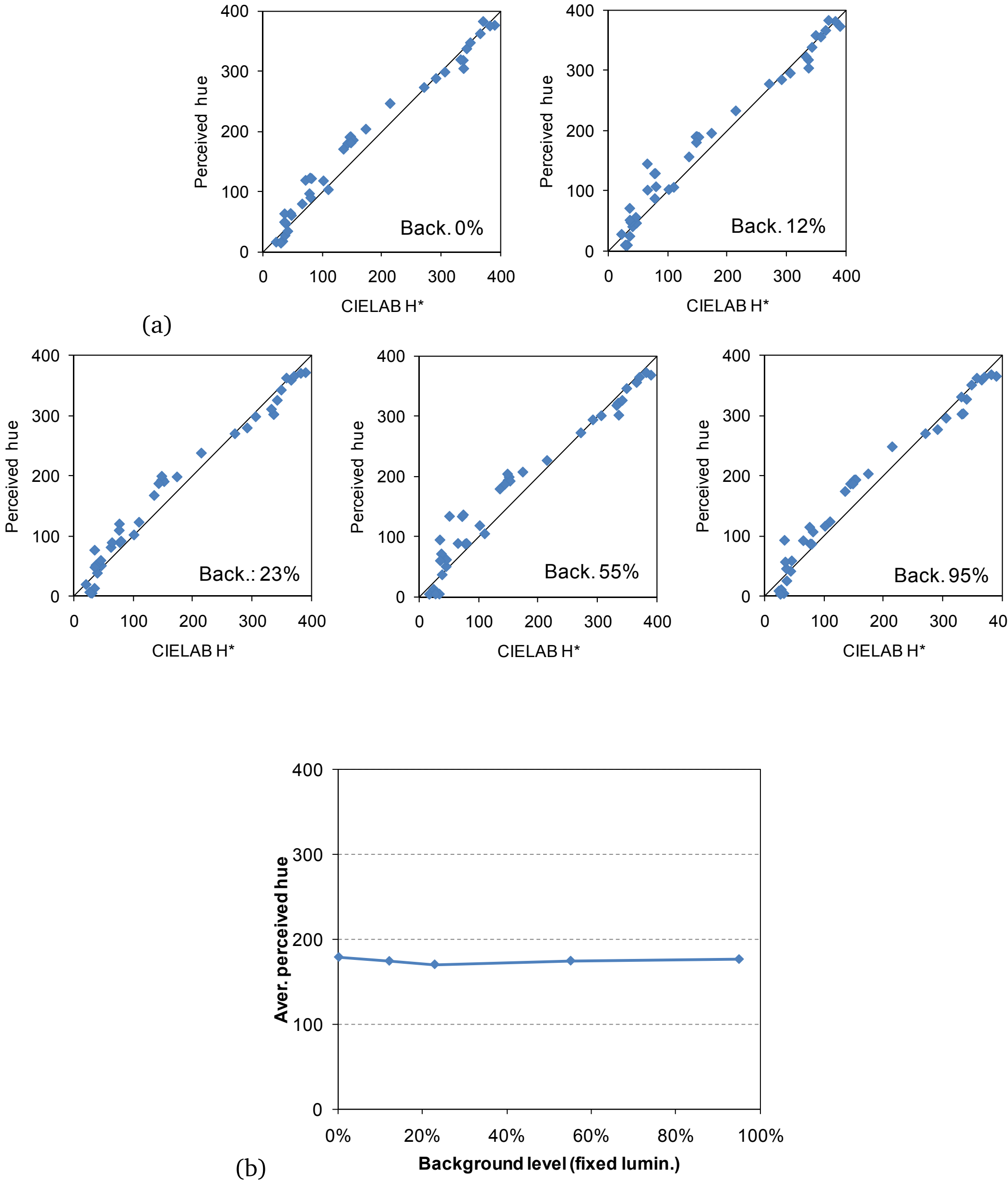

Figure 4.18: *(a) Hue perception for different background levels (phases 8, 9, 10, 11, and 12). (b) Average hue perception for different background levels.*

7941K) of 37% (both with two others). The CV value of perceived hue between 6197K and 7941K is 5.86%. In the low colour temperature (1803K), yellowish colours appear more reddish, and bluish colours appear more reddish. As observed in [Li et al., 2002], our experimental data sets also show *inconsistent* chromatic adaptation in perceiving hue under different colour temperatures and that perceived colourfulness also changes depending on the colour temperature of the light source.

4.5.8 Surround Effect on Colour Appearance

The perceived colour appearance under different surrounds (dark and average – 0% and 20% of the peak luminance) is presented in Figure 4.20. 40 colour patches were observed by the participants under a peak luminance of 2 196 cd/m^2, a background ratio of 23%, and a correlated colour temperature of 6197K. In dark surround settings (0%), we used a dark room with all indoor lights turned off. In average surround settings (20%), florescent-type bulbs illuminated the environment in order to make the surround 20% as bright as the peak luminance [Moroney et al., 2002]. Participants judged colour appearance in average bright viewing conditions. We note that perceived lightness,

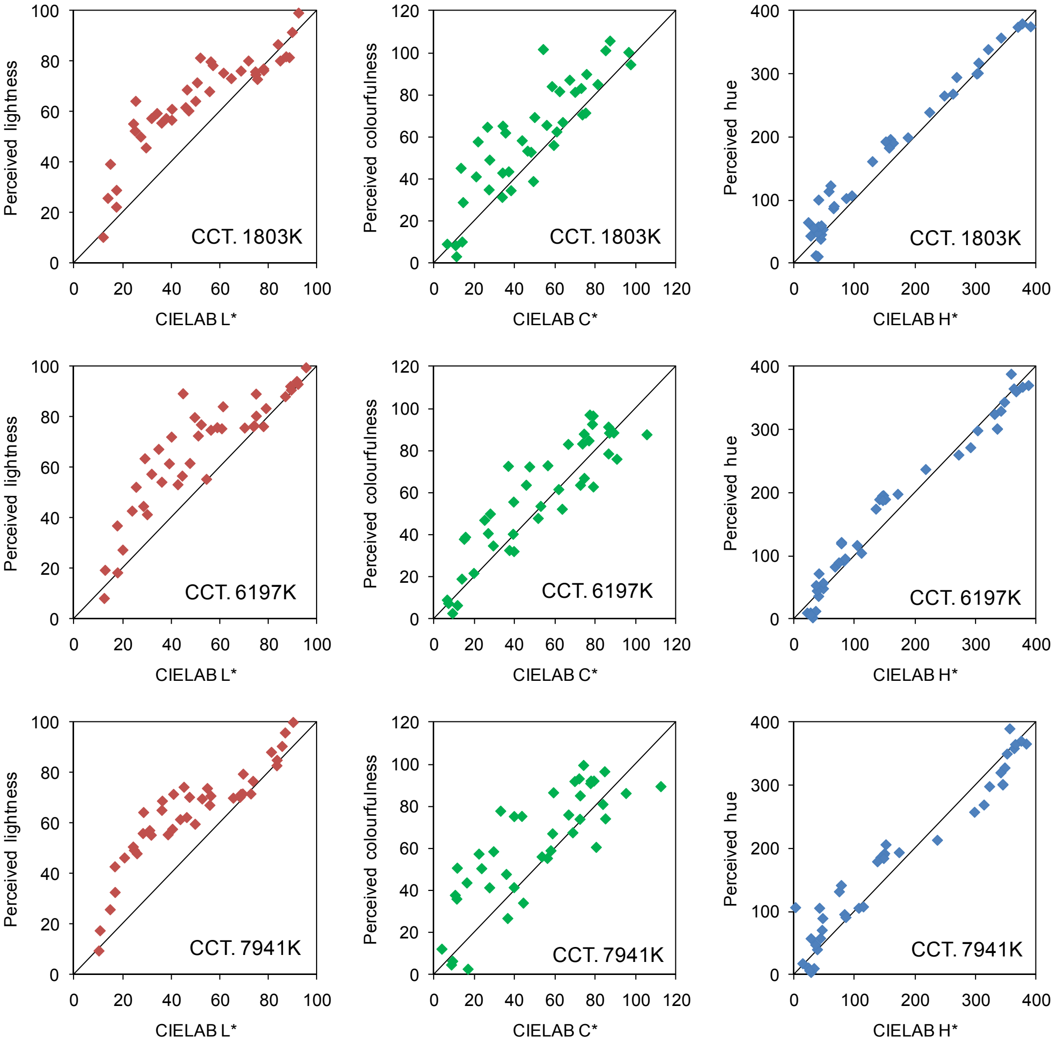

Figure 4.19: Colour perception for different colour temperatures (phases 14, 7, and 13).

colourfulness, and hue are almost identical [CV: (L) 9.16%, (C) 14.70%, and (H) 9.07% — less than the short-term repeatability] between the two different surrounds. For the minor changes in perceived hue, we suggest that the cause was the difference in colour temperature of the surround light (3323K) and viewing display (6197K).

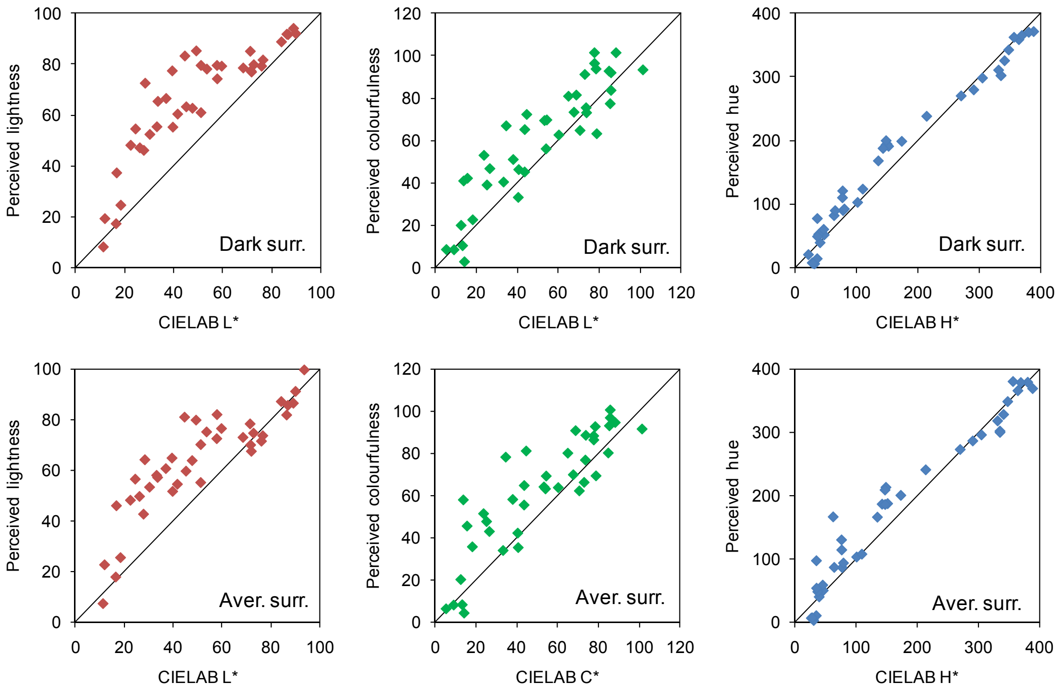

Figure 4.20: *Colour perception for different surrounds (phases 7 and 15).*

4.6 Discussion

In order to achieve high levels of luminance, we built a novel display device by utilising two HMI bulbs, which substitute the fluorescent back-lit unit in an LCD display. Its maximum level of luminance is approximately 30,000 cd/m^2. However, we performed experiments up to 16,860 cd/m^2 and abandoned higher levels of luminance as the luminances were too uncomfortable for the participants.

We mainly measured the impact of luminance and background level changes on colour perception. Hence, our experimental data contains limited variation of media and viewing conditions. For the variation of appearance on different media, LUTCHI data can be integrated as our data is compatible with LUTCHI data.

4.6.1 Perceived Lightness Appearance

The perceived lightness of the *medium* colours (not dark and not bright) increases when the luminance level increases. The average perceived lightness increases with increased peak luminance. This means that the shape of the perceived lightness curve changes due to the peak luminance. This was also shown by Stevens and Stevens [1963], and is called the *Stevens effect*. They attempted to model the perceived lightness curve as a power function. However, the perceived lightness turns out to have more complex trends than a simple power function. This Stevens-influenced modelling is observed in other colour appearance models, e.g., CIELAB, LLAB, RLAB, and so on. We model this luminance effect on lightness in a more rigorous way (see Chapter 5 for more details) than others.

The perceived lightness of *all* the colours clearly increases with a darker background. When the background luminance level increases, the average perceived lightness decreases (of all the colours), as shown by Bartleson and Breneman [1967]. This effect is called the *simultaneous contrast effect*. This phenomena is also modelled in our colour appearance model (see Chapter 5).

4.6.2 Perceived Colourfulness Appearance

Colourfulness shows a similar trend to lightness. The perceived colourfulness of *brighter* colours increases. At higher luminance levels, perceived colourfulness increases, which is known as the *Hunt effect* [Hunt, 2004]. This shows that the *slope* of the perceived colourfulness trends changes due to the peak luminance.

The perceived colourfulness of the medium-dark colours mainly increases, which was also indicated by the participants in post-experiment interviews. The average perceived colourfulness increases against a darker background, as shown in the *simultaneous contrast effect* [Albers, 1963]. These two colourfulness phenomena are also modelled in our colour appearance model (see Chapter 5).

4.6.3 Perceived Hue Appearance

Hue is generally constant with regard to variation in luminance, background, and surround, which is consistent with previous data. However, perceived hue presents a variation in colour temperature of the light source. Reddish light (low colour temperature) makes colours appear slightly more reddish, and greenish-and-bluish light (high colour temperature) makes colours appear slightly more bluish. Lesser degrees of adaptation occurred under the low colour temperature (1803K), following Li et al. [2002]'s findings. These *inconsistent colour constancy* phenomena are modelled through a process called *chromatic adaptation modelling* (see Chapter 5).

4.7 Summary

Current display devices cannot display five-orders of magnitude of luminance and therefore cannot cover the working dynamic range of the human visual system. Hence, we built a new high-luminance display device, which enables us to conduct colour appearance experiments under high luminance levels. Our experiments followed the methodology of previous LUTCHI colour experiments; therefore, our data set is compatible with in the existing colour appearance data. However, our colour appearance data set extends the range of luminance up to 16 860 $\mathrm{cd/m^2}$.

We summarise important findings and trends observed in our experimental data. If the luminance level increases, then lightness and colourfulness both increase. This confirms the Stevens and Hunt effects. In contrast, if the background luminance level increases, lightness and colourfulness both decrease, confirming the simultaneous contrast effect. Most of our findings are consistent with the LUTCHI data sets, and similar trends can be observed in both data sets. However, the LUTCHI data sets quantify these colour appearance phenomena mostly under approximately 690 cd/m^2, but our data set covers luminance up to 16 860 cd/m^2. Although our colour appearance data includes less various media than the LUTCHI data sets and less variation in colour temperature, it covers the five-orders of magnitude of luminance. The range of the experimental data corresponds to the working range of the human visual system. This experimental contribution enables us to derive a new colour appearance model for an extended range of luminance levels. Accordingly, our numerical model covers the full range of colour perception of the human visual system. The next chapter describes our colour appearance model.

Chapter 5

A Colour Appearance Model for Extended Luminance Levels

A colour appearance model (CAM) converts from *physical measurements* to *perceptual quantities*. This conversion differs amongst existing colour appearance models and involves numerical transfer functions that are matched to psychophysical observation data. These data are, in general, not publicly available and only implicitly embedded into CAMs derived from these data. The only available psychophysical data is from the LUTCHI experiments. Luo et al. [1991a,b, 1993a,b, 1995] measured human perception based mainly on reflective materials and low dynamic range conditions. The luminance level of these measurements is lower than that of many everyday situations in reality. For this reason, we conducted our own high-luminance colour experiments. These experiments, explained in the previous chapter, yielded a novel measurement of perceived colour appearance under *extended* luminance levels (up to 16 860 $\mathrm{cd/m^2}$). The dynamic range of the acquired appearance data set is close to that of the human visual system (about five-order magnitude). This enables us to numerically derive a new colour appearance model for *high-dynamic-range* luminance.

In this chapter, a novel colour appearance model is presented to improve *accuracy* in predicting human colour perception. This model is able to predict not only *image appearance* as can other colour appearance models, but also *real-world observation of the human visual system*. The following section describes a forward appearance model and is followed by an analytical inverse model. Both models will be used to complete a cross-media colour reproduction technique for *high-dynamic-range* imaging in the next chapter.

5.1 Data Sets

For the developments of our colour appearance model, we use the *maximum likelihood* approach, which derives a model based on training data without taking prior information. However, performance on the whole training set is not a good indicator of predictive performance on the seen data due to the problem of *over-fitting* [Bishop, 2006]. Insofar as we have 19 phases, our approach is to use some of the available phases as input to a range of models, and to compare the models with independent phases as a *validation set*. We subgroup certain phases with four different criteria:

luminance-varying phases (1, 2, 4, 7, 10, 17, and 19) — *group L*, background-varying phases (8, 9, 10, 11, and 12) — *group B*, colour temperature-varying phases (10, 14, and 15) — *group T*, and surround-varying phases (10, 15) — *group S*. For modelling distinctive colour appearance phenomena in our experiments (*Stevens*, *Hunt*, and *simultaneous contrast* effects, see Chapter 4), we mainly use *group L* and *B* as *training* sets for predicting these phenomena. We used *group T* for chromatic adaptation and *group S* for surround effect. The other independent phases (3, 5, 6, 16, and 18) were used as a *validation* set, called *group V*. In addition, although the LUTCHI data set has colour samples under limited range of luminances, we also used them (R-HL, LT, and CRT) as a *third test set* for *cross-validation* and validation on different media.

5.2 Forward Model

We propose a new colour appearance model that closely follows Müller [1930]'s zone theory in order to perform well under high-luminance conditions. The model consists of three main components: chromatic adaptation, cone response, and visual cortex response for each perceptual colour attribute. It aims to accurately predict lightness, colourfulness and hue, including the *Hunt effect* (colourfulness increases with luminance levels), the *Stevens effect* (lightness contrast changes with different luminance levels), and *simultaneous contrast effect* (lightness and colourfulness changes with background luminance levels), as observed in Chapter 4. Additional correlates of brightness, chroma, saturation, hue quadrature, and Cartesian colour opponent coordinates will be derived as well.

First, we model input parameters for this forward model as follow:

- Absolute CIE tristimulus values (observed main colours): XYZ,
- Absolute tristimulus values of the reference white point: $X_w Y_w Z_w$,
  (where Y_w corresponds to the peak luminance level L_w),
- Level of luminance adaptation: L_a [unit: cd/m^2]
  (luminance of viewing stimuli at about 10-degree angle),
- A medium type: E (e.g., paper, CRT, transparency, or high-luminance display).

The CIE defines colour elements as a light source (spectral energy), an object (normalised reflectance ratio on each wavelength), and a standard observer (presented as colour matching functions). Following this standard, previous colour appearance models take the *normalised reflectance* property (CIEXYZ, normalised to Y=100) for test colours. However, as shown in Chapter 4, absolute luminance matters in perceived colour appearance. The absolute scale of the measured radiance (CIEXYZ) can be very useful information for predicting colour appearance under high luminance levels. Therefore, we use absolute CIEXYZ measurements instead of normalised CIEXYZ. A spectroradiometer or a characterised HDR camera system [Kim and Kautz, 2008a] (see Chapter 3) can be used to measure absolute radiance. Our model also requires as input reference white point measurements on an absolute scale. Finally, our model requires the level of luminance adaptation by measuring the luminance of the viewing stimuli of a 10-degree viewing area. In our experimental set, luminance adaptation level comprises 88% of the background luminance, 4% of the test colour luminance, 4% of the reference white luminance, and 4% of the reference colourfulness luminance (see Figure 4.5). This weighted-average luminance of this 10-degree viewing area is used as an input parameter for the level of luminance adaptation, following [Moroney et al., 2002]. In the following, we explain all the components of our model.

5.2.1 Chromatic Adaptation

Humans perceive object colours as *constant* under different illumination (called *colour constancy*). This is generally true; however, as shown in Section 4.5.7, lesser degrees of chromatic adaptation may occur under lower colour temperatures such as the CIE illuminant A (white appears slightly yellow, see Figure 4.19). Once our eye has adapted to a certain viewing condition, the perceived colours seem to be scaled by the adapted brightest colour. We assume that this scaling is only performed in cone colour space. Further, certain colours seem more sensitive than others depending their own hue. Such an *inconsistency* of the chromatic adaptation was discovered in surface colour research [Lam, 1985]. This *inconsistent* chromatic adaptation, called a *chromatic adaptation transform* (CAT), has been researched extensively, e.g., Bradford transform (BFD), CMCCAT97s, CMCCAT2000, and CIECAT02. These transforms were derived from data sets [Helson et al., 1952; McCann et al., 1976; Breneman, 1987; Mori et al., 1991; Kuo et al., 1995; Braun and Fairchild, 1996] and enable us to predict corresponding colours in changes of spectral characteristics of illuminant. However, most of these data sets are not publicly available.

Chromatic adaptation is as large as a research field as appearance modelling for cross media; hence, generally previous CATs have been researched independently of colour appearance models. As the focus of our experiments was to extend the luminance range of colour appearance models, we exclude modelling chromatic adaptation from our research scope. Instead, we adopt one of the previously developed chromatic adaptation transforms. We tested a selection of transforms: the HPE transform (LMS cone space, used in RLAB) [Estévez, 1979], the BFD transform (used in CIECAT97s) [Lam, 1985], and the CIECAT02 transform (used in CIECAM02) [Li et al., 2002]. *Group L* of the luminance-varying phases (1, 2, 4, 7, 10, 17, and 19) is used for testing, assuming that the eye has adapted to the light source completely. As shown in Figure 5.1, the three colour transforms perform *consistently* better in terms of hue than raw calculations of CIELAB (von Kries chromatic adaptation in CIEXYZ). Therefore, these three colour transforms are worth considering in order to predict *inconsistent* chromatic adaptation with respect to *hue*. Among these, the HPE transform unfortunately changes the perceived chroma. The BFD and CIECAT02 transforms present similar performance with the CIECAT02 transform slightly outperforming the BFD transform in terms of colourfulness and hue. The BFD transform also has an invertibility problem [Fairchild, 2005]. Therefore, we chose and adopted the CIECAT02 model as our chromatic adaptation transform. Colourfulness errors increase slightly after applying transforms in all cases, but note that *chromatic adaptation transform* is used to predict *hue changes* with respect to illumination. Perceived colourfulness will be modelled later.

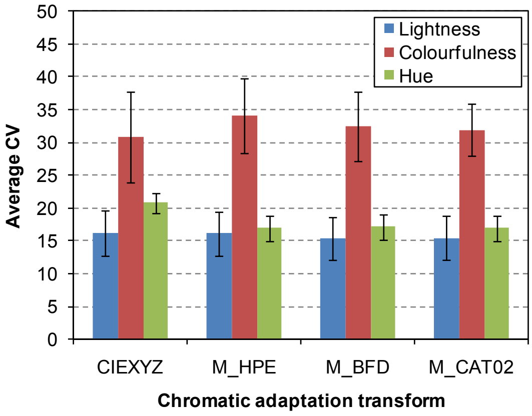

Figure 5.1: *We compare three chromatic adaptation transforms (with CIEXYZ): the HPE transform (LMS cone colour space), the BFD transform, and CIECAT02. These three chromatic transforms are plugged into the CIELAB colour space structure as a form of von Kries chromatic adaptation. The calculated L*, C*, H* values are compared with perceptual measurements in phases 1, 2, 4, 7, 10, 17, and 19. Overall, CIECAT02 performs better than the other transforms.*

In Equation (5.1), we transform the chromatically adapted cone signal, which is linear to incident radiation into the eye in *absolute* terms:

$$\begin{bmatrix} R_C \\ G_C \\ B_C \end{bmatrix} = \mathbf{M}_{\mathrm{CAT02}} \cdot \begin{bmatrix} X \\ Y \\ Z \end{bmatrix}, \quad \mathbf{M}_{\mathrm{CAT02}} = \begin{bmatrix} 0.7328 & 0.4296 & -0.1624 \\ -0.7036 & 1.6975 & 0.0061 \\ 0.0030 & 0.0136 & 0.9834 \end{bmatrix}. \tag{5.1}$$

It takes the incident (absolute) XYZ_{D50} values and transforms them to new RGB_C values, accounting for chromatic adaptation based on the reference white. It is important to note that, in contrast to previous models, we do not normalise the signal but keep its absolute scale; i.e., the white-adapted RGB_C has the same scale [use Y_w in Equation (5.2)] as the original XYZ:

$$\begin{bmatrix} R'_C \\ G'_C \\ B'_C \end{bmatrix} = \mathbf{M}_{\mathrm{D}} \cdot \begin{bmatrix} R_C \\ G_C \\ B_C \end{bmatrix}, \quad \mathbf{M}_{\mathrm{D}} = \begin{bmatrix} Y_w/R_w & 0 & 0 \\ 0 & Y_w/G_w & 0 \\ 0 & 0 & Y_w/B_w \end{bmatrix}. \tag{5.2}$$

In the original CIECAT02 transform, a parameter D is used to estimate the *degree of chromatic adaptation* by taking into account the *level of luminance adaptation* L_a [see Equation (2.90) and (2.91)]. This parameter linearly interpolates the degree between 100% white adaptation and no adaptation, depending on the luminance adaptation level. As shown in Figure 5.2, the parameter D varies between 0.66–0.80 (F constant for dark surround — 0.8), and it starts to saturate from a luminance level of 310 cd/m^2. This means a higher luminance level than 310 cd/m^2 will be adapted in the same was as lower levels.

In our luminance-varying phases (group L), no distinguishing difference in the degree of chromatic adaptation was observed up to 16 860 cd/m^{2}in our experimental data. CVs of predicted

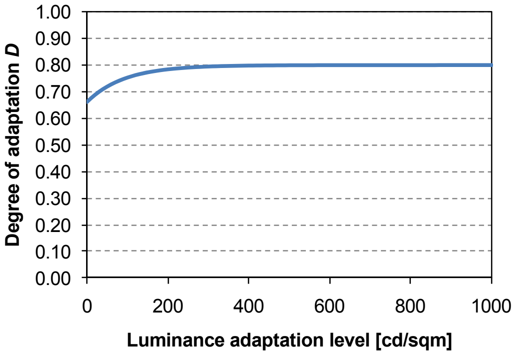

Figure 5.2: *The degree of chromatic adaptation parameter D in CIECAT02. The X axis shows the input luminance level, and the Y axis presents the interpolation parameter D [see Equation (2.90)]. In this experimental dark surround, the parameter D only varies between 0.66–0.80 and starts to saturate after 310* $\mathrm{cd/m^2}$ *of luminance adaptation level.*

lightness, colourfulness, and hue *without* D were 15.47, 31.96, and 16.98; CVs of predicted lightness, colourfulness, and hue *with* D were 15.62, 31.74, and 16.74. These two prediction results with/without the D parameter are almost identical to each other. Therefore, although we adopted the chromatic transform matrix M_{CAT02} from CIECAT02, we exclude the nonlinear interpolation with the *degree of adaptation function* D.

5.2.2 Cone Responses

Biological and physiological structures and mechanisms of the human eye are still obscured by a lack of knowledge. According to previous research [Müller, 1930; Vos and Walraven, 1971; Estévez, 1979; Hunt, 1995], we have a different population ratio of LMS cones [Vos and Walraven, 1971], which is related to a colour space [Estévez, 1979]. Most models have adopted a ratio based on a compromise of physiological evidence (LMS cone colour space) [Estévez, 1979] and psychophysical experiments resulting in a 40:20:1 ratio of LMS cones [Vos and Walraven, 1971].

Based on previous knowledge, the human eye is believed to exhibit a non-linear response on each cone channel. Following Stevens [1961], this is usually modelled as a power function (exponent: 1/2 [de Vries, 1943; Rose, 1948] or 1/3 [CIE, 1986]) derived from psychophysical experimental data. Older colour appearance models, such as CIELAB, RLAB, and LLAB modelled cone response within XYZ space and assumed a simple power function as a response curve, which reflects early physiological assumptions [de Vries, 1943; Rose, 1948] (see Section 2.3.4 for more details of other models). Modern *Hunt94-based* models (Hunt94, CIECAM97s, FC, Fairchild, and CIECAM02) transform the chromatically adapted (and normalised) XYZ tristimulus values into LMS cone space, commonly using the HPE transform [Estévez, 1979]. Note that RLAB uses the HPE transform only for chromatic adaptation. These CAMs modelled cone response with hyperbolic functions of the form shown in Equation (2.11). However, existing models (and in particular

CIECAM02), use a constant σ in Equation (2.11) (following Boynton and Whitten [1970]) which causes the hyperbolic function [see Equation (2.93)] to resemble a power function (see Figure 5.3), as mentioned by Kwak [2003].

Most applications of dynamic cone response functions take as input normalised cone signals and a fixed adaptation point. Models based on Hunt94 [Hunt, 1995] use the F_L function, which takes the adaptation level L_a as input, in order to translate the relative input colour information into a quasi-absolute scale. Our cone model is based on two insights. First, the V_m in the original equation [see Equation (2.11)] is not the reference white, but the *maximum saturation point of cones*. This means that the model works in terms of *absolutes*. Second, based on findings by Valeton and van Norren [1983], the σ should be decided by the *absolute level of luminance adaptation*. As mentioned by Hunt [1998] and Fairchild [2005], cones that contribute photopic vision are highly concentrated in the fovea (1.5–2°) and more sparsely populated throughout the peripheral retina. There are no rods in the central fovea and there is a blind spot at a 12–15° angle from the fovea. As the *luminance of the adapting field*, generally background, has been assumed the level of *luminance adaptation* by most appearance models, e.g., CIECAM97s and CIECAM02, σ can be decided by measuring the actual luminance of viewing stimuli at a 10° angle; or, in an imaging application, measuring the averaged luminance value and using it as an input value.

In our model, tristimulus values (from chromatic adaptation) are transformed into LMS cone space using the Hunt-Pointer-Estévez (HPE) transform [Estévez, 1979]:

$$\begin{bmatrix} L \\ M \\ S \end{bmatrix} = \mathbf{M}_{\mathrm{HPE}} \cdot \mathbf{M}_{\mathrm{CAT02}}^{-1} \cdot \begin{bmatrix} R'_C \\ G'_C \\ B'_C \end{bmatrix}, \quad \mathbf{M}_{\mathrm{HPE}} = \begin{bmatrix} 0.38971 & 0.68898 & -0.07868 \\ -0.22981 & 1.18340 & 0.04641 \\ 0.00000 & 0.00000 & 1.00000 \end{bmatrix}. \tag{5.3}$$

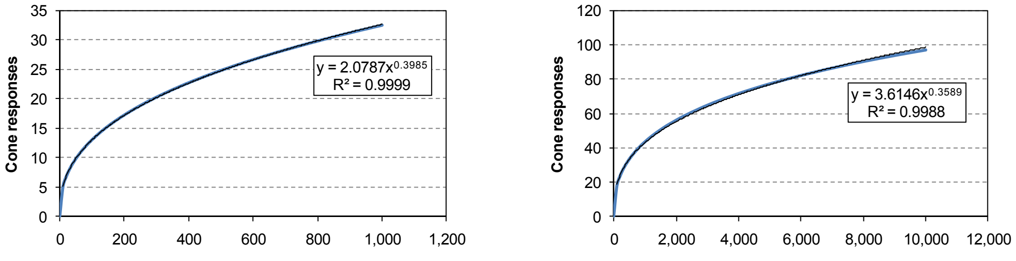

(a) (b)

Figure 5.3: *These plots show a cone response curve modelled by CIECAM02 up to (a) 1 000 cd/m^2 and (b) 10 000 cd/m^2. Although it has the form of a hyperbolic function, the actual outputs resemble a power function that has an exponent between 1/2.51–1/2.79. The squared correlation coefficients (R^2) between a power function and the CIECAM02 cone response function are (a) 0.9999 and (b) 0.9988.*

We then model the cones' absolute responses according to Equation (2.11):

$$
\begin{aligned}
L' &= \frac{L^{n_c}}{L^{n_c}+L_a^{n_c}}\,, \\
M' &= \frac{M^{n_c}}{M^{n_c}+L_a^{n_c}}\,, \\
S' &= \frac{S^{n_c}}{S^{n_c}+L_a^{n_c}}\,.
\end{aligned}
\tag{5.4}
$$

We have only replaced the σ from the original equation (where it was given in troland units) with the absolute level of adaptation L_a measured in $\mathrm{cd/m^2}$ (assuming that both units are related almost linearly for the working range of the adaptation level, e.g., $10\mathrm{td} \approx 1\,\mathrm{cd/m^2}$). The adaptation level should ideally be the average luminance of the 10° viewing field (it serves as an input parameter to our model). This adapting parameter of the level of luminance adaptation implicitly contains the level of background luminance. It allows our model to predict the *simultaneous contrast effect* with respect to lightness and colourfulness. Noting that the exponent parameter n_c in the original Equation (2.11) is derived from primate cone responses ($n_c = 0.74$ [Valeton and van Norren, 1983]), we have separately derived n_c from our experimental data as $n_c = 0.57$ by using an *exhaustive search* (the iterative numerical optimisation with a certain range of constrains on the entire likelihood data of lightness from the training data sets). See Figure 5.4 for an example of the predicted cone response by using our model.

5.2.3 Achromatic Attributes

Before the cone signals are transported to our visual cortex, it is believed that they are decomposed into two types of signals: *achromatic* and *colour opponent* signals by the ganglion cells, based on

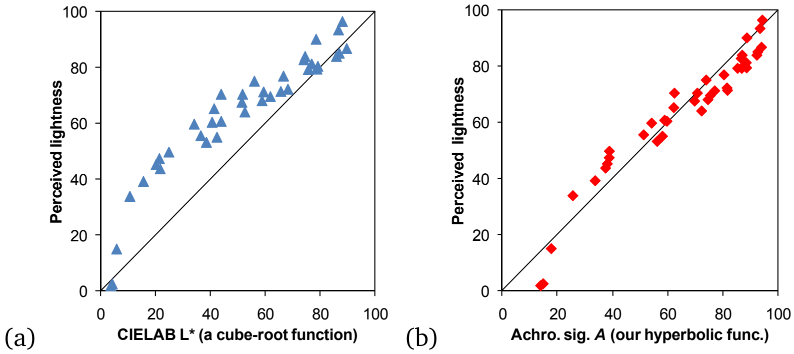

Figure 5.4: *These two plots compare achromatic signals (lightness) of a cube-root power function model (the same as in CIELAB) and our proposed hyperbolic function model [compared with perceived lightness in phase 19 (16 400 cd/m^2)]. A power-function-based model [plot(a)] forms a curve away from the diagonal for high luminances. The CV between perceptual lightness and L* values is 28.07%. In contrast, our model's intermediate achromatic signals A/A_w (weighted summation of three cone responses) [plot(b)] are closer to the diagonal, which means our predictions of lightness are much closer to the actual perception. The CV between perceptual lightness and normalised achromatic signals is 10.33%.*

zone theory [Müller, 1930]. The actual biological and physiological structures and mechanisms are still unclear due to a lack of evidence. It is believed that LMS cones have a roughly *40:20:1* proportion in the retina [Vos and Walraven, 1971]. The summation of the three cone signals is believed to produce an *achromatic signal* in retinal ganglion cells in modern colour appearance modelling. Our model takes the weighted *summation* as an *achromatic signal*. The relative ratio of the achromatic signal to the *reference white* produces *lightness-to-be* signal. The signal A is then defined as:

$$A = (40L' + 20M' + S')/61. \tag{5.5}$$

Lightness is defined as the ratio between the achromatic signal A and the achromatic signal of reference white A_w, since the observer was asked to relate the two. See Figure 5.4 for an example of the predicted achromatic signals. The accuracy of the achromatic signals is decided by that of the cone response functions. As shown in Chapter 4, lightness perception trends are more complicated than a simple power function. Power-function-based models (from CIELAB to CIECAM02) tend to form a curve off from the diagonal for high luminances, which shows the differences between the actual perception and the model's prediction. Our intermediate achromatic signal (the summation of three cone responses) is closer to the actual perceived values.

However, as is shown in Figure 5.4(b), the A/A_w in our model still shows an inverse sigmoidal shape. Hence, we assume that the visual cortex has an additional contrast enhancement process that resembles an inverse sigmoidal function. We solve the undetermined inverse hyperbolic function by using an iterative numerical optimisation on the likelihood data for lightness from the training data sets. $g(x)$ derives the lightness J' from a given cone signal A related to A_w:

$$J' = g\left(\frac{A}{A_w}\right), \tag{5.6}$$

with

$$g(x) = \left[\frac{-(x - \beta_j)\sigma_j^{n_j}}{x - \beta_j - \alpha_j}\right]^{1/n_j}. \tag{5.7}$$

The values of the parameters are derived from our experimental data, yielding $\alpha_j = 0.89, \beta_j = 0.24, \sigma_j = 0.65$, and $n_j = 3.65$. Note that J' may yield values below zero and above one hundred, in which case it should be clamped. This corresponds to the case where the observer cannot distinguish dark colours from even darker colours and bright colours from even brighter ones. Our lightness perception function allows us to predict the *Stevens effect* to a high accuracy, see Figure 5.5.

As already mentioned in Chapter 4, the perceived lightness values vary with different media, even though the physical stimuli are otherwise identical. By testing our model with other media data from the LUTCHI data sets, we observed our model showing media dependency and no surround dependency, unlike other models, e.g., Hunt94, LLAB, and CIECAM97s (see Section 2.3.4). We have decided to incorporate these media differences explicitly in our model in order to improve lightness

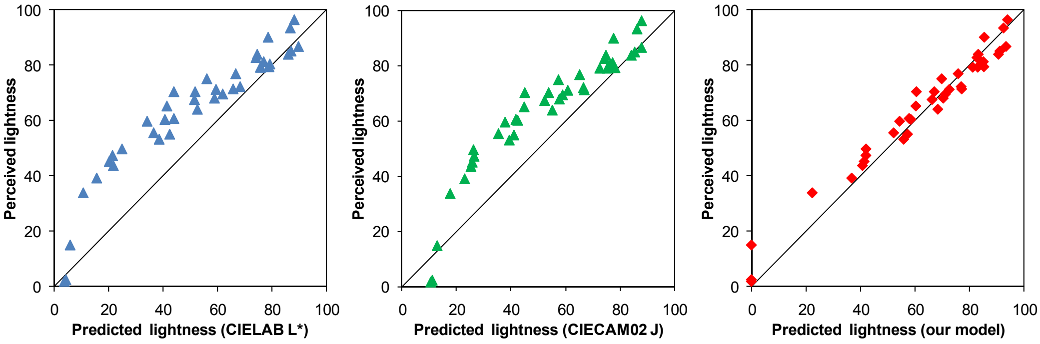

(a) CIELAB L* (b) CIECAM02 J (c) Our model J

Figure 5.5: *These three plots compare the perceived lightness against the predicted lightness in phase 19 (16 400 cd/m^2). (a) plots the predicted lightness perception by CIELAB (L*). (b) plots the prediction of lightness by CIECAM02 (J). The lightness predictions of the CIELAB and the CIECAM02 present similar trends (a curve off the diagonal). (c) shows the lightness prediction of our model (J). It is the results of Equation (5.6) and (5.7) on the achromatic signals [see Figure 5.4(b)]. The CVs between perceptions and predictions are (a) 28.07%, (b) 21.17%, and (c) 8.03%.*

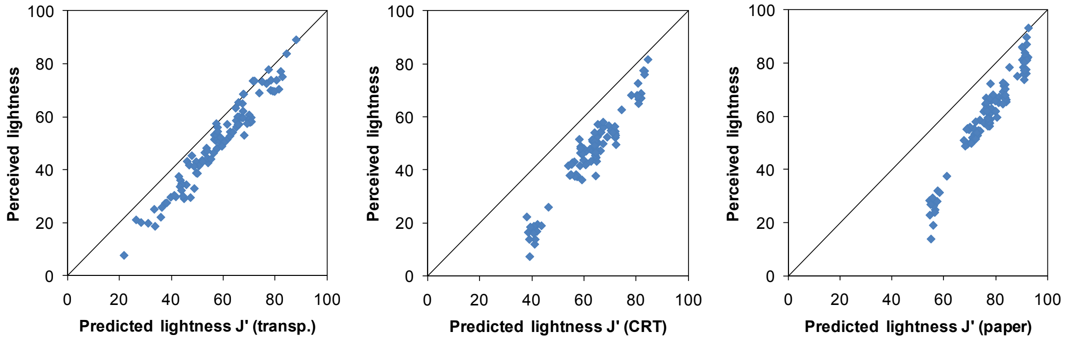

(a) Transparency (J') (b) CRT display (J') (c) Paper (J')

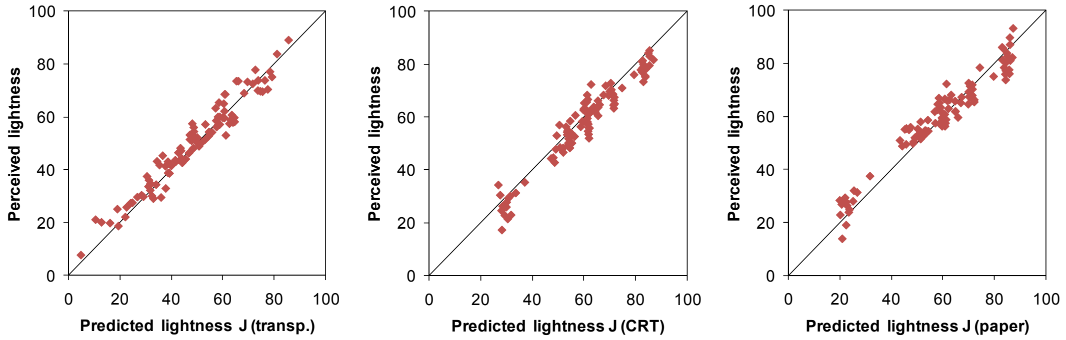

(d) Transparency (J) (e) CRT display (J) (f) Paper (J)

Figure 5.6: *By testing our initial lightness model with other media data from the LUTCHI data sets, our initial model presents media dependency in predicting lightness like other models. We therefore incorporate these lightness differences explicitly in our model in order to improve prediction. Plots (a), (b), and (c) represent the initial lightness prediction J' against transparency (LT phase in the LUTCHI data sets), CRT display (CRT phase), and paper (R-HL phase). Plots (d), (e), and (f) show the final lightness predictions J through modelling media dependency [CVs: (d) 8.66%, (e) 8.16% , and (f) 7.85%]*

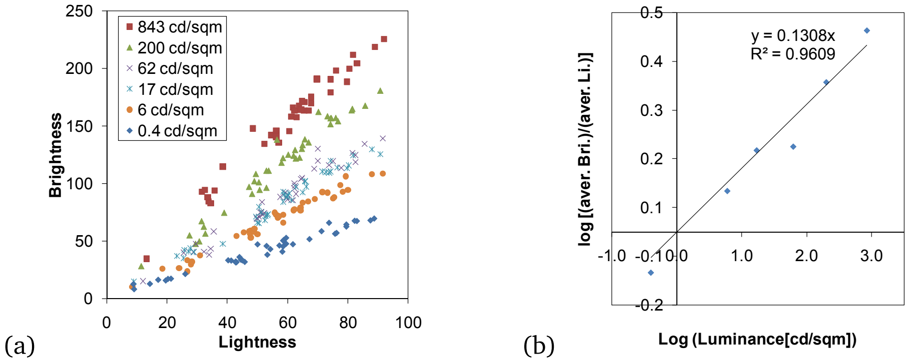

Figure 5.7: *(a) plots perceived brightness against perceived lightness in R-VL group phases [Luo et al., 1993a] in the LUTCHI data sets. The perceived brightness increases linearly according to the perceived lightness. The slope of the brightness is affected by the level of peak luminance. (b) shows the least-squares fitting of the relationship between brightness and lightness with respect to luminance. The logarithm of (brightness/lightness) increases in a slope of 0.1308 according to the logarithm of luminance (squared correlation coefficient* $R^2 = 0.9608$*).*

prediction, yielding a media-dependent lightness value:

$$J = 100\left[E\left(J' - 1\right) + 1\right], \tag{5.8}$$

where the parameter E is different for each medium. A value of $E = 1.0$ corresponds to a high-luminance LCD display, transparent advertising media yield $E = 1.2175$, CRT displays are $E = 1.4572$, and reflective paper is $E = 1.7526$. The lightness contrast J is optimised from our data; reflective media (R-HL), CRT, and transmittance (LT) phases are from the LUTCHI data sets. Figure 5.6 shows the differences between J' and J.

Brightness was not measured in our experiments. We used R-VL phases [Luo et al., 1993a] from the LUTCHI data sets, which is the only data set to have a lightness and brightness comparison. These few phases with both lightness and brightness measurements indicate that these two properties have a linear relationship [see Figure 5.7(a)]. We found that luminance has a linear relationship to *brightness/lightness* in the log-log domain [see Figure 5.7(b)]. We therefore define brightness as:

$$Q = J\left(L_w\right)^{n_q}. \tag{5.9}$$

The parameter is driven from experimental data and yields $n_q = 0.1308$.

5.2.4 Chromatic Attributes

Retinal ganglion cells are believed to convert cone signals into *colour opponent signals* a and b, which are based on differences between the cone responses. We adopt previous psychophysical results on

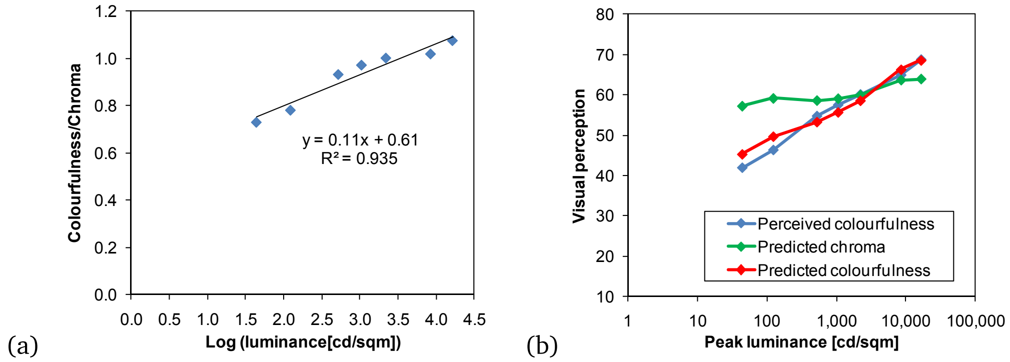

Figure 5.8: *(a) shows the least-squares fitting of the slope of (colorfulness/chroma) and its offset. The colourfulness increases with a slope of 0.11 with an offset of 0.61 according to the logarithm of luminance ($R^2 = 0.935$). (b) plots perceived average colourfulness against peak luminance in luminance-varying phases (group L) in our data sets. The average predicted colourfulness (red line) matches the average perceived colourfulness (blue line) with a CV of 3.83%. The green line represents predicted chroma.*

how the responses are combined together [Vos and Walraven, 1971; Hunt, 1991], yielding:

$$\textit{Redness} - \textit{Greenness} \qquad a = \frac{1}{11}\left(11L' - 12M' + S'\right), \tag{5.10}$$

$$\textit{Yellowness} - \textit{Blueness} \qquad b = \frac{1}{9}\left(L' + M' - 2S'\right). \tag{5.11}$$

Chroma C is the colourfulness judged in proportion to the brightness of the reference white, i.e., it should be independent of luminance L_w (like lightness). It is commonly based on the magnitude of a and b [CIE, 1986]:

$$C = \alpha_k \left(\sqrt{a^2 + b^2}\right)^{n_k}. \tag{5.12}$$

Note that it is possible to optimise the parameters α_k and n_k after modelling colourfulness, for which we have actual perceptual data. We further know that colourfulness should increase with the luminance level (*Hunt effect*, see Chapter 4 for findings). Hence, we found the relationship between chroma (the *magnitude* of a and b) and *colourfulness* to be linear in the logarithm of the reference white luminance L_w:

$$M = C(\alpha_m \log_{10} L_w + \beta_m). \tag{5.13}$$

From this we can derive parameters for colourfulness as well as chroma based on our data and the constraint that chroma does not change with luminance: $\alpha_k = 456.5$, $n_k = 0.62$, $\alpha_m = 0.11$, and $\beta_m = 0.61$. These parameters were numerically optimised on the likelihood data of colourfulness from training data sets. See Figure 5.8 and 5.9 for comparison.

Saturation is independent of brightness and colourfulness. It is modelled by the square-root of

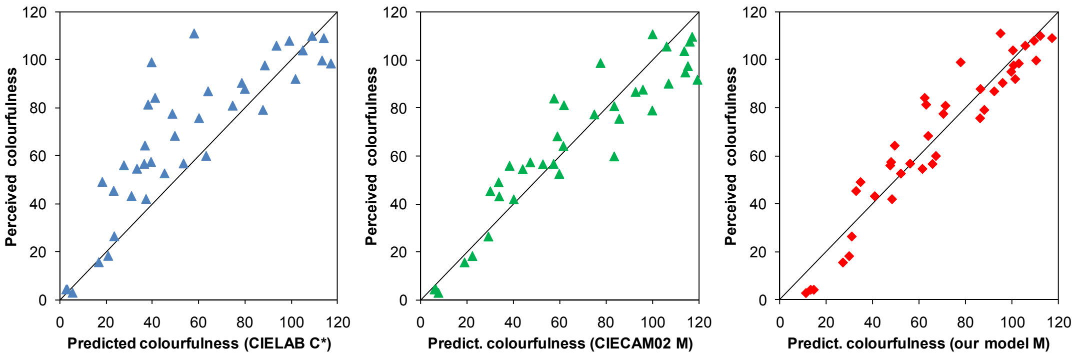

(a) CIELAB C* (b) CIECAM02 M (c) Our model M

Figure 5.9: *These three plots compare the perceived colourfulness against the predicted colourfulness in phase 19 (16 400 cd/m^2). (a) plots the predicted colourfulness perception by CIELAB (C*) with a CV of 31.23%. (b) plots the prediction of colourfulness by CIECAM02 (J) with a CV of 19.67%. (c) presents the colourfulness prediction of our model (M) with a CV of 14.15%. CIELAB C* shows a comparative variation in predicting colourfulness. CIECAM02 M presents better predictions than CIELAB C* (scaled by a colourfulness scalar 1.23). Our model's colourfulness values are closer to the diagonal with smaller variation, which means our predictions are much closer to the actual perception.*

brightness over colourfulness (defined by Hunt [1998]), following Moroney et al. [2002]:

$$s = 100\sqrt{\frac{M}{Q}}. \tag{5.14}$$

The hue angle is derived by converting colour opponent signals of a and b into *polar* coordinates:

$$h = \frac{180}{\pi}\tan^{-1}(b/a). \tag{5.15}$$

This *hue* angle (0°–360°) could be used directly as a prediction of perceived hue. However, the hue angle in psychophysical experiments is scaled from 0 to 400 (see Section 4.3.1 for more details on the hue estimation). Therefore, the computed *hue angle* is interpolated in the perceptually uniform scale to match the perceptual *hue quadrature* used in the experiments. The perceptual *hue quadrature* [$H = \text{huequad}(h)$] has been shown in [Hunt, 1991] to improve accuracy, which we adopt in our model as well:

$$H = H_1 + \frac{100(h-h_1)/e_1}{(h-h_1)/e_1 + (h_2-h)/e_2}, \tag{5.16}$$

where e is $e = \frac{1}{4}\left[\cos\left(h\frac{\pi}{180}+2\right)+3.8\right]$. e_1 and h_1 are the values of e and h, respectively, for the unique hues having the nearest lower value of h in Table 5.1; e_2 and h_2 are the values of e and h, respectively, for the unique hues having the nearest higher value of h in Table 5.1. H_1 is 0, 100, 200, or 300 according to whether red, yellow, green or blue, respectively, is the hue having the nearest lower value of h. See Figure 5.10 for comparison.

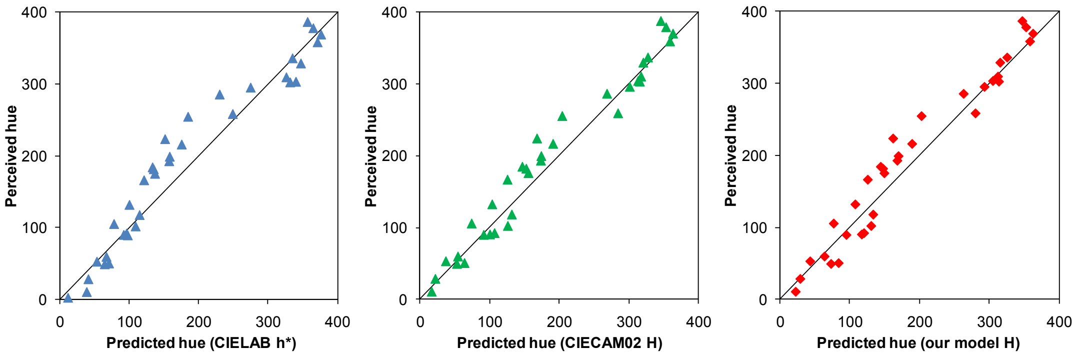

(a) CIELAB h* (b) CIECAM02 H (c) Our model H

Figure 5.10: *These three plots compare the perceived hue against the predicted hue in phase 19 (16 400 cd/m^2). (a) plots the predicted hue perception by CIELAB (h*) with a CV of 23.11%. For only plotting purpose, h* is scaled to 400. (b) plots the prediction of hue by CIECAM02 (H) with a CV of 12.60%. (c) presents the hue prediction of our model (H) with a CV of 13.86%. CIELAB h* shows a comparative variation in predicting hues around green primaries. In contrast, CIECAM02 and our model's hue values are closer to the diagonal, which means our predictions are closer to the actual perception. Both hue estimates are almost identical.*

Unique Hue	Red	Yellow	Green	Blue
Hue quadrature H	0	100	200	300
Hue angle h	20.14	90.00	164.25	237.53
Eccentricity e	0.7741	0.7227	0.9884	1.1976

Table 5.1: *Hue eccentricity parameters for unique hues. Adapted from [Hunt, 1991].*

Finally, the colour coordinates introduced above can form a three-dimensional colour space (lightness, chroma, and hue). The hue angle can be represented in Cartesian coordinates with respect to the three-dimensional colour space (comprising lightness J, chroma C, and hue h):

$$\textit{Redness} - \textit{Greenness} \qquad a_C = C\cos\left(h\frac{\pi}{180}\right), \tag{5.17}$$

$$\textit{Yellowness} - \textit{Blueness} \qquad b_C = C\sin\left(h\frac{\pi}{180}\right). \tag{5.18}$$

The next section summarises our analytical inverse model of these forward calculations.

5.3 Inverse Model

The development of our colour appearance model is motivated by the complete colour reproduction pipeline (see Section 2.1 for more details). A forward device transform allows us to convert device-dependent signals to physically-meaningful device-independent coordinates. Forward appearance model transforms these physically-meaningful coordinates to perceptually-uniform appearance scales. These two stages yield the estimation of colour perception, but two inverse stages are required to complete colour communication for reproducing estimated colours on a different medium [CIE, 2004] (see Chapter 6 for more details on our colour reproduction pipeline). Therefore, *analytical invertibility* of the device characterisation (especially output devices) and the colour appearance model is essential for application of the appearance model.

With colour reproduction as context, we developed our model while considering *analytical invertibility*. The proposed mathematical pipeline in Section 5.2 is analytically invertible, and does not require any iterative estimation (such as *Newton's method*) to invert them. First, we model input parameters for this inverse model as follows:

- Perceptual colour appearance values: J (lightness), M (colourfulness), and h (hue),
- Absolute tristimulus values of the reference white point (of a target media): $X_w Y_w Z_w$,
- Level of luminance adaptation (in viewing the target media): L_a [unit: cd/m^2] (luminance of viewing stimuli at about a 10-degree angle),
- A target medium type: E (e.g., paper, CRT, transparency, or high-luminance display).

Our forward model takes physical input values of reference white, luminance adaptation level, and medium type; our inverse model takes perceptual input values of reference white, luminance adaptation level, and medium type (specifying the output medium viewing conditions) and outputs physical values.

Our inverse model first computes achromatic white point A_w of the target device using Equations (5.4) and (5.5). Then, it computes brightness Q from lightness J [see Equation (5.9) for optimised parameters]:

$$J = Q/(L_w)^{n_q}. \tag{5.19}$$

Then, the lightness J is used to compute the achromatic signal A [see Equations (5.6), (5.7), and (5.8)]:

$$J' = (J/100 - 1)/E + 1, \tag{5.20}$$

$$A = A_w \left(\frac{\alpha_j J'^{n_j}}{J'^{n_j} + \sigma_j^{n_j}} + \beta_j \right). \tag{5.21}$$

For inverting colourfulness, Chroma C is first calculated from colourfulness M [see Equation (5.13)]:

$$C = M/(\alpha_m log_{10} L_w + \beta_m). \tag{5.22}$$

The chroma value C is then used for deriving colour opponent signals a and b from chroma C and hue angle h [see Equations (5.12) and (5.15)]:

$$a = \cos(\pi h/180)\left(C/\alpha_k\right)^{1/n_k}, \tag{5.23}$$

$$b = \sin(\pi h/180)\left(C/\alpha_k\right)^{1/n_k}. \tag{5.24}$$

Once we have the achromatic signal A and opponents a and b, this allows us to compute non-linear cone signals $L'M'S'$:

$$\begin{bmatrix} L' \\ M' \\ S' \end{bmatrix} = \begin{bmatrix} 1.0000 & 0.3215 & 0.2053 \\ 1.0000 & -0.6351 & -0.1860 \\ 1.0000 & -0.1568 & -4.4904 \end{bmatrix} \begin{bmatrix} A \\ a \\ b \end{bmatrix}. \tag{5.25}$$

The non-linear cone signals $L'M'S'$ are then converted to linear cone signals LMS [see Equation (5.4)]:

$$L = \left(\frac{-L_a^{n_c} L'}{L' - 1} \right)^{1/n_c}, \tag{5.26}$$

$$M = \left(\frac{-L_a^{n_c} M'}{M' - 1} \right)^{1/n_c}, \tag{5.27}$$

$$S = \left(\frac{-L_a^{n_c} S'}{S' - 1} \right)^{1/n_c}. \tag{5.28}$$

After that, our model computes tristimulus XYZ_{D50} from cone signals LMS using the HPE transform [see Equation (5.3)]. Finally, our model applies an inverse chromatic adaptation transform to the white point of the target medium [see Equation (5.1) and (5.2)]. The next section presents the performance of our model in predicting human colour perception when compared with other colour appearance models (CIELAB, RLAB, and CIECAM02).

5.4 Results

The following sections provide qualitative and quantitative analysis of our model. We have applied our model, as well as CIELAB, RLAB, and CIECAM02, to our perceptual data sets (for high-luminance conditions) and the LUTCHI data sets (for low-luminance conditions). However, using our data set with the LUTCHI data set has a drawback. The colourfulness data sets are not directly compatible without first applying a calibrating scalar, i.e., a colourfulness scalar should be derived before applying the data set to a model.

5.4.1 Estimations under High Luminances

Modelling accuracy results under luminance-varying phases can be found in Figure 5.11. The group L phases (1, 2, 4, 7, 10, 17, and 19) are used. The luminance levels vary from 44 to 16 400 cd/m^2 with a fix background ratio (23%). Our prediction in terms of lightness is *statistically significantly* (one-side t-test with alpha = 0.05) better than the predictions of the other models and also very *consistent* up to high luminances. The average CV [see Equation (2.12)] value (11.51%) is as large as the long-term repeatability CV value (11.83%) for the averaged human observer (see Table 4.2). This means that our model performance is as accurate as the variation of the experimental data. Other models achieve a less accurate prediction and, importantly, their prediction quality *fluctuates* considerably between phases. Colourfulness is also predicted *significantly* better with our model than with the other models. Our colourfulness prediction is very *consistent*. The average CV value (17.15%) is similar to the CV value between short-term repeated runs of the same experiment (17.23%). In particular, RLAB performs significantly worse than other models in predicting colourfulness, and the prediction quality in CIELAB fluctuates more than other models. Hue is predicted similarly among CIELAB, CIECAM02, and our model (average CV: 14.74%), and the hue prediction of CIECAM02 is better than others [see Figure 5.13 (a), (c), and (e) for average comparison]. This result indicates that our CAM models the *Stevens* and *Hunt* effects (observed in our experimental data) to a high accuracy.

Figure 5.12 shows modelling accuracy results against different background ratios (group B). Phases from 8 to 12 are used. The background ratio varies from 0 (black) to 95% (white). Our prediction in terms of lightness is *significantly* better than the others. The average CV value (12.26%) is roughly as large as the long-term repeatability CV value (11.83%) for the average human observer. Other models achieve a less accurate prediction. CIECAM02 and our model predictions are getting better against a darker background, but CIELAB and RLAB performance are getting better against a brighter background. Colourfulness is also predicted *significantly* better than the other models and is very *consistent*. The average CV value (15.86%) is lower than the CV value of short-term repeatability (17.23%). In particular, the performances of CIECAM02 and CIELAB fluctuate between different backgrounds. Hue prediction is very similar to the other models (average CV: 14.38%) except RLAB. This result shows that our CAM models the *simultaneous contrast effect* to a high accuracy in terms of *lightness* and *colourfulness* as observed in our experimental data. See Figure 5.13 (b), (d), and (f) for average comparison.

Chromatic adaptation results can be found in Figure 5.14. Group T (phases 7, 13, and 14) of our data sets is used. As before, our prediction of lightness is *significantly* better than the other models and is very *consistent*. The average CV value is 12.26% (as large as the long-term repeatability). The colourfulness prediction of our model is also better in all cases (average CV: 18.77%). Hue prediction is very similar to the other models. Our chromatic adaptation transform is adapted from CIECAM02, but the performance of our model (average CV: 16.34) in three different colour temperatures is better than CIECAM02 (average CV: 17.21) because of the different modelling structure and optimisation of the model. Our model can predict inconsistent chromatic adaptation to a high accuracy [see Figure 5.16 (a), (c), and (e) for an average comparison].

Our model does not include a surround parameter, but the surround effect is implicitly modelled by using the level of luminance adaptation (which implicitly contains a surround measurement). Surround effect results can be found in Figure 5.15. Group S (phases 10 and 15) compares two different surround levels: dark and average (20% of the peak luminance). The lightness prediction of our model is *statistically significantly* better than other models and very *consistent*. The average CV value is 13.98%. The lightness prediction of CIECAM02 with an average surround is comparatively worse than with a dark surround. The colourfulness prediction of our model is also better with both surrounds (average CV: 17.34). Hue prediction is very similar to the other models as before (average CV: 14.87). Hue estimation with an average surround increases from 12.30% to 17.45% due to the difference of colour temperatures of the light source (main colour stimuli) and the surround light sources. This indicates that our model can predict the surround effect well. See Figure 5.16(b), (d), and (f) for a comparison of their averages.

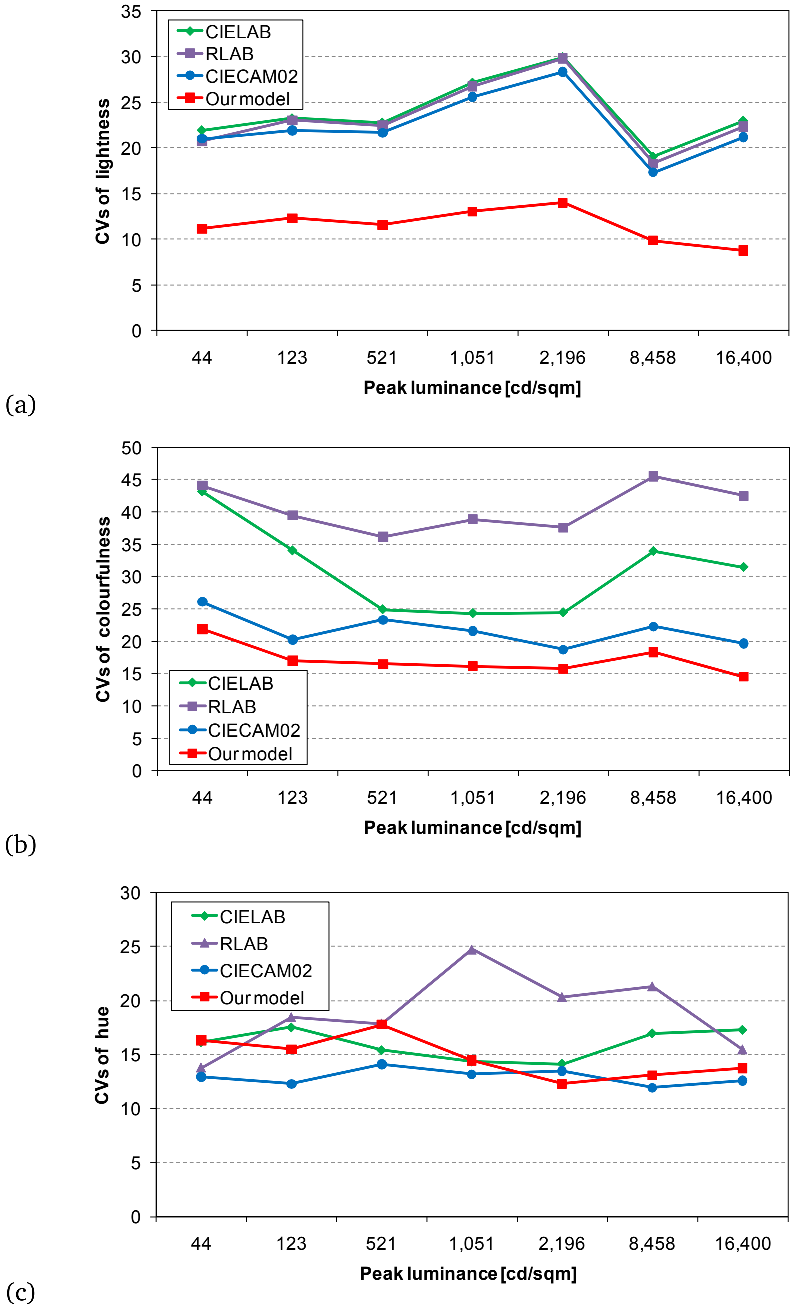

Figure 5.11: *Results of estimations in luminance-varying phases* group L *(44–16 400 cd/m^2) with a fix background ratio (23%). We compare a few phases (1, 2, 4, 7, 10, 17, and 19) of our experiment in terms of lightness, colourfulness, and hue prediction error (CV) with CIELAB, RLAB, and CIECAM02. Our model performs statistically significantly better than the other models in terms of lightness and colourfulness, which means our model can predict the* Stevens effect *to a high accuracy. Colourfulness prediction is also better in all cases, which means our model can predict the* Hunt effect *to a high accuracy. Hue prediction is very similar to the other models even though CIECAM02 is better especially under low luminances.*

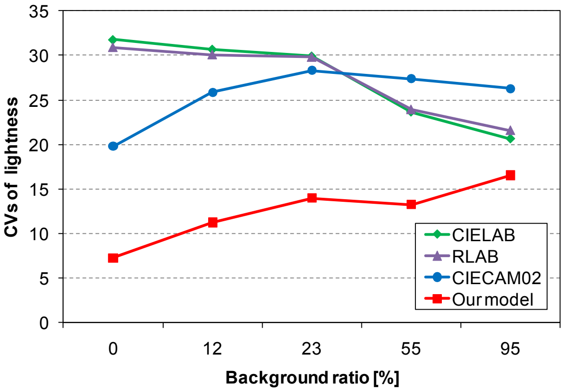

(a)

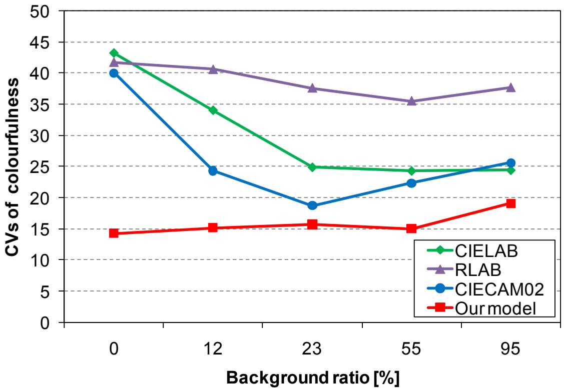

(b)

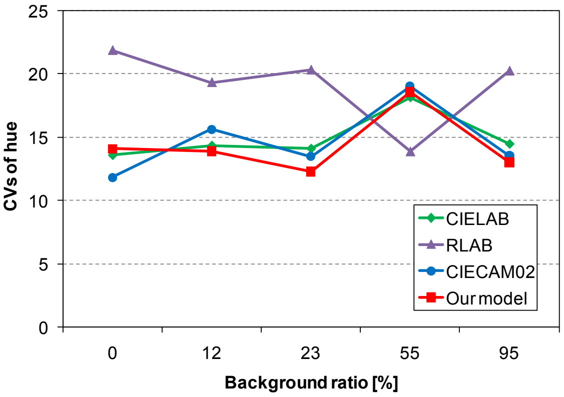

(c)

Figure 5.12: *Results of estimations in background-varying phases* group B *(0-95%) under a luminance of 2 241 cd/m^2. We compare these phases (8–12) of our experiment in terms of lightness, colourfulness, and hue prediction error. Our model performs statistically significantly better than the other models in terms of lightness and colourfulness. This means that our model can predict the* simultaneous contrast effect *to a high accuracy. Hue prediction is very similar to the other models except RLAB.*

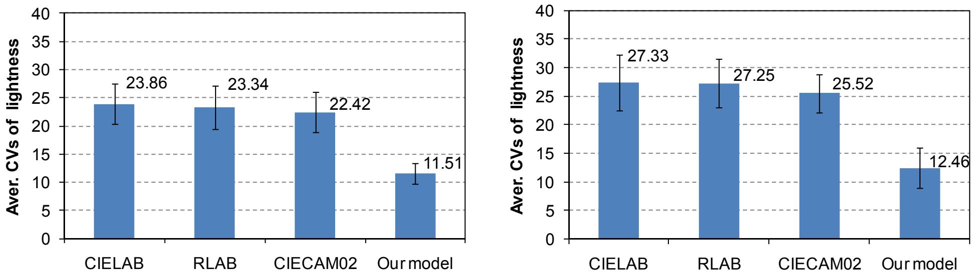

(a) Lightness (group L) (b) Lightness (group B)

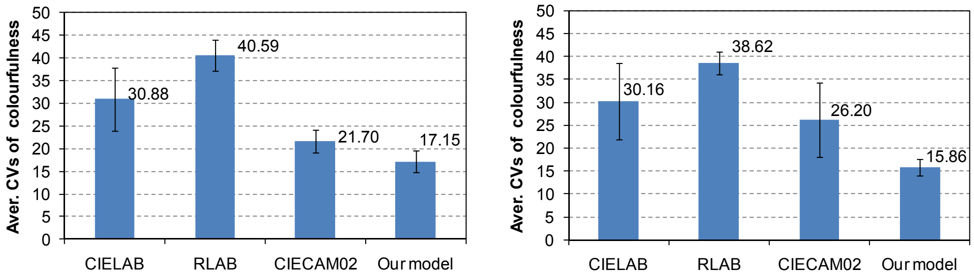

(c) Colourfulness (group L) (d) Colourfulness (group B)

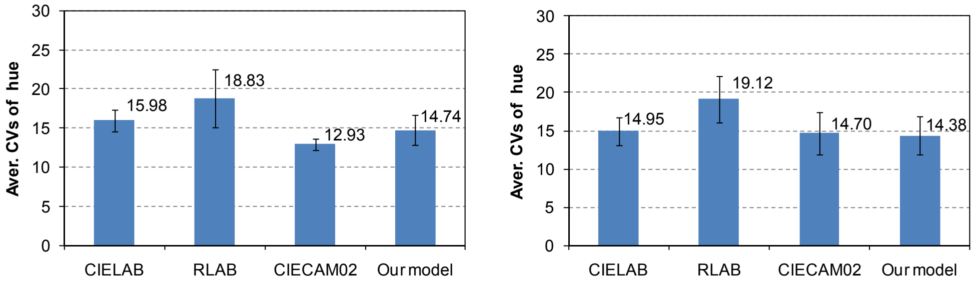

(e) Hue (group L) (f) Hue (group B)

Figure 5.13: *These plots compare the average CV errors in estimating colour appearance in terms of lightness, colourfulness, and hue with luminance-varying phases (group L) and background-varying phases (group B). Our model performs* significantly better than others in predicting lightness and colourfulness in both groups. *Hue prediction is almost identical to CIECAM02 and CIELAB.*

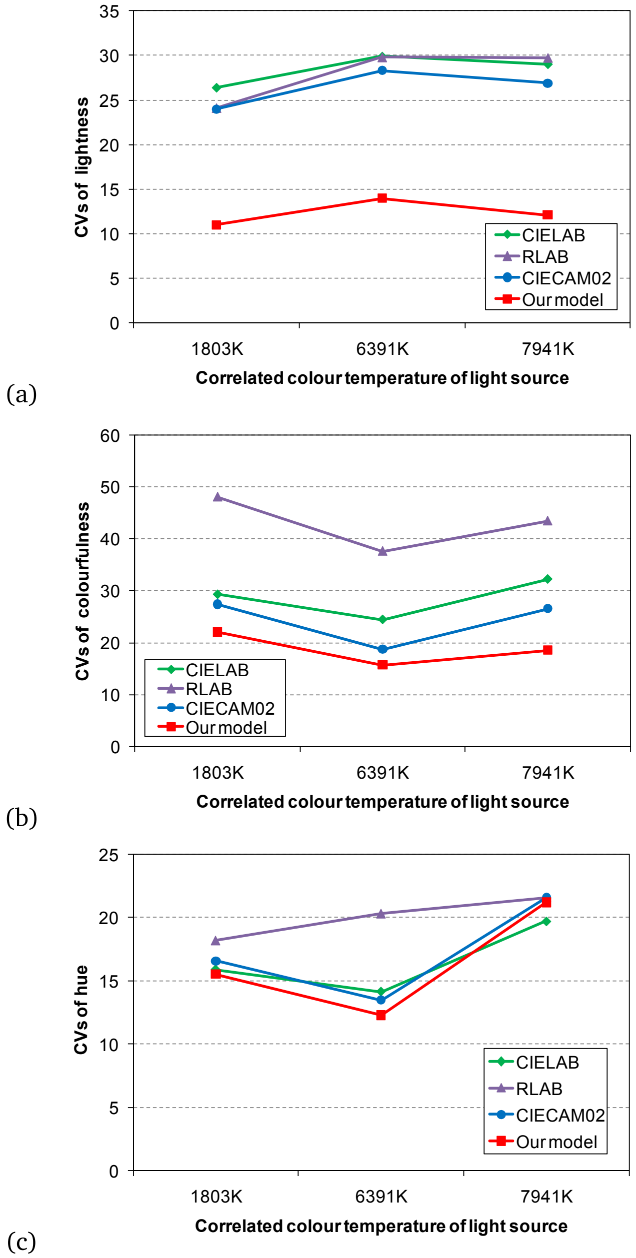

Figure 5.14: *Results of estimations in colour-temperature-varying phases (group T) under a luminance of 1 233 cd/m*^{2}*. We compare the colour temperature-varying phases (7, 13, and 14) of our experiment in terms of lightness, colourfulness, and hue prediction error (CV) with CIELAB, RLAB, and CIECAM02. Our model performs significantly better than the other models in terms of lightness. Colourfulness prediction of our model is also better in all cases. Hue prediction is very similar to the other models.*

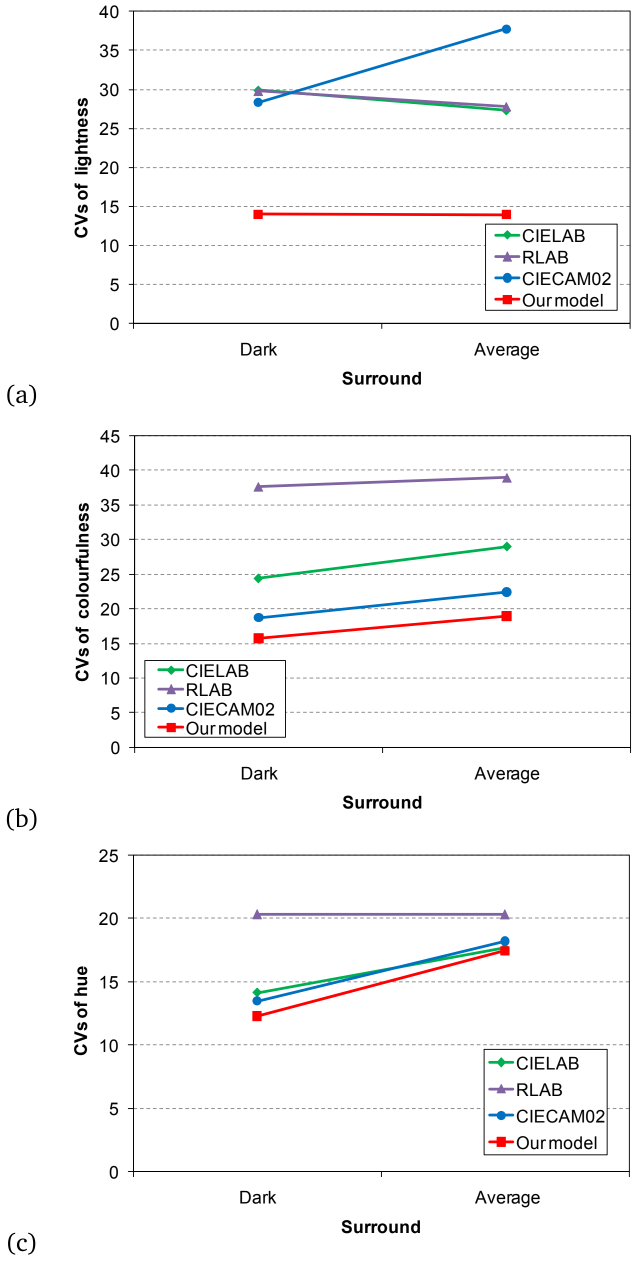

Figure 5.15: *Results of estimations in surround-varying phases (group S) under a luminance of 2 201 cd/m^2. We compare the surround-varying phases (10 and 15) of our experiment in terms of lightness, colourfulness, and hue prediction error with CIELAB, RLAB, and CIECAM02. Our model performs significantly better than the other models in predicting lightness. Colourfulness prediction is also better in all cases. Hue prediction is very similar to the other models, except RLAB.*

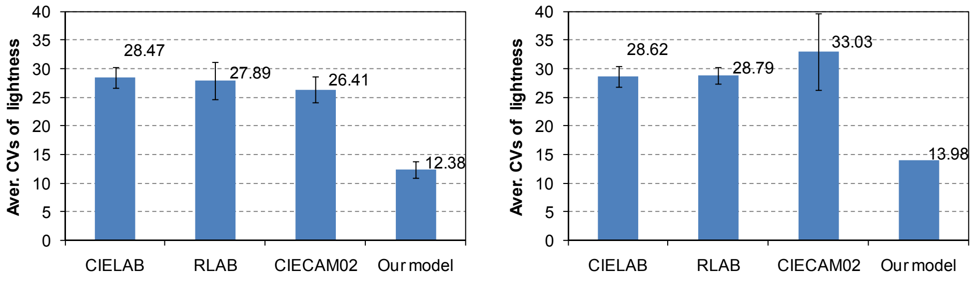

(a) Lightness (group T) (b) Lightness (group S)

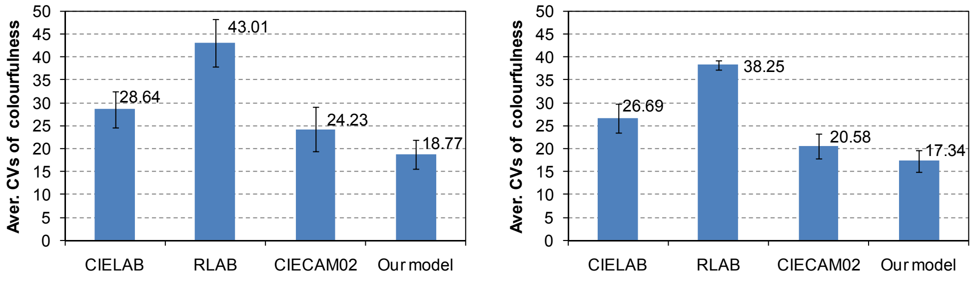

(c) Colourfulness (group T) (d) Colourfulness (group S)

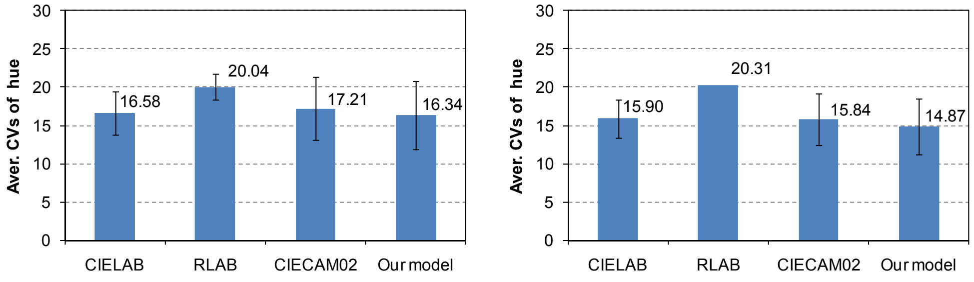

(e) Hue (group T) (f) Hue (group S)

Figure 5.16: *These plots compare the average CV errors in estimating colour appearance in terms of lightness, colourfulness, and hue with colour-temperature-varying phases (group T) and surround-varying phases (group S). Our model performs* significantly *better than others in predicting lightness. Colourfulness prediction is also better in all cases. Hue prediction is almost identical to CIECAM02 and CIELAB.*

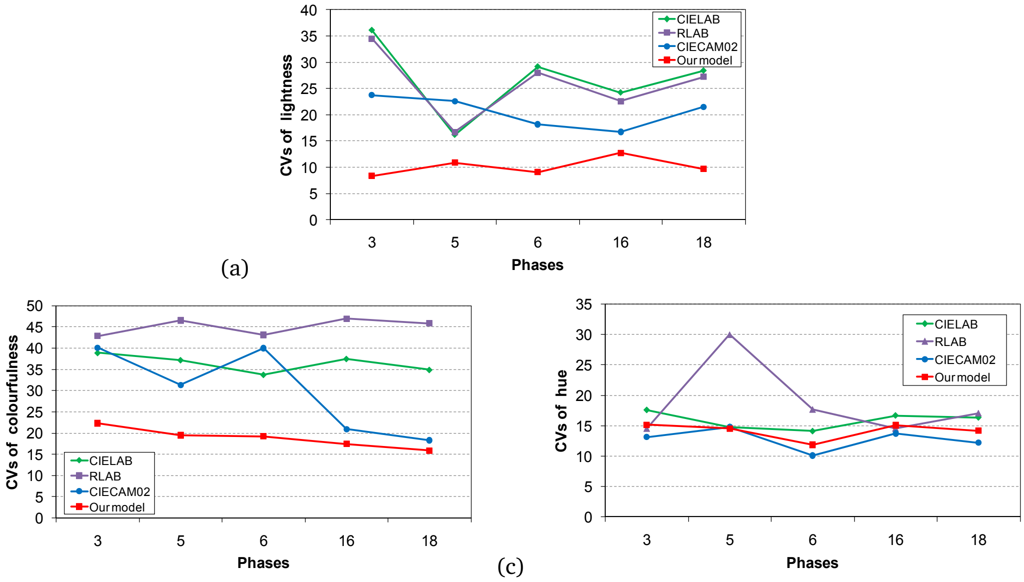

(a)

(b)

(c)

Figure 5.17: *Results of estimations in a validation set (phases 3, 5, 6, 16, and 18). We compare the group V phases of our experiment in terms of lightness, colourfulness, and hue prediction errors (CV) with CIELAB, RLAB, and CIECAM02. Our model performs significantly better than the other models in terms of lightness even on these independent test phases. Colourfulness prediction is also better in all cases. Hue prediction is very similar to the other models, except RLAB.*

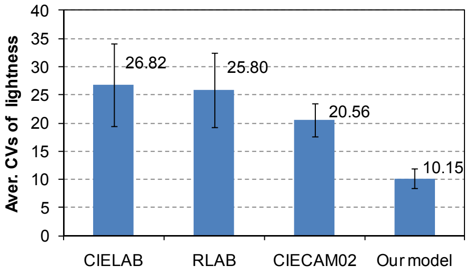

(a) Lightness (group V)

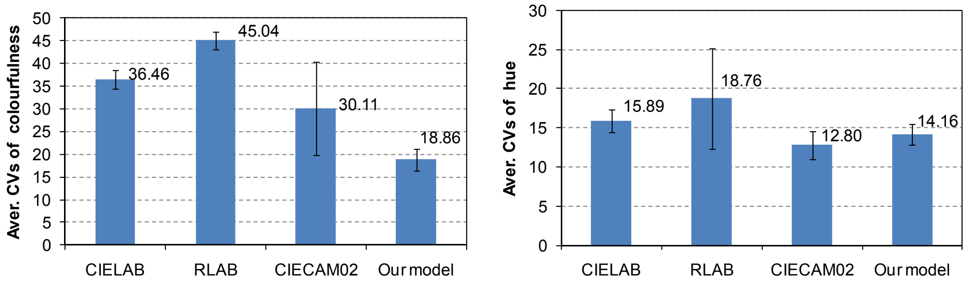

(b) Colourfulness (group V)

(c) Hue (group V)

Figure 5.18: *These three plots compare the average CV errors in estimating colour appearance in terms of lightness, colourfulness, and hue with a validation set (phases 3, 5, 6, 16, and 18). Our model performs significantly better than others in predicting lightness and colourfulness. Hue prediction is similar to CIECAM02 and CIELAB.*

The previous data sets are included in the *maximum likelihood optimisation* to derive our colour appearance model. We have independent data sets (phases 3, 5, 6, 16, and 18 — group V), which are used as test phases for *cross-validation* of our model. These data sets have a variation of different peak luminances and different backgrounds. Therefore, these results are a good indicator of predictive performance under high luminance levels. As shown in Figure 5.17, our model prediction in terms of lightness is *statistically significantly* better than in other models and is also very *consistent*. The average CV value (10.15%) is as large as the CV values in our training data (11.83% — group L). This proves that our model is free from over-fitting issues. Other models achieve a less accurate prediction, and the performance of the CIELAB and RLAB models fluctuates between phases. Colourfulness prediction of our model is also *significantly* better than the others and is very *consistent* (average CV: 18.86 — similar to the training group L: 17.15%). Hue is predicted by our model similarly to CIELAB and CIECAM02. The average CV is 14.16%, similar to the CV of 14.74% in our training data set (group L). In other words, our model predicts lightness and colourfulness *consistently* to a higher accuracy than other models. See Figure 5.18 for a comparison of average CV.

Figure 5.19 summarises the main result of all phases (including the training and test data sets). Our prediction in terms of lightness is *significantly* better than the other models and is very *consistent*. The CV value is approximately as large as the repeatability CV value for a human observer, which indicates that our model's performance is as accurate as the variation of the experimental data. Other models achieve a less accurate prediction and, importantly, their prediction quality *fluctuates* considerably between phases. Colourfulness is also predicted very *consistently* by our model and is generally much better than the other models. As before, the CV value is similar to the CV value between two repeated runs of the same experiment. This again indicates that our model's colourfulness prediction performance is as accurate as the variation of the experimental data. The other models' performance varies significantly, not only between models, but also between phases. Hue is predicted very similarly between all models, where even the simple CIELAB model performs well. See Appendix A.6 for the entire results.

5.4.2 Estimations on Different Media

We further investigate how our model predicts the data from the LUTCHI data set. This allows us to test our model's performance on different media like paper, transparency, or CRT, and it validates our model's performance by using a *third test set* as a *cross-validation*. We use a number of phases from three different groups (R-HL, CRT, and LT) in the LUTCHI data sets as these are samples of photopic vision in the LUTCHI data set.

Figure 5.20 quantitatively compares the predictions of CIECAM02 and our model on different media against perceived colour appearance. (a), (b), and (c) show the detail lightness, colourfulness, and hue from R-HL phase 2; (d), (e), and (f) show the detail from CRT phase 1; (g), (h), and (i) present the detail of LT phase 1. Our lightness, colourfulness, and hue predictions are very much along the diagonal, indicating that our model covers the dominant perceptual phenomena.

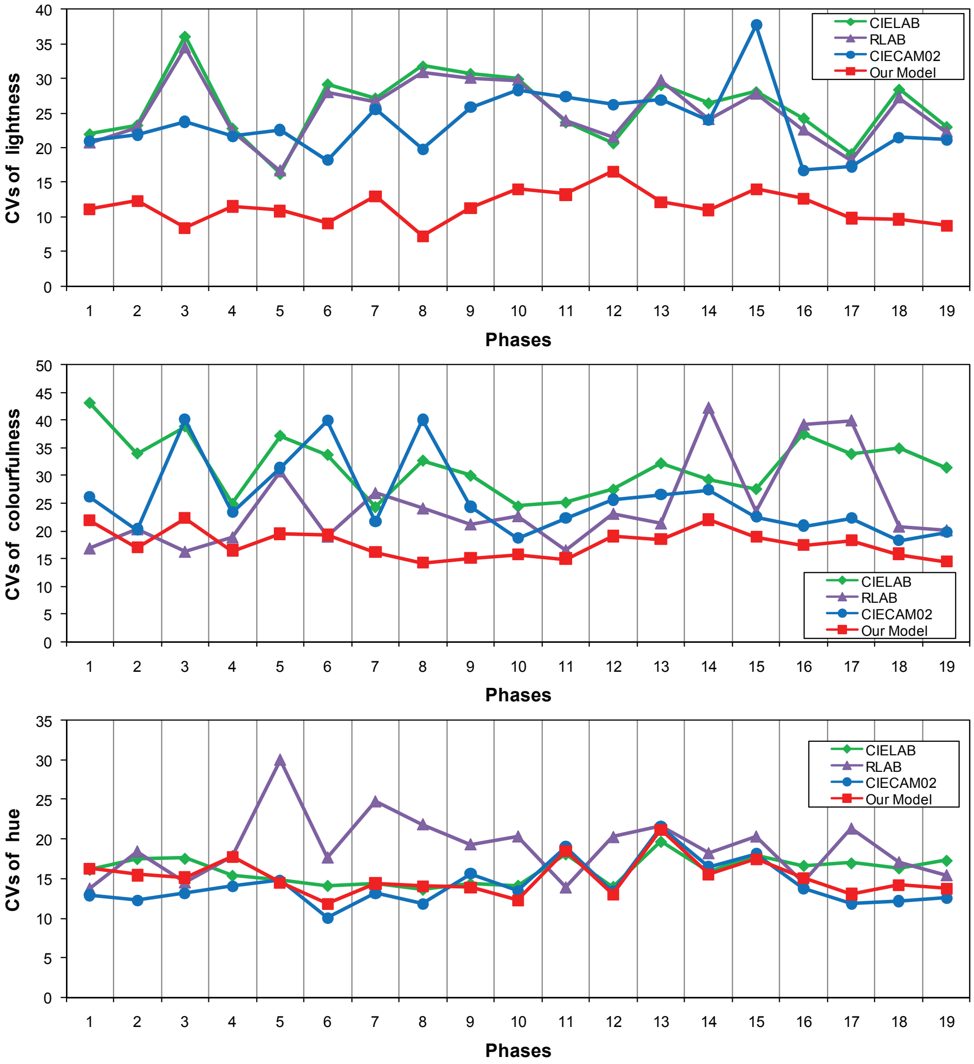

Figure 5.19: *We compare all 19 phases of our experiment (including the training and test data sets) in terms of lightness, colourfulness, and hue prediction error (CV) with CIELAB, RLAB, and CIECAM02. Our model performs consistently better than the other models in terms of lightness. Colourfulness prediction is better in almost all cases. Hue prediction is very similar to the other models, even though CIECAM02 is minimally better at lower luminances.*

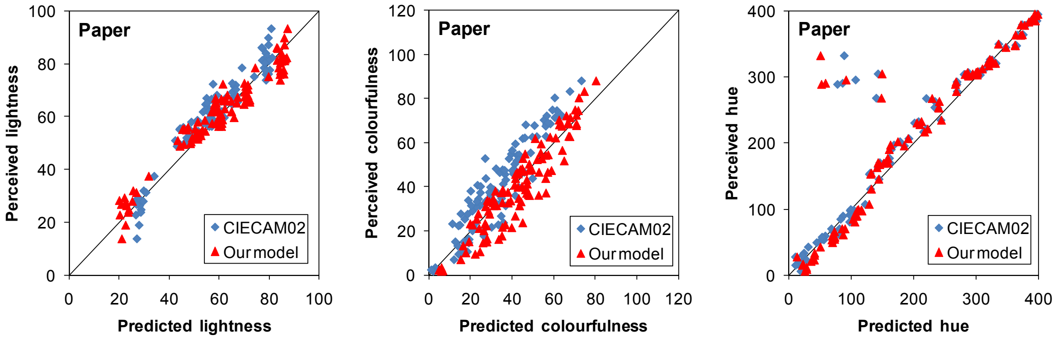

(a) R-HL phase 2 (lightness) (b) R-HL phase 2 (colourfulness) (c) R-HL phase 2 (hue)

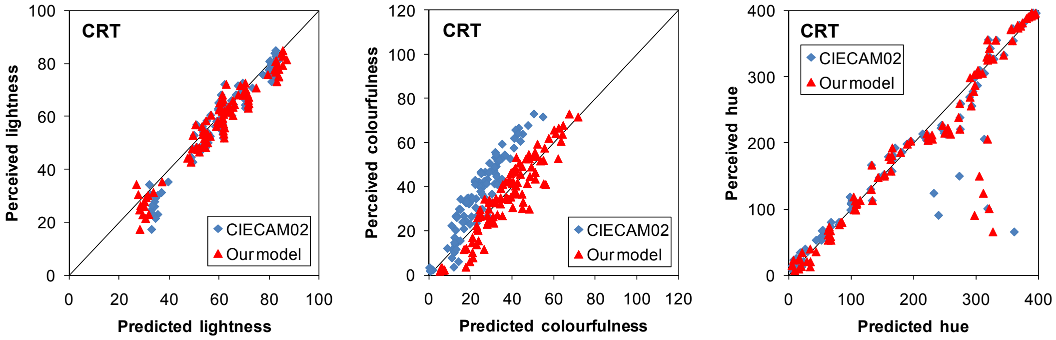

(d) CRT phase 1 (lightness) (e) CRT phase 1 (colourfulness) (f) CRT phase 1 (hue)

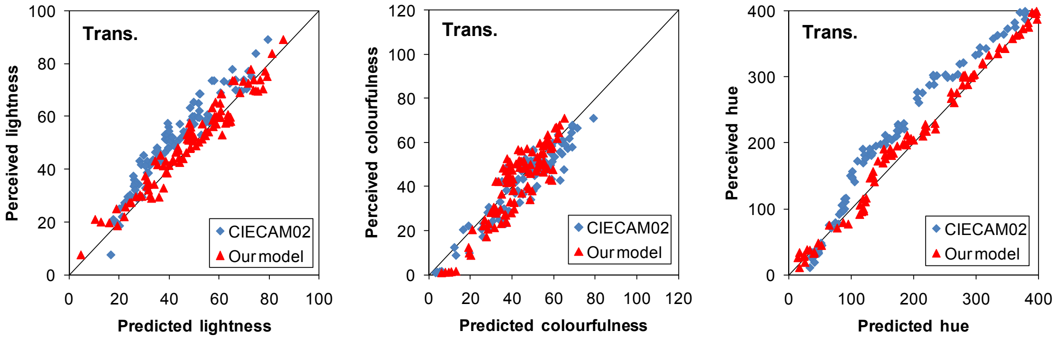

(g) LT phase 1 (lightness) (h) LT phase 1 (colourfulness) (i) LT phase 1 (hue)

Figure 5.20: *Quantitative comparison of the prediction of colour appearance on different media against perceived colour appearance (from LUTCHI data sets). R-HL phase 2 has a background ratio of 6.2% under a luminance of 252 cd/m^2. CRT phase 1 has a background ratio of 20% under a luminance of 44 cd/m^2. LT phase 1 has a background ratio of 16% under a luminance of 2 259 cd/m^2. (The colourfulness scalar of our data was 0.65 against the LUTCHI LT data set.) It can be seen that our model achieves very good lightness, colourfulness, and hue prediction. CIECAM02 is not able to predict lightness and hue on transparency, and colourfulness on paper and CRT media. In particular, the hue measurements on paper and CRT media in the LUTCHI data sets present comparable offsets with certain colours. As CIECAM02 and our model show similar patterns of offset, we suspect the offsets are measurement errors of the hue appearance in the original LUTCHI data sets.*

However, CIECAM02 incorrectly estimates lightness [see Figure 5.20(g)], yielding values that form a curve off the diagonal. This indicates that CIECAM02 underestimates lightness perception under high luminances. Colourfulness and hue predictions of CIECAM02 also show mismatches to the actual perception [see Figure 5.20(b), (e), and (i)]. These effects can be noticed in other phases as well: the predicted appearance forms a curve instead of a diagonal line as would be expected.

Figure 5.21 summarises the results of the LUTCHI data sets. We ran all four models (CIELAB, RLAB, CIECAM02, and our model) on a number of phases from the data sets [transparency, reflective media (paper), and CRT]. The average CV error of lightness is 10.84%, similar to the average CV of 11.41% for our entire data set. The average CV error of hue is 14.59%, which is almost identical to the error of 15.14% in our data. The average CV error of colourfulness (20.25%) is slightly more than the error of 17.76% in our data. In summary, our model outperforms the other colour appearance models in terms of lightness, colourfulness, and hue, even though the LUTCHI data set was not the main basis for the derivation of our model.

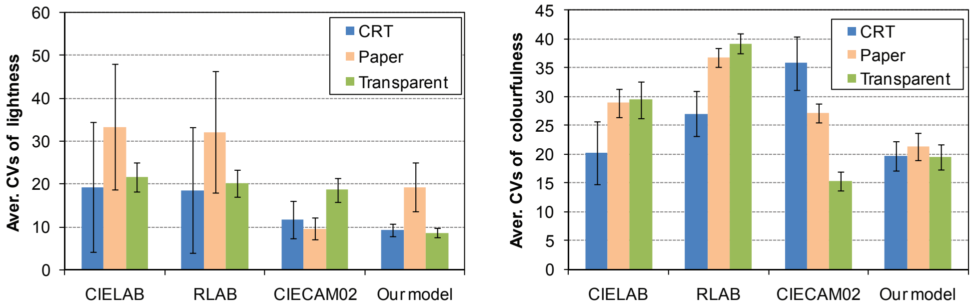

(a) Lightness (b) Colourfulness

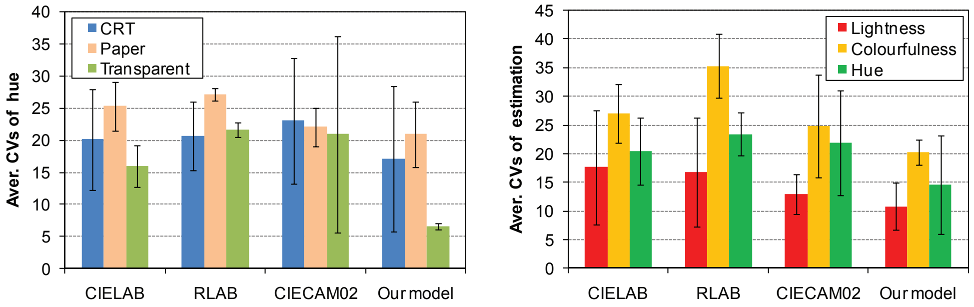

(c) Hue (d) Overall

Figure 5.21: *This figure quantitatively compares the average CV error (and standard deviation) of estimated lightness, colourfulness, and hue when applied to several phases of the LUTCHI data set. In particular, we use the LT phases (transparency), R-HL phases (reflective media), and CRT phases. Our model achieves the best overall prediction. Further, the variation in error is rather small for our lightness and colourfulness prediction, indicating that our model performs consistently.*

5.5 Discussion

In the development of our colour appearance model, we have chosen to fit most constants in our model, instead of relying on previous results. We have considered *high-dynamic-range* colour reproduction, i.e., the invertibility of our model, as well as tried to avoid over-fitting during the optimisation. Although we developed our appearance model with inspiration from zone theory [Müller, 1930], we tried to avoid using physiological constants which were derived from primate measurements, for instance, parameter $n = 0.74$ in Equation (2.11). This primate-driven parameter has been adopted in previous CAMs. We found that 0.57 fits better to our experimental data. Hence, we believe that the human visual system may have different responsivity from that of the primate. It is worth noting that colour appearance models are only computational models of colour appearance and as such do not try to describe how human vision actually works.

As shown in Chapter 4, the response of the human visual system presents complicated non-linear characteristics for a given physical stimuli. Modelling these non-linear characteristics with a few sets of equations is a challenging task. For example, the simplest approach might be to use a polynomial function. The function could be easily fitted through linear regression to a high accuracy for the given data set. However, polynomial equations could be over-fitted to the given training data and are not invertible when of a higher order than the second order. Therefore, particularly for modelling lightness, we use hyperbolic functions. This enables us to model lightness to a significantly higher accuracy than other models while keeping analytical invertibility. However, these types of equations cannot be solved by linear solving. Therefore, we conducted an *exhaustive search* to find the *maximum likelihood* for a given training data set. We validated our model through *cross-validation* with *independent* data sets and *third test sets* (see Figure 5.17 and 5.21). However, this numerical optimisation is still open to development; our freely available experimental data [Kim et al., 2009] may provide further opportunities.

Our psychophysical experiments and colour appearance model focused on high-luminance *photopic* vision rather than dim (mesopic) or dark (scotopic) vision because our research was motivated by the advent of *high-dynamic-range imaging*, which deals with higher levels of luminance. For instance, our colour appearance model does not model the rods' contribution under dark luminance conditions. If the peak luminance level is under $\sim 10\,\mathrm{cd/m^2}$ the performance of our model may decrease insofar as the rods and the cones have different sensitivities to the luminance. For mesopic vision (phase 1, under $43\,\mathrm{cd/m^2}$ luminance), our model still outperforms other models (average CV: 11.15% in predicting lightness), see Figure 5.21.

Our model does not take a separate background parameter. Our model is only driven by the adaptation luminance level and the peak luminance level. In contrast, the CIECAM02 model uses the luminance adaptation level and the background luminance level respectively. We share the same definition of the *level of luminance adaptation* [Moroney et al., 2002], which means the amount of luminance in an approximately 10-degree viewing angle. However, we found that the measurement of the level of luminance adaptation implicitly contains the background luminance level (as the background is a main part of the adapting field). This means that the separation between the luminance adaptation level and the background luminance level is a *redundant* parameterisation. Therefore for applications of a colour appearance model with respect to colour reproduction, the decision to use a background luminance level is questionable [Fairchild, 2005]. Hence, we chose an approach that derives our model without an explicit background luminance level parameter.

Our model also does not take a separate surround parameter as in our experiment its influence was not significant. Even though our model does not have an explicit parameter for surround, its effect could be taken into account by changing the adaptation level accordingly. In our experiments, we were able to build only a limited range of surround (average level — 20% of the peak luminance) because our main colour stimuli is already very bright. We were not able to create a high-luminance viewing surround because of the limitations with light sources that is large and bright enough to cover the room. As a result, our experiment did not fully investigate how the surround influences perception at high luminances, but the measured influence on the perceived attributes was minimal, as was also observed in [Breneman, 1977].

5.6 Summary

We have presented a new colour appearance model that has been designed from the ground up to work for an extended luminance range. As no colour perception data was available for high luminance ranges, we have first conducted a large psychophysical magnitude experiment to fill this gap. Based on our data, as well as previous data, we have developed a model that predicts lightness, colourfulness and hue to a high accuracy for different luminance ranges, levels of adaptation, and media. In contrast to other CAMs, our method works with absolute luminance scales, which we believe is an important difference and key to achieving good results. The next chapter demonstrates an application of our colour appearance model to complete a high-fidelity colour reproduction pipeline for high-dynamic-range imaging.

Chapter 6

Colour Reproduction in High-Dynamic-Range Imaging

The previous chapter describes a novel colour appearance model (CAM) which is derived from our experimental data sets of perceptual attributes measured under high levels of luminance. This computational model of human colour vision allows us to convert physically-meaningful high-dynamic-range (HDR) radiance values (obtained from HDR characterisation) to perceptually-uniform colour appearance attributes. These forward calculations yield perceptual coordinates for a given physical stimulus. The perceptual coordinates are reproducible on a new output medium such that the colour appearance model is analytically invertible, i.e., perceptual lightness, colourfulness, and hue values can be mathematically inverted into physical quantities (e.g., CIEXYZ) with a new set of target viewing parameters as input. These physical coordinates of an output device are then converted to device signals through an inverse device characterisation model. This chapter introduces a colour reproduction pipeline to achieve high-fidelity reproduction of real-world radiance values on any output medium and then evaluates the perceived similarity of the reproductions to the real scenes through a series of psychophysical experiments.

6.1 Image Reproduction

This section introduces an image reproduction pipeline for reproducing high-dynamic-range scenes on an output display device. The proposed pipeline achieves a high level of fidelity in the reproductions, as shown by psychophysical evaluations. The imaging characterisation method, introduced in Chapter 3, is used to capture high-dynamic-range scenes. The appearance model, described in Chapter 5, is used to complete the visual communication at each stage. This section proposes an HDR imaging system by combining these previously described elements.

6.1.1 Reproduction Pipeline

Suppose we are taking an HDR image of a real-world landscape with an HDR camera system. As presented in Chapter 3, our characterisation method enables us to convert such an HDR RGB image into a physically-meaningful CIEXYZ radiance map (on an absolute scale). Our colour appearance model for high-luminance levels (covering the dynamic range of the human visual system, see Chapter 5) then allows us to convert the physically-meaningful coordinates into perceptually-uniform coordinates of colour appearance, e.g., lightness, chroma, and hue (see Figure 6.1). This completes the forward communication of HDR colour information from the real world to human perception. On the other hand, suppose we already have a reproduction of a real-world landscape, say a digital photograph of the landscape on an sRGB display. Insofar as we have a characterisation model of the display, we can convert RGB signals of the image into actual physical radiance values in CIEXYZ. Once we have the physical coordinates of the displayed image, we can convert these values to perceptual appearance attributes by using our colour appearance model. This enables us to predict the perception of the photograph under a given viewing environment. At this point, we have two sets of perceptual coordinates: the perception of the real-world landscape and that of the reproduction of the landscape. The closer the reproduction perceptual coordinates are to those of the real world, the more *faithful* the duplication with respect to visual perception. *High-fidelity* colour reproduction of the real world is achievable in this approach.

The perception of colour reproduction is a *metameric sensation*, i.e., the relationship can be represented as a *many-to-one* function with viewing environment parameters. Imagine that two sets of perceived colours are identical. This means that two different observations on different media under

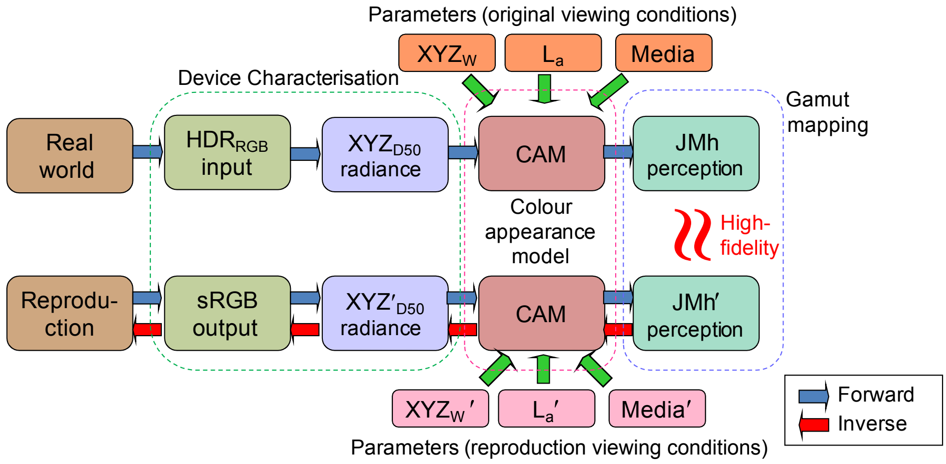

Figure 6.1: *High-fidelity colour reproduction pipeline for HDR imaging. In observing the real world, an HDR camera system captures real-world radiance as input. The HDR characterisation model converts the captured HDR image into a physically-meaningful radiance map. A forward colour appearance model then converts physical radiances to perceptual coordinates, e.g., lightness, colourfulness, and hue (*JMh*). Imagine that we observe a reproduction of the real world. A forward output device characterisation model converts device signals to physical radiance values. The forward colour appearance model with output viewing conditions converts physical radiances to the perceptual coordinates (*JMh'*) of the observation of the reproduction. If* JMh' *matched* JMh*, we would believe that the reproduction appears* faithfully *identical to the real world. Aiming for high fidelity, we directly map* JMh *to* JMh'*. Ensuring that our forward colour appearance and characterisation models are analytically invertible, we apply these inverse models to* JMh' *we finally achieve high-fidelity colour reproduction on an output medium.*

two different viewing conditions yield identical perceptions, i.e., the reproduction of the real world appears the same as the original real world. We have introduced an *analytically invertible* forward mathematical transform to convert physical quantities to perceptual quantities. Therefore, perceptual coordinates are transformable to physical coordinates by using the *inverse colour appearance model*. The parameters of the inverse model are set to specify the viewing environment conditions of the target observation. The converted physical coordinates are reproducible on an output device by using an *inverse device characterisation* (from the physical coordinates to the device signals). This allows us to reproduce *metameric colour reproduction* with newly given target environmental conditions (see Figure 6.1).

For instance, colour reproduction of HDR images is achieved by first taking an absolute HDR radiance map (containing physically meaningful $CIEXYZ$ values) and applying our CAM, which yields perceptual attributes, e.g., lightness, colourfulness, and hue (JMh). These attributes are then converted to absolute $CIEXYZ$ for a specific target display and target viewing condition by applying the inverse CAM. Finally, $CIEXYZ$ coordinates are transformed into device-dependent coordinates (e.g., sRGB) for display.

6.1.2 Colour Connection Space

As mentioned earlier, the perceptual coordinates of input/output medium are connected in a perceptual colour space to complete colour reproduction. If we use absolute perceptual coordinates for colours, we can reproduce such absolute perceptual quantities (e.g, brightness and colourfulness) on output media. If we use relative perceptual coordinates, we will reproduce only relative colour coordinates (e.g., lightness and chroma) on output media. We call these Cartesian 3D coordinate systems *colour connection spaces*.

As our colour appearance model provides both relative and absolute coordinates of perceptual colour attributes, we have four different options for a colour connection space to complete colour communication: (1) brightness, colourfulness, and hue (QMh), (2) brightness, chroma, and hue (QCh), (3) lightness, colourfulness, and hue (JCh), and (4) lightness, chroma, and hue (JCh). For a colour connection space, when *relative* colours are used, the entire colour information in an image is normalised by the specifications of a target medium. For instance, lightness and chroma are relative brightness and colourfulness normalised by reference white on a target medium (see Section 2.3.1 for definitions), and accordingly output brightness and colourfulness depend on the reference white of the target medium. This means that once we use relative colour coordinates, we could never achieve absolutely identical reproduction of the source input on the output as long as we have a white point and colour gamut of the output medium that is different from the real world. On the other hand, when *absolute* colours are used, theoretically all colour information is kept in this colour-connecting stage. However, if the maximum brightness level or colour gamut of the target medium is lower or smaller than the original, the original colour information could be saturated by the specifications of the output medium. Thus, if the output medium has a higher maximum brightness and a wider colour gamut than the source medium, we can use absolute colour coordinates. However, if the output produces less brightness and has a smaller colour gamut than the source input, using relative coordinates is a better choice to avoid significant saturation of the colour information.

In the experimental context of this thesis, the luminance level of our target LCD display device (∼250 cd/m^2) is much lower than that of the real world assuming ordinary reproduction conditions of HDR imaging. Real-world brightness is obviously not reproducible on any of the target media. Therefore, we decided to use relative coordinates for connecting achromatic colour information by using *lightness*. This narrows the possible colour connection spaces to JMh and JCh colour spaces. Second, as shown in Section 2.4, our target output device presents an almost identical colour gamut to the sRGB colour space, which covers most colours in the real world [Pointer, 1982] (see Figure 2.14). We decided to use absolute coordinates for chromatic information by using *colourfulness* instead of chroma. *Chroma* quantifies the relative intensity of each hue, disregarding absolute intensity, whereas *colourfulness* preserves the absolute intensity of each hue (see Section 2.3.1). Therefore, using *colourfulness* coordinates is a better choice to reproduce the original colour information without loss of any information (achieving higher fidelity) with the condition that the output medium could produce the same colourfulness as the input medium. However, if the gamut boundary of the output medium is unknown or significantly smaller than that of the input medium, *chroma* could be a safer choice for the colour space because we could avoid unpredictable saturation of the colour information in reproduction although the overall colourfulness would be *shrunk* or *expanded* depending on the specification of the output medium with chroma mapping. In summary, the JMh colour space is chosen as our main colour connection space considering our experimental conditions. The perceptual performances of JMh and JCh are evaluated in Section 6.2.

6.1.3 Parameters

Our forward colour appearance model requires absolute CIEXYZ radiance values with three parameters as input: absolute CIEXYZ values of the reference white of the scene, the level of luminance for global adaptation, and the medium type that is observed. Measuring the absolute CIEXYZ radiance values of a scene is achievable by using a spectroradiometer or an HDR characterisation method [Kim and Kautz, 2008a], presented in Chapter 3. The absolute CIEXYZ values of the reference white of the scene are able to be chosen in an automatic or a manual manner: automatically selecting CIEXYZ values of the maximum brightest pixel value or our estimating-illumination method (see Chapter 3), or manually selecting the reference white point. We conducted manual measurements of the reference white for our experimental scenes carefully in order to avoid any measurement error caused by camera noises. For the level of luminance adaptation, we used an averaged luminance level by using the *geometric mean* of luminance as it is believed to be a good approximation of the average luminance [Pattanaik et al., 2000; Reinhard et al., 2002, 2005]. In order to avoid infinite errors in calculating the geometric mean, we calculated the geometric mean of the luminance by using the exponential of the arithmetic mean of log luminances with a minimum value:

$$L_a = \exp\left(\frac{\sum_{x,y} \log\left(\delta + Y\left(x,y\right)\right)}{\mid Y \mid}\right), \tag{6.1}$$

where δ is 1.0E-30, Y is the luminance of each pixel (x,y), and $\mid Y \mid$ is the cardinality of Y. The input medium parameter is decided by which medium is observed. In the case of a real-world scene, we use a high-luminance LCD display with parameter $E = 1.0$ [see Equation (5.8)] as this corresponds to real-world observations (see Chapter 5).

Our inverse colour appearance model requires perceptual colour attributes JMh or JCh with three parameters as input: absolute CIEXYZ values of the reference white of an output device, a level of luminance adaptation of the observation, and a target medium type. For our experimental conditions, we set the target medium to an sRGB calibrated LCD display (having a peak luminance level of 250 cd/m^2) assuming that the display is observed in dim conditions (10% of the peak luminance level), following [IEC, 2003] for standardised sRGB viewing conditions, i.e., the reference white of the output device for our inverse colour appearance model was (237.62, 250.00, 272.21) in CIEXYZ. The level of luminance adaptation level was set to 25 cd/m^2. In addition, for a general purpose target medium, we used the transparent advertising media parameter ($E = 1.2175$) for a general sRGB display device with an average surround, which was assumed to have characteristics between our *high-luminance LCD* display and a *CRT* display. Therefore, the printed thesis might appear differently depending on printer characteristics and its viewing conditions. The following section demonstrates actual applications of the reproduction of HDR images onto a general sRGB target medium with comparison to other methods.

6.1.4 Qualitative Results

As mentioned in Chapter 5, our colour appearance model can be used to predict perceptual phenomena. Figure 6.2 demonstrates an example of the *simultaneous contrast effect*. Our colour appearance model can be used to match the appearance of images with different backgrounds. The two images appear identical even though the one on the right is actually lighter and more colourful (see Section 4.5). This is achieved by modifying the target luminance adaptation level when applying our colour appearance model. Compared to a black background, a white background increases luminance adaptation.

In Figure 6.3, we demonstrate media-dependent reproduction. The left image printed on paper is perceptually equivalent to the right image displayed on an LCD display (assuming a calibrated device in dim viewing conditions). If both are viewed on an LCD display, the left image appears brighter. This is due to the fact that luminance perception for paper decreases, and our colour appearance model compensates for it.

Figure 6.4 qualitatively compares colour reproduction with CIECAM02 [Moroney et al., 2002], iCAM06 [Kuang et al., 2007], and our model [Kim et al., 2009]. A high-dynamic-range scene is captured by our HDR camera system and converted into a CIEXYZ radiance map (on an absolute

Figure 6.2: *Appearance matching with respect to the background effect. The two colour charts will appear similar (assuming that a calibrated display with a gamma of 2.2 in dim viewing conditions). When comparing the two images without the backgrounds, it can be seen that the right colour chart is actually lighter and more colourful.*

Figure 6.3: *Appearance matching with respect to media dependency. Our model can be used to match colour appearance on different media. Starting from a radiometrically calibrated $CIEXYZ$ float image [Kim and Kautz, 2008a], the left image printed on* paper *will appear very similar to the right image when displayed on an LCD* display *(assuming calibrated devices in dim viewing conditions under a luminance of 119 cd/m^2).*

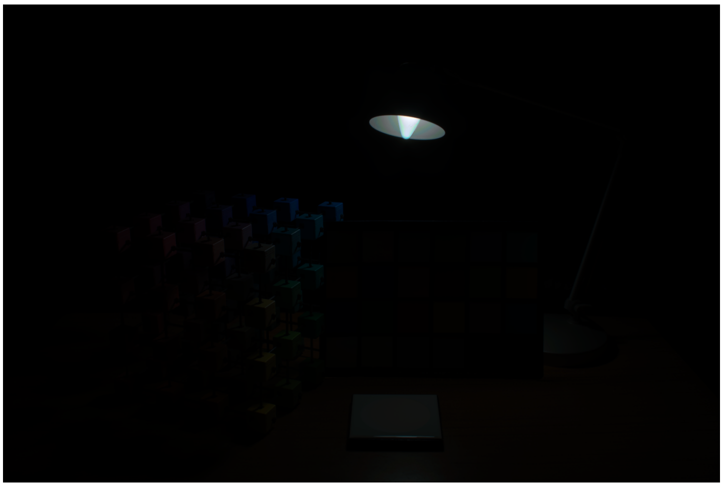

(a) CIECAM02

(b) iCAM06

(c) Our model

Figure 6.4: *Qualitative comparison of perceptual predictions of CIECAM02* (top)*, iCAM06* (middle)*, and our model* (bottom)*. As the HDR image contains high-dynamic-range luminances, CIECAM02 fails to predict visual perception. As can be seen, CIECAM02 is not designed to handle HDR images. iCAM06 is a hybrid model to combine the revised CIECAM02 and an HDR tone-mapping algorithm. Its result shows halo artefacts on the colour chart and hue deterioration. Measured peak luminance of this scene was 1 382 cd/m*^{2}.

scale). The peak luminance level of the scene was 1 391 cd/m^2. Image (a) shows the result for CIECAM02, which underestimates the perceived lightness, as observed in qualitative comparison [see Figure 5.5(b)]. As the HDR image contains high-dynamic-range luminances, CIECAM02 fails to predict visual perception. As can be seen, CIECAM02 is not designed to handle HDR images. Image (b) shows a results of iCAM06 (a combination of the revised CIECAM02 and a bilateral tone-mapping algorithm [Durand and Dorsey, 2002]). Original colourfulness and hue are altered by the model, and halo artifacts are observed around square patches on the colour chart. Image (c) presents the result of our model. Our model reproduction is much closer to actual perception with HDR images as demonstrated in quantitative comparisons (see Section 5.4).

Figures 6.5 and 6.6 compare the use of our colour appearance model for tone-mapping with CIECAM02, Reinhard et al. [2002]'s method, and iCAM06. Our model's results are consistent throughout with good luminance compression. Colours are slightly more saturated than with the other two models, which is due to our model preserving the original colourfulness impression. Figures 6.7, 6.8, and 6.9 present more results with ordinary HDR images. The next section describes *quantitative* evaluation of the *perceptual similarity* of our reproduction model to the real scene with comparison of other methods.

6.2 Experimental Evaluation

We conducted a series of psychophysical experiments to evaluate the *fidelity (accuracy)* of the reproduction of real scenes. Two real scenes were arranged to be compared with their reproductions (on a calibrated LCD display). Participants were asked to compare the real scene and its reproduction in terms of how similar to the real scene the reproduction is. The participants produced a five-point scoring scale by comparing the reproduction to the real scene. The data from this *paired comparison plus category* experiments was analysed with Torgerson's *Law of Categorical Judgement* [Torgerson, 1958] (extended Thurstone's Law of Comparative Judgement), as shown in [Kim and MacDonald, 2006; Kuang et al., 2007; Ritschel et al., 2008; Yu et al., 2009].

6.2.1 Stimuli

In order to measure the perceptual similarity of HDR reproductions to real-world scenes, we arranged two real scenes with high-dynamic-range luminances in a dark room (see Figure 6.10 for the experimental setup). The scenes were captured by our HDR imaging system (using a Canon 350D camera, see Chapter 3). The HDR images were characterised to produce *physically-meaningful* HDR radiance maps in absolute terms [Kim and Kautz, 2008a]. The calibrated HDR radiance maps (absolute CIEXYZ) were reproduced on a characterised LCD display with three different HDR tone-mapping algorithms ([Reinhard et al., 2002], [Durand and Dorsey, 2002], and [Reinhard and Devlin, 2005]), an image appearance model (iCAM06), and our method (using JMh and JCh colour connection spaces). We used an Apple Cinema HD Display 23" monitor with a maximum luminance of 275.6 cd/m^2 whose gamma was calibrated to 2.2 following the sRGB colour specification [IEC, 2003]. Figure 6.11 shows a screen shot of the stimulus. Participants were seated in front of the

(a) CIECAM02 (b) Reinhard et al. (2002)

(c) iCAM06 (d) Our model

Figure 6.5: *Qualitative comparison of visual predictions of (a) CIECAM02, (b) Reinhard et al.'s tone-mapping algorithm, (c) the iCAM06 image appearance model, and (d) our colour appearance model. The target display is assumed to be sRGB with a peak luminance level of 250* cd/m^2 *and a gamma of 2.2 (dim viewing conditions, adapting luminance is assumed to be 10% of peak luminance). Our model takes into account not only tone but also original colourfulness. Estimated peak luminance: 13 405* cd/m^2*. Image courtesy of Paul Debevec.*

(a) CIECAM02 (b) Reinhard et al. (2002)

(c) iCAM06 (d) Our model

Figure 6.6: *Qualitative comparison of visual predictions. Absolute HDR radiance maps are tone-mapped using (a) CIECAM02, (b) Reinhard et al.'s tone-mapping algorithm, (c) the iCAM06 image appearance model, and (d) our colour appearance model. Different from other methods, our model does not struggle with local adaptation artefacts like halos. Estimated peak luminance: 1 199* $\mathrm{cd/m^2}$*. Image courtesy of Yuanzhen Li.*

(a) Reinhard et al. (2002)

(b) iCAM06

(c) Our model

Figure 6.7: *Qualitative comparison of visual predictions of (a) Reinhard et al.'s local tone mapping* (top)*, (b) an image appearance model, iCAM06,* (middle)*, and (c) our model* (bottom)*. Estimated peak luminance: 8 774 cd/m^2. Image courtesy of Martin Cadik.*

(a) Reinhard et al. (2002)

(b) iCAM06

(c) Our model

Figure 6.8: *Qualitative comparison of visual predictions of (a) Reinhard et al.'s local tone mapping* (top)*, (b) an image appearance model, iCAM06,* (middle)*, and (c) our model* (bottom)*. Estimated peak luminance: 18 238 cd/m*^{2}*. Image courtesy of Dani Lischinski.*

(a) Reinhard et al. (2002)

(b) iCAM06

(c) Our model

Figure 6.9: *Qualitative comparison of visual predictions of (a) Reinhard et al.'s local tone mapping* (top)*, (b) an image appearance model, iCAM06,* (middle)*, and (c) our model* (bottom)*. Estimated peak luminance: 13 437 cd/m*^{2}*. Image courtesy of Greg Ward.*

screen at a distance of approximately 60–100cm. All stimulus reproductions were presented twice against a middle-gray background (∼20% background ratio) in a random order, i.e., each reproduction is shown twice in each phase with consideration of training and measurement accuracy. The actual data is averaged from these twice-repeated data. Figure 6.12, 6.13, 6.14, and 6.15 present the actual reproductions used as visual stimuli for the experiment.

6.2.2 Experimental Procedure

The goal of our psychophysical experiments was to *quantify perceptual similarity* of reproductions to their original real scene. The *paired comparison plus category method* [Scheffé, 1952] was used (see Figure 6.10), using a five-point scoring scale (see Figure 6.11). The technique is a combination of a five-point category rating scale and a pair comparison. Participants estimate the difference between a pair (the real scene and the reproduction) and assign a number to this difference. These categories are labelled with the following descriptions: *(1) not similar, (2) slightly similar, (3) moderately similar, (4) very much similar, and (5) extremely similar*, adapted from [Bartleson, 1984; Meilgaard et al., 1991].

The paired comparison plus category experiments were conducted in three sessions on two days. Two different scenes were built and used as stimuli in the same way. Ten colour-normal participants took part in each experiment. In the experiments, three of the participants were female computer scientists with an imaging background; the other participants were male with a computer graphics or science background. The participants were given instructions beforehand which contained a brief description of the task.

On each day, participants were given a real scene and a series of reproduced scenes in a dark room (see Figure 6.10 for experimental setting). They were asked to compare the real scene and the reproduced scene with three criteria. In the first phase, they were asked to assign a score (1–5) to how similar each reproduction was to the real scene in terms of *realism* (considering all visual aspects). In the second, they were asked to score lightness reproduction such as tone, contrast, lightness, and shadow. In the third, they were asked to score colour reproduction, e.g., how similar the reproduced colour chart was to the real colour chart.

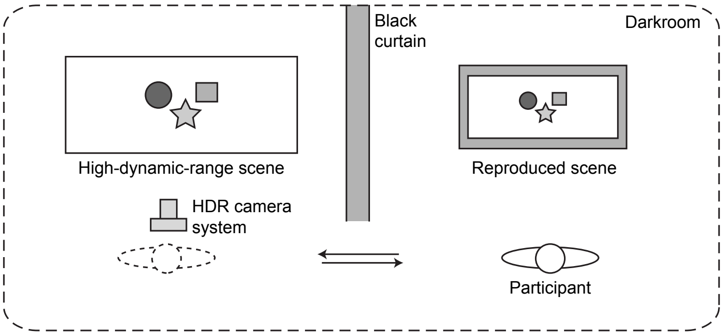

Figure 6.10: *Schematic diagram of psychophysical experiments for evaluating visual accuracy in reproductions.*

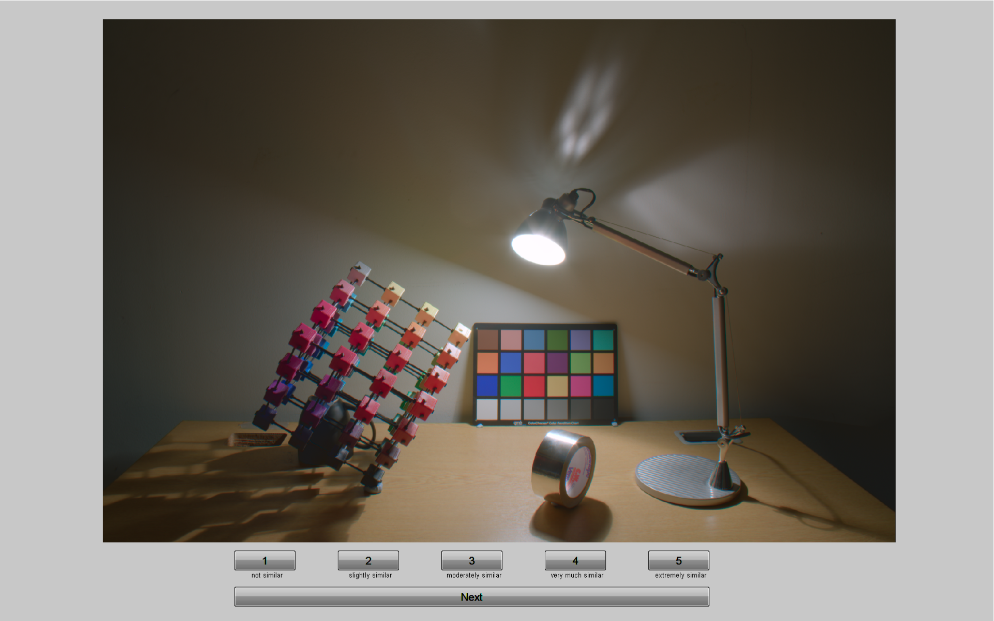

Figure 6.11: *Screen capture of a reproduction stimulus. Participants observed six different reproductions in a dark room, compared with the captured real scene. The participants were allowed to compare the real scene and the reproduced scene anytime they felt it necessary. The category of the reproduction was judged based on their memory.*

The experiment was conducted in a controlled environment under dark viewing conditions, following sRGB standard viewing conditions. Participants were asked to adapt to the illumination conditions for 5-10 minutes before starting the experiment. The participants were allowed to compare the real scene and the reproduced scene anytime they felt it necessary. The category of the reproduction was judged based on their memory.

In the experiment, the participants made six estimates (six reproduction methods compared to a reference for each of the two scenes) in terms of three different criteria: *realism reproduction*, *lightness reproduction*, and *colour reproduction* for each phase. The same set of stimuli were repeated seamlessly twice to achieve a higher accuracy (average data was used for analysis). In completing three phases, participants spent approximately 20–30 minutes. See Table 6.1 for a summary of the experimental evaluation (see Appendix A.7).

The *inter-observer variance* of the ten participants of all phases (average variation of each participant to an average result) was 14.81%. Three observers repeated the same experiment twice in order to judge *repeatability*. The average variation between the two experiments was 12.96%.

6.2.3 Quantitative Results and Analysis

The category experiment yielded similarity scores on a five-point scale relating the reference real scenes to the reproduced images. We analysed this data using perceptual scaling. The five-point scores were scaled using the "Law of Categorical Judgement" [Torgerson, 1954, 1958]. This is an

(a) Durand and Dorsey [2002]

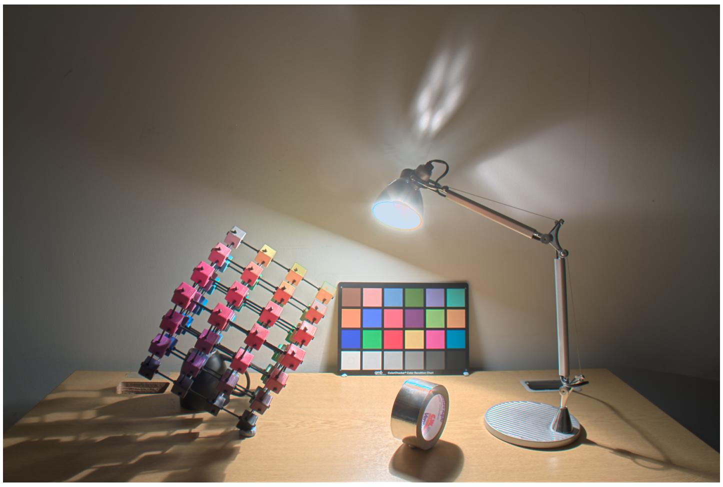

(b) Reinhard et al. [2002]

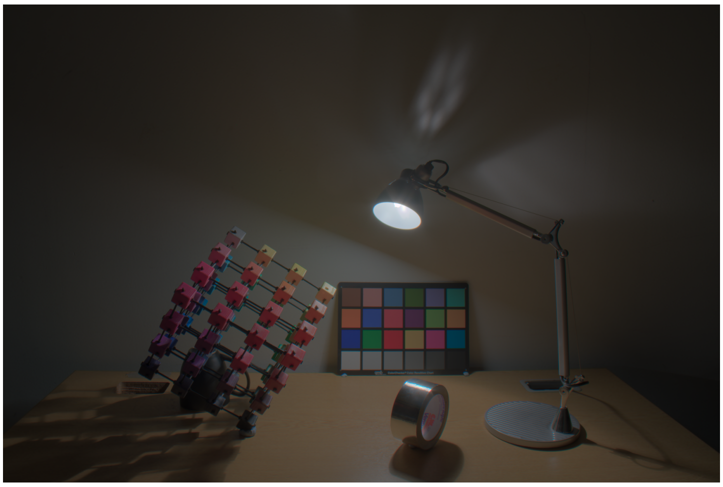

(c) Reinhard and Devlin [2005]

Figure 6.12: *Comparison of perceptual predictions of Durand and Dorsey [2002]* (top)*, Reinhard et al. [2002]* (middle)*, and Reinhard and Devlin [2005]* (bottom)*. These reproductions are compared with a real scene as ground truth (scene one).*

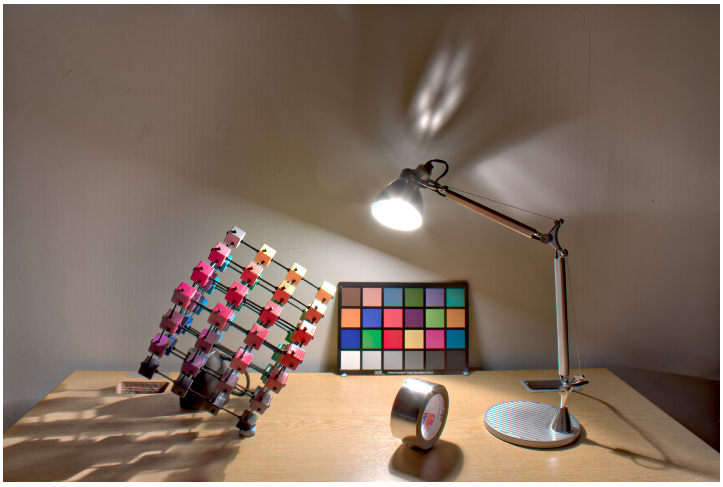

(a) iCAM06

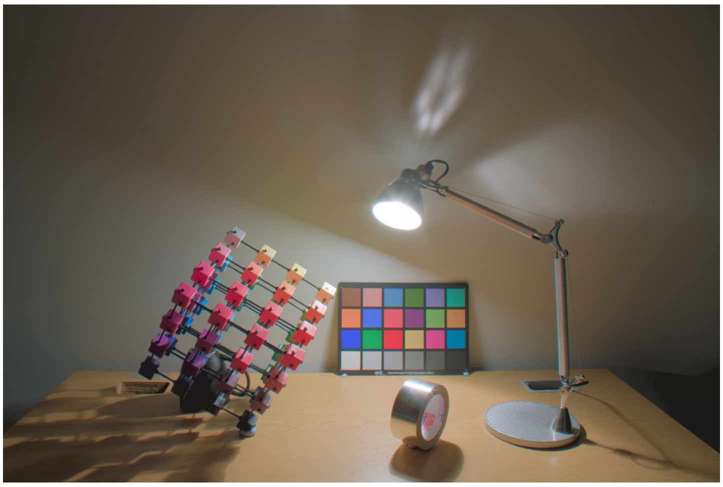

(b) Our model (JMh)

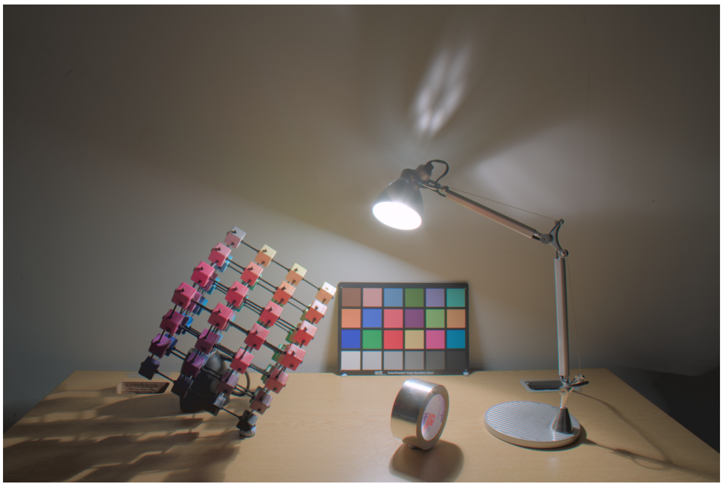

(c) Our model (JCh)

Figure 6.13: *Comparison of perceptual predictions of iCAM06* (top)*, our model by using the JMh colour space* (middle)*, and our model by using JCh colour space* (bottom)*. These reproductions are compared with a real scene as ground truth (scene one).*

(a) Durand and Dorsey [2002]

(b) Reinhard et al. [2002]

(c) Reinhard and Devlin [2005]

Figure 6.14: *Comparison of perceptual predictions of Durand and Dorsey [2002]* (top), *Reinhard et al. [2002]* (middle), *and Reinhard and Devlin [2005]* (bottom). *These reproductions are compared with a real scene as ground truth (scene two).*

(a) iCAM06

(b) Our model (JMh)

(c) Our model (JCh)

Figure 6.15: *Comparison of perceptual predictions of iCAM06* (top)*, our model by using the JMh colour space* (middle)*, and our model by using JCh colour space* (bottom)*. These reproductions are compared with a real scene as ground truth (scene two).*

	Observers	Phases	Methods	Scenes	Estimates
Numbers	10	3	6	2	72

Table 6.1: *Summary of our evaluation experiment. In each phase, six reproductions were shown twice. Two scenes were used. Each participant totalled 72 estimations, which took approximately 20–30 minutes per participant.*

extension to Thurstone [1959]'s pair-comparison scaling that allows for several categories. First, the frequency matrix **FM** of N participants for each score was computed for each reproduction. A cumulative frequency matrix was then computed from the lowest score to the highest score. A *logistic psychometric model* **LG** (following Condition D in the Law of Categorical Judgement — assuming that all the discriminal dispersions and correlations are constant, independent of category or sample [Engeldrum, 2000]), was derived from the cumulative frequency matrix:

$$\mathbf{LG} = \ln\left(\frac{\mathbf{FM}+1/2}{N-\mathbf{FM}+1/2}\right). \tag{6.2}$$

Also, from the normalised frequency matrix **FM**, *z scores* were computed through the *normal-inverse* statistic function. Then, a linear least squares-fit was used to find the best fit from the **LG** to the z scores (see Figure 6.16 for an example). The difference of the *response scales* for each method between neighbouring categories were averaged to find *category boundary estimates*. Finally, the differences between category boundary estimates and response scales yields *perceptually-uniform scales* for the given stimuli [Morovic, 2008]. These *scale* values can be related to the original categories (from *not similar* to *extremely similar*). The estimated scale values are on a *perceptually-uniform* scale, which allows one to judge relative differences in similarity of the reproduced HDR images to the captured real-world scene. The results are summarised with estimated category boundaries in Figures 6.18 (see Figure 6.12 and 6.13 for actual stimuli) and 6.19 (see Figure 6.14 and 6.15).

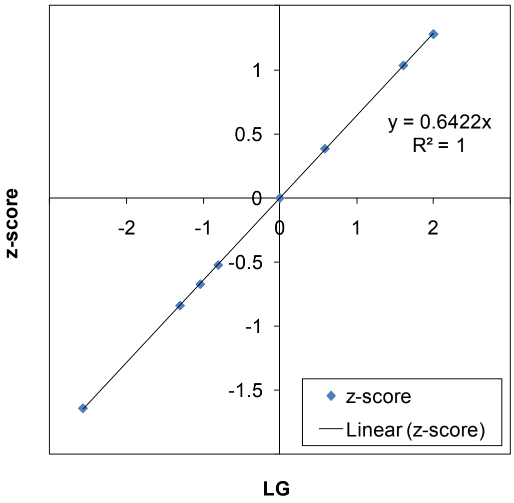

Figure 6.16: *An example of a linear least-squares fit from LG to z-score (from a phase of lightness reproduction in scene two).*

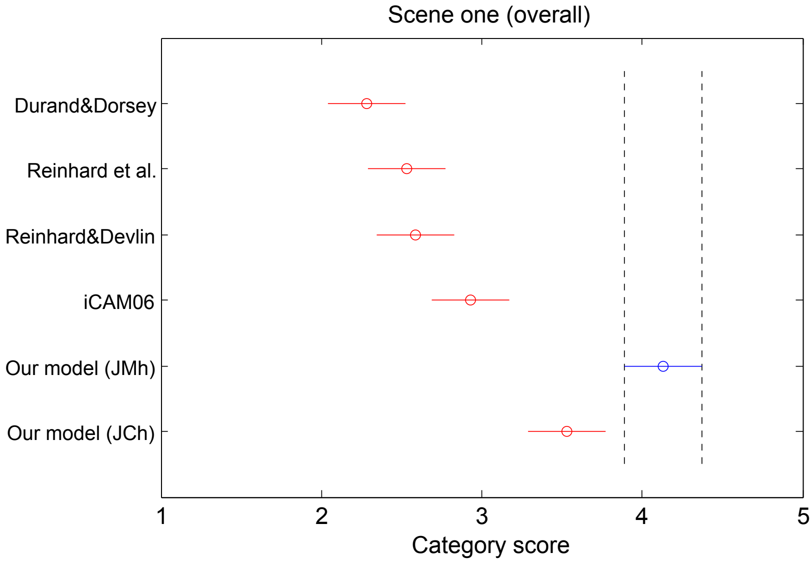

(a)

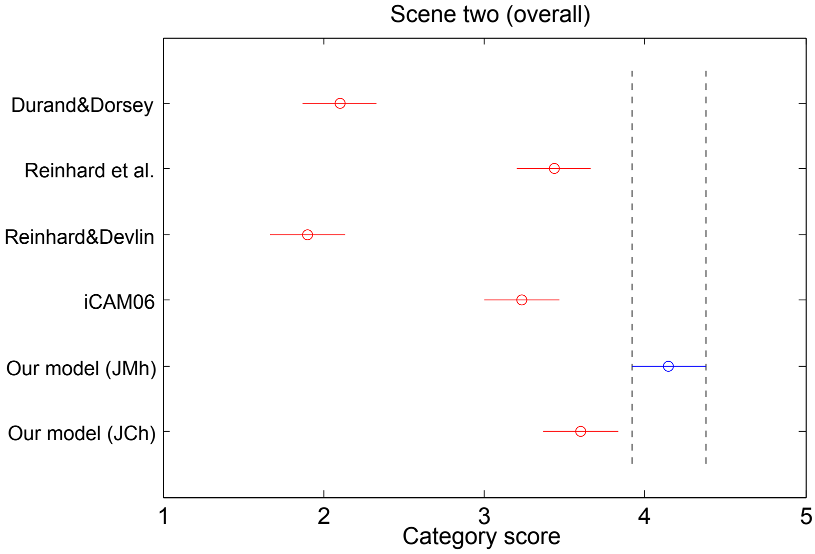

(b)

Figure 6.17: *Overall quantitative comparison of visual predictions of Durand and Dorsey [2002], Reinhard et al. [2002], Reinhard and Devlin [2005], iCAM06, and our model (JMh and JCh colour spaces) with real scenes (scene one and two). Our JMh model has overall mean of category scores* significantly *different from other five methods in both scenes (one-way ANOVA, F-test, alpha=0.05): (scene one) F-value=34.48, p-value=0.0, (scene two) F-value=59.77, p-value=0.0. The dotted lines indicate 95% confidence interval. It is compared in terms of the reproductions of realism, lightness, and colourfulness. Descriptions of scores: (1) not similar, (2) slightly similar, (3) moderately similar, (4) very much similar, and (5) extremely similar.*

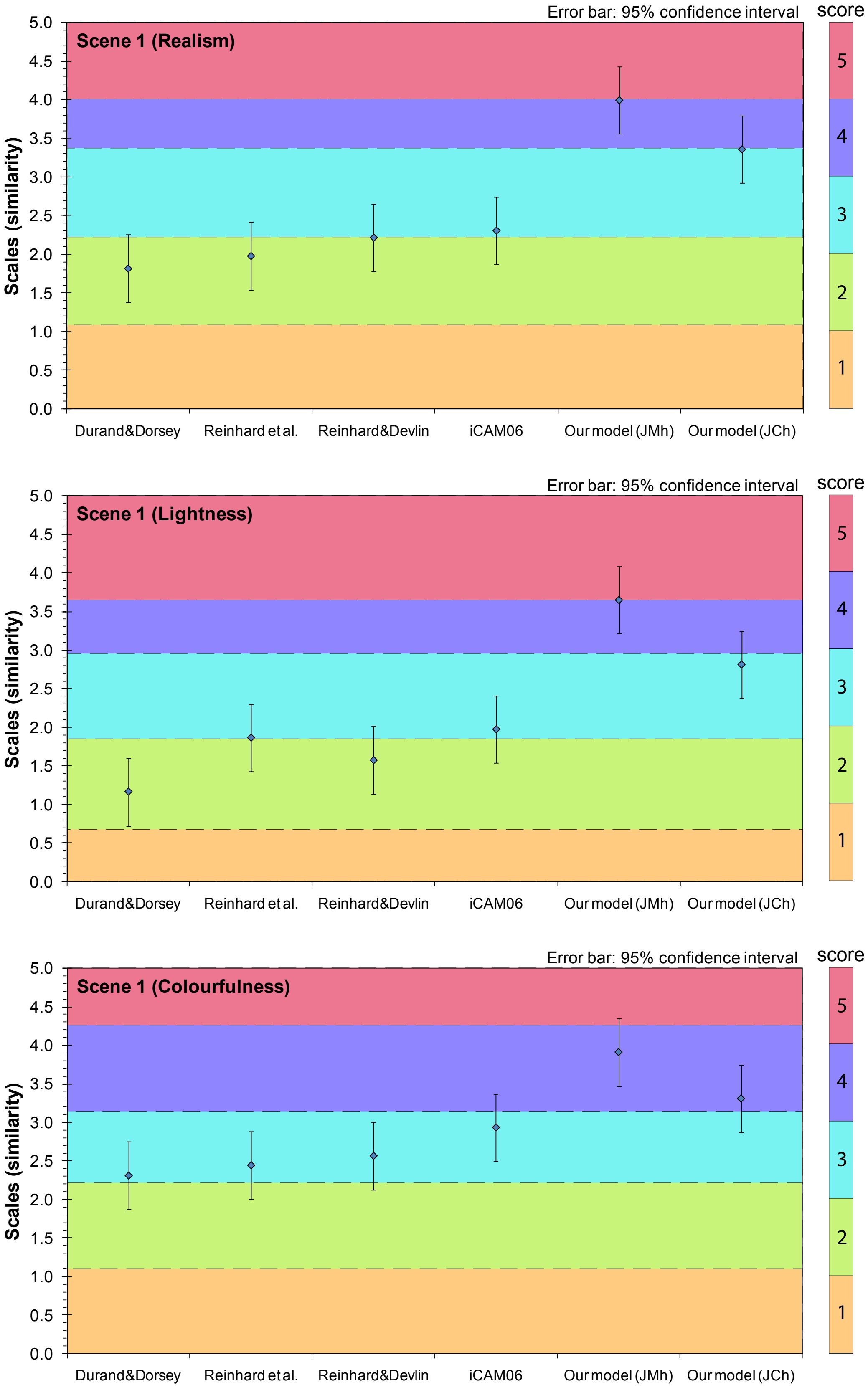

Figure 6.18: *Quantitative comparison of visual predictions of Durand and Dorsey [2002], Reinhard et al. [2002], Reinhard and Devlin [2005], iCAM06, and our model (JMh and JCh colour spaces) with a real scene (scene one). It is compared in terms of the reproductions of realism, lightness, and colourfulness. Descriptions of scores: (1) not similar, (2) slightly similar, (3) moderately similar, (4) very much similar, and (5) extremely similar.*

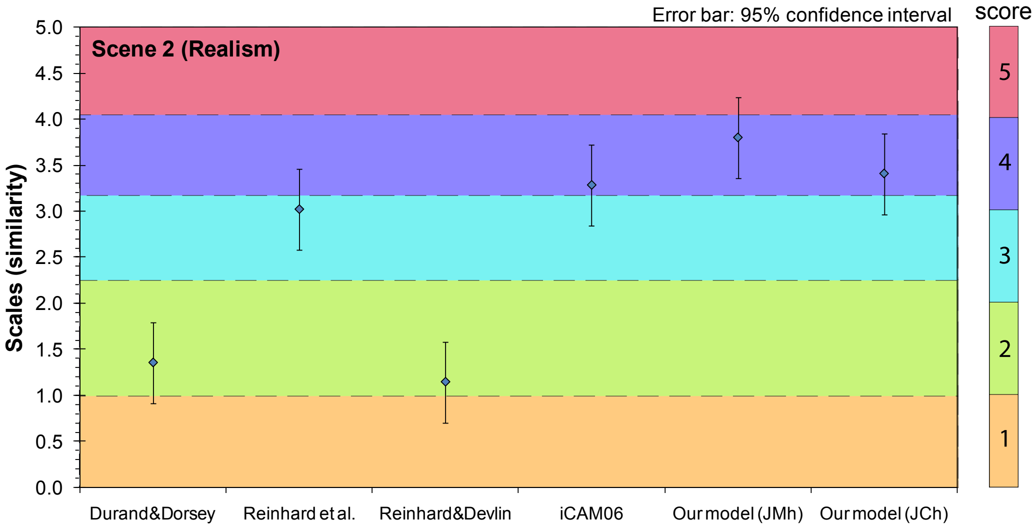

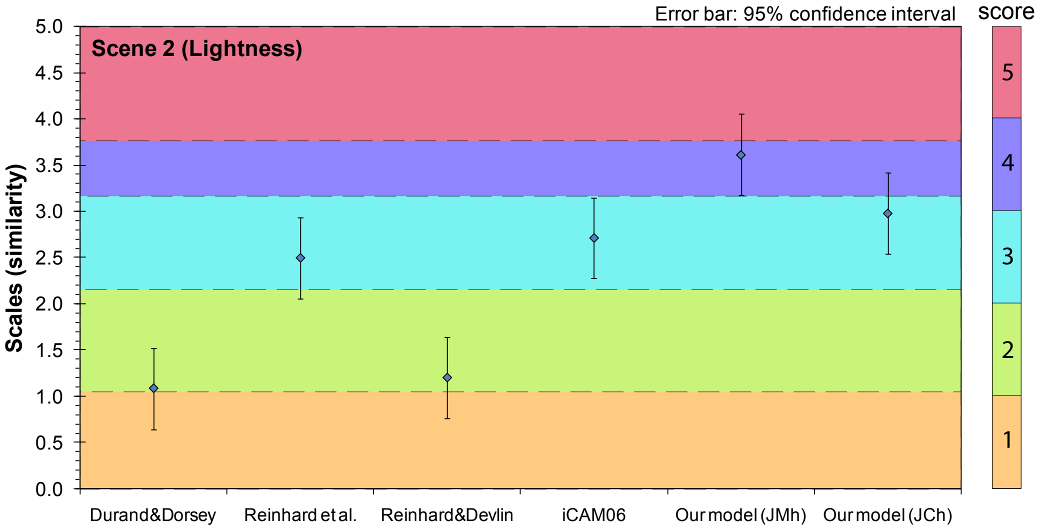

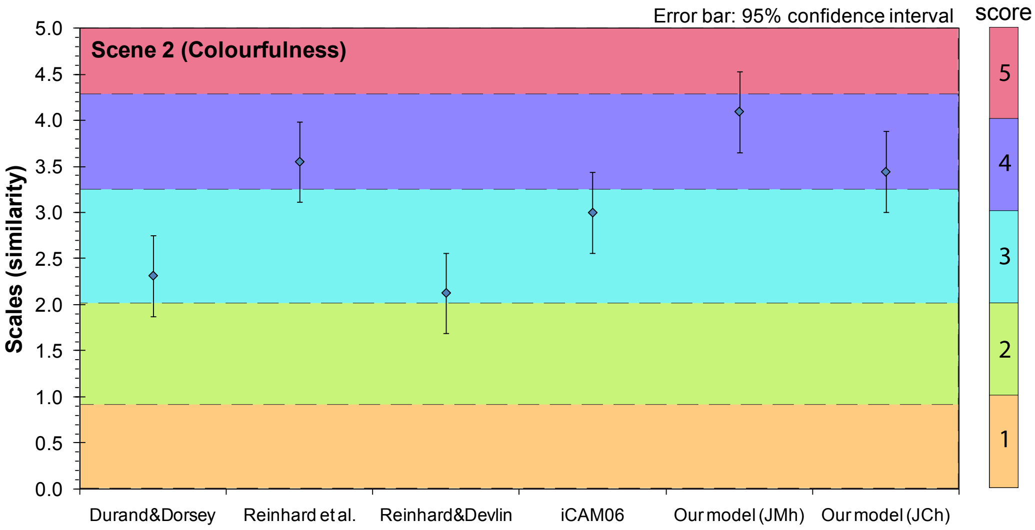

Figure 6.19: *Quantitative comparison of visual predictions of Durand and Dorsey [2002], Reinhard et al. [2002], Reinhard and Devlin [2005], iCAM06, and our model (JMh and JCh colour spaces) with a real scene (scene two). It is compared in terms of the reproductions of realism, lightness, and colourfulness. Descriptions of scores: (1) not similar, (2) slightly similar, (3) moderately similar, (4) very much similar, and (5) extremely similar.*

Our reproductions using the JMh colour connection space were all considered *very much similar* to the reference scene in all scenes. Our JMh method *statistically significantly* outperforms the other methods in all phases of all scenes (one-way ANOVA, F-test, alpha=0.05). See Figure 6.17. Our reproductions using the JCh colour space were considered *very much similar* or *moderately similar*. Our JCh method mostly outperforms the other methods. However, its performance was significantly lower than our JMh method in all cases. In one phase of *realism reproduction* in scene two, our JCh method presents similar but better performance than iCAM06. Reinhard et al. [2002] shows a better performance than our JCh method in one phase of *colour reproduction* in scene two.

6.3 Discussion

As shown in Figure 6.18 and 6.19, the performance of the presented HDR tone-mapping algorithms depends on the scene. Scene one contains fewer objects than scene two but has more obvious colour samples and luminance changes (e.g., light and shadow). In post interviews, the participants said that they felt the task was much easier for scene one as the shadow and colour differences (using the colour chart as a reference) were more obvious than in scene two. Participants felt more confident in judging the similarity of colourfulness (with scene one) by comparing the colour chart in the real scene to that in the reproductions. Participants commented that the overall change in luminances in scene one is clearer than that of scene two (see Figure 6.12, 6.13, 6.14, and 6.15) and this helped lightness judgement. Scene two contains more ordinary objects than scene one but does not contain any standard object like the GretagMacbeth ColorChecker. As shown in Figure 6.19, participants felt the reproductions of a few tone-mapping algorithms (Reinhard et al. [2002] and iCAM06) were more similar to the real scene in scene two than in scene one. These two methods were ranked between *slightly similar* and *moderately similar* in scene one, but were ranked between *moderately similar* and *very much similar* in scene two. Their performance became closer to that of our JCh method. This indicates that our JCh method may not distinctively outperform the other methods with ordinary scenes (e.g., without standard objects like a colour chart). However, the performance of our JMh method was ranked top in all scenes with *statistical significance*.

Our reproduction system using the JMh colour connection space significantly outperforms other methods as our pipeline takes perceptual transformation of colour attributes into account. The 1:1 perceptual mapping in our JMh colour space yields *high-fidelity colour reproduction*. However, our system has limitations when used with current HDR imaging technology. First, current available HDR images have been generated using uncalibrated HDR imaging systems. This means that our JMh reproduction system is not fully compatible with existing HDR images. Hence, in order to obtain absolute scale in uncalibrated HDR images, we empirically scale existing HDR images to reasonable levels (see Figure 6.5). The complete application requires characterisation procedures for input/output devices [Kim and Kautz, 2008a]. In addition, if the specification of an output device is not available (e.g., non sRGB colour device), our JCh model may be a safer choice for colour reproduction on unknown devices. In this case, the colourfulness intensity will depend on the colour specifications of the output medium.

The scope of this thesis limits the mapping from an input to an output colour gamut as a *direct 1:1 mapping*. Colours outside the target gamut were simply clamped. This enables the faithful reproduction of perceived colours with high fidelity such that they are inside the gamut. However, it does not include any image enhancement for out-of-gamut colours. If we would like to improve the *preference* of users, rather than *faithfulness* in reproduction, it would be interesting to study a gamut mapping algorithm that scales and adapts perceptual colours intelligently.

As shown in Equation (6.1), we calculate the average luminance adaptation by employing the geometric mean, which is empirically believed to work well for tone-mapping [Reinhard et al., 2005]. However, the actual mathematical relationship between the geometric mean and the spatial coherence of the luminance adaptation is currently unknown. This would be worth studying in the future. In addition, the impact and correlation between luminance adaptation and surround luminance levels is not explored in this thesis.

6.4 Summary

This chapter presented a novel HDR imaging pipeline that is built on our HDR characterisation method and colour appearance model. It also describes the psychophysical evaluation of the reproduction performance, compared with other HDR tone reproduction and image appearance models. A series of psychophysical experiments were conducted to quantify the perceptual similarity of the reproductions to the reference real scene. As a result, the proposed colour reproduction system, called the JMh colour space model, outperformed other HDR tone reproduction methods and an image appearance model with statistical significance. This result cross-validates the quantitative evaluation of our colour appearance model (see Chapter 5). Consequently, our JMh colour reproduction system provides a good basis for high-fidelity colour reproduction for high-dynamic-range imaging.

Chapter 7

Discussion and Future Work

The aim of this thesis was to develop a colour reproduction system for high-dynamic-range (HDR) imaging. Classical colour reproduction systems fail to reproduce HDR images because the current characterisation methods and colour appearance models (CAM) fail to cover the dynamic range of luminance in HDR images. HDR tone-mapping algorithms have been developed to reproduce HDR images on low-dynamic-range (LDR) media such as LCD displays. However, these models have been based on theoretical assumptions, due to a lack of physical and psychological measurements. Hence, we revisited the key infrastructure of classical colour reproduction elements (the characterisation method and the colour appearance model), reformulating them for high-dynamic-range imaging through a series of physical and psychological experiments. To this end, the most essential elements of colour reproduction, the device characterisation and the colour appearance model, were investigated with respect to high-dynamic-range imaging. First, our HDR characterisation method enables us to measure high-dynamic-range radiances to a high accuracy, competing with very expensive spectroradiometers in accuracy (Chapter 3). Second, modelling colour appearance requires significant effort to prepare before the mathematic development. We firstly built a high-luminance display to obtain a controllable high-luminance viewing environments. We conducted a psychophysical experiment on this display to measure colour appearance attributes of human colour perception (Chapter 4). A novel numerical model was derived from a novel experimental data set, which covers the full range of the human visual system (Chapter 5). Our colour appearance model predicts perceptual colour attributes under high luminance levels to a high accuracy. Finally, our colour reproduction system is built on our novel HDR characterisation and colour appearance models. This system outperforms other HDR reproduction methods with statistical significance (Chapter 6). The following sections summarise findings and discuss each chapter.

7.1 High-Dynamic-Range Characterisation

Current camera characterisation methods for low-dynamic-range camera systems were established with classical colorimetry, which interprets a colour with three essential elements: a light source, an object, and an observer. These characterisation models were numerically derived from a set of physical measurements of reflective colour samples and camera responses to the physical radiation.

A light source is required to obtain camera responses from the reflective targets. The numerical transform of the characterisation model bakes the actual spectral characteristics into the characterisation model. The imaging sensor of the digital camera is illuminated by radiant power, which is the sum of the product of the spectral energy of the light source and reflectance property of the target surface. Therefore, separate measurements of the light source and reflectance for building a characterisation model are not only redundant, but also contribute to worse performance and luminance dependency as in previous characterisation methods.

Our scientific insights into characterisation are that the reflective targets only offer a low dynamic range which make them a bad choice for HDR imaging, and that characterisation based on reflective targets requires both the reflectance of the target and the spectrum of the illuminant to be known. Therefore, we proposed the use of a novel back-lit transparency colour target, specifically designed for HDR imaging, offering a higher dynamic range and wider colour gamut. Thus, our characterisation method only requires the emitted radiant power to be known, which can be measured using a spectroradiometer. This enables us to accurately characterise a digital camera used for HDR imaging. The achieved accuracy of the characterised HDR camera system is similar to the accuracy of a spectroradiometer. Our characterisation model transforms HDR RGB images into physically-meaningful CIEXYZ radiance maps in absolute scale. The captured CIEXYZ radiance can be white-balanced by our illuminant estimation method for display. In addition, the combination of a new transparency colour target, HDR imaging, and characterisation theory yields significantly higher accuracy in measuring real-world radiation. The big advantage using our HDR characterisation method is that such highly-accurate measurement is provided not at a point as with a spectroradiometer but as an whole image. This provides greater *efficiency* in measuring radiance when compared to a spectroradiometer.

The performance of our characterisation method depends on the optical quality of the digital camera, including lens flare, vignetting, veiling glare, and the infrared filter. Modelling these optical phenomena is worth future study. Also, the measurement used in our method returns radiometric CIEXYZ values, not radiance at each wavelength. This means that our method still allows potential measurement errors with metameric colours as is the case with any other target-based models.

7.2 High-Luminance Colour Experiments

Our HDR characterisation method interprets colour specifications of device-dependent HDR RGB images into highly accurate and physically-meaningful radiance values in the form of absolute CIEXYZ. However, this is not sufficient for HDR colour reproduction as the given physical colours are perceived differently under different viewing environment conditions. Therefore, perceptual attributes need to be measured and modelled to allow for HDR colour reproduction.

Colour appearance modelling was developed to predict colour appearance attributes under given viewing conditions. CAMs interpret physical colours *perceptually*. Colour appearance models have previously been derived numerically from experimental measurements of colour appearance. However, currently-available colour appearance measurements present only a limited dynamic range of luminance. The range of colours in the available data sets are at most three orders of magnitude. This was limited by the available display technology in the early 1990s. Therefore, a novel high-luminance display device was built to yield a controllable high-luminance viewing environment, where a series of psychophysical experiments were conducted to produce colour appearance data under high luminance levels up to five-order magnitude (covering the dynamic range of the human visual system).

From the high-luminance colour experiments, we found that if the luminance level increases, then lightness and colourfulness both increase. This confirms the Stevens and Hunt effects. In contrast, if the background luminance level increases, lightness and colourfulness both decrease, confirming the simultaneous contrast effect. Most of our findings are consistent with previous colour appearance data sets under low luminance, and similar trends can be observed in both data sets. However, the previous data sets quantify these colour appearance phenomena to at most three orders of magnitude of luminance (690 $\mathrm{cd/m^2}$), but our data set covers luminance up to five orders of magnitude of luminance (16 860 $\mathrm{cd/m^2}$).

Although our colour appearance data includes fewer different media than previous appearance data and less variation in colour temperature, it covers five orders of magnitude of luminance. The range of the experimental data corresponds to the working range of the human visual system. This experimental data set enables us to derive a novel colour appearance model for an extended range of luminance levels. Accordingly, our numerical model covers the full range of colour perception of the human visual system.

7.3 Colour Appearance Model

A colour appearance model describes a conversion from physical measurements to perceptual quantities. This conversion differs amongst existing CAMs and involves numerical transfer functions that are matched to psychophysical observation data. Our CAM is mainly derived from our observation data under high-luminance levels. Our model is based on two insights. First, the modelling approaches of current CAMs are based on classical colourimetry using relative colour coordinates. As shown in our colour experiments, colour perception changes according to the absolute levels of luminances. Modelling and optimisation in our model were based on absolute-scaled quantities of physical measurements. Second, a physiologically-derived cone response function [Valeton and van Norren, 1983] has been broadly used in existing CAMs. This function has two parameters. One parameter was previously taken from primate measurements. In contrast, our CAM uses this data and optimises the cone model purely based on our high-luminance experimental observations. The other parameter is modelled as a constant in other CAMs and differs amongst existing CAMs. However, through investigation of physiological literature, we found that this parameter should change dynamically according to the level of luminance adaptation, which we adopt in our model. Our cone response function enables us to cover the full working range of the human visual system and to predict the simultaneous contrast effect with various level of luminance adaptation.

As a result, the lightness and colourfulness predictions of our model were statistically significantly better than the predictions of the other models and also very consistent up to high level of luminances. The variation of the predictions on the test data sets reaches that of the psychological measurements. This means that it would be difficult to achieve a better lightness and colourfulness prediction than that from our model. Hue predictions were almost identical with current standard models. Our model was also tested on previous appearance data, which allows us to cross-validate our model's performance on different media such as paper, transparency, or CRT. Our model outperformed the other CAMs even with this data set, presenting similar accuracy to that of our CAM with our high-luminance data set.

Our psychophysical experiments and colour appearance model focused on high-luminance photopic vision rather than mesopic or scotopic vision as our research was motivated by the advent of high-dynamic-range imaging, which deals with higher levels of luminance. Therefore, our model does not include the contribution of rods under dark luminance conditions. Our model also does not take a separate background parameters because we believe that the explicit measurement of luminance in a 10° viewing angle already includes the background luminance level implicitly, which is confirmed in our result variation (measurement data is fitted well by our model). We also do not include a separate surround parameter, as our data and previous experiments (see Section 4.5.8) showed that this parameter has no significant influence on perception.

As is well known from previous research, colour appearance depends on the medium. Considering our research goal, we chose high-luminance and high-dynamic-range media rather than reflective media. Furthermore, our research scope does not include chromatic adaptation experiments, and we rely on previous CAT models. This is a worthwhile area for future study. Eye ball movement and light scattering within the eye may be an interesting direction of study. Our research scope focuses on 2° colour perception (sensed by the fovea, the main concentration of colour receptors, that comprises approximately 2° diameter of the visual field [Hunt, 1998]) rather than 10° perception (sensed by the fovea and rods together before the blind spot in a 10-12° diameter of the visual field). Using 10° observations, reflective media, increasing variation in surround conditions, and mesopic/scotopic-level luminances are all worth future study.

7.4 High-Dynamic-Range Colour Reproduction

Our HDR characterisation method enables us to convert device-dependent HDR images to physically-meaningful radiance maps. Our colour appearance model allows us to convert physical coordinates to perceptually-uniform colour appearance attributes. These perceptual coordinates from the forward application of our model are reproducible on a target medium with new viewing parameters as input. With colour reproduction in mind, we developed all our model equations to have analytical invertibility. Our inverse CAM is able to convert perceptual coordinates back to physical quantities. These physical quantities are easily reproducible using inverse output device characterisation. This completes the pipeline for image reproduction of the real world onto a target medium.

We conducted a series of psychophysical experiments to evaluate accuracy of real-world reproduction. Real scenes were built to be compared with their reproductions. Our reproduction system using the JMh colour connection space outperforms other reproduction methods with statistical significance in all scenes, as our system takes into account perception under high luminance. These experimental results match the previous quantitative results of our CAM for cross-validation.

Our colour reproduction system is fully independent of existing HDR imaging systems. The entire pipeline needs to be used in order to achieve high-fidelity reproduction as our method supersedes existing HDR methods. The scope of this thesis did not include gamut mapping and we use direct 1:1 mapping. This enables the faithful reproduction of the perceived colours with high fidelity. A user preference study, called a gamut mapping algorithm, can be a worthwhile area for future study. In addition, the numerical relationship between the averaged luminance adaptation and its spatial coherence within vision is worth studying in the future.

Chapter 8

Conclusion

The focus of this thesis has been the development of a colour reproduction system for high-dynamic-range imaging, which enables us to reproduce the visual perception of the human visual system on any target medium. With this context, we revisited the key infrastructure of classical colour reproduction elements, reformulating them for high-dynamic-range imaging. We developed an HDR characterisation method that enables us to measure high-dynamic-range radiances to a high accuracy. This method measures the physical radiance values of the real world as an image with significant accuracy, rivaling spectroradiometers. This allows us to obtain physically-meaningful HDR radiance maps with a standard digital camera. However, this is not sufficient for HDR colour reproduction as the given physical colours under high luminance ranges are perceived differently due to their viewing environment conditions. Hence, we built a novel high-luminance display and conducted a psychophysical experiment to measure the perceptual colour attributes under a wide range of luminance levels. This enables us to quantify human perception, covering the full range of the human visual system. A novel colour appearance model was then derived from the experimental data. Our model predicts perceptual colour attributes of lightness and colourfulness under high luminance levels with significant accuracy. This completes the colour reproduction pipeline with respect to high-dynamic-range imaging. Finally, our reproduction system was built on these fundamental contributions, our novel HDR characterisation and colour appearance models. A psychophysical evaluation showed that our HDR reproduction system outperforms other methods with statistical significance. Our colour reproduction system provides high-fidelity colour reproduction for high-dynamic-range imaging.

Appendix A

Supplementals

A.1 Notation

L	Radiance (luminance),	I	Radiant intensity,
F	Luminous flux,	Φ	Radiant power (flux),
B	Radiosity,	P	Spectral power distribution of light,
E	Irradiance (Illuminance),	S	Surface reflectance (or transmittance),
ω_i	Incoming direction,	ω_o	Outgoing direction,
K_m	Maximum photographic luminous efficacy,	$\mathbf{M},\mathbf{N}$	Matrices,
$\mathbf{M}^{-1}$	Inverse matrix,	$\mathbf{M}^{\top}$	Matrix transposition,
$\mathbf{M}\cdot\mathbf{N}$	Matrix multiplication,	λ	Wavelength [nm],
J	Lightness,	M	Colourfulness,
H	Hue quadrature,	Q	Brightness,
C	Chroma,	h	Hue angle,
a_C	Cartesian coordinate of red–green,	b_C	Cartesian coordinate of yellow–blue,
s	Saturation,	A	Achromatic signal,
a	Colour opponent signals of red–green,	b	Colour opponent signals of yellow–blue,
ΔE^*_{ab}	Colour difference in CIELAB,	ΔE_{00}	Colour difference (CIEDE2000).

A.2 Relative Camera Transforms

	Forward transform		
	R	G	B
X	0.5730	0.2459	0.0243
Y	0.2486	0.9000	-0.1486
Z	0.0459	-0.1865	0.9108

	Inverse transform		
	X	Y	Z
R	2.0085	-0.5795	-0.1481
G	-0.5915	1.3206	0.2312
B	-0.2223	0.2996	1.1528

Table A.1: *Relative characterisation for Canon 350D. The forward transform for Canon 350D was computed from reference colour samples and corresponding input radiance.*

A.3 Physical Measurements in HDR Characterisation

Radiometric measurements							Canon 350D measurements				
Index	Patch#	X	Y[cd/m^2]	Z	u’	v’	X	Y[cd/m^2]	Z	u’	v’
1	A1	62.07	55.00	41.80	0.2452	0.4889	61.29	54.78	45.81	0.2403	0.4832
2	A2	74.51	52.30	34.86	0.3093	0.4885	72.08	52.05	38.09	0.2981	0.4844
3	A3	85.72	51.15	30.13	0.3635	0.4880	83.24	53.10	33.44	0.3398	0.4876
4	A4	95.19	43.70	20.02	0.4696	0.4851	97.18	51.87	23.59	0.4109	0.4935
5	A5	249.08	223.40	163.09	0.2436	0.4917	239.85	212.94	165.53	0.2441	0.4876
6	A6	274.88	207.10	133.65	0.2907	0.4928	269.27	208.48	138.88	0.2825	0.4921
7	A7	315.96	201.30	115.16	0.3433	0.4922	309.22	205.33	124.13	0.3288	0.4913
8	A8	351.65	188.70	90.75	0.4072	0.4916	350.27	203.21	103.26	0.3778	0.4932
9	A9	661.76	684.00	507.90	0.2127	0.4946	637.25	660.40	502.79	0.2115	0.4932
10	A10	692.45	671.60	481.01	0.2269	0.4951	672.97	651.20	479.57	0.2266	0.4933
11	A11	707.64	643.60	442.52	0.2422	0.4955	690.25	630.87	452.93	0.2398	0.4932
12	A12	775.76	630.60	396.90	0.2716	0.4967	752.35	624.11	396.62	0.2662	0.4969
13	A13	1536.87	1754.00	1429.26	0.1913	0.4912	1448.50	1679.81	1381.64	0.1882	0.4910
14	A14	1705.22	1876.00	1516.60	0.1983	0.4909	1573.24	1745.80	1374.06	0.1974	0.4928
15	A15	1718.63	1913.00	1403.91	0.1985	0.4972	1625.68	1823.93	1316.89	0.1974	0.4984
16	A16	1691.10	1910.00	1489.51	0.1943	0.4938	1571.64	1796.83	1326.75	0.1934	0.4975
17	A17	1735.75	1914.00	1487.13	0.1989	0.4935	1593.96	1749.30	1339.92	0.2002	0.4943
18	A18	1667.42	1893.00	1375.70	0.1951	0.4983	1470.06	1660.50	1206.57	0.1960	0.4982
19	A19	1635.99	1816.00	1520.63	0.1957	0.4888	1484.88	1654.36	1355.82	0.1956	0.4903
20	A20	139.73	69.14	49.70	0.4215	0.4693	135.13	75.67	52.68	0.3785	0.4768
21	A21	563.15	419.80	314.33	0.2887	0.4842	518.17	391.66	295.22	0.2848	0.4843
22	A22	1129.88	1117.00	680.27	0.2268	0.5045	1027.31	1009.54	633.15	0.2274	0.5028
23	B1	89.74	82.78	51.33	0.2417	0.5016	89.97	82.36	57.19	0.2404	0.4952
24	B2	107.30	84.73	35.98	0.2888	0.5131	106.04	84.60	43.89	0.2815	0.5053
25	B3	125.88	87.83	24.25	0.3321	0.5214	121.11	88.15	31.32	0.3151	0.5161
26	B4	143.16	80.74	2.83	0.4202	0.5332	142.27	86.02	9.81	0.3893	0.5295
27	B5	336.62	316.30	183.19	0.2391	0.5056	327.33	304.71	188.12	0.2397	0.5021
28	B6	365.03	297.90	120.40	0.2811	0.5161	357.58	294.29	132.46	0.2767	0.5124
29	B7	402.06	283.60	74.66	0.3296	0.5230	396.35	286.82	92.62	0.3186	0.5187
30	B8	442.68	260.20	35.90	0.3976	0.5258	440.29	275.90	55.78	0.3711	0.5232
31	B9	810.86	859.30	614.60	0.2087	0.4975	792.55	825.11	606.72	0.2115	0.4954
32	B10	832.46	845.10	540.55	0.2201	0.5027	820.97	823.40	550.50	0.2215	0.4999
33	B11	832.20	807.50	471.41	0.2318	0.5061	822.38	794.46	483.83	0.2318	0.5039
34	B12	922.23	814.50	359.25	0.2595	0.5156	905.39	799.19	373.52	0.2584	0.5133
35	B13	1458.45	1705.00	1462.16	0.1857	0.4884	1402.16	1647.50	1369.41	0.1856	0.4906
36	B14	1544.23	1610.00	1413.15	0.2064	0.4841	1473.92	1555.87	1313.97	0.2050	0.4870
37	B15	1682.46	1887.00	1187.28	0.2006	0.5062	1580.56	1784.79	1124.01	0.1993	0.5063
38	B16	1359.44	1526.00	1196.96	0.1953	0.4933	1323.02	1498.13	1170.19	0.1938	0.4938
39	B17	1566.54	1652.00	1209.22	0.2091	0.4960	1462.77	1537.75	1158.15	0.2089	0.4942
40	B18	1505.11	1783.00	1230.39	0.1885	0.5024	1418.09	1660.18	1162.56	0.1903	0.5013

Table A.2: *Radiometric measurements of training colour samples (transparency) by a spectroradiometer (Jeti Specbos 1200) and Canon 350D measurements by HDR characterisation (bright-side IT8.7/1 – patch index: 1-40).*

Radiometric measurements							Canon 350D measurements				
Index	Patch#	X	Y[cd/m^2]	Z	u'	v'	X	Y[cd/m^2]	Z	u'	v'
41	B19	1438.32	1601.00	1479.45	0.1925	0.4820	1326.12	1478.13	1357.06	0.1924	0.4825
42	B20	123.06	79.54	31.62	0.3489	0.5073	120.28	83.02	40.99	0.3232	0.5020
43	B21	382.46	269.80	100.32	0.3234	0.5133	364.02	259.57	113.29	0.3167	0.5081
44	B22	743.61	678.90	374.95	0.2468	0.5070	687.28	626.56	359.23	0.2463	0.5051
45	C1	179.17	182.90	103.80	0.2216	0.5090	175.59	175.98	110.64	0.2232	0.5032
46	C2	194.16	186.20	69.29	0.2431	0.5245	189.39	180.15	78.38	0.2423	0.5185
47	C3	209.88	189.10	41.30	0.2648	0.5368	202.51	180.43	50.63	0.2646	0.5305
48	C4	221.93	183.00	7.42	0.2970	0.5510	212.04	177.56	12.38	0.2912	0.5487
49	C5	633.05	647.00	323.02	0.2239	0.5150	635.20	635.92	340.53	0.2269	0.5112
50	C6	648.79	621.50	181.47	0.2468	0.5319	654.88	626.96	199.48	0.2458	0.5294
51	C7	682.13	610.00	92.34	0.2699	0.5431	677.16	607.72	109.55	0.2676	0.5404
52	C8	742.59	592.10	13.75	0.3073	0.5513	706.87	564.46	19.64	0.3062	0.5502
53	C9	963.61	1042.00	697.37	0.2063	0.5019	950.18	998.07	709.28	0.2106	0.4977
54	C10	960.63	1018.00	582.37	0.2137	0.5096	942.98	995.44	599.42	0.2134	0.5069
55	C11	973.57	1002.00	475.51	0.2234	0.5174	968.29	983.64	490.16	0.2253	0.5149
56	C12	1054.88	995.20	227.79	0.2532	0.5374	1029.45	983.47	250.09	0.2491	0.5354
57	C13	1371.93	1663.00	1498.88	0.1781	0.4857	1336.75	1649.87	1407.92	0.1764	0.4899
58	C14	1458.92	1449.00	1407.14	0.2129	0.4757	1402.82	1384.45	1351.37	0.2140	0.4751
59	C15	1703.74	1909.00	989.48	0.2046	0.5158	1640.46	1848.88	961.51	0.2034	0.5158
60	C16	1102.99	1233.00	955.53	0.1964	0.4940	1088.48	1194.15	943.90	0.1994	0.4923
61	C17	1387.87	1386.00	959.97	0.2215	0.4978	1340.95	1331.81	940.15	0.2222	0.4966
62	C18	1377.55	1709.00	1051.47	0.1827	0.5099	1327.24	1613.51	1000.99	0.1861	0.5089
63	C19	1226.63	1365.00	1466.04	0.1880	0.4707	1133.42	1253.52	1290.49	0.1904	0.4739
64	C20	309.09	241.30	39.59	0.3055	0.5366	296.64	233.25	54.21	0.2998	0.5304
65	C21	519.28	517.20	265.63	0.2289	0.5130	496.30	486.50	263.16	0.2313	0.5101
66	C22	629.10	567.00	254.77	0.2542	0.5155	586.77	526.34	255.99	0.2537	0.5121
67	D1	121.49	131.20	76.63	0.2095	0.5091	123.57	130.05	84.46	0.2123	0.5028
68	D2	123.00	132.90	49.69	0.2172	0.5279	124.15	131.90	58.35	0.2180	0.5212
69	D3	124.49	136.40	30.18	0.2202	0.5429	127.44	135.97	37.48	0.2236	0.5369
70	D4	124.64	136.90	7.84	0.2264	0.5596	122.64	132.61	10.14	0.2290	0.5571
71	D5	486.96	539.00	271.90	0.2075	0.5167	507.36	553.00	287.39	0.2100	0.5150
72	D6	476.63	532.10	149.27	0.2141	0.5377	479.92	537.68	162.01	0.2126	0.5358
73	D7	453.86	511.60	73.12	0.2175	0.5516	445.41	502.70	79.18	0.2167	0.5502
74	D8	453.52	518.20	17.21	0.2191	0.5634	433.33	489.29	7.30	0.2224	0.5650
75	D9	1111.98	1241.00	613.08	0.2062	0.5179	1081.20	1189.82	627.83	0.2078	0.5145
76	D10	1086.73	1223.00	346.66	0.2123	0.5377	1078.51	1198.42	370.50	0.2139	0.5348
77	D11	1048.63	1185.00	171.48	0.2169	0.5515	1065.41	1188.01	176.34	0.2195	0.5507
78	D12	1060.35	1212.00	67.87	0.2181	0.5610	1019.54	1161.55	47.54	0.2194	0.5625
79	D13	1304.36	1623.00	1522.87	0.1727	0.4834	1288.30	1618.15	1480.31	0.1718	0.4854
80	D14	1387.78	1315.00	1386.15	0.2197	0.4683	1343.14	1272.77	1329.41	0.2200	0.4690

Table A.3: *Radiometric measurements of training colour samples (transparency) by a spectroradiometer (Jeti Specbos 1200) and Canon 350D measurements by HDR characterisation (bright-side IT8.7/1 – patch index: 41-80).*

Radiometric measurements							Canon 350D measurements				
Index	Patch#	X	Y[cd/m^2]	Z	u'	v'	X	Y[cd/m^2]	Z	u'	v'
81	D15	1689.15	1897.00	798.97	0.2076	0.5247	1691.36	1923.33	795.53	0.2055	0.5257
82	D16	840.61	936.20	712.42	0.1975	0.4950	861.79	933.98	721.79	0.2023	0.4934
83	D17	1225.97	1153.00	726.33	0.2369	0.5013	1219.78	1136.97	750.30	0.2377	0.4985
84	D18	1259.78	1616.00	842.58	0.1798	0.5189	1212.71	1530.33	831.40	0.1819	0.5166
85	D19	1036.21	1149.00	1395.34	0.1846	0.4605	977.00	1085.54	1290.35	0.1849	0.4623
86	D20	83.71	87.95	38.04	0.2207	0.5218	87.66	87.92	47.72	0.2263	0.5106
87	D21	754.43	750.40	43.67	0.2485	0.5562	702.43	695.24	46.44	0.2493	0.5552
88	D22	981.35	1142.00	1369.00	0.1767	0.4626	877.69	1012.16	1230.30	0.1777	0.4612
89	E1	166.93	194.60	111.49	0.1952	0.5120	170.41	193.09	123.02	0.1984	0.5058
90	E2	156.30	197.00	73.29	0.1877	0.5322	158.53	191.51	86.67	0.1927	0.5237
91	E3	142.09	198.20	46.45	0.1746	0.5481	145.52	194.63	53.74	0.1804	0.5430
92	E4	131.04	207.00	12.33	0.1601	0.5692	129.32	201.89	7.33	0.1627	0.5714
93	E5	695.18	835.70	429.02	0.1915	0.5181	724.04	847.47	458.36	0.1955	0.5150
94	E6	613.05	804.10	266.13	0.1820	0.5371	636.36	814.45	288.34	0.1856	0.5343
95	E7	559.20	801.90	151.07	0.1715	0.5534	565.34	806.92	145.84	0.1725	0.5541
96	E8	507.96	787.20	81.79	0.1618	0.5640	500.57	778.51	63.27	0.1619	0.5665
97	E9	1102.24	1277.00	815.66	0.1942	0.5062	1095.99	1269.32	807.86	0.1943	0.5064
98	E10	1024.48	1247.00	618.44	0.1899	0.5199	1035.48	1240.58	659.16	0.1916	0.5164
99	E11	956.07	1213.00	485.20	0.1856	0.5298	989.63	1258.73	515.00	0.1848	0.5290
100	E12	915.95	1239.00	343.54	0.1784	0.5431	914.79	1226.43	352.79	0.1796	0.5419
101	E13	1235.53	1577.00	1531.82	0.1676	0.4813	1240.89	1599.82	1525.77	0.1665	0.4829
102	E14	1283.05	1152.00	1319.84	0.2279	0.4603	1281.34	1147.15	1273.59	0.2297	0.4628
103	E15	1683.11	1885.00	655.51	0.2109	0.5314	1698.82	1909.29	690.20	0.2097	0.5302
104	E16	634.64	706.20	542.36	0.1975	0.4944	656.85	718.90	572.47	0.1997	0.4917
105	E17	1075.93	945.60	559.26	0.2541	0.5025	1080.41	954.86	573.35	0.2524	0.5019
106	E18	1141.92	1508.00	684.15	0.1769	0.5258	1136.84	1484.65	696.13	0.1784	0.5241
107	E19	862.38	949.40	1329.85	0.1807	0.4475	836.24	888.61	1298.54	0.1852	0.4428
108	E20	198.26	249.80	47.47	0.1940	0.5500	193.42	236.08	55.18	0.1984	0.5448
109	E21	622.21	790.20	166.41	0.1918	0.5481	598.15	751.87	168.19	0.1933	0.5466
110	E22	246.03	498.90	339.87	0.1125	0.5132	254.58	482.17	344.01	0.1195	0.5094
111	F1	112.89	143.10	103.19	0.1758	0.5013	121.64	145.14	118.25	0.1834	0.4923
112	F2	95.31	143.30	86.56	0.1522	0.5150	107.49	148.67	100.25	0.1630	0.5072
113	F3	80.48	144.30	79.26	0.1297	0.5231	92.86	150.92	94.60	0.1407	0.5144
114	F4	60.92	143.00	62.22	0.1018	0.5379	74.92	152.21	74.99	0.1160	0.5303
115	F5	338.96	446.50	304.10	0.1706	0.5056	355.91	456.71	321.66	0.1742	0.5030
116	F6	279.85	450.80	257.52	0.1432	0.5192	292.35	448.31	274.59	0.1491	0.5146
117	F7	223.50	438.80	209.72	0.1202	0.5312	242.63	445.39	231.45	0.1274	0.5262
118	F8	195.05	415.00	190.33	0.1116	0.5343	223.23	438.11	208.86	0.1203	0.5313
119	F9	763.00	930.40	671.02	0.1824	0.5005	781.09	922.97	712.24	0.1864	0.4956
120	F10	671.47	912.20	602.81	0.1662	0.5079	684.98	907.85	628.39	0.1693	0.5047

Table A.4: *Radiometric measurements of training colour samples (transparency) by a spectroradiometer (Jeti Specbos 1200) and Canon 350D measurements by HDR characterisation (bright-side IT8.7/1 – patch index: 81-120).*

Radiometric measurements							Canon 350D measurements				
Index	Patch#	X	Y[cd/m^2]	Z	u’	v’	X	Y[cd/m^2]	Z	u’	v’
121	F11	592.91	893.40	531.76	0.1521	0.5158	622.86	900.07	566.22	0.1575	0.5120
122	F12	534.95	908.50	494.07	0.1368	0.5226	565.07	923.74	510.28	0.1417	0.5212
123	F13	1178.32	1536.00	1548.79	0.1633	0.4789	1200.79	1560.33	1588.86	0.1635	0.4781
124	F14	1185.38	1007.00	1264.54	0.2361	0.4513	1194.98	1006.96	1247.57	0.2385	0.4522
125	F15	1696.57	1896.00	536.35	0.2138	0.5375	1708.62	1903.50	583.49	0.2135	0.5352
126	F16	461.95	510.20	394.57	0.1987	0.4938	483.94	525.73	414.17	0.2014	0.4922
127	F17	936.69	763.20	410.73	0.2752	0.5044	950.98	785.90	449.81	0.2700	0.5020
128	F18	1048.87	1437.00	570.28	0.1725	0.5319	1039.24	1394.73	591.17	0.1752	0.5289
129	F19	694.75	757.00	1243.16	0.1761	0.4318	664.59	724.49	1204.24	0.1755	0.4305
130	F20	51.06	99.19	25.21	0.1265	0.5529	57.06	99.10	32.55	0.1391	0.5434
131	F21	154.58	330.70	58.45	0.1169	0.5626	155.28	316.83	60.11	0.1221	0.5604
132	F22	269.93	522.30	77.40	0.1295	0.5639	252.66	478.50	74.16	0.1321	0.5627
133	G1	80.90	99.24	87.57	0.1766	0.4875	92.68	105.25	104.84	0.1867	0.4770
134	G2	72.62	102.00	93.73	0.1542	0.4873	83.81	108.39	108.96	0.1646	0.4790
135	G3	61.55	98.86	97.24	0.1341	0.4846	73.93	106.21	111.76	0.1477	0.4774
136	G4	45.36	99.00	107.80	0.0979	0.4806	59.85	108.63	123.62	0.1162	0.4746
137	G5	351.40	449.90	382.65	0.1704	0.4909	383.97	475.87	415.95	0.1751	0.4884
138	G6	296.98	453.40	406.54	0.1428	0.4906	317.34	465.07	426.65	0.1481	0.4882
139	G7	238.79	430.10	412.58	0.1205	0.4883	265.97	444.93	441.52	0.1287	0.4845
140	G8	210.96	416.50	415.35	0.1095	0.4865	243.13	449.79	434.12	0.1173	0.4882
141	G9	780.10	948.10	768.12	0.1803	0.4931	799.67	954.41	793.48	0.1828	0.4909
142	G10	693.74	936.00	800.17	0.1620	0.4916	709.41	929.82	840.02	0.1652	0.4872
143	G11	619.27	916.90	816.67	0.1472	0.4905	650.70	944.52	852.65	0.1498	0.4892
144	G12	551.84	921.90	847.84	0.1304	0.4903	586.80	936.04	881.49	0.1359	0.4878
145	G13	1126.68	1500.00	1567.95	0.1591	0.4765	1156.75	1563.62	1606.01	0.1572	0.4782
146	G14	1099.24	882.90	1204.07	0.2449	0.4426	1100.98	889.21	1197.54	0.2442	0.4438
147	G15	1705.58	1899.00	441.87	0.2165	0.5423	1727.77	1930.67	471.30	0.2153	0.5413
148	G16	317.72	347.80	277.54	0.1996	0.4916	341.25	367.02	301.73	0.2022	0.4892
149	G17	803.82	603.50	283.15	0.3003	0.5073	858.41	661.52	325.43	0.2920	0.5064
150	G18	961.86	1357.00	461.88	0.1695	0.5380	978.34	1350.04	482.19	0.1726	0.5358
151	G19	560.46	599.10	1167.94	0.1718	0.4131	542.10	576.68	1138.06	0.1720	0.4117
152	G20	91.73	194.40	74.01	0.1136	0.5417	107.05	199.72	89.56	0.1270	0.5331
153	G21	160.71	281.90	204.10	0.1285	0.5073	174.85	286.56	212.05	0.1369	0.5048
154	G22	43.63	57.57	112.89	0.1401	0.4159	48.60	59.87	115.41	0.1504	0.4168
155	H1	83.92	98.83	104.05	0.1787	0.4735	94.37	105.13	120.30	0.1857	0.4656
156	H2	76.46	99.52	129.49	0.1562	0.4575	89.08	107.10	146.45	0.1669	0.4515
157	H3	70.79	100.60	160.63	0.1373	0.4392	82.69	107.50	173.53	0.1493	0.4366
158	H4	57.29	97.82	216.68	0.1054	0.4048	71.67	105.60	237.61	0.1210	0.4013
159	H5	291.72	354.90	382.37	0.1726	0.4723	321.18	375.05	415.57	0.1786	0.4692
160	H6	265.90	356.40	473.30	0.1513	0.4562	284.66	372.42	489.74	0.1551	0.4566

Table A.5: *Radiometric measurements of training colour samples (transparency) by a spectroradiometer (Jeti Specbos 1200) and Canon 350D measurements by HDR characterisation (bright-side IT8.7/1 – patch index: 121-160).*

Radiometric measurements							Canon 350D measurements				
Index	Patch#	X	Y[cd/m^2]	Z	u'	v'	X	Y[cd/m^2]	Z	u'	v'
161	H7	230.30	346.60	574.60	0.1288	0.4361	253.25	360.26	609.16	0.1353	0.4332
162	H8	205.73	337.30	662.90	0.1134	0.4185	235.38	356.66	695.37	0.1227	0.4184
163	H9	824.06	947.40	830.57	0.1881	0.4865	862.10	974.58	877.41	0.1904	0.4842
164	H10	784.93	944.00	940.00	0.1767	0.4782	808.49	964.29	950.66	0.1784	0.4788
165	H11	734.91	919.10	1019.35	0.1672	0.4705	754.51	924.36	1048.25	0.1699	0.4683
166	H12	669.74	934.10	1340.06	0.1432	0.4495	682.44	943.45	1349.61	0.1446	0.4497
167	H13	1069.91	1451.00	1576.80	0.1553	0.4737	1118.34	1534.94	1654.95	0.1537	0.4746
168	H14	1011.17	768.10	1145.72	0.2533	0.4329	1031.46	782.48	1179.18	0.2530	0.4319
169	H15	1713.50	1891.00	340.02	0.2204	0.5473	1774.26	1970.11	360.56	0.2190	0.5471
170	H16	209.19	229.20	181.07	0.1997	0.4923	234.14	248.20	202.91	0.2051	0.4892
171	H17	697.70	483.00	186.80	0.3282	0.5112	740.46	532.62	222.56	0.3152	0.5101
172	H18	860.00	1240.00	339.02	0.1680	0.5450	886.76	1244.10	369.30	0.1717	0.5421
173	H19	445.52	466.30	1086.04	0.1666	0.3923	436.78	447.37	1070.55	0.1687	0.3887
174	H20	48.51	74.83	101.78	0.1314	0.4562	58.40	80.36	114.86	0.1452	0.4497
175	H21	140.05	240.30	315.37	0.1194	0.4611	154.78	243.15	333.56	0.1289	0.4556
176	H22	41.19	20.08	48.10	0.3385	0.3713	43.33	23.55	48.35	0.3200	0.3913
177	I1	132.74	142.70	196.45	0.1855	0.4486	145.45	150.52	211.75	0.1915	0.4458
178	I2	136.91	146.10	294.68	0.1705	0.4093	144.85	150.52	298.23	0.1757	0.4108
179	I3	137.41	145.70	431.45	0.1519	0.3625	143.13	144.51	443.51	0.1572	0.3572
180	I4	134.93	141.40	647.85	0.1285	0.3030	132.45	128.08	654.95	0.1318	0.2869
181	I5	429.58	469.50	487.10	0.1923	0.4730	445.20	483.29	523.63	0.1922	0.4694
182	I6	426.45	462.70	627.40	0.1844	0.4502	452.61	472.03	672.86	0.1895	0.4448
183	I7	416.76	449.10	751.36	0.1772	0.4297	433.31	467.80	774.18	0.1774	0.4308
184	I8	404.57	429.40	1032.99	0.1627	0.3886	405.47	433.30	1038.51	0.1619	0.3892
185	I9	881.06	971.30	882.15	0.1947	0.4830	926.56	990.60	938.21	0.1993	0.4793
186	I10	860.63	949.80	967.58	0.1911	0.4746	907.80	979.38	1010.70	0.1949	0.4731
187	I11	848.50	930.50	1038.99	0.1894	0.4672	906.02	978.68	1101.71	0.1918	0.4663
188	I12	853.30	924.00	1323.37	0.1827	0.4451	884.04	951.10	1347.22	0.1842	0.4460
189	I13	1022.52	1410.00	1553.91	0.1524	0.4729	1083.06	1519.05	1592.33	0.1512	0.4773
190	I14	934.79	673.80	1073.73	0.2622	0.4252	960.37	699.42	1082.76	0.2613	0.4282
191	I15	1671.97	1838.00	263.38	0.2227	0.5508	1750.36	1924.76	269.29	0.2228	0.5512
192	I16	126.32	138.70	111.37	0.1989	0.4913	146.51	154.33	132.14	0.2051	0.4860
193	I17	600.47	381.90	115.99	0.3597	0.5148	655.83	434.16	151.66	0.3441	0.5126
194	I18	786.28	1169.00	262.09	0.1646	0.5506	805.83	1165.98	276.49	0.1685	0.5487
195	I19	353.49	361.50	988.59	0.1617	0.3722	341.54	352.01	948.85	0.1613	0.3741
196	I20	199.38	249.00	472.13	0.1490	0.4188	203.04	244.08	474.10	0.1536	0.4155
197	I21	308.62	433.00	769.73	0.1355	0.4276	315.90	425.24	784.04	0.1397	0.4230
198	I22	22.83	23.38	3.34	0.2381	0.5486	26.92	27.41	7.55	0.2337	0.5355
199	J1	44.84	40.54	75.05	0.2043	0.4155	52.54	46.85	84.15	0.2085	0.4184
200	J2	52.62	39.51	132.74	0.2017	0.3408	55.25	42.54	129.87	0.2041	0.3535

Table A.6: *Radiometric measurements of training colour samples (transparency) by a spectroradiometer (Jeti Specbos 1200) and Canon 350D measurements by HDR characterisation (bright-side IT8.7/1 – patch index: 161-200).*

Radiometric measurements							Canon 350D measurements				
Index	Patch#	X	Y[cd/m^2]	Z	u’	v’	X	Y[cd/m^2]	Z	u’	v’
201	J3	59.79	37.27	225.62	0.1846	0.2589	56.18	32.80	217.08	0.1874	0.2461
202	J4	69.08	35.27	365.91	0.1629	0.1872	54.28	19.49	341.07	0.1585	0.1280
203	J5	265.59	267.20	316.28	0.2034	0.4605	291.33	282.80	345.34	0.2092	0.4570
204	J6	292.03	272.70	441.92	0.2046	0.4300	319.86	291.41	472.28	0.2095	0.4294
205	J7	305.00	263.50	562.40	0.2052	0.3989	308.07	267.16	563.68	0.2052	0.4003
206	J8	333.18	253.70	812.46	0.2027	0.3472	326.19	234.90	813.02	0.2075	0.3362
207	J9	759.97	820.60	751.34	0.1984	0.4820	804.34	854.33	790.69	0.2012	0.4808
208	J10	768.36	810.00	828.78	0.1995	0.4732	816.04	851.79	902.29	0.2003	0.4703
209	J11	772.41	787.00	913.88	0.2017	0.4624	815.60	818.59	988.11	0.2032	0.4588
210	J12	818.59	771.50	1229.72	0.2036	0.4318	833.62	782.34	1247.38	0.2044	0.4317
211	J13	1002.69	1406.00	1592.45	0.1493	0.4709	1052.99	1482.59	1631.95	0.1494	0.4734
212	J14	867.42	593.20	1012.07	0.2710	0.4170	912.05	630.23	1047.55	0.2701	0.4199
213	J15	1671.11	1813.00	191.89	0.2270	0.5542	1731.78	1893.32	188.06	0.2257	0.5551
214	J16	66.18	72.04	59.91	0.1996	0.4888	82.77	86.03	74.73	0.2073	0.4847
215	J17	497.63	286.00	61.53	0.4003	0.5177	550.09	338.13	95.39	0.3724	0.5151
216	J18	725.19	1092.00	187.21	0.1642	0.5563	743.39	1087.54	192.53	0.1686	0.5551
217	J19	276.44	272.10	898.80	0.1567	0.3471	265.05	251.48	903.87	0.1571	0.3354
218	J20	37.88	15.55	210.57	0.1678	0.1550	28.97	7.98	191.68	0.1601	0.0992
219	J21	255.08	239.60	544.35	0.1861	0.3934	263.22	237.69	557.16	0.1914	0.3889
220	J22	16.17	26.03	4.46	0.1540	0.5578	20.63	30.06	8.16	0.1664	0.5454
221	K1	73.64	65.53	78.97	0.2277	0.4559	82.25	73.76	90.12	0.2255	0.4550
222	K2	90.37	64.78	109.79	0.2598	0.4190	95.93	71.11	114.70	0.2547	0.4248
223	K3	102.26	59.56	141.44	0.2881	0.3775	105.97	62.86	141.43	0.2877	0.3840
224	K4	122.02	53.94	190.48	0.3248	0.3231	126.41	58.13	179.59	0.3289	0.3404
225	K5	218.69	196.30	230.31	0.2270	0.4584	241.41	214.10	255.12	0.2289	0.4568
226	K6	264.42	196.00	310.93	0.2557	0.4264	280.97	212.31	325.09	0.2531	0.4303
227	K7	296.17	183.40	385.93	0.2817	0.3925	309.65	195.02	392.13	0.2808	0.3979
228	K8	340.63	167.10	512.42	0.3108	0.3430	347.59	174.36	485.53	0.3146	0.3551
229	K9	667.09	674.00	634.29	0.2104	0.4784	728.41	719.45	686.13	0.2146	0.4769
230	K10	700.97	653.10	709.43	0.2221	0.4655	739.83	690.84	760.59	0.2211	0.4645
231	K11	748.80	641.10	816.99	0.2337	0.4502	787.05	671.11	868.82	0.2339	0.4487
232	K12	858.20	620.60	1054.26	0.2575	0.4190	881.03	642.22	1052.65	0.2578	0.4228
233	K13	968.57	1369.00	1580.58	0.1476	0.4695	1022.28	1448.70	1658.80	0.1475	0.4702
234	K14	806.35	529.70	956.03	0.2776	0.4103	831.43	564.50	976.50	0.2720	0.4155
235	K15	1652.55	1761.00	130.42	0.2323	0.5569	1702.16	1818.10	126.47	0.2320	0.5575
236	K16	30.57	33.73	27.86	0.1972	0.4896	42.57	44.27	38.04	0.2075	0.4854
237	K17	411.75	216.40	27.61	0.4403	0.5207	458.80	265.31	53.11	0.3992	0.5193
238	K18	666.77	1006.00	123.98	0.1654	0.5614	683.95	1014.76	119.98	0.1682	0.5615
239	K19	226.41	215.20	832.51	0.1522	0.3254	219.78	205.20	833.96	0.1516	0.3184
240	K20	102.89	58.06	207.69	0.2577	0.3272	101.27	57.67	198.77	0.2592	0.3322

Table A.7: *Radiometric measurements of training colour samples (transparency) by a spectroradiometer (Jeti Specbos 1200) and Canon 350D measurements by HDR characterisation (bright-side IT8.7/1 – patch index: 201-240).*

Radiometric measurements							Canon 350D measurements				
Index	Patch#	X	Y[cd/m^2]	Z	u’	v’	X	Y[cd/m^2]	Z	u’	v’
241	K21	411.55	324.90	654.39	0.2271	0.4034	406.68	319.03	649.37	0.2278	0.4021
242	K22	15.72	31.86	48.76	0.0983	0.4481	24.24	38.31	57.47	0.1257	0.4470
243	L1	75.29	68.07	65.25	0.2331	0.4741	86.87	79.15	77.53	0.2306	0.4728
244	L2	93.20	67.66	70.06	0.2828	0.4619	102.06	76.47	79.55	0.2744	0.4626
245	L3	102.08	61.10	71.55	0.3311	0.4459	114.43	71.81	84.61	0.3167	0.4471
246	L4	116.20	53.21	72.67	0.4105	0.4229	131.08	68.03	76.46	0.3797	0.4434
247	L5	223.18	196.80	186.49	0.2390	0.4743	254.42	222.59	217.29	0.2397	0.4719
248	L6	274.74	193.10	202.42	0.2908	0.4599	299.60	214.79	222.51	0.2861	0.4615
249	L7	308.87	176.20	208.09	0.3455	0.4434	333.28	198.60	226.27	0.3340	0.4478
250	L8	344.20	163.30	219.58	0.3988	0.4257	376.84	197.45	225.30	0.3755	0.4427
251	L9	666.78	675.90	556.44	0.2138	0.4876	712.67	716.63	605.43	0.2147	0.4857
252	L10	717.37	662.50	579.61	0.2315	0.4811	772.99	709.17	640.13	0.2319	0.4788
253	L11	754.65	634.20	595.51	0.2504	0.4735	823.16	694.27	656.67	0.2493	0.4731
254	L12	833.94	613.60	623.33	0.2801	0.4638	920.09	685.24	681.89	0.2779	0.4656
255	L13	879.10	1281.00	1530.48	0.1424	0.4670	948.62	1376.78	1614.36	0.1435	0.4686
256	L14	634.14	360.00	768.83	0.3041	0.3885	683.15	396.73	786.15	0.3039	0.3971
257	L15	1580.28	1579.00	41.61	0.2490	0.5597	1647.26	1640.83	9.52	0.2506	0.5618
258	L16	0.91	0.87	0.84	0.2209	0.4751	6.84	6.66	3.79	0.2315	0.5075
259	L17	209.71	92.58	1.15	0.5237	0.5202	240.90	126.38	15.12	0.4416	0.5213
260	L18	540.56	783.50	33.12	0.1745	0.5690	544.67	792.46	0.02	0.1753	0.5737
261	L19	116.62	90.08	580.72	0.1453	0.2526	106.20	74.49	565.06	0.1456	0.2297
262	L20	158.68	85.98	148.30	0.3352	0.4087	169.72	97.57	151.91	0.3250	0.4204
263	L21	416.18	326.20	363.01	0.2602	0.4588	439.78	342.93	381.95	0.2614	0.4586
264	L22	48.63	28.06	2.01	0.4090	0.5310	54.38	34.67	7.22	0.3650	0.5235
265	Dmin	2119.82	2346.00	1816.99	0.1983	0.4938	2179.67	2556.41	1877.51	0.1889	0.4985
266	N1	1660.37	1848.00	1455.37	0.1968	0.4929	1743.47	2010.82	1550.42	0.1908	0.4950
267	N2	1511.22	1690.00	1347.91	0.1956	0.4922	1616.26	1845.68	1383.88	0.1933	0.4965
268	N3	1361.14	1524.00	1217.15	0.1953	0.4921	1428.66	1626.15	1244.10	0.1934	0.4952
269	N4	1168.89	1299.00	1029.69	0.1969	0.4924	1232.35	1371.09	1122.58	0.1959	0.4903
270	N5	988.05	1098.00	885.53	0.1965	0.4913	1090.82	1202.39	942.53	0.1987	0.4929
271	N6	855.00	950.00	769.53	0.1964	0.4910	940.16	1023.24	866.59	0.1991	0.4876
272	N7	705.68	785.60	640.03	0.1959	0.4907	791.58	857.17	721.40	0.2002	0.4878
273	N8	597.38	663.00	532.48	0.1968	0.4915	668.50	729.19	596.34	0.1996	0.4899
274	N9	498.70	556.10	459.63	0.1952	0.4898	552.69	607.39	519.64	0.1970	0.4871
275	N10	413.79	459.60	385.10	0.1956	0.4888	462.07	504.43	433.62	0.1981	0.4866
276	N11	336.89	372.00	317.60	0.1962	0.4874	370.12	404.84	352.77	0.1974	0.4857
277	N12	263.65	291.40	247.04	0.1962	0.4879	301.92	323.45	277.69	0.2017	0.4863
278	N13	216.97	240.40	206.35	0.1954	0.4871	239.73	254.51	235.83	0.2012	0.4807
279	N14	174.66	194.30	161.92	0.1954	0.4892	199.72	215.84	192.45	0.1990	0.4839
280	N15	135.74	150.10	129.26	0.1957	0.4868	159.53	170.08	153.55	0.2012	0.4827

Table A.8: *Radiometric measurements of training colour samples (transparency) by a spectroradiometer (Jeti Specbos 1200) and Canon 350D measurements by HDR characterisation (bright-side IT8.7/1 – patch index: 241-280).*

Radiometric measurements							Canon 350D measurements				
Index	Patch#	X	Y[cd/m^2]	Z	u'	v'	X	Y[cd/m^2]	Z	u'	v'
281	N16	101.13	111.10	95.53	0.1969	0.4868	117.16	123.88	115.94	0.2017	0.4799
282	N17	74.20	81.02	69.83	0.1980	0.4864	87.47	92.46	86.23	0.2019	0.4802
283	N18	52.18	56.92	48.01	0.1988	0.4879	62.74	65.75	61.97	0.2032	0.4792
284	N19	35.01	38.32	32.24	0.1982	0.4881	41.46	44.40	40.89	0.1998	0.4814
285	N20	20.50	22.47	19.10	0.1977	0.4875	26.74	28.32	26.51	0.2014	0.4799
286	N21	13.02	14.29	12.67	0.1962	0.4846	17.58	18.72	18.05	0.1995	0.4779
287	N22	5.23	5.71	5.06	0.1971	0.4846	9.03	9.50	9.12	0.2018	0.4779
288	Dmax	0.83	0.80	0.79	0.2176	0.4732	3.67	3.78	3.31	0.2086	0.4840
289	A1	0.92	0.88	0.57	0.2325	0.5003	1.68	1.64	1.21	0.2236	0.4939
290	A2	0.97	0.72	0.39	0.2998	0.5008	1.86	1.58	1.11	0.2579	0.4923
291	A3	1.20	0.77	0.38	0.3456	0.4989	2.09	1.62	1.03	0.2845	0.4945
292	A4	1.37	0.66	0.32	0.4481	0.4857	2.36	1.56	0.85	0.3323	0.4961
293	A5	3.62	3.48	2.23	0.2316	0.5010	5.14	4.91	3.41	0.2311	0.4964
294	A6	4.13	3.31	1.96	0.2769	0.4993	5.78	4.81	3.03	0.2659	0.4975
295	A7	4.48	2.98	1.63	0.3314	0.4960	6.37	4.68	2.74	0.3009	0.4967
296	A8	5.19	2.83	1.34	0.4019	0.4930	7.42	4.75	2.45	0.3448	0.4971
297	A9	10.58	11.65	7.83	0.2027	0.5021	13.71	14.68	9.97	0.2079	0.5008
298	A10	11.27	11.67	7.68	0.2153	0.5017	14.03	14.42	9.40	0.2171	0.5020
299	A11	11.80	11.50	7.38	0.2286	0.5014	14.41	14.07	8.87	0.2287	0.5024
300	A12	12.48	10.81	6.34	0.2578	0.5024	15.88	13.95	8.35	0.2538	0.5019
301	A13	27.62	33.27	24.14	0.1844	0.4998	32.10	38.21	26.37	0.1876	0.5025
302	A14	30.43	35.29	24.74	0.1920	0.5010	34.79	39.95	26.02	0.1954	0.5049
303	A15	31.86	37.45	24.29	0.1912	0.5057	35.08	40.98	25.85	0.1929	0.5071
304	A16	32.12	38.27	25.74	0.1880	0.5040	33.54	39.80	25.11	0.1901	0.5074
305	A17	31.28	36.36	24.81	0.1922	0.5026	35.74	40.51	26.43	0.1978	0.5045
306	A18	30.43	36.41	23.30	0.1883	0.5069	34.64	40.87	25.43	0.1913	0.5081
307	A19	30.60	35.67	25.99	0.1902	0.4988	32.90	38.25	26.86	0.1915	0.5009
308	A20	1.95	0.99	0.66	0.4153	0.4744	3.28	2.17	1.49	0.3250	0.4848
309	A21	8.96	7.07	5.08	0.2752	0.4885	11.58	9.30	6.64	0.2708	0.4895
310	A22	19.60	20.59	11.51	0.2160	0.5105	22.64	23.34	13.08	0.2198	0.5099
311	B1	1.20	1.18	0.62	0.2312	0.5116	1.99	2.00	1.24	0.2233	0.5039
312	B2	1.41	1.19	0.41	0.2753	0.5227	2.31	2.08	1.00	0.2533	0.5128
313	B3	1.61	1.21	0.30	0.3117	0.5271	2.60	2.10	0.87	0.2833	0.5148
314	B4	1.92	1.16	0.12	0.3902	0.5305	2.91	2.06	0.52	0.3302	0.5239
315	B5	4.86	4.88	2.50	0.2272	0.5133	6.50	6.54	3.53	0.2257	0.5109
316	B6	5.11	4.48	1.54	0.2657	0.5241	7.08	6.24	2.59	0.2612	0.5179
317	B7	5.49	4.13	0.94	0.3126	0.5290	7.70	6.04	1.89	0.2962	0.5229
318	B8	6.52	3.96	0.46	0.3875	0.5296	8.82	5.94	1.29	0.3465	0.5252
319	B9	12.46	14.01	9.13	0.1994	0.5044	15.64	17.43	10.72	0.2022	0.5073
320	B10	13.35	14.44	8.40	0.2093	0.5093	16.26	17.37	9.88	0.2122	0.5102

Table A.9: *Radiometric measurements of training colour samples (transparency) by a spectroradiometer (Jeti Specbos 1200) and Canon 350D measurements by HDR characterisation (bright-side IT8.7/1 – patch index: 281-288 and dark-side – patch index: 289-320).*

Radiometric measurements							Canon 350D measurements				
Index	Patch#	X	Y[cd/m^2]	Z	u'	v'	X	Y[cd/m^2]	Z	u'	v'
321	B11	13.22	13.72	7.33	0.2194	0.5123	16.68	17.28	9.01	0.2203	0.5134
322	B12	14.17	13.37	5.35	0.2456	0.5214	18.21	17.30	7.04	0.2437	0.5210
323	B13	27.26	33.52	24.99	0.1802	0.4986	28.82	34.98	25.42	0.1830	0.4999
324	B14	27.51	30.31	23.70	0.1989	0.4931	29.94	32.45	24.22	0.2032	0.4955
325	B15	30.06	35.56	19.33	0.1935	0.5150	32.55	38.27	20.35	0.1950	0.5159
326	B16	24.34	28.76	19.78	0.1890	0.5025	27.17	31.56	21.53	0.1923	0.5026
327	B17	27.69	30.96	20.05	0.2006	0.5046	30.12	33.06	20.89	0.2046	0.5054
328	B18	27.18	33.70	20.50	0.1830	0.5105	29.48	35.45	21.81	0.1881	0.5091
329	B19	25.33	29.55	24.09	0.1873	0.4917	27.33	31.35	25.20	0.1907	0.4922
330	B20	1.71	1.12	0.40	0.3470	0.5114	2.81	2.22	1.11	0.2849	0.5066
331	B21	5.51	4.13	1.40	0.3076	0.5187	7.33	5.73	2.33	0.2925	0.5144
332	B22	11.46	11.15	5.76	0.2339	0.5120	13.91	13.40	7.04	0.2359	0.5109
333	C1	2.33	2.58	1.22	0.2085	0.5196	3.36	3.54	2.03	0.2148	0.5093
334	C2	2.45	2.53	0.78	0.2293	0.5328	3.54	3.58	1.46	0.2298	0.5229
335	C3	2.68	2.59	0.45	0.2500	0.5436	3.76	3.67	0.97	0.2438	0.5350
336	C4	2.85	2.56	0.12	0.2740	0.5537	4.00	3.67	0.46	0.2651	0.5464
337	C5	9.02	9.86	4.20	0.2128	0.5235	11.36	12.17	5.59	0.2157	0.5199
338	C6	9.28	9.54	2.39	0.2327	0.5381	11.94	12.20	3.29	0.2332	0.5361
339	C7	9.56	9.18	1.13	0.2538	0.5484	12.19	11.68	1.97	0.2522	0.5438
340	C8	10.70	9.20	0.27	0.2863	0.5538	13.01	11.25	0.66	0.2832	0.5511
341	C9	14.64	16.77	10.00	0.1977	0.5096	17.89	20.04	12.31	0.2013	0.5075
342	C10	14.74	16.57	8.50	0.2042	0.5164	17.76	19.84	10.06	0.2055	0.5168
343	C11	14.63	16.17	6.92	0.2105	0.5236	18.11	19.55	8.27	0.2155	0.5234
344	C12	15.94	16.18	3.08	0.2380	0.5436	19.48	19.46	4.31	0.2402	0.5400
345	C13	22.28	28.26	22.41	0.1736	0.4954	25.91	32.58	23.98	0.1767	0.4999
346	C14	22.87	23.96	21.22	0.2051	0.4836	26.81	27.87	23.38	0.2082	0.4871
347	C15	28.68	34.55	15.29	0.1935	0.5245	32.45	38.06	16.77	0.1986	0.5240
348	C16	18.04	21.24	14.68	0.1896	0.5022	20.60	23.98	16.07	0.1923	0.5037
349	C17	22.36	23.66	14.76	0.2122	0.5051	25.95	27.01	16.41	0.2161	0.5061
350	C18	23.42	30.35	16.03	0.1778	0.5185	26.57	34.12	17.49	0.1799	0.5197
351	C19	19.95	23.22	22.04	0.1837	0.4811	22.00	25.38	23.19	0.1863	0.4837
352	C20	4.21	3.53	0.39	0.2887	0.5447	5.74	4.99	1.11	0.2734	0.5352
353	C21	7.55	7.99	3.71	0.2180	0.5191	9.68	10.07	4.83	0.2210	0.5172
354	C22	9.20	8.87	3.66	0.2402	0.5210	11.11	10.67	4.49	0.2407	0.5201
355	D1	1.58	1.83	0.84	0.2003	0.5220	2.36	2.63	1.48	0.2041	0.5116
356	D2	1.49	1.68	0.44	0.2128	0.5398	2.38	2.62	1.06	0.2118	0.5258
357	D3	1.55	1.80	0.33	0.2099	0.5484	2.41	2.76	0.78	0.2092	0.5383
358	D4	1.58	1.88	0.16	0.2089	0.5592	2.43	2.81	0.39	0.2123	0.5529
359	D5	6.67	7.84	3.43	0.1983	0.5244	8.42	9.87	4.31	0.1987	0.5244
360	D6	6.42	7.70	1.72	0.2021	0.5453	8.28	9.63	2.49	0.2067	0.5411

Table A.10: *Radiometric measurements of training colour samples (transparency) by a spectroradiometer (Jeti Specbos 1200) and Canon 350D measurements by HDR characterisation (dark-side IT8.7/1 – patch index: 321-360).*

Radiometric measurements							Canon 350D measurements				
Index	Patch#	X	Y[cd/m^2]	Z	u'	v'	X	Y[cd/m^2]	Z	u'	v'
361	D7	6.34	7.63	0.78	0.2060	0.5577	8.07	9.57	1.23	0.2079	0.5545
362	D8	6.31	7.78	0.26	0.2039	0.5656	7.97	9.70	0.34	0.2063	0.5651
363	D9	16.37	19.53	8.54	0.1955	0.5248	19.78	22.95	9.89	0.2009	0.5246
364	D10	16.83	20.24	4.76	0.2011	0.5442	19.59	23.29	5.62	0.2031	0.5433
365	D11	15.96	19.53	2.26	0.2022	0.5568	19.04	23.15	2.72	0.2034	0.5564
366	D12	16.82	21.18	0.87	0.1996	0.5654	19.83	24.07	0.75	0.2070	0.5654
367	D13	20.82	26.96	22.25	0.1693	0.4932	23.76	30.98	23.81	0.1698	0.4980
368	D14	21.44	21.26	20.56	0.2133	0.4759	23.75	23.17	21.82	0.2175	0.4775
369	D15	28.07	33.71	12.00	0.1971	0.5325	31.21	36.45	13.32	0.2021	0.5309
370	D16	12.86	15.04	10.19	0.1912	0.5031	15.32	17.91	11.52	0.1924	0.5060
371	D17	19.12	19.01	11.06	0.2266	0.5070	21.45	20.98	12.07	0.2304	0.5071
372	D18	20.69	27.87	12.38	0.1739	0.5271	23.35	30.49	13.22	0.1795	0.5274
373	D19	15.93	18.31	20.26	0.1814	0.4690	18.00	20.51	21.91	0.1840	0.4716
374	D20	1.12	1.25	0.43	0.2117	0.5317	1.89	2.04	0.97	0.2140	0.5187
375	D21	11.04	11.91	0.49	0.2310	0.5607	13.24	14.16	0.61	0.2329	0.5602
376	D22	15.41	18.53	19.83	0.1747	0.4726	16.80	20.01	20.70	0.1773	0.4751
377	E1	2.08	2.57	1.15	0.1887	0.5247	2.97	3.52	1.86	0.1935	0.5163
378	E2	1.89	2.51	0.72	0.1813	0.5417	2.79	3.51	1.32	0.1880	0.5318
379	E3	1.91	2.76	0.51	0.1704	0.5540	2.74	3.70	0.94	0.1792	0.5455
380	E4	1.70	2.78	0.18	0.1548	0.5694	2.49	3.86	0.32	0.1621	0.5663
381	E5	9.54	12.13	5.37	0.1838	0.5259	11.71	14.59	6.28	0.1879	0.5265
382	E6	8.73	12.36	3.25	0.1713	0.5456	10.92	14.64	3.97	0.1802	0.5435
383	E7	8.26	12.42	1.85	0.1651	0.5586	9.88	14.31	2.08	0.1712	0.5581
384	E8	8.02	13.02	0.98	0.1555	0.5681	9.64	15.16	0.92	0.1607	0.5690
385	E9	16.54	20.34	11.32	0.1861	0.5148	19.18	22.82	13.06	0.1914	0.5126
386	E10	15.48	19.93	8.70	0.1818	0.5267	18.12	22.95	9.84	0.1850	0.5271
387	E11	14.47	19.49	6.73	0.1770	0.5364	17.66	23.46	7.58	0.1800	0.5382
388	E12	14.19	20.28	4.57	0.1709	0.5496	17.23	24.10	5.30	0.1746	0.5496
389	E13	21.33	28.22	24.28	0.1649	0.4908	22.24	29.29	22.99	0.1677	0.4969
390	E14	18.73	17.68	19.01	0.2197	0.4667	21.63	20.42	20.19	0.2227	0.4731
391	E15	27.24	33.07	9.64	0.1973	0.5390	31.20	36.17	10.72	0.2060	0.5373
392	E16	9.31	10.69	7.49	0.1938	0.5008	11.09	12.63	8.49	0.1963	0.5029
393	E17	15.76	14.67	7.84	0.2431	0.5091	18.24	16.86	9.32	0.2440	0.5073
394	E18	19.11	26.15	10.09	0.1731	0.5329	20.74	28.22	10.84	0.1741	0.5329
395	E19	12.94	14.59	18.96	0.1793	0.4549	14.20	15.77	20.44	0.1821	0.4547
396	E20	2.69	3.55	0.51	0.1872	0.5559	3.80	4.78	0.99	0.1937	0.5483
397	E21	9.06	12.12	2.00	0.1841	0.5541	11.28	14.52	2.62	0.1905	0.5515
398	E22	3.91	7.63	4.46	0.1187	0.5213	5.03	9.22	5.27	0.1263	0.5214
399	F1	1.31	1.74	1.02	0.1720	0.5139	2.06	2.57	1.67	0.1809	0.5071
400	F2	1.15	1.76	0.91	0.1519	0.5231	1.93	2.71	1.50	0.1638	0.5180

Table A.11: *Radiometric measurements of training colour samples (transparency) by a spectroradiometer (Jeti Specbos 1200) and Canon 350D measurements by HDR characterisation (dark-side IT8.7/1 – patch index: 361-400).*

Radiometric measurements							Canon 350D measurements				
Index	Patch#	X	Y[cd/m^2]	Z	u’	v’	X	Y[cd/m^2]	Z	u’	v’
401	F3	1.02	1.83	0.79	0.1323	0.5340	1.78	2.78	1.39	0.1490	0.5252
402	F4	0.78	1.75	0.57	0.1086	0.5480	1.58	2.84	1.14	0.1328	0.5372
403	F5	4.35	5.95	3.51	0.1671	0.5143	5.84	7.58	4.69	0.1748	0.5106
404	F6	3.44	5.70	2.74	0.1416	0.5280	5.10	7.84	3.91	0.1517	0.5249
405	F7	2.93	5.77	2.26	0.1218	0.5395	4.41	7.91	3.27	0.1327	0.5358
406	F8	2.72	5.71	2.05	0.1151	0.5437	4.08	7.68	3.03	0.1272	0.5384
407	F9	10.34	13.19	8.37	0.1773	0.5088	12.34	15.37	9.81	0.1813	0.5079
408	F10	9.76	13.84	7.80	0.1622	0.5174	11.49	15.60	8.98	0.1688	0.5154
409	F11	8.81	13.67	6.98	0.1501	0.5240	10.71	15.97	8.31	0.1556	0.5223
410	F12	8.16	14.06	6.30	0.1372	0.5318	10.13	16.80	7.48	0.1424	0.5313
411	F13	18.81	25.35	22.29	0.1615	0.4897	20.28	26.90	23.38	0.1642	0.4902
412	F14	16.76	14.74	17.73	0.2303	0.4558	18.92	16.66	19.24	0.2318	0.4591
413	F15	26.10	31.53	7.61	0.2000	0.5437	29.31	34.87	8.81	0.2026	0.5422
414	F16	6.33	7.29	5.21	0.1928	0.4997	8.07	8.96	6.58	0.1991	0.4971
415	F17	12.86	11.13	5.52	0.2620	0.5101	15.21	13.29	6.58	0.2596	0.5105
416	F18	16.44	23.32	7.64	0.1690	0.5393	18.32	25.49	8.01	0.1725	0.5402
417	F19	9.85	10.84	16.83	0.1767	0.4376	11.41	12.53	18.14	0.1798	0.4444
418	F20	0.73	1.34	0.29	0.1346	0.5558	1.38	2.14	0.73	0.1550	0.5399
419	F21	2.18	4.54	0.59	0.1210	0.5671	3.20	6.13	0.95	0.1304	0.5630
420	F22	4.34	8.29	0.88	0.1322	0.5681	5.04	9.33	0.98	0.1362	0.5676
421	G1	0.86	1.12	0.83	0.1707	0.5002	1.53	1.81	1.41	0.1861	0.4946
422	G2	0.83	1.20	0.90	0.1542	0.5016	1.46	1.88	1.52	0.1708	0.4943
423	G3	0.72	1.17	0.98	0.1358	0.4965	1.38	1.93	1.62	0.1573	0.4936
424	G4	0.51	1.10	1.03	0.1015	0.4925	1.24	2.01	1.76	0.1352	0.4935
425	G5	4.33	5.71	4.39	0.1679	0.4982	5.72	7.34	5.53	0.1729	0.4989
426	G6	3.62	5.62	4.52	0.1427	0.4984	5.04	7.38	5.85	0.1512	0.4983
427	G7	3.10	5.53	4.82	0.1234	0.4952	4.53	7.52	6.22	0.1332	0.4977
428	G8	2.78	5.37	4.79	0.1138	0.4947	4.13	7.28	6.21	0.1252	0.4966
429	G9	10.59	13.37	9.68	0.1764	0.5010	12.25	15.21	11.07	0.1791	0.5003
430	G10	9.98	13.79	10.39	0.1610	0.5004	11.33	15.46	11.16	0.1638	0.5028
431	G11	8.92	13.44	10.59	0.1473	0.4992	10.63	15.62	11.88	0.1516	0.5010
432	G12	8.27	13.93	10.90	0.1324	0.5016	10.01	16.37	12.49	0.1366	0.5028
433	G13	16.49	22.82	20.81	0.1566	0.4876	18.84	25.72	21.90	0.1602	0.4921
434	G14	14.73	12.17	16.40	0.2390	0.4444	16.53	13.87	17.67	0.2382	0.4497
435	G15	26.57	31.78	6.05	0.2038	0.5485	28.15	33.22	6.14	0.2066	0.5487
436	G16	3.95	4.47	3.20	0.1960	0.4991	5.34	5.89	4.40	0.1999	0.4959
437	G17	10.49	8.27	3.55	0.2890	0.5126	12.75	10.13	4.65	0.2855	0.5103
438	G18	14.88	21.92	5.84	0.1648	0.5462	16.67	23.74	6.24	0.1704	0.5458
439	G19	7.53	7.94	15.09	0.1752	0.4157	8.52	9.19	16.14	0.1750	0.4246
440	G20	1.23	2.52	0.74	0.1193	0.5498	2.07	3.61	1.33	0.1372	0.5396

Table A.12: *Radiometric measurements of training colour samples (transparency) by a spectroradiometer (Jeti Specbos 1200) and Canon 350D measurements by HDR characterisation (dark-side IT8.7/1 – patch index: 401-440).*

Radiometric measurements							Canon 350D measurements				
Index	Patch#	X	Y[cd/m^2]	Z	u'	v'	X	Y[cd/m^2]	Z	u'	v'
441	G21	2.15	3.72	2.36	0.1322	0.5148	3.06	4.83	3.24	0.1436	0.5101
442	G22	0.49	0.63	1.25	0.1432	0.4142	1.09	1.29	1.88	0.1675	0.4450
443	H1	0.95	1.16	1.07	0.1763	0.4842	1.53	1.77	1.60	0.1858	0.4845
444	H2	0.80	1.06	1.26	0.1562	0.4658	1.45	1.76	1.95	0.1719	0.4704
445	H3	0.80	1.14	1.69	0.1393	0.4467	1.44	1.83	2.34	0.1610	0.4586
446	H4	0.60	0.98	2.07	0.1116	0.4100	1.35	1.82	3.26	0.1406	0.4260
447	H5	3.49	4.36	4.31	0.1706	0.4796	4.61	5.51	5.41	0.1781	0.4792
448	H6	3.09	4.18	5.12	0.1523	0.4636	4.26	5.59	6.63	0.1579	0.4658
449	H7	2.73	4.01	6.32	0.1334	0.4410	3.89	5.38	8.33	0.1418	0.4420
450	H8	2.40	3.75	7.05	0.1203	0.4229	3.69	5.47	9.18	0.1302	0.4347
451	H9	10.60	12.70	10.02	0.1834	0.4945	12.54	14.74	11.59	0.1868	0.4943
452	H10	10.39	12.86	11.71	0.1743	0.4854	12.12	14.66	12.96	0.1789	0.4871
453	H11	9.65	12.41	12.53	0.1654	0.4786	11.66	14.82	14.19	0.1686	0.4823
454	H12	9.16	12.79	16.77	0.1458	0.4580	10.84	15.11	18.38	0.1482	0.4647
455	H13	15.78	22.09	20.94	0.1540	0.4850	17.39	24.03	21.66	0.1570	0.4884
456	H14	13.50	10.49	15.46	0.2486	0.4346	15.38	12.09	16.35	0.2504	0.4427
457	H15	24.98	29.71	4.34	0.2066	0.5529	26.87	31.37	4.63	0.2102	0.5522
458	H16	2.44	2.76	1.96	0.1963	0.4996	3.64	4.03	2.83	0.2008	0.4997
459	H17	8.81	6.34	2.16	0.3192	0.5169	10.33	7.83	3.11	0.3012	0.5140
460	H18	12.83	19.42	4.09	0.1622	0.5524	14.41	21.19	4.35	0.1669	0.5523
461	H19	5.58	5.82	13.02	0.1692	0.3970	6.63	6.88	14.44	0.1731	0.4042
462	H20	0.54	0.82	0.99	0.1366	0.4668	1.19	1.54	1.76	0.1610	0.4683
463	H21	1.76	2.88	3.58	0.1264	0.4654	2.58	3.90	4.74	0.1370	0.4661
464	H22	0.48	0.24	0.58	0.3299	0.3711	0.92	0.72	0.93	0.2541	0.4470
465	I1	1.43	1.56	2.08	0.1841	0.4519	2.02	2.17	2.57	0.1910	0.4620
466	I2	1.46	1.57	3.06	0.1708	0.4133	2.09	2.22	3.88	0.1778	0.4249
467	I3	1.53	1.60	4.57	0.1560	0.3670	2.10	2.19	5.48	0.1635	0.3834
468	I4	1.47	1.41	6.77	0.1370	0.2956	2.04	1.97	8.38	0.1435	0.3128
469	I5	4.84	5.40	5.28	0.1904	0.4780	6.05	6.68	6.52	0.1924	0.4778
470	I6	4.80	5.30	6.81	0.1833	0.4555	5.90	6.52	8.10	0.1844	0.4585
471	I7	4.65	5.08	8.09	0.1769	0.4349	5.85	6.35	9.69	0.1796	0.4391
472	I8	4.83	5.04	11.97	0.1661	0.3899	5.60	5.89	13.64	0.1660	0.3929
473	I9	10.60	12.21	10.14	0.1891	0.4902	12.55	14.11	11.82	0.1934	0.4891
474	I10	10.59	11.92	11.64	0.1888	0.4783	12.35	13.91	12.96	0.1900	0.4817
475	I11	10.69	12.08	12.72	0.1859	0.4726	12.49	13.89	14.32	0.1894	0.4739
476	I12	10.45	11.57	16.11	0.1799	0.4482	12.51	13.84	17.94	0.1828	0.4547
477	I13	14.50	20.37	19.80	0.1529	0.4831	16.21	22.74	21.19	0.1541	0.4863
478	I14	11.45	8.42	13.49	0.2570	0.4252	13.30	10.06	14.67	0.2555	0.4349
479	I15	24.20	28.51	3.07	0.2100	0.5565	25.57	30.02	3.20	0.2107	0.5565
480	I16	1.38	1.58	1.09	0.1947	0.5016	2.29	2.52	1.76	0.2017	0.5000

Table A.13: *Radiometric measurements of training colour samples (transparency) by a spectroradiometer (Jeti Specbos 1200) and Canon 350D measurements by HDR characterisation (dark-side IT8.7/1 – patch index: 441-480).*

Radiometric measurements							Canon 350D measurements				
Index	Patch#	X	Y[cd/m^2]	Z	u’	v’	X	Y[cd/m^2]	Z	u’	v’
481	I17	7.20	4.69	1.28	0.3539	0.5186	8.81	6.13	1.96	0.3303	0.5174
482	I18	11.59	17.77	3.01	0.1614	0.5569	12.71	19.10	3.01	0.1649	0.5577
483	I19	4.26	4.20	11.51	0.1674	0.3714	5.11	4.97	13.38	0.1705	0.3733
484	I20	2.41	2.94	5.43	0.1535	0.4213	3.14	3.68	6.62	0.1604	0.4234
485	I21	3.66	4.90	8.49	0.1426	0.4297	4.62	6.19	9.78	0.1455	0.4394
486	I22	0.27	0.26	0.07	0.2466	0.5342	0.68	0.76	0.37	0.2077	0.5182
487	J1	0.47	0.44	0.70	0.2050	0.4318	0.87	0.85	1.13	0.2064	0.4493
488	J2	0.47	0.34	1.24	0.2024	0.3294	0.92	0.82	1.71	0.2011	0.4016
489	J3	0.60	0.34	2.30	0.1905	0.2429	0.94	0.66	2.80	0.1948	0.3085
490	J4	0.72	0.30	3.83	0.1724	0.1616	1.01	0.57	4.66	0.1721	0.2185
491	J5	2.88	2.96	3.22	0.2023	0.4679	3.76	3.86	4.11	0.2032	0.4694
492	J6	3.22	3.03	4.72	0.2050	0.4340	3.98	3.85	5.69	0.2020	0.4396
493	J7	3.27	2.87	6.05	0.2029	0.4007	4.08	3.62	7.01	0.2053	0.4104
494	J8	3.59	2.68	9.14	0.2017	0.3387	4.26	3.28	10.34	0.2015	0.3495
495	J9	8.76	9.76	8.28	0.1947	0.4880	10.15	11.42	9.08	0.1946	0.4925
496	J10	8.89	9.68	9.43	0.1950	0.4777	10.42	11.15	10.60	0.1990	0.4791
497	J11	8.89	9.37	10.66	0.1960	0.4648	10.76	11.18	11.88	0.2010	0.4700
498	J12	9.51	9.10	14.43	0.2010	0.4326	11.11	10.65	15.64	0.2040	0.4401
499	J13	13.78	19.75	19.70	0.1493	0.4815	14.93	21.31	20.16	0.1512	0.4855
500	J14	10.62	7.33	12.79	0.2673	0.4151	11.88	8.56	13.44	0.2632	0.4265
501	J15	23.87	27.76	2.16	0.2137	0.5592	24.77	28.40	2.09	0.2168	0.5592
502	J16	0.71	0.79	0.49	0.2024	0.5068	1.37	1.50	0.99	0.2038	0.5028
503	J17	5.99	3.47	0.67	0.3990	0.5201	6.92	4.49	1.20	0.3560	0.5189
504	J18	10.32	16.03	2.02	0.1607	0.5617	11.36	17.18	1.89	0.1654	0.5628
505	J19	3.28	3.07	10.27	0.1637	0.3448	3.79	3.70	11.23	0.1633	0.3581
506	J20	0.48	0.19	2.33	0.1860	0.1657	0.72	0.46	2.79	0.1818	0.2581
507	J21	2.91	2.69	6.17	0.1884	0.3919	3.52	3.35	6.84	0.1895	0.4058
508	J22	0.16	0.26	0.08	0.1488	0.5442	0.60	0.76	0.34	0.1823	0.5253
509	K1	0.70	0.63	0.67	0.2303	0.4663	1.18	1.13	1.16	0.2183	0.4710
510	K2	0.84	0.58	1.02	0.2667	0.4143	1.32	1.07	1.44	0.2423	0.4442
511	K3	0.99	0.57	1.34	0.2920	0.3783	1.44	1.02	1.79	0.2606	0.4146
512	K4	1.28	0.56	2.08	0.3216	0.3166	1.66	0.93	2.38	0.2924	0.3675
513	K5	2.24	2.05	2.32	0.2243	0.4618	3.00	2.80	3.01	0.2215	0.4666
514	K6	2.51	1.89	3.08	0.2504	0.4242	3.44	2.70	4.02	0.2457	0.4340
515	K7	2.97	1.84	4.16	0.2760	0.3847	3.72	2.52	4.77	0.2670	0.4061
516	K8	3.61	1.71	6.00	0.3055	0.3256	4.24	2.30	6.31	0.2941	0.3591
517	K9	7.26	7.59	6.87	0.2049	0.4820	8.66	8.86	8.02	0.2093	0.4814
518	K10	7.64	7.35	7.96	0.2156	0.4666	9.00	8.62	8.83	0.2186	0.4707
519	K11	8.31	7.34	9.15	0.2279	0.4529	9.76	8.67	10.17	0.2294	0.4581
520	K12	9.61	7.02	12.34	0.2530	0.4158	10.99	8.21	12.91	0.2542	0.4275

Table A.14: *Radiometric measurements of training colour samples (transparency) by a spectroradiometer (Jeti Specbos 1200) and Canon 350D measurements by HDR characterisation (dark-side IT8.7/1 – patch index: 481-520).*

Radiometric measurements							Canon 350D measurements				
Index	Patch#	X	Y[cd/m^2]	Z	u'	v'	X	Y[cd/m^2]	Z	u'	v'
521	K13	12.91	18.78	19.09	0.1468	0.4803	13.92	20.02	19.52	0.1493	0.4834
522	K14	9.91	6.47	11.91	0.2778	0.4081	10.63	7.36	12.04	0.2706	0.4215
523	K15	22.82	26.08	1.38	0.2183	0.5613	23.42	26.71	1.10	0.2192	0.5625
524	K16	0.32	0.35	0.25	0.2025	0.4984	0.83	0.93	0.61	0.2006	0.5040
525	K17	4.58	2.41	0.28	0.4407	0.5218	5.40	3.32	0.74	0.3757	0.5204
526	K18	9.22	14.40	1.24	0.1611	0.5661	10.01	15.14	1.07	0.1667	0.5670
527	K19	2.59	2.32	9.23	0.1592	0.3208	2.94	2.69	10.03	0.1604	0.3300
528	K20	1.02	0.52	2.20	0.2646	0.3035	1.45	0.96	2.63	0.2428	0.3645
529	K21	4.49	3.58	7.17	0.2253	0.4043	5.05	4.11	7.76	0.2241	0.4112
530	K22	0.18	0.30	0.34	0.1263	0.4737	0.60	0.79	0.80	0.1611	0.4792
531	L1	0.68	0.64	0.52	0.2297	0.4865	1.15	1.11	0.96	0.2221	0.4827
532	L2	0.78	0.57	0.56	0.2834	0.4659	1.25	1.04	0.88	0.2569	0.4799
533	L3	0.92	0.56	0.65	0.3265	0.4472	1.42	1.06	1.01	0.2791	0.4683
534	L4	1.17	0.54	0.74	0.4073	0.4230	1.69	1.07	1.06	0.3241	0.4600
535	L5	2.17	1.98	1.77	0.2335	0.4793	2.93	2.75	2.35	0.2287	0.4831
536	L6	2.52	1.79	1.83	0.2892	0.4621	3.42	2.65	2.51	0.2697	0.4704
537	L7	2.91	1.64	2.08	0.3449	0.4373	3.76	2.45	2.60	0.3111	0.4564
538	L8	3.60	1.65	2.28	0.4092	0.4220	4.48	2.50	2.75	0.3564	0.4482
539	L9	6.95	7.32	5.67	0.2078	0.4925	8.31	8.64	6.73	0.2104	0.4918
540	L10	7.61	7.34	6.18	0.2234	0.4848	8.69	8.34	6.80	0.2255	0.4868
541	L11	8.28	7.20	6.52	0.2438	0.4770	9.45	8.37	7.38	0.2406	0.4794
542	L12	9.04	6.80	6.72	0.2756	0.4665	10.63	8.24	7.63	0.2706	0.4721
543	L13	11.65	17.04	18.02	0.1450	0.4773	12.53	18.45	17.93	0.1461	0.4840
544	L14	7.19	4.01	9.39	0.3011	0.3779	8.07	4.87	9.43	0.2953	0.4005
545	L15	20.90	22.90	0.48	0.2285	0.5634	19.97	22.02	0.15	0.2278	0.5651
546	L16	0.03	0.03	0.06	0.1818	0.4091	0.46	0.50	0.28	0.2070	0.5116
547	L17	2.43	1.08	0.10	0.5135	0.5135	3.20	1.88	0.39	0.3940	0.5194
548	L18	7.48	11.41	0.39	0.1664	0.5711	7.74	11.64	0.04	0.1697	0.5741
549	L19	1.28	0.88	5.97	0.1581	0.2445	1.51	1.12	6.82	0.1562	0.2597
550	L20	1.61	0.84	1.58	0.3398	0.3989	2.05	1.30	1.92	0.3000	0.4290
551	L21	4.25	3.41	3.85	0.2539	0.4584	4.99	4.16	4.30	0.2488	0.4661
552	L22	0.47	0.30	0.07	0.3629	0.5212	0.85	0.70	0.31	0.2770	0.5126
553	Dmin	24.81	29.18	19.83	0.1901	0.5031	24.08	27.95	18.41	0.1932	0.5046
554	N1	18.28	21.54	14.98	0.1893	0.5018	17.89	21.03	14.57	0.1898	0.5020
555	N2	16.03	18.71	13.30	0.1905	0.5003	16.28	18.73	12.92	0.1937	0.5017
556	N3	13.73	15.97	11.30	0.1912	0.5005	14.68	16.93	11.73	0.1933	0.5015
557	N4	11.64	13.44	9.70	0.1921	0.4992	12.90	14.60	10.34	0.1963	0.4998
558	N5	9.80	11.37	8.17	0.1913	0.4995	11.28	12.98	9.20	0.1931	0.5001
559	N6	8.31	9.62	6.97	0.1916	0.4989	9.77	11.16	8.03	0.1942	0.4990
560	N7	6.91	7.95	5.89	0.1923	0.4974	8.10	9.11	6.79	0.1961	0.4966

Table A.15: *Radiometric measurements of training colour samples (transparency) by a spectroradiometer (Jeti Specbos 1200) and Canon 350D measurements by HDR characterisation (dark-side IT8.7/1 – patch index: 521-560).*

Radiometric measurements							Canon 350D measurements				
Index	Patch#	X	Y[cd/m^2]	Z	u'	v'	X	Y[cd/m^2]	Z	u'	v'
561	N8	5.97	6.87	4.92	0.1929	0.4995	6.74	7.70	5.41	0.1947	0.5004
562	N9	4.77	5.47	4.10	0.1924	0.4967	5.84	6.61	4.84	0.1955	0.4977
563	N10	3.90	4.50	3.30	0.1917	0.4983	4.80	5.48	3.93	0.1944	0.4992
564	N11	3.25	3.69	2.79	0.1945	0.4958	4.02	4.58	3.48	0.1934	0.4956
565	N12	2.54	2.87	2.15	0.1955	0.4962	3.45	3.84	2.84	0.1982	0.4969
566	N13	1.97	2.26	1.69	0.1923	0.4968	2.82	3.11	2.42	0.1985	0.4933
567	N14	1.57	1.78	1.29	0.1959	0.4985	2.34	2.58	1.89	0.2006	0.4970
568	N15	1.18	1.34	1.03	0.1938	0.4949	1.83	2.01	1.52	0.2006	0.4948
569	N16	0.86	0.98	0.72	0.1944	0.4978	1.41	1.57	1.14	0.1997	0.4977
570	N17	0.70	0.77	0.57	0.1987	0.4974	1.17	1.27	0.95	0.2025	0.4953
571	N18	0.47	0.54	0.37	0.1968	0.5019	0.91	1.00	0.73	0.2019	0.4971
572	N19	0.35	0.38	0.30	0.2020	0.4921	0.70	0.76	0.55	0.2036	0.4972
573	N20	0.16	0.17	0.16	0.2042	0.4804	0.53	0.58	0.41	0.2032	0.4981
574	N21	0.14	0.14	0.14	0.2122	0.4759	0.44	0.48	0.33	0.2018	0.5005
575	N22	0.08	0.08	0.08	0.2045	0.4669	0.36	0.40	0.27	0.2004	0.5018
576	Dmax	0.07	0.07	0.06	0.2330	0.4823	0.34	0.39	0.25	0.1985	0.5048

Table A.16: *Radiometric measurements of training colour samples (transparency) by a spectroradiometer (Jeti Specbos 1200) and Canon 350D measurements by HDR characterisation (dark-side IT8.7/1 – patch index: 561-576).*

Nikon D100 measurements							Nikon D40 measurements				
Index	Patch#	X	Y[cd/m^2]	Z	u’	v’	X	Y[cd/m^2]	Z	u’	v’
1	A1	64.45	55.63	47.93	0.2472	0.4802	64.56	55.33	46.44	0.2498	0.4817
2	A2	73.73	52.57	40.87	0.2994	0.4804	74.46	53.47	38.16	0.3005	0.4856
3	A3	85.64	53.81	36.74	0.3415	0.4828	87.71	55.39	35.26	0.3425	0.4867
4	A4	99.44	52.51	26.30	0.4117	0.4892	100.15	53.07	25.62	0.4117	0.4909
5	A5	250.70	220.99	169.04	0.2462	0.4884	247.17	214.87	164.48	0.2494	0.4879
6	A6	277.98	208.55	140.75	0.2904	0.4903	279.18	207.17	140.30	0.2933	0.4897
7	A7	310.72	203.00	125.38	0.3330	0.4896	312.73	202.51	122.79	0.3364	0.4901
8	A8	351.33	200.71	103.13	0.3828	0.4920	357.82	205.16	102.65	0.3824	0.4933
9	A9	641.06	656.62	503.18	0.2137	0.4925	641.74	644.70	483.92	0.2182	0.4932
10	A10	673.75	643.83	475.69	0.2292	0.4928	663.54	627.43	467.15	0.2313	0.4920
11	A11	703.12	633.17	452.24	0.2433	0.4931	700.72	630.73	437.50	0.2443	0.4947
12	A12	768.91	617.86	414.98	0.2726	0.4929	764.57	622.33	396.32	0.2709	0.4962
13	A13	1491.29	1722.17	1389.58	0.1894	0.4922	1450.57	1708.46	1376.12	0.1859	0.4927
14	A14	1597.99	1789.56	1391.51	0.1960	0.4938	1595.55	1779.78	1392.89	0.1966	0.4933
15	A15	1650.75	1882.77	1303.23	0.1953	0.5013	1635.09	1844.62	1285.57	0.1972	0.5006
16	A16	1612.23	1841.61	1383.86	0.1932	0.4964	1596.38	1833.54	1372.49	0.1922	0.4968
17	A17	1614.16	1791.49	1373.76	0.1980	0.4945	1611.72	1808.42	1367.50	0.1963	0.4956
18	A18	1593.73	1818.15	1268.34	0.1951	0.5009	1571.93	1820.89	1281.89	0.1921	0.5007
19	A19	1513.41	1681.36	1380.48	0.1961	0.4901	1521.87	1699.51	1431.34	0.1944	0.4885
20	A20	142.02	80.14	56.27	0.3755	0.4767	150.14	88.56	67.73	0.3571	0.4739
21	A21	532.42	395.41	304.34	0.2887	0.4824	537.15	398.55	305.95	0.2890	0.4826
22	A22	1057.45	1026.46	637.76	0.2303	0.5030	1052.75	1023.53	637.46	0.2299	0.5029
23	B1	92.63	83.44	58.82	0.2436	0.4938	93.77	82.30	57.66	0.2499	0.4934
24	B2	109.14	85.04	45.46	0.2870	0.5031	108.67	84.30	43.72	0.2890	0.5043
25	B3	125.23	88.88	32.24	0.3221	0.5144	125.55	87.57	31.91	0.3272	0.5135
26	B4	143.55	85.94	12.01	0.3910	0.5266	147.46	88.44	10.61	0.3917	0.5286
27	B5	336.95	310.18	186.22	0.2429	0.5031	336.84	302.85	189.79	0.2473	0.5002
28	B6	369.92	297.69	139.15	0.2817	0.5101	372.95	297.06	133.52	0.2853	0.5112
29	B7	405.91	287.28	94.55	0.3248	0.5172	396.94	281.21	94.33	0.3242	0.5167
30	B8	443.81	273.00	58.24	0.3766	0.5213	442.69	271.69	58.13	0.3774	0.5211
31	B9	801.36	827.33	610.67	0.2131	0.4950	789.42	814.48	596.23	0.2134	0.4954
32	B10	821.34	807.71	563.16	0.2246	0.4970	809.14	806.04	538.40	0.2230	0.4998
33	B11	832.30	798.40	483.22	0.2335	0.5040	840.19	797.17	482.04	0.2359	0.5037
34	B12	922.64	814.23	384.85	0.2582	0.5128	908.40	796.44	383.98	0.2594	0.5117
35	B13	1438.76	1708.99	1424.08	0.1836	0.4907	1393.93	1645.57	1424.89	0.1837	0.4879
36	B14	1488.13	1564.12	1379.06	0.2046	0.4840	1484.32	1553.39	1339.74	0.2061	0.4854
37	B15	1622.99	1847.58	1129.96	0.1984	0.5081	1651.08	1875.89	1147.48	0.1987	0.5080
38	B16	1375.77	1564.33	1129.28	0.1949	0.4987	1342.37	1507.30	1184.33	0.1952	0.4932
39	B17	1521.93	1603.60	1170.99	0.2093	0.4961	1543.22	1623.78	1188.96	0.2095	0.4959
40	B18	1446.67	1704.55	1171.70	0.1895	0.5025	1445.42	1720.68	1193.83	0.1875	0.5022

Table A.17: *Nikon D100 and D40 measurements by HDR characterisation (bright-side IT8.7/1 – patch index: 1-40).*

Nikon D100 measurements							Nikon D40 measurements				
Index	Patch#	X	Y[$\mathrm{cd/m^2}$]	Z	u’	v’	X	Y[$\mathrm{cd/m^2}$]	Z	u’	v’
41	B19	1355.17	1490.14	1394.39	0.1944	0.4809	1372.71	1535.13	1396.46	0.1921	0.4833
42	B20	127.70	87.73	43.79	0.3243	0.5013	138.90	98.73	56.17	0.3107	0.4969
43	B21	378.76	268.46	116.37	0.3186	0.5082	375.63	270.13	120.27	0.3138	0.5077
44	B22	711.46	628.58	375.97	0.2526	0.5021	695.11	618.67	363.14	0.2513	0.5032
45	C1	181.52	177.90	113.90	0.2275	0.5016	178.73	171.23	108.88	0.2326	0.5014
46	C2	193.52	179.55	77.31	0.2482	0.5182	192.75	178.47	77.09	0.2486	0.5180
47	C3	202.50	178.60	50.57	0.2670	0.5299	205.65	179.45	50.46	0.2698	0.5297
48	C4	217.14	178.29	13.48	0.2962	0.5473	218.23	178.35	12.92	0.2977	0.5474
49	C5	633.62	641.75	343.56	0.2245	0.5116	628.07	615.72	324.53	0.2318	0.5113
50	C6	650.36	616.67	193.95	0.2482	0.5295	646.06	606.95	199.22	0.2497	0.5279
51	C7	665.84	595.31	107.05	0.2686	0.5403	657.40	581.07	106.90	0.2713	0.5395
52	C8	712.84	570.05	20.20	0.3058	0.5502	718.34	569.25	21.07	0.3083	0.5497
53	C9	955.23	1010.51	705.22	0.2096	0.4989	943.14	997.75	678.90	0.2102	0.5004
54	C10	956.10	989.64	601.60	0.2172	0.5059	972.10	997.71	581.49	0.2199	0.5078
55	C11	982.86	998.91	495.92	0.2252	0.5151	962.20	979.55	482.41	0.2250	0.5155
56	C12	1054.71	984.38	258.85	0.2542	0.5338	1053.27	989.45	256.28	0.2528	0.5344
57	C13	1331.58	1625.14	1464.23	0.1769	0.4859	1338.10	1646.10	1429.13	0.1765	0.4887
58	C14	1458.22	1454.81	1395.13	0.2124	0.4767	1422.73	1435.07	1375.03	0.2102	0.4771
59	C15	1667.24	1881.97	953.55	0.2036	0.5171	1658.88	1894.14	965.75	0.2013	0.5171
60	C16	1097.48	1205.21	952.56	0.1992	0.4923	1089.92	1206.86	947.02	0.1979	0.4930
61	C17	1370.89	1369.44	949.27	0.2215	0.4978	1367.68	1361.18	943.38	0.2222	0.4977
62	C18	1334.08	1624.72	975.70	0.1864	0.5107	1344.69	1671.21	1010.42	0.1827	0.5108
63	C19	1175.30	1284.41	1408.06	0.1906	0.4687	1164.46	1302.99	1399.67	0.1870	0.4708
64	C20	305.47	239.05	56.94	0.3008	0.5296	316.74	249.43	70.30	0.2968	0.5258
65	C21	520.66	498.47	281.39	0.2355	0.5074	519.81	493.80	276.14	0.2375	0.5076
66	C22	606.52	531.15	262.45	0.2592	0.5107	609.86	530.69	261.23	0.2608	0.5106
67	D1	125.54	128.57	88.56	0.2165	0.4988	129.99	129.88	86.16	0.2225	0.5002
68	D2	126.91	132.07	59.99	0.2219	0.5195	127.92	130.41	59.17	0.2262	0.5190
69	D3	128.83	135.28	37.65	0.2269	0.5361	129.15	132.80	38.57	0.2310	0.5343
70	D4	125.05	135.61	10.19	0.2284	0.5574	124.35	130.99	11.64	0.2342	0.5550
71	D5	502.46	535.64	296.58	0.2132	0.5114	493.97	529.17	289.29	0.2125	0.5121
72	D6	482.71	531.10	157.86	0.2164	0.5357	483.43	519.46	163.42	0.2206	0.5334
73	D7	452.85	499.80	81.38	0.2211	0.5490	452.70	491.96	77.42	0.2245	0.5490
74	D8	434.45	494.25	1.70	0.2213	0.5664	431.12	480.96	9.33	0.2247	0.5641
75	D9	1103.50	1223.29	617.57	0.2072	0.5167	1097.43	1201.37	612.25	0.2095	0.5160
76	D10	1083.96	1215.29	362.17	0.2125	0.5362	1089.69	1192.01	354.82	0.2176	0.5355
77	D11	1049.79	1192.57	175.96	0.2157	0.5514	1057.79	1193.75	159.82	0.2176	0.5526
78	D12	1022.02	1171.17	49.05	0.2182	0.5626	1044.25	1186.30	52.84	0.2199	0.5620
79	D13	1302.09	1631.68	1498.19	0.1721	0.4851	1305.03	1672.15	1476.66	0.1694	0.4883
80	D14	1378.06	1316.65	1341.30	0.2192	0.4711	1331.03	1276.62	1334.99	0.2174	0.4692

Table A.18: *Nikon D100 and D40 measurements by HDR characterisation (bright-side IT8.7/1 – patch index: 41-80).*

Nikon D100 measurements							Nikon D40 measurements				
Index	Patch#	X	Y[cd/m²]	Z	u'	v'	X	Y[cd/m²]	Z	u'	v'
81	D15	1698.16	1924.84	793.36	0.2061	0.5257	1696.67	1935.82	794.89	0.2049	0.5261
82	D16	868.25	935.97	746.37	0.2025	0.4913	854.49	928.62	707.97	0.2022	0.4943
83	D17	1230.54	1138.41	738.19	0.2399	0.4993	1206.77	1124.27	717.60	0.2387	0.5003
84	D18	1232.41	1570.07	815.64	0.1810	0.5189	1246.35	1590.58	821.46	0.1808	0.5192
85	D19	984.65	1079.72	1312.52	0.1865	0.4602	985.24	1079.17	1337.70	0.1860	0.4584
86	D20	94.67	94.55	52.78	0.2266	0.5092	103.72	104.00	63.55	0.2237	0.5048
87	D21	715.97	700.14	45.62	0.2522	0.5549	723.20	701.98	52.04	0.2536	0.5538
88	D22	901.26	1026.50	1242.67	0.1800	0.4613	894.38	1029.84	1245.25	0.1782	0.4616
89	E1	176.94	196.86	122.03	0.2025	0.5068	170.68	189.97	118.67	0.2022	0.5064
90	E2	160.56	190.67	85.52	0.1960	0.5236	162.63	189.07	85.57	0.1998	0.5227
91	E3	148.92	195.00	55.05	0.1839	0.5418	151.26	195.86	54.94	0.1859	0.5417
92	E4	127.91	198.82	8.75	0.1631	0.5705	128.32	196.89	9.86	0.1650	0.5696
93	E5	713.15	838.01	440.42	0.1953	0.5164	701.34	825.90	431.91	0.1950	0.5167
94	E6	628.71	814.04	277.05	0.1840	0.5359	626.59	796.86	281.83	0.1867	0.5342
95	E7	559.05	784.70	145.97	0.1751	0.5531	553.90	768.66	148.70	0.1768	0.5521
96	E8	500.18	776.42	61.37	0.1623	0.5667	497.91	762.16	64.37	0.1643	0.5658
97	E9	1131.11	1304.06	831.35	0.1951	0.5062	1088.94	1256.78	814.84	0.1946	0.5053
98	E10	1037.17	1260.13	631.25	0.1900	0.5195	1030.34	1238.36	631.25	0.1917	0.5184
99	E11	980.99	1260.23	506.36	0.1833	0.5299	979.11	1224.89	503.83	0.1877	0.5284
100	E12	934.10	1244.48	346.51	0.1810	0.5426	932.74	1240.48	349.54	0.1812	0.5423
101	E13	1242.19	1584.24	1557.55	0.1674	0.4804	1247.56	1610.86	1513.83	0.1666	0.4840
102	E14	1293.97	1153.13	1320.94	0.2295	0.4602	1270.94	1148.06	1304.91	0.2269	0.4611
103	E15	1720.06	1920.00	679.84	0.2113	0.5307	1669.74	1927.96	669.49	0.2049	0.5323
104	E16	660.58	704.03	560.66	0.2048	0.4911	665.45	717.83	575.20	0.2023	0.4910
105	E17	1074.25	934.38	593.35	0.2547	0.4985	1095.86	958.58	569.84	0.2551	0.5020
106	E18	1142.74	1483.74	692.35	0.1794	0.5242	1151.31	1503.55	678.90	0.1789	0.5257
107	E19	814.18	898.14	1264.35	0.1801	0.4471	830.31	916.31	1245.74	0.1814	0.4503
108	E20	197.87	235.88	56.55	0.2026	0.5435	205.56	245.32	69.93	0.2008	0.5391
109	E21	606.06	743.18	169.67	0.1977	0.5454	606.51	745.53	170.40	0.1972	0.5455
110	E22	261.10	466.43	345.39	0.1259	0.5062	266.62	475.38	354.71	0.1260	0.5056
111	F1	123.76	146.39	116.83	0.1854	0.4934	123.78	142.94	114.00	0.1897	0.4929
112	F2	108.56	147.87	102.30	0.1649	0.5053	108.89	144.87	102.01	0.1683	0.5038
113	F3	94.82	148.34	94.26	0.1457	0.5130	95.83	145.95	96.01	0.1490	0.5105
114	F4	78.72	150.55	79.47	0.1223	0.5261	74.65	143.58	75.57	0.1216	0.5263
115	F5	360.28	454.74	326.61	0.1766	0.5015	363.04	447.40	323.74	0.1805	0.5005
116	F6	296.24	446.90	275.46	0.1514	0.5139	300.64	443.81	277.39	0.1544	0.5127
117	F7	244.92	439.00	221.13	0.1307	0.5273	246.92	432.91	224.96	0.1332	0.5254
118	F8	219.55	416.35	207.23	0.1239	0.5288	219.96	411.41	211.33	0.1252	0.5271
119	F9	769.99	917.80	687.64	0.1855	0.4976	771.87	905.49	679.34	0.1883	0.4972
120	F10	691.34	910.46	619.78	0.1706	0.5056	679.08	904.54	606.34	0.1691	0.5067

Table A.19: *Nikon D100 and D40 measurements by HDR characterisation (bright-side IT8.7/1 – patch index: 81-120).*

Nikon D100 measurements							Nikon D40 measurements				
Index	Patch#	X	Y[$\mathrm{cd/m^2}$]	Z	u’	v’	X	Y[$\mathrm{cd/m^2}$]	Z	u’	v’
121	F11	630.03	902.02	554.44	0.1593	0.5130	621.12	895.89	561.42	0.1578	0.5121
122	F12	562.29	919.85	522.53	0.1412	0.5198	554.68	901.40	507.39	0.1422	0.5201
123	F13	1191.33	1584.50	1570.24	0.1606	0.4806	1198.22	1581.90	1546.42	0.1621	0.4815
124	F14	1181.74	1005.55	1235.21	0.2367	0.4532	1169.50	1006.17	1238.37	0.2342	0.4533
125	F15	1724.61	1916.26	563.79	0.2145	0.5363	1733.50	1962.38	547.97	0.2113	0.5382
126	F16	493.22	520.40	420.37	0.2064	0.4899	486.48	513.85	414.45	0.2062	0.4900
127	F17	958.23	780.76	444.66	0.2737	0.5018	962.32	779.26	455.31	0.2746	0.5003
128	F18	1055.33	1409.35	557.39	0.1769	0.5314	1045.77	1415.35	546.47	0.1749	0.5326
129	F19	674.62	715.22	1181.44	0.1805	0.4306	688.41	740.17	1202.57	0.1788	0.4326
130	F20	61.28	101.63	36.00	0.1447	0.5400	68.09	109.36	47.01	0.1473	0.5322
131	F21	159.85	314.39	59.04	0.1265	0.5600	160.72	311.15	67.05	0.1278	0.5568
132	F22	257.66	476.25	69.32	0.1354	0.5633	259.26	474.89	78.97	0.1361	0.5609
133	G1	91.29	102.71	103.39	0.1880	0.4760	92.55	102.81	100.25	0.1913	0.4781
134	G2	84.52	106.11	112.86	0.1678	0.4740	84.07	105.21	107.21	0.1695	0.4773
135	G3	74.13	103.93	113.09	0.1503	0.4742	73.25	99.53	112.46	0.1539	0.4706
136	G4	62.56	107.19	129.27	0.1216	0.4687	61.03	104.56	124.12	0.1220	0.4701
137	G5	367.45	449.66	411.62	0.1761	0.4848	372.28	451.17	399.97	0.1786	0.4869
138	G6	314.26	453.89	433.05	0.1493	0.4851	309.58	439.81	422.26	0.1515	0.4843
139	G7	266.37	432.79	450.07	0.1314	0.4804	262.25	426.19	435.61	0.1318	0.4818
140	G8	241.12	421.14	448.82	0.1220	0.4795	238.79	418.98	445.19	0.1215	0.4798
141	G9	800.02	951.12	802.89	0.1831	0.4898	791.91	938.80	782.65	0.1839	0.4906
142	G10	710.77	936.45	822.96	0.1650	0.4893	706.55	928.31	802.00	0.1659	0.4904
143	G11	648.84	957.12	840.21	0.1481	0.4915	641.10	906.74	876.21	0.1520	0.4837
144	G12	592.25	950.35	902.32	0.1350	0.4872	584.51	944.91	885.08	0.1343	0.4884
145	G13	1139.53	1524.24	1574.36	0.1587	0.4775	1155.44	1559.48	1623.56	0.1571	0.4771
146	G14	1101.21	890.94	1196.57	0.2440	0.4441	1113.85	902.65	1187.67	0.2446	0.4460
147	G15	1727.24	1962.65	457.84	0.2123	0.5428	1756.00	1954.49	462.33	0.2164	0.5419
148	G16	353.84	361.61	313.50	0.2107	0.4844	357.66	369.92	308.41	0.2094	0.4873
149	G17	858.65	642.11	329.65	0.2992	0.5034	848.21	641.51	313.55	0.2973	0.5059
150	G18	961.61	1329.44	461.72	0.1726	0.5368	972.71	1345.77	459.71	0.1726	0.5374
151	G19	545.91	573.36	1131.57	0.1741	0.4115	553.36	575.92	1141.36	0.1754	0.4108
152	G20	106.49	195.45	85.95	0.1292	0.5337	113.00	198.60	98.85	0.1334	0.5275
153	G21	175.74	274.23	222.56	0.1418	0.4979	179.77	276.61	224.05	0.1438	0.4978
154	G22	52.10	59.91	123.11	0.1579	0.4084	54.86	65.25	118.22	0.1581	0.4230
155	H1	95.49	104.01	119.60	0.1896	0.4647	94.96	101.90	118.24	0.1920	0.4636
156	H2	88.47	103.15	149.38	0.1698	0.4455	87.92	103.32	140.97	0.1707	0.4513
157	H3	83.67	105.93	180.01	0.1513	0.4309	83.89	105.82	175.81	0.1526	0.4332
158	H4	72.49	103.92	236.33	0.1239	0.3996	72.35	101.91	235.38	0.1254	0.3975
159	H5	309.84	357.56	406.14	0.1798	0.4669	314.52	356.66	411.99	0.1823	0.4652
160	H6	284.33	358.37	495.47	0.1591	0.4513	284.71	351.70	487.72	0.1621	0.4507

Table A.20: *Nikon D100 and D40 measurements by HDR characterisation (bright-side IT8.7/1 – patch index: 121-160).*

Nikon D100 measurements							Nikon D40 measurements				
Index	Patch#	X	Y[cd/m^2]	Z	u’	v’	X	Y[cd/m^2]	Z	u’	v’
161	H7	248.18	347.06	600.27	0.1368	0.4305	249.27	346.31	590.88	0.1382	0.4319
162	H8	228.78	336.15	697.46	0.1243	0.4109	228.98	339.03	682.22	0.1244	0.4145
163	H9	847.41	969.55	874.31	0.1882	0.4844	858.03	965.30	859.17	0.1916	0.4849
164	H10	798.08	957.03	938.45	0.1777	0.4793	806.38	943.34	957.59	0.1809	0.4762
165	H11	759.55	929.67	1065.44	0.1697	0.4674	756.34	932.69	1043.03	0.1692	0.4696
166	H12	697.54	961.31	1393.58	0.1446	0.4483	696.28	941.98	1404.33	0.1463	0.4453
167	H13	1111.71	1544.22	1586.52	0.1532	0.4787	1115.74	1542.96	1610.30	0.1534	0.4774
168	H14	1032.79	784.68	1167.79	0.2533	0.4331	1011.65	770.71	1141.76	0.2530	0.4336
169	H15	1697.34	1897.54	348.44	0.2176	0.5473	1719.40	1943.86	358.67	0.2152	0.5475
170	H16	232.30	241.99	206.72	0.2073	0.4859	246.88	254.34	208.12	0.2107	0.4885
171	H17	744.27	522.62	228.69	0.3212	0.5074	741.69	522.14	222.85	0.3210	0.5084
172	H18	883.23	1244.74	359.20	0.1712	0.5430	880.15	1253.95	351.95	0.1697	0.5440
173	H19	427.97	440.86	1032.52	0.1688	0.3914	432.84	443.50	1031.55	0.1701	0.3921
174	H20	59.59	79.04	115.71	0.1497	0.4467	67.29	87.39	126.45	0.1532	0.4475
175	H21	157.04	237.98	334.28	0.1328	0.4529	157.24	233.97	329.63	0.1351	0.4523
176	H22	46.03	27.41	51.25	0.3014	0.4038	48.76	30.97	55.02	0.2876	0.4109
177	I1	146.74	148.32	219.79	0.1937	0.4404	142.35	143.57	205.95	0.1954	0.4435
178	I2	142.99	145.85	307.75	0.1758	0.4034	148.91	147.79	308.43	0.1810	0.4042
179	I3	142.96	144.44	440.02	0.1575	0.3582	141.94	142.89	438.86	0.1576	0.3570
180	I4	128.92	133.36	633.31	0.1280	0.2979	132.15	132.15	635.89	0.1314	0.2957
181	I5	443.78	467.87	511.40	0.1973	0.4681	440.22	458.46	488.44	0.2005	0.4698
182	I6	435.66	465.49	652.55	0.1859	0.4468	432.15	457.52	625.08	0.1885	0.4490
183	I7	419.89	451.71	750.75	0.1778	0.4303	425.90	442.21	761.61	0.1823	0.4259
184	I8	399.45	415.45	1038.26	0.1639	0.3837	400.80	419.25	1003.74	0.1653	0.3890
185	I9	912.64	1003.36	906.18	0.1954	0.4834	913.58	982.27	913.58	0.1987	0.4808
186	I10	873.89	953.96	1007.85	0.1920	0.4716	882.16	949.76	1016.32	0.1941	0.4702
187	I11	884.32	962.66	1085.88	0.1904	0.4663	881.09	954.36	1099.55	0.1906	0.4644
188	I12	856.93	924.50	1353.25	0.1825	0.4430	883.13	945.92	1348.13	0.1848	0.4453
189	I13	1051.36	1452.72	1595.24	0.1522	0.4732	1080.08	1492.08	1614.70	0.1526	0.4744
190	I14	949.36	697.65	1065.02	0.2599	0.4298	958.84	708.59	1067.43	0.2593	0.4312
191	I15	1720.42	1889.67	255.19	0.2232	0.5516	1723.27	1902.46	287.75	0.2215	0.5501
192	I16	149.04	153.53	131.13	0.2095	0.4856	160.06	163.73	137.32	0.2114	0.4867
193	I17	648.77	421.70	153.75	0.3490	0.5104	642.73	421.81	155.05	0.3458	0.5106
194	I18	803.05	1178.38	272.63	0.1665	0.5496	803.84	1171.44	267.03	0.1677	0.5498
195	I19	340.72	339.48	975.88	0.1630	0.3654	349.26	345.07	970.93	0.1656	0.3680
196	I20	204.75	243.55	466.77	0.1558	0.4169	213.55	247.78	477.26	0.1593	0.4159
197	I21	308.61	412.26	752.86	0.1411	0.4240	307.27	405.02	747.80	0.1425	0.4226
198	I22	29.25	29.47	11.34	0.2315	0.5249	33.07	33.30	18.31	0.2252	0.5101
199	J1	53.42	47.20	86.50	0.2093	0.4161	51.53	44.65	82.80	0.2126	0.4144
200	J2	56.78	43.33	135.95	0.2038	0.3499	58.20	43.39	137.84	0.2074	0.3479

Table A.21: *Nikon D100 and D40 measurements by HDR characterisation (bright-side IT8.7/1 – patch index: 161-200).*

Nikon D100 measurements							Nikon D40 measurements				
Index	Patch#	X	Y[cd/m^2]	Z	u’	v’	X	Y[cd/m^2]	Z	u’	v’
201	J3	57.20	35.36	216.31	0.1850	0.2574	56.96	36.43	215.34	0.1824	0.2624
202	J4	54.01	24.82	332.72	0.1517	0.1568	56.14	29.76	328.60	0.1509	0.1800
203	J5	278.90	273.00	341.73	0.2066	0.4551	285.38	273.67	346.99	0.2102	0.4535
204	J6	305.99	280.40	458.91	0.2078	0.4285	315.55	283.04	472.52	0.2111	0.4261
205	J7	305.23	259.49	575.10	0.2061	0.3943	312.26	261.29	574.06	0.2098	0.3950
206	J8	319.41	242.12	785.55	0.2025	0.3455	324.96	242.85	789.21	0.2052	0.3450
207	J9	772.13	831.70	781.97	0.1981	0.4800	777.60	825.75	772.37	0.2009	0.4801
208	J10	803.73	824.66	855.95	0.2042	0.4715	806.50	830.93	870.42	0.2031	0.4709
209	J11	801.57	808.54	966.18	0.2026	0.4597	813.14	813.31	975.27	0.2041	0.4592
210	J12	825.88	776.83	1209.96	0.2051	0.4340	828.95	781.62	1252.01	0.2033	0.4313
211	J13	1050.15	1483.34	1667.68	0.1484	0.4717	1057.47	1473.60	1659.99	0.1503	0.4713
212	J14	890.93	620.93	1007.72	0.2694	0.4225	889.05	614.61	1018.96	0.2701	0.4202
213	J15	1689.91	1839.88	182.01	0.2266	0.5550	1710.91	1851.75	193.99	0.2276	0.5542
214	J16	85.26	85.68	76.37	0.2132	0.4821	93.93	94.68	80.79	0.2139	0.4851
215	J17	547.17	331.45	95.59	0.3770	0.5138	537.51	327.07	93.92	0.3755	0.5141
216	J18	732.51	1086.41	182.27	0.1667	0.5563	737.23	1082.03	184.49	0.1683	0.5558
217	J19	258.55	255.64	833.58	0.1568	0.3489	270.89	261.72	869.06	0.1593	0.3462
218	J20	29.48	12.72	189.86	0.1493	0.1449	34.04	18.78	190.31	0.1535	0.1906
219	J21	253.13	232.42	546.20	0.1883	0.3890	255.52	232.22	538.42	0.1909	0.3904
220	J22	23.16	31.73	11.95	0.1731	0.5338	26.40	34.58	18.67	0.1757	0.5177
221	K1	84.81	74.04	94.34	0.2295	0.4507	84.00	71.43	91.99	0.2347	0.4491
222	K2	98.20	70.11	119.47	0.2604	0.4183	98.05	70.10	114.29	0.2628	0.4227
223	K3	107.36	65.30	142.97	0.2833	0.3877	111.05	67.53	142.99	0.2860	0.3913
224	K4	122.23	59.74	176.54	0.3158	0.3473	122.58	59.22	178.81	0.3169	0.3445
225	K5	235.36	207.13	250.20	0.2300	0.4555	240.84	207.46	254.75	0.2340	0.4535
226	K6	271.80	200.73	327.16	0.2550	0.4237	278.27	206.18	317.09	0.2575	0.4293
227	K7	298.55	189.58	386.57	0.2776	0.3966	305.18	194.72	385.51	0.2785	0.3999
228	K8	339.24	174.30	487.73	0.3072	0.3552	336.91	174.52	493.90	0.3038	0.3540
229	K9	693.12	685.71	675.95	0.2132	0.4745	695.92	688.61	668.17	0.2136	0.4756
230	K10	720.74	662.29	757.29	0.2230	0.4611	730.82	661.57	744.47	0.2268	0.4620
231	K11	783.10	663.58	853.42	0.2356	0.4491	774.27	661.24	834.04	0.2347	0.4510
232	K12	873.56	635.82	1051.55	0.2576	0.4218	865.29	629.73	1075.13	0.2557	0.4187
233	K13	1013.33	1428.03	1633.79	0.1483	0.4702	1024.23	1437.25	1650.95	0.1488	0.4698
234	K14	837.48	562.42	947.73	0.2765	0.4177	850.48	574.15	970.70	0.2749	0.4176
235	K15	1691.13	1809.26	109.56	0.2320	0.5584	1705.08	1817.25	120.68	0.2326	0.5577
236	K16	46.08	46.34	40.75	0.2135	0.4830	52.39	52.87	44.31	0.2142	0.4863
237	K17	444.17	252.90	54.65	0.4036	0.5171	443.07	252.87	55.82	0.4025	0.5168
238	K18	677.53	1011.69	110.39	0.1675	0.5626	673.07	997.50	112.63	0.1685	0.5620
239	K19	208.60	197.04	808.31	0.1493	0.3173	220.13	205.27	799.61	0.1545	0.3242
240	K20	101.57	60.19	196.92	0.2547	0.3396	105.43	64.11	203.91	0.2512	0.3437

Table A.22: *Nikon D100 and D40 measurements by HDR characterisation (bright-side IT8.7/1 – patch index: 201-240).*

		Nikon D100 measurements					Nikon D40 measurements				
Index	Patch#	X	Y[cd/m^2]	Z	u’	v’	X	Y[cd/m^2]	Z	u’	v’
241	K21	397.92	313.75	626.45	0.2279	0.4043	407.33	315.61	640.92	0.2306	0.4021
242	K22	26.39	38.46	59.42	0.1350	0.4429	28.51	40.69	65.57	0.1365	0.4383
243	L1	92.12	83.81	84.97	0.2297	0.4702	83.92	73.07	74.17	0.2394	0.4689
244	L2	105.80	79.81	86.31	0.2709	0.4599	100.80	72.82	80.85	0.2809	0.4565
245	L3	118.05	75.97	89.27	0.3096	0.4482	112.05	69.99	80.97	0.3191	0.4484
246	L4	132.96	71.45	82.93	0.3659	0.4424	125.95	65.45	77.16	0.3762	0.4399
247	L5	248.78	215.71	218.65	0.2403	0.4689	246.33	209.64	208.76	0.2453	0.4697
248	L6	298.48	211.91	226.01	0.2873	0.4590	293.48	207.08	220.62	0.2890	0.4589
249	L7	329.08	196.99	226.73	0.3320	0.4472	313.28	187.11	218.10	0.3320	0.4462
250	L8	367.14	191.98	219.31	0.3761	0.4425	364.38	191.91	222.17	0.3728	0.4418
251	L9	702.22	710.63	609.03	0.2130	0.4849	700.24	696.94	583.10	0.2171	0.4861
252	L10	747.56	684.67	614.98	0.2325	0.4791	743.97	679.10	614.01	0.2330	0.4785
253	L11	794.03	671.57	638.28	0.2485	0.4728	800.25	668.10	639.68	0.2512	0.4719
254	L12	872.47	649.98	657.65	0.2771	0.4645	887.07	654.72	666.73	0.2792	0.4637
255	L13	913.07	1334.38	1598.43	0.1420	0.4669	931.02	1354.07	1620.16	0.1427	0.4669
256	L14	653.15	385.35	750.19	0.3009	0.3994	660.93	393.15	759.78	0.2991	0.4004
257	L15	1584.03	1598.42	-2.98	0.2480	0.5630	1614.00	1604.47	11.56	0.2511	0.5615
258	L16	12.89	13.06	8.80	0.2193	0.4997	16.32	16.47	10.83	0.2206	0.5011
259	L17	236.37	122.76	17.69	0.4437	0.5185	245.20	128.75	19.21	0.4390	0.5187
260	L18	525.75	766.61	-1.85	0.1750	0.5740	533.83	772.69	5.26	0.1759	0.5728
261	L19	103.32	82.82	546.26	0.1385	0.2498	111.11	88.75	548.21	0.1440	0.2587
262	L20	168.23	96.80	154.51	0.3229	0.4181	167.70	98.39	153.76	0.3187	0.4207
263	L21	428.17	329.87	385.52	0.2622	0.4545	421.04	328.24	371.12	0.2608	0.4574
264	L22	56.15	36.87	11.45	0.3490	0.5156	58.54	38.78	15.24	0.3413	0.5088
265	Dmin	2126.75	2411.78	1915.30	0.1931	0.4928	2120.00	2438.94	1904.74	0.1909	0.4942
266	N1	1655.90	1942.30	1527.69	0.1872	0.4942	1718.26	1957.42	1568.09	0.1921	0.4923
267	N2	1567.32	1799.14	1405.20	0.1913	0.4941	1548.59	1775.02	1387.93	0.1916	0.4940
268	N3	1408.41	1599.83	1264.04	0.1929	0.4931	1405.73	1583.77	1268.70	0.1941	0.4921
269	N4	1226.09	1390.55	1092.23	0.1934	0.4935	1223.92	1338.37	1131.58	0.1983	0.4878
270	N5	1043.54	1173.03	941.47	0.1945	0.4919	1043.75	1154.80	961.54	0.1965	0.4891
271	N6	904.22	998.35	837.52	0.1967	0.4885	906.56	991.02	827.04	0.1987	0.4886
272	N7	755.87	833.96	701.14	0.1967	0.4884	754.80	809.90	704.97	0.2010	0.4854
273	N8	633.78	689.96	593.87	0.1986	0.4865	649.66	698.06	582.28	0.2020	0.4883
274	N9	532.52	580.66	507.47	0.1979	0.4855	543.79	581.67	516.40	0.2011	0.4839
275	N10	446.83	481.71	416.37	0.2003	0.4859	450.43	472.77	417.10	0.2049	0.4839
276	N11	358.84	382.23	347.06	0.2012	0.4822	369.07	386.86	346.17	0.2047	0.4829
277	N12	291.86	310.17	277.97	0.2020	0.4831	294.02	308.54	288.73	0.2032	0.4797
278	N13	238.56	254.74	232.11	0.2006	0.4821	245.92	256.56	232.86	0.2052	0.4818
279	N14	193.90	206.70	186.05	0.2013	0.4829	198.04	205.06	190.97	0.2059	0.4798
280	N15	155.89	161.32	155.07	0.2051	0.4775	159.38	165.68	152.33	0.2055	0.4808

Table A.23: *Nikon D100 and D40 measurements by HDR characterisation (bright-side IT8.7/1 – patch index: 241-280).*

Nikon D100 measurements							Nikon D40 measurements				
Index	Patch#	X	Y[cd/m^2]	Z	u'	v'	X	Y[cd/m^2]	Z	u'	v'
281	N16	114.60	120.65	110.55	0.2032	0.4813	118.95	122.39	113.45	0.2073	0.4799
282	N17	87.98	89.47	87.04	0.2081	0.4761	94.09	94.21	90.00	0.2118	0.4771
283	N18	63.81	65.00	63.24	0.2078	0.4762	67.31	67.53	64.66	0.2113	0.4770
284	N19	44.79	45.16	44.77	0.2091	0.4745	46.51	46.26	45.43	0.2122	0.4749
285	N20	27.23	27.89	28.17	0.2055	0.4735	29.88	30.02	31.11	0.2084	0.4711
286	N21	19.11	19.54	18.84	0.2074	0.4769	21.90	22.24	22.18	0.2076	0.4743
287	N22	11.40	11.76	11.21	0.2059	0.4780	13.69	13.81	14.29	0.2076	0.4713
288	Dmax	6.58	6.95	6.18	0.2034	0.4835	9.35	9.85	10.06	0.1999	0.4733
289	A1	2.72	2.66	2.13	0.2217	0.4886	2.33	2.18	1.72	0.2322	0.4881
290	A2	3.00	2.65	2.05	0.2450	0.4877	2.50	2.11	1.63	0.2562	0.4864
291	A3	3.33	2.78	2.13	0.2592	0.4864	2.82	2.18	1.60	0.2790	0.4867
292	A4	3.92	2.98	2.04	0.2868	0.4898	3.32	2.34	1.53	0.3092	0.4896
293	A5	6.38	6.08	4.32	0.2307	0.4950	5.72	5.23	3.75	0.2400	0.4933
294	A6	7.04	5.98	4.16	0.2581	0.4927	6.43	5.24	3.35	0.2705	0.4960
295	A7	7.80	5.99	3.88	0.2856	0.4932	7.30	5.26	3.21	0.3050	0.4938
296	A8	9.13	6.21	3.60	0.3228	0.4944	8.31	5.36	2.90	0.3411	0.4952
297	A9	14.62	15.40	10.44	0.2111	0.5005	13.67	14.37	9.46	0.2122	0.5021
298	A10	15.05	15.09	10.25	0.2212	0.4990	14.22	14.11	9.48	0.2237	0.4993
299	A11	15.74	15.31	9.69	0.2294	0.5020	15.03	14.00	9.08	0.2383	0.4995
300	A12	19.74	17.54	11.95	0.2478	0.4953	16.48	14.12	8.36	0.2602	0.5016
301	A13	31.89	37.42	25.52	0.1905	0.5029	30.46	35.78	23.87	0.1907	0.5041
302	A14	33.96	38.95	25.51	0.1956	0.5046	32.66	36.98	24.99	0.1973	0.5025
303	A15	34.87	40.47	24.75	0.1948	0.5086	33.52	38.46	22.74	0.1976	0.5101
304	A16	34.72	40.72	25.29	0.1925	0.5080	33.37	38.38	24.84	0.1953	0.5053
305	A17	34.84	40.26	25.09	0.1952	0.5075	33.60	38.01	24.58	0.1984	0.5049
306	A18	34.13	39.90	24.44	0.1934	0.5087	33.87	39.57	23.29	0.1943	0.5107
307	A19	32.88	38.02	25.54	0.1935	0.5034	32.15	36.38	25.03	0.1970	0.5015
308	A20	4.95	3.68	2.60	0.2914	0.4873	4.19	2.87	2.10	0.3131	0.4823
309	A21	12.29	9.97	7.00	0.2690	0.4908	11.58	9.04	6.48	0.2778	0.4883
310	A22	23.06	23.43	13.15	0.2228	0.5094	22.68	22.58	12.22	0.2279	0.5106
311	B1	2.96	2.86	2.07	0.2270	0.4945	2.58	2.44	1.69	0.2325	0.4964
312	B2	3.31	2.97	1.92	0.2472	0.4984	2.89	2.47	1.49	0.2603	0.5008
313	B3	3.63	3.10	1.81	0.2611	0.5024	3.20	2.57	1.35	0.2794	0.5050
314	B4	4.12	3.18	1.57	0.2916	0.5062	3.62	2.61	1.06	0.3152	0.5112
315	B5	7.25	7.12	4.25	0.2286	0.5054	6.97	6.53	3.90	0.2391	0.5040
316	B6	8.19	7.23	3.55	0.2576	0.5111	7.60	6.50	2.88	0.2672	0.5143
317	B7	8.77	7.07	2.97	0.2836	0.5142	8.17	6.26	2.20	0.3006	0.5184
318	B8	10.13	7.11	2.57	0.3257	0.5139	9.30	6.22	1.78	0.3447	0.5186
319	B9	16.77	18.20	11.59	0.2066	0.5048	15.47	16.38	10.56	0.2113	0.5034
320	B10	17.27	17.92	10.64	0.2172	0.5072	16.06	16.29	9.69	0.2219	0.5065

Table A.24: *Nikon D100 and D40 measurements by HDR characterisation (bright-side IT8.7/1 – patch index: 281-288 and dark-side – patch index: 289-320).*

Nikon D100 measurements							Nikon D40 measurements				
Index	Patch#	X	Y[cd/m^2]	Z	u’	v’	X	Y[cd/m^2]	Z	u’	v’
321	B11	17.68	17.68	9.97	0.2261	0.5087	16.63	16.35	9.13	0.2300	0.5087
322	B12	19.13	17.75	8.01	0.2473	0.5163	17.89	16.32	7.01	0.2523	0.5176
323	B13	28.45	34.61	23.74	0.1839	0.5034	26.88	31.98	23.04	0.1868	0.4999
324	B14	30.41	32.92	23.70	0.2043	0.4977	29.17	31.35	22.90	0.2054	0.4966
325	B15	33.20	38.12	20.37	0.1994	0.5151	32.22	36.40	19.07	0.2028	0.5155
326	B16	27.37	31.83	21.05	0.1928	0.5044	26.54	29.91	20.02	0.1983	0.5029
327	B17	30.45	33.21	20.60	0.2063	0.5063	29.71	31.95	19.88	0.2090	0.5057
328	B18	29.64	36.20	20.25	0.1872	0.5144	28.22	34.41	19.63	0.1871	0.5134
329	B19	27.25	31.47	23.54	0.1913	0.4969	26.57	30.64	23.41	0.1910	0.4956
330	B20	4.20	3.54	2.28	0.2614	0.4969	3.53	2.77	1.63	0.2823	0.4988
331	B21	8.64	6.86	3.34	0.2845	0.5079	7.92	6.01	2.61	0.2993	0.5107
332	B22	14.85	14.05	7.81	0.2385	0.5078	14.12	13.19	6.74	0.2432	0.5113
333	C1	4.20	4.31	2.64	0.2188	0.5053	3.72	3.77	2.28	0.2216	0.5056
334	C2	4.44	4.39	2.16	0.2317	0.5146	3.99	3.82	1.78	0.2393	0.5160
335	C3	4.71	4.46	1.84	0.2439	0.5206	4.23	3.91	1.38	0.2526	0.5250
336	C4	4.95	4.54	1.40	0.2566	0.5290	4.55	4.00	1.01	0.2690	0.5328
337	C5	11.94	12.61	6.08	0.2177	0.5174	11.13	11.44	5.45	0.2237	0.5172
338	C6	12.71	12.61	4.28	0.2369	0.5286	11.81	11.50	3.41	0.2428	0.5320
339	C7	13.04	12.35	2.92	0.2520	0.5368	12.23	11.27	2.10	0.2607	0.5407
340	C8	14.12	12.23	1.79	0.2783	0.5424	13.07	11.05	1.06	0.2872	0.5464
341	C9	18.50	20.34	11.88	0.2060	0.5096	16.95	18.22	10.69	0.2103	0.5088
342	C10	18.76	20.29	10.55	0.2116	0.5147	17.46	18.68	9.45	0.2143	0.5157
343	C11	19.13	20.14	9.26	0.2193	0.5194	17.93	18.94	8.23	0.2195	0.5217
344	C12	20.79	20.63	5.41	0.2399	0.5359	19.41	19.08	4.44	0.2435	0.5384
345	C13	25.31	31.42	23.29	0.1787	0.4992	24.17	30.19	21.96	0.1781	0.5005
346	C14	27.06	28.45	22.24	0.2080	0.4919	26.00	26.77	21.20	0.2118	0.4905
347	C15	32.05	37.52	16.05	0.1994	0.5252	29.71	34.07	14.61	0.2033	0.5245
348	C16	21.69	24.61	16.42	0.1971	0.5033	20.26	22.80	15.39	0.1985	0.5024
349	C17	26.39	27.26	16.25	0.2180	0.5068	25.04	25.47	15.52	0.2208	0.5053
350	C18	26.82	33.98	17.52	0.1821	0.5191	24.14	29.95	15.69	0.1855	0.5179
351	C19	23.22	26.28	22.73	0.1913	0.4870	21.60	24.44	22.11	0.1901	0.4839
352	C20	7.08	6.08	2.24	0.2699	0.5211	6.29	5.26	1.58	0.2797	0.5265
353	C21	10.66	10.74	5.49	0.2266	0.5135	9.72	9.70	4.87	0.2291	0.5140
354	C22	12.39	11.57	5.42	0.2452	0.5150	11.53	10.66	4.49	0.2493	0.5189
355	D1	3.06	3.21	2.09	0.2130	0.5024	2.69	2.77	1.74	0.2175	0.5042
356	D2	3.17	3.34	1.78	0.2162	0.5129	2.76	2.86	1.38	0.2221	0.5167
357	D3	3.24	3.50	1.55	0.2147	0.5216	2.79	2.90	1.14	0.2246	0.5252
358	D4	3.23	3.59	1.23	0.2130	0.5317	2.85	3.06	0.85	0.2218	0.5369
359	D5	9.27	10.30	5.08	0.2072	0.5178	8.50	9.22	4.54	0.2120	0.5173
360	D6	9.28	10.53	3.21	0.2099	0.5359	8.52	9.38	2.67	0.2168	0.5369

Table A.25: *Nikon D100 and D40 measurements by HDR characterisation (dark-side IT8.7/1 – patch index: 321-360).*

Nikon D100 measurements							Nikon D40 measurements				
Index	Patch#	X	Y[cd/m^2]	Z	u'	v'	X	Y[cd/m^2]	Z	u'	v'
361	D7	8.86	10.08	2.32	0.2122	0.5432	8.18	9.24	1.52	0.2162	0.5495
362	D8	9.02	10.48	1.42	0.2115	0.5532	8.05	9.41	0.68	0.2129	0.5599
363	D9	20.06	23.02	10.23	0.2026	0.5231	18.69	21.37	9.31	0.2037	0.5238
364	D10	20.56	23.71	6.50	0.2079	0.5392	18.88	21.57	5.61	0.2102	0.5403
365	D11	19.93	23.39	3.88	0.2085	0.5505	18.62	21.61	3.12	0.2115	0.5523
366	D12	19.73	23.85	1.93	0.2059	0.5600	18.86	22.69	1.03	0.2082	0.5636
367	D13	23.16	29.83	22.68	0.1719	0.4984	22.62	28.90	22.17	0.1731	0.4977
368	D14	24.53	24.13	21.62	0.2174	0.4812	23.66	23.10	19.97	0.2200	0.4834
369	D15	31.39	36.16	13.46	0.2045	0.5299	29.52	34.42	12.07	0.2029	0.5322
370	D16	16.19	18.27	12.41	0.1978	0.5021	15.02	16.82	11.04	0.2000	0.5038
371	D17	22.09	21.72	12.42	0.2293	0.5076	20.84	20.07	11.20	0.2346	0.5081
372	D18	23.57	30.65	13.73	0.1798	0.5259	21.68	27.93	12.58	0.1813	0.5255
373	D19	18.12	20.71	20.48	0.1858	0.4777	17.14	19.14	20.02	0.1882	0.4728
374	D20	2.98	3.11	1.95	0.2150	0.5045	2.33	2.33	1.35	0.2255	0.5074
375	D21	13.64	14.22	1.51	0.2357	0.5529	12.79	13.22	0.87	0.2393	0.5568
376	D22	16.68	19.88	19.37	0.1789	0.4797	16.03	18.72	18.91	0.1813	0.4765
377	E1	3.63	4.03	2.50	0.2027	0.5068	3.22	3.55	2.09	0.2055	0.5093
378	E2	3.44	4.05	1.97	0.1963	0.5200	3.07	3.55	1.54	0.2018	0.5242
379	E3	3.37	4.27	1.62	0.1864	0.5318	2.91	3.67	1.17	0.1896	0.5372
380	E4	3.22	4.50	1.21	0.1735	0.5447	2.74	3.87	0.70	0.1741	0.5539
381	E5	12.14	14.66	6.88	0.1921	0.5222	11.18	13.34	6.09	0.1948	0.5230
382	E6	11.24	14.71	4.61	0.1830	0.5388	10.60	13.69	3.94	0.1861	0.5410
383	E7	10.41	14.75	2.97	0.1731	0.5518	9.59	13.54	2.26	0.1747	0.5553
384	E8	10.08	15.40	1.88	0.1634	0.5618	9.16	14.05	1.16	0.1640	0.5661
385	E9	19.04	22.51	12.32	0.1934	0.5146	17.96	21.10	11.37	0.1950	0.5152
386	E10	18.65	22.96	9.90	0.1899	0.5262	17.40	21.21	9.18	0.1917	0.5257
387	E11	17.81	23.00	8.25	0.1839	0.5341	16.68	21.30	7.14	0.1865	0.5361
388	E12	17.79	24.23	5.88	0.1784	0.5467	16.27	21.87	5.24	0.1808	0.5467
389	E13	21.63	28.27	22.77	0.1683	0.4950	20.79	27.22	20.83	0.1692	0.4984
390	E14	21.98	20.65	19.78	0.2248	0.4752	21.40	19.71	18.87	0.2291	0.4747
391	E15	29.24	34.39	10.74	0.2026	0.5361	29.24	33.50	10.09	0.2081	0.5365
392	E16	11.87	13.36	9.22	0.1978	0.5012	11.38	12.46	8.45	0.2034	0.5015
393	E17	19.09	17.52	9.58	0.2458	0.5076	18.10	16.15	8.56	0.2532	0.5082
394	E18	20.69	27.32	10.90	0.1787	0.5309	20.15	26.50	10.18	0.1799	0.5321
395	E19	14.75	16.65	18.94	0.1837	0.4663	14.39	15.99	18.65	0.1855	0.4640
396	E20	4.55	5.48	1.82	0.1976	0.5348	3.93	4.63	1.26	0.2036	0.5400
397	E21	11.26	14.39	2.99	0.1908	0.5486	10.78	13.64	2.48	0.1935	0.5509
398	E22	5.67	9.58	5.80	0.1359	0.5170	4.97	8.53	5.36	0.1334	0.5152
399	F1	2.70	3.10	2.35	0.1917	0.4961	2.31	2.62	1.87	0.1956	0.4995
400	F2	2.53	3.16	2.17	0.1791	0.5040	2.09	2.65	1.62	0.1793	0.5107

Table A.26: *Nikon D100 and D40 measurements by HDR characterisation (dark-side IT8.7/1 – patch index: 361-400).*

Nikon D100 measurements							Nikon D40 measurements				
Index	Patch#	X	Y[cd/m^2]	Z	u’	v’	X	Y[cd/m^2]	Z	u’	v’
401	F3	2.42	3.32	2.05	0.1661	0.5120	1.90	2.69	1.54	0.1619	0.5164
402	F4	2.27	3.43	1.93	0.1529	0.5186	1.70	2.76	1.33	0.1440	0.5275
403	F5	6.45	8.08	5.11	0.1806	0.5085	5.80	7.19	4.51	0.1824	0.5087
404	F6	5.74	8.14	4.62	0.1621	0.5169	5.00	7.19	4.06	0.1600	0.5175
405	F7	4.97	8.08	3.84	0.1443	0.5282	4.31	7.24	3.22	0.1405	0.5316
406	F8	4.82	8.12	3.66	0.1402	0.5310	4.01	7.16	3.11	0.1327	0.5337
407	F9	13.14	16.10	9.96	0.1847	0.5093	11.98	14.46	9.06	0.1871	0.5083
408	F10	12.13	16.17	9.20	0.1719	0.5156	11.06	14.56	8.49	0.1735	0.5140
409	F11	11.51	16.48	8.91	0.1613	0.5197	10.30	14.97	7.80	0.1596	0.5217
410	F12	10.68	16.71	8.14	0.1495	0.5263	9.68	15.57	7.09	0.1463	0.5298
411	F13	20.46	27.28	22.18	0.1650	0.4948	18.89	24.94	20.29	0.1665	0.4946
412	F14	19.84	17.74	17.74	0.2341	0.4707	18.75	16.19	17.66	0.2383	0.4632
413	F15	29.16	33.89	8.69	0.2070	0.5412	28.20	32.40	8.05	0.2095	0.5417
414	F16	8.95	9.72	6.90	0.2040	0.4986	8.11	8.77	6.06	0.2054	0.5001
415	F17	16.39	14.20	7.15	0.2613	0.5095	15.26	12.69	6.26	0.2720	0.5089
416	F18	18.52	25.34	8.52	0.1746	0.5376	17.61	23.90	7.68	0.1764	0.5389
417	F19	11.78	12.95	17.54	0.1821	0.4506	10.99	11.78	17.20	0.1838	0.4430
418	F20	2.14	2.88	1.50	0.1717	0.5202	1.50	2.11	0.92	0.1670	0.5290
419	F21	3.79	6.51	1.45	0.1434	0.5538	3.09	5.55	1.04	0.1382	0.5582
420	F22	5.42	9.24	1.63	0.1455	0.5585	4.73	8.38	1.06	0.1416	0.5644
421	G1	2.15	2.35	2.09	0.1968	0.4843	1.72	1.87	1.59	0.1992	0.4872
422	G2	2.22	2.51	2.19	0.1912	0.4867	1.59	1.90	1.67	0.1815	0.4871
423	G3	2.01	2.51	2.27	0.1729	0.4861	1.51	1.90	1.72	0.1714	0.4863
424	G4	1.89	2.60	2.51	0.1561	0.4834	1.34	1.96	1.87	0.1476	0.4855
425	G5	6.36	7.73	5.85	0.1819	0.4974	5.61	6.83	5.30	0.1810	0.4960
426	G6	5.60	7.79	6.20	0.1588	0.4971	5.01	6.96	5.55	0.1590	0.4969
427	G7	4.98	7.58	6.68	0.1434	0.4918	4.31	6.82	5.93	0.1386	0.4935
428	G8	4.84	7.67	6.42	0.1391	0.4961	4.09	6.69	5.84	0.1341	0.4938
429	G9	12.97	16.14	10.85	0.1804	0.5051	11.85	14.22	10.14	0.1855	0.5008
430	G10	11.90	15.53	11.42	0.1705	0.5008	10.78	14.06	10.38	0.1705	0.5005
431	G11	11.00	15.60	11.75	0.1570	0.5010	10.10	14.38	10.68	0.1567	0.5019
432	G12	10.60	16.69	12.72	0.1417	0.5022	9.38	14.84	11.04	0.1415	0.5038
433	G13	18.43	25.23	21.37	0.1599	0.4926	17.31	23.14	19.88	0.1633	0.4911
434	G14	17.56	14.79	17.06	0.2417	0.4581	16.51	13.70	16.15	0.2441	0.4559
435	G15	28.03	32.68	6.31	0.2087	0.5475	26.11	30.05	5.92	0.2112	0.5468
436	G16	6.40	6.96	5.08	0.2032	0.4969	5.66	5.92	4.32	0.2107	0.4960
437	G17	13.79	11.04	5.32	0.2824	0.5086	12.38	9.66	4.24	0.2913	0.5114
438	G18	16.55	22.98	6.55	0.1738	0.5430	15.32	21.42	5.73	0.1732	0.5449
439	G19	9.15	9.76	16.17	0.1794	0.4305	8.55	9.00	15.28	0.1805	0.4277
440	G20	2.62	4.03	1.98	0.1520	0.5255	2.02	3.31	1.39	0.1451	0.5335

Table A.27: *Nikon D100 and D40 measurements by HDR characterisation (dark-side IT8.7/1 – patch index: 401-440).*

Nikon D100 measurements							Nikon D40 measurements				
Index	Patch#	X	Y[cd/m^2]	Z	u’	v’	X	Y[cd/m^2]	Z	u’	v’
441	G21	3.63	5.22	3.84	0.1554	0.5027	3.09	4.58	3.05	0.1529	0.5091
442	G22	1.60	1.78	2.37	0.1813	0.4522	1.21	1.34	1.89	0.1795	0.4472
443	H1	2.07	2.22	2.22	0.1972	0.4755	1.70	1.79	1.68	0.2034	0.4794
444	H2	1.99	2.25	2.53	0.1840	0.4675	1.59	1.78	1.97	0.1862	0.4683
445	H3	2.00	2.37	2.95	0.1727	0.4598	1.50	1.77	2.36	0.1708	0.4534
446	H4	1.89	2.37	3.64	0.1562	0.4409	1.38	1.78	3.11	0.1480	0.4281
447	H5	5.19	5.88	5.65	0.1884	0.4795	4.65	5.33	5.00	0.1868	0.4815
448	H6	4.83	5.90	6.67	0.1704	0.4686	4.34	5.34	6.19	0.1685	0.4667
449	H7	4.33	5.73	8.24	0.1505	0.4485	3.81	5.16	7.47	0.1473	0.4481
450	H8	4.19	5.82	9.35	0.1403	0.4381	3.55	5.06	8.55	0.1351	0.4334
451	H9	12.88	14.82	11.08	0.1920	0.4969	12.02	13.72	10.51	0.1929	0.4952
452	H10	12.31	14.73	12.39	0.1821	0.4902	11.42	13.62	11.68	0.1821	0.4888
453	H11	11.87	14.66	13.57	0.1742	0.4842	10.94	13.37	12.80	0.1751	0.4815
454	H12	10.99	14.89	17.68	0.1529	0.4663	10.02	13.67	16.58	0.1513	0.4646
455	H13	17.12	23.80	20.54	0.1571	0.4916	15.90	21.89	19.75	0.1577	0.4883
456	H14	15.78	12.52	16.01	0.2508	0.4479	14.72	11.54	14.72	0.2538	0.4477
457	H15	26.90	31.16	4.91	0.2114	0.5509	25.64	29.57	4.36	0.2126	0.5518
458	H16	4.53	4.75	3.67	0.2090	0.4925	3.74	3.95	2.83	0.2093	0.4974
459	H17	11.59	8.66	3.78	0.3033	0.5100	10.58	7.72	3.00	0.3126	0.5133
460	H18	14.80	21.28	4.95	0.1698	0.5490	13.79	19.56	4.28	0.1723	0.5501
461	H19	7.11	7.35	14.27	0.1775	0.4129	6.37	6.65	13.14	0.1750	0.4112
462	H20	1.77	2.08	2.32	0.1774	0.4689	1.25	1.49	1.74	0.1728	0.4658
463	H21	3.07	4.17	4.99	0.1524	0.4656	2.52	3.57	4.34	0.1461	0.4649
464	H22	1.59	1.30	1.48	0.2488	0.4582	1.20	0.88	1.04	0.2725	0.4530
465	I1	2.62	2.64	3.21	0.2020	0.4583	2.23	2.27	2.58	0.2026	0.4641
466	I2	2.61	2.64	4.28	0.1894	0.4319	2.19	2.19	3.64	0.1907	0.4287
467	I3	2.60	2.71	5.89	0.1710	0.4003	2.19	2.14	5.36	0.1736	0.3824
468	I4	2.49	2.55	8.23	0.1522	0.3507	2.02	2.04	7.57	0.1463	0.3318
469	I5	6.59	7.08	6.61	0.1987	0.4805	5.89	6.29	6.00	0.1995	0.4787
470	I6	6.58	6.98	8.16	0.1940	0.4627	5.93	6.13	7.47	0.1969	0.4587
471	I7	6.26	6.66	9.85	0.1843	0.4417	5.72	5.95	8.88	0.1882	0.4402
472	I8	6.20	6.64	12.75	0.1722	0.4148	5.59	5.66	12.42	0.1748	0.3989
473	I9	13.07	14.48	11.16	0.1982	0.4941	12.01	13.01	10.54	0.2012	0.4904
474	I10	12.67	14.07	12.41	0.1942	0.4853	11.91	12.95	11.42	0.1983	0.4847
475	I11	12.66	14.03	13.79	0.1915	0.4774	11.94	12.89	12.57	0.1965	0.4774
476	I12	12.92	13.99	17.80	0.1871	0.4559	11.51	12.39	15.59	0.1887	0.4568
477	I13	16.22	22.53	20.65	0.1559	0.4873	15.02	20.80	19.12	0.1563	0.4870
478	I14	14.40	10.99	14.81	0.2576	0.4422	13.41	10.09	13.50	0.2612	0.4425
479	I15	26.02	29.41	3.89	0.2174	0.5528	24.44	27.57	3.16	0.2185	0.5545
480	I16	3.25	3.35	2.68	0.2108	0.4900	2.51	2.56	1.84	0.2163	0.4963

Table A.28: *Nikon D100 and D40 measurements by HDR characterisation (dark-side IT8.7/1 – patch index: 441-480).*

Nikon D100 measurements							Nikon D40 measurements				
Index	Patch#	X	Y[cd/m^2]	Z	u’	v’	X	Y[cd/m^2]	Z	u’	v’
481	I17	10.13	7.11	2.84	0.3234	0.5107	8.44	5.74	1.98	0.3363	0.5141
482	I18	13.10	19.11	3.75	0.1686	0.5530	11.85	17.51	2.82	0.1675	0.5569
483	I19	5.49	5.52	12.94	0.1729	0.3907	4.87	4.86	11.86	0.1719	0.3859
484	I20	3.59	4.05	6.73	0.1697	0.4314	3.05	3.42	5.88	0.1692	0.4276
485	I21	4.94	6.29	10.05	0.1528	0.4372	4.45	5.74	9.11	0.1511	0.4382
486	I22	1.12	1.15	0.87	0.2132	0.4929	0.77	0.77	0.46	0.2249	0.5054
487	J1	1.42	1.38	1.69	0.2091	0.4563	1.03	0.95	1.20	0.2182	0.4528
488	J2	1.47	1.33	2.23	0.2093	0.4258	1.05	0.87	1.75	0.2165	0.4048
489	J3	1.51	1.30	3.17	0.1982	0.3834	1.09	0.83	2.66	0.2026	0.3477
490	J4	1.48	1.17	4.91	0.1757	0.3116	1.11	0.78	4.25	0.1734	0.2745
491	J5	4.37	4.29	4.34	0.2136	0.4724	3.85	3.72	3.82	0.2166	0.4709
492	J6	4.65	4.35	5.94	0.2120	0.4463	4.09	3.75	5.12	0.2159	0.4460
493	J7	4.65	4.23	7.03	0.2089	0.4267	4.23	3.60	6.56	0.2169	0.4159
494	J8	5.00	4.11	10.08	0.2064	0.3817	4.40	3.48	9.28	0.2085	0.3708
495	J9	10.76	11.62	9.32	0.2020	0.4910	9.91	10.53	8.61	0.2046	0.4893
496	J10	10.71	11.19	10.08	0.2052	0.4824	9.80	10.19	9.27	0.2058	0.4816
497	J11	11.08	11.11	11.90	0.2076	0.4685	10.41	10.59	10.68	0.2070	0.4735
498	J12	11.62	11.25	15.46	0.2050	0.4465	10.57	10.04	14.30	0.2072	0.4428
499	J13	14.98	20.97	19.55	0.1543	0.4862	13.79	19.13	18.38	0.1550	0.4838
500	J14	12.79	9.27	13.23	0.2671	0.4357	11.95	8.38	12.39	0.2734	0.4315
501	J15	24.68	28.05	2.59	0.2178	0.5570	23.74	26.75	1.99	0.2204	0.5586
502	J16	2.19	2.28	1.86	0.2087	0.4889	1.56	1.58	1.14	0.2172	0.4962
503	J17	8.16	5.42	2.01	0.3418	0.5109	7.32	4.61	1.29	0.3645	0.5164
504	J18	11.36	16.91	2.24	0.1673	0.5601	10.56	15.73	1.83	0.1677	0.5618
505	J19	4.12	3.98	11.21	0.1693	0.3675	3.70	3.57	10.31	0.1676	0.3645
506	J20	1.15	0.93	3.31	0.1839	0.3338	0.74	0.54	2.66	0.1756	0.2899
507	J21	3.99	3.70	6.96	0.1983	0.4144	3.53	3.21	6.41	0.1991	0.4075
508	J22	1.04	1.13	1.18	0.1933	0.4722	0.62	0.74	0.43	0.1920	0.5121
509	K1	1.78	1.67	1.77	0.2221	0.4677	1.36	1.22	1.19	0.2334	0.4727
510	K2	1.96	1.68	1.94	0.2377	0.4582	1.53	1.21	1.48	0.2542	0.4510
511	K3	2.16	1.67	2.32	0.2521	0.4400	1.73	1.22	1.80	0.2724	0.4318
512	K4	2.56	1.71	2.87	0.2770	0.4183	2.11	1.28	2.35	0.2969	0.4063
513	K5	3.68	3.34	3.36	0.2309	0.4707	3.12	2.77	2.89	0.2343	0.4674
514	K6	4.23	3.35	4.31	0.2510	0.4472	3.69	2.80	3.79	0.2589	0.4416
515	K7	4.55	3.22	5.14	0.2663	0.4246	3.95	2.63	4.33	0.2800	0.4198
516	K8	5.24	3.24	6.56	0.2849	0.3967	4.60	2.61	5.90	0.2989	0.3825
517	K9	9.22	9.42	7.76	0.2122	0.4879	8.36	8.27	7.14	0.2172	0.4839
518	K10	9.67	9.07	9.18	0.2232	0.4712	8.88	8.24	8.04	0.2270	0.4735
519	K11	10.44	9.20	10.33	0.2328	0.4614	9.70	8.37	9.13	0.2385	0.4632
520	K12	11.93	8.98	13.55	0.2547	0.4316	10.95	8.11	11.96	0.2599	0.4332

Table A.29: *Nikon D100 and D40 measurements by HDR characterisation (dark-side IT8.7/1 – patch index: 481-520).*

Nikon D100 measurements							Nikon D40 measurements				
Index	Patch#	X	Y[cd/m^2]	Z	u’	v’	X	Y[cd/m^2]	Z	u’	v’
521	K13	14.04	19.80	19.03	0.1526	0.4841	12.89	18.21	17.20	0.1526	0.4854
522	K14	11.81	8.25	12.52	0.2729	0.4289	10.79	7.37	11.06	0.2793	0.4292
523	K15	23.74	26.54	1.67	0.2225	0.5596	21.92	24.21	1.15	0.2257	0.5608
524	K16	1.59	1.66	1.40	0.2073	0.4869	0.94	0.96	0.67	0.2166	0.4983
525	K17	6.98	4.41	1.58	0.3585	0.5097	6.09	3.64	0.85	0.3855	0.5181
526	K18	10.03	14.90	1.51	0.1686	0.5633	9.26	13.82	1.03	0.1687	0.5662
527	K19	3.31	3.14	9.61	0.1671	0.3566	2.88	2.67	9.06	0.1644	0.3426
528	K20	2.15	1.62	3.14	0.2393	0.4066	1.64	1.09	2.50	0.2576	0.3846
529	K21	5.68	4.63	7.97	0.2295	0.4207	5.29	4.12	7.35	0.2372	0.4161
530	K22	0.99	1.16	1.36	0.1767	0.4642	0.59	0.74	0.79	0.1686	0.4733
531	L1	1.74	1.67	1.49	0.2224	0.4807	1.34	1.22	0.98	0.2364	0.4862
532	L2	1.94	1.68	1.52	0.2446	0.4773	1.54	1.22	1.07	0.2676	0.4764
533	L3	2.16	1.74	1.48	0.2643	0.4787	1.75	1.26	1.13	0.2923	0.4715
534	L4	2.61	1.82	1.55	0.3027	0.4735	2.14	1.34	1.17	0.3317	0.4684
535	L5	3.67	3.32	2.77	0.2375	0.4839	3.15	2.76	2.32	0.2445	0.4821
536	L6	4.21	3.27	3.04	0.2700	0.4719	3.74	2.76	2.46	0.2842	0.4732
537	L7	4.77	3.23	3.12	0.3050	0.4644	4.12	2.62	2.47	0.3241	0.4640
538	L8	5.66	3.49	3.25	0.3338	0.4637	5.02	2.86	2.67	0.3590	0.4603
539	L9	8.93	9.02	6.72	0.2173	0.4938	8.18	8.19	6.12	0.2190	0.4934
540	L10	9.43	9.00	7.02	0.2280	0.4894	8.72	7.97	6.36	0.2367	0.4868
541	L11	10.21	8.86	7.76	0.2456	0.4792	9.32	7.91	6.75	0.2515	0.4802
542	L12	11.30	8.71	8.17	0.2715	0.4710	10.43	7.85	7.03	0.2797	0.4732
543	L13	12.27	17.76	18.09	0.1474	0.4801	11.31	15.97	16.34	0.1509	0.4793
544	L14	9.00	5.71	9.78	0.2903	0.4145	8.34	5.10	8.69	0.3008	0.4137
545	L15	21.24	22.93	0.62	0.2314	0.5622	20.22	21.61	-0.01	0.2349	0.5648
546	L16	1.02	1.09	1.03	0.1996	0.4793	0.50	0.51	0.38	0.2152	0.4937
547	L17	4.57	2.82	1.13	0.3633	0.5052	3.78	2.16	0.49	0.4016	0.5165
548	L18	7.80	11.51	0.54	0.1713	0.5690	7.27	10.70	0.10	0.1731	0.5730
549	L19	1.93	1.56	7.15	0.1644	0.3006	1.55	1.24	6.38	0.1577	0.2842
550	L20	2.89	2.01	2.43	0.2867	0.4485	2.40	1.50	1.90	0.3142	0.4410
551	L21	5.63	4.55	4.65	0.2562	0.4663	5.29	4.17	3.99	0.2652	0.4703
552	L22	1.49	1.25	0.87	0.2597	0.4929	1.03	0.78	0.39	0.2981	0.5049
553	Dmin	23.09	26.74	17.44	0.1938	0.5051	22.01	25.18	15.90	0.1968	0.5065
554	N1	18.13	20.45	14.57	0.1967	0.4993	17.14	19.43	12.78	0.1976	0.5040
555	N2	16.73	18.95	13.13	0.1967	0.5011	15.62	17.54	11.52	0.1994	0.5039
556	N3	14.69	16.70	11.43	0.1961	0.5019	13.69	15.31	10.62	0.1990	0.5007
557	N4	12.98	14.56	10.07	0.1984	0.5010	12.30	13.49	9.53	0.2022	0.4992
558	N5	11.50	12.71	8.83	0.2012	0.5003	10.87	11.96	8.22	0.2022	0.5009
559	N6	9.96	10.97	7.95	0.2008	0.4977	9.19	10.03	7.29	0.2026	0.4973
560	N7	8.60	9.51	6.82	0.2005	0.4984	7.75	8.44	5.98	0.2034	0.4988

Table A.30: *Nikon D100 and D40 measurements by HDR characterisation (dark-side IT8.7/1 – patch index: 521-560).*

Nikon D100 measurements							Nikon D40 measurements				
Index	Patch#	X	Y[cd/m^2]	Z	u’	v’	X	Y[cd/m^2]	Z	u’	v’
561	N8	7.41	8.10	5.77	0.2028	0.4985	6.68	7.12	5.07	0.2076	0.4979
562	N9	6.34	7.00	5.07	0.2005	0.4979	5.72	6.11	4.38	0.2069	0.4976
563	N10	5.54	5.96	4.46	0.2046	0.4951	4.77	5.15	3.69	0.2049	0.4980
564	N11	4.61	4.93	3.91	0.2042	0.4913	3.98	4.26	3.09	0.2066	0.4969
565	N12	3.98	4.23	3.39	0.2052	0.4906	3.36	3.52	2.63	0.2098	0.4945
566	N13	3.43	3.64	3.04	0.2046	0.4878	2.81	2.93	2.27	0.2098	0.4922
567	N14	2.90	3.06	2.60	0.2049	0.4867	2.34	2.41	1.82	0.2130	0.4933
568	N15	2.48	2.58	2.17	0.2080	0.4868	1.89	1.92	1.51	0.2146	0.4904
569	N16	2.06	2.12	1.89	0.2086	0.4826	1.50	1.51	1.14	0.2172	0.4929
570	N17	1.62	1.67	1.44	0.2082	0.4854	1.23	1.23	0.89	0.2199	0.4951
571	N18	1.37	1.39	1.23	0.2110	0.4832	1.04	1.01	0.77	0.2236	0.4913
572	N19	1.15	1.19	1.11	0.2068	0.4793	0.77	0.77	0.58	0.2193	0.4925
573	N20	1.01	1.06	0.93	0.2052	0.4842	0.63	0.64	0.48	0.2170	0.4933
574	N21	0.87	0.92	0.87	0.2017	0.4789	0.52	0.52	0.41	0.2170	0.4900
575	N22	0.77	0.83	0.80	0.1980	0.4776	0.43	0.44	0.34	0.2148	0.4906
576	Dmax	0.69	0.76	0.76	0.1943	0.4756	0.39	0.40	0.33	0.2124	0.4871

Table A.31: *Nikon D100 and D40 measurements by HDR characterisation (dark-side IT8.7/1 – patch index: 561-576).*

Radiometric measurements							Canon 350D measurements				
Index	Patch#	X	Y[cd/m^2]	Z	u'	v'	X	Y[cd/m^2]	Z	u'	v'
1	A1	995.63	769.20	168.81	0.3054	0.5309	1012.00	794.99	183.49	0.3001	0.5305
2	B1	3334.80	2572.00	657.77	0.3039	0.5274	3313.93	2616.25	731.45	0.2962	0.5261
3	C1	1141.34	1150.00	802.56	0.2195	0.4976	1152.74	1145.77	756.85	0.2237	0.5003
4	D1	745.52	778.40	153.67	0.2315	0.5438	756.09	778.77	143.24	0.2350	0.5447
5	E1	1306.82	1153.00	799.08	0.2489	0.4942	1255.95	1117.23	759.71	0.2476	0.4955
6	F1	1230.12	1523.00	672.44	0.1886	0.5253	1210.60	1474.50	648.31	0.1916	0.5251
7	A2	3782.08	2603.00	161.71	0.3493	0.5409	3665.68	2597.90	252.28	0.3379	0.5388
8	B2	814.61	747.00	989.62	0.2174	0.4485	813.86	748.64	899.14	0.2208	0.4571
9	C2	2441.79	1472.00	310.03	0.3838	0.5205	2437.53	1562.42	360.51	0.3617	0.5217
10	D2	581.89	407.50	276.14	0.3094	0.4875	576.17	413.30	256.70	0.3054	0.4930
11	E2	2007.70	2164.00	231.15	0.2284	0.5539	1876.52	2020.10	195.06	0.2291	0.5549
12	F2	2266.96	1780.00	97.39	0.3099	0.5475	2201.09	1732.40	96.03	0.3092	0.5476
13	A3	389.11	343.60	672.03	0.2059	0.4091	389.15	337.37	600.45	0.2147	0.4187
14	B3	1093.39	1443.00	265.01	0.1858	0.5519	1116.02	1423.04	256.35	0.1922	0.5513
15	C3	1652.94	892.00	102.73	0.4310	0.5233	1749.88	1064.67	174.89	0.3836	0.5252
16	D3	3919.03	3417.00	202.02	0.2810	0.5513	3756.82	3296.34	229.62	0.2788	0.5505
17	E3	1646.87	991.60	467.07	0.3676	0.4980	1672.82	1068.57	472.59	0.3500	0.5030
18	F3	419.54	573.30	519.02	0.1587	0.4879	417.65	556.89	498.19	0.1627	0.4882
19	A4	7008.98	6508.00	2488.92	0.2501	0.5225	6296.21	5806.93	2193.75	0.2519	0.5227
20	B4	4046.31	3787.00	1494.28	0.2477	0.5217	3710.41	3455.20	1380.44	0.2487	0.5211
21	C4	2192.16	2053.00	815.23	0.2475	0.5215	2006.57	1863.14	732.82	0.2496	0.5215
22	D4	954.32	890.70	356.41	0.2481	0.5211	868.45	817.09	309.70	0.2472	0.5233
23	E4	349.61	327.80	133.37	0.2468	0.5206	334.58	314.37	121.86	0.2471	0.5224
24	F4	109.86	102.30	41.44	0.2485	0.5206	97.08	90.51	36.41	0.2483	0.5209
25	A1	2.41	1.80	0.44	0.3137	0.5272	3.32	2.74	0.80	0.2842	0.5267
26	B1	7.22	5.30	1.47	0.3169	0.5234	8.24	6.52	1.94	0.2947	0.5246
27	C1	2.69	2.61	1.84	0.2272	0.4960	3.70	3.53	1.99	0.2361	0.5074
28	D1	1.81	1.82	0.47	0.2372	0.5367	2.85	2.71	0.65	0.2512	0.5366
29	E1	3.08	2.60	1.72	0.2608	0.4953	3.76	3.27	1.84	0.2577	0.5046
30	F1	2.84	3.27	1.53	0.2011	0.5211	2.99	3.30	1.46	0.2106	0.5222
31	A2	6.84	4.62	0.64	0.3505	0.5327	7.51	5.57	0.87	0.3209	0.5352
32	B2	1.63	1.36	1.64	0.2419	0.4542	2.84	2.49	1.99	0.2464	0.4855
33	C2	4.90	2.88	0.72	0.3900	0.5157	6.00	4.13	1.06	0.3373	0.5225
34	D2	1.59	1.07	0.61	0.3267	0.4946	2.61	2.05	0.87	0.2901	0.5130
35	E2	3.76	3.89	0.56	0.2358	0.5488	4.49	4.55	0.80	0.2390	0.5449
36	F2	4.61	3.56	0.57	0.3088	0.5365	4.63	3.79	0.63	0.2926	0.5383
37	A3	0.93	0.80	1.21	0.2246	0.4348	2.16	1.92	1.41	0.2452	0.4911
38	B3	1.98	2.41	0.59	0.1985	0.5436	3.28	3.53	0.91	0.2225	0.5388
39	C3	3.51	1.93	0.33	0.4197	0.5193	4.99	3.45	0.82	0.3369	0.5245
40	D3	6.79	5.70	0.60	0.2887	0.5452	7.94	6.75	0.90	0.2839	0.5429
41	E3	3.41	2.02	0.91	0.3743	0.4989	4.45	3.17	1.25	0.3188	0.5118
42	F3	1.28	1.45	1.08	0.1949	0.4968	2.00	2.01	1.14	0.2246	0.5083
43	A4	8.69	7.78	3.24	0.2573	0.5182	9.74	8.84	3.39	0.2556	0.5217
44	B4	5.39	4.87	2.02	0.2551	0.5187	6.76	6.18	2.32	0.2540	0.5227
45	C4	3.47	3.17	1.29	0.2529	0.5198	4.81	4.32	1.61	0.2586	0.5222
46	D4	1.90	1.68	0.71	0.2600	0.5173	3.46	3.01	1.06	0.2672	0.5232
47	E4	1.05	0.93	0.35	0.2617	0.5215	2.39	2.09	0.73	0.2661	0.5232
48	F4	0.72	0.65	0.22	0.2588	0.5256	1.79	1.54	0.48	0.2716	0.5263

Table A.32: *Radiometric measurements of test colour samples (transparency) by a spectroradiometer (Jeti Specbos 1200) and Canon 350D measurements by HDR characterisation (bright & dark-sides GretagMacbeth ColorCheckers).*

Nikon D100 measurements							Nikon D40 measurements				
Index	Patch#	X	Y[cd/m²]	Z	u’	v’	X	Y[cd/m²]	Z	u’	v’
1	A1	1563.51	1209.45	300.38	0.3054	0.5309	1529.01	1168.31	300.86	0.3065	0.5269
2	B1	5388.68	4041.83	1114.36	0.3039	0.5274	4730.72	3579.01	1109.47	0.3065	0.5217
3	C1	1754.96	1663.61	1152.08	0.2195	0.4976	1724.44	1645.95	1140.15	0.2312	0.4965
4	D1	1123.48	1132.00	216.52	0.2315	0.5438	1097.44	1109.21	212.98	0.2389	0.5433
5	E1	1938.59	1643.50	1131.49	0.2489	0.4942	1929.11	1619.97	1113.76	0.2610	0.4931
6	F1	1818.31	2146.55	1003.45	0.1886	0.5253	1782.92	2054.50	987.00	0.2005	0.5200
7	A2	5816.25	3963.53	403.72	0.3493	0.5409	5127.59	3598.59	347.07	0.3410	0.5385
8	B2	1320.94	1140.22	1366.04	0.2174	0.4485	1295.98	1116.05	1302.31	0.2362	0.4577
9	C2	3758.13	2325.53	565.57	0.3838	0.5205	3523.91	2200.79	547.96	0.3692	0.5188
10	D2	1042.99	721.89	417.94	0.3094	0.4875	995.71	693.53	401.29	0.3160	0.4953
11	E2	2780.15	2951.69	299.99	0.2284	0.5539	2690.60	2773.74	301.36	0.2381	0.5523
12	F2	3267.35	2520.37	151.11	0.3099	0.5475	3177.95	2468.17	133.69	0.3131	0.5471
13	A3	625.19	541.31	888.94	0.2059	0.4091	611.49	527.14	859.59	0.2204	0.4275
14	B3	1632.16	2016.94	396.01	0.1858	0.5519	1599.64	1902.93	395.86	0.2042	0.5466
15	C3	2659.14	1573.26	282.62	0.4310	0.5233	2594.40	1537.27	267.46	0.3923	0.5230
16	D3	5609.20	4854.46	290.62	0.2810	0.5513	5287.17	4467.88	306.34	0.2888	0.5491
17	E3	2544.93	1595.77	722.79	0.3676	0.4980	2544.25	1592.41	711.83	0.3563	0.5017
18	F3	661.74	818.98	759.73	0.1587	0.4879	638.28	786.74	728.27	0.1746	0.4842
19	A4	9909.69	9027.25	3347.35	0.2501	0.5225	8842.42	8049.25	3065.92	0.2549	0.5220
20	B4	5719.89	5271.14	1910.92	0.2477	0.5217	5165.40	4543.92	1916.52	0.2613	0.5172
21	C4	2880.11	2672.47	1049.17	0.2475	0.5215	2911.87	2612.87	1074.60	0.2570	0.5188
22	D4	1326.38	1197.24	485.98	0.2481	0.5211	1289.35	1176.01	466.36	0.2537	0.5207
23	E4	505.84	463.13	193.00	0.2468	0.5206	504.86	460.81	193.03	0.2526	0.5187
24	F4	155.71	141.03	60.98	0.2485	0.5206	152.71	139.86	56.38	0.2524	0.5202
25	A1	10.97	7.94	3.41	0.3137	0.5272	8.81	6.19	2.65	0.3218	0.5082
26	B1	26.26	18.00	6.48	0.3169	0.5234	22.04	15.09	5.20	0.3341	0.5145
27	C1	13.21	10.24	6.54	0.2272	0.4960	10.40	8.02	5.07	0.2852	0.4946
28	D1	8.68	7.13	2.95	0.2372	0.5367	5.80	4.81	1.66	0.2799	0.5220
29	E1	14.53	10.67	6.25	0.2608	0.4953	11.16	8.15	4.88	0.3016	0.4955
30	F1	9.90	8.71	4.46	0.2011	0.5211	7.50	6.69	3.54	0.2533	0.5082
31	A2	22.38	15.15	4.50	0.3505	0.5327	19.25	12.59	3.44	0.3524	0.5188
32	B2	11.99	8.88	5.70	0.2419	0.4542	8.62	6.17	4.60	0.2999	0.4830
33	C2	19.40	12.74	4.77	0.3900	0.5157	15.01	9.38	3.12	0.3635	0.5114
34	D2	14.44	10.09	5.05	0.3267	0.4946	9.92	6.49	3.22	0.3397	0.4995
35	E2	15.01	12.36	4.17	0.2358	0.5488	10.77	8.92	2.59	0.2828	0.5269
36	F2	16.10	11.57	3.78	0.3088	0.5365	12.01	8.55	2.37	0.3261	0.5221
37	A3	7.72	5.99	4.40	0.2246	0.4348	5.28	3.97	3.34	0.2820	0.4774
38	B3	10.18	8.95	3.85	0.1985	0.5436	7.41	6.59	2.97	0.2573	0.5149
39	C3	19.47	12.97	4.81	0.4197	0.5193	14.38	8.99	3.20	0.3622	0.5094
40	D3	24.46	18.33	5.26	0.2887	0.5452	18.78	13.86	3.34	0.3174	0.5270
41	E3	18.43	12.44	5.46	0.3743	0.4989	13.43	8.61	3.89	0.3481	0.5024
42	F3	7.60	6.27	4.07	0.1949	0.4968	5.01	4.15	2.90	0.2640	0.4916
43	A4	27.13	20.67	8.86	0.2573	0.5182	22.80	17.43	7.25	0.2980	0.5126
44	B4	19.46	15.35	6.66	0.2551	0.5187	14.96	11.63	5.27	0.2915	0.5101
45	C4	14.23	11.46	5.07	0.2529	0.5198	10.08	7.94	3.51	0.2887	0.5115
46	D4	10.92	8.79	4.20	0.2600	0.5173	6.48	5.14	2.45	0.2853	0.5086
47	E4	7.83	6.34	3.13	0.2617	0.5215	4.02	3.19	1.61	0.2840	0.5062
48	F4	5.48	4.48	2.36	0.2588	0.5256	2.87	2.29	1.24	0.2802	0.5036

Table A.33: *Nikon D100 and D40 measurements of test colour samples by HDR characterisation (bright & dark-sides GretagMacbeth ColorCheckers).*

A.4 Physical Measurements of the High-Luminance Display

High-luminance display signals					Normalised radiometric measurements					
Index	Patch#	R	G	B	X	Y	Z	L	A	B
1	A1	0	0	0	0.37	0.6	0.37	5.42	-8.4	2.38
2	A2	0	0	85	1.64	1.29	6.45	11.23	11.11	-38.56
3	A3	0	0	170	8.66	5.48	39.55	28.05	34.05	-80.58
4	A4	0	0	255	27.38	18.12	125.73	49.65	45.68	-116.98
5	A5	0	85	0	2.59	5.23	0.8	27.38	-37.32	32.07
6	A6	0	85	85	4.33	6.74	7.81	31.21	-25.8	-9.74
7	A7	0	85	170	11.53	10.85	42.35	39.33	7.83	-64.74
8	A8	0	85	255	30.32	23.62	128.67	55.7	30.94	-108.32
9	A9	0	170	0	16.56	34.94	3.63	65.7	-74.24	70.28
10	B1	0	170	85	18.76	36.96	11.56	67.25	-69.12	39.64
11	B2	0	170	170	26.71	41.85	48.81	70.77	-48.05	-18.3
12	B3	0	170	255	46.06	55.17	137.52	79.14	-19.22	-73.12
13	B4	0	255	0	47.7	100.57	9.66	100.22	-105.5	102.52
14	B5	0	255	85	51.21	104.93	19.33	101.88	-103.16	79.93
15	B6	0	255	170	59.79	110.56	58.15	103.95	-90.65	28.81
16	B7	0	255	255	79.6	124.53	148.25	108.8	-68.87	-27.99
17	B8	85	0	0	4.51	3.08	0.71	20.38	23.39	21.78
18	B9	85	0	85	6.03	3.96	6.56	23.55	27.96	-17.83
19	C1	85	0	170	13.61	8.45	40.72	34.91	40.9	-70.3
20	C2	85	0	255	32.67	21.44	127.7	53.43	49.3	-111.65
21	C3	85	85	0	7.42	8.79	1.22	35.57	-9.58	39.76
22	C4	85	85	85	9.25	10.15	8.07	38.11	-4.37	1.14
23	C5	85	85	170	17.14	14.73	43.32	45.26	17.09	-55.73
24	C6	85	85	255	36.54	27.83	131	59.73	35.41	-102.76
25	C7	85	170	0	22.38	40.16	4.16	69.58	-61.6	73.65
26	C8	85	170	85	24.85	42.3	12.37	71.08	-57.15	43.87
27	C9	85	170	170	32.46	46.76	43.5	74.04	-40.26	-6.35
28	D1	85	170	255	53.09	61.36	137.91	82.57	-15.08	-67.41
29	D2	85	255	0	54.23	107.07	10.29	102.67	-98.78	104.68
30	D3	85	255	85	58.24	111.95	19.74	104.45	-96.52	83.5
31	D4	85	255	170	66.95	117.15	59.81	106.28	-84.33	31.16
32	D5	85	255	255	87.13	131.54	148.97	111.1	-64.45	-24.42
33	D6	170	0	0	25.64	15.93	2.1	46.89	50.46	49.63
34	D7	170	0	85	27.44	17	7.27	48.27	51.89	21.79
35	D8	170	0	170	35.14	21.55	40.8	53.55	57.37	-38.25
36	D9	170	0	255	55.23	35.01	125.92	65.75	62.86	-89.33
37	E1	170	85	0	29.61	22.94	2.74	55.01	31.28	58.17
38	E2	170	85	85	32.2	24.86	9.02	56.94	32.5	30.12
39	E3	170	85	170	40.29	29.49	43.41	61.21	40.99	-28.34
40	E4	170	85	255	61	43.39	131.24	71.82	50.69	-82.07
41	E5	170	170	0	45.87	55.46	5.65	79.3	-20.48	82.51
42	E6	170	170	85	48.52	57.97	13.18	80.72	-19.21	58.22
43	E7	170	170	170	58.17	64.39	50.2	84.17	-9.28	3.22
44	E8	170	170	255	78.51	78.01	138.23	90.78	6.63	-53.45
45	E9	170	255	0	78.76	124.28	11.82	108.72	-70.17	110.38
46	F1	170	255	85	83.7	130.29	20.81	110.69	-69.12	92.06
47	F2	170	255	170	93.08	136.55	59.65	112.69	-60.55	42.37
48	F3	170	255	255	114.23	151.23	148.85	117.15	-44.84	-13.92
49	F4	255	0	0	85.32	52.04	3.33	77.3	77.87	92.25
50	F5	255	0	85	87.45	53.25	8.21	78.02	78.73	69.44

Table A.34: *Device signals and corresponding radiometric measurements of the high-luminance display (patch index: 1-50).*

High-luminance display signals					Normalised radiometric measurements					
Index	Patch#	R	G	B	X	Y	Z	L	A	B
51	F6	255	0	170	94.87	57.64	43.21	80.54	81.19	5.23
52	F7	255	0	255	113.69	70.4	129.77	87.19	83.43	-54.69
53	F8	255	85	0	89	59.32	4	81.47	66.72	95.1
54	F9	255	85	85	91.47	61.49	9.76	82.64	66.11	71.9
55	G1	255	85	170	98.97	65.8	45.62	84.89	69.5	9.78
56	G2	255	85	255	118.12	78.75	133.96	91.12	73.28	-50.39
57	G3	255	170	0	105.84	93.8	7.05	97.55	26.33	107.69
58	G4	255	170	85	108.2	96.51	14.29	98.64	25.46	86.15
59	G5	255	170	170	116.49	101.74	52.68	100.67	29.64	28.92
60	G6	255	170	255	136.03	115.28	142.32	105.63	36.51	-30.17
61	G7	255	255	0	139.3	164.4	13.3	120.91	-24.88	127.19
62	G8	255	255	85	143.59	170.47	22.62	122.57	-26.31	108.98
63	G9	255	255	170	151.99	175.54	62.58	123.93	-21.25	58.85
64	H1	255	255	255	171.92	189.87	152.32	127.64	-12.83	2.29
65	H2	0	0	15	0.33	0.53	0.37	4.76	-7.06	1.16
66	H3	0	0	30	0.4	0.64	0.39	5.81	-8.92	2.57
67	H4	0	0	51	0.41	0.58	0.78	5.27	-6.25	-5.55
68	H5	0	0	115	3.24	2.26	13.59	16.8	19.99	-53.1
69	H6	0	0	145	5.53	3.61	24.63	22.35	27.52	-67.56
70	H7	0	0	204	14.18	8.93	65.23	35.85	40.44	-95.55
71	H8	0	0	225	18.45	11.74	85.17	40.81	43.29	-104.2
72	H9	0	0	240	22.6	14.59	103.94	45.07	45.06	-110.73
73	I1	0	15	0	0.37	0.56	0.39	5.09	-6.9	1.46
74	I2	0	30	0	0.38	0.61	0.44	5.51	-8.26	1.17
75	I3	0	51	0	0.64	1.2	0.54	10.55	-19.8	7.94
76	I4	0	115	0	5.92	12.43	1.51	41.89	-52.27	47.13
77	I5	0	145	0	10.66	22.42	2.44	54.47	-63.8	59.66
78	I6	0	204	0	26.1	55.04	5.5	79.06	-86.3	82.8
79	I7	0	225	0	34.21	72.2	7.04	88.07	-94.61	91.37
80	I8	0	240	0	40.04	84.5	8.18	93.67	-99.68	96.5
81	I9	15	0	0	0.4	0.62	0.37	5.58	-7.79	2.69
82	J1	30	0	0	0.5	0.68	0.34	6.16	-6.23	4.19
83	J2	51	0	0	1.52	1.31	0.49	11.37	7.35	10.36
84	J3	115	0	0	9.08	5.9	1.06	29.15	32.84	31.02
85	J4	145	0	0	16.97	10.68	1.6	39.04	42.98	41.19
86	J5	204	0	0	41.46	25.56	2.79	57.62	60.07	62.22
87	J6	225	0	0	54.08	33.21	3.22	64.33	66.08	70.65
88	J7	240	0	0	62.96	38.57	3.35	68.44	69.8	76.85
89	J8	0	20	20	0.44	0.63	0.38	5.65	-6.67	2.48
90	J9	20	0	20	0.42	0.61	0.42	5.53	-6.99	1.63
91	K1	20	20	0	0.43	0.68	0.38	6.11	-8.84	3.31
92	K2	0	225	225	55.84	87.14	103.88	94.8	-60.81	-24.94
93	K3	225	0	225	75.59	46.38	87.41	73.79	74.02	-49.09
94	K4	225	225	0	95.22	115.5	10.56	105.71	-26.68	109.03
95	K5	20	20	20	0.5	0.68	0.48	6.16	-6.33	1.64
96	K6	51	51	51	2.44	3.06	2.39	20.27	-9.6	1.09
97	K7	128	128	128	26.33	29	23.22	60.78	-6.57	1.3
98	K8	204	204	204	94.15	103.76	82.41	101.44	-10.14	2.54
99	K9	225	225	225	122.29	134.74	106.92	112.12	-11.02	2.83

Table A.35: *Device signals and corresponding radiometric measurements of the high-luminance display (patch index: 51-99).*

A.5 Instruction for Colour Experiments

In an experiment trial, during the time allowed for the participant's eye to adapt to the environment lighting, observers were read this following instruction by a experimenter, adapted from [Kwak, 2003].

Instructions

Please sit comfortably and look at the test pattern. You will be shown a series of test colours in a random order. Your task will be to tell me what lightness, colourfulness and hue you see. You will enter corresponding numbers by using a keyboard. There is no time limit for each test colour and you can take as long as required until you report your estimations.

Lightness scaling Use the reference white as a standard, which has a lightness of 100, and your imaginary black, which has a lightness of zero. Describe the test colour by assigning a number, which is in the right relationship to the reference white and the imaginary black. (The reference white is displayed in the test pattern.)

Colourfulness scaling Colourfulness is an attribute of a visual sensation according to which an area appears to exhibit more or less of its hue. A neutral colour has no colourfulness, represented by zero on your scale. You are asked to assign a reasonable number to describe the colourfulness of the test colour. This is an open-ended scale since no top limit is set. The reference colourfulness patch in the test pattern should be remembered as 40 so that all subsequent test colours can be related to it.

Hue scaling There are four psychological primaries: red, yellow, green and blue. These four colours can be arranged as points around a circle and lie at opposite ends of x and y axes. You are asked to describe a hue as a proportion of two neighbouring primaries. First, decide whether or not you perceive any hue at all. If not, please reply 'Neutral'. On the other hand if the test colour does not appear neutral then decide which of the four primaries is predominant. Next decide whether or not you see a trace of any other primary hue. If so, identify it. Finally, estimate the proportions in which the two primaries stand, e.g. an orange colour may be 60% yellow and 40% red.

A.6 Colour Appearance Data

This appendix provides the psychophysical experimental data which was used to develop our model. The data comprises three main parts: (1) physical measurements of colour stimuli (absolute XYZ coordinates measured with a spectroradiometer; Y in $[\mathrm{cd/m^2}]$), (2) perceptual attribute estimates (averaged over six participants) of the stimuli in terms of lightness J', colourfulness M', and hue quadrature H', and (3) colour appearance attributes predicted by our colour appearance model in terms of lightness J, colourfulness M, hue quadrature H, brightness Q, chroma C, hue angle h, and saturation s.

In each phase, 40 main colour patches were observed on a high-luminance display under different viewing conditions (different peak luminance level, background, ambient surround, and colour temperature, see Table A.36). Six observers who passed the Ishihara and City University vision tests for normal colour vision participated in the experiments. Each participant completed a total of 2,280 estimations (19 phases with 40 patches and 3 estimates each), which took about 10 hours per participant. The averaged repeatability in terms of CV was 11.83% for lightness, 22.82% for colourfulness, and 11.42% for hue. Note that our experimental results are compatible with the LUTCHI data [Luo et al., 1991a].

The lightness attribute has a scale of 0–100 relative to the brightness of reference white. The colourfulness attribute has an absolute scale of 0 to unlimited. The hue attribute varies from 0 to 400: redness (0) - yellowness (100) - greenness (200) - blueness (300) - redness (400); observers were allowed to judge a hue as undefined (denoted as 'N/A' below) if the shown patch was too dark, too bright, or neutral.

Phase	Medium	CCT	Reference White (Abs.)			La(10°)	Background (Abs.)				Ambient
Number	Type	[K]	X	Y[$\mathrm{cd/m^2}$]	Z	[$\mathrm{cd/m^2}$]	%	X	Y[$\mathrm{cd/m^2}$]	Z	Luminance
1	LCD	5935	32.51	43.88	25.72	12.06	24.52%	8.64	10.76	7.66	dark
2	LCD	6265	93.68	122.90	84.06	31.26	21.81%	21.94	26.81	20.98	dark
3	LCD	6265	376.08	493.60	348.19	30.07	0.34%	1.22	1.68	1.23	dark
4	LCD	6265	396.71	521.00	371.57	144.29	23.82%	103.97	126.90	104.31	dark
5	LCD	6197	419.38	562.60	373.03	466.17	87.11%	366.89	490.10	326.54	dark
6	LCD	6197	800.51	1067.00	714.78	70.00	0.32%	2.43	3.37	2.46	dark
7	LCD	6197	800.22	1051.00	736.81	269.90	22.06%	189.58	231.80	183.53	dark
8	LCD	6390	1712.46	2176.00	1689.59	136.44	0.22%	3.59	4.76	4.12	dark
9	LCD	6392	1721.81	2189.00	1697.69	367.61	12.16%	229.77	266.20	234.15	dark
10	LCD	6391	1726.31	2196.00	1702.69	576.71	22.90%	422.04	502.90	427.31	dark
11	LCD	6387	1732.94	2205.00	1708.66	1204.03	55.06%	1012.64	1214.00	1010.70	dark
12	LCD	6388	1758.09	2241.00	1729.44	2009.94	94.87%	1667.67	2126.00	1636.72	dark
13	LCD	7941	995.40	1274.00	1293.24	312.49	21.16%	228.16	269.55	314.68	dark
14	LCD	1803	1063.72	1233.00	356.61	284.36	19.17%	217.84	236.35	73.20	dark
15	LCD	6391	1730.32	2201.40	1705.62	604.76	22.90%	432.93	533.92	429.98	average
16	Trans.	5823	6890.34	8519.00	5936.19	941.70	5.61%	408.02	477.60	256.97	dark
17	Trans.	5823	6849.58	8458.00	5911.69	2120.66	21.41%	1499.62	1811.00	1062.72	dark
18	Trans.	5921	13676.05	16860.00	12201.60	1860.80	5.49%	791.12	926.00	523.38	dark
19	Trans.	5937	13295.61	16400.00	11918.19	4183.52	21.81%	2963.80	3577.00	2194.24	dark

Table A.36: *Summary of viewing conditions for all 19 phases.*

Physical measurements				Perceptual estimates			Predicted appearance						
Colour	X	Y[cd/m²]	Z	J′	M′	H′	J	M	H	Q	C	h	s
1	0.61	0.56	0.30	8.67	12.44	0.25	1.00	27.35	-11.8	1.64	34.59	8.46	408.40
2	0.44	0.50	0.30	2.00	2.33	N/A	1.00	15.05	N/A	1.64	19.04	N/A	302.97
3	1.31	0.85	4.93	32.50	64.28	305.00	30.33	60.32	312.7	49.73	76.30	262.98	110.13
4	0.69	0.79	0.35	6.67	6.75	77.50	23.80	18.95	21.3	39.03	23.97	36.66	69.68
5	1.98	1.42	0.37	43.00	50.84	1.33	39.00	50.56	5.8	63.95	63.95	24.76	88.92
6	2.60	1.56	8.57	41.33	64.26	325.83	41.64	62.39	316.9	68.29	78.92	270.91	95.58
7	0.62	0.94	0.50	15.83	30.28	179.17	27.50	13.02	196.9	45.09	16.46	161.03	53.73
8	3.36	2.04	14.17	52.00	61.81	305.83	45.22	70.18	306.9	74.16	88.76	251.80	97.28
9	1.00	1.79	0.41	39.50	55.77	207.50	39.39	34.51	158.4	64.60	43.64	126.78	73.08
10	4.64	3.07	0.59	55.00	60.54	10.50	50.61	63.05	10.7	83.00	79.74	28.58	87.16
11	1.80	2.00	0.51	31.17	27.80	127.00	42.55	32.86	55.3	69.77	41.57	61.07	68.63
12	1.51	2.90	0.48	42.67	55.22	190.00	46.39	43.96	157.6	76.08	55.60	126.16	76.01
13	3.03	2.37	2.02	46.17	48.29	372.50	46.54	46.47	369.6	76.32	58.78	347.94	78.03
14	2.90	4.18	5.21	47.33	34.51	275.33	52.58	36.42	304.3	86.22	46.07	246.63	65.00
15	8.58	5.52	0.70	68.33	52.87	6.67	59.22	70.35	20.3	97.12	88.98	35.88	85.11
16	6.56	4.27	0.85	52.83	57.80	3.83	55.43	66.23	9.9	90.90	83.76	27.95	85.36
17	4.06	3.44	11.91	53.33	52.41	320.33	51.54	57.14	313.8	84.51	72.27	265.06	82.22
18	6.53	5.48	10.96	55.17	39.94	349.17	58.53	49.34	333.9	95.98	62.40	299.49	71.69
19	10.06	6.78	0.84	61.83	62.88	36.17	62.22	68.93	25.0	102.02	87.18	39.44	82.19
20	3.43	4.62	6.41	49.00	38.09	283.67	54.23	38.54	307.7	88.93	48.75	253.47	65.84
21	3.34	6.58	1.15	59.50	50.56	187.50	58.22	49.07	159.5	95.47	62.07	127.63	71.69
22	9.63	7.34	0.89	58.67	57.49	54.50	62.96	63.28	36.1	103.24	80.03	47.58	78.29
23	12.91	9.54	15.52	62.33	42.42	363.67	68.17	54.80	350.7	111.79	69.31	324.08	70.02
24	12.88	10.57	2.40	57.83	38.24	52.00	68.98	55.04	24.7	113.12	69.61	39.19	69.75
25	4.98	7.59	5.42	54.83	24.06	232.00	61.31	21.52	276.9	100.55	27.22	218.14	46.26
26	6.70	8.31	16.89	63.83	37.24	296.67	63.41	49.03	306.0	103.99	62.01	250.06	68.67
27	16.90	15.00	13.88	67.83	44.30	369.50	75.81	43.06	361.7	124.32	54.46	338.37	58.85
28	5.20	10.39	1.00	65.83	51.39	181.33	65.34	61.27	152.0	107.15	77.50	122.01	75.62
29	16.57	17.14	5.95	66.17	35.76	72.50	77.59	37.05	29.6	127.24	46.86	42.79	53.96
30	15.79	17.06	1.45	69.17	61.28	91.17	76.84	61.20	91.1	126.01	77.41	84.51	69.69
31	19.50	20.00	18.41	73.67	27.74	374.50	81.49	33.10	351.4	133.63	41.86	325.03	49.77
32	18.31	19.75	9.07	76.00	29.21	60.83	80.70	29.95	9.7	132.35	37.88	27.75	47.57
33	16.15	17.81	1.56	69.00	63.58	91.67	77.69	60.71	93.4	127.39	76.78	85.95	69.03
34	9.05	17.46	2.71	77.83	57.62	180.83	75.18	54.11	154.5	123.29	68.43	123.88	66.25
35	20.65	25.84	15.39	82.00	3.09	N/A	86.88	13.41	N/A	142.47	16.96	N/A	30.68
36	18.55	27.94	9.15	85.50	27.74	167.83	87.84	30.66	140.6	144.05	38.78	114.00	46.14
37	21.31	28.42	2.29	90.00	70.67	103.17	88.42	63.10	119.6	145.00	79.80	100.83	65.97
38	24.41	30.88	16.30	88.17	4.65	82.83	92.15	14.13	22.9	151.11	17.87	37.84	30.58
39	21.22	30.34	2.84	92.83	64.35	111.67	90.04	60.75	125.9	147.65	76.84	104.62	64.15
40	27.32	33.76	24.28	100.00	1.44	N/A	95.46	17.05	N/A	156.55	21.56	N/A	33.00

Table A.37: *Physical measurements, perceptual estimates, and our model's predictions (Phase 1).*

Physical measurements				Perceptual estimates			Predicted appearance						
Colour	X	Y[cd/m^2]	Z	J′	M′	H′	J	M	H	Q	C	h	s
1	2.03	1.79	0.99	10.83	17.88	9.00	18.87	32.42	-6.2	35.41	38.60	14.10	95.69
2	1.35	1.61	0.87	2.83	4.47	50.00	1.00	15.22	33.3	1.88	18.12	45.55	284.83
3	4.48	2.79	17.89	33.67	68.77	304.17	33.24	65.86	311.7	62.37	78.42	261.17	102.76
4	2.17	2.53	0.94	8.00	11.74	74.17	28.91	25.03	58.7	54.25	29.80	63.40	67.92
5	6.63	4.61	1.30	40.33	54.01	2.50	42.06	57.61	7.2	78.92	68.60	25.84	85.44
6	9.05	5.25	30.85	46.17	68.51	334.17	44.17	66.65	317.6	82.88	79.36	272.13	89.67
7	1.94	3.13	1.59	23.67	35.88	200.33	32.23	22.07	182.9	60.48	26.28	147.37	60.41
8	11.45	6.74	49.71	60.33	71.36	267.83	47.08	74.93	306.4	88.34	89.22	250.86	92.10
9	3.16	6.01	1.17	43.67	58.28	210.00	42.68	45.23	158.8	80.08	53.86	127.12	75.16
10	15.26	9.99	1.87	57.17	65.50	4.17	53.32	69.88	15.6	100.04	83.21	32.31	83.58
11	5.95	6.69	1.62	43.17	34.53	126.17	45.71	39.26	69.8	85.76	46.74	70.84	67.66
12	4.86	9.63	1.50	51.83	55.61	191.67	49.35	53.16	157.7	92.60	63.29	126.28	75.77
13	10.14	7.86	7.24	47.33	46.51	375.00	49.43	50.53	372.1	92.76	60.16	350.84	73.80
14	9.75	14.17	18.62	51.83	39.92	275.67	55.64	37.99	300.7	104.40	45.23	238.92	60.32
15	28.02	17.81	2.24	72.33	62.82	12.00	61.96	77.22	24.8	116.25	91.95	39.26	81.50
16	21.27	13.69	2.90	63.67	57.17	9.00	57.98	72.43	12.8	108.79	86.24	30.18	81.59
17	14.13	11.83	42.42	62.00	51.86	327.67	54.45	59.27	313.9	102.18	70.57	265.39	76.16
18	21.82	18.18	38.37	60.00	48.68	349.17	61.31	50.97	335.2	115.04	60.69	301.60	66.56
19	32.85	22.11	2.52	67.83	70.82	44.17	65.16	75.59	32.6	122.26	90.00	44.99	78.63
20	11.81	15.83	23.14	53.83	35.68	278.67	57.49	39.43	305.3	107.87	46.95	248.62	60.46
21	10.88	21.90	3.94	62.33	61.04	190.33	61.36	56.96	159.7	115.13	67.82	127.83	70.34
22	31.73	24.31	2.79	59.50	60.09	52.50	66.18	69.72	44.8	124.18	83.01	53.76	74.93
23	42.90	31.55	54.69	68.67	46.60	365.00	71.36	57.09	352.5	133.91	67.98	326.51	65.30
24	42.19	34.80	8.60	68.50	63.93	50.83	72.43	58.55	30.4	135.90	69.71	43.41	65.64
25	16.77	25.49	19.44	58.17	31.24	239.50	64.65	23.20	255.7	121.30	27.63	201.72	43.74
26	23.01	28.32	60.21	74.17	50.83	300.83	66.78	50.15	304.6	125.30	59.72	247.10	63.27
27	55.72	49.57	49.14	73.83	35.20	359.50	79.64	43.47	364.2	149.43	51.76	341.49	53.94
28	16.71	33.71	3.38	67.33	64.72	188.33	68.39	69.10	152.2	128.32	82.28	122.16	73.38
29	53.72	55.68	20.54	68.83	34.82	57.83	81.35	39.86	40.6	152.63	47.47	50.79	51.11
30	51.81	56.58	5.15	71.17	72.14	92.50	81.05	67.56	97.2	152.07	80.44	88.29	66.65
31	64.64	66.23	65.07	72.33	24.89	361.17	85.89	32.21	354.3	161.17	38.35	328.83	44.70
32	60.30	65.35	32.24	76.33	25.63	60.33	85.15	31.05	23.4	159.77	36.97	38.21	44.09
33	52.93	58.99	5.31	73.17	72.06	81.17	81.93	67.78	99.9	153.73	80.70	89.96	66.40
34	29.44	57.45	9.58	83.83	60.51	178.33	79.09	60.41	155.0	148.41	71.93	124.24	63.80
35	68.72	86.00	54.73	83.17	3.87	100.40	92.18	12.39	19.5	172.97	14.75	35.28	26.77
36	61.10	92.38	32.47	83.83	26.46	187.00	93.17	35.47	143.4	174.83	42.24	115.95	45.04
37	69.41	93.51	7.78	87.67	74.78	119.17	93.68	70.30	123.4	175.79	83.70	103.10	63.24
38	80.86	102.40	58.25	88.67	6.54	92.00	98.11	15.93	61.7	184.09	18.97	65.43	29.42
39	68.30	98.26	9.56	87.50	71.09	138.33	95.01	67.61	128.7	178.27	80.50	106.29	61.58
40	90.04	111.20	85.51	99.67	1.63	N/A	101.60	13.38	N/A	190.63	15.93	N/A	26.49

Table A.38: *Physical measurements, perceptual estimates, and our model's predictions (Phase 2).*

Physical measurements				Perceptual estimates			Predicted appearance						
Colour	X	Y[cd/m^2]	Z	J'	M'	H'	J	M	H	Q	C	h	s
1	3.98	3.11	1.23	28.71	59.45	12.00	26.80	49.78	-0.6	60.30	54.93	19.52	90.86
2	2.00	2.25	1.20	22.71	23.45	94.86	1.00	22.37	46.4	2.25	24.68	54.88	315.27
3	12.12	6.55	54.72	44.71	78.01	308.00	40.27	83.45	310.7	90.64	92.08	259.34	95.95
4	4.29	4.70	1.37	31.14	38.64	126.43	33.80	38.35	68.5	76.08	42.32	69.96	71.00
5	19.38	12.55	2.66	46.71	59.89	7.71	49.62	77.74	6.2	111.66	85.78	25.06	83.44
6	26.96	14.53	100.40	55.71	78.48	336.14	51.32	75.54	317.9	115.49	83.36	272.76	80.88
7	3.25	5.83	2.84	40.86	51.77	193.14	35.85	33.05	187.9	80.68	36.47	152.03	64.00
8	37.60	20.32	174.31	61.57	87.33	306.14	54.79	85.99	306.1	123.31	94.88	250.16	83.50
9	6.73	13.78	2.10	44.71	63.39	189.43	47.60	62.32	160.7	107.13	68.77	128.61	76.27
10	50.34	31.42	4.80	58.71	68.92	11.43	61.29	85.11	13.4	137.93	93.91	30.65	78.55
11	14.94	15.70	2.91	46.14	46.81	100.71	50.87	55.55	74.1	114.49	61.29	73.63	69.65
12	11.84	24.79	3.19	57.43	72.34	185.00	54.97	69.86	158.6	123.70	77.08	126.97	75.15
13	29.48	20.84	19.49	53.29	49.26	373.29	55.86	66.75	370.9	125.72	73.65	349.50	72.86
14	26.67	38.05	57.55	55.71	52.99	277.43	61.21	45.09	299.4	137.77	49.76	236.99	57.21
15	101.12	62.46	7.03	78.29	72.72	16.43	70.52	86.60	22.2	158.70	95.56	37.31	73.87
16	73.91	45.77	7.46	72.00	62.62	7.43	66.29	84.51	10.0	149.19	93.25	28.04	75.26
17	42.31	32.35	142.31	64.00	63.65	327.57	60.42	65.57	313.9	135.98	72.35	265.40	69.44
18	69.73	54.11	130.56	70.86	44.53	347.14	67.85	54.78	335.4	152.71	60.44	301.92	59.89
19	118.82	75.96	7.02	83.57	75.80	30.00	73.16	86.10	31.5	164.64	95.01	44.18	72.32
20	32.51	42.52	72.61	57.14	35.65	278.14	62.86	46.15	304.8	141.48	50.93	247.64	57.12
21	29.90	62.32	10.42	64.86	59.75	185.86	67.01	67.06	161.6	150.81	74.00	129.30	66.68
22	111.26	79.33	8.23	77.14	69.29	45.86	73.42	80.10	44.3	165.24	88.38	53.43	69.62
23	150.53	104.20	192.87	80.57	53.88	358.57	78.12	58.94	352.0	175.82	65.03	325.76	57.90
24	152.22	116.60	25.10	78.71	44.39	48.14	79.23	64.55	27.0	178.31	71.23	40.87	60.17
25	47.64	72.60	59.87	64.43	29.76	230.71	69.96	25.63	260.5	157.45	28.28	205.32	40.35
26	72.33	83.96	212.76	74.71	56.58	284.29	72.34	52.91	303.8	162.82	58.38	245.57	57.01
27	196.50	163.40	167.20	82.43	31.64	369.86	84.80	45.65	362.6	190.85	50.38	339.49	48.91
28	50.02	103.90	10.61	78.29	78.02	198.57	74.22	77.10	153.0	167.04	85.08	122.72	67.94
29	189.77	185.10	65.43	79.57	28.18	49.71	86.19	42.07	37.5	193.97	46.42	48.56	46.57
30	181.71	185.00	15.76	71.71	83.53	88.00	85.57	73.51	97.9	192.59	81.11	88.73	61.78
31	224.22	216.50	231.01	86.57	12.34	372.17	89.19	33.38	353.1	200.73	36.83	327.23	40.78
32	209.32	213.70	104.63	85.71	24.45	52.71	88.68	33.11	19.5	199.57	36.53	35.28	40.73
33	185.40	192.70	16.70	82.14	89.69	94.29	86.22	72.86	100.5	194.04	80.39	90.27	61.27
34	90.14	181.00	28.83	87.00	49.99	181.71	83.20	63.51	156.5	187.25	70.08	125.37	58.24
35	230.13	279.00	188.02	95.57	2.44	90.00	93.10	13.78	7.6	209.54	15.20	26.15	25.64
36	199.61	300.90	107.13	91.29	19.57	173.86	93.68	33.19	143.7	210.83	36.62	116.14	39.68
37	240.67	310.60	26.70	95.14	75.00	103.29	94.43	70.36	123.0	212.51	77.64	102.81	57.54
38	277.13	338.40	201.47	98.29	4.15	77.00	97.07	15.65	55.2	218.46	17.27	61.01	26.76
39	235.29	330.50	32.61	94.57	75.78	105.43	95.43	67.03	128.2	214.77	73.97	106.01	55.87
40	316.13	374.50	320.99	100.00	1.97	N/A	99.42	15.85	N/A	223.75	17.49	N/A	26.62

Table A.39: *Physical measurements, perceptual estimates, and our model's predictions (Phase 3).*

Physical measurements				Perceptual estimates			Predicted appearance						
Colour	X	Y[$\mathrm{cd/m^2}$]	Z	J'	M'	H'	J	M	H	Q	C	h	s
1	9.16	7.98	4.02	15.57	38.10	6.71	19.04	36.37	3.6	43.15	40.02	22.97	91.81
2	6.06	7.32	3.85	6.71	6.87	66.00	1.00	17.39	22.0	2.27	19.13	37.19	276.97
3	20.51	12.82	85.04	36.43	80.24	301.86	33.32	71.67	305.6	75.53	78.86	249.17	97.41
4	10.82	12.83	4.38	19.00	31.57	129.14	31.77	29.66	57.6	72.00	32.64	62.62	64.19
5	30.53	20.90	6.19	39.57	55.90	7.43	42.47	63.33	13.8	96.25	69.68	30.91	81.11
6	41.56	24.10	142.99	48.71	78.74	330.14	44.41	71.71	312.5	100.67	78.90	262.70	84.40
7	9.07	15.38	8.09	25.29	49.74	195.00	33.98	26.48	187.7	77.01	29.14	151.81	58.64
8	50.87	30.70	224.51	58.86	74.69	299.57	47.01	80.76	300.4	106.56	88.86	238.43	87.06
9	14.56	28.62	5.81	43.86	64.39	195.00	43.65	49.87	158.2	98.93	54.87	126.62	71.00
10	66.86	42.69	8.51	57.57	79.69	5.29	52.99	76.76	23.6	120.09	84.46	38.37	79.95
11	27.09	30.92	7.31	36.71	41.42	119.00	46.27	43.46	70.1	104.87	47.82	71.00	64.38
12	22.76	46.24	7.43	48.71	60.89	192.29	50.47	58.49	156.4	114.38	64.36	125.28	71.51
13	47.16	36.61	36.23	45.14	51.02	369.43	50.14	54.64	374.5	113.65	60.12	353.64	69.34
14	45.42	66.68	89.77	54.71	43.16	262.00	56.50	41.17	300.2	128.06	45.30	237.85	56.70
15	117.67	73.41	9.99	79.71	78.48	9.71	61.10	84.14	35.4	138.49	92.58	47.02	77.95
16	92.49	58.18	13.58	66.14	68.11	7.00	57.60	79.41	23.6	130.54	87.38	38.39	78.00
17	64.20	55.26	192.04	59.43	59.16	323.14	55.04	62.71	309.7	124.75	69.00	257.34	70.90
18	101.07	85.40	179.74	59.00	57.92	354.57	62.23	54.08	336.9	141.05	59.51	304.20	61.92
19	135.23	90.72	10.80	76.43	87.41	34.29	64.15	81.68	44.8	145.39	89.87	53.77	74.95
20	52.89	71.18	106.59	53.86	38.63	294.29	57.71	42.35	303.9	130.80	46.59	245.78	56.90
21	48.97	99.74	20.43	64.00	70.25	188.71	61.93	60.07	157.9	140.36	66.09	126.45	65.42
22	134.40	104.00	12.86	67.29	78.35	47.14	65.80	74.57	51.9	149.15	82.05	58.72	70.71
23	186.12	138.80	247.22	65.43	73.81	358.86	71.40	60.80	355.6	161.82	66.90	330.64	61.30
24	177.17	148.90	43.04	68.29	54.41	44.86	72.07	61.04	36.5	163.34	67.16	47.81	61.13
25	76.86	116.30	94.50	50.14	33.23	221.43	65.30	25.30	263.0	148.02	27.84	207.27	41.35
26	100.83	126.80	267.11	75.29	46.65	296.00	66.99	53.57	302.3	151.84	58.94	242.32	59.40
27	234.65	212.30	222.34	74.00	44.30	380.71	79.27	45.86	367.4	179.68	50.46	345.39	50.52
28	75.81	154.20	17.66	71.14	83.62	186.00	69.24	73.25	151.2	156.92	80.60	121.44	68.32
29	229.05	242.10	101.05	70.00	31.80	57.86	81.44	40.56	39.4	184.60	44.62	49.92	46.87
30	215.15	239.60	23.68	78.43	91.76	89.29	80.54	72.22	99.1	182.55	79.46	89.42	62.90
31	271.71	281.80	287.69	76.71	36.49	374.29	85.47	34.11	356.9	193.72	37.53	332.31	41.96
32	252.87	277.50	150.11	75.14	24.60	54.71	84.73	31.98	19.0	192.05	35.19	34.92	40.81
33	219.63	249.40	24.63	74.71	84.26	91.43	81.40	72.28	101.1	184.50	79.52	90.58	62.59
34	128.48	250.80	49.00	85.00	72.98	184.57	79.34	62.62	153.5	179.84	68.90	123.12	59.01
35	284.65	356.70	242.66	86.57	5.59	78.33	91.16	12.67	-3.1	206.62	13.94	17.20	24.76
36	259.59	389.50	153.34	88.57	32.13	176.71	92.80	36.01	141.5	210.33	39.62	114.62	41.38
37	285.73	388.40	37.88	92.29	92.38	102.57	92.81	73.76	122.9	210.36	81.15	102.75	59.21
38	334.78	424.90	260.98	92.43	12.43	98.57	97.10	15.74	35.4	220.09	17.32	47.04	26.74
39	282.70	408.60	46.24	93.43	68.66	111.71	94.20	70.91	128.4	213.50	78.02	106.12	57.63
40	369.89	460.90	365.11	99.14	1.77	N/A	100.45	13.53	N/A	227.67	14.89	N/A	24.38

Table A.40: *Physical measurements, perceptual estimates, and our model's predictions (Phase 4).*

Physical measurements				Perceptual estimates			Predicted appearance						
Colour	X	Y[$\mathrm{cd/m^2}$]	Z	J′	M′	H′	J	M	H	Q	C	h	s
1	14.89	16.22	9.01	9.83	15.28	6.67	18.85	20.23	2.0	43.16	22.17	21.73	68.47
2	12.06	15.74	8.90	3.67	3.16	31.25	10.11	9.88	62.0	23.15	10.83	65.63	65.34
3	25.48	20.64	85.85	31.50	58.73	300.83	29.50	55.28	314.9	67.54	60.58	267.12	90.47
4	16.32	20.73	9.20	15.00	17.32	109.17	27.44	17.86	68.8	62.83	19.58	70.15	53.32
5	35.58	28.81	10.75	36.00	38.44	7.50	37.02	43.51	4.4	84.77	47.68	23.61	71.64
6	46.06	31.81	141.97	35.83	62.00	339.50	39.15	60.83	319.8	89.63	66.66	276.14	82.39
7	14.52	23.07	12.53	18.83	24.46	202.50	29.15	17.42	188.4	66.73	19.09	152.56	51.10
8	55.27	38.40	221.08	53.00	60.07	300.83	41.77	69.44	310.7	95.64	76.10	259.32	85.21
9	20.22	36.53	10.59	40.67	45.20	189.17	38.08	33.30	162.9	87.17	36.49	130.27	61.80
10	71.85	50.93	13.17	49.17	60.73	1.67	46.96	59.00	8.7	107.50	64.66	27.00	74.09
11	32.85	39.25	11.94	29.67	26.00	100.50	40.67	30.27	67.9	93.10	33.18	69.56	57.02
12	28.17	53.75	12.23	48.33	54.98	194.17	44.29	41.14	161.1	101.41	45.09	128.91	63.70
13	51.71	44.18	39.47	39.17	42.09	374.50	44.01	41.17	369.7	100.77	45.12	348.04	63.92
14	49.94	73.59	90.45	49.50	27.44	275.67	49.98	35.08	302.3	114.41	38.44	242.42	55.37
15	122.11	81.54	14.72	59.33	58.98	6.67	54.68	69.46	14.5	125.18	76.12	31.45	74.49
16	97.09	66.34	18.08	53.83	55.17	1.67	51.30	64.02	6.0	117.44	70.16	24.87	73.83
17	68.03	62.18	189.32	50.50	55.52	336.33	48.77	56.98	316.1	111.65	62.44	269.49	71.44
18	104.13	92.00	177.24	53.33	49.39	346.67	55.51	50.08	334.0	127.08	54.88	299.69	62.78
19	140.51	99.33	15.44	66.33	56.42	23.33	57.69	68.80	21.9	132.08	75.40	37.12	72.17
20	58.77	80.35	110.11	52.33	33.29	279.00	51.60	37.47	307.1	118.13	41.06	252.23	56.32
21	53.88	106.80	24.09	59.00	46.59	188.33	55.15	48.19	163.4	126.26	52.81	130.67	61.78
22	138.44	111.50	17.32	60.83	49.50	52.00	59.08	62.70	33.3	135.26	68.71	45.51	68.09
23	188.69	145.60	243.26	67.00	51.97	N/A	64.52	57.85	N/A	147.72	63.40	N/A	62.58
24	180.66	156.20	45.98	61.50	44.48	56.50	65.14	55.53	21.0	149.14	60.85	36.44	61.02
25	80.60	122.60	94.44	57.33	23.51	240.00	58.34	22.25	268.2	133.57	24.38	211.22	40.81
26	103.80	132.70	260.87	63.00	38.39	294.83	60.13	51.38	306.7	137.66	56.31	251.36	61.10
27	236.88	219.00	218.80	69.50	37.34	369.67	72.33	45.19	360.7	165.60	49.52	337.12	52.24
28	79.58	159.60	21.22	67.00	55.48	180.00	62.10	60.22	154.9	142.18	65.99	124.18	65.08
29	231.19	248.20	101.06	64.00	27.21	58.17	74.42	39.09	31.1	170.39	42.84	43.93	47.90
30	218.04	245.90	27.47	62.50	60.27	86.67	73.61	62.26	87.9	168.53	68.23	82.52	60.78
31	273.64	288.50	282.17	72.00	38.28	363.67	78.74	35.55	351.0	180.27	38.95	324.41	44.41
32	254.64	283.40	148.32	68.83	30.49	60.67	77.82	31.78	13.1	178.16	34.83	30.44	42.24
33	222.32	255.50	28.02	64.83	59.71	103.67	74.47	62.67	91.1	170.50	68.68	84.50	60.63
34	131.98	256.40	50.96	74.50	50.20	176.67	72.23	56.40	158.0	165.37	61.80	126.52	58.40
35	290.17	368.20	240.55	77.50	9.37	55.60	85.22	13.45	-10.0	195.11	14.74	10.26	26.25
36	262.18	396.30	151.46	84.50	21.22	173.67	86.52	34.78	142.9	198.09	38.12	115.59	41.90
37	288.47	395.50	41.19	88.17	65.07	99.67	86.72	66.68	118.3	198.53	73.07	100.09	57.96
38	336.41	431.80	255.25	84.67	13.81	68.40	91.41	15.60	38.2	209.27	17.09	49.04	27.30
39	290.00	422.40	49.36	85.67	46.69	115.83	88.85	65.38	125.3	203.42	71.64	104.22	56.69
40	371.86	468.30	357.84	97.00	5.89	361.60	95.41	16.82	342.5	218.44	18.43	312.49	27.75

Table A.41: *Physical measurements, perceptual estimates, and our model's predictions (Phase 5).*

Physical measurements				Perceptual estimates			Predicted appearance						
Colour	X	Y[cd/m^2]	Z	J′	M′	H′	J	M	H	Q	C	h	s
1	15.20	11.17	3.08	26.86	64.01	7.57	36.21	62.39	2.5	90.14	66.15	22.13	83.19
2	8.93	10.66	3.32	23.29	27.38	95.00	33.34	35.08	55.8	82.99	37.20	61.37	65.02
3	37.50	21.34	169.15	46.14	76.47	304.29	45.30	87.99	310.4	112.78	93.30	258.58	88.33
4	19.32	22.96	4.60	32.00	45.66	91.00	44.83	49.63	71.7	111.59	52.63	72.05	66.69
5	60.24	38.53	7.29	50.86	69.41	14.43	53.44	83.98	8.2	133.03	89.05	26.64	79.45
6	80.85	44.77	282.50	53.00	78.11	332.86	55.47	75.82	318.0	138.08	80.40	272.94	74.10
7	15.05	28.34	12.34	37.57	52.78	207.57	46.51	40.25	186.7	115.78	42.68	150.93	58.96
8	97.79	58.54	442.85	61.86	82.53	302.14	57.90	86.79	305.8	144.14	92.03	249.49	77.60
9	27.57	58.63	7.38	49.14	84.07	190.00	55.43	72.07	160.8	138.00	76.42	128.66	72.27
10	136.63	84.80	12.76	67.71	66.28	10.86	63.64	88.80	14.6	158.43	94.15	31.52	74.87
11	56.31	64.76	10.90	49.86	42.75	111.43	58.17	59.93	76.9	144.79	63.55	75.47	64.34
12	44.64	95.72	10.66	53.86	76.70	186.29	61.72	76.94	158.8	153.64	81.58	127.12	70.77
13	96.36	74.20	70.82	57.71	53.88	376.00	61.41	62.77	372.1	152.87	66.55	350.93	64.08
14	91.58	139.00	180.29	58.57	56.73	279.86	67.62	43.36	296.3	168.34	45.98	234.30	50.75
15	240.78	148.10	15.66	80.14	70.87	19.14	71.31	90.51	24.2	177.51	95.97	38.81	71.40
16	188.73	116.40	22.76	78.86	74.39	15.86	68.02	86.36	11.5	169.33	91.58	29.15	71.42
17	128.63	113.40	379.68	60.29	57.98	326.00	66.14	60.88	313.7	164.65	64.55	264.93	60.81
18	206.42	177.80	355.38	68.00	62.94	350.00	73.05	50.49	335.7	181.85	53.53	302.27	52.69
19	279.91	187.80	17.06	83.00	78.74	33.43	74.45	86.89	33.2	185.33	92.13	45.43	68.47
20	110.76	153.60	218.66	59.71	43.45	277.00	69.27	42.69	303.7	172.44	45.26	245.23	49.76
21	100.13	209.10	39.16	68.00	67.01	189.71	72.70	64.54	162.0	180.99	68.44	129.60	59.72
22	276.80	216.10	21.50	73.71	61.72	57.14	76.04	79.50	46.5	189.29	84.30	54.93	64.81
23	380.63	288.30	486.59	83.00	55.65	356.86	81.34	54.67	352.9	202.47	57.97	326.96	51.96
24	362.81	309.20	84.16	82.14	54.70	49.00	81.76	56.89	29.2	203.53	60.33	42.52	52.87
25	158.12	243.60	187.83	64.43	36.95	241.71	75.93	24.64	253.1	189.02	26.13	199.84	36.10
26	202.69	263.80	527.10	74.57	50.48	302.29	77.39	49.16	303.2	192.64	52.13	244.20	50.52
27	479.49	441.70	438.30	82.86	36.43	369.86	88.01	39.71	364.0	219.10	42.10	341.22	42.57
28	155.84	323.00	31.27	81.29	83.74	186.71	79.32	78.74	153.1	197.46	83.49	122.85	63.15
29	468.16	502.30	198.77	83.71	34.57	61.71	89.66	35.26	41.2	223.18	37.39	51.19	39.75
30	440.76	497.70	43.19	80.14	99.45	92.00	88.76	73.67	99.1	220.96	78.11	89.42	57.74
31	555.70	586.10	565.95	89.43	23.80	362.43	92.90	28.61	354.4	231.26	30.33	329.00	35.17
32	517.18	575.70	297.02	89.43	24.11	52.57	92.24	26.90	23.8	229.63	28.52	38.50	34.22
33	450.83	518.60	45.04	82.57	88.78	95.29	89.47	73.41	101.6	222.73	77.84	90.81	57.41
34	261.57	517.90	94.47	87.43	44.58	186.14	87.83	59.01	156.7	218.63	62.57	125.53	51.95
35	587.85	747.40	481.91	97.43	3.38	70.00	97.17	10.19	26.5	241.90	10.81	40.50	20.53
36	531.05	804.10	301.86	93.57	27.05	178.29	97.95	30.15	144.3	243.82	31.97	116.55	35.17
37	582.80	801.40	70.25	91.86	77.91	99.57	97.71	70.64	123.6	243.22	74.90	103.20	53.89
38	682.66	877.20	511.94	97.86	3.08	82.40	100.78	12.47	64.6	250.87	13.22	67.36	22.30
39	587.93	856.40	91.54	96.00	70.57	110.00	99.05	65.36	128.6	246.58	69.30	106.28	51.48
40	747.91	946.50	712.76	99.86	2.12	N/A	102.70	11.16	N/A	255.65	11.83	N/A	20.89

Table A.42: *Physical measurements, perceptual estimates, and our model's predictions (Phase 6).*

Physical measurements				Perceptual estimates			Predicted appearance						
Colour	X	Y[$\mathrm{cd/m^2}$]	Z	J'	M'	H'	J	M	H	Q	C	h	s
1	18.47	15.90	7.26	19.29	21.64	8.43	21.03	39.43	10.1	52.25	41.84	28.11	86.87
2	12.62	15.32	7.36	8.14	8.97	81.67	6.46	19.97	69.9	16.04	21.19	70.87	111.57
3	40.05	25.76	165.02	36.86	87.75	300.86	34.11	74.54	303.8	84.75	79.10	245.57	93.78
4	21.82	26.05	8.53	18.29	18.92	120.71	32.77	31.58	84.3	81.42	33.51	80.23	62.28
5	62.15	42.48	11.43	42.71	63.50	8.57	43.18	66.98	15.2	107.28	71.07	32.04	79.01
6	81.19	47.98	274.36	52.14	75.84	329.43	44.87	74.09	314.2	111.47	78.62	265.90	81.53
7	18.14	31.33	15.63	27.29	37.83	197.29	34.92	29.25	185.7	86.77	31.04	149.91	58.07
8	99.06	61.58	434.33	63.43	87.47	301.43	47.54	83.63	300.0	118.10	88.74	237.54	84.15
9	29.71	59.26	11.17	44.57	72.48	195.14	44.59	53.89	156.7	110.79	57.19	125.54	69.75
10	136.99	87.83	16.74	67.14	82.87	0.86	53.76	80.19	22.8	133.57	85.10	37.79	77.48
11	57.26	65.64	14.54	41.29	40.55	118.57	47.55	46.78	87.2	118.13	49.64	82.06	62.93
12	46.04	94.62	14.35	54.14	72.20	194.43	51.18	62.40	155.0	127.16	66.21	124.20	70.05
13	93.91	73.67	68.92	57.29	55.51	370.29	50.62	56.35	370.7	125.77	59.79	349.22	66.93
14	90.40	135.60	174.35	53.14	46.84	259.71	57.12	42.53	294.6	141.90	45.13	232.86	54.75
15	241.14	150.90	18.90	89.14	91.10	11.14	61.85	87.89	35.0	153.67	93.26	46.77	75.63
16	187.31	118.20	25.95	72.00	83.08	5.43	58.18	82.79	16.9	144.54	87.86	33.35	75.68
17	127.49	112.60	372.54	61.43	63.47	324.29	55.71	64.28	310.7	138.40	68.21	259.20	68.15
18	201.15	173.00	345.78	61.57	61.43	343.57	62.78	55.04	335.6	155.97	58.41	302.14	59.41
19	281.05	189.70	21.72	79.71	88.22	35.00	65.18	84.94	48.1	161.93	90.13	56.06	72.42
20	108.00	148.50	211.22	56.57	49.82	271.43	58.71	43.30	302.6	145.86	45.95	243.01	54.49
21	98.40	202.50	40.18	72.43	72.75	189.00	62.50	63.26	159.4	155.28	67.13	127.60	63.83
22	275.22	213.80	24.93	76.86	96.82	47.14	66.57	77.92	61.1	165.39	82.68	65.03	68.64
23	374.15	281.80	475.78	75.71	62.69	365.00	71.98	62.37	352.8	178.82	66.19	326.91	59.06
24	360.18	303.50	83.12	75.29	52.10	43.57	72.70	63.52	33.2	180.61	67.40	45.46	59.30
25	153.28	234.80	181.96	55.29	38.79	236.71	65.79	26.51	261.7	163.45	28.13	206.24	40.27
26	197.16	253.40	514.03	74.71	53.47	298.29	67.31	55.16	301.2	167.22	58.54	240.00	57.44
27	472.12	429.70	428.10	75.57	47.73	367.57	79.76	46.85	362.3	198.16	49.71	339.12	48.62
28	150.99	309.70	33.72	84.00	84.56	188.71	69.60	77.09	150.0	172.91	81.80	120.57	66.77
29	463.43	491.60	194.92	76.43	40.24	55.71	81.98	42.41	41.1	203.66	45.01	51.12	45.64
30	436.86	486.90	45.97	76.14	92.39	91.00	81.09	75.60	108.4	201.46	80.23	94.46	61.26
31	549.70	574.80	560.14	83.29	32.51	360.29	86.11	34.24	352.8	213.93	36.33	326.84	40.00
32	506.39	556.30	286.24	76.14	34.68	52.14	84.93	33.60	19.4	211.01	35.66	35.24	39.91
33	445.04	505.00	47.59	80.29	96.37	94.57	81.87	75.68	110.4	203.39	80.31	95.57	61.00
34	255.79	503.90	94.37	89.00	66.75	187.29	79.63	65.74	154.5	197.83	69.76	123.88	57.65
35	579.74	732.10	476.38	88.00	7.35	70.86	91.96	13.11	3.2	228.46	13.91	22.66	23.96
36	519.82	785.10	296.01	90.57	32.00	173.71	92.99	38.22	143.2	231.02	40.55	115.78	40.67
37	572.08	778.80	71.85	92.00	88.34	115.86	92.82	77.30	126.4	230.61	82.02	104.89	57.90
38	666.43	849.30	498.26	92.86	6.37	88.33	96.93	17.41	52.3	240.81	18.47	58.99	26.89
39	578.88	837.90	92.68	94.00	78.35	103.57	94.95	73.53	129.8	235.90	78.03	107.03	55.83
40	741.05	930.00	711.74	99.43	2.60	388.33	100.53	12.62	346.5	249.77	13.39	318.26	22.48

Table A.43: *Physical measurements, perceptual estimates, and our model's predictions (Phase 7).*

Physical measurements				Perceptual estimates			Predicted appearance						
Colour	X	Y[cd/m^2]	Z	J'	M'	H'	J	M	H	Q	C	h	s
1	26.96	19.66	6.83	32.17	75.63	16.67	34.22	62.28	1.3	93.51	63.73	21.18	81.61
2	15.28	17.79	7.17	28.17	41.67	119.17	30.06	32.67	48.2	82.13	33.44	56.17	63.07
3	69.17	38.91	315.77	46.17	83.51	304.67	43.14	89.73	310.8	117.89	91.82	259.51	87.24
4	32.56	37.24	9.03	38.00	59.22	122.00	42.26	49.44	67.9	115.47	50.60	69.57	65.44
5	110.87	69.29	14.86	54.17	79.89	16.83	52.23	87.45	7.6	142.73	89.49	26.12	78.27
6	150.90	82.11	546.02	57.33	75.05	337.50	53.66	78.67	318.4	146.63	80.51	273.57	73.25
7	25.41	46.37	23.81	37.17	58.34	204.17	44.04	42.13	190.2	120.35	43.12	154.25	59.17
8	194.29	111.30	904.19	59.83	85.83	318.33	56.38	90.85	305.9	154.06	92.98	249.82	76.79
9	45.04	94.48	14.53	49.33	79.65	191.67	52.89	73.70	163.1	144.52	75.43	130.43	71.41
10	266.28	160.80	26.01	67.83	79.34	18.00	63.03	93.71	13.9	172.24	95.91	31.03	73.76
11	97.35	106.80	20.31	49.83	56.45	123.00	55.93	62.47	72.9	152.83	63.93	72.82	63.93
12	73.59	156.40	20.82	53.67	77.93	190.83	59.25	79.75	161.3	161.90	81.61	129.00	70.18
13	173.95	127.80	127.11	53.83	53.38	376.50	59.56	67.31	374.3	162.74	68.89	353.37	64.31
14	157.95	231.40	337.18	55.50	52.65	273.33	65.04	46.31	294.3	177.72	47.40	232.54	51.05
15	506.80	303.00	34.45	80.50	94.61	27.50	71.68	95.39	22.7	195.88	97.63	37.66	69.79
16	381.79	229.10	44.99	72.67	73.38	15.00	67.85	91.63	11.9	185.39	93.77	29.47	70.30
17	238.64	196.90	757.07	67.17	57.00	319.33	63.90	64.77	313.6	174.61	66.29	264.74	60.91
18	382.49	310.00	698.89	73.17	55.02	347.50	70.93	54.07	336.8	193.81	55.34	304.09	52.82
19	597.45	381.00	37.28	78.33	86.80	34.67	74.78	92.67	31.6	204.34	94.84	44.30	67.34
20	192.48	256.90	412.99	57.17	51.13	288.17	66.68	45.45	303.0	182.20	46.51	243.82	49.95
21	169.12	351.40	72.06	61.00	69.89	185.83	70.24	70.29	164.0	191.93	71.93	131.15	60.52
22	573.77	417.30	45.18	70.67	83.39	60.83	75.70	85.55	42.6	206.86	87.55	52.19	64.31
23	776.34	550.20	1004.81	79.67	59.94	362.50	80.46	59.96	355.3	219.87	61.36	330.25	52.22
24	761.52	596.70	156.64	83.00	62.71	47.17	81.32	65.24	28.1	222.22	66.77	41.71	54.18
25	274.64	414.30	351.75	66.33	41.15	246.67	73.42	27.88	249.3	200.61	28.53	197.05	37.28
26	381.07	461.60	1102.55	77.00	66.00	298.83	75.06	53.85	302.8	205.09	55.11	243.53	51.24
27	985.09	836.70	885.98	85.17	58.61	375.33	87.02	45.13	367.7	237.77	46.19	345.77	43.57
28	269.18	556.10	62.21	73.17	86.53	180.00	76.97	83.54	155.2	210.34	85.49	124.37	63.02
29	950.59	939.70	377.88	78.83	48.02	64.17	88.46	42.28	37.6	241.73	43.27	48.62	41.82
30	901.72	933.90	91.14	83.00	88.81	97.00	87.75	77.98	92.2	239.77	79.80	85.21	57.03
31	1126.00	1099.00	1192.29	88.83	32.11	382.83	91.51	32.42	357.8	250.05	33.18	333.46	36.01
32	1043.65	1076.00	576.42	84.83	38.30	49.83	90.91	33.04	22.4	248.40	33.81	37.47	36.47
33	920.98	972.70	95.48	82.83	89.43	90.33	88.42	77.55	94.9	241.62	79.37	86.85	56.65
34	467.24	921.90	183.53	81.83	64.72	181.33	85.60	64.77	158.6	233.91	66.28	126.94	52.62
35	1157.77	1394.00	989.90	96.50	5.00	63.67	95.45	13.32	19.6	260.83	13.63	35.35	22.59
36	1003.61	1486.00	592.74	92.67	37.07	170.83	95.92	35.08	144.6	262.12	35.91	116.79	36.59
37	1175.48	1518.00	151.34	92.50	87.71	118.33	96.47	74.44	120.3	263.60	76.18	101.26	53.14
38	1365.29	1658.00	1053.42	97.83	4.88	80.00	99.20	16.33	53.0	271.08	16.71	59.48	24.54
39	1164.67	1619.00	189.70	91.67	80.02	103.67	97.63	70.04	127.2	266.79	71.68	105.39	51.24
40	1541.92	1824.00	1635.45	100.00	3.71	2.50	101.47	13.81	345.9	277.28	14.14	317.42	22.32

Table A.44: *Physical measurements, perceptual estimates, and our model's predictions (Phase 8).*

Physical measurements				Perceptual estimates			Predicted appearance						
Colour	X	Y[cd/m^2]	Z	J'	M'	H'	J	M	H	Q	C	h	s
1	32.10	25.53	11.73	29.17	52.39	27.67	22.34	47.01	8.3	61.10	48.09	26.66	87.71
2	20.32	23.68	12.25	18.83	22.08	144.50	1.00	22.63	68.2	2.73	23.15	69.79	287.68
3	73.89	44.56	320.57	47.33	96.64	303.33	34.72	80.89	304.6	94.94	82.75	247.15	92.30
4	37.54	43.11	14.00	28.00	48.33	128.67	33.58	36.82	81.9	91.82	37.67	78.65	63.33
5	116.75	75.50	19.71	51.67	76.07	9.67	44.63	76.24	15.0	122.05	78.00	31.87	79.04
6	156.41	88.25	552.54	54.17	80.61	337.83	46.07	78.40	314.9	125.99	80.21	267.11	78.89
7	30.34	52.27	28.84	39.83	63.45	195.33	35.62	33.40	188.4	97.40	34.17	152.57	58.56
8	200.54	118.90	910.13	63.33	87.69	317.00	49.09	89.09	300.0	134.24	91.15	237.60	81.47
9	50.03	100.70	19.43	54.67	80.99	190.00	45.21	60.63	159.6	123.63	62.04	127.69	70.03
10	270.63	166.10	30.76	64.50	86.03	9.67	55.61	88.94	23.7	152.06	91.00	38.48	76.48
11	102.81	113.10	25.55	50.00	57.01	128.33	48.36	52.57	84.6	132.25	53.79	80.42	63.05
12	78.53	162.30	26.11	56.50	78.77	189.50	51.71	68.82	157.5	141.40	70.41	126.12	69.76
13	180.15	134.60	133.17	55.50	53.13	372.50	52.09	63.05	374.5	142.44	64.51	353.61	66.53
14	162.87	238.30	340.50	57.33	43.58	277.00	57.63	46.11	290.3	157.60	47.17	229.13	54.09
15	512.09	309.10	40.05	80.83	94.49	24.50	64.60	95.18	36.4	176.65	97.38	47.78	73.40
16	385.79	234.10	49.54	75.50	78.92	9.83	60.52	90.85	20.3	165.50	92.94	35.89	74.09
17	244.90	204.00	764.67	62.17	54.20	322.00	56.54	67.89	310.3	154.61	69.46	258.53	66.26
18	389.97	318.40	706.11	65.50	56.78	357.50	63.75	58.00	337.6	174.33	59.34	305.17	57.68
19	601.81	386.60	42.80	84.17	94.76	40.33	67.82	92.93	47.7	185.47	95.07	55.76	70.78
20	199.16	265.40	420.99	52.50	38.42	284.17	59.39	46.38	301.0	162.42	47.46	239.60	53.44
21	174.30	357.80	77.13	66.67	69.88	188.83	62.96	68.28	161.1	172.16	69.86	128.86	62.98
22	577.72	422.50	49.99	72.50	85.50	46.17	68.74	85.47	58.1	187.99	87.45	62.97	67.43
23	781.73	557.10	1010.82	80.17	75.93	365.83	73.79	66.37	356.6	201.78	67.90	331.84	57.35
24	770.86	606.60	164.88	77.50	58.56	47.50	74.88	70.19	36.2	204.76	71.82	47.65	58.55
25	279.60	420.30	356.39	60.17	40.90	232.50	66.21	29.17	248.2	181.07	29.85	196.25	40.14
26	386.74	469.70	1104.73	75.17	57.75	295.00	68.04	58.76	300.3	186.08	60.11	238.17	56.19
27	991.40	844.00	894.23	81.00	54.22	380.83	81.13	51.25	368.2	221.88	52.44	346.29	48.06
28	272.45	559.00	66.25	76.67	95.12	N/A	69.96	82.51	N/A	191.31	84.42	N/A	65.67
29	957.74	948.80	386.90	76.17	48.42	55.83	82.87	47.47	42.9	226.63	48.56	52.39	45.76
30	909.49	942.80	95.64	79.00	84.88	87.00	82.16	80.19	103.1	224.68	82.04	91.63	59.74
31	1134.49	1109.00	1201.68	82.83	42.70	382.50	86.50	37.73	358.3	236.56	38.60	334.09	39.93
32	1054.31	1089.00	588.07	82.33	47.62	70.83	85.84	37.87	25.0	234.75	38.74	39.42	40.16
33	926.32	979.50	100.94	78.00	91.94	106.67	82.90	79.75	105.3	226.72	81.59	92.81	59.31
34	471.99	928.90	186.70	82.83	70.23	180.00	79.53	69.62	156.1	217.49	71.23	125.10	56.58
35	1164.59	1403.00	996.03	89.17	7.83	51.17	91.39	15.68	20.9	249.93	16.04	36.35	25.05
36	1014.08	1499.00	603.34	84.83	42.73	156.17	92.09	40.12	144.5	251.83	41.04	116.67	39.91
37	1176.79	1519.00	153.58	91.33	83.09	102.00	92.73	80.09	124.6	253.58	81.94	103.79	56.20
38	1372.22	1668.00	1062.09	92.67	9.02	101.00	96.36	19.27	55.7	263.52	19.72	61.32	27.04
39	1170.06	1626.00	195.66	93.83	82.02	105.67	94.35	76.04	129.3	258.01	77.79	106.72	54.29
40	1553.40	1840.00	1643.56	99.50	3.35	355.00	99.62	16.55	345.7	272.44	16.93	317.12	24.65

Table A.45: *Physical measurements, perceptual estimates, and our model's predictions (Phase 9).*

Physical measurements				Perceptual estimates			Predicted appearance						
Colour	X	Y[cd/m^2]	Z	J'	M'	H'	J	M	H	Q	C	h	s
1	36.36	30.91	16.09	19.00	22.33	19.43	14.64	39.51	3.0	40.06	40.42	22.51	99.32
2	24.46	28.85	16.45	7.86	8.24	81.00	1.00	18.58	52.7	2.74	19.00	59.28	260.57
3	78.02	49.80	324.49	37.00	81.31	301.86	31.38	74.99	308.9	85.86	76.71	255.80	93.46
4	42.02	48.66	18.49	17.00	19.68	120.00	30.18	31.11	72.1	82.56	31.83	72.35	61.39
5	120.75	80.69	23.88	47.86	64.99	6.43	41.59	68.94	9.6	113.79	70.52	27.68	77.84
6	160.77	93.70	557.49	54.29	77.22	325.57	43.09	75.81	317.4	117.90	77.55	271.76	80.19
7	34.72	57.82	33.30	24.29	40.71	198.29	32.33	29.07	189.6	88.45	29.73	153.65	57.33
8	204.71	123.70	916.05	72.29	93.24	302.29	46.09	86.34	304.1	126.10	88.32	246.08	82.75
9	54.39	106.30	23.67	46.86	66.75	194.00	42.21	53.68	162.0	115.48	54.91	129.58	68.18
10	276.38	172.30	35.18	65.14	80.75	4.86	52.74	83.96	16.6	144.29	85.89	33.12	76.28
11	107.70	119.10	29.99	45.86	38.79	109.29	45.44	47.15	76.4	124.30	48.23	75.12	61.59
12	82.91	168.10	30.33	55.14	72.14	192.71	48.75	62.46	160.1	133.38	63.89	128.13	68.43
13	184.94	140.30	137.80	52.14	50.83	371.57	49.13	59.02	374.3	134.41	60.37	353.41	66.27
14	167.62	244.20	345.62	55.00	52.80	270.00	54.67	44.46	292.7	149.58	45.48	231.22	54.52
15	516.69	314.30	44.01	83.00	91.86	13.00	61.70	92.38	26.4	168.81	94.50	40.48	73.98
16	392.10	240.90	54.89	77.14	91.05	5.43	57.68	87.27	14.5	157.80	89.27	31.45	74.37
17	249.67	209.80	771.03	66.29	64.57	310.71	53.60	67.24	312.6	146.63	68.79	262.88	67.72
18	394.28	323.40	711.39	63.00	62.43	342.57	60.77	58.05	337.1	166.25	59.38	304.49	59.09
19	607.33	392.60	47.01	85.00	101.32	38.29	64.99	90.55	36.2	177.80	92.63	47.62	71.36
20	203.55	270.80	425.92	60.14	46.52	279.57	56.41	45.30	302.3	154.33	46.34	242.39	54.18
21	179.38	364.90	81.62	62.43	69.54	190.43	60.06	65.17	163.1	164.31	66.67	130.45	62.98
22	583.19	428.50	53.70	79.29	93.64	50.57	65.90	83.17	47.1	180.29	85.08	55.41	67.92
23	790.41	565.60	1020.46	79.29	63.02	358.86	71.05	67.36	355.7	194.39	68.91	330.75	58.87
24	773.39	611.10	168.50	79.00	73.20	51.43	72.06	70.43	30.4	197.14	72.05	43.36	59.77
25	285.66	428.00	363.07	60.71	41.95	237.86	63.34	28.70	248.7	173.29	29.36	196.63	40.69
26	390.95	475.50	1109.04	77.86	69.25	298.29	65.13	59.35	302.0	178.19	60.71	241.75	57.71
27	995.20	849.50	899.16	78.29	55.88	370.43	78.53	52.62	367.9	214.84	53.82	345.93	49.49
28	278.72	568.00	72.23	74.00	72.94	187.14	67.19	78.95	N/A	183.81	80.77	N/A	65.54
29	963.83	956.20	392.42	76.71	44.94	59.29	80.40	48.61	39.2	219.97	49.73	49.80	47.01
30	912.69	946.80	100.76	77.14	101.34	89.00	79.64	78.45	96.0	217.87	80.25	87.56	60.01
31	1140.21	1117.00	1207.43	81.43	46.06	365.29	84.24	39.19	357.9	230.46	40.09	333.64	41.24
32	1059.86	1097.00	593.89	79.00	40.18	48.00	83.54	39.14	23.0	228.54	40.04	37.94	41.38
33	931.38	986.20	105.40	79.57	96.27	91.43	80.47	78.33	98.2	220.16	80.13	88.91	59.65
34	479.58	939.80	194.29	84.86	75.31	199.29	77.00	69.18	157.7	210.67	70.77	126.24	57.31
35	1172.12	1413.00	1004.82	88.57	8.15	76.43	89.54	16.37	20.4	244.96	16.74	35.94	25.85
36	1021.02	1508.00	608.72	91.57	32.91	167.43	90.29	41.50	144.7	247.00	42.46	116.82	40.99
37	1186.78	1531.00	162.75	91.43	83.53	101.86	91.14	79.41	122.0	249.34	81.23	102.27	56.43
38	1377.69	1674.00	1069.43	91.86	10.09	88.86	94.95	20.23	54.7	259.76	20.69	60.63	27.90
39	1173.43	1632.00	195.67	93.86	92.63	122.86	92.76	77.12	127.9	253.78	78.89	105.82	55.13
40	1559.29	1849.00	1647.77	100.00	2.48	362.50	98.69	17.48	345.8	269.99	17.89	317.23	25.45

Table A.46: *Physical measurements, perceptual estimates, and our model's predictions (Phase 10).*

Physical measurements				Perceptual estimates			Predicted appearance						
Colour	X	Y[cd/m^2]	Z	J'	M'	H'	J	M	H	Q	C	h	s
1	49.58	47.11	29.37	14.83	23.00	4.17	8.98	28.80	-2.2	24.59	29.45	18.07	108.23
2	37.73	45.13	29.66	6.17	3.68	133.33	1.00	13.14	34.4	2.74	13.44	46.29	219.13
3	91.19	65.99	337.87	39.00	72.28	320.83	28.31	63.67	313.9	77.50	65.12	265.41	90.64
4	54.88	64.50	31.39	12.83	21.77	132.83	26.76	22.68	59.6	73.26	23.19	64.01	55.63
5	134.07	96.98	37.30	42.00	52.69	12.33	38.01	55.75	4.0	104.05	57.02	23.29	73.20
6	174.42	110.20	571.64	44.17	66.81	325.33	39.52	68.58	320.1	108.17	70.14	276.61	79.62
7	47.75	73.75	46.27	20.83	30.61	206.67	28.90	21.53	190.9	79.12	22.02	154.95	52.16
8	216.29	138.90	926.17	60.50	86.00	300.83	42.30	78.78	309.0	115.80	80.57	255.86	82.48
9	67.25	121.90	36.76	45.17	58.39	198.33	38.46	41.46	164.8	105.27	42.41	131.85	62.76
10	288.80	188.00	48.19	53.67	68.32	7.50	48.82	72.76	9.7	133.65	74.41	27.75	73.78
11	119.97	134.20	43.00	39.33	37.62	135.67	41.54	37.39	66.0	113.71	38.24	68.27	57.34
12	96.10	184.40	43.07	53.83	66.32	192.83	44.91	50.62	162.9	122.93	51.78	130.30	64.17
13	197.85	156.30	150.70	51.00	53.14	367.17	45.24	50.41	374.1	123.83	51.55	353.22	63.80
14	180.39	260.10	357.36	47.67	50.74	271.67	50.66	39.84	296.7	138.67	40.74	234.65	53.60
15	529.04	330.10	56.79	80.17	86.06	4.50	57.72	83.90	17.0	157.98	85.81	33.39	72.88
16	404.24	256.10	67.63	66.00	71.27	4.67	53.67	78.14	8.3	146.90	79.91	26.68	72.93
17	261.43	224.70	780.50	63.17	64.33	317.00	49.58	63.24	315.3	135.70	64.68	267.85	68.26
18	407.67	339.80	724.80	61.83	59.50	345.00	56.71	55.32	336.4	155.23	56.58	303.47	59.70
19	620.04	408.50	60.21	70.50	75.24	36.50	61.01	83.06	24.6	166.99	84.95	39.13	70.53
20	216.13	286.60	438.18	54.50	45.12	293.17	52.36	41.48	304.1	143.34	42.42	246.09	53.80
21	192.17	380.60	94.48	63.83	57.59	191.67	55.98	57.39	165.6	153.24	58.70	132.41	61.20
22	593.58	442.40	66.71	63.83	68.51	50.00	61.82	75.94	34.9	169.21	77.66	46.67	66.99
23	801.97	580.70	1032.89	77.33	57.85	355.00	66.99	65.85	354.6	183.38	67.35	329.24	59.93
24	785.28	625.90	181.03	70.33	59.68	71.00	68.05	67.64	24.2	186.27	69.18	38.78	60.26
25	297.68	443.00	374.63	61.33	41.39	225.83	59.19	26.71	249.7	162.03	27.32	197.31	40.60
26	403.71	491.10	1118.72	73.67	54.82	300.00	61.05	57.57	304.4	167.11	58.87	246.82	58.69
27	1009.22	866.40	913.82	75.17	45.63	371.33	74.75	52.50	367.5	204.62	53.69	345.51	50.65
28	290.08	581.30	84.08	71.33	76.95	186.33	63.05	70.73	156.9	172.59	72.34	125.63	64.02
29	973.73	969.50	404.23	70.50	46.23	61.33	76.64	48.30	34.9	209.78	49.39	46.69	47.98
30	923.96	961.50	111.43	68.33	82.90	87.50	75.95	73.08	86.2	207.89	74.74	81.44	59.29
31	1151.32	1131.00	1220.32	78.50	35.66	363.50	80.74	40.07	357.4	221.00	40.98	332.96	42.58
32	1071.39	1111.00	606.96	75.33	35.55	59.67	79.99	39.60	20.7	218.95	40.50	36.19	42.53
33	943.27	1001.00	117.52	75.83	80.91	88.33	76.84	72.89	88.9	210.34	74.54	83.13	58.87
34	492.78	954.60	207.90	79.17	54.22	203.33	73.14	65.69	160.0	200.20	67.18	128.01	57.28
35	1183.60	1427.00	1016.75	77.83	11.72	94.17	86.55	16.93	18.4	236.91	17.31	34.42	26.73
36	1029.10	1518.00	619.36	82.50	36.14	178.50	87.30	41.92	145.0	238.97	42.87	117.04	41.88
37	1196.33	1545.00	171.57	89.33	70.59	117.83	88.47	76.36	117.9	242.18	78.10	99.80	56.15
38	1387.22	1687.00	1077.89	88.00	11.94	88.33	92.68	21.13	52.6	253.70	21.61	59.20	28.86
39	1186.33	1646.00	211.88	92.33	67.91	104.33	90.34	74.04	125.5	247.28	75.72	104.34	54.72
40	1568.55	1861.00	1656.54	98.17	2.34	N/A	97.09	18.54	N/A	265.76	18.96	N/A	26.41

Table A.47: *Physical measurements, perceptual estimates, and our model's predictions (Phase 11).*

Physical measurements				Perceptual estimates			Predicted appearance						
Colour	X	Y[cd/m^2]	Z	J′	M′	H′	J	M	H	Q	C	h	s
1	64.47	68.09	43.88	9.17	9.78	17.50	19.75	21.07	3.3	54.17	21.53	22.74	62.37
2	52.69	66.23	44.25	2.50	2.18	N/A	13.83	9.68	N/A	37.93	9.89	N/A	50.52
3	106.44	87.19	354.74	32.17	70.68	301.67	28.83	55.30	315.1	79.09	56.51	267.59	83.61
4	70.16	85.91	46.17	6.33	7.19	106.00	27.59	17.90	69.9	75.67	18.29	70.88	48.64
5	149.33	118.10	51.59	35.17	50.71	8.00	36.89	45.99	4.2	101.20	47.00	23.46	67.42
6	190.11	131.60	589.65	39.17	75.21	326.33	38.32	61.92	320.6	105.13	63.28	277.56	76.75
7	62.76	95.13	60.95	21.67	35.23	202.50	29.16	18.91	191.3	80.00	19.33	155.39	48.62
8	232.62	160.80	946.58	53.00	75.73	302.50	40.97	71.97	310.8	112.38	73.55	259.46	80.03
9	82.17	143.30	51.11	33.67	48.20	192.50	37.27	34.85	166.8	102.23	35.62	133.46	58.39
10	304.82	209.60	62.67	49.50	71.04	10.17	47.00	63.46	8.2	128.92	64.85	26.61	70.16
11	135.93	156.40	57.56	28.00	30.11	113.83	40.18	31.30	66.6	110.21	31.99	68.69	53.29
12	111.05	206.00	57.49	50.17	67.57	192.33	43.22	43.17	164.7	118.57	44.12	131.70	60.34
13	214.36	178.50	166.53	40.33	52.44	364.50	43.61	43.08	374.2	119.63	44.03	353.35	60.01
14	196.07	282.30	373.73	48.67	48.16	269.33	48.72	35.95	297.3	133.65	36.74	235.21	51.86
15	545.97	352.40	71.90	68.50	77.26	3.67	55.62	75.84	14.1	152.58	77.50	31.18	70.50
16	420.25	277.80	81.63	55.50	73.06	2.50	51.65	69.69	7.0	141.67	71.22	25.69	70.13
17	278.14	247.50	800.73	56.17	59.00	330.17	47.77	58.68	316.0	131.02	59.96	269.22	66.92
18	425.59	363.50	744.02	56.67	63.01	350.00	54.64	51.54	335.9	149.88	52.67	302.64	58.64
19	634.39	429.30	73.83	66.50	72.85	24.67	58.77	75.79	21.3	161.21	77.45	36.63	68.57
20	232.35	309.30	455.13	49.00	47.12	276.00	50.38	37.82	304.5	138.21	38.65	246.90	52.31
21	207.44	403.30	108.79	59.83	63.42	192.50	53.86	51.35	166.8	147.74	52.47	133.40	58.95
22	611.09	465.50	81.66	59.17	62.76	40.67	59.64	69.18	30.9	163.60	70.70	43.76	65.03
23	816.35	601.60	1047.62	63.67	63.67	358.33	64.63	62.46	353.9	177.28	63.83	328.33	59.36
24	800.25	647.70	195.95	63.17	55.26	44.83	65.72	63.39	22.1	180.29	64.78	37.23	59.30
25	315.06	467.60	392.51	54.33	47.49	247.50	57.06	24.82	249.6	156.51	25.36	197.25	39.82
26	419.86	515.10	1135.37	68.00	56.71	295.00	58.87	54.64	305.3	161.49	55.84	248.59	58.17
27	1025.71	890.70	932.00	69.00	41.73	367.17	72.47	50.35	367.2	198.78	51.45	345.10	50.33
28	307.56	606.00	100.16	71.17	70.58	185.83	60.86	63.44	158.1	166.93	64.83	126.58	61.65
29	991.90	996.00	421.38	69.00	42.27	58.00	74.43	46.28	33.6	204.17	47.29	45.73	47.61
30	939.85	984.60	128.08	60.83	63.02	86.00	73.70	67.11	81.8	202.16	68.58	78.63	57.62
31	1170.49	1158.00	1241.17	68.33	44.30	363.17	78.61	39.14	356.9	215.63	40.00	332.30	42.61
32	1086.37	1133.00	623.79	69.17	41.58	56.00	77.72	38.39	19.6	213.20	39.23	35.40	42.43
33	958.30	1024.00	130.35	61.67	76.98	85.83	74.59	67.49	85.3	204.61	68.97	80.83	57.43
34	511.26	983.20	222.32	71.17	65.95	185.83	70.95	61.69	160.9	194.61	63.04	128.70	56.30
35	1203.23	1454.00	1035.93	71.67	17.30	92.17	84.61	16.63	17.1	232.09	16.99	33.45	26.77
36	1052.80	1551.00	637.58	76.67	34.76	173.33	85.54	40.80	145.0	234.65	41.70	117.03	41.70
37	1216.31	1574.00	187.93	70.83	71.30	115.50	86.75	71.60	115.8	237.97	73.17	98.64	54.85
38	1411.07	1722.00	1103.10	78.00	22.07	91.50	91.28	20.72	52.2	250.38	21.17	58.95	28.77
39	1205.44	1675.00	227.17	74.00	51.51	123.00	88.70	70.05	124.5	243.32	71.59	103.72	53.66
40	1586.78	1889.00	1672.76	87.00	14.33	361.33	95.86	18.57	345.4	262.95	18.98	316.62	26.58

Table A.48: *Physical measurements, perceptual estimates, and our model's predictions (Phase 12).*

Physical measurements				Perceptual estimates			Predicted appearance						
Colour	X	Y[cd/m^2]	Z	J′	M′	H′	J	M	H	Q	C	h	s
1	18.12	15.64	12.15	17.50	43.53	17.00	1.00	37.27	-3.8	2.55	39.17	16.47	382.49
2	12.63	14.82	12.55	9.50	12.15	105.00	1.00	16.25	24.0	2.55	17.08	38.69	252.55
3	56.36	28.96	254.19	42.83	91.79	300.83	29.97	75.92	312.4	76.34	79.78	262.52	99.72
4	20.63	24.11	13.04	25.83	37.65	131.17	27.67	28.95	60.2	70.50	30.43	64.38	64.09
5	59.75	40.71	18.30	46.33	74.97	10.17	40.42	65.87	4.8	102.99	69.22	23.93	79.97
6	109.20	53.76	435.71	50.67	85.90	327.83	42.04	77.22	318.9	107.11	81.15	274.51	84.91
7	17.93	29.17	22.82	32.67	50.53	193.33	30.40	25.66	189.6	77.46	26.97	153.65	57.56
8	148.27	72.66	701.15	64.33	89.17	301.67	45.00	85.97	307.4	114.66	90.35	252.86	86.59
9	28.21	55.57	16.58	49.33	77.53	191.67	41.47	51.02	160.1	105.65	53.62	128.14	69.49
10	134.69	85.58	27.14	57.17	86.24	3.00	51.44	80.40	11.2	131.05	84.50	28.93	78.33
11	53.16	60.29	21.40	48.00	57.18	141.17	44.26	44.78	70.0	112.75	47.05	70.93	63.02
12	43.33	89.14	20.90	55.33	75.06	189.17	48.23	60.32	158.2	122.88	63.39	126.67	70.06
13	96.94	71.49	106.11	56.00	41.31	365.83	47.93	59.22	369.7	122.11	62.23	348.09	69.64
14	103.47	133.70	267.55	55.50	50.30	257.50	54.22	43.99	302.4	138.15	46.22	242.62	56.43
15	243.20	151.00	32.47	71.50	90.61	9.17	59.74	88.55	20.4	152.21	93.06	35.96	76.27
16	187.93	117.10	40.50	68.83	75.71	5.83	55.99	83.98	9.2	142.66	88.25	27.36	76.72
17	163.13	115.90	592.40	65.17	60.39	320.17	52.62	68.45	315.2	134.05	71.93	267.80	71.45
18	232.08	174.30	551.84	61.50	67.27	350.00	59.75	60.16	336.0	152.23	63.22	302.75	62.86
19	283.22	187.70	34.20	74.33	91.78	39.17	62.79	86.69	29.6	159.98	91.10	42.79	73.61
20	124.58	147.60	328.79	57.67	58.32	269.00	55.81	45.99	307.1	142.19	48.34	252.18	56.88
21	96.41	198.20	57.50	62.33	55.87	205.83	59.76	63.12	160.8	152.25	66.33	128.68	64.39
22	274.80	209.40	39.03	70.33	91.59	70.00	63.93	79.23	41.5	162.87	83.26	51.41	69.75
23	426.50	290.50	774.27	73.83	73.88	358.67	69.01	67.55	352.2	175.81	70.99	326.03	61.99
24	369.77	303.10	125.60	67.17	66.80	46.67	69.91	66.29	24.8	178.12	69.66	39.24	61.00
25	163.89	233.00	278.67	59.67	35.87	213.00	62.83	26.10	270.7	160.08	27.42	213.18	40.38
26	252.86	265.20	837.77	69.67	58.77	298.17	64.51	58.18	305.7	164.36	61.14	249.38	59.50
27	523.31	442.30	690.95	70.00	55.15	370.33	76.53	51.88	362.2	194.99	54.52	339.06	51.58
28	147.56	308.70	48.90	70.83	99.22	185.33	66.80	77.90	152.5	170.19	81.87	122.37	67.66
29	482.56	496.10	298.96	71.50	47.56	57.00	78.48	44.38	32.7	199.96	46.64	45.06	47.11
30	440.94	489.00	69.24	70.33	92.85	95.00	77.75	76.84	96.0	198.10	80.75	87.54	62.28
31	609.87	588.60	907.43	76.67	33.96	365.00	82.09	39.58	352.6	209.13	41.60	326.57	43.51
32	539.69	571.10	451.72	71.67	41.21	56.67	81.42	35.65	12.6	207.44	37.47	30.01	41.46
33	449.89	508.50	71.58	71.67	84.80	90.33	78.51	76.99	98.5	200.01	80.91	89.05	62.04
34	258.43	512.40	139.13	79.50	73.67	184.00	76.44	66.96	155.7	194.75	70.37	124.74	58.64
35	624.66	750.10	755.00	88.17	4.65	106.00	87.40	15.38	-13.3	222.67	16.16	6.94	26.28
36	541.65	804.90	455.34	85.00	26.66	178.83	88.47	37.86	142.3	225.40	39.79	115.21	40.98
37	583.99	802.70	107.27	82.83	96.21	105.00	88.79	79.53	122.4	226.20	83.58	102.49	59.29
38	727.91	889.00	805.43	95.83	6.40	88.67	92.40	16.79	30.8	235.40	17.65	43.70	26.71
39	582.57	856.10	132.44	90.50	80.71	107.17	90.32	76.59	127.9	230.10	80.48	105.85	57.69
40	831.79	977.10	1181.01	100.00	2.64	390.00	95.43	18.99	342.8	243.14	19.96	312.94	27.95

Table A.49: *Physical measurements, perceptual estimates, and our model's predictions (Phase 13).*

Physical measurements				Perceptual estimates			Predicted appearance						
Colour	X	Y[cd/m^2]	Z	J′	M′	H′	J	M	H	Q	C	h	s
1	28.46	21.50	3.35	25.67	57.75	42.83	27.10	44.11	5.6	68.76	46.43	24.55	80.09
2	17.35	17.63	3.89	10.17	9.15	100.00	15.96	20.19	23.7	40.49	21.25	38.45	70.61
3	22.33	23.80	62.90	39.17	83.97	300.83	33.56	72.31	306.2	85.13	76.11	250.42	92.16
4	30.84	29.89	4.38	22.17	28.94	113.33	33.41	32.00	46.9	84.75	33.68	55.22	61.44
5	102.99	65.38	4.78	50.00	69.31	11.83	46.82	71.33	15.0	118.78	75.09	31.86	77.50
6	64.61	52.80	106.70	55.17	87.03	338.33	46.12	68.13	317.1	116.99	71.71	271.18	76.31
7	19.32	30.00	7.65	28.83	45.20	198.67	32.32	29.96	211.7	81.99	31.53	171.53	60.45
8	50.89	56.43	171.21	64.17	101.03	299.67	47.28	84.00	301.4	119.95	88.43	240.55	83.69
9	32.40	55.43	7.58	52.33	64.68	195.83	42.09	46.18	181.0	106.79	48.61	145.64	65.76
10	233.44	141.60	6.84	61.00	83.11	10.17	57.81	83.21	22.1	146.66	87.59	37.26	75.32
11	82.19	75.65	7.80	45.67	49.11	122.50	47.91	46.08	54.1	121.54	48.51	60.24	61.58
12	49.35	87.51	10.63	57.33	65.23	187.50	48.54	52.75	179.2	123.15	55.53	144.03	65.45
13	139.25	100.30	27.98	59.33	43.53	378.33	53.00	59.24	382.9	134.45	62.36	402.95	66.38
14	75.50	124.40	72.85	57.33	61.96	264.83	54.60	49.89	283.1	138.50	52.52	223.16	60.02
15	418.33	248.60	7.15	81.33	100.21	37.83	66.50	90.05	32.0	168.69	94.78	44.58	73.06
16	322.52	193.70	10.00	68.67	84.98	10.67	62.58	85.34	21.7	158.76	89.83	36.93	73.32
17	102.69	111.90	148.02	55.50	56.06	317.00	55.08	61.92	310.1	139.73	65.18	258.08	66.57
18	232.54	200.00	138.40	60.33	53.35	356.67	63.53	51.43	341.5	161.16	54.14	310.98	56.49
19	483.43	298.80	9.50	79.83	94.36	45.00	69.52	87.36	35.8	176.37	91.95	47.35	70.38
20	95.33	140.90	88.35	56.67	42.94	267.83	56.68	47.86	294.7	143.80	50.38	232.89	57.69
21	103.49	188.20	26.16	61.67	58.29	190.00	59.54	55.56	183.7	151.04	58.48	148.11	60.65
22	460.25	309.70	12.52	78.33	105.61	53.33	69.92	80.46	41.0	177.39	84.70	51.05	67.35
23	503.33	368.20	190.79	75.33	81.58	373.67	74.44	61.12	362.1	188.86	64.34	338.92	56.89
24	579.82	415.40	37.59	73.17	71.43	47.50	75.52	68.71	27.5	191.58	72.32	41.28	59.89
25	158.49	227.70	80.50	64.17	41.15	238.67	63.52	33.04	258.7	161.13	34.77	203.97	45.28
26	147.83	234.80	214.67	71.50	62.48	294.17	64.79	61.29	292.9	164.36	64.52	231.34	61.07
27	657.96	533.90	177.46	80.17	52.79	374.50	81.38	49.43	375.0	206.46	52.03	354.22	48.93
28	167.00	292.50	29.23	68.00	101.57	192.17	66.45	61.71	172.1	168.57	64.96	137.80	60.51
29	679.57	591.10	90.37	74.67	38.93	57.50	82.76	47.31	28.5	209.94	49.80	42.03	47.47
30	670.89	587.80	33.47	75.83	89.74	86.33	82.00	65.41	74.8	208.04	68.86	74.11	56.07
31	710.51	656.50	235.77	76.33	31.41	379.17	85.95	36.33	365.6	218.04	38.24	343.14	40.82
32	715.61	655.60	129.02	77.00	34.59	55.33	85.29	39.10	16.9	216.38	41.15	33.35	42.51
33	678.30	603.80	36.53	72.83	70.57	89.83	82.60	63.89	76.0	209.55	67.25	74.89	55.22
34	281.14	479.90	61.97	76.17	65.58	182.33	75.68	55.41	176.8	191.99	58.33	141.84	53.72
35	729.03	787.80	211.55	86.67	8.50	64.17	89.81	16.82	5.0	227.84	17.70	24.14	27.17
36	639.23	809.50	148.55	80.17	34.96	160.83	89.42	31.37	151.3	226.85	33.02	121.55	37.18
37	821.76	868.80	58.23	81.83	81.27	102.33	91.57	59.48	106.7	232.29	62.61	93.53	50.60
38	863.08	933.40	230.01	91.50	10.23	59.17	94.94	18.59	32.3	240.86	19.57	44.79	27.78
39	796.50	902.10	70.22	81.50	66.96	106.67	92.47	55.99	117.9	234.57	58.94	99.81	48.86
40	919.57	1004.00	322.02	99.17	3.23	N/A	97.80	15.87	N/A	248.10	16.70	N/A	25.29

Table A.50: *Physical measurements, perceptual estimates, and our model's predictions (Phase 14).*

Physical measurements				Perceptual estimates			Predicted appearance						
Colour	X	Y[cd/m^2]	Z	J'	M'	H'	J	M	H	Q	C	h	s
1	41.90	38.26	21.58	22.50	35.59	398.00	24.21	35.84	1.6	66.24	36.66	21.43	73.56
2	30.09	36.34	21.96	7.17	6.12	166.67	18.72	16.69	53.5	51.22	17.07	59.82	57.08
3	83.74	57.29	330.69	45.83	90.83	301.83	33.53	72.56	311.6	91.77	74.22	260.97	88.92
4	47.43	55.88	23.82	17.67	20.02	114.50	32.44	28.80	68.4	88.77	29.46	69.87	56.96
5	126.35	88.11	29.47	48.00	64.74	7.00	42.33	65.82	6.8	115.84	67.32	25.48	75.38
6	166.52	101.17	563.47	56.33	93.13	328.00	43.72	74.44	318.7	119.66	76.14	274.09	78.87
7	40.19	65.07	38.63	25.33	57.90	200.50	34.16	27.69	190.3	93.49	28.32	154.33	54.42
8	209.69	130.72	920.62	64.00	91.60	299.83	46.49	84.89	306.4	127.22	86.83	250.79	81.69
9	59.78	113.34	29.10	49.50	78.23	213.17	42.83	50.91	163.9	117.21	52.08	131.06	65.91
10	281.38	179.36	40.56	57.00	80.12	3.33	52.88	81.75	13.0	144.72	83.62	30.31	75.16
11	112.75	125.92	35.28	42.50	47.60	130.33	45.82	44.95	71.8	125.41	45.97	72.16	59.87
12	88.44	175.44	35.56	57.83	81.15	209.00	49.04	60.06	161.8	134.21	61.43	129.41	66.90
13	190.25	147.50	143.06	53.17	58.10	368.83	49.39	57.19	374.3	135.15	58.50	353.40	65.05
14	172.98	251.26	350.88	51.50	51.35	272.83	54.75	43.73	294.5	149.84	44.72	232.77	54.02
15	522.12	321.78	49.44	80.83	100.67	10.83	61.69	90.77	21.5	168.83	92.85	36.82	73.33
16	396.83	247.60	59.74	64.67	66.22	7.50	57.69	85.65	11.3	157.87	87.60	29.04	73.66
17	254.56	216.58	774.80	60.50	62.18	318.00	53.69	66.51	313.8	146.93	68.03	265.13	67.28
18	400.00	331.02	717.04	59.50	63.74	348.33	60.76	57.48	336.7	166.27	58.79	303.90	58.80
19	612.21	399.60	52.22	79.67	94.68	40.50	64.92	89.14	30.4	177.66	91.17	43.38	70.83
20	208.73	277.80	430.64	54.33	42.87	286.33	56.44	44.66	303.1	154.47	45.68	243.99	53.77
21	184.48	371.60	86.82	63.67	69.23	187.50	60.02	63.85	164.3	164.26	65.31	131.44	62.35
22	587.87	435.24	59.45	70.00	92.74	50.50	65.81	81.72	41.1	180.10	83.58	51.10	67.36
23	793.36	571.04	1023.32	72.33	69.33	365.50	70.87	66.98	355.2	193.95	68.51	330.07	58.76
24	778.26	617.60	173.40	76.33	69.86	48.50	71.91	69.92	27.6	196.81	71.51	41.34	59.60
25	290.53	434.64	367.67	55.00	45.46	240.83	63.25	28.47	249.1	173.10	29.12	196.89	40.55
26	396.47	482.60	1114.08	75.00	64.08	295.83	65.05	58.98	303.0	178.03	60.32	243.91	57.56
27	1001.32	857.46	905.04	72.83	63.14	378.83	78.40	52.43	367.7	214.56	53.62	345.73	49.43
28	283.60	574.08	76.99	81.83	88.61	186.67	67.06	77.58	155.4	183.52	79.35	124.56	65.02
29	967.56	962.04	396.56	67.33	55.46	59.00	80.22	48.45	37.5	219.54	49.56	48.54	46.98
30	917.54	953.92	105.41	69.83	88.32	86.67	79.50	77.54	91.6	217.55	79.30	84.81	59.70
31	1144.50	1122.80	1212.58	73.50	35.22	378.33	84.07	39.20	357.7	230.06	40.09	333.30	41.28
32	1063.12	1101.20	597.83	71.33	33.85	54.17	83.33	39.12	22.1	228.04	40.01	37.24	41.42
33	936.05	992.68	109.94	74.50	86.41	93.83	80.32	77.45	94.2	219.81	79.22	86.45	59.36
34	484.57	945.68	198.95	78.17	76.84	186.17	76.83	68.62	158.7	210.27	70.19	127.05	57.13
35	1176.26	1418.20	1008.69	87.00	7.88	97.50	89.38	16.39	19.3	244.60	16.76	35.10	25.89
36	1024.12	1512.40	612.35	81.67	42.10	166.17	90.11	41.48	144.8	246.60	42.43	116.87	41.01
37	1190.34	1537.40	165.43	85.50	96.93	103.33	91.01	79.10	120.3	249.08	80.90	101.21	56.35
38	1382.70	1681.80	1073.19	91.00	8.05	87.00	94.87	20.27	53.7	259.63	20.73	59.93	27.94
39	1179.99	1639.60	204.01	86.33	80.22	107.83	92.69	76.19	126.9	253.67	77.93	105.24	54.81
40	1561.99	1852.60	1651.22	99.50	4.07	380.00	98.57	17.60	345.7	269.74	18.00	317.14	25.54

Table A.51: *Physical measurements, perceptual estimates, and our model's predictions (Phase 15).*

Physical measurements				Perceptual estimates			Predicted appearance						
Colour	X	Y[cd/m^2]	Z	J′	M′	H′	J	M	H	Q	C	h	s
1	12.36	12.02	6.71	6.67	26.18	395.00	1.00	20.03	0.9	3.27	19.22	20.87	247.65
2	14.21	15.49	6.33	6.83	25.88	87.50	1.00	19.68	48.3	3.27	18.88	56.25	245.47
3	51.61	28.08	234.05	21.33	101.00	301.17	1.00	75.71	310.7	3.27	72.64	259.23	481.44
4	159.01	71.32	13.59	33.33	117.14	2.50	25.85	93.72	-2.6	84.46	89.91	17.67	105.34
5	511.93	135.80	2169.70	40.00	94.91	327.67	40.63	101.43	313.4	132.71	97.31	264.30	87.42
6	418.63	212.50	12.62	48.50	121.52	399.50	44.34	104.78	16.7	144.82	100.52	33.15	85.06
7	585.45	233.60	2808.28	48.67	89.46	305.33	45.39	105.75	302.8	148.28	101.45	243.40	84.45
8	264.38	256.10	6.70	38.17	54.78	98.33	44.59	80.01	87.2	145.66	76.76	82.03	74.12
9	119.30	325.00	99.72	44.67	94.71	195.67	45.70	68.08	189.4	149.27	65.32	153.46	67.53
10	957.14	609.00	74.48	64.17	85.15	12.83	57.55	94.79	28.0	187.99	90.94	41.61	71.01
11	211.41	708.70	39.54	58.33	96.46	199.17	55.60	103.37	168.3	181.63	99.17	134.61	75.44
12	657.73	808.80	138.87	43.33	68.82	148.67	59.44	65.66	111.3	194.16	62.99	96.06	58.15
13	965.47	890.40	904.20	53.50	66.49	360.00	61.80	47.30	358.3	201.87	45.38	334.11	48.41
14	1431.62	928.80	464.40	60.67	91.11	5.17	63.56	84.73	-8.3	207.62	81.28	12.07	63.88
15	439.37	972.10	1256.21	58.50	78.05	247.50	60.57	70.49	263.6	197.85	67.63	207.69	59.69
16	1128.14	1053.00	2896.00	62.33	60.79	309.83	63.81	64.40	312.2	208.44	61.79	262.14	55.59
17	337.86	1084.00	63.89	60.00	97.23	196.67	61.43	105.91	166.4	200.66	101.61	133.09	72.65
18	1548.81	1519.00	2556.04	60.17	47.17	334.17	69.35	49.32	325.8	226.55	47.31	286.41	46.66
19	2090.34	1573.00	16.19	63.33	105.80	51.17	70.23	115.08	84.2	229.42	110.41	80.13	70.83
20	2207.29	1598.00	3118.45	61.50	79.90	370.33	71.39	67.01	348.0	233.21	64.28	320.38	53.60
21	2223.13	1882.00	34.78	64.17	95.39	52.00	72.70	110.68	93.4	237.49	106.18	85.95	68.27
22	1498.01	2092.00	1956.12	61.50	44.62	253.33	73.36	32.71	282.6	239.65	31.38	222.78	36.95
23	2477.33	2169.00	697.35	66.83	57.64	39.17	75.54	59.96	32.2	246.74	57.52	44.72	49.30
24	1096.26	2361.00	320.34	69.17	82.15	190.83	74.03	84.74	160.9	241.81	81.29	128.71	59.20
25	2971.35	2735.00	2586.56	69.67	51.42	387.83	79.63	44.22	363.0	260.13	42.42	340.06	41.23
26	1996.49	2798.00	3759.46	73.00	66.34	288.50	78.26	46.00	293.1	255.66	44.13	231.57	42.42
27	1999.92	2992.00	1854.77	73.33	44.31	231.00	79.41	30.24	204.1	259.40	29.01	166.76	34.14
28	3451.11	3706.00	1282.88	74.33	30.81	59.33	84.75	44.61	67.0	276.83	42.80	68.97	40.14
29	3511.12	3739.00	3300.11	78.50	20.09	393.33	85.09	28.26	353.1	277.97	27.12	327.28	31.89
30	3543.47	3909.00	53.29	77.17	107.60	92.00	84.78	119.38	121.6	276.93	114.53	102.01	65.66
31	2040.48	3922.00	247.14	76.67	101.35	190.33	83.32	99.50	148.5	272.17	95.46	119.54	60.46
32	3806.31	4037.00	1768.59	77.67	32.40	53.33	86.65	37.30	45.5	283.04	35.78	54.24	36.30
33	3336.75	4281.00	2187.57	85.17	16.74	197.50	87.11	24.81	125.4	284.54	23.80	104.29	29.53
34	3723.35	4348.00	104.65	79.17	110.79	94.50	86.88	112.21	123.8	283.80	107.65	103.33	62.88
35	2496.79	4348.00	466.46	77.67	78.83	172.50	85.89	84.52	147.0	280.56	81.08	118.42	54.89
36	3595.13	5319.00	1464.41	81.17	50.63	184.17	91.27	51.61	144.0	298.16	49.52	116.38	41.61
37	4016.11	5489.00	172.26	84.17	102.45	105.00	91.50	108.89	132.3	298.90	104.47	108.58	60.36
38	4494.54	5512.00	2632.77	87.17	17.47	101.67	93.12	26.94	96.2	304.17	25.85	87.64	29.76
39	4762.91	5719.00	4159.67	96.50	2.99	N/A	94.19	9.54	N/A	307.67	9.15	N/A	17.61
40	4116.73	5933.00	340.81	83.67	108.50	118.00	93.39	96.16	134.6	305.06	92.25	110.07	56.14

Table A.52: *Physical measurements, perceptual estimates, and our model's predictions (Phase 16).*

Physical measurements				Perceptual estimates			Predicted appearance						
Colour	X	Y[$\mathrm{cd/m^2}$]	Z	J'	M'	H'	J	M	H	Q	C	h	s
1	31.89	36.11	20.98	2.00	4.42	380.00	1.00	12.89	26.1	3.26	12.37	40.20	198.76
2	34.40	40.08	21.13	2.17	5.55	N/A	1.00	13.88	N/A	3.26	13.32	N/A	206.25
3	73.95	54.12	257.68	15.83	94.28	303.33	1.00	58.67	315.2	3.26	56.31	267.81	424.00
4	184.53	98.45	29.46	22.83	102.07	398.83	1.00	71.14	-3.8	3.26	68.28	16.45	466.90
5	543.14	162.50	2238.20	32.00	91.97	299.33	34.47	95.55	316.3	112.51	91.70	269.84	92.15
6	450.86	242.70	27.47	38.83	101.58	398.00	38.69	87.98	10.6	126.25	84.43	28.49	83.48
7	623.63	267.00	2907.38	41.17	86.49	300.00	39.94	98.67	306.6	130.34	94.69	251.20	87.01
8	296.72	292.80	22.27	37.33	60.28	102.50	39.16	61.51	76.9	127.79	59.03	75.48	69.38
9	141.17	356.20	115.61	41.33	79.43	199.17	39.87	58.44	189.6	130.12	56.08	153.67	67.02
10	1006.43	653.20	92.51	55.67	76.72	10.17	52.35	86.52	22.5	170.83	83.03	37.54	71.17
11	241.28	763.10	57.11	55.50	86.23	213.33	50.48	89.85	171.2	164.73	86.23	137.10	73.85
12	695.66	855.60	157.55	46.67	48.92	127.50	54.14	58.66	108.5	176.69	56.29	94.53	57.62
13	1026.10	953.90	955.07	50.33	54.12	356.67	56.74	45.16	358.3	185.19	43.34	334.15	49.38
14	1510.38	993.00	501.16	61.17	78.35	2.83	58.57	81.47	-8.4	191.15	78.19	11.94	65.28
15	472.89	1029.00	1309.59	53.00	74.05	264.33	55.37	67.31	264.9	180.71	64.60	208.70	61.03
16	1185.02	1115.00	3004.45	62.67	63.30	308.00	58.71	65.61	313.5	191.60	62.97	264.62	58.52
17	362.11	1129.00	77.16	58.17	83.18	211.67	56.09	95.82	169.2	183.05	91.96	135.41	72.35
18	1621.87	1596.00	2662.74	61.83	51.85	339.50	64.40	51.03	325.9	210.17	48.97	286.63	49.27
19	2189.50	1655.00	28.66	68.67	109.71	50.00	65.56	103.18	72.2	213.95	99.02	72.38	69.44
20	2296.66	1676.00	3235.94	64.00	74.84	370.83	66.51	68.99	347.2	217.04	66.21	319.20	56.38
21	2328.70	1978.00	44.38	66.00	92.75	50.00	68.14	101.10	84.4	222.38	97.03	80.27	67.43
22	1563.74	2183.00	2029.92	62.50	50.43	265.67	68.54	33.56	282.5	223.70	32.20	222.70	38.73
23	2574.96	2262.00	731.73	68.83	56.87	33.67	70.87	61.37	29.9	231.30	58.89	43.04	51.51
24	1154.15	2475.00	339.74	68.17	81.38	190.00	69.39	83.65	162.6	226.46	80.28	130.02	60.78
25	3091.92	2858.00	2681.91	67.83	59.53	374.17	75.34	46.24	363.2	245.88	44.37	340.20	43.37
26	2094.67	2927.00	3899.40	70.50	54.51	294.17	73.91	48.40	295.1	241.19	46.45	233.23	44.80
27	2083.35	3114.00	1920.36	72.17	40.21	223.50	75.04	32.12	202.4	244.89	30.82	165.72	36.21
28	3600.76	3865.00	1342.36	80.33	27.05	55.00	81.08	47.16	64.6	264.59	45.26	67.36	42.22
29	3635.44	3877.00	3417.92	76.67	26.87	384.50	81.31	30.28	352.9	265.35	29.06	327.04	33.78
30	2109.65	4042.00	272.38	78.33	90.55	175.50	79.32	97.76	150.2	258.85	93.82	120.73	61.46
31	3670.72	4054.00	65.44	75.33	102.33	88.67	81.26	111.77	117.1	265.20	107.27	99.39	64.92
32	3981.29	4230.00	1857.74	74.83	34.38	53.00	83.36	39.97	44.6	272.06	38.35	53.63	38.33
33	3437.79	4418.00	2249.42	80.33	17.46	155.00	83.51	27.11	126.6	272.54	26.02	105.01	31.54
34	3842.10	4495.00	120.09	75.00	96.35	93.00	83.57	107.16	120.5	272.73	102.84	101.34	62.68
35	2596.52	4523.00	485.99	79.17	79.81	175.83	82.39	86.19	148.0	268.88	82.72	119.16	56.62
36	3767.22	5573.00	1544.55	84.50	42.95	176.67	88.91	55.05	144.6	290.16	52.83	116.75	43.56
37	4644.97	5701.00	2723.72	88.00	18.96	92.17	90.76	29.58	96.4	296.20	28.39	87.81	31.60
38	4181.37	5707.00	201.80	86.67	97.32	102.50	89.25	105.89	131.0	291.27	101.62	107.77	60.29
39	4942.49	5924.00	4327.15	96.67	2.35	N/A	92.15	10.74	N/A	300.73	10.31	N/A	18.90
40	4274.83	6157.00	360.46	81.67	93.56	109.17	91.41	97.24	134.1	298.32	93.32	109.75	57.09

Table A.53: *Physical measurements, perceptual estimates, and our model's predictions (Phase 17).*

Physical measurements				Perceptual estimates			Predicted appearance							
Colour	X	Y[cd/m^2]	Z	J'	M'	H'	J	M	H	Q	C	h	s
1	24.34	24.33	13.60	3.00	22.70	0.40	1.00	19.62	7.5	3.57	18.25	26.06	234.35
2	28.45	31.05	13.62	6.50	9.44	93.80	1.00	19.88	46.9	3.57	18.50	55.26	235.95
3	109.33	60.53	504.19	24.17	102.26	302.17	1.00	78.86	310.1	3.57	73.36	258.01	469.89
4	344.91	155.20	30.85	40.83	117.41	394.17	28.46	98.40	-2.4	101.65	91.54	17.84	98.39
5	1088.84	292.20	4631.31	44.50	94.88	329.67	41.29	104.50	313.6	147.47	97.22	264.83	84.18
6	898.29	451.00	25.71	56.17	120.77	N/A	45.36	110.30	N/A	162.02	102.61	N/A	82.51
7	1237.86	503.00	5962.05	52.50	97.53	301.67	46.05	108.88	302.6	164.47	101.29	243.01	81.36
8	535.36	517.60	16.90	44.33	59.71	95.33	44.94	81.89	86.0	160.49	76.18	81.31	71.43
9	243.90	671.70	214.07	49.67	80.84	198.33	46.29	71.02	189.6	165.32	66.07	153.67	65.54
10	2031.34	1278.00	160.66	61.17	93.70	11.33	58.41	99.07	27.8	208.64	92.17	41.50	68.91
11	439.42	1477.00	82.77	66.33	96.45	194.17	56.32	107.77	167.8	201.15	100.26	134.25	73.20
12	1352.83	1664.00	300.56	51.50	59.05	139.17	60.00	67.71	111.3	214.31	62.99	96.08	56.21
13	2017.78	1849.00	1933.10	61.17	57.21	358.33	62.49	49.08	359.1	223.20	45.66	335.09	46.89
14	3005.41	1926.00	992.92	68.17	84.73	399.17	64.29	88.59	-8.2	229.64	82.41	12.10	62.11
15	927.66	2052.00	2704.55	62.67	81.95	293.83	61.43	72.83	262.5	219.39	67.75	206.89	57.62
16	2369.41	2207.00	6178.95	70.00	58.46	310.33	64.55	65.83	312.0	230.54	61.24	261.83	53.44
17	682.56	2210.00	135.66	69.67	99.43	211.33	61.87	109.70	166.4	220.96	102.05	133.08	70.46
18	3249.59	3171.00	5487.03	69.17	58.52	341.00	70.15	50.43	326.0	250.57	46.92	286.68	44.86
19	4318.54	3210.00	27.96	76.33	117.69	55.33	70.78	121.00	84.8	252.79	112.56	80.50	69.18
20	4625.45	3326.00	6649.08	68.33	87.31	370.33	72.18	69.11	348.7	257.80	64.29	321.24	51.78
21	4597.17	3850.00	72.42	66.50	104.67	51.67	73.32	115.15	93.2	261.88	107.12	85.80	66.31
22	3082.79	4321.00	4168.25	73.17	43.88	271.00	74.04	34.08	280.3	264.46	31.71	220.84	35.90
23	5121.67	4448.00	1492.25	72.00	64.54	29.50	76.21	62.17	31.2	272.21	57.84	43.96	47.79
24	2231.99	4864.00	686.41	73.50	90.94	191.67	74.71	87.62	161.2	266.83	81.51	128.97	57.31
25	6157.79	5637.00	5507.23	73.17	58.26	10.83	80.40	45.67	363.5	287.17	42.49	340.65	39.88
26	4145.83	5802.00	8015.02	73.67	56.21	295.83	79.07	47.24	292.1	282.40	43.94	230.66	40.90
27	4098.75	6146.00	3942.69	76.00	33.53	232.00	80.09	31.58	203.9	286.07	29.38	166.67	33.23
28	7106.92	7600.00	2716.28	84.50	27.69	57.83	85.53	46.21	66.7	305.47	42.99	68.77	38.89
29	7254.22	7705.00	7029.93	88.83	24.10	384.50	85.93	28.87	353.4	306.93	26.86	327.73	30.67
30	7217.23	7933.00	111.41	81.83	118.85	90.67	85.34	123.90	121.6	304.82	115.26	102.01	63.75
31	4139.24	8022.00	535.82	84.17	111.77	173.33	84.00	102.37	148.8	300.02	95.23	119.72	58.41
32	7771.79	8212.00	3756.60	84.00	30.52	43.17	87.28	38.37	44.4	311.73	35.69	53.49	35.08
33	7543.19	8791.00	236.97	82.33	125.17	86.67	87.41	114.88	123.6	312.21	106.87	103.17	60.66
34	6845.62	8796.00	4653.72	92.00	9.57	161.67	87.93	25.73	127.3	314.05	23.94	105.44	28.62
35	5157.02	9056.00	1017.39	79.00	84.54	173.17	86.99	86.94	147.3	310.69	80.88	118.68	52.90
36	7377.39	10950.00	3168.49	85.17	40.51	177.50	92.24	52.71	144.7	329.44	49.03	116.86	40.00
37	9256.02	11340.00	5617.57	93.00	12.21	80.00	94.10	27.72	96.6	336.10	25.79	87.89	28.72
38	8294.38	11350.00	366.19	85.17	113.10	101.67	92.58	112.80	132.4	330.67	104.94	108.63	58.41
39	9756.02	11660.00	8853.97	96.83	2.67	N/A	94.96	10.23	N/A	339.15	9.52	N/A	17.37
40	8441.72	12200.00	724.31	88.83	120.79	105.00	94.37	99.37	134.7	337.08	92.44	110.14	54.29

Table A.54: *Physical measurements, perceptual estimates, and our model's predictions (Phase 18).*

Physical measurements				Perceptual estimates			Predicted appearance							
Colour	X	Y[cd/m^2]	Z	J'	M'	H'	J	M	H	Q	C	h	s
1	64.08	73.06	44.65	1.83	4.16	N/A	1.00	12.78	N/A	3.56	11.90	N/A	189.50
2	71.30	83.41	46.37	2.50	4.16	N/A	1.00	14.08	N/A	3.56	13.11	N/A	198.89
3	152.66	111.80	546.27	15.00	81.23	302.50	1.00	60.95	314.7	3.56	56.77	266.86	413.85
4	388.52	205.70	61.51	33.83	98.89	395.83	16.53	75.04	-3.4	58.82	69.90	16.87	112.95
5	1131.57	340.70	4677.55	39.17	94.96	328.83	35.11	98.48	316.7	124.94	91.73	270.58	88.79
6	954.02	510.10	60.85	45.17	110.92	398.33	39.88	92.36	10.4	141.93	86.02	28.30	80.67
7	1302.90	561.80	6104.10	47.33	98.38	303.33	40.56	101.67	306.5	144.35	94.70	251.04	83.92
8	583.15	575.20	45.51	43.67	56.54	105.00	39.25	63.50	76.6	139.67	59.14	75.28	67.42
9	287.49	731.40	249.81	49.67	84.06	215.83	40.60	60.75	190.0	144.48	56.58	154.12	64.84
10	2091.48	1341.00	194.78	59.67	86.80	10.17	53.12	90.74	22.1	189.03	84.52	37.25	69.28
11	481.80	1540.00	113.83	55.50	90.28	198.83	50.92	93.64	170.8	181.22	87.22	136.76	71.88
12	1401.97	1725.00	338.97	53.17	54.50	131.67	54.61	60.12	108.0	194.35	55.99	94.25	55.62
13	2090.73	1930.00	1999.23	60.33	55.91	358.33	57.26	47.13	359.1	203.79	43.90	335.07	48.09
14	3088.20	2005.00	1043.93	65.17	75.58	2.17	59.13	85.43	-8.4	210.45	79.57	11.97	63.71
15	973.04	2114.00	2764.06	55.00	77.41	285.50	56.04	69.70	264.2	199.44	64.92	208.13	59.12
16	2438.32	2284.00	6300.84	70.33	59.85	309.50	59.32	67.34	313.5	211.11	62.72	264.52	56.48
17	732.90	2286.00	167.61	60.67	97.59	192.50	56.63	98.71	169.2	201.54	91.94	135.39	69.98
18	3328.01	3255.00	5585.21	67.50	52.55	336.00	65.08	52.38	326.4	231.61	48.79	287.38	47.56
19	4394.58	3288.00	55.72	70.33	107.84	48.83	65.93	107.42	71.8	234.64	100.05	72.10	67.66
20	4719.83	3412.00	6780.75	64.00	80.81	386.67	67.21	71.58	347.9	239.17	66.67	320.20	54.71
21	4696.31	3954.00	103.29	75.00	105.80	50.00	68.66	103.81	82.8	244.34	96.69	79.27	65.18
22	3164.93	4429.00	4264.17	68.00	49.00	258.33	69.20	34.90	281.0	246.28	32.51	221.46	37.64
23	5199.51	4531.00	1523.84	71.17	68.21	28.00	71.44	63.98	28.9	254.23	59.60	42.33	50.17
24	2308.14	4988.00	732.18	69.50	87.77	223.33	69.99	85.87	163.0	249.09	79.98	130.38	58.71
25	6271.83	5753.00	5622.41	71.33	57.34	369.17	76.03	48.29	363.5	270.58	44.98	340.58	42.25
26	4267.48	5959.00	8199.61	76.83	64.17	295.17	74.71	49.94	294.2	265.88	46.52	232.46	43.34
27	4220.96	6311.00	4063.33	72.17	45.27	254.50	75.83	33.16	203.5	269.88	30.88	166.38	35.05
28	7198.48	7710.00	2791.25	82.67	41.86	59.17	81.70	48.70	63.8	290.74	45.36	66.81	40.93
29	7367.16	7823.00	7154.88	83.83	26.33	378.00	82.17	31.42	353.5	292.43	29.26	327.89	32.78
30	7378.83	8125.00	139.22	79.17	108.95	89.83	82.03	115.54	116.9	291.92	107.62	99.23	62.91
31	4219.20	8156.00	579.06	79.17	91.91	175.00	80.14	100.83	150.4	285.20	93.92	120.86	59.46
32	7984.78	8454.00	3873.57	81.17	43.10	52.50	84.08	41.38	43.4	299.23	38.54	52.74	37.18
33	6935.08	8903.00	4746.89	90.00	15.50	166.00	84.42	27.53	126.3	300.43	25.65	104.82	30.27
34	7696.87	8989.00	248.94	79.33	109.86	91.67	84.33	110.91	120.3	300.10	103.31	101.22	60.79
35	5183.23	9081.00	1057.18	80.33	79.04	181.33	83.19	88.00	148.4	296.06	81.97	119.42	54.52
36	7504.09	11150.00	3230.11	83.83	56.69	184.00	89.77	56.65	145.0	319.47	52.76	117.06	42.11
37	9299.93	11400.00	5682.85	93.33	18.16	89.17	91.67	30.34	95.5	326.24	28.26	87.23	30.50
38	8399.19	11490.00	418.34	85.00	99.65	101.67	90.34	109.69	131.0	321.49	102.17	107.76	58.41
39	9947.84	11880.00	9037.32	96.33	2.76	N/A	93.18	11.54	N/A	331.61	10.75	N/A	18.65
40	8604.66	12420.00	764.81	86.67	103.85	117.50	92.65	100.21	134.0	329.72	93.34	109.70	55.13

Table A.55: *Physical measurements, perceptual estimates, and our model's predictions (Phase 19).*

A.7 Similarity Experimental Data

This appendix provides the psychophysical experimental data which was used to evaluate our reproduction model. Two real scenes were compared with six different reproduction methods: HDR tone-mapping algorithms ([Reinhard et al., 2002], [Durand and Dorsey, 2002], and [Reinhard and Devlin, 2005]), an image appearance model (iCAM06), and our methods (JMh and JCh colour connection spaces). Ten participants for each scene judged *similarity* of the reproductions to their reference real-world scene, using a five-point scoring scale, in terms of *realism*, *lightness*, and *colour* reproductions. These scale categories were labelled with the following descriptions: *1. (not similar), 2. (slightly similar), 3. (moderately similar), 4. (very much similar), and 5. (extremely similar)*.

Participant	Criteria	Durand&Dorsey	Reinhard et al.	Reinhard&Devlin	iCAM06	Our model (JMh)	Our model (JCh)
1	Realism	3.5	2.0	2.5	1.5	3.5	3.5
	Lightness	2.5	1.0	2.0	1.5	4.0	3.0
	Colour	2.0	2.0	2.0	2.5	3.5	3.0
2	Realism	2.0	3.5	2.5	1.0	5.0	3.0
	Lightness	1.5	2.5	2.0	2.5	5.0	4.0
	Colour	2.5	3.0	3.5	4.0	5.0	3.0
3	Realism	2.5	2.5	3.5	2.0	4.0	3.5
	Lightness	3.0	2.5	2.5	2.0	4.5	5.0
	Colour	4.0	2.0	3.5	3.0	3.5	4.0
4	Realism	2.0	1.0	2.5	2.0	4.0	4.5
	Lightness	2.0	1.0	1.5	2.0	4.0	2.5
	Colour	2.0	2.5	2.0	3.5	5.0	3.5
5	Realism	1.5	2.0	2.0	2.5	4.0	3.5
	Lightness	1.0	4.0	1.0	3.5	4.0	2.0
	Colour	3.0	3.5	2.5	2.5	4.5	3.0
6	Realism	2.0	2.0	2.0	3.5	3.5	3.0
	Lightness	2.0	3.5	2.0	4.0	3.0	3.0
	Colour	2.0	3.0	2.0	4.0	3.0	3.5
7	Realism	2.0	2.0	3.5	3.0	4.0	3.0
	Lightness	2.5	2.0	3.5	3.0	4.5	4.5
	Colour	2.0	2.5	2.0	4.0	3.5	3.5
8	Realism	2.0	3.0	3.0	4.5	4.0	3.5
	Lightness	2.0	3.5	3.0	4.0	4.0	3.5
	Colour	1.0	2.5	1.5	4.5	3.5	2.5
9	Realism	3.0	3.5	4.0	3.0	4.5	4.0
	Lightness	2.0	4.0	2.5	2.5	4.5	4.0
	Colour	4.5	4.5	5.0	3.0	4.0	5.0
10	Realism	1.5	2.0	1.0	3.0	5.0	4.0
	Lightness	2.5	1.5	3.5	3.5	4.5	4.0
	Colour	2.5	1.5	3.5	2.5	5.0	4.0

Table A.56: *Physical measurements of perceived similarity of a real scene (scene one).*

Participant	Criteria	Durand&Dorsey	Reinhard et al.	Reinhard&Devlin	iCAM06	Our model (JMh)	Our model (JCh)
1	Realism	3.0	2.5	3.0	3.5	4.5	4.0
	Lightness	2.5	1.5	4.0	2.5	3.0	3.5
	Colour	3.5	2.0	4.0	3.5	3.0	3.0
2	Realism	2.0	4.0	1.5	3.0	4.5	3.0
	Lightness	2.0	3.5	1.0	2.0	5.0	4.0
	Colour	2.0	4.5	3.5	2.5	5.0	3.5
3	Realism	1.0	2.5	1.0	3.5	3.5	3.5
	Lightness	1.0	3.5	1.0	4.0	3.5	3.5
	Colour	2.5	3.5	1.5	4.0	5.0	3.5
4	Realism	2.0	4.0	2.0	3.0	4.0	3.0
	Lightness	1.5	3.0	1.0	3.0	4.0	2.5
	Colour	3.0	3.5	3.0	2.0	4.0	4.0
5	Realism	1.5	4.0	1.0	3.0	3.5	3.5
	Lightness	1.0	3.0	1.0	2.5	4.5	3.0
	Colour	3.0	3.5	2.5	4.0	3.5	4.5
6	Realism	1.5	3.0	1.5	3.5	4.0	3.5
	Lightness	2.5	3.5	1.5	3.0	3.5	3.0
	Colour	2.0	4.0	1.0	3.0	4.0	3.0
7	Realism	1.5	3.5	1.5	4.0	5.0	3.5
	Lightness	1.5	4.0	1.5	3.0	5.0	3.5
	Colour	3.0	5.0	2.5	4.0	5.0	5.0
8	Realism	2.5	4.5	2.0	4.5	5.0	5.0
	Lightness	1.5	3.5	1.0	2.5	4.5	3.5
	Colour	3.0	4.5	4.0	3.5	5.0	4.5
9	Realism	2.0	2.5	1.0	4.0	4.0	4.5
	Lightness	1.0	3.5	1.0	4.5	3.5	4.0
	Colour	2.0	4.0	1.0	3.0	4.5	4.0
10	Realism	2.0	3.0	1.5	3.0	3.5	3.0
	Lightness	2.0	2.0	2.0	2.5	3.5	4.0
	Colour	3.5	4.0	3.0	3.0	4.0	2.0

Table A.57: *Physical measurements of perceived similarity of a real scene (scene two).*

Bibliography

Akyüz, A. O. and Reinhard, E. 2006. Color appearance in high-dynamic-range imaging. *J. Electron. Imaging*, 15(3):1–12.

Albers, J. 1963. *Interaction of Color*. Yale University Press, New Haven.

ANSI 1999. Graphic technology - color transmission target for input scanner calibration. Technical Report ANSI IT8.7/1-1993 (R1999), American National Standards Institute.

Attridge, G. G. 2000. Sensitometry. In Jacobson, R., Ray, S., Attridge, G. G., and Axford, N., editors, *The Manual of Photography*, pages 218–246. Focal Press, Oxford, 9th edition.

Barnard, K., Cardei, V., and Funt, B. V. 2002. A comparison of computational color constancy algorithms – part I: Methodology and experiments with synthesized data. *IEEE Trans. Image Processing*, 11(9):972–984.

Barnard, K. and Funt, B. V. 2002. Camera characterization for color research. *Color Res. Appl.*, 27(3):153–164.

Bartleson, C. and Breneman, E. 1967. Brightness perception in complex fields. *J. Opt. Soc. Am.*, 57(7):953–957.

Bartleson, C. J. 1979. Changes in color appearance with variations in chromatic adaptation. *Color Res. Appl.*, 4(3):119–138.

Bartleson, C. J. 1984. Chapter 8. In Bartleson, C. J. and Grum, F., editors, *Optical Radiation Measurements, Vol. 5 Visual Measurements*. Academic Press, Orlando.

Battle, D. R. 1997. The measurement of colour. In McDonald, R., editor, *Colour Physics for Industry*, pages 57–80. Soc. Dyers Col., Bradford, 2nd edition.

Berns, R. and Katoh, N. 2002. Methods for characterizing displays. In Green, P. and MacDonald, L. W., editors, *Colour Engineering*, pages 143–164. John Wiley, Chichester.

Berns, R. S., Motta, R. J., and Gorzynski, M. E. 1993. CRT colorimetry. Part I: Theory and practice. *Color Res. Appl.*, 18(5):299–314.

Bishop, C. M. 2006. *Pattern Recognition and Machine Learning.* Springer, New York.

Boynton, R. M. and Whitten, D. N. 1970. Visual adaptation in monkey cones: recordings of late receptor potentials. *Science*, 170(3965):1423–1426.

Braun, G. J. and Fairchild, M. D. 1999. Image lightness rescaling using sigmoidal contrast enhancement functions. In *Proc. Color Imaging Conf.*, pages 380–393. IS&T.

Braun, K. M. and Fairchild, M. D. 1996. Psychophysical generation of matching images for cross-media colour reproduction. In *Proc. Color Imaging Conf.*, pages 214–220, Springfield, Virginia. IS&T.

Breneman, E. J. 1977. Perceived saturation in complex stimuli viewed in light and dark surrounds. *J. Opt. Soc. Am.*, 67(5):657–662.

Breneman, E. J. 1987. Corresponding chromaticities for different states of adaptation to complex visual fields. *J. Opt. Soc. Am.*, 4A:1115–1129.

Buchsbaum, G. 1980. A spatial processor model for object colour perception. *J. the Franklin Institute*, 310(1):1–26.

Carroll, J., Neitz, J., and Neitz, M. 2002. Estimates of L:M cone ratio from ERG flicker photometry and genetics. *J. Vision*, 2(8):531–542.

Chiu, K., Herf, M., Shirley, P., Swamy, S., Wang, C., and Zimmerman, K. 1993. Spatially non-uniform scaling functions for high contrast images. In *Proc. Graphics Interface '93*, pages 245–253, San Francisco. Morgan Kaufmann.

CIE 1981. An analytic model for describing the influence of lighting parameters upon visual performance. CIE Pub. 19/2.1, Commission Internationale de l'Eclairage (CIE), Vienna.

CIE 1983. The basis of physical photometry. Publication CIE 18.2-1983, Commission Internationale de l'Eclairage (CIE), Vienna.

CIE 1986. Colorimetry. CIE Pub. 15.2, Commission Internationale de l'Eclairage (CIE), Vienna.

CIE 1995. Industrial colour difference evaluation. CIE Pub. 116, Commission Internationale de l'Eclairage (CIE), Vienna.

CIE 1998. The CIE 1997 interim colour appearance model (simple version), CIECAM97s. CIE Pub. 131, Commission Internationale de l'Eclairage (CIE), Vienna.

CIE 2001. Improvement to industrial colour difference equation. CIE Pub. 142, Commission Internationale de l'Eclairage (CIE), Vienna.

CIE 2004. CIE TC8-01 Technical Report, A Colour Apperance Model for Color Management System: CIECAM02. Publication CIE 159-2004, Commission Internationale de l'Eclairage (CIE), Vienna.

Clarke, F. J., McDonald, R., and Rigg, R. 1984. Modification to the JPC79 colour-difference formula. *J. Soc. Dyers Col.*, 100:117–148.

Coffin, D. 2009. Decoding raw digital photos in linux. http://www.cybercom.net/∼dcoffin/dcraw/.

De Valois, R. L., De Valois, K. K., Switkes, E., and Mahon, L. 1997. Hue scaling of isoluminant and cone-specific lights. *Vision Res.*, 37(7):885–897.

de Vries, H. 1943. The quantum character of light, its bearing upon threshold of vision, the differential sensitivity and visual acuity of the eye. *Physica*, 10:553–564.

Debevec, P. E. and Malik, J. 1997. Recovering high dynamic range radiance maps from photographs. In *Proc. ACM SIGGRAPH '97*, pages 369–378.

Dolby 2008. Dolby's High-Dynamic-Range Technologies: Breakthrough TV Viewing. Technical report, Dolby Laboratories, Inc.

Drago, F., Myszkowski, K., Annen, T., and Chiba, N. 2003. Adaptive logarithmic mapping for displaying high contrast scenes. *Computer Graphics Forum*, 22(3):419–426.

Durand, F. and Dorsey, J. 2002. Fast bilateral filtering for the display of high-dynamic-range images. *ACM Trans. Graph. (Proc. SIGGRAPH 2002)*, 21(3):257–266.

d'Zmura, M. and Lennie, P. 1986. Mechanisms of color constancy. *J. Opt. Soc. Am.*, 3:1662–1672.

Ebner, F. and Fairchild, M. 1998. Development and testing of a color space (IPT) with improved hue uniformity. In *Proc. Color Imaging Conf.*, pages 8–13. IS&T.

Engeldrum, P. G. 2000. *Psychometric Scaling: A Toolkit for Imaging Systems Development*. Imcotek Press, Winchester, MA.

Estévez, O. 1979. *On the Fundermental Data-Base of Normal and Dichromatic Colour Vision*. Ph.D. thesis, University of Amsterdam.

Fairchild, M. D. 1991. Formulation and testing of an incomplete-chromaticadaptation model. *Color Res. Appl.*, 16(4):243–250.

Fairchild, M. D. 2001. A revision of CIECAM97s for practical applications. *Color Res. Appl.*, 26(6):418–427.

Fairchild, M. D. 2005. *Color Appearance Models*. John Wiley, Chichester, 2nd edition.

Fattal, R., Lischinski, D., and Werman, M. 2002. Gradient domain high dynamic range compression. *ACM Trans. Graph. (Proc. SIGGRAPH 2002)*, 21(3):249–256.

Fechner, G. 1963. *Elements of Psychophysics*, volume 1. New York.

Ferwerda, J. A., Pattanaik, S. N., Shirley, P., and Greenberg, D. P. 1996. A model of visual adaptation for realistic image synthesis. In *Proc. ACM SIGGRAPH '96*, pages 249–258.

Finlayson, G. D., Hordley, S. D., and Hubel, P. M. 2001. Color by correlation: A simple, unifying framework for color constancy. *IEEE Trans. Pattern Anal. Mach. Intell*, 23(11):1209–1221.

Finlayson, G. D., Hubel, P. M., and Hordley, S. 1997. Color by correlation. In *Proc. Color Imaging Conf.*, pages 6–11. IS&T.

Funt, B., Ciurea, F., and McCann, J. 2000. Retinex in MATLAB. In *Proc. Color Imaging Conf.*, pages 112–121, Springfield, Virginia. IS&T.

Gehler, P. V., Rother, C., Blake, A., Minka, T., and Sharp, T. 2008. Bayesian color constancy revisited. In *Proc. IEEE Conf. Comput. Vision and Pattern Recognition (CVPR)*, pages 1–8.

Gijsenij, A. and Gevers, T. 2007. Color constancy using natural image statistics. In *Proc. IEEE Conf. Comput. Vision and Pattern Recognition (CVPR)*, pages 1–8.

Gilblom, D. L. and Yoo, S. K. 2004. Infrared and ultraviolet imaging with a CMOS sensor having layered photodiodes. In *Proc. Electron. Imaging*, volume 5301, pages 186–192, San Jose. SPIE/IS&T.

Göesele, M., Heidrich, W., and Seidel, H.-P. 2001. Color calibrated high dynamic range imaging with ICC profiles. In *Proc. Color Imaging Conf.*, pages 286–290. IS&T.

Helson, H. 1938. Fundamental problem in color vision. I. The pinciple governing changes in hue, saturation, and lightness of non-selective samples in chromatic illumination. *J. Exp. Psych.*, 23:439–476.

Helson, H., Judd, D. B., and Warren, M. H. 1952. Object-color changes from daylight to incandescent filament illumination. *Illum. Eng.*, 47:221–233.

Hirakawa, K. and Parks, T. W. 2003. Adaptive homogeneity-directed demosaicing algorithm. In *Proc. IEEE Int. Conf. Image Processing (ICIP)*, pages 669–672.

Holm, W. and Krochmann, J. 1975. Ermittlung der ähnlichsten Farbtemperatur. *Die Farbe*, 24(1/6):91–96.

Holst, G. C. 1998. *CCD Arrays Cameras and Displays*. SPIE - Int. Soc. Opt. Eng., Bellingham, 2nd edition.

Hood, D. C., Finkelstein, M. A., and Buckingham, E. 1979. Psychophysical tests of models of the response function. *Vision Res.*, 19:401–406.

Hordley, S. D. 2006. Scene illuminant estimation: Past, present, and future. *Color Res. Appl.*, 31(4):303–314.

Hubel, P., Holm, J., and Finlayson, G. 1999. Illuminant estimation and colour correction. In McDonald, L. W. and Luo, M. R., editors, *Colour Imaging, Vision and Technology*, pages 73–95. John Wiley & Sons Ltd, Chichester, West Sussex.

Hunt, R. W. G. 1952. Light and dark adaptation and the perception of color. *J. Opt. Soc. Am.*, 42(3):190–199.

Hunt, R. W. G. 1982. A model of colour vision for predicting colour appearance. *Color Res. Appl.*, 7(2):95–112.

Hunt, R. W. G. 1987. A model of colour vision for predicting colour appearance in various viewing conditions. *Color Res. Appl.*, 12(6):297–314.

Hunt, R. W. G. 1991. Revised colour-appearance model for related and unrelated colours. *Color Res. Appl.*, 16(3):146–165.

Hunt, R. W. G. 1994. An improved predictor of colourfulness in a model of colour vision. *Color Res. Appl.*, 19(1):23–26.

Hunt, R. W. G. 1995. *The Reproduction of Colour*. Fountain Press, Kingston Upon Thames, 5th edition.

Hunt, R. W. G. 1998. *Measuring Colour*. Fountain Press, Kingston Upon Thames, 3rd edition.

Hunt, R. W. G. 2004. *The Reproduction of Colour*. John Wiley, Chichester, 6th edition.

Hunt, R. W. G., Li, C. J., Juan, L. Y., and Luo, M. R. 2002. Further improvements to CIECAM97s. *Color Res. Appl.*, 27(3):164–170.

Hunt, R. W. G., Li, C. J., and Luo, M. R. 2003. Dynamic cone response functions for models of colour appearance. *Color Res. Appl.*, 28(2):82–88.

Hunt, R. W. G. and Pointer, M. R. 1985. A colour-appearance transform for the CIE 1931 standard colorimetric observer. *Color Res. Appl.*, 10(3):165–179.

ICC 2004. International color consortium specification. Technical Report ICC.1:2004-10, International Color Consortium (ICC).

IEC 2003. Multimedia systems and equipment - color measurement and management. Technical Report IEC61966-2-1:2003, International Electrotechnical Commission (IEC), Geneva.

IEEE 1985. *IEEE Standard for Binary Floating-Point Arithmetic*. IEEE Std 754-1985.

Inanici, M. and Galvin, J. 2004. Evaluation of high dynamic range photography as a luminance mapping technique. Paper LBNL-57545, LBNL.

Inglis, A. F. and Luther, A. C. 1996. *Video Engineering*. McGraw-Hill, Inc, New York, 2nd edition.

ISO 2006. Graphic technology and photography — colour characterisation of digital still cameras (dscs) — part 1: Stimuli, metrology and test procedures. Technical Report ISO:17321-1:2006, International Organization for Standardization (ISO).

Janesick, J. R. 2001. *Scientific Charge-Coupled Devices*. SPIE - Int. Soc. Opt. Eng., Bellingham, WA.

Johnson, G. M. and Fairchild, M. D. 2003. Rendering HDR images. In *Proc. Color Imaging Conf.*, pages 36–41. IS&T.

Johnson, T. 2002. Methods for characterizing colour scanners and digital cameras. In Green, P. and MacDonald, L. W., editors, *Colour Engineering, achieving device, independent colour*, pages 165–178. John Wiley & Sons Inc., Chichester, West Sussex.

Kajiya, J. T. 1986. The rendering equation. In *Proc. ACM SIGGRAPH '86*, pages 143–150.

Kim, E.-S., Lee, S.-H., Jang, S.-W., and Sohng, K.-I. 2005. Adaptive colorimetric characterization of camera for the variation of white balance. *IEICE Trans. Electron.*, E88C(11):2086–2089.

Kim, M. H. and Kautz, J. 2008a. Characterization for high dynamic range imaging. *Computer Graphics Forum (Proc. EUROGRAPHICS '08)*, 27(2):691–697.

Kim, M. H. and Kautz, J. 2008b. Consistent tone reproduction. In *Proc. the 10th IASTED Int. Conf. Comput. Graphics and Imaging (CGIM 2008)*, pages 152–159, Innsbruck. IASTED/ACTA Press.

Kim, M. H. and Kautz, J. 2009. Consistent scene illumination using a chromatic flash. In *Proc. Eurographics Workshop on Computational Aesthetics (CAe2009)*, pages 83–89, British Columbia. Eurographics Association.

Kim, M. H. and MacDonald, L. W. 2006. Rendering high dynamic range images. In *Proc. the 17th Anuual EVA Conference 2006*, pages 22.1–11, Middlesex. EVA Conferences International (ECI).

Kim, M. H., Weyrich, T., and Kautz, J. 2009. Modeling human color perception under extended luminance levels. *ACM Trans. Graph. (Proc. SIGGRAPH 2009)*, 28(3):27:1–9.

Kleinschmidt, J. and Dowling, J. E. 1975. Intracellar recordings from gecko photoreceptors during light and dark adaptation. *J. Gen. Physiol.*, 66:617–648.

Krawczyk, G., Goesele, M., and Seidel, H.-P. 2005. Photometric calibration of high dynamic range cameras. Research Rep. MPI-I-2005-4-005, MPI Informatik, Saarbrücken.

Kuang, J., Yamaguchi, H., Johnson, G. M., and Fairchild, M. D. 2004. Testing HDR image rendering algorithms. In *Proc. Color Imaging Conf.*, pages 315–320. IS&T.

Kuang, J. T., Johnson, G. M., and Fairchild, M. D. 2007. iCAM06: A refined image appearance model for HDR image rendering. *J. Visual Communication and Image Representation*, 18(5):406–414.

Kunkel, T. and Reinhard, E. 2009. A neurophysiology-inspired steady-state color appearance model. *J. Opt. Soc. Am. A*, 26(4):776–782.

Kuo, W. G., Luo, M. R., and Bez, H. E. 1995. Various chromatic adaptation transforms tested using new colour appearance data in textiles. *Color Res. Appl.*, 20:313–327.

Kwak, Y. 2003. *Quantifying the colour appearance of displays*. Ph.D. thesis, University of Derby.

Kwak, Y. and MacDonald, L. W. 2001. Accurate prediction of colours on liquid crystal displays. In *Proc. Color Imaging Conf.*, pages 355–360. IS&T.

Lam, K. M. 1985. *Metamerism and colour constancy*. Ph.D. thesis, University of Bradford.

Laming, D. 1997. *The Measurement of Sensation*. Oxford University Press, New York.

Land, E. H. 1977. The retinex theory of color vision. *Scientific American*, 237(6):108–128.

Land, E. H. and McCann, J. J. 1971. Lightness and retinex theory. *J. Opt. Soc. Am.*, 61(1):1–11.

Li, C., Luo, M. R., Rigg, B., and Hunt, R. W. G. 2002. CMC 2000 chromatic adaptation transform: CMCCAT2000. *Color Res. Appl.*, 27(1):49–58.

Li, Y., Sharan, L., and Adelson, E. H. 2005. Compressing and companding high dynamic range images with subband architectures. *ACM Trans. Graph (Proc. SIGGRAPH 2005)*, 24(3):836–844.

Lucas Digital Ltd. 2006. Reading and writing OpenEXR image files with the IlmImf library. http://www.openexr.com/ReadingAndWritingImageFiles.pdf.

Luo, M. R., Clarke, A. A., Rhodes, P. A., Schappo, A., Scrivener, S. A. R., and Tait, C. J. 1991a. Quantifying colour appearance. Part I. LUTCHI colour appearance data. *Color Res. Appl.*, 16(3):166–180.

Luo, M. R., Clarke, A. A., Rhodes, P. A., Schappo, A., Scrivener, S. A. R., and Tait, C. J. 1991b. Quantifying colour appearance. Part II. Testing colour models performance using LUTCHI colour appearance data. *Color Res. Appl.*, 16(3):181–197.

Luo, M. R., Cui, G., and Rigg, B. 2001. The development of the CIE 2000 colour difference formula. CIEDE2000. *Color Res. Appl.*, 26(5):340–350.

Luo, M. R., Gao, X. W., Rhodes, P. A., Xin, H. J., Clarke, A. A., and Scrivener, S. A. R. 1993a. Quantifying colour appearance. Part III. Supplementary LUTCHI colour appearance data. *Color Res. Appl.*, 18(2):98–113.

Luo, M. R., Gao, X. W., Rhodes, P. A., Xin, H. J., Clarke, A. A., and Scrivener, S. A. R. 1993b. Quantifying colour appearance. Part IV. Transmissive media. *Color Res. Appl.*, 18(3):191–209.

Luo, M. R., Gao, X. W., and Scrivener, S. A. R. 1995. Quantifying colour appearance. Part V. Simultaneous contrast. *Color Res. Appl.*, 20(1):18–28.

Luo, M. R. and Hunt, R. W. G. 1998. Testing colour appearance models using corresponding – colour and magnitude – estimation data sets. *Color Res. Appl.*, 23(3):147–153.

Luo, M. R., Lo, M.-C., and Kuo, W.-G. 1996. The LLAB (l:c) colour model. *Color Res. Appl.*, 21(6):412–429.

Luo, M. R. and Morovic, J. 1996. Two unsolved issues in colour management — colour appearance and gamut mapping. In *5th International Conference on High Technology*, pages 136–147, Chiba.

Luo, M. R. and Rigg, B. 1987. Colour difference formular BFD Part 1 – Development of the formula. *J. Soc. Dyers Col.*, 103:86–94.

Luo, M. R., Xu, H., Tang, X., and Zhou, F. 1997. Testing colour models performance using unrelated colour appearance data. In *Proc. International Colour Association (AIC '97)*, pages 175–178.

MacDonald, L. W. 1993. Gamut mapping in perceptual colour space. In *Proc. Color Imaging Conf.*, pages 193–196. IS&T.

MacDonald, L. W. and Ji, W. 2002. Colour characterisation of a high-resolution digital camera. In *Proc. European Conf. Color in Graphics, Image, and Vision (CGIV)*, volume 1, pages 433–437. IS&T.

Mann, S. 1993. Compositing multiple pictures of the same scene. In *Proc. the 46th Annual IS&T Conference*, pages 50–52, Cambridge. IS&T.

Mann, S. and Picard, R. W. 1995. On being undigital with digital cameras. In *Proc. the 48th Annual IS&T Conference*, pages 422–428, Cambridge. IS&T.

Mantiuk, R., Mantiuk, R., Tomaszewska, A., and Heidrich, W. 2009. Color correction for tone mapping. *Computer Graphics Forum (Proc. EUROGRAPHICS 2009)*, 28(2):193–202.

Martínez-Verdú, F., Pujol, J., and Capilla, P. 2000. Calculation of the color-matching functions of digital cameras from their complete spectral responsitivities. In *Proc. Color Imaging Conf.*, pages 211–216. IS&T.

Martínez-Verdú, F., Pujol, J., and Capilla, P. 2003. Characterization of a digital camera as an absolute tristimulus colorimeter. *Journal of Imaging Science and Technology*, 47(4):279–374.

McCann, J. J., McKee, S. P., and Taylor, T. H. 1976. Quantitative studies in retinex theory: a comparison between theoretical predictions and observer responses to the "color mandarin" experiments. *Vision Res.*, 16:445–458.

Meilgaard, M., Gail, C., and Carr, B. 1991. *Sensory Evaluation Techniques*. CRC Press, Boca Raton, 2nd edition.

Meylan, L. and Süsstrunk, S. 2004. Color image enhancement using a Retinex-based adaptive filter. In *IS&T Second European Conference on Color in Graphics, Image, and Vision (CGIV)*, volume 2, pages 359–363.

Michaelis, L. and Menten, M. L. 1913. The kinetics of the inversion effect. *Biochemische Zeitschrift*, 49:333–369.

Miller, G. S. and Hoffman, C. R. 1984. Illumination and reflection maps: Simulated objects in simulated and real environments. In *SIGGRAPH '84 Advanced Computer Graphics Animation course notes*.

Mitsunaga, T. and Nayar, S. K. 1999. Radiometric self calibration. In *Proc. IEEE Conf. Comput. Vision and Pattern Recognition (CVPR)*, pages 374–380.

Morgenstern, T., Bornhoeft, G., and Goerlich, S. 2004. Miniaturized spectroradiometer. Light 2004, JETI Technische Instrumente GmbH, Brno.

Mori, L., Sobagaki, H., Komatsubara, H., and Ikeda, K. 1991. Field trials on CIE chromatic adaptation formula. In *Proc. the CIE 22nd session*, pages 55–58. MIT Press.

Moroney, N., Fairchild, M. D., Hunt, R. W. G., Li, C., Luo, M. R., and Newman, T. 2002. The CIECAM02 color appearance model. In *Proc. Color Imaging Conf.*, pages 23–27. IS&T.

Morovic, J. 1985. *To Develop a Universal Gamut Mapping Algorithm*. Ph.D. thesis, University of Derby.

Morovic, J. 2008. *Color Gamut Mapping*. John Wiley & Sons Ltd, Chichester, 1nd edition.

Müller, G. E. 1930. Über die Farbenempfindungen. *Z. Psychol.*, page Erganzungsbände 17 and 18.

Naka, K. I. and Rushton, W. A. 1966. S-potentials from luminosity units in the retina of fish (cyprinidae). *Journal of Physiology*, 185(587–599).

Nayar, S. and Mitsunaga, T. 2000. High dynamic range imaging: Spatially varying pixel exposures. In *Proc. IEEE Conf. Comput. Vision and Pattern Recognition (CVPR)*, pages 472–479.

Nielsen, M. and Stokes, M. 1998. The creation of the sRGB ICC Profile. In *Proc. Color Imaging Conf.*, pages 253–257. IS&T.

Normand, C., Fornaro, P., and Gschwind, R. 2007. Automated digital camera sensor characterization. In *Proc. Electron. Imaging*, volume 6502, pages 311–318. SPIE/IS&T.

Ohta, N. and Robertson, A. R. 2005. *Colorimetry*. John Wiley, Chichester, 1st edition.

Pattanaik, S. N., Ferwerda, J. A., Fairchild, M. D., and Greenberg, D. P. 1998. A multiscale model of adaptation and spatial vision for realistic image display. In *Proc. ACM SIGGRAPH '98*, pages 287–298.

Pattanaik, S. N., Tumblin, J. E., Yee, H., and Greenberg, D. P. 2000. Time-dependent visual adaptation for realistic real-time image display. In *Proc. ACM SIGGRAPH 2000*, pages 47–54.

Perlin, K. and Hoffert, E. M. 1989. Hypertexture. *Computer Graphics*, 23(3):253–262.

Perona, P. and Malik, J. 1990. Scale-space and edge detection using anisotropic diffusion. *IEEE Trans. Pattern Analysis and Machine Intelligence*, PAMI-12(7):629–639.

Pointer, M. R. 1980. The concept of colourfulness and its use for deriving grids for assessing colour appearance. *Color Res. Appl.*, 5(2):99–107.

Pointer, M. R. 1982. The gamut of real surface colours. *Color Res. Appl.*, 5(3):145–155.

Pointer, M. R., Attridge, G. G., and Jacobson, R. E. 2001. Practical camera characterization for color measurement. In *Proc. Image Processing, Image Quality, Image Capture Systems Conference (PICS)*, pages 246–251.

Purkinje, J. E. 1825. Neue beiträge zur kenntniss des sehens in subjectiver hinsicht. pages 109–110. Reimer, Berlin.

Rahman, Z. U., Jobson, D. J., and Woodell, G. A. 1996. Multi-scale retinex for color image enhancement. In *Proc. IEEE Int. Conf. Image Processing (ICIP)*, pages III: 1003–1006.

Ray, S. F. 2000a. Camera features. In Jacobson, R., Ray, S., Attridge, G. G., and Axford, N., editors, *The Manual of Photography*, pages 131–175. Focal Press, Oxford, 9th edition.

Ray, S. F. 2000b. The geometry of image formation. In Jacobson, R., Ray, S., Attridge, G. G., and Axford, N., editors, *The Manual of Photography*, pages 39–71. Focal Press, Oxford, 9th edition.

Reinhard, E. and Devlin, K. 2005. Dynamic range reduction inspired by photoreceptor physiology. *IEEE Transactions on Visualization and Computer Graphics*, 11(1):13–24.

Reinhard, E., Stark, M., Shirley, P., and Ferwerda, J. 2002. Photographic tone reproduction for digital images. *ACM Trans. Graph. (Proc. SIGGRAPH 2002)*, 21(3):267–276.

Reinhard, E., Ward, G., Pattanaik, S., and Debevec, P. 2005. *High Dynamic Range Imaging: Acquisition, Display and Image-Based Lighting*. Morgan Kaufmann.

Ritschel, T., Grosch, T., Kim, M. H., Seidel, H.-P., Dachsbacher, C., and Kautz, J. 2008. Imperfect shadow maps for efficient computation of indirect illumination. *ACM Trans. Graph. (Proc. SIGGRAPH Asia 2008)*, 27(5):129:1–8.

Robertson, M. A., Borman, S., and Stevenson, R. L. 1999. Dynamic range improvement through multiple exposures. In *Proc. IEEE Int. Conf. Image Processing (ICIP)*, volume 3, pages 159–163.

Robertson, M. A., Borman, S., and Stevenson, R. L. 2003. Estimation-theoretic approach to dynamic range enhancement using multiple exposures. *J. Electron. Imaging*, 12(2):219–228.

Rose, A. 1948. The sensitivity performance of the human eye on an absolute scale. *J. Opt. Soc. Am.*, 38:196–208.

Rosenberg, C. R., Minka, T. P., and Ladsariya, A. 2003. Bayesian color constancy with non-gaussian models. In *Neural Information Processing Systems (NIPS)*. MIT Press.

Saito, K. 1995. Electronic image pickup device. Japanese Patent 07-254965.

Scheffé, H. 1952. An analysis of variance for paired comparisons. *Jour. Amer. Stat. Assoc.*, 47(259):381–400.

Schlick, C. 1994. Quantization techniques for the visualization of high dynamic range pictures. In *Photorealistic Rendering Techniques*, Eurographics, pages 7–20. Springer.

Seetzen, H., Heidrich, W., Stuerzlinger, W., Ward, G., Whitehead, L., Trentacoste, M., Ghosh, A., and Vorozcovs, A. 2004. High dynamic range display systems. *ACM Trans. Graph. (Proc. SIGGRAPH 2004)*, 23(3):760–768.

Seetzen, H., Li, H., Ye, L., Heidrich, W., Whitehead, L., and Ward, G. 2006. Observations of luminance, contrast and amplitude resolution of displays. *SID Symposium*, 37(1):1229–1233.

Shortis, M. R., Bellman, C. J., Robson, S., Johnston, G. J., and Johnson, G. W. 2006. Stability of zoom and fixed lenses used with digital SLR cameras. 36(5):285–290.

Shortis, M. R., Seager, J. W., Harvey, E. S., and Robson, S. 2005. The influence of Bayer filters on the quality of photogrammetric measurement. In *Proc. SPIE Vol. 5665 Videometrics VIII*, pages 164–171.

Stevens, S. and Stevens, J. 1963. Brightness function: Effects of adaptation. *J. Opt. Soc. Am.*, 53(3):375–385.

Stevens, S. S. 1957. On the psychophysical law. *Psychological Review*, 64:153–181.

Stevens, S. S. 1961. To honour Fechner and repeal his law: A power function, not a log function describes the operating characteristic of a sensory system. *Science*, 133:80–86.

Stevens, S. S. 1971. Issues in psychophysical measurement. *Psychological Review*, 78:426–450.

Stiles, W. S. and Burch, J. M. 1959. NPL colour-matching investigation: Final report. *Optica Acta*, 6:1–26.

Stone, M. C., Cowan, W. B., and Beatty, J. C. 1988. Color gamut mapping and the printing of digital color images. *ACM Trans. Graph.*, 7(4):249–292.

Talvala, E.-V., Adams, A., Horowitz, M., and Levoy, M. 2007. Veiling glare in high dynamic range imaging. *ACM Trans. Graph. (Proc. SIGGRAPH 2007)*, 26(3):37:1–10.

Thurstone, L. L. 1959. *The measurement of values*. the University of Chicago, Chicago.

Tomasi, C. and Manduchi, R. 1998. Bilateral filtering for gray and color images. In *Proc. IEEE Int. Conf. Comput. Vision (ICCV)*, pages 839–846.

Torgerson, W. S. 1954. A law of categorical judgement. In Clark, L. H., editor, *Consumer Behaviour*, pages 92–93. New York University Press, New York.

Torgerson, W. S. 1958. *Theory and Methods of Scaling*. Wiley, New York.

Tumblin, J. and Rushmeier, H. E. 1991. Tone reproduction for realistic computer generated images. Tech. Report GI GIT-GVU-91-13, Georgia Institute of Tech.

Tumblin, J. and Rushmeier, H. E. 1993. Tone reproduction for realistic images. *IEEE Comput. Graphics Appl.*, 13(6):42–48.

Tumblin, J. and Turk, G. 1999. LCIS: A boundary hierarchy for detail-preserving contrast reduction. In *Proc. ACM SIGGRAPH '99*, pages 83–90.

Valeton, J. M. and van Norren, D. 1983. Light adaptation of primate cones: an analysis based on extracellular data. *Vision Res.*, 23(12):1539–1547.

van de Weijer, J. and Gevers, T. 2005. Color constancy based on the grey-edge hypothesis. In *Proc. IEEE Int. Conf. Image Processing (ICIP)*, pages 722–725.

von Kries, J. 1970. Chromatic adaptation. In MacAdam, D. L., editor, *Sources of Color Science*, pages 109–119. MIT Press, Cambridge.

Vos, J. J. 1978. Colorimetric and photometric properties of a 2-deg fundamental observer. *Color Res. Appl.*, 3:125–128.

Vos, J. J. and Walraven, P. L. 1971. On the derivation of the foveal receptor primaries. *Vision Res.*, 11(8):799–818.

Walls, H. J. and Attridge, G. G. 1977. *Basic Photo Science*. Focal Press, London.

Ward, G. 1992. Real pixels. In Arvo, J., editor, *Graphics Gems II*, pages 80–83. Academic Press.

Ward, G. 1994. A contrast-based scalefactor for luminance display. In Heckbert, P. S., editor, *Graphics Gems IV*, pages 415–421. Academic Press Professional, Boston, MA.

Ward, G., Rushmeier, H. E., and Piatko, C. D. 1997. A visibility matching tone reproduction operator for high dynamic range scenes. *IEEE Trans. Visualization and Computer Graphics*, 3(4):291–306.

Wyszecki, G. and Stiles, W. S. 1982. *Color Science: Concepts and Methods, Quantitative Data and Formulae*. John Wiley and Sons, New York.

Xiao, F., DiCarlo, J. M., Catrysse, P. B., and Wandell, B. A. 2002. High dynamic range imaging of natural scenes. In *Proc. Color Imaging Conf.*, pages 337–342. IS&T.

Yamada, K., Nakano, T., and Yamamoto, S. 1995. Wide dynamic range vision sensor for autonomous vehicles. In *Proc. IEEE Int. Conf. Robotics and Automation*, pages 770–775.

Yamada, T. 2006. CCD image sensors. In Nakamura, J., editor, *Image Sensors and Signal Processing for Digital Still Cameras*, pages 95–141. CRC Press, Broken Sound Parkway.

Yu, I., Cox, A., Kim, M. H., Ritschel, T., Grosch, T., Dachsbacher, C., and Kautz, J. 2009. Perceptual influence of approximate visibility in indirect illumination. *ACM Trans. Appl. Percept. (Presented at APGV 2009)*, 6(4):24:1–14.

Index